AN ABSTRACT OF THE DISSERTATION OF

Federico Cernuschi Rodilosso for the degree of Doctor of Philosophy in Geology presented on December 1, 2015.

Title: The Geology and Geochemistry of the Haquira East Porphyry Copper Deposit of Southern Peru: Insights on the Timing, Temperature and Lifespan of the Magmatic-hydrothermal Alteration and Mineralization

Abstract approved:

John H. Dilles

This dissertation is informally divided into three major sections. In the first section (Chapter 2) I use data from field mapping, isotopic geochronology, whole rock geochemistry and trace element concentrations in zircons to examine the petrology, geochemistry and ages of the Haquira East porphyry copper deposit of southern Peru. In the second section (Chapters 3 – 6) I investigate the timing, temperature, zonation and lifespan of the magmatic-hydrothermal alteration and Cu-Mo mineralization by applying field mapping, whole rock geochemistry, petrography, geothermometry, spectral, X-ray and cathodoluminiscense imaging of rock samples. The timescales of the magmatic-hydrothermal system was constrained by isotopic dating, diffusion of titanium in quartz and the novel approach of oxygen diffusion via $\delta^{18}O$ of quartz analyzed by secondary ion mass spectrometry. These data are also used construct cross-sections and 3D models. In the final section (Chapter 7) I describe the production and evaluation of a calibration for portable X-ray spectrometers that could potentially be applied to further investigate porphyry copper deposits.

Haquira East is a moderate grade porphyry copper-molybdenum-gold deposit (688 Mt ore at 0.59 wt. % Cu, containing 4.7 Mt Cu, 37,000 t Mo and 0.9 M oz Au) in the Eocene-Oligocene Andahuaylas-Yauri porphyry belt of southern Peru. Based on a Re/Os age of

molybdenite, the copper and molybdenum mineralization and hydrothermal alteration at Haquira East formed at ~33.85 Ma. These ores are associated with dominantly granodioritic intrusions that range from 34.5 to 33.5 Ma in age and represent some of the youngest intrusions of the Andahuaylas-Yauri batholith between 40 and 32 Ma. In this study, new U-Pb zircon ages of these intrusions ages were determined via laser ablation inductively coupled mass spectroscopy (LA-ICP-MS) and sensitive high resolution ion microprobe in reverse geometry (SHRIMP-RG). At Haquira East, the regional Eocene-Oligocene shortening of the Incaic orogeny resulted in the folding of Jurassic-Cretaceous meta-sedimentary rock into the northwest-trending and northeast-overturned Tocone syncline that is associated with northwest-striking and southwest-dipping thrust faults. The magmatism was synchronous with the deformation and began with the ~34.5 Ma andesitic to dacitic Lahuani sills and was followed by the ~34.2 to 33.5 Ma Haquira granodiorite stock and the slightly younger, narrow and subvertical Haquira porphyry dikes of similar composition. Several sets of Haquira porphyry dikes were emplaced synchronously with the porphyry copper and molybdenum mineralization, veining and K-silicate hydrothermal alteration. At the waning stages of the magmatism (~33.5), the dacitic Pararani porphyry dikes were emplaced along a north-south strike and closely followed in time with D veins, sericitic halos and sericitically-altered hydrothermal breccias.

Whole-rock trace element modeling indicates that the Haquira East magmas originated in a garnet-bearing basaltic-andesite to andesite zone of melt-assimilation-storage-hybridization (MASH) in the lower crust below ~25 km depth. Andesite melts from the MASH zone were injected into an inferred granodiorite magma chamber at ~10km depth beneath Haquira East, where the oxidized and water-rich magma fractionated hornblende and small amounts of plagioclase, together with traces of titanite, apatite, zircon and magnetite. Intrusions sourced in this chamber have enrichments in Sr/Y (>60) and V/Sc (>12), depletions in the light rare earth elements (REE) and high mid-REE/heavy-REE ratios inherited from melts derived from the MASH zone where garnet is residual. Similarly, the intrusions that were emplaced closely in time with the mineralization have high Eu_N/Eu_N* (0.4 to 0.8) and Ce_N/Ce_N* (200 to 5000) in zircon compared to older intrusions (LA-ICP-MS, and SHRIMP-RG) further evidencing the high oxidation state and water content of the magma.

New core logging observations, ICP-MS whole rock geochemical data and short wave infrared spectroscopy data document the sequence and spatial distribution of veins, hydrothermal alteration zones and Cu-Mo-bearing sulfide ore zones and are summarized in cross-sections and three-dimensional models. From oldest to youngest, the sequence of veins consists of biotite veins/micro-breccias, aplite dikes, deep quartz (DQ) veins, actinolite veins with plagioclase halos and epidote veins, early dark micaceous (EDM) halos with bornite-chalcopyrite, Cu-sulfide±quartz veinlets with chalcopyrite and/or bornite, banded molybdenite-quartz (BMQ) veins, B-type quartz-bornite-chalcopyrite veins, D-type pyrite-quartz-sericite veins with sericitic halos, and fractures with green and white intermediate argillic halos containing mixtures of illite-smectite-chlorite-kaolinite ± pyrite. The areas with the highest density of EDM halos constitute the high-grade copper ore. Scanning electron microscopy imaging (QEMSCAN) have been used to identifiy mineralogy, textures and zoning of hydrothermal alteration zones. The EDM halos are formed by hydrothermal biotite, muscovite, K-feldspar, with rare quartz and corundum replacing magmatic plagioclase and hornblende and carry up to 10-15 volume % disseminated bornite and chalcopyrite. Later BMQ veins host the high-grade molybdenum ore, whereas late B veins contribute both copper and molybdenum to the ores. The copper ore shell forms a continuous high-grade ore zone (>0.5 wt. %) in the Haquira stock, but is lower grade where it projects into the relatively non-reactive meta-sedimentary, mostly quartzite, wall rock, likely as a result of a limited supply of iron to enable copper-iron sulfide precipitation. In contrast, molybdenite mineralization forms a roughly symmetric shell overlapping both the stock and quartzite with an axis of symmetry located along the southwest flank of the Haquira granodiorite stock.

The abundance of EDM halos, lack of A veins and the dearth of unmixed fluid inclusion assemblages in quartz veins and prescense of two phase (liquid + vapor) fluid inclusions (P>1.5 kbar) suggest that Haquira East was emplaced at significant depths. The emplacement depth of Haquira is estimated at ~10 km, at greater depth than shallower and outcropping Acojasa intrusion to the south, emplaced at ~ 8 km according to hornblende barometry (~2.0 ± 0.5 kb). The veining, hydrothermal alteration and mineralization formed at this depth magmatic hydrothermal fluid was released from an inferred magmatic cupola, hydro-fractured the wall rock and depressurized from ~3 kb at lithostatic pressure to >1.2 kb at close to hydrostatic pressure without unmixing into a vapor and brine phase.

The temperature evolution of the magmatic-hydrothermal system was estimated by mineral phase equilibria and the application of different geothermometers. For TitaniQ geothermometry, Ti-in-quartz of veins and dikes was measured by electron microprobe (EMP) and LA-ICP-MS (1 ppm to > 100 ppm) on samples that were previously imaged by secondary electron microscope cathodoluminescense, Temperatures were also estimated through Ti-in-zircon (2 ppm to 13 ppm, via SHRIMP-RG), Ti-in-biotite (~1.0 to 2.3wt.%, via EMP) and the δ^{34}S compositions of pyrite-anhydrite and chalcopyrite-anhydrite pairs (-1.4 ‰ to -0.1‰ and 7.5

‰ to 10.2‰ respectively). Porphyry dikes, aplites and DQ veins formed first between ~720ºC and 650ºC. Copper was introduced later in EDM halos at ~500ºC and was followed by molybdenite in BMQ veins at ~650ºC during a thermal reversal. A second stage of copper and molybdenum was introduced in B veins at ~550°C. Late D veins with pyrite and sericite formed first at ~450ºC and later at ~350ºC. Diffusion modeling of both Ti (EMP) and $\delta^{18}O$ gradients (via secondary ion mass spectrometry, ~10.7 ‰ to ~12.7‰) across initially abrupt quartz growth boundaries yields a calculated maximum lifespan for the Haquira East porphyry of 170,000 years for the period from initial fluid injection at >650 ºC to cooling below ~ 350 ºC. However, the high-grade copper and molybdenum ore formed relatively rapidly in less than 30,000 years.

In the last chapter of this dissertation two calibrations were produced and tested for a Bruker Tracer IV portable X-ray fluorescence portable spectrometer (pXRF). Concentrations of Al_2O_3, CaO, FeO*, K_2O, MnO, TiO_2 and, in lesser degree, SiO_2 were accurately reproduced together with Cr, Cu, Nb, Ni, Sr, Y, Zr and less accurately V in powdered basaltic samples, and Nb, Pb, Rb, Sr, Y, Zn, Zr and, less accurately, Ba in powdered rhyolitic samples. The pXRF is particularly reliable for measuring relatively immobile elements (*e.g.* Nb, Zr, Ti and Y), which are often resistant to hydrothermal alteration and weathering. Therefore pXRFs may be useful for lithogeochemical mapping of hydrothermally altered rocks that are zoned around porphyry copper deposits.

The Geology and Geochemistry of the Haquira East Porphyry Copper Deposit of Southern Peru: Insights on the Timing, Temperature and Lifespan of the Magmatic-hydrothermal Alteration and Mineralization

by
Federico Cernuschi Rodilosso

A DISSERTATION

submitted to

Oregon State University

in partial fulfillment of
the requirements for the
degree of

Doctor of Philosophy

Presented December 1, 2015
Commencement June 2016

Doctor of Philosophy dissertation of Federico Cernuschi Rodilosso presented on December 1, 2015.

APPROVED:

Major Professor, representing Geology

Dean of the College of Earth, Ocean, and Atmospheric Sciences

Dean of the Graduate School

I understand that my dissertation will become part of the permanent collection of Oregon State University libraries. My signature below authorizes release of my dissertation to any reader upon request.

Federico Cernuschi Rodilosso, Author

ACKNOWLEDGEMENTS

It has been seven years since I first moved to the US to start my graduate studies. It all started in 2008 when I was living in Montevideo, I called my wife Silvina de Brum and told her of my opportunity to complete a Masters in the United States. Although my funding was secure, it was a risky move for her to be in a new country without any employment or study prospects. She was bold, she said yes immediately, and I am eternally thankful. Gracias Silvi! Little did we know, seven years later we would still be in the USA, her with a Masters, me with a PhD, and both of us with two adorable children, Mila and Luca. If I am still relatively sane after my PhD is because of them. Starting a family and being students was not easy, but it made it all more meaningful and If I had to do it all over again I would do it the same way. This period in the US would not have been possible without the support our parents: Nelson, Lydia, Daniel y Eugenia, who were often far away but always there for us. They provide such a strong foundation, that I know building our own family is so much easier than others who are not so fortunate.

A lot happened in seven years, a lot has changed, and the guy going back to Uruguay is not the same guy that left seven years ago. I am proud to say that I gave as much as I could, and I took as much as I could. I am different: professionally, academically and as a human being. I am the Pacific Northwest hipster gaucho now, but most importantly I believe that my close friends and colleagues are a bit of a *rio platense*. And I guess that is part of what this was all about.

I wouldn't be writing this if it wasn't for George Schroeder and Alex Raab from Orosur, who seven years ago trusted me to do a research about Lascano and the Laguna Merín basin of Uruguay. That project would turn into my master's research and would bring me to Corvallis two days before classes would begin. The project also led me to my Masters and Ph.D. advisor John Dilles. John is a superb geologist, a fantastic advisor and one of the most ethical and nice persons I know. I like to think that after so many years some of those qualities percolated into myself. John taught me to think critically, to be constantly looking for excellence, and to be humble. I was always careful to follow him and pick up as many of the ideas he was constantly dropping as he goes along. I made an effort to not just be a Salieri stealing from Mozart, but to make his tunes my own. John transformed into my mentor and my friend, and I will always be grateful for everything he did for me. Through John I met another epic geologist, his wife, Anita Grunder. She has always been there for me and my family, and has become a great friend as well. From her I learned that if you know what you are doing and you make the effort of truly communicating with people, you can make almost anything happen. In short, I am grateful and lucky that the Grunder-Dilles family has become our extended family in the US.

In my transition from Masters to PhD research I was fortunate to work with Scott Halley, a one-of-a-kind Australian geochemist, who not only taught me so much about rock and chemistry, but also showed me how to think as an academic and work professionally in the mining-exploration industry. He recommended John and I to First Quantum, who had recently acquired what would become to be my PhD research site, the Haquira porphyry copper deposit of southern Peru. There is a long list of people from First Quantum that I would like to thank. The vice president of exploration, Mike Christie trusted me enough to fully fund my PhD to work at Haquira. He has been absolutely fantastic and always encouraged me to further interact with other First Quantum geologist and with other exploration projects around the world. Thank you Mike! For similar reasons I thank Tim Ireland, Mclean Trott, Matt Booth, Steve Beresford, Chris Winjs and many more from First Quantum, lots of local geos at Arequipa, Peru and Kevin Heather, John Black and Neil Barr from Antares.

My PhD committee, Anita Grunder, Adam Kent and Andrew Meigs as well as my graduate council representative Dave Graham have been fantastic and a great support through all this process. Similarly, I was lucky enough to engage several coauthors in my research and they are all acknowledged in the coauthors page. I would like to mention here Phil Gans and Marco Einaudi. Both of them did field work at Haquira before I worked there and I was able to use so much of their data including core-logs, sections, maps and notes. It was a great opportunity to be able to look at the rocks, make my observations, and at the same time be able to see their own observations and interpretations. I learned a lot by doing that, and I think of them as advisors too. I would also like to thank my fellow student coauthors at OSU: Stephanie Grocke, Nansen Olson, Mark Ford and Darrick Boschmann. I am proud of having engaged them in my projects, and grateful that they took time out of their own projects to work with me. It was a wonderful experience. Similarly, a lot of other VIPER students and professor such as Ashley Bromley, Matt Loewen, Luc Farmer, Chris Longton, Julia Cohen, Alison Koleszar, Erin Lieuallen, Rob Harris, Frank Tepley, Richard Bradshaw, Dale Burns and many more where always there for me and I am thankful for the time that we shared. I would like to thank Nora Utevsky and Silvina de Brum for a tremendous help formatting my thesis and index.

My American brother, Morgan Salisbury deserves a whole paragraph. He has been a great friend since I first arrived to the US, a true ambassador of the country and has been constantly supporting me as a friend, as a geologist and as a scientist. I am particularly grateful for his endless nights of editing my English in my Master thesis, in my PhD thesis and everything I wrote in between.

I was lucky to have many awesome friends through all my time in the US, friends who included us into their community, and who will always remain great friends. Barry Walker Jr., Valerie Osterberg, Stephanie Grocke, Nikki Moore, Julia Rosen, Josh Holmes, Chris and Danielle Madugo, Yann and Joanna Gavillot, Ashley Streig, Bobby Babbra, Michelle Zellers, Nansen Olson, Nora Utevsky, Henri Sanville, Jeannie Holliday, Halley Ohms, Caren Barcelo, Steven Highland, Carole and Darrell, Levi, Tammy, Travis, Jordan, Steve, and many more. Thank you all!

CONTRIBUTION OF AUTHORS

Chapter 2: John Dilles contributed with the field work, design of the research, interpretation of the results and edits for this chapter. Phillip Gans, Kevin Heather and Neil Barr contributed with previous field data and interpretations. Anita Grunder assisted the trace element modeling. Nansen Olson and Adam Kent assisted the analysis, data reduction and interpretation of the trace element in zircon studies. Mclean Trott and Tim Ireland helped interpret the results and provided additional field data. Robert Creaser performed Re-Os in molybdenite age dating.

Chapter 3: John Dilles contributed with the field work, design of the research and interpretation of the results. Marco Einaudi contributed his previously collected field data and interpretations. Kalin Kouzmanov performed the QEMSCAN analyses. Scott Halley compiled and contributed to the interpretation of the SWIR data.

Chapter 4: John Dilles helped to establish the research question and with interpreting the results.

Chapter 5: John Dilles helped design the experiments and contributed with the results and interpretations. John Valley and Kouki Kitajima assisted with SIMS analyses and standardization. Frank Tepley assisted with EMP analyses and standardization. Stephanie Grocke assisted the diffusion modeling. All the authors contributed with the interpretation of the data and added to, and edited, this chapter.

Chapter 6: John Dilles helped to design the experiments and to interpret the results. Brian Rusk and Yongmei Zhang performed the microthermometry analysis of fluid inclusions and contributed to the interpretations of the results.

Chapter 7: Mark Ford assisted with the pXRF calibration for rhyolitic powders and with testing the calibration for rhyolitic and basaltic rocks. Darrick Boschmann performed the calibration for basaltic powders, with assistence from Richard Conrey. John Dilles helped design the testing protocol of the experiments and assisted with the interpretation of the results. All the authors contributed with edits for this chapter.

TABLE OF CONTENTS

TABLE OF CONTENTS (Continued)

TABLE OF CONTENTS (Continued)

LIST OF FIGURES

LIST OF FIGURES

LIST OF TABLES

LIST OF APPENDICES

LIST OF DIGITAL APPENDICES (CD-ROM in Pocket)

Appendix 1 – Supplementary data and figures for chapter 2
Appendix 2– Supplementary data and figures for chapter 3
Appendix 3 – Supplementary data and figures for chapter 4
Appendix 4 – Supplementary data and figures for chapter 5
Appendix 5 – Supplementary data and figures for chapter 6
Appendix 6 – Supplementary data and figures for chapter 7

LIST OF PLATES

LIST OF MOVIES

DEDICATION

I dedicate this project to the people of Peru. To my gracious hosts while I studied one of their ore deposits in the beautiful highlands of the central Andes. If the results of the research presented in this dissertation lead, either directly or indirectly, to the economic exploitation of Peruvian ores, I sincerely hope that it benefits the Peruvian people, and that it is performed in the most environmentally sustainable manner possible. Let the future mining developments help in particular those who need it the most, those who live in the mining districts, and especially those I met in the high Andes with whom I was often only able to communicate through gestures. They made a southamerican lowlander feel at home. To my Andean brothers, let's make the best out of it.

Le dedico este proyecto a la gente de Perú. A mis amables anfitriones durante mi estadía para estudiar uno de sus depósitos minerales en los hermosos Andes centrales. Si los resultados de la investigación presentada en esta disertación lleva directa o indirectamente a la explotación económica de depósitos minerales peruanos, deseo sinceramente que beneficie a los peruanos y que las explotaciones se realicen de la mejor forma posible y sustentable para el medio ambiente. Que los desarrollos mineros del futuro ayuden en particular a aquellos que lo necesitan más, a los que viven en los distritos mineros y especialmente a aquellos que conocí en la altitud de la cordillera y con los que muchas veces sólo me pude comunicar a través de gestos. Hicieron que un sudamericano de la llanura se sintiera como en su casa. A mis hermanos andinos, hagamos que todo sea para mejor.

CHAPTER I

GENERAL INTRODUCTION

1.1 Porphyry copper deposits and the global supply of copper

Porphyry-type deposits include porphyry copper±molybdenum±gold deposits in which copper is the chief economic metal. These deposits are large, ranging from ~100 Mt (million metric tons) to ~5 Bt (billion metric tons) ore materials grading from ~0.2 to >1.2 wt.% copper with variable amounts of molybdenum and gold. Porphyry deposits are extremely important to the global supply of metals, as they are the world's main source of copper, supply most its molybdenum and are also significant contributors of gold and silver.

Copper is a fundamental metal that accompanied the evolution of humanity since its early adoption for tool making about 8,000 BP and later triggered the bronze-age revolution when copper was alloyed with tin about 5,000 BP. More recently, tool making shifted to other materials such as steel, but copper remained in high demand during the Industrial age for its electrical conductivity properties and its high malleability that enables the construction of wires for power transmission. The beginning of the massification of electric power supply in the late 1800's marks the start of the extensive use of copper for wire making. As developed countries in Europe and North America completed the construction of most of their power grid, the demand for copper for wiring shifted to emerging economies such as China and India sustaining a high copper demand to the present day. Copper production raised from ~2,000 Mt in the 1950's to ~18,100 Mt in 2013. Nowadays, vast areas of the world still do not have access to electric power. However, these areas are being wired, or will likely be wired in the near future, further sustaining a high demand for copper. Furthermore, technological advances to reduce the dependency on fossil fuels and its impact on global climate change rely on electric energy and demand copper for their construction. The massification of wind turbines, solar panels and electric transportation is forecasted to double the global copper consumption by 2050. Most of this new demand will come from developed countries that are starting to build new infrastructure for clean energy production.

Although global consumption of copper has been rising for about one hundred years and its demand is forecasted to keep rising, the discovery of new, world-class porphyry deposits have not keep apace. This contradiction is likely explained by the fact that the increase in the copper production was enabled by the development of new and better mining technologies. However, similar advances in the understanding of the formation processes of porphyry systems (and other copper deposits) were not achieved with the same magnitude. The improvement of our scientific understanding of these processes is what ultimately feeds the development of new exploration concepts and techniques that lead to discoveries. We can presume that most of the world-class outcropping deposits have been already discovered and are currently being mined, or will be mined soon. Exploration has been shifting to poorly exposed or concealed prospects around the world. Therefore a more detailed scientific understanding of the processes that lead to the formation of Cu±Mo±Au porphyry deposits is necessary, and will be a key factor for successful future mineral exploration.

1.2 Contributing to the understanding of porphyry copper deposits

The sulfide and oxide minerals that constitute the ore in porphyry copper deposits are precipitated in narrow veins and hydrothermal alteration halos from high temperature magmatic-hydrothermal fluids accompanying the emplacement of porphyritic dikes emanating from intrusive cupolas of deeper granitic plutons. Because of the nature of the mineralization, studying the magmatism related to porphyry mineralization and the magmatic-hydrothermal alteration is necessary to advance the understanding of porphyry copper deposits.

This dissertation primarily investigates the magmatism and the magmatic-hydrothermal alteration and mineralization at the Haquira East porphyry copper deposit of southern Peru. Haquira East is a moderate grade Cu-Mo deposit with less Au (688 Mt copper at 0.59% and a 0.3% cutoff and ~140 ppm Mo) and is part of the Eocene-Oligocene Andahuaylas-Yauri porphyry belt of southern Peru (see Fig. 2.1 in Chapter 2). This belt could be considered a continuation of the better-explored and studied Eocene-Oligocene porphyry belt of Chile that hosts large porphyry copper deposits such as Escondida, Chuquicamata and Collahuasi. Extensive drill core from previous exploration work from Antares Minerals LTD and First Quantum Minerals LTD provides a unique opportunity to map, sample and study porphyry dikes, veins, mineralization and hydrothermal alteration throughout the deposit.

Chapter 2 focuses on the petrology, age and geochemistry of the Haquira East intrusions in relation to the regional deformation and shortening that affected southern Peru during the Eocene and Oligocene. Although porphyry copper deposits could form in a variety of stress regimes, there is an apparent correlation between contractional settings and large porphyry copper deposits such as those of the Laramide orogeny of southwest North America, the Eocene-Oligocene and Miocene-Pliocene belts of the central Andes, the Miocene belt of Iran and the Pliocene belts of New Guinea and the Philippines. To further understand the timing of intrusions and mineralization events at Haquira East and its relation to the contractional events, I focused my studies on the porphyry/vein cross-cutting relations and the deformation recorded in the wall rock, intrusions and veins.

It is further argued that compression, and associated crustal thickening, is responsible for the mineralogical and chemical characteristics of many porphyry-related magmas themselves. To further understand these processes at the Haquira East magmatic system, I investigated the trace element whole-rock magmatic compositions and trace element compositions of zircon crystals to produce a petrogenetic model that elucidates the oxidation state, water content and depth of origin of the involved magmas. Similarly, it has been argued that the biggest copper endowment in the Eocene porphyry belt of northern Chile is related to its youngest pulses of magmatism, as opposed to later magmatic events. I explore the validity of this hypothesis for southern Peru copper porphyry deposits by obtaining and comparing U-Pb ages of zircon, Re/Os ages of molybdenite and ^{40}Ar/^{39}Ar ages of hydrothermal muscovite from Haquira East and other deposit of the Andahuaylas-Yauri belt.

Chapter 3 expands on the study of the hydrothermal veining, alteration and mineralization described in chapter 2. Previous field-based studies of the hydrothermal alteration and mineralization in porphyry copper deposits set the basis for the development of general models on porphyry deposit genesis and enabled more recent and specific studies. This type of research has also provided the basis for the development of successful exploration techniques that contributed to the discovery of porphyry deposit elsewhere. Haquira East is a particularly interesting porphyry copper deposit because it was formed in two different wall-rock lithologies with contrasting mineralogical compositions, thus providing the opportunity to study the influence of the wall-rock composition in copper and molybdenum mineralization. In chapter 3, I studied the porphyry and vein cross-cutting relationships at Haquira East by field mapping and core logging, and added the application of modern techniques such as quantitative evaluation of minerals by scanning electron microscopy (QEMSCAN, energy dispersive spectroscopy) and short wave infrared spectroscopy to study the mineralogy of hydrothermal veins and halos. I also compiled the mapped results in surface maps and cross-sections through the deposit and combined these field-based data with drill core whole-rock trace element data to further investigate the details of the magmatic-hydrothermal system using recent 3D visualization and modeling software. This methodology enabled me to reconstruct the relative timing of porphyry emplacement, vein/halo formation and hydrothermal paragenesis as well as the vein/halo distribution and their relation to the copper and molybdenum ores.

Chapter 4 explores deeper into the temperature and timing of formation of the copper mineralization at Haquira East, and porphyry copper deposits elsewhere. The temperature of Cu-sulfide deposition and the formation of high grade copper ore in porphyry copper deposits has been the subject of strong debate for at least a decade. Vein cross-cutting relations, mineral phase equilibria and sulfur isotope data apparently indicates copper precipitation temperatures above 400ºC and stable with hydrothermal biotite and potassic-feldspar bearing K-silicate alteration. More recent studies that employ secondary electron microscope cathodoluminescense (SEM-CL) imaging of quartz, coupled with in-situ TitaniQ geothermometry and fluid inclusion data, however, suggest that copper deposition took place at temperatures below 400ºC and therefore in stability with sericitic alteration. In chapter 4 I obtain SEM-CL imaging of quartz in veins from Haquira East and coupled it with the relative timing of veining developed in chapter 3, and Ti-in-quartz data that are presented chapters 5 and 6, to investigate the timing and temperature of copper deposition at Haquira East. I re-evaluated and compared the findings with previously published data from deposits elswhere and obtain new data on the Batu Hijau deposit of Indonesia for detailed comparison.

Chapter 5, explores the question of the timescales of porphyry copper deposits formation. The Re/Os ages of molybdenite presented in chapter 2 suggest that the copper and molybdeum ores were formed in relatively short periods of time that cannot be resolved by conventional isotopic age dating techniques. In chapter 5 I obtained estimates for the duration of the magmatic-hydrothermal fluid flow at >350ºC using diffusion profiles of titanium (Ti) and $\delta^{18}O$ analyzed along transects of quartz in Fe, Cu, and/or Mo sulfide-bearing hydrothermal veins and igneous quartz. The $\delta^{18}O$ of quartz analyzed by secondary ion mass spectrometry is a novel approach for quantifying hydrothermal timescales and this is the first study to apply the technique to ore deposit research. In this chapter, I reconstruct the evolution of the geothermal gradient through time and provide maximum timeframes for the formation of the copper and molybdenum ores and the subsequent cooling of the magmatic-hydrothermal system.

Chapter 6 presents preliminary findings on the temperature and pressure evolution of porphyry magmatic-hydrothermal systems. Some of the temperature estimates presented here are also discussed, and aid in the interpretations, in chapters 4 and 5. In conjunction with estimating magmatic-hydrothermal temperatures for Haquira East, I investigate the depth of emplacement of pre- to post-mineralization intrusions, porphyry dikes and veins using a combination of Ti-in-quartz, Ti-in-zircon and Ti-in-biotite geothermometry, hornblende barometry, fluid inclusion data and $\delta^{34}S$ compositions of sulfide-sulfate pairs. It has been argued that deeply emplaced porphyry deposits show significant differences with shallowly emplaced deposits. I investigate these differences by comparing the pressure-temperature data of the deeply (~10 km) emplaced Haquira East with newly obtained data from the shallowly emplaced (~1.5 km) Batu Hijau porphyry copper-gold deposit of Indonesia.

Chapter 7 explores the use of relatively recently developed and mass-produced portable X-ray fluorescence spectrometers (p-XRF) for whole-rock analyses and applications in lithogeochemistry. Significant portions of the research presented in the previous chapters rely heavily on obtaining and interpreting high quality geochemical data. In chapter 7, I describe the production and testing of two p-XRF calibrations using whole-rock powdered samples: one for basaltic and another for rhyolitic compositions. The calibrations were further tested to study their accuracy and precision by measuring samples previously analyzed with standard and commercially available instruments (*i.e.* bench top wave dispersive XRF).

All the chapters were developed with the collaboration and assistance of a diverse group of coauthors, including researchers from Oregon State University and other universities and exploration geologists from around the world. The coauthors are listed at the beginning of each chapter and their contributions are summarized in the pre-pages of this dissertation.

CHAPTER II

GEOLOGY, AGE AND PETROGENESIS OF ORE-FORMING MAGMAS AT THE HAQUIRA EAST PORPHYRY COPPER DEPOSIT, PERU.

Federico Cernuschi
John H. Dilles
Philip Gans
Kevin Heather
Neil Barr
Anita Grunder
Nansen Olson
Adam Kent
Mclean Trott
Timothy Ireland
Robert Creaser

Draft to be submitted to Economic Geology
A journal of the Society of Economic Geologists

2.1 Abstract

The Eocene-Oligocene Andahuaylas-Yauri belt magmatism took place during, to near the end of, the Incaic period of intense compression and deformation associated with east to northeast subduction beneath the western margin of South America. Most of the magmatism of the belt ranges in age from ~ 40 to 32 Ma (U-Pb in zircon). The ~33.85 Ma (Re-Os in molybdenite) Cu-Mo-mineralization and hydrothermal alteration at the Haquira East porphyry copper deposit is associated with some of the youngest dated intrusions of the belt at ~34.5 to 33.5 Ma (U-Pb in zircon). At the Haquira East region the shortening was locally oriented with a southwest to northeast strike as demonstrated by the northwest to southeast-striking and southwest-dipping thrust faults, and the northwest to southeast-trending and northeast-overturned Tocone syncline. The Incaic regional compression thickened the crust, resulting in garnet-bearing basaltic-andesite to andesite melt-assimilation-storage-hybridization (MASH) zone in the lower crust below ~25 km depth. Melts from the MASH zone were injected into a mid- to upper-crust andesitic-dacitic magma chamber beneath Haquira East, where an oxidized and water-rich magma fractionated hornblende and small amounts of plagioclase, together with traces of titanite, apatite, zircon and magnetite. Intrusions sourced in this chamber have enrichments in Sr/Y and depletions in light rare earth elements (REEs), Nb, Ta, P and Zr, together with low mid-REEs)/heavy-REEs inherited from the garnet residual material in the MASH zone. At ~34.5 Ma the andesitic to dacitic Lahuani sills conformably intruded the meta-sedimentary Jurassic-Cretaceous wall rock and the axial plane of the actively forming Tocone syncline. During the peak activity of the Haquira magma chamber, the ~34.2 to 33.5 Ma dacitic-trachydacitic Haquira granodiorite stock and the slightly younger set of narrow and subvertical Haquira porphyry dikes intruded the Tocone overturned syncline. The intrusion of the Haquira porphyry dikes was intimately related to the porphyry Cu-Mo mineralization, veining and high temperature hydrothermal alteration. At the waning stages of the magmatism (~33.5 Ma), the dacitic Pararani dikes intruded closely in time with lower temperature sericite-pyrite-muscovite veins. After ore formation and towards the end of shortening, the area was tilted ~10º to 20º to the northeast. Uplift and erosion shallowed the geology to near-surface depths from an estimated ~10 km depth of formation based on similar porphyry copper deposits elsewhere and observed fluid inclusion assemblages. The pre-mineralization Haquira granodiorite stock and the syn-mineralization Haquira porphyry dikes have high Eu_N/Eu_N* (0.4 to 0.8) and Ce_N/Ce_N* (200 to 5000) in zircon in comparison to older intrusions. Both Eu_N/Eu_N* in zircon and whole-rock Sr/Y and V/Sc increase with fractionation and are higher than average arc intrusions, further suggesting the role of oxidized, water-rich and

sulfur-rich magmas in the formation of the Haquira East porphyry deposit. However, these ratios reach a maximum in the immediately post-mineralization Pararani porphyry dikes.

2.2 Introduction

Porphyry Cu±Mo±Au deposits are large and profitable mineral deposits that occur in mineral belts in convergent margin associated with shallowly emplaced arc-type granitoids and are formed by magmatic-hydrothermal processes (Seedorff *et al.,* 2005). Decades of mineral exploration and research has significantly increased the geologic understanding of porphyry copper deposits (*i.e.* Sillitoe, 2010). However, key aspects of the porphyry copper geology, such as the petrogenesis of ore-productive magmas and its relationship with the stress regime of the arc are yet to be fully understood.

With the aim of contributing to the understanding of these processes we studied the field geology, whole-rock chemistry, trace element concentrations in zircon and isotopic ages of intrusions related and un-related to porphyry copper mineralization in the Haquira area of the Eocene-Oligocene Andahuaylas-Yauri porphyry belt of southern Peru.

The Andahuaylas-Yauri belt could be considered a continuation of the better explored and studied Eocene-Oligocene porphyry belt of Chile that hosts large porphyry copper deposits like Escondida, Chuquicamata and Collahuasi (Sillitoe and Perelló, 2005, Fig. 2.1). In southern Peru, the Eocene-Oligocene (*ca.* 48-32 Ma) Andahuaylas-Yauri batholith and related porphyry stocks, dikes and sills intruded a compressionally deformed sequence of Jurassic-Cretaceous quartzite, meta-siltstone, meta-mudstone and limestone (Perelló *et al.,* 2003).

Until recently, only copper skarns hosted in the Ferrobamba Formation limestones at Tintaya, Coroccohuayco, Las Bambas and other localities, were known in the Andahuaylas-Yauri belt (Fig. 2.1). However, recent discoveries such as Haquira East (Heather *et al.,* 2012) and Antilla (Perelló and Posso, 2011) identified porphyry copper deposits hosted in non-outcropping granodiorite of the Andahuaylas-Yauri batholith. Similarly, porphyry copper deposit mineralization has been found associated to the Coroccohuayco (249 Mt at 1.01 weight % Cu; Xstrata, 2014) and Antapaccay skarns (740 Mt at 0.50 weight % Cu; Xstrata, 2014) of the Tintaya cluster (Chelle-Michou *et al.,* 2015; Jones *et al.,* 2007).

Haquira East is a moderate grade Cu-Mo deposit with less Au (688 Mt copper at 0.59% and a 0.3% cutoff and ~140 ppm Mo; Antares, 2010) hosted in a subvertical granodiorite stock emplaced in the northwest to southeast-trending and overturned quartzite and meta-siltstone within the Tocone syncline (Fig. 2.2). Previous exploration work from Antares Minerals LTD and

First Quantum Minerals LTD provide extensive drill-hole core that enabled cross-cutting observations of porphyry and veins, as well as samples of porphyry intrusions of the concealed porphyry copper deposit.

The available isotopic ages that constrain the magmatic activity and mineralization in the belt were obtained through K-Ar (Perelló *et al.* 2003). However, more reliable and modern isotopic dating techniques are necessary to better constrain the intrusion and mineralization ages. In this study, we obtained U-Pb in zircon, ^{40}Ar/^{39}Ar in muscovite and Re-Os in molybdenite isotopic ages from intrusions and veins from the Haquira East deposit.

We complement the data set with samples from the nearby Haquira West deposit, and the porphyry copper prospects Cristo de los Andes further south and Dolores further east, together with the Zincore regional prospect further east (Fig. 2.2). Haquira West is located 2 km west of Haquira East and presents a similar geology with high Cu and Mo grades and is currently being explored by First Quantum Minerals LTD (388 Mt at 0.47 weight % Cu; Antares, 2010). Cristo de los Andes and Dolores prospects have strong evidence of vein-hosted porphyry copper mineralization. The Zincore prospect only presents Pb-Zn carbonate replacement occurrences such as the Yanque prospect (Mondillo *et al.,* 2014), but for the moment there is no known porphyry copper mineralization.

The relationship between porphyry copper deposit formation and regional stress is still debated. Porphyry copper deposits form in a variety of stress regimes (Tosdal and Richards, 2001), however there is a correlation between contractional settings and large porphyry copper deposits like in the Laramide orogeny of southwest North America, the Eocene-Oligocene and Miocene-Pliocene belts of the central Andes, the Miocene belt of Iran and the Pliocene belts of New Guinea and the Phillipines (Sillitoe, 1998; Sillitoe, 2010 and references therein). To further understand the timing of intrusions and mineralization events at Haquira East and its relation to the contractional events that formed the Tocone syncline, we studied the intrusion and intrusion/mineralization cross-cutting relations and deformation recorded in the wall rock, intrusions and veins.

Similarly, it has been argued that the compression regime were some large porphyry copper deposits have been emplaced is responsible for the mineralogical and chemical characteristics of porphyry-related magmas, and has been associated to crustal thickening. Andesitic arc intrusions having high Sr/Y and V/Sc whole rock ratios, and a depletion of middle- and heavy-rare earths (MREEs and HREEs) are related to porphyry copper mineralization worldwide (Ayusso, 2010; Richards, 2011; Loucks, 2014). To explain some of these compositions, some authors argue for either lower crustal, or mid- to shallow-crustal processes. In thick crust, fractionation of garnet or contamination with deep crustal melts equilibrated with garnet coupled with the absence of plagioclase fractionation is expected (*i.e.* Hamilton, 1981; DeBari and Sleep, 1991; Chiaradia, 2009). In thin crust or shallower parts of thick crust, trace element compositions may be due to the fractionation of hornblende-titanite-zircon and suppression of plagioclase fractionation in oxidized and water-rich magmas (Sisson, 1994; Kelin *et al.,* 1997; Richards, 2011). Hornblende is crystallized at high water contents (> 4wt%, Naney, 1978), which will in turn suppress the crystallization of plagioclase (Moore and Carmichael, 1998) while titanite requires high oxidation states (Foley and Wheller, 1990). However, this shallow magma chamber hypothesis could also argue for magmatism under a compressional setting. A compressional regime is thought to promote the formation of large mid- to upper-crustal magma chambers (Takada, 1994) that could produce enough hydrothermal fluids after fractionation to produce large porphyry copper deposits during (Sillitoe, 1998). To further understand these processes and the petrogenesis of the intrusions at Haquira East, we investigated the trace element whole-rock magmatic compositions. These data allowed the production of a petrogenetic model for the compositional diversity, in order to investigate the oxidation state, water content and depth of origin of the involved magmas.

Insights on these processes can also be obtained from mineral chemistry. Variations in REE composition of zircons from barren to ore-related intrusions, have been observed in magmas from different arc setting around the world (Ballard *et al.,* 2002; Dilles *et al.,* 2015). Zircons are resistant minerals that can remain unaltered during late stage magmatic crystallization and hydrothermal alteration processes, retaining the chemical composition from their magmatic formation. Rare earth elements (REE) present +3 valence in magmas and increasingly partition into zircon from light REE to heavy REE as the ionic radius decreases (REE contraction). However, Eu and Ce can also occur as Eu^{2+} and Ce^{4+}, in which case Eu^{2+} will partition less than Eu^{3+} and Ce^{4+} will partition more than Ce^{3+} into zircon (Hoskin and Schalterger, 2003). Variations in Eu_N/Eu_N^* and $Ce^{(IV)}/Ce^{(III)}$ have been linked with high magmatic water contents (Dilles *et al.,* 2015) that suppress plagioclase crystallization and/or high oxidation states (Ballard *et al.,* 2002; Burnham and Berry, 2012) and have been proposed to be related to high sulfur concentrations of the magmas and late magmatic oxidation due to SO_2 degassing (Dilles *et al.,* 2015). To further evaluate the role of magmatic water and oxidation state in the formation of porphyry copper deposits at the Andahuaylas-Yari belt, we studied the trace element composition of zircons from intrusion from Haquira East, Cristo de los Andes, Dolores and Zincore.

2.3 Regional geology

Eocene granitic rocks intrude the folded Jurassic-Cretaceous greenschist meta-sedimentary rocks of the Andahuaylas-Yauri belt (Fig. 2.2, Perelló *et al.,* 2003), a sequence of up to 4.5 km stratigraphic thickness. At Haquira East and surroundings, the base of the sedimentary succession is dominated by deep marine black shale with minor intercalations of siltstone and sandstone of the Mid Jurassic Chuquibambilla Formation, which is the lower unit of the Yura Group (Ligarda, 1989). The Chuquibambilla Formation is overlain by a sequence of shallow marine to deltaic Cretaceous sedimentary rocks. The base is composed of thick quartzite units intercalated with thinner layers of siltsone of the Soraya Formation (Pecho, 1981). The Soraya is overlain by red-brown shale and thinly bedded siltstone with minor intercalations of sandstone of the Mara Formation (Pecho, 1981). The Mara Formation is overlain by Upper-Cretaceous shallow platform limestone of the Ferrobamba Formation (Marocco, 1978; Pecho, 1981).

During the Incaic orogeny, between the late Paleocene and the Eocene-Oligocene, the Jurassic-Cretaceous strata were deformed into northwest to east-west-trending folds that are closely associated with and displaced by northwest to east-west-striking and north-vergent thrust faults (Maher, 2010; Carlotto, 1998; Fig. 2.2). Some of the folds, as the Tocone syncline at Haquira East, are overturned to the northeast or to the north. The Eocene portion of this orogeny was characterized by a broadening and landward migration of the magmatic arc, which has been interpreted as resulting from a change of steep-slab subduction to flat-slab subduction that accompanied the crust thickening associated with folding and thrust faulting (Noble *et al.,* 1984; Mamani *et al.,* 2010). The ~300 x 100 km Andahuaylas-Yauri batholith and related dikes and sills were emplaced during the Eocene to early Oligocene. Two magmatic pulses are recognized based on K-Ar ages of magmatic amphibole, biotite and K-feldspar in granitic rocks (Perelló *et al.,* 2003). The first, and smaller-volume pulse was dominated by mafic magmas (gabbros and diorites) emplaced between ~48 to 43 Ma. The second, and more voluminous pulse was related to the porphyry copper deposits and skarns, and was dominated by granodioritic magmas and emplaced between ~40 to 32 Ma. Recent U-Pb zircon ages obtained by laser ablation inductively coupled mass spectrometry (LA-ICP-MS) and isotope dilution thermal ionization mass spectrometry (ID-TIMS) from the Coroccohuayco porphyry-skarn Cu deposit suggest a smaller lifespan for the magmatism. A gabbrodiorite complex was emplaced ~40.4 Ma, whereas the ore-related granodioritic magmatism followed at ~35.6 Ma after a ~5 Ma long magmatic lull (Chelle-Michou *et al.,* 2014). Similarly, magmatic-hydrothermal events at the nearby Antapaccay-porphyry copper deposit-skarn span between 39.9 and 32.5 Ma (no method description available, Jones *et al.,* 2007).

U-Pb in hydrothermal titanite and Re/Os in molybdenite indicate that the mineralization took place at Coroccohuayco during a short period of time near the end of the Andahuaylas-Yauri magmatism, between ~35.7 and 35.6 Ma (Chelle-Michou *et al.,* 2015). A post-mineralization alkaline basalt gives a ^{40}Ar/^{39}Ar age of 26.6 Ma, and was interpreted to be related to the initiation of the slab roll-back after the flat-subduction Andahuaylas-Yauri episode (Chelle-Michou *et al.,* 2015) and could be related to the deposition of the Tacaza Group (Klinck et al., 1986; Carlotto, 1998).

Southwest of Haquira East, ~28 Ma Oligocene trachyandesite, andesite and rhyolite tuff of the Tacaza Group fill valleys in the Jurassic-Cretaceous basement (Fig. 2.2). The source of these eruptions was likely located outside of the belt to the southwest.

2.4 Methodology

Detailed logging and geochemical sampling were conducted on drill cores from holes drilled at Haquira East, Haquira West, Cristo de los Andes and accompanied by reconnaissance geologic mapping of the area during several field seasons between 2011 and 2013. Drill hole core samples from Dolores and surface samples from Zincore were provided by First Quantum Minerals LTD.

Standard transmitted and reflected light microscopy and petrographic techniques were used to describe the mineralogy and textures of the rocks. Thirty three split drill core samples of the freshest and vein-less pieces of core from Haquira East, together with four surface samples and twenty three 1 to 2 meter split core whole-rock samples from Dolores and Zincore, were analyzed for major and trace elements at ALS-Chemex. A lithium metaborate/tetraborate fusion was followed by dissolution using a dilute nitric digestion and analyzed by inductively coupled plasma optical emission spectrometry (ICP-OES) for major elements and inductively coupled plasma mass spectroscopy (ICP-MS) to measure trace element compositions. Major elements for all samples were normalized to 100% volatile-free. See the appendix for additional analytical details and a complete dataset.

Two muscovite separates were prepared at Oregon State University (OSU) using standard mineral separation procedures. Plateau ages from 12 and 13 incremental heating steps were obtained via ^{40}Ar/^{39}Ar. Analyses were made at OSU Noble Gas Mass Spectometry lab using a Mass Analyzer Products model 215-50 rare gas mass spectrometer with an all-metal extraction system, after irradiation in the OSU TRIGA experimental reactor (see Koppers and Duncan, 2003). Inverse isochrons (^{36}Ar/^{39}Ar vs. ^{39}Ar/^{40}Ar) were used to identify excess argon. Plateau ages were calculated as the weighted mean of 11 and 12 consecutive heating steps, representing at least 95% of the released gas. Errors are reported at 2 standard deviations of the mean and listed with the MSWD.

Nineteen zircon separates where analyzed to determinate rare earth element concentrations and to obtain U-Pb ages: five at the Sensitive High Resolution Ion-Microprobe in reverse geometry (SHRIMP-RG) at the Stanford-USGS Micro Analysis Center at Stanford University and fourteen at OSU using a laser ablation inductively couple plasma mass spectroscopy (LA-ICP-MS), where the five SHRIMP-RG samples were also analyzed for trace elements. Zircons, concentrated by standard heavy mineral separation processes and panning, were hand selected for final purity and mounted on double-sided tape on glass slides in 1 x 6 mm rows, cast in a 25 mm diameter by 4 mm thick epoxy disc, ground and polished to a 1 micron finish. The zircons were imaged with a Gatan MiniCL cathodoluminescence detector of the FEI Quanta 600F environmental SEM (Scanning Electron Microscope) at OSU to identify internal structure, inclusions and physical defects, inherited cores and overgrowth rims.

The LA-ICP-MS analyses at OSU used a Photon Machines Analyte G2 coupled with a Thermo XseriesII Quadrupole mass spectrometer, operating at 7 Hz with a 30 μm fixed spot and ~ 20 μm depth (Loewen and Kent, 2012; Dumitru et al., 2013). Measured trace elements include ^{31}P, ^{49}Ti, ^{50}Ti, ^{89}Y, ^{93}Nb, ^{139}La, ^{140}Ce, ^{141}Pr, ^{146}Nd, ^{147}Sm, ^{153}Eu, ^{157}Gd, ^{159}Tb, ^{163}Dy, ^{165}Ho, ^{166}Er, ^{169}Tm, ^{172}Yb, ^{175}Lu, ^{178}Hf, ^{179}Hf, ^{206}Pb, ^{207}Pb, ^{208}Pb, ^{232}Th, ^{235}U, ^{238}U and concentrations were standardized using the Plešovice standard (Sláma *et al.,* 2008) using an Excel application (LaserTram, Kent *et al.* 2004). Spot analyses that included apatite or other inclusions were discarded by monitoring light rare earth element and phosphorous concentrations. U-Pb isotopic ratios were standardized using Temora-1 zircon (418.6 Ma, Black *et al.,* 2004), as a primary standard (analyzed every 5 unknowns) and Plešovice (337.15 Ma, Sláma *et al.,* 2008) as a secondary standard. ^{206}Pb/^{207}Pb, ^{206}Pb/^{238}U and ^{207}Pb/^{235}U ratios for individual analyses were linearly extrapolated to the start of ablation to correct for laser-induced fractionation. Measured ^{207}Pb/^{206}Pb ratios were corrected for common lead using a Tera-Wasserburg Concordia plot.

For the SHRIMP-RG, the plugs were coated in gold at the SUMAC facility in Stanford. Secondary ions were sputtered from the target spot using an O_2^- primary ion beam, which was accelerated at 10 kV and had an intensity varying from 3.0 to 4.0 nA. The primary ion beam spot had a diameter between 22-28 microns and a depth of ~1.0-1.5 microns for the analyses performed in this study. The acquisition routine includes analysis of ^{30}Si^{16}O^{+}, ^{48}T^{+}, ^{49}Ti^{+}, ^{56}Fe^{+}, ^{89}Y^{+}, ^{139}La^{+}, ^{140}Ce^{+}, ^{146}Nd^{+}, ^{147}Sm^{+}, ^{153}Eu^{+}, ^{155}Gd^{+}, ^{163}Dy, ^{16}O^{+}, ^{166}Er^{16}O^{+}, ^{172}Yb^{16}O^{+}, a high mass normalizing species (^{90}Zr$_{2}$^{16}O^{+}), followed by ^{180}Hf^{16}O^{+}, ^{204}Pb^{+}, a background measured at 0.045 mass units above the ^{204}Pb^{+} peak, ^{206}Pb^{+}, ^{207}Pb^{+}, ^{208}Pb^{+}, ^{232}Th^{+}, ^{238}U^{+}, ^{232}Th^{16}O^{+}, and ^{238}U^{16}O^{+}. Trace element concentrations (Y, Hf, REE) were measured briefly (0.2 to 3 sec/mass) immediately before the geochronology peaks, and in mass order. A separate run was done to measure only trace elements with better precision at a rate 2 to 15 sec/mass. These analyses include ^{27}Al^{+}, ^{31}P^{+}, ^{40}Ca^{+}, ^{45}Sc^{+}, ^{48}Ti^{+}, ^{49}Ti^{+}, ^{51}V^{+}, ^{56}Fe^{+}, ^{89}Y^{+}, ^{93}Nb^{+}, ^{139}La^{+}, ^{140}Ce^{+}, ^{146}Nd^{+}, ^{147}Sm^{+}, ^{153}Eu^{+}, ^{155}Gd^{+}, ^{159}Tb^{16}O^{+}, ^{163}Dy^{16}O^{+}, ^{165}Ho^{+}, ^{166}Er^{16}O^{+}, ^{1169}Tm^{16}O^{+}, ^{1172}Yb^{16}O^{+}, ^{175}Lu^{16}O^{+}, ^{180}Hf^{16}O^{+}, ^{206}Pb^{+}, ^{248}Th^{+} and ^{254}U^{+}. All peaks were measured on a single EPT® discrete-dynode electron multiplier operated in pulse counting mode. All SHRIMP analyses were performed with 5 scans (peak-hopping cycles from mass 46 through 254), and counting times on each peak are varied according to the sample age and the U and Th concentrations to improve counting statistics and age precision. Measurements are made at mass resolutions of M/DM = 8000-9000 (10% peak height), which eliminates interfering molecular species, particularly for the REE. U, Th and all of the measured trace elements were standardized against the MAD-green standard (4196 ppm U, Barth and Wooden, 2010), which was mounted on a separate setup mount. Calculated model ages for zircon are standardized relative to Temora-2 (^{206}Pb/^{238}U age = 416.8 Ma; Black *et al.,* 2004), which were analyzed repeatedly throughout the duration of the analytical session (every five analyses). Data reduction for geochronology follows the methods described by Williams (1997), and Ireland and Williams (2003), and uses the MS Excel add-in programs Squid 2.51 and Isoplot 3.76 (Ludwig, 2009; 2013). The measured ^{206}Pb/^{238}U was corrected for common Pb using ^{207}Pb, whereas ^{207}Pb/^{206}Pb was corrected using ^{204}Pb. The common-Pb correction was based on a model Pb composition from Stacey and Kramers (1975). No addition error is propagated for the uncertainty in the common-Pb composition. All reported ^{206}Pb/^{238}U and ^{207}Pb/^{206}Pb model ages and uncertainties (2σ) include error summed in quadrature from the external reproducibility (1s SD) of the standard Temora-2 during an individual analytical session (16-24 hours). Data reduction for the trace element concentrations was performed in MS Excel. Average count rates of each element of interest are ratioed to the appropriate high mass normalizing species (see above) to account for any primary current drift, and the derived ratios for the unknowns are compared to an average of those for the standards to determine concentrations.

For both SHRIMP and LA-ICP-MS data, concordant ages within error of one another (n=4 to 18) are used to compare weighted mean ages with a standard error of the mean reported at

2σ (95 % confidence). The individual spot analyses that yield ages older than the main population of each sample were interpreted as inherited grains or mixtures between inherited and magmatic grains and were not used for the age calculation. For the LA-ICP-MS data, the analyses that yield outlying younger ages were interpreted as the result of Pb loss and were discarded from the age calculation of the sample. Analyses with 2σ error ellipses that were more than 8% discordant were also discarded from the age calculation.

Five Re-Os ages were obtained at Creaser Laboratory at University of Alberta. For each sample, a molybdenite mineral separate was produced by metal-free crushing followed by gravity and magnetic concentration methods. Methods used for molybdenite analysis are described in detail by Selby and Creaser (2004) and Markey *et al.* (2007). The ^{187}Re and ^{187}Os concentrations in molybdenite were determined by isotope dilution using negative thermal ionization mass spectrometry techniques following Carius-tube, solvent extraction and anion chromatography separation of Re and Os. A mixed double spike containing known amounts of isotopically enriched ^{185}Re, ^{190}Os, and ^{188}Os analysis was used. Isotopic analysis is made using a ThermoScientific Triton mass spectrometer by Faraday collector. Total procedural blanks for Re and Os are less than <3 picograms and 2 picograms, respectively, which are insignificant for the Re and Os concentrations in molybdenite. The Chinese molybdenite powder HLP-5 (Markey *et al.,* 1998), was analyzed as a standard. For this control sample over a period of two years, an average Re-Os age of 221.56 ± 0.40 Ma (1σ uncertainty, n=10) is obtained that is identical to the age of 221.0 ± 1.0 Ma reported by Markey *et al.* (1998).

2.5 Results

South of Haquira East, the older Chuquibambilla Formation is thrust over the Soraya Formation (Fig. 2.2, Fig. 2.3 insert). The Soraya Formation is folded along a northwest to southeast axis into the north-vergnet overturned Tocone syncline, that exposes the younger Mara Formation along the syncline axis as illustrated in cross-section 1900NW (Fig. 2.3). The overturned syncline is accompanied by thrust faults parallel to the south dipping axial plane. Two of these thrusts bound and offset the Mara Formation in the syncline axis. The block to the southwest stands at a steeper angle than the block to the northeast.

2.5.1 Intrusions and relation to ores

The petrography of the intrusions is summarized in Table 2.1 and representative analyses are shown in Table 2.2. Photographs illustrating the main textural and mineralogical characteristics of each unit are provided in Plate 2.1.

Two types of plagioclase-hornblende-biotite rich Lahuani sills that range between 1 to 15 m in thickness were emplaced into the Soraya and Mara Formations. The sills were likely deformed by the folding but are cut by the axial plane thrust faults. There are two compositional types of Lahuani sills but the mineralogy and textures are gradational. Nonetheless, the Lahuani type A (Plate 2.1A) sills tend to be fine-grained and equigranular and intensely sheared, whereas the Lahuani type B sills (Plate 2.1B) tend to have plagioclase phenocrysts set in a fine-grained and less sheared matrix (Plate 2.1F). In cross-section 1900NW, most of the Lahuani type A sills were intercepted in the axial plane of the Tocone syncline where they intrude the Mara formation, whereas the Lahuani type B sills were intruded away from the axial plane along sedimentary contacts of the Soraya and Mara formations. The Lahuani type A sills are quartz monzodiorites that range in composition between 59 and 62 weight % SiO_2 and 6.0 to 6.5 weight % $Na_2O + K_2O$ and are dominantly microporphyritic (Table 2.1, Fig. 2.4A). The Lahuani type B sills are quartz monzodiorites to granodiorites and range between 62 and 65 weight % SiO_2 and 6.7 to 7.5 weight % $Na_2O + K_2O$ and tend to be plagioclase porphyritic. Both groups of Lahuani sills are distinguishable in trace element composition as evidenced by ratios such as Th/Sc and Ti/Nb (Fig. 2.4B).

The Haquira granodiorite stock does not crop out but is intersected y drill core as a ~1 km x 0.5 km, NW-elongated plug-like body. The stock plunges 70º to 80º to the southwest and it has been drilled to a maximum depth of ~ 1 km, however it appears to continue below that depth. It is intruded in the center to north side of the Tocone syncline, both into the upright limb to the northeast and the overturned limb to the southwest. Three end-member textural variations with gradational contacts between them can be identified in the Haquira granodiorite stock (Table 2.1, Plate 2.1C, D, E). All of them are plagioclase-hornblende porphyritic with lesser biotite, and one of the textural variations present sparse quartz phenocrysts. Their matrix varies from 10 to 30 volume % (0.05 to 0.1 mm) fine-grained quartz and K-feldspar. Compositionally, the three textural types are quartz-monzodiorites to granodiorites, and the least altered samples range between 62 and 66 weight % SiO_2 and 7.0 to 8.3 weight % $K_2O + Na_2O$ and have identical trace element compositions (Fig. 2.4A, B). Internal contacts are common, but not necessarily separating different textural facies, and are evidenced by steeply dipping hornblende and igneous biotite lineations and weak foliations.

The Haquira porphyry dikes are a set of narrow (20 cm to 3 m wide) sub-vertical dikes that cross-cut the Haquira granodiorite stock. Compositionally the dikes are indistinguishable from the stock (Fig. 2.4), however, the dikes differ in texture and contain plagioclase (30 vol. %), hornblende (5 vol. %), lesser biotite, and rare quartz phenocrysts, in a quartz and K-feldspar aplitic matrix (45 to 60 vol. %) of 0.01 to 0.05 mm grain size (Table 2.1, Plate 2.1F, G). In deep core samples many of the Haquira porphyry dikes cross-cut aplites and deep quartz veins (DQ) in the area of highest vein density, below the Haquira East high grade copper ore (Plate 2.1G). However, the dikes are cross-cut by much less abundant sets of those same aplites and DQ veins. Some aplites and DQ veins are intensely folded (Plate 2.1G), and is more evident when these veins are intruded in the silstone wall rock (Plate 2.1M). Folded veins are also found in the Haquira stock. The Haquira porphyry dikes are not evidently deformed, and cross-cut the folded aplites and DQ veins (Plate 2.1G). Similarly, later banded quartz-molybdenite (BMQ) veins are folded (Plate 2.1L), whereas folding in the closely contemporaneous chalcopyrite-bornite bearing veins and alteration halos is less evident. Cu- and Mo-bearing veins and halos are both cross-cut some Haquira porphyry dikes and are cut by later sets Haquira porphyry dikes indicating contemporaneous emplacement (Plate 2.1H; Cernuschi *et al.,* 2012).

The high-grade copper ore (> 0.5 wt. %) at Haquira East is formed by a high density of bornite and chalcopyrite bearing Early Dark Micaceous halos (EDM) and later B veins (Einaudi, 2008) and sits above the zone of highest density of Haquira porphyry dikes, aplites and DQ veins (Fig. 2.3). The highest grades of molybdenum ore (>100 ppm) have a distribution similar to the high-grade copper ore and is hosted by banded molybdenite-quartz (BMQ) veins and later molybdenite bearing B-veins (Cernuschi *et al.,* 2013). The Haquira granodiorite stock hornblendes are intensely altered to hydrothermal biotite in both the deep zone with the highest density of Haquira porphyry dikes and low-grade copper, and in the shallower high-grade copper-ore zone,.

The Pararani dikes are the last intrusions that cross-cut all the other lithologies and veins, and do not contain hydrothermal biotite replacing the hornblende. Nonetheless, feldspars and hornblendes are commonly altered to sericite, illite and chlorite. These dikes are granodiorite to quartz monzodiorite in composition and contain plagioclase, hornblende and quartz phenocrysts together with less abundant poikilitic K-feldspar megacrysts with an aplitic quartz-K-feldspar groundmass (0.01 to 0.05 mm, 20 to 45 vol. %) matrix. The dikes have a narrow range of SiO_2

between 66 and 67 weight %, and vary between 7.7 and 8.3 weight % $Na_2O + K_2O$. Based on outcrops and drill-hole intercepts at Haquira East, the Pararani porphyry dikes are north-south striking and subvertical tabular bodies that range between 5 and 30 m thickness. These dikes tend to amalgamate into wider bodies in some areas, and divide into several thinner sinuous bodies in others. Fine-grained quenched margins are a common feature of these dikes.

The late pyrite-sericite rich D veins with sericitic alteration halos cross-cut the Pararani porphyry dikes and all the older intrusions and veins. Similarly, there is at least one sericitically altered hydrothermal pebble breccia that cross-cuts the Pararani dikes (Fig. 2.3). The main breccia at Haquira East is north-south striking, 5 to 20 m wide tabular body, that dips ~70º to the west. It is a polymictic breccia composed of 1 to 20 cm angular to rounded clasts of quartzite, siltstone, Haquira porphyries and Pararani porphyries in a matrix supported in rock flour with sericite and pyrite. Some of the Haquira porphyry clasts in the breccia have Cu-Mo-bearing veins that truncate against the matrix.

The Haquira granodiorite stock plunges ~70º to 80º southwest and suggests that the Haquira deposit has been tilted ≤ 20º to the northeast after formation (Fig. 2.3). Weakly foliated hydrothermal biotite in the Haquira stock and folded BMQ veins in the stock and the meta-sedimentary wall rock suggests tilting is related to post-mineralization shortening.

2.5.2 Haquira West, Cristo de los Andes, Dolores and Zincore

Haquira West is located 2 km west of Haquira East (Fig. 2.2). Granodiorite intrusions similar to the Haquira stock and the Haquira porphyry dikes are recognized but some variability exists. The copper and molybdenum mineralization is less defined, and hosted in similar veins as the ones described for Haquira East. The Pararani porphyry dikes are the latest intrusions and post-date the mineralization at Haquira West.

Cristo de los Andes is located ~8 km to the south of Haquira East and near the outcrops of the Acojasa granodiorite batholith (Fig. 2.2). The Soraya and Mara Formations are intruded by equigranular to porphyritic granodiorites to quartz monzodiorites. There is no defined high grade Cu-Mo mineralization, but the presence of abundant DQ, BMQ and Cu-sulfide veins together with K-silicate and sericitic alteration is indicative of porphyry style mineralization.

Dolores is located ~30 km east of Haquira East in granodiorite outcrops of the Andahuaylas batholith (Fig. 2.2). Intrusions range from quartz diorite to tonalite. Porphyry dikes with aplitic groundmass, DQ and Cu-sulfide quartz veins indicate porphyry style mineralization. An early quartz diorite porphyritic intrusion is not related to the mineralization, whereas the Cu-ore is hosted in granodiorite to diorite porphyritic intrusions. Granodiorite and tonalite porphyritic intrusions cross-cut the Cu-ore. The Zincore prospect is located ~15 km northeast of Dolores (Fig. 2.2). Porphyritic intrusions there are similar to the ones at Dolores, although there is currently no known porphyry copper mineralization.

2.5.3 Geochronology

U-Pb zircon, $^{40}Ar/^{39}Ar$ and Re/Os ages are reported in Table 2.3 and the data are available in the appendix. Errors are reported at 2 standard deviation. The U-Pb inverse concordia plots are presented in Figure 2.5 and $^{40}Ar/^{39}$ Ar plateau ages and inverse isochrones are shown in Figure 2.6. U-Pb weighted average and probability plots are available in the appendix.

The intrusions from each of the PCD and prospects show distinct but partially overlapping age ranges: Dolores (LA-ICP-MS: ~50, 43-38 Ma), Zincore (LA-ICP-MS: ~40-34 Ma), Cristo de los Andes (LA-ICP-MS: ~38.5-36 Ma), Haquira East (SHRIMP-RG: (~34.5, ~34.2 to 33.5 Ma).

U-Pb zircon ages for each sample were calculated using only the individual zircon spot analyses that produced a Gaussian distribution and lying within two standard deviation of the mean. This mean age is interpreted as the age of magmatic cooling and crystallization of zircon. Most of the samples (LA-ICP-MS and SHRIMP-RG) present at least 1, and up to 14, individual zircon spot analyses that yield younger or older ages, outliers of the Gaussian distribution of ages. The younger ages are considered to be produced by Pb-loss, and the older ages to be produced by inherited or antecrystic grains. Inherited grains are particularly common in sample FC-HAQ-135 (Lahuani sill B: 34.41 ± 0.50, SHRIMP-RG), where several 100 to 1000 Ma grains were identified (Figure 2.5). We use the weighted mean of concordant individual zircon ages and consider it robust for all the samples, based on MSWDs ranging between 0.81 and 2.2. Only sample FC-HAQ-145 (Haquira porphyry dike: 33.57 ± 0.74 Ma, SHRIMP-RG) has a higher MSWD of 3.1 based on an age calculated with only 6 individual analyses. However, this age is considered robust since it overlaps in error with sample FC-HAQ-034 (33.98 ± 0.31 Ma, SHRIMP-RG) of the same lithology and calculated with 13 individual analyses.

Zircon samples from the intrusion at Dolores, Zincore and Cristo de los Andes were analyzed with LA-ICP-MS. The LA-ICP-MS analyzes gave larger errors (0.97 to 3.2 Ma) than the SHRIMP-RG analyses (0.31 to 0.74 Ma). These ages range from the same age up to 10 M.y. older than the SHRIMP-RG ages obtained from Haquira East. However, most of the ages overlap with previously reported K-Ar and U-Pb ages for the Andahuaylas-Yauri. The exception is sample 24167 from a quartz-diorite porphyry from Dolores that gives a considerable older age of 49.8 ± 1.6 Ma.

The Re/Os in molybdenite ages from banded quartz-molybdenite vein and B-vein samples present small two standard deviation errors of ~ 0.14 Ma, and are considered to yield robust ages. The three analyzed samples from Haquira East average ~33.85 ± 0.2 Ma, and overlap within error with one sample from the close-by Haquira West prospect that yield an age of ~ 33.64 ± 0.14 Ma. One sample from Cristo de los Andes gives an older age of 36.30 ± 0.15 Ma, that is analytically identical to its replicate (Table 2.3).

The two $^{40}Ar/^{39}Ar$ ages of muscovite have weighted mean plateaus produced by 95% of the ^{39}Ar gas released (Fig. 2.6). Sample FC-HAQ-128, from a fracture-filling coarse muscovite in the meta-sedimentary wall rock, gave a plateau age of 37.04 ± 0.19 Ma (MSWD=0.09). This age has one initial low-temperature heating step that yielded a younger age than the plateau. This step represents only 5 % of the ^{39}Ar gas, is attributed to Ar-loss in the rims of the crystal grains, and was discarded from the age calculation. Sample FC-HAQ-079, from fine-grained muscovite in the sericitic halo of a D vein, gave a plateau age of 33.18 ±0.21 Ma (MSWD=0.09). This sample shows excess Ar for the first two heating steps, represents 5% of the ^{39}Ar released and was discarded for the age calculation. The excess Ar is attributed to a recoil effect affecting the fine-grained muscovite crystals.

2.6 Discussion

2.6.1 Porphyry intrusion, mineralization and deformation at Haquira East

Magmatism started at Haquira East with the intrusion of the pre-mineralization andesitic to dacitic Lahuani sills. These sills record the most intense deformation of all the intrusions in their sheared contacts and intense alignment of hornblendes on its matrix (Plate 2.1K). The Lahuani sills were intruded within the sedimentary contacts of the wall rock prior to, or more likely during, the southwest to northeast shortening events that lead to the formation of the Tocone syncline (Fig. 2.2). This deformation was related to the Incaic orogeny and the east to northeast subduction of the Nazca plate under the South American plate. Southeast of Haquira, the deformation is recorded in northwest-striking folds and faults that accommodated shortening in the southwest to northeast direction. West of Haquira, folds and faults are oriented east-west and accommodate shortening in the south to north direction (Fig. 2.2). This structural orientation is apparently a product of the Abancay deflection further to the northwest. The unusual orientation at the Andahuaylas-Yauri belt may be due to the subduction of the Nazca ridge and to other pre-existing basement features (Fig. 2.1). Haquira East is located where the orientation of the Tocone syncline axis bends from southeast-northwest to east-west. Part of the change in orientation is accommodated by unconstrained late northeast striking faults that apparently displace contiguous blocks left-laterally. At the west margin of Haquira East the Tocone syncline grades into an east-west striking thrust fault. The Tocone thrust faults locally bend to a northeast-southwest strike immediately west of Haquira Est (Gans, 2008; Fig. 2.2).

It is possible that further deformation occurred during the intrusion of the Haquira granodiorite stock. The stock might have pushed up its wall rock, tilting and partially stretching the Mara formation block to the southwest of the Haquira granodiorite stock (Gans, 2008; Fig. 2.3). The Haquira granodiorite stock is a composite intrusion, and despite the several textural facies that are recognized, they are all dacitic to trachydacitic and are not mappable as individual units (Table 2.1). However, the presence of sub-vertical internal contacts (not necessarily between different textural facies), evidenced by the flow foliation alignment of hornblende and biotite between the feldspars, indicates that several emplacement events took place under compression, and that the stock probably grew as a series of smaller northwest-trending dike-like bodies that amalgamated into one larger unit.

The early aplites, DQ and BMQ veins are commonly folded, suggesting that the compression and shortening was active at least during the first stages of the magmatic-hydrothermal system. Later veins are less evidently folded, and mostly present later and minor fractures and faults. These observations could suggest that the magnitude of the compression diminished, or that temperatures declined by the time of emplacement of later veins and halos. It is likely that when the magmatic-hydrothermal system was well established, veins were shielded from deformation by the pressure of hydrothermal fluid up-flow. By the time the magmatic-hydrothermal system was completely developed at Haquira East, the magmatic-hydrothermal fluid pressures equaled and temporally surpassed the regional compression forces. It has been proposed that the hydro-fractures that guide the porphyry dike and vein emplacement in porphyry copper deposits, forms when the magmatic-hydrothermal fluid pressures exceeds the sum of the local stresses and tensile stress of the rock (Tosdal and Richards, 2001; Cox, 2005). The lack of deformation in the later veins does not necessary indicate a decrease in the regional compression, and could be explained by a decrease in temperatures after the peak development of the porphyry magmatic-hydrothermal up-flow zone. Lastly, the aplites, DQ and BMQ veins are more commonly folded in the meta-siltstones and shales compared to the quartzites and Haquira granodiorite stock This might be explained based on the rheological difference between the more ductile and mica-rich siltstones and shales against the slightly less ductile quartzite and Haquira stock.

The Haquira granodiorite stock is the main host of the mineralization, and the porphyry copper deposit veining and hydrothermal alteration affects all of its textural facies equally and cross-cuts its internal contacts. The southeast end of the stock is K-silicate altered and cross-cut by Haquira porphyry dikes, aplites, DQ, BMQ and B veins and EDM halos. The northwest of the stock is Na-Ca altered and cross-cut by actinolite veins. Later D veins, sericitic halos and intermediate argillic halos cross-cut through all the stock (see Chapter 3). The porphyry copper deposit magmatic-hydrothermal system developed after the emplacement of the Haquira granodiorite stock. The high-grade copper forms an inverted cup shape on top of a low-grade copper core. This is the typical shape of the high-grade copper in several porphyry copper deposits elsewhere, as governed by favorable pressure, temperature and fluid composition conditions for copper deposition during the hydrothermal and mineralizing fluid flow (*Seedorff et al.* 2005, Landtwing *et al.* 2010; Redmond and Einaudi 2010). However, at Haquira East the stock is strongly mineralized with copper, although copper grades are low in the meta-sedimentary wall rock (Fig. 2.3). There is no evidence of significant fault displacement along the contact. The low-grade copper mineralization and high-grade molybdenum ore-shell form inverted cup shapes that are continuous throughout the meta-sedimentary and granodiorite wall rocks. Similarly, the DQ and BMQ veins are symmetrically distributed through both wall rock types. These observations suggest that the magmatic-hydrothermal fluid migrated equally through both wall rock types. An explanation for the high grade Cu-ore asymmetry can be hypothesized based on the wall rock compositional contrast and the availability of iron to trigger the precipitation of Cu-sulfides (Cernuschi *et al.,* 2013; see Chapter 3). Based on the location of the high-grade copper shell and the low-grade core, and the distribution of veins and hydrothermal alteration, the locus of the input of high temperature hydrothermal fluid can be inferred to be located close to the southwest flank of the Haquira granodiorite stock in cross-section 1900NW (Fig. 2.3, Cernuschi *et al.,* 2013, see Chapter 3). The highest density Haquira porphyry dikes were identified in this zone, and suggest that the emplacement of the dikes was related to the input of hydrothermal fluids.

In the deeper parts of the deposit, the Haquira porphyry dikes cross-cuts zones with high density of aplites and DQ veins in the Haquira granodiorite stock and the meta-sedimentary wall rock. However, the dikes are also cross-cut by less dense zones of these same veins types, positioning the intrusion of the Haquira porphyry dikes during the period of high temperature magmatic-hydrothermal events that produced the DQ veins. In shallower areas, the Haquira porphyry dikes cross-cut some of Cu-Mo-bearing B veins and EDM halos, and are in turn cross-cut by later sets of the same vein and halo types. These observations indicate that several sets of dikes were emplaced from the early and high temperature magmatic-hydrothermal events to the later Cu-Mo-ore forming events. Therefore, the Haquira porphyry dikes are inferred to be at least in part related to, and maybe even causative of, the porphyry copper deposit magmatic-hydrothermal system and mineralization.

There is little information to constrain the strike of the steeply-dipping Haquira porphyry dikes due to the lack of outcrops and oriented drill-hole core. The dikes are narrow and discontinuous based on drill core space at 150 to 200 m, which complicates the task of connecting individual bodies along and between cross sections. The only direct evidence of attitude comes from one outcropping dike 500 meters to the northeast of the Haquira stock, which strikes N50ºE and dips more than 90 º to the east (Gans, 2008). An acceptable fit of some individual dikes along and between cross-sections can be achieved by projecting northeast-striking dikes. A similar fit can be achieved by projecting northwest-striking dikes, following the elongation of the Haquira granodiorite stock. Orthogonal cross-cutting sets of dikes have been observed in drill core, suggesting that the dikes were emplaced along two conjugate strikes.

The Pararani porphyry dikes and hydrothermal breccias post-date the Cu-Mo-ore, K-silicate alteration and Haquira porphyry dikes. The Pararani dikes are subvertical, strike north-south and cross-cut by the hydrothermal breccias that also strike north-south but dip 70º W. Both dikes and breccias are sericitically altered and were apparently emplaced along swarms of D veins and sericitic halos, suggesting that all were emplaced closely in time.

The lack of A veins and abundance of Cu-ore forming EDM halos suggest that Haquira East was emplaced deeply (Cernuschi *et al.,* 2013). Shallow porphyry deposits are constituted by Cu-sulfides hosted in A veins, whereas deep deposits tend to be constituted by Cu-sulfides in EDM halos (Proffett, 2009). As complied by Seedorff *et al.* (2005), depths range from ~1 km for porphyry deposits with A veins (*e.g.* Batu Hijau, Indonesia) to ≥8 km in porphyry deposits with EDM halos (Butte, Montana). The lack of vapor-rich and halite-bearing fluid inclusion in veins from Haquira East indicates that the deposit was emplaced at high pressures (> 1.4 kb) that inhibited un-mixing of the magmatic-hydrothermal fluid into immiscible vapor and brine phases as commonly observed in shallower copper deposits elsewhere (e.g. Bingham, Utah, Landtwing *et al.,* 2010). The fluid inclusion assemblages resemble those observed at the deeper parts of Butte, Montana and suggests a greater depth of ~10 km for Haquira East (see Chapter 6).

It has been proposed that the regional compression resulted in concomitant uplift of the central Andes and enhanced erosion during the Eocene-Oligocene (Oncken *et al.,* 2006 and references therein). The Haquira East area must have experienced rapid uplift and erosion in order to expose the porphyry Cu-Mo mineralization formed at ~10 km depth (Fig. 2.3). The exhumation took place between the ore formation at ~33.85 Ma and the deposition of the valley-filling Oligocene Tacaza volcanics to the southwest at ~28 Ma (Mamani *et al.,* 2009; Fig. 2.2).

2.6.2 Age of igneous rocks and mineralization in the Andahuaylas-Yauri belt

All the dated intrusions overlap in age with previously reported ages for the Andahuaylas-Yauri belt (Perelló *et al.*, 2003) and recent age data from the Tintaya district (Fig. 2.7a; Jones *et al.,* 2007; Chelle-Michou *et al.,* 2014). U-Pb in zircons ages evidenced distinct but partially overlapping ages for each of the dated PCDs and prospects (Fig. 2.7A). The magmatic activity migrated through time in the Andahuaylas-Yauri belt following a progression from Dolores (~50, ~43 to 38 Ma), to Zincore (~40 to 34 Ma) and Cristo de los Andes (~38.5 to 36 Ma) and finalizing at Haquira East (~34.5, ~34.2 to 33.5 Ma). The Re/Os ages of molybdenite and one ^{40}Ar/^{39}Ar muscovite age support the hypothesis that the hydrothermal activity and mineralization at Cristo de los Andes, Haquira West and Haquira East is closely associated in time with the magmatic activity at each of the porphyry copper deposit centers. A high temperature magmatic-hydrothermal system was active first at Cristo de los Andes at ~36.3 Ma, and later at Haquira East at ~33.85 Ma and HaquiraWest at ~33.64 (Fig. 2.7A, B).

2.6.2.1 Dolores, Zincore and Cristo de los Andes

The Dolores prospect is defined by the oldest isotopic ages. Only one of the dated intrusions, a quartz-diorite porphyry (24167: 49.8 ± 1.6 Ma) not related to the mineralization, has an age >43 Ma (Fig. 2.7A). The remaining five dated intrusions range from ~ 43 to 38 Ma. Two samples of granodioritic to dioritic porphyries that host the veins carrying the mineralization overlap within error between ~ 43 to 42 Ma (23539: 43.1 ± 3.2 Ma; 21082: 42.4 ± 1.7 Ma). Three samples of intrusions that cross-cut the mineralized veins has slightly younger ages that overlap within error between ~ 40 to 38 Ma (granodioritic porphyries 24480: 40.2 ± 2.6 Ma and 23338: 39.1 ± 1.5 ma; tonalite 19541: 38.5 ± 2.5 Ma). Therefore, the mineralization must have occurred after the emplacement of the host intrusions between ~43 to 42 Ma, and before the post-mineralization intrusions between ~ 40 to 38 Ma.

The intrusions from the Zincore prospect partially overlap in age with Dolores, and have a range of ~ 41 to 34 Ma. However, the samples from Zincore are not associated with known porphyry copper deposits, skarns or significant Cu-Mo anomalies. The intrusions from the Zincore area overlap in age with the post-mineralization intrusions from nearby Dolores, and also with the mineralized intrusions from Haquira East.

2.6.2.2 Haquira East, Haquira West and Cristo de los Andes

Intrusions at Cristo de los Andes range from ~38.5 to 36 Ma. Here, the dated intrusions are younger than intrusions from Dolores, overlap in age with some intrusion from Zincore and are older than the intrusions from Haquira East. The age range at Cristo de los Andes is constrained by a granodioritic porphyry (FC-HAQ-182: 36.7 ± 1.7 Ma) that, based on preliminary mapping post-dates the copper mineralization but is affected by sericitic alteration. Six kilometers to the east, a sample of the large and equigranular monzodiorite to granodiorite Acojasa intrusion of the Andahuaylas-Yauri batholith has a similar age (FC-HAQ-177: 37.3 ± 1.4 Ma).

The dated intrusions at Haquira East are the youngest of all the sampled intrusions at ~34.5 Ma and 34.2 to 33.5 Ma (Fig. 8b). At Haquira East, the magmatism started with the pre-mineralization Lahuani sills at ~34.41 ± 0.50 Ma (FC-HAQ-135) and continued between ~34.2 and 33.5 Ma with the pre-mineralization of the Haquira granodiorite stock (FC-HAQ-017: 33.85 ± 0.36 Ma), the syn-mineralization emplacement of the Haquira porphyry dikes (FC-HAQ-034: 33.98 ±0.31 Ma), and the post-Cu-Mo-mineralization Pararani porphyry dikes (FC-HAQ-164: 34.15 ± 0.37). The different zircon ages of the pre- to post-Cu-Mo-mineralization intrusions are not resolvable at the 95% confidence level. According to these data, the magmatism at Haquira East spanned a maximum of ~ 1 M.y.

The lifespan of the magmatic-hydrothermal system can be partially constrained from the Re-Os and the $^{40}Ar/^{39}Ar$ ages. However, the $^{40}Ar/^{39}Ar$ in muscovite data deserve further discussion. The coarse-grained muscovite that fills a fracture in the meta-sedimentary wall rock (FC-HAQ-128) gave a $^{40}Ar/^{39}Ar$ age of 37.04 ± 0.19 Ma, whereas the fine-grained muscovite from the sericitic halo of a D vein (FC-HAQ-079) gave a younger age of 33.18 ± 0.21 Ma. The latter age is slightly younger than the U-Pb in zircon SHRIMP-RG ages of intrusions and the Re/Os ages in molybdenite and can be interpreted in terms of the cooling of the magmatic-hydrothermal system after the high temperature molybdenite mineralization or the post-metamorphic cooling as Haquira East is a deeply emplaced deposit (~10 km). However, the coarse-grained muscovite of sample FC-HAQ-128 is 3 M.y. older than the intrusion ages and Re-

OS ages of molybdenite and there is no geologic explanation for the older FC-HAQ-128 age. If this age reflects a real hydrothermal event at ~37 Ma, it would have been wholly or partially reset by the later ~34 to 33 Ma magmatic-hydrothermal events. Since sample FC-HAQ-128 was obtained from the meta-sedimentary wall rock, one plausible explanation is that the coarse-grained muscovite includes older detrital or metamorphic muscovite. The ^{40}Ar/^{39}Ar age reflects only partial resetting of the pre-intrusion muscovite by the younger intrusions and hydrothermal alteration. For this reason, the ^{40}Ar/^{39}Ar age of samples FC-HAQ-128 will not be considered in the interpretations.

Re/Os ages of molybdenite from Haquira East and West partially overlap in error but suggest that the mineralization at Haquira West at ~ 33.64 Ma might be slightly younger than the mineralization at Haquira East at ~33.84 Ma. At Haquira East, the Re/Os ages of molybdenite in early BMQ veins (FC-HAQ-001: 33.86±0.14 Ma; FC-HAQ-020: 33.75±0.14 Ma) are practically identical to the Re/Os ages of molybdenite in later Cu-Mo-bearing B veins (FC-HAQ-156: 33.93±0.14 Ma, Table 2.3).

In summary, at Haquira East the Re-Os and ^{40}Ar/^{39}Ar age data suggests a short period of molybdenum and copper mineralization at ~33.85 Ma followed by post-intrusion and post-hydrothermal cooling through the Ar-closure temperature (~350-325 ºC) by ~33.2 Ma (Fig 2.7B).

2.6.2.3 Magmatism age and Cu-endowment

Haquira East is the biggest Cu-resource of all the porphyry copper deposits and prospects studied here. Haquira East is also the youngest dated mineralization at ~ 33.85 Ma, and is associated with some of the youngest dated magmatism of the Andahuaylas-Yauri belt at ~ 34.2 to 33.5 Ma (Fig. 2.7). Isotopic age data from the Tintaya district, another significant Cu-resource, indicates magmatism and mineralization at the same age range. U-Pb in hydrothermal titanite and Re/Os in molybdenite from the Coroccohuayco PCD-skarn indicate that the mineralization there took place between 35.7 and 35.6 Ma (Chelle-Michou *et al.,* 2015). Similarly, magmatic-hydrothermal events at Antapaccay-PCD-skarn started at 39.9 Ma and reached 32.0 Ma (no method description available, Jones *et al.,* 2007) (Fig. 2.7).

With the available data, it is apparent that the youngest magmatism produced some of the biggest Cu-ore deposits known to date at the Andahuaylas-Yauri belt (~ 35 to 32 Ma). A similar temporal relation between magmatism and the Cu-endowment has been argued for the better explored and studied Eocene-Oligocene porphyry copper deposit belt of Chile, where more isotopic age data are available and some of the biggest Cu-deposits (e.g. Chuquicamata) are associated with ~32 Ma magmatism (Camus, 2003). This magmatism has been interpreted as the result of the deepening of a lower crust MASH zone in result of a compressional regime and crust thickening (Ireland, 2010).

2.6.3 Petrology, oxidation state, water and sulfur content of magmas

2.6.3.1 Rare earth elements in zircon

Representative analyses of trace element concentrations in zircons by SHRIMP-RG and LA-ICP-MS are presented in Table 2.4. All the analyses are depleted in light rare earth elements and elevated heavy rare earth elements in comparison to chondrite, with positive Ce anomalies and negative Eu anomalies, as described for arc magmas elsewhere (see Dilles *et al.,* 2015). The biggest elemental variation among the samples is found in the magnitude of the Ce and Eu anomalies. Data are normalized to chondrite (noted as $_N$) below.

Eu_N/Eu_N* was calculated using the Eu* as the geometric mean of Sm_N and Sm_N by fitting a straight line between Sm_N and Sm_N and intrapolating the concentration at the Eu_N position as if all the Eu present had a +3 valence (Eu_N*). Ce_N/Ce_N* was calculated applying a similar principle [$Ce_N/Ce_N* = (Ce_N/(La_N*Pr_N)^{1/2}$]. However, La is found in very low concentrations in zircon and the LA-ICP-MS analyses for this element were generally below detection limit. For this reason a straight line was fitted from the Nd_N and Sm_N concentrations, and the concentration at the Ce_N position was extrapolated from the mid rare earth data as if all the Ce present had a +3 valence (Ce_N*). $Ce^{(IV)}/Ce^{(III)}$ was calculated following the procedure described by Ballard *et al.* (2002) for which the Ce whole-rock concentration was used.

High Eu_N/Eu_N* and $Ce^{(IV)/}Ce^{(III)}$ (or Ce_N/Ce_N*, see below) ratios in zircon were recognized in several of the analyzed intrusions of the Andahuaylas-Yauri belt (Fig. 10, 11). It has been proposed that high Eu_N/Eu_N^* and $Ce^{(IV)/}Ce^{(III)}$ ratios reflect high oxidation states and/or high magmatic water contents (Ballard *et al.,* 2002; Burnham and Berry, 2012; Dilles *et al.,* 2015) that suppress plagioclase crystallization, and are associated with the high sulfur concentrations of the magmas and late magmatic oxidation due to SO_2 degassing (Dilles *et al.,* 2015). Alternatively, Chelle-Michou *et al.* (2014) proposed that the high $Ce^{(IV)/}Ce^{(III)}$ ratios (Ce/Nd as a proxy) recognized in some of the Coroccohuayco intrusions are inherited from lower crustal melts, on the basis that there is no correlation between Ce/Nd, age or $\varepsilon Hf_{(T)}$. However, all the granodiorite porphyry rocks at Coroccohuayco have higher Ce/Nd than the earlier gabbro-diorite intrusions, which could be interpreted in terms of SO_2 of degassing of the felsic rocks in comparison to the earlier mafic rocks.

The Haquira East zircon samples were analyzed using SHRIMP-RG and LA-ICP-MS, and the different ways to evaluate the Ce_N/Ce_N* ratios are compared below. When individual samples from Haquira East are compared, the Eu_N/Eu_N* and $Ce^{(IV)/}Ce_N^{(III)}$ ratios calculated from the SHRIMP-RG data (Fig. 2.8A) are similar to the ratios calculated from the LA-ICP-MS data (Fig. 2.8A and Table 2.4). When all the samples are grouped according to lithology, the ranges of the SHRIMP-RG and LA-ICP-MS Eu_N/Eu_N* and $Ce^{(IV)/}Ce_N^{(III)}$ ratios of each group are almost identical. Similarly, the $Ce^{(IV)/}Ce^{(III)}$ ratios calculated following the procedure described by Ballard *et al.* (2002) are almost identical to the Ce_N/Ce_N* ratio calculated by fitting a straight line from the Nd_N and Sm_N concentrations. This method is preferable over calculating Ce_N/Ce_N* as $(Ce_N/(La_N*Pr_N)^{1/2}$, as La was generally below detection limit for the samples analyzed by LA-ICP-MS, and as noted before, La and Pr are susceptible to contamination by small melt and apatite in zircons (Ballard *et al.,* 2002; Lee, 2008; Wang *et al.,* 2013). Also, the calculation of $Ce^{(IV)/}Ce^{(III)}$ requires the whole-rock composition of the sample and the assumption that the whole-rock Ce concentration is the same as the Ce concentration of the melt at the time of the zircon crystallization, which may not be a valid assumption (Dilles *et al.,* 2015). Similarly, other inconsistencies of the $Ce^{(IV)/}Ce^{(III)}$ ratio as a proxy for oxidation state has been noted before (Wang *et al.,* 2013; Trail *et al.,* 2011). For these reasons our calculation of Ce_N/Ce_N* is preferable, but it is used with reservation, and emphasis is given to the interpretations of the Eu_N/Eu_N* ratio which I considered to be more reliable.

At Haquira East, where vein and porphyry cross-cutting relationships enables the grouping of the sampled intrusions in terms of their relationship with mineralization, the highest Eu_N/Eu_N* and Ce_N/Ce_N* ratios were found in the immediately pre-Cu-Mo-mineralization Haquira granodiorite stock, in the syn-Cu-Mo-mineralization Haquira porphyry dikes and in the immediately post-Cu-Mo-mineralization Pararani porphyry dikes (Fig. 2.8, 2.9). The pre-mineralization Lahuani sills and the barren Acojasa intrusion near Cristo de los Andes have Eu_N/Eu_N* commonly below 0.5 and rarely reach 0.7, whereas Ce_N/Ce_N* mostly remains below 500. The samples of Haquira granodiorite stock, the Haquira porphyry dikes and the Pararani porphyry dikes have higher Eu_N/Eu_N* between 0.4 and 0.8, and Ce_N/Ce_N* between 200 and 5000. When using the $Ce^{(IV)/}Ce^{(III)}$, these samples overlap with the ore-productive samples from the Eocene El Abra-Chuquicamata porphyry deposits from Chile analyzed by Ballard *et al.* (2002), and have higher Eu_N/Eu_N* and $Ce^{(IV)/}Ce^{(III)}$ ratios than zircons from intrusions not related to mineralization.

When the analyzed samples from intrusions from Cristo de los Andes, Dolores, and Zincore are plotted, only the samples from the Dolores porphyry copper deposit have high Eu_N/Eu_N* and Ce_N/Ce_N* ratios with the exception of quartz-diorite sample (24167), which is at least 5 M.y. older than the mineralization-related intrusions from Dolores (Fig. 11a). When Eu_N/Eu_N* is plotted against Hf, which can be used as a proxy for crystallization or fractionation, the pre-mineralization samples (Lahuani sills from Haquira East, the Acojasa intrusion near Cristo de los Andes, all the samples from Zincore and sample 24167 from Dolores) form an array in which Eu_N/Eu_N* decreases as Hf increases. In samples of intrusions that host or post-date the mineralization at Dolores, Eu_N/Eu_N* increase as Hf increases, whereas intrusions contemporaneous with the mineralization at Haquira East form a trend of no change in Eu_N/Eu_N* as Hf increases (Fig. 2.9B). These samples overlap with the field of porphyry copper pluton samples from elsewhere, such as Yerington in Nevada and Chuquicamata-El Abra and El Salvador in Chile, which have high Eu_N/Eu_N* values that increase as Hf increases (Dilles *et al.,* 2015).

The rare earth element data in zircons provide evidence that although all the sampled intrusions are relatively oxidized and water-rich, the mineralization-related intrusions are defined by even higher water contents and oxidation states. The post-mineralization samples, such as the Pararani porphyry dikes at Haquira East, have the highest Eu_N/Eu_N* and Ce_N/Ce_N* ratios. Although the Pararani porphyry dikes apparently represent the most oxidized and water-rich magmatism, they immediately post-date the mineralization and did not form known ore deposits. Similarly, the Eu_N/Eu_N* and Ce_N/Ce_N* ratios of some of the Dolores intrusions are higher than the Haquira East intrusions, and the Eu_N/Eu_N* increases a greater amount as Hf increases. This might indicate that the magmas at Dolores were more oxidized and water-rich compared to the magmas at Haquira East, despite the bigger Cu-endowment identified at Haquira East. On the basis of the zircons sampled here, the water content and oxidation state of each of the different magmatic episodes in different areas of the Andahuaylas-Yauri belt increased from the non-ore-related to late ore-related intrusions, as noted before for porphyry copper deposit related intrusions elsewhere (Dilles, 1987; Richards *et al.,* 2012; Dilles *et al.,* 2015). From this perspective, intrusions with zircon Eu_N/Eu_N* and Ce_N/Ce_N* ratios that overlap with the productive fields described by Ballard *et al.* (2002) and Dilles *et al.* (2015) have similar chances of being related to porphyry copper deposits regardless of the ratio values. Similarly, the highest Eu_N/Eu_N* and Ce_N/Ce_N* ratios are not necessarily associated to the syn-mineralization intrusions, and are more likely related to immediately post-mineral dikes, as previously noted for post-Cu-mineralization dikes at Yerington, Nevada and El Salvador, Chile (Dilles *et al.,* 2015).

It has been proposed that magmas could gain a higher oxidation state after losing SO_2-rich magmatic-hydrothermal ore fluids during late-stage crystallization of magma bodies in the upper crust (Dilles *et al.,* 2015). If this is correct, the rare earth element ratios in zircons might not only indicate high water contents and suppression of plagioclase crystallization, but also that the ore-productive magmas were sulfur rich.

2.6.3.2 Petrogenesis of ore forming magmas

The TiO_2, P_2O_4 and alkali compositions of the sampled intrusions (among other elements) has a wide scatter at a given SiO_2 and do not form consistent arrangements that indicate crystal fractionation (Fig. 2.4A). The magmatic diversity observed at Haquira East, thus, cannot be explained by simple fractionation of a single magmatic source. We propose that the magmas evolved in middle to shallow crustal chambers that were periodically re-injected by basaltic andesite to andesite magmas that evolved simultaneously in a lower crust MASH zone (mixing-assimilation-storage-homogenization). The presence of mantle-derived melts in MASH zones has been long recognized as the source for a variety of arc-related magmatic processes (Hildreth and Moorbath, 1988). Dilles (1987) proposed that basaltic andesite melts ascend to shallower crustal levels where assimilation and fractionation processes produce more felsic melts that accumulate in magma chambers from where later porphyry dikes are sourced. It has also been recognized that in order to sustain shallow crust magma chambers throughout the timescales observed for porphyry copper deposit related magmatism, periodical re-injections of MASH zone derived melts, or injections from other sub-products stored in the mid-crust, are necessary (Tosdal *et al.,* 2009).

To test the petrogenesis of the igneous rocks at Haquira East, linear magma mixing and fractionation paths were calculated using standard approaches (Rollinson, 1993). Rayleigh fractionation calculations were performed using the equation $C_L/C_o = f^{(D-1)}$ where C_L is the liquid composition, C_o is the parent liquid composition, f is the fractionation factor and D is the bulk partition coefficient between mineral and melt for each element. Mineral–melt partition coefficients were taken from Rollinson (1993) and the GERM database (GERM, 2014) and are listed in the appendix. When available, the most recent experimental partition coefficients were used. Linear magma mixing tests were calculated with the formula $(A–B)_{MIX} = f_*A + (1-f)_*B)$ where f represents the mass fraction (0 to 1) and A and B are the concentration of an element in mixing end member magmas.

Two fractional crystallization paths were calculated for an andesite parental magma composition (Fig. 2.10a). Path (A) describes magma evolution in the lower crust where garnet is stable (Loucks, 2004), high water contents suppress plagioclase crystallization and temperature is above the maximum temperature of hornblende crystallization (Annen *et al.,* 2006). Mineral proportions were set at 70 wt. % pyroxene and 30 wt. % garnet. A second path (B) for magma describes crystallizing in the mid to shallow crust at lower temperatures and high water contents that enhanced the crystallization of hornblende stable, diminished the crystallization of plagioclase and where low temperature trace phases are stable. Mineral proportions were set at 40 wt.% hornblende, 40 wt. % clinopyroxene, 15 wt. % plagioclase, 2 wt. % titanite, 1 wt. % apatite, 1 wt. % zircon and 1 wt. % magnetite. The results of the modeling are presented here using a Sr/Y versus Dy/Yb plot (Fig. 2.10A). Additionally, the modeling results for La, Sm, Tb, Yb, Nb, P, Ta, Ni, Zr yield similar conclusions for roles of crystal fractionation via processes A and B.

There is an increase of Sr/Y and La/Yb ratios with decreasing ages of intrusions from the andesitic Lahuani sills, to the andesitic to trachydacitic Haquira granodiorite stock and Haquira porphyry dikes, and to the dacitic Pararani porphyry dikes (Fig. 9a). The increase in Sr/Y can be explained both by the garnet-fractionating path A and the hornblende and trace mineral phases fractionation path B.

The importance of hornblende to explain high Sr/Y ratio values has been recognized for adakite-like compositions of arc magmatic rocks elsewhere (Richards, 2011). High magmatic water contents suppress the crystallization of plagioclase (Moore and Carmichael, 1998) because hydroxylation breaks the polymerizing Si-O-Al bonds (Burnham, 1979; Stolper, 1982). Thus, elements compatible in plagioclase such as Sr, are enriched in the residual melt when plagioclase crystallization is surpessed. Hornblende crystallization requires <950 ºC and > 4 weight % water in dacitic melts (Naney, 1979; Costa *et al.,* 2006) and its fractionation depletes the melt in hornblende-compatible trace elements such as Ti, Sc and Y. Hornblende and clinopyroxene, however, have similar partition coefficients for middle and heavy rare earth elements, which differ from the REE partition coefficients in garnet, which preferentially incorporate the heavy rare earth elements (Romick *et al.,* 1992; Castillo *et al.,* 1999 and Rooney *et al.,* 2011). Thus, middle-rare earth element/heavy-rare earth element ratios such as Dy/Yb, Sm/Yb or Tb/Yb are not expected to increase with hornblende or pyroxene fractionation, but they would increase with garnet fractionation. At Haquira East, middle-rare earth element/heavy-rare earth element ratios increase from early to late intrusions, and support a role for the fractionation of garnet (Fig.

2.10A). Garnet is only stable at high pressures in basaltic to andesitic melts (~1 Mpa at 900 ºC, Loucks, 2014) which suggest the presence of a thickened crust that would position the MASH zone below ~ 25 km depth. This lower crustal garnet-fractionation is represented by fractionation path A (Fig. 2.10A).

Other trace elements indicate fractionation processes at lower temperatures in hydrous magmas in the shallower crust. La and other light rare earth elements are depleted through time, together with Nb, Ta, P and Zr, indicating the fractionation of magnetite, titanite, apatite and zircon, which are the trace phases included in the fractionating assemblage B. This is further supported by Ti-in-zircon crystallization temperatures that indicate crystallization in the range of ~650 to 750 ºC (Chapter 6).

The whole-rock trace element data always plot in arrays comprehended between the garnet-fractionating path A and the hornblende and trace mineral phases fractionation path B, which suggests that both fractional crystallization processes contributed to magma compositions (Fig. 2.10A). One possible explanation is that fractionating path A processes occurred in the lower crust MASH zone and produced basaltic andesite to andesite melt that were periodically re-injected into a mid- to upper-crust magma chamber that further evolved through fractionating path B. This process is illustrated in the Sr/Y and La/Yb plot by mixing lines between fractionation paths A and B (Fig. 2.10A) and it is schematically illustrated in Figure 2.10B. In Figure 2.10A some samples of each intrusion plot in close linear arrangements oblique to the mineral fractionation path A and B. Some of these oblique arrangements of samples can be partially fitted by mixing lines between both fractionation trends, further supporting the re-injection model. A mixing line between a 5 % fractionated batch from path A (a1) and 5 % fractionated batch from path B (b1) exemplifies a first mixing event that could explain some of the Lahuani sills compositions (Fig.. 2.10A). A lower crust melt of composition (a1) is injected into an upper crust magma reservoir of composition (b1). Subsequently, both the lower crust reservoir and the upper crust magma chamber will fractionate and evolve to compositions (a2) and (b2) respectively. After a new injection of melt (a2) into the upper crustal magma chamber of composition (b2), some degree of mixing can produce at least part of the Haquira granodiorite stock and the Haquira porphyry dikes compositions (Fig. 2.10a). Similarly, compositions (a3) and (b3) exemplify a third re-injection event that produced the Pararani porphyry dikes. However, it is very likely that more than three re-injections and partial mixing events occurred and the mixing lines in Figure 2.10A are intended to be an illustration of the processes and not an exact fit for the individual sample compositions.

Alternatively, if higher degrees of homogenization are achieved after each re-injection and mixing event, the new starting composition of the upper crust fractionating path B would be shifted towards higher Dy/Yb ratios. If this was the case, after the parent composition evolved to (a1) in the lower crust and (b1) in the upper crust and they mixed after re-injection into the upper crustal magma chamber the resulting composition would plot somewhere along the mixing line between a1 and b1 depending on the mixed proportions of a1 and b1. Starting from this point, the upper crustal magma chamber would then fractionate along path B. In this scenario of near 100% homogenization, the samples in Figure 2.10A would be required to be fit by several parallel lines representing fractionation B-like trends at increasingly higher Dy/Yb ratios and higher Sr/Y starting points.

Regardless of the precise dynamics of the involved processes, the model fractionation experiments provide evidence that both fractionation processes A and B are necessary to describe the observed compositions. Additional evidence for this two-stage fractionation model is provided by other intrusions in the Andauyalas-Yauri belt during the Eocene-Oligocene. As discussed before, the intrusive rocks at Haquira-East were formed during to near the end of regional compressive events in the late Eocene to earliest Oligocene. Mamani *et al.* (2009) proposed that these events produced uplift, folding and thickening of the crust not only at Haquira East, but in a broader belt of the central Andes in northern Chile and southern Peru. Thus, a thick crust (>30 km) that stabilized garnet in a MASH zone at the mantle/lower crust boundary was likely present at the time of the magmatic activity at Haquira East. Similarly, extensive outcrops of the late Eocene to early Oligocene Andahuaylas-Yauri batholith evidence widely distributed magma in shallow crust of southern Peru. The intrusions of the batholith contain hornblende and trace mineral phases such as titanite, apatite and zircon, and are inferred to have fractionated these minerals in the middle or upper curst. Furthermore, upper crustal fractionation of hornblende, zircon and titanite along with other mineral phases, in 4 to 9 km deep magma chambers has been proposed for intrusions of the Andahuaylas-Yauri batholith coeval with the Coroccohuayco Cu-Mo skarns of the Tintaya cluster (Chelle-Michou *et al.,* 2014).

2.6.3.3 Variations in whole-rock trace elements

Samples of the immediately pre- to immediately post-Cu-Mo-mineralization at Haquira East have higher Sr/Y (>60) and V/Sc (>12) whole-rock ratio values at a given SiO_2 composition compared to the pre-mineralization samples, and overlap with the ore-productive intrusion fields defined by Loucks (2014). The Sr/Y and V/Sc ratio values of pre-mineralization samples partially overlap with the average volcanic arc fields (Fig. 2.11A), which are defined using whole-rock samples from intrusions related and un-related to mineralization from arcs around the world. A better correlation between the Haquira East samples and the ore-productive fields is found in terms of the Sr/Y ratio than the V/Sc ratio. In the V/Sc versus SiO_2 plot, all the samples plot in the ore-productive intrusion field. Nonetheless, the pre-mineralization samples show lower V/Sc ratios than the samples of intrusions emplaced closely in time with the Cu-Mo-mineralization.

As discussed above, Sr/Y values can be used to track garnet fractionation and high water contents of magmas. Additionaly, high V/Sc ratio values also indicate oxidized and hydrous magmas, as early magnetite can be suppressed by high water contents. Similarly, as the oxidation state of magmas increases from NNO=0 to NNO=+3, the magnetite/melt partition coefficient of vanadium drops from ~20 to ~1 (Toplis and Corgne, 2002). Therefore, vanadium acts incompatibly in strongly oxidized magmas whereas scandium remains compatible in hornblende, with the result of increasing the V/Sc ratios (NNO>1, Loucks, 2014).

For the sampled intrusions of the Andahuaylas-Yauri belt, there is an agreement between the samples that have indications of high oxidation state and magmatic water contents on the basis of high whole-rock Sr/Y and V/Sc ratios, and the samples that have indications of high oxidation state and high magmatic water based on the rare earth element compositions of zircons (Fig. 2.11B). Samples of intrusions that show small negative Eu anomalies in zircon (larger Eu_N/Eu_N^* ratios), and lager positive Ce anomalies (larger Ce_N/Ce_N^* ratios), also have high Sr/Y ratio values in whole-rock composition. Similarly the whole-rock V/Sc ratio is higher for samples with small negative Eu anomalies (larger Eu_N/Eu_N^* ratios) and larger positive Ce anomalies (larger Ce_N/Ce_N^* ratios) in zircons (Fig 2.11B). Both rare earth element concentrations in zircon and trace element in whole-rock are, thus, useful indicators of petrogenetic processes that are important in the genesis of ore-productive magmas.

2.7 Conclusions

Magmatism at Haquira East took place in the late Eocene to earliest Oligocene between ~34.9 to 33.5 Ma during regional compression related to the east/northeast subduction of the Nazca plate under the western margin of the South American plate. Most of the magmatism at Haquira East is related to the formation of the relatively large porphyry Cu-Mo deposit, and it is some of the youngest magmatism related to the large Andahuaylas-Yauri batholith of southern Peru.

As a response to the regional shortening, the Jurassic-Cretaceous meta-sedimentary wall rock at Haquira East was folded into the southeast-northwest trending Tocone syncline that arcs into an east-west trending fold further west. Andesitic to dacitic Lahuani sills were emplaced at ~34.5 Ma (Fig. 2.12A). The Lahuani sills intruded sedimentary contacts in the wall rock and into the folding axial plane of the Tocone syncline. The Tocone syncline was then overturned to the north/northeast while east-west/southwest-northeast-striking and south-dipping thrust faults juxtaposed the older Chuquibambilla Formation on top of the younger Soraya Formation. Similar thrust faults produced minor offsets and displacements between the Soraya and Mara Formations within the syncline (Fig. 2.12B). The Lahuani magma was originally produced in an inferred lower-crust MASH zone. Magma injection into the mid- to upper-crust then developed an inferred small magma chamber (Fig. 2.12A) that would later grow into the larger Haquira magma chamber and form part of the Andahuaylas-Yauri batholith (Fig. 2.12B).

The more voluminous granodioritic magmatism took place between ~34.2 and 33.5 Ma during the peak activity of the inferred Haquira magma chamber, concealed at depth below Haquira East (Fig. 2.12B). On the basis of trace element modeling we infer that a hydrous and oxidized magma fractionated hornblende, small amounts of plagioclase and trace mineral phase, which was periodically re-injected with basaltic andesite and andesite from a garnet-fractionating lower crust MASH zone. This petrogenesis is responsible for high Sr/Y and V/Sc ratio whole-rock values and high Eu_N/Eu_N* and Ce_N/Ce_N* ratios in zircon observed in the granodioritic intrusions of Haquira East. These intrusions comprise the immediately pre-mineralization Haquira granodiorite stock, the syn-mineralization Haquira porphyry dikes and the immediately post-mineralization Pararani porphyry dikes.

The Haquira granodiorite stock was emplaced as a series of dike-like bodies that intruded in a short period of time and while they were still hot, amalgamating into a single 0.5 x 1 km northwest-southeast elongate stock. The slightly later Haquira porphyry dikes were emplaced in several successive sets together with the K-silicate alteration-stable magmatic-hydrothermal veins and the Cu-Mo-mineralization at ~ 33.85 Ma (Fig. 2.12B). The emplacement of the Pararani porphyry dikes followed immediately while diminished activity in the magma chamber at Haquira occurred at greater depth. The sericitically altered hydrothermal breccias and sericitic alteration-stable veins and halos were emplaced closely in time with the Pararani porphyry dikes. Deep magma injection ceased after the Pararani porphyry dikes, producing the consequent end of the magmatism at Haquira East.

Further compression tilted the geology of Haquira East between 10º and 20º to the north/northeast. Rapid uplift and erosion shallowed the Haquira East intrusions and the high grade Cu-Mo mineralization from an inferred depth of formation of ~10 km at ~33.85 Ma, to its present close to surface position. Most of the erosion took place before the deposition of the ~28 Ma Tacaza volcanics further to the southwest (Fig. 2.12C).

The observations at Haquira East support the previously described relation between compression and the formation of some porphyry copper deposits, as well as the intimate relation between the emplacement of porphyry dikes and the formation of the Cu-Mo-ore. The regional compression prevented the early magma extrusion from upper crust chambers. Water rich and oxidized granodioritic magma evolved in these chambers as they were re-injected by basaltic-andesite melts from deep MASH zones. Magmatic-hydrothermal fluids that scavenge Cu and Mo from the magma, accumulated on cupolas in the shallower areas of the chambers. The regional compression prevented the ejection of the fluid until the hydrostatic pressure surpassed the regional stress, causing the hydro fracturing of its roof wall rock. In these instances, several batches of the Cu-Mo-ore-forming magmatic-hydrothermal fluid accumulated in the cupolas were ejected, together with small quantities of magma that formed the Haquira porphyry dikes and aplites.

2.8 Acknowledgements

I would like thank First Quantum Minerals INC. for supporting this PhD and allowing us to work at their core-sheds and field site in Peru with the support of all their staff. To Matt Coble for the assistance with the SHRIMP-RG analyses and Richard Bradshaw for the assistance with the LA-ICP-MS analyses.

2.9 References

Antares, 2010, Antares press–release: New Haquira global resource, February 26th, 2010, 6 p.

Ayusso, R.A., 2010, Trace element geochemistry, *in* porphyry copper model: Scientific Investigation Report 2010–5070–B. U.S. Department of the Interior U.S. Geological Survey.

Ballard, J.R., Palin, J.M., and Campbell, I.H., 2002, Relative oxidation states of magmas inferred from $Ce^{(IV)/}Ce^{(III)}$ in zircon: Application to porphyry copper deposits of northern Chile: Contributions to Mineralogy and Petrology, v. 144, p. 347–364.

Barth, A.P., and Wooden, J.L., 2010, Coupled elemental and isotopic analyses of polygenetic zircons from granitic rocks by ion microprobe, with implications for melt evolution and the source of granitic magmas: Chemical Geology, v. 277, p. 149–159.

Black, L.P., Kamo, S.L., Allen, C.M., Davis, D.W., Aleinikoff, J.N., Valley, J.W., Mundil, R., Campbell, I.H., Korsch, R.J., Williams, I.S., Foudoulis, C., 2004, Improved $^{206}Pb/^{238}U$ microprobe geochronology by the monitoring of a trace–element–related matrix effect; SHRIMP, ID–TIMS, ELA–ICP–MS and oxygen isotope documentation for a series of zircon standards: Chemical Geololgy, v. 205, p. 115–140.

Burnham, A.D., and Berry, A.J., 2012, An experimental study of trace element partitioning between zircon and melt as a function of oxygen fugacity: Geochimica et Cosmochimica, Acta, v. 95, p. 196–212.

Burnham, C.W., 1979, The importance of volatile constituents, *in* Yoder, H.S. Jr., ed., The evolution of the igneous rocks: Fiftieth anniversary perspectives, Princeton University Press, Princeton, N. J., p. 439–482.

Camus, F., 2003, Geología de las sistemas porfíricos en los Andes de Chile: Santiago de Chile, Servicio Nacional de Geología y Minera, 267 p.

Carlotto, V., 1998, Evolution andine et raccourcissement au niveau de Cusco (13º–16º), Pérou: Enregistrement sédimentaire, chronologie, contrôles paléogeógraphiques, évolution cinématique [Unpublished Ph.D. thesis]: Grenoble, France, Université Joseph Fourier, 203 p.

Castillo, P.R., Janney, P.E., and Solidum, R.U., 1999, Petrology and geochemistry of Camiguin Island, southern Philippines: Insights to the source of adakites and other lavas in a complex arc setting: Contributions to Mineralogy and Petrology, v. 134, p. 33–51.

Cernuschi, F., Dilles, J. H., and Creaser, R., 2013, Hydrothermal alteration, SWIR–mineral mapping, vein distribution and age of the Haquira–East Cu–Mo porphyry: 12th SGA Biennial Meeting 2013, Proceedings, v. 2, p. 782–785.

Cernuschi, F., Einaudi, M.T, Dilles, J.H., Heather, K.B., and Barr, N. C., 2012, Hydrothermal veins, porphyry geochemistry and mineralization zonation of the Haquira–East Porphyry Cu–Mo Deposit, Perú: SEG Conference 2012, Lima, Peru.

Chelle–Michou, C., Chiaradia, M., Ovtcharova, M., Ulianov, A., and Wotzlaw, J.F., 2014, Zircon petrochronology reveals the temporal link between porphyry systems and the magmatic evolution of their hidden plutonic roots (the Eocene Coroccohuayco Deposit, Peru): Lithos v. 198–199, no. 0, p. 129–40.

Chiaradia, M., 2009, Adakite–like magmas from fractional crystallization and melting–assimilation of mafic lower crust (Eocene Macuchi arc, Western Cordillera, Ecuador): Chemical Geology, v. 265, p. 468–487.

Clement, S.W.J., and Compston, W., 1994, Ion probe parameters for very high resolution without loss of sensitivity: U.S. Geological Survey Circular, no. 1107, 62 p.

Costa F., Scaillet, B., and Pichavant, M., 2004, Petrological and experimental constraints on the pre–eruption conditions of Holocene dacite from Volcan San Pedro (36_S, Chilean Andes) and the importance of sulphur in silicic subduction–related magmas: Journal of Petrology, v. 45, p. 855–881.

Cox, S., 2005, Coupling between deformation, fluid pressures and fluid flow in ore–producing hydrothermal environments: Economic Geology 100th Anniversary Volume, p. 39–75.

DeBari, S.M., and Sleep, N.H., 1991, High–Mg, low–Al bulk composition of the Talkeetna island arc, Alaska: Implications for primary magmas and the nature of arc crust: Geological Society of America, Bulletin, v. 103, p. 37–47.

Dilles, J.H., 1987, Petrology of the Yerington batholith, Nevada: Evidence for evolution of porphyry copper ore fluids: Economic Geology, v. 82, p.1750–1789.

Dilles, J.H., Kent, A.J.R., Wooden, J.L., Tosdal, R.M., Koleszar, A., Lee, R.G., and Farmer, L.P., 2015, Zircon compositional evidence for sulfur–degassing from ore–forming arc magmas: Economic Geology, v. 110, no. 1, p. 241–51, doi:10.2113/econgeo.110.1.241.

Dumitru, T.A., Ernst, W.G., Wright, J.E., Wooden, J.L., Wells, R.E., Farmer, L.P., Kent, A.J.R., and Graham, S.A., 2013, Eocene extension in Idaho generated massive sediment floods into the Franciscan Trench and into the Tyee, Great Valley, and Green River Basins: Geology, v. 41, no. 2, p. 187–190.

Einaudi, M.T., 2008, Distribution of vein types, alteration, sulfides, and metal grades. Haquira Cu–Mo–Au deposit, departamento de Apureímac, Perú: Unpublished Report for Antares Minerals Inc. (September): 47 p.

Foley, S.F., and Wheller, G.E., 1990, Parallels in the origin of the geochemical signatures of island arc volcanics and continental potassic igneous rocks: The role of residual titanites: Chemical Geology, v. 85, p. 1–18.

Gans, P., 2009, Geology of the Haquira copper deposit: New information and iynthesis: Internal report for Antares Minerals, 9 p.

Geissman, J., Van Der Voo, R., Kelly, W., and Brimhall, Jr., G., 1980, Paleomagnetism, rock magnetism, and aspects of structural deformation of the Butte mining district, Butte, Montana: Journal of Geology, v. 88, p. 129–159.

Germ, 2014, Geochemical earth reference model. Partition coefficient database: http://earthref.org/KDD/

Hamilton, W.B., 1981, Crustal evolution by arc magmatism. Philosophical Transactions: Royal Society of London, v. 301, p. 279–291.

Heather, K.B., Black, J.E., Gamarra, H., Einaudi, M., Barr, N.C. and Robeto, J., 2012, Discovery and development of the Haquira Cu–Mo–Au porphyry deposit, Peru: A super giant in the making? SEG Orange NSW talk, presentation, 27–06–2012.

Hildreth, W., and Moorbath, S., 1988, Crustal Contributions to Arc Magmatism in the Andes of Central Chile: Contributions to Mineralogy and Petrology, v. 98, n. 4, p. 455–489.

Houston, R.A., and Dilles, J.H., 2013, Structural geologic evolution of the Butte district, Montana: Economic Geology, v. 108, no. 6, p. 1397–1424, doi:10.2113/econgeo.108.6.1397.

INGEMMET, 2001, Geologic maps from the instituto geoloógico, minero y metalúrgico del Perú, digital edition. Including: Mapa geológico del cuadrángulo Santo Tomás, hojas 29r–I, 29r–II, 29r–III, 29r–IV, escala 1:50.000, Mapa geológico del cuadrángulo Livitaca, hoja 29–s, escala 1:100.0000.

Ireland, T., 2010, Geological framework of the mineral deposits of the Collahuasi district, Región de Tarapacá, Chile [unpublished PhD Thesis]: University of Tasmania, 412 pp.

Ireland, T.R., and Williams, I.S., 2003, Considerations in zircon geochronology by SIMS, Reviews in Mineralogy and Geochemistry, v. 53, p. 215–241, Hanchar, J.M., and Hoskin, W.O., editors.

Jones, B., Kamenetsky, V.S., Davidson, P., and Allen, C.M., 2007, Antapaccay porphyry Cu–Au deposit: A product of Andean tectonism and evolving magmatism, late Eocene–early Oligocene Abancay batholith, Altiplano, southern Peru, *in* Ores and orogenesis: A symposium honoring the career of William R. Dickinson: Tucson, Arizona, Arizona Geological Society, p. 132–133.

Kent, A.J.R., Jacobsen, B., Peate, D.W., Waight, T.E., and Baker, J.A., 2004, Isotope dilution MC–ICP–MS rare earth element analysis of geochemical reference materials NIST SRM 610, NIST SRM 612, NIST SRM 614, BHVO–2G, BHVO–2, BCR–2G, JB–2, WS–1, W–2, AGV–1, AGV–2: Geostandards Newsletter, v. 28, no. 3, p. 417–430.

Klein, M., Stosch, H.G., and Seck, H.A., 1997, Partitioning of high field strength and rare–earth elements between amphibole and quartz–dioritic to tonalitic melts: An experimental study: Chemical Geology, v. 138, p. 257–271.

Klinck, B.A., Ellison, R.A., and Hawkins, M.P., 1986, The geology of the Cordillera Occidental and Altiplano west of Lake Titicaca, southern Peru: Lima, British Geological Survey, Instituto Geológico Minero y Metalúrgico, 353 p.

Koppers, A., and Duncan, B., 2003, High–resolution 40Ar/39Ar dating of the oldest oceanic basement basalts in the western Pacific basin: Geochemistry, Geophysics, Geosystems v. 4, no. 11, p. 1–20.

Landtwing, M.R., Furrer, C., Redmond, P.B., Pettke, T., Guillong, M., and Heinrich, C.A., 2010, The Bingham Canyon Porphyry Cu–Mo–Au Deposit. III. Zoned copper–gold ore deposition by magmatic vapor expansion: Economic Geology, v. 105, no. 1, p. 91–118.

Le Maitre, R.W., Bateman, P., Dudek, A., Keller, J., Lameyre, J., Le Bas, M.J., Sabine, P.A., Schmid, R., Sorensen, H., Streckeisen, A., Woolley, A.R., and Zanettin, B., 1989, A classification of igneous rocks and glossary of terms: Recommendations of the international union of geological sciences subcommission on the systematics of igneous rocks, Blackwell Scientific, Oxford.

Lee, R.G., 2008, Genesis of the El Salvador porphyry copper deposit, Chile and distribution of epithermal alteration at Lassen Peak, California [unpublished Ph.D. thesis]: Corvallis, OR, Oregon State University, 322 p.

Ligarda, R., 1989, Estudio geológico del cuadrángulo de Curahuasi (Departamento deApurimac) [Bachelor thesis]: Cusco, Universidad Nacional San Antonio Abad.

Loewen, M.W., and Kent, A.J., 2012, Sources of elemental fractionation and uncertainty during the analysis of semi–volatile metals in silicate glasses using LA–ICP–MS: Journal of Analytical and Atomic Spectrometry, v. 27, p. 1502–1508

Loucks, R.R., 2014, Distinctive Composition of Copper–Ore–Forming Arcmagmas: Australian Journal of Earth Sciences, v. 61, no, 1, p 5–16.

Ludwig, K.R., 2009, Squid 2, A user's manual, Berkeley Geochronology Center Special, Publication No. 5, 110 p.

Ludwig, K.R., 2012, Isoplot 3.75, a geochronological toolkit for Excel, Berkeley Geochronology Center Special Publication No. 5, 75 p.

Maher, K.C., 2010, Skarn alteration and mineralization at Coroccohuayco, Tintaya district, Peru: Economic Geology, v. 105, p. 263–283.

Mamani, M., Wörner, G., and Sempere, T., 2010, Geochemical variations in igneous rocks of the Central Andean orocline (13ºS to 18ºS): Tracing crustal thickening and magma generation through time and space: Geological Society of America Bulletin, v. 122, p. 162–182.

Markey, R.J., Stein, H.J., and Morgan, J.W., 1998, Highly precise Re–Os dating for molybdenite using alkaline fusion and NTIMS, Talanta, v. 45, p. 935–946.

Markey, R.J., Stein, H.J., Hannah, J.L., Selby, D., and Creaser, R.A., 2007, Standardizing Re–Os geochronology: A new molybdenite Reference Material (Henderson, USA) and the stoichiometry of Os salts: Chemical Geology, v. 244, p. 74–87.

Mondillo, N., Boni, M., Balassone, G., and Villa, I.M., 2014, The Yanque prospect (Peru): From polymetallic Zn–Pb mineralization to a nonsulfide deposit: Economic Geology, v. 109, p. 1735–1762.

Moore, G.M., and Carmichael, I.S.E., 1998, The hydrous phase equilibria (to 3 kbar) of an andesite and basaltic andesite from western Mexico: Constraints on water content and conditions of phenocryst growth: Contributions to Mineralogy and Petrology, v. 130, p. 304–319.

Naney, M.T., 1977, Phase Equilibria and Crystallization in Iron and Magnesium–bearing Granitic Systems [Unpublished Ph.D. thesis]: Stanford University.

Noble, D.C., McKee, E.H., Eyzaguirre, V.R., and Marocco, R., 1984, Age and regional tectonic and metallogenetic implications of igneous activity and mineralization in the Andahuaylas–Yauri belt of southern Peru: Economic Geology, v. 79, p. 172–176.

Oncken, O., Hindle, D., Kley, J., Elger, K., Victor, P., and Schemmann, K., 2006, Deformation of the Central Andean Upper Plate system—Facts, Fiction, and Constraints for Plateau Models: The Andes, p. 3–27.

Pecho, V., 1981, Geología de los cuadrángulos de Chalhuanca, Antabamba y Santo Tomás: Instituto de Geología, Minería y Metalurgia, Boletín n. 35, 67 p.

Perelló, J., Carlotto, V., Zarate, A., Ramos, P., Posso, H., Neyra, C., Caballero, A., Fuster, N., and Muhr, R., 2003, Porphyry–style alteration and mineralization of the middle Eocene to early Oligocene Andahuaylas–Yauri Belt: Economic Geology, v. 98, no. 8, p. 1575–1605.

Perelló, J. and Posso, C., 2011, Antilla: a supergene enriched porphyry copper deposit in the Andahuaylas–Yauri belt: ^{11}th SGA Biennial Metting, 26th–29th September 2011, Antofagasta, Chile, p. 917–920.

Proffett, 1979, Ore deposits of the western United States, A summary: Nevada Bureau of Mines and Geology, Report 33, p. 13–32.

Redmond, P.B., and Einaudi, M.Y., 2010, The Bingham Canyon Porphyry Cu–Mo–Au Deposit. I. Sequence of Intrusions, Vein Formation, and Sulfide Deposition: Economic Geology, v. 105, no. 1, p. 43.

Richards, J.P., 2011, High Sr./Y Arc magmas and porphyry Cu ±Mo ±Au deposits: Just add water: Economic Geology, v. 106, no. 7, p. 1075–1081.

Richards, J.P., Spell, T., Rameh, E., Razique, A., and Fletcher, T., 2012, High Sr/Y magmas reflect arc maturity, high magmatic water content, and porphyry Cu ± Mo ± Au potential: Examples from the Tethyan arcs of central and eastern Iran and western Pakistan: Economic Geology, v. 107, p. 295–332.

Rollinson, H.R., 1993, Using geochemical data: Evaluation, presentation, interpretation. J. Wiley & Sons, New, 352 pp.

Romick, J.D., Kay, S.M., and Kay, R.W., 1992, The influence of amphibole fractionation on the evolution of calc–alkaline andesite and dacite tephra from the central Aleutians, Alaska: Contributions to Mineralogy and Petrology, v. 112, p. 101–118.

Rooney, T.O., Franceschi, P., and Hall, C.M., 2011, Water–saturated magmas in the Panama Canal region: A precursor to adakite–like magma generation?: Contributions to Mineralogy and Petrology, v. 161, p. 373–388.

Seedorff, E., Dilles, J.H., Proffett, J.M., Jr., Einaudi, M.T., Zurcher, L., Stavast, W.J.A., Johnson, D.A., and Barton, M.D., 2005, Porphyry deposits: Characteristics and origin of hypogene features: Economic Geology 100TH Anniversay Volume, p. 251−298.

Selby, D. and Creaser, R.A., 2004, Macroscale NTIMS and microscale LA–MC–ICP–MS Re–Os isotopic analysis of molybdenite: Testing spatial restrictions for reliable Re–Os age determinations, and implications for the decoupling of Re and Os within molybdenite: Geochimica et Cosmochimica, Acta, v. 68, p. 3897–3908.

Sillitoe, R.H., 1998, Major regional factors favoring large size, high hypogene grade, elevated gold content and supergene oxidation and enrichment of porphyry copper deposits, *in* Porter, T.M., ed., Porphyry and hydrothermal copper and gold deposits: A global perspective: Adelaide, Australian Mineral Foundation, p. 21−34.

Sillitoe, R.H., 2010, Porphyry Copper Systems: Economic Geology, v. 105, no. 1, p. 3–41.

Sillitoe, R.H., and Perelló, J., 2005, Andean copper province: Tectonomagmatic settings, deposit types, metallogeny, exploration, and discovery: Economic Geology 100TH Anniversary Volume, p. 845−890.

Sisson, T.W., 1994, Hornblende–melt trace–element partitioning measured by ion microprobe: Chemical Geology, v. 117, p. 331–344.

Sláma, J., Košler, J., Condon, D.J., Crowley, J.L., Gerdes, A., Hanchar, J.M., Horstwood, M.S.A., Morris, G.A., Nasdala, L., Norberg N., Schaltegger, U., Schoene, B., Tubrett, M.N., and Whitehouse, M.J., 2008, Plešovice zircon – a new natural reference material for U–Pb and Hf isotopic microanalysis: Chemical Geology, v. 249, no. 1–2, p. 1–35.

Stacey, J. and Kramers, J.D., 1975, Approximation of terrestrial lead isotope evolution by a two–stage model: Earth and Planetary Science Letters, v. 26, p. 207–221.

Stolper E., 1982, Water in silicate glasses: An infrared spectroscopic technique, Contributions to Mineralogy and Petrology, v. 81, p. 1–17.

Streck, M.J., and Dilles, J.H., 1998, Sulfur Evolution of Oxidized Arc Magmas as Recorded in Apatite from a Porphyry Copper Batholith: Geology v. 26, no. 6: 523.

Takada, A., 1994, The influence of regional stress and magmatic input on styles of monogenetic and polygenetic volcanism: Journal of Geophysical Research, v. 99, p. 563−573.

Tosdal, R.M., Dilles, J.H., and Cooke, D.R., 2009, From Source to Sinks in Auriferous Magmatic–Hydrothermal Porphyry and Epithermal Deposits, Elements v. 5, p. 289–295, doi:10.2113/gselements.5.5.289.

Tosdal, R.M., and Richards, J.P., 2001, Magmatic and structural controls on the development of porphyry Cu ± Mo ± Au deposits: Reviews in Economic Geology, v. 14, p. 157−181.

Trail, D., Watson, E.B., and Tailby, N.D., 2011, The oxidation state of Hadean magmas and implications for early Earth's atmosphere: Nature, v. 480, p. 79−82.

Wang, F., Liu, S–A; Li, S., and He, Y., 2013, Contrasting zircon Hf–O isotopes and trace elements between ore–bearing and ore–barren adakitic rocks in central–eastern China: Implications for genetic relation to Cu–Au mineralization: Lithos, v. 156−159, p. 97−111.

Williams, I.S., 1998, U–Th–Pb geochronology by ion microprobe, *in* McKibben, M.A., Shanks III, W.C., Ridley, W.I., (Editors), Applications of microanalytical techniques to understanding mineralizing processes, Reviews in Economic Geology Special Publication 7: p. 1–35

Xstrata, 2014, Mineral resources and ore reserves as at 31 December 2014: Annual Report, 64 p. glencorexstrata.com.

2.10 Figures and Tables

Table 2.1. Petrography of the Haquira East intrusions

Lithology	Relation to ore	Texture		Felsic sites	Mafic sites	Matrix	Composition	Phot
Lahuani (La) sills	Pre-mineralization	Microporphyritic to equigranular. Common tectonic foliation.	A	40% plagioclase, euhedral, 2-5 mm.	5-10% hornblende. 1-2 mm. 5-10% biotite, 0.5-1 mm.	40% microcristalline. 0.05-0.1 mm. ksp, quartz, ± hornblende.	Quartz-monzodiorite (Andesite)	A
			B	40-50% plagioclase, subhedral, 1-2 (5) mm	20-30% hornblende, acicular. 1-2 mm. < 3% biotite.	20% microcristalline to aphanitic. 0.05-0.1 mm. K-fdsp, quartz, ± hornblende.	Quartz-monzodiorite to granodiorite. (Andesite to dacite)	B, K
Haquira granodiorite (HG) stock	Pre-mineralization	Transitional porphyritic tending to equigranular	A	50-70% plagioclase, subhedral, 2-7 mm.	10-15% hornblende. 1-2 mm. 10-15% biotite, 2-3 mm.	10-20% fine grained. 0.1 mm, ksp, quartz.	Quartz monzodiorite to granodiorite (Dacite to trachydacite)	C
			B	50-60% plagioclase, subhedral, 2-5 mm.	20-25% hornblende. 1-2 mm. 10-15% biotite, 2-3 mm.	10 % fine grained. 0.1 mm, ksp, quartz.		D
			C	60% plagioclase, subhedral, 3-6 mm. 0.5-2% quartz, subhedral quartz.	5-10%, hornblende. 1 mm. 5-10% biotite, 1 mm.	20-30% fine grained. 0.05-0.1 mm, ksp, quartz.		E
Haquira porphyry (Hp) dikes	Syn-Cu-Mo-mineralization	Porphyritic		30% plagioclase, subhedral, (80%, 5-8 mm and 20%, 1 mm). Ocasional quartz	5%, hornblende. 1 mm. 10% biotite, 2-3mm.	45-60% aplitic. 0.01-0.05 mm, Ksp, quartz.		F, G, H, J
Pararani porphyry (Pp) dikes	Post-Cu-Mo-mineralization (coeval with sericitic alteration)			30-60% plagioclase, subhedral (15%, 1-3 mm, 85%, 1 mm). 1% K-feldspar poikilitic anhedral megacrysts (<2 cm). 1-3% quartz, subhedral, 5-10 mm.	10-20 % hornblende, 1 mm.	30-45% aplitic. 0.01-0.05 mm, ksp, quartz.	Granodiorite to quartz monzodiorite. (Dacite)	I

Note: Compositional names are given after normative calculations from chemical compositions followed by the compositional range in TAS diagram in parenthesis. Trace minerals for all the intrusions are: magnetite, apatite, zircon and titanite.

Table 2.2. Representative whole rock analyses

	Lahuani sills A		Lahuani sills B		Haquira porphyry stock		Haquira porphyry dikes		Pararani porphyry dikes		Acojasa granodiorite		Cristo de los Andes ppy.
	FC-HAQ-142	FC-HAQ-144	FC-HAQ-135	FC-HAQ-137	FC-HAQ-17	FC-HAQ-34	FC-HAQ-145	FC-HAQ-154	FC-HAQ-160	FC-HAQ-164	FC-HAQ-175	FC-HAQ-177	FC-HAQ-182
wt. %													
Al_2O_3	16.00	16.50	16.15	16.30	16.10	16.85	16.55	15.65	15.75	15.85	18.30	17.55	16.30
CaO	4.15	4.01	4.78	3.96	3.46	2.86	2.35	3.55	2.02	3.20	6.55	5.47	1.22
Fe_2O_3	6.29	5.28	3.72	5.24	3.42	4.21	4.09	3.55	3.33	3.22	3.81	4.94	3.75
K_2O	2.77	2.62	3.47	2.77	3.33	2.85	2.89	3.17	2.70	2.55	1.02	1.56	2.98
MgO	2.67	2.33	2.17	2.31	1.54	1.92	1.59	1.47	1.33	1.54	1.56	1.40	2.08
MnO	0.12	0.09	0.07	0.09	0.08	0.08	0.08	0.09	0.08	0.09	0.10	0.14	0.07
Na_2O	3.45	3.78	3.98	4.17	4.02	4.63	4.26	4.12	4.82	4.69	5.31	4.07	5.22
P_2O_5	0.25	0.28	0.20	0.23	0.22	0.18	0.25	0.24	0.27	0.22	0.27	0.25	0.21
SiO_2	61.30	62.80	64.00	63.20	64.40	65.50	66.30	65.30	67.80	67.20	63.40	64.90	65.30
TiO_2	0.58	0.58	0.50	0.50	0.45	0.49	0.44	0.45	0.35	0.37	0.53	0.52	0.47
LOI	1.48	1.37	0.64	1.71	1.44	0.86	1.32	1.37	1.14	1.80	0.57	0.41	1.52
Total	99.31	99.89	99.95	100.68	98.73	100.69	100.36	99.31	99.82	101.00	101.52	101.31	99.33
ppm													
Ba	1275	1235	1410	990	1565	1295	1185	1995	1195	1485	466	513	1115
Ce	49.4	56.6	46.0	47.1	45.9	46.0	35.3	46.1	30.4	33.4	44.1	45.6	48.2
Co	15.3	14.5	12.0	11.9	10.2	15.9	13.1	9.8	11.2	8.8	5.7	8.3	11.6
Cr	70	70	80	70	60	70	60	50	60	60	60	50	70
Cs	3.4	1.4	0.5	0.7	2.1	0.9	1.0	0.8	1.4	1.6	0.6	1.2	1.2
Cu	2970	2040	2090	38	818	1815	871	504	11	11	11	8	3030
Dy	3.0	3.6	2.7	2.8	2.4	2.6	2.2	2.2	1.5	1.6	2.6	2.9	2.6
Er	1.6	1.5	1.4	1.3	1.2	1.4	1.0	1.1	0.9	0.7	1.6	1.7	1.4
Eu	1.0	1.0	0.8	0.9	1.0	1.0	0.7	0.8	0.6	0.7	0.9	1.1	1.1
Ga	21.0	19.7	18.6	17.9	21.2	21.5	19.2	18.8	19.7	18.9	19.5	18.1	19.6
Gd	3.4	3.5	3.0	2.8	2.7	3.1	1.7	2.6	2.0	2.0	3.2	3.1	3.5
Hf	3.9	3.5	4.0	3.9	3.4	3.6	3.9	4.2	3.4	3.6	3.5	3.2	3.7
Ho	0.6	0.6	0.5	0.5	0.4	0.4	0.5	0.5	0.3	0.3	0.5	0.5	0.5
La	24.8	28.2	23.0	23.2	22.3	23.2	17.8	23.3	15.6	16.8	22.2	24.7	24.2
Lu	0.3	0.2	0.3	0.3	0.2	0.2	0.2	0.2	0.1	0.1	0.2	0.3	0.2
Mo	5	4	12	4	3	5	5	2	3	2	2	3	2
Nb	5.8	6.1	6.5	6.1	6.5	6.0	5.8	5.0	3.5	3.3	6.3	5.1	3.7
Nd	20.0	23.5	18.8	18.3	18.8	19.7	15.3	19.4	13.2	14.1	17.9	17.7	24.3
Ni	43	43	44	65	45	187	44	32	38	33	32	35	51
Pb	7	7	9	8	11	9	16	9	25	14	7	6	7
Pr	5.5	6.4	5.0	5.0	5.0	5.2	4.0	5.4	3.5	3.9	4.9	5.0	6.0
Rb	79.5	69.6	63.0	80.8	73.9	67.3	72.8	58.9	81.7	71.6	32.3	52.0	66.6
Sc	13.2	13.5	11.1	10.6	8.0	8.1	9.0	7.8	6.0	6.1	9.0	7.7	9.4
Sm	3.5	4.6	3.6	2.8	3.2	3.4	2.7	3.8	2.7	2.8	4.0	3.9	4.7
Sn	1	1	2	1	BDL	1	1	2	1	2	1	1	2
Sr	886	949	943	757	954	1045	835	1005	899	924	472	431	750
Ta	0.5	0.5	0.5	0.5	0.6	0.5	0.5	0.4	0.3	0.3	0.5	0.5	0.4
Tb	0.5	0.6	0.4	0.4	0.4	0.4	0.3	0.4	0.3	0.3	0.5	0.5	0.5
Th	8.5	8.9	8.3	8.8	7.1	7.8	7.3	7.4	6.3	6.3	7.2	7.5	6.1
Tm	0.3	0.3	0.2	0.3	0.2	0.2	0.2	0.2	0.1	0.1	0.2	0.3	0.2
U	2.7	2.9	2.6	2.5	2.6	2.4	3.2	2.3	2.6	2.6	1.9	1.9	1.7
V	159	152	125	127	123	147	112	106	87	92	100	84	117
W	9.0	12.0	5.0	6.0	11.0	6.0	15.0	7.0	4.0	3.0	2.0	1.0	2.0
Y	16	18	16	15	14	14	12	13	9	9	16	16	15
Yb	1.5	1.7	1.4	1.5	1.3	1.2	1.2	1.3	1.0	1.0	1.7	1.6	1.3
Zn	67	60	56	53	52	50	67	53	79	72	57	60	68
Zr	129	121	127	134	112	123	122	152	115	123	129	118	136

Note: BDL = Below detection limit. See appendix for analythical details and sample location

Table 2.3. Isotopic ages

Sample	Age (Ma)	MSWD	Lithology	Method	Mineral
Haquira East					
FC-HAQ-017	33.85 ± 0.36	1.5	Haquira porphyry stock	U-Pb SHRIMP	Zircon
FC-HAQ-034	33.98 ± 0.31	1.4	Haquira porphyry dike		
FC-HAQ-135	34.41 ± 0.50	1.37	Lahuani sill (B)		
FC-HAQ-145	33.57 ± 0.74	3.1	Haquira porphyry dike		
FC-HAQ-164	34.15 ± 0.37	1.6	Pararani porphyry dike		
FC-HAQ-079	33.18 ± 0.21	0.04	D vein halo	^{40}Ar-^{39}Ar	Musc.
FC-HAQ-128	37.04 ± 0.19	0.09	Coarse muscovite in fracture		
FC-HAQ-001	33.86 ± 0.14		Banded molybdenite vein	Re-Os	Molybdenite
FC-HAQ-029	33.75 ± 0.14		Banded molybdenite vein		
FC-HAQ-156	33.93 ± 0.14		B vein (Bn-Cpy-Mo)		
Haquira West					
FC-HAQ-172	33.64 ± 0.14		Banded molybdenite vein		
Cristo de los Andes					
FC-HAQ-170	36.30 ± 0.15		Banded molybdenite vein		
replicate	36.31 ± 0.15				
FC-HAQ-182	36.7 ± 1.7	0.81	Cristo porphyry	U-Pb LA-ICP-MS	Zircon
Acojasa granodiorite					
FC-HAQ-177	37.3 ± 1.4	1.16	Acojasa granodiorite		
Dolores					
19541	38.5 ± 2.6	1.40	Tonalite porphyry		
21082	42.4 ± 1.7	1.12	Diorite porphyry		
23338	39.1 ± 1.5	1.20	Feldspar porphyry		
23539	43.1 ± 3.2	1.80	Quartz-monzonite porphyry		
24167	49.8 ± 1.6	1.12	Quartz-diorite porphyry		
24480	40.2 ± 2.6	2.20	Andesitic porphyry		
Zincore					
5205	33.8 ± 0.97	1.16	Diorite		
5217	37.8 ± 1.2	1.30	Microdiorite		
5228	36.2 ± 1.1	1.01	Hornblende diorite		
5301	39.3 ± 2.0	1.30	Diorite		
5308	39.4 ± 1.7	0.93	Quartz diorite		
5385	34.3 ± 1.6	0.83	Microdiorite		

Note: See appendix for sample locations. **Abbreviations:** Musc. = Muscovite, MSWD = Mean Standard Weigthed Deviation

Table 2.4. Representative analyses of trace elements in zircon

Lithology	Spot	La	Ce	Pr	Nd	Sm	Eu	Gd	Tb	Dy	Ho	Er	Tm	Yb	Lu	Hf	Eu_N/Eu_N*	$Ce^{(IV)}/Ce^{(III)}$	Ce_N/Ce_N*	Ce_N/Nd_N
		(ppm)																		
SHRIMP-RG																				
Acojasa granodiorite	FC-HAQ-117-01	0.12	7.48		0.75	1.59	0.76	13.49	4.57	49.73	20.77	93.78	22.53	213.87	44.99	10741	0.50	73	132	8
Lahuani sills B	FC-HAQ-135-02	0.01	23.57		0.79	1.28	0.56	8.55	2.32	26.40	9.51	38.95	8.63	72.58	13.45	10437	0.51	139	229	22
Haquira porphyry stock	FC-HAQ-017-11	0.03	40.34		0.85	2.10	1.40	24.09	9.37	116.55	55.92	275.95	66.18	614.07	127.07	12333	0.58	679	1188	40
	FC-HAQ-034-20	0.00	37.89		0.46	1.24	0.86	17.60	6.59	89.79	40.51	215.82	55.60	522.34	107.96	11884	0.56	1275	2097	62
Pararani porphyry dikes	FC-HAQ-164-06	0.01	10.85		0.12	0.41	0.27	3.76	1.59	22.94	12.32	75.69	21.91	249.69	66.00	14010	0.66	2434	3413	68
LA-ICP-MS																				
Acojasa granodiorite	FCHAQ177-01	0.10	10.47	0.06	0.47	0.90	0.41	9.56	3.45	46.92	18.10	95.71	26.13	239.89	59.43	13256	0.42	48	73	4
Lahuani sills B	FCHAQ135-18	0.19	44.73	0.37	1.39	2.53	1.36	24.33	7.28	89.12	32.50	171.48	36.18	280.30	66.74	9383	0.48	80	129	9
Haquira porphyry stock	FCHAQ017-19	BDL	41.33	0.03	0.49	1.38	0.89	12.36	4.41	71.55	27.20	158.54	39.43	429.96	78.51	9638	0.56	352	566	23
	FCHAQ034-21	BDL	44.83	0.02	0.33	1.53	1.18	16.68	5.72	75.33	31.44	148.26	36.45	356.61	85.73	11194	0.61	462	772	36
Pararani porphyry dikes	FCHAQ164-13	0.02	52.96	0.01	0.33	1.76	1.14	14.74	6.03	91.42	42.10	217.85	59.62	573.60	102.51	10076	0.57	580	1220	44

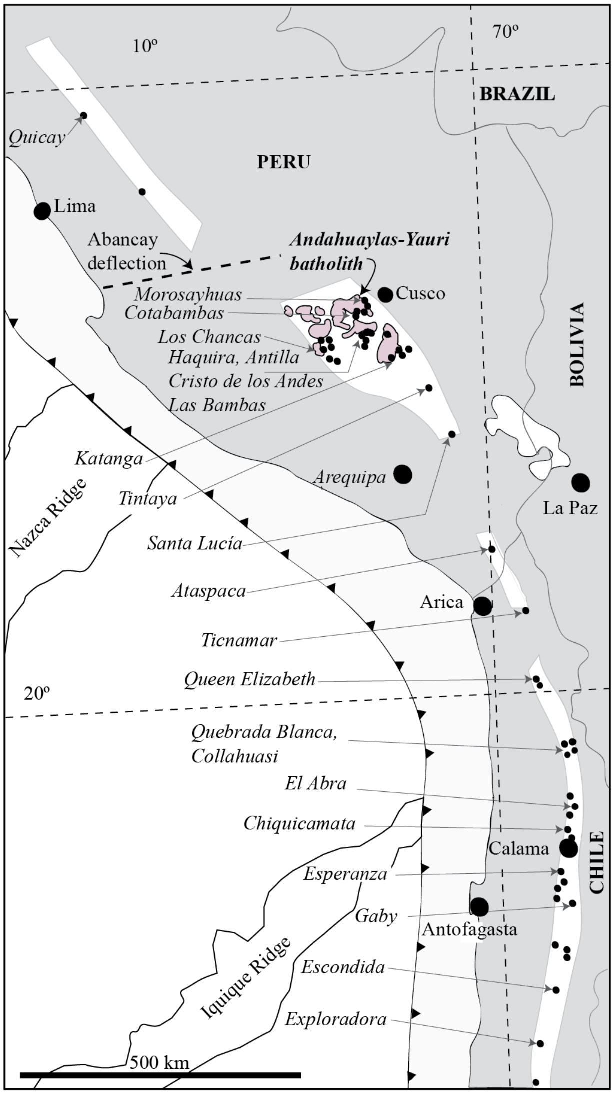

Figure 2.1. Location of the Andahuaylas-Yauri batholith and Haquira East in relation to the Eocene-Oligocene Andean belt of porphyry copper deposits. Modified from Perelló *et al.* (2003).

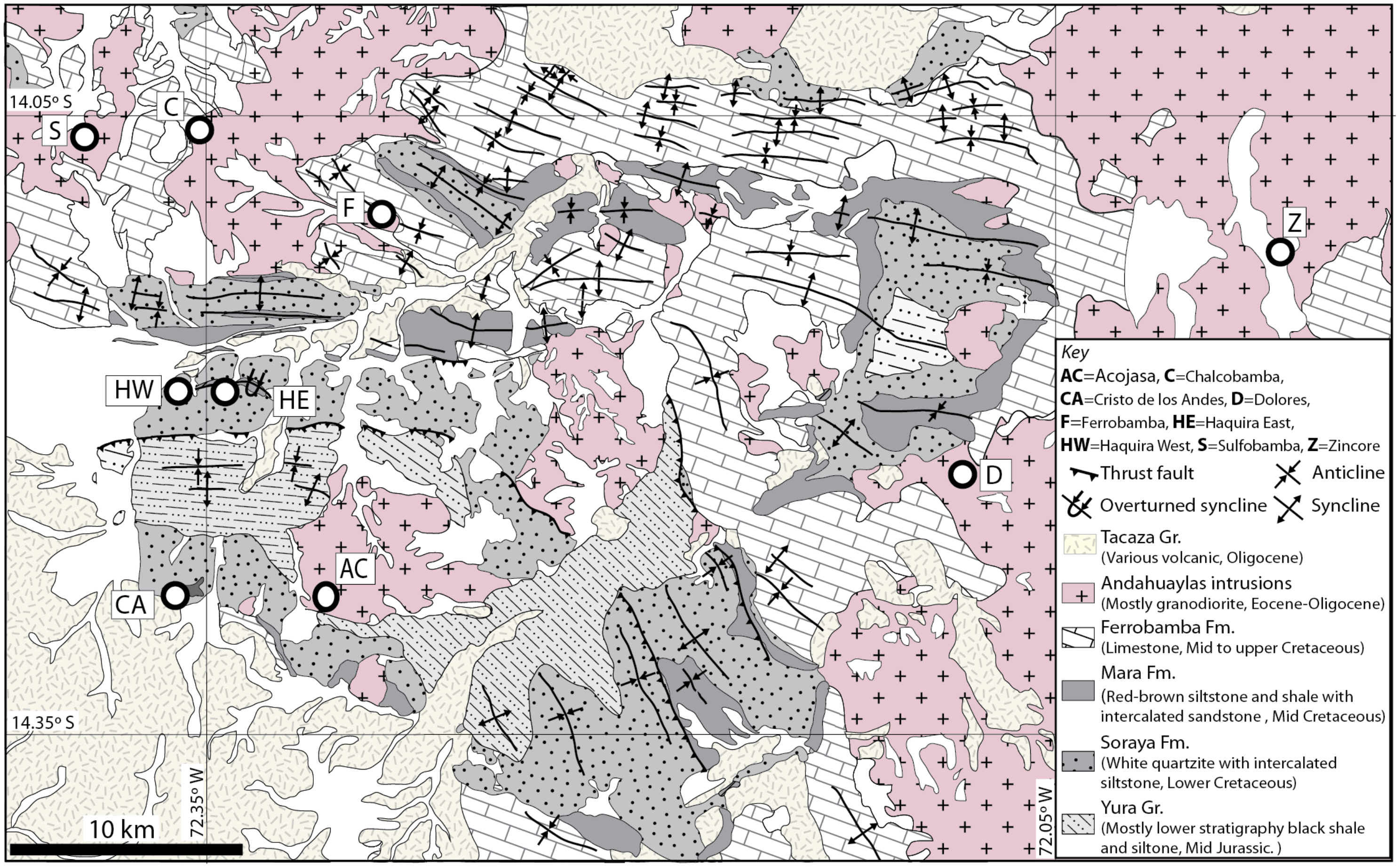

Figure 2.2. Geology map simplified from INGEMMET (2001) showing the location of the PCDs, skarns and prospects in relation to the Eocene-Oligocene Andahuaylas-Yauri batholith, the Jurassic-Cretaceous meta-sedimentary walk rock, and the younger Oligocene volcanics.

Figure 2.3. Cross-section 1900NW through the Haquira East PCD modified from Gans (2009). The Haquira granodiorite stock and dikes the quartzite and meta-siltstone beds of the Soraya Formation and red sandstone and mudstone of the Mara Formation in the thrust-faulted axis of the overturned Tocone syncline. The insert shows the location of the section and geology in map view.

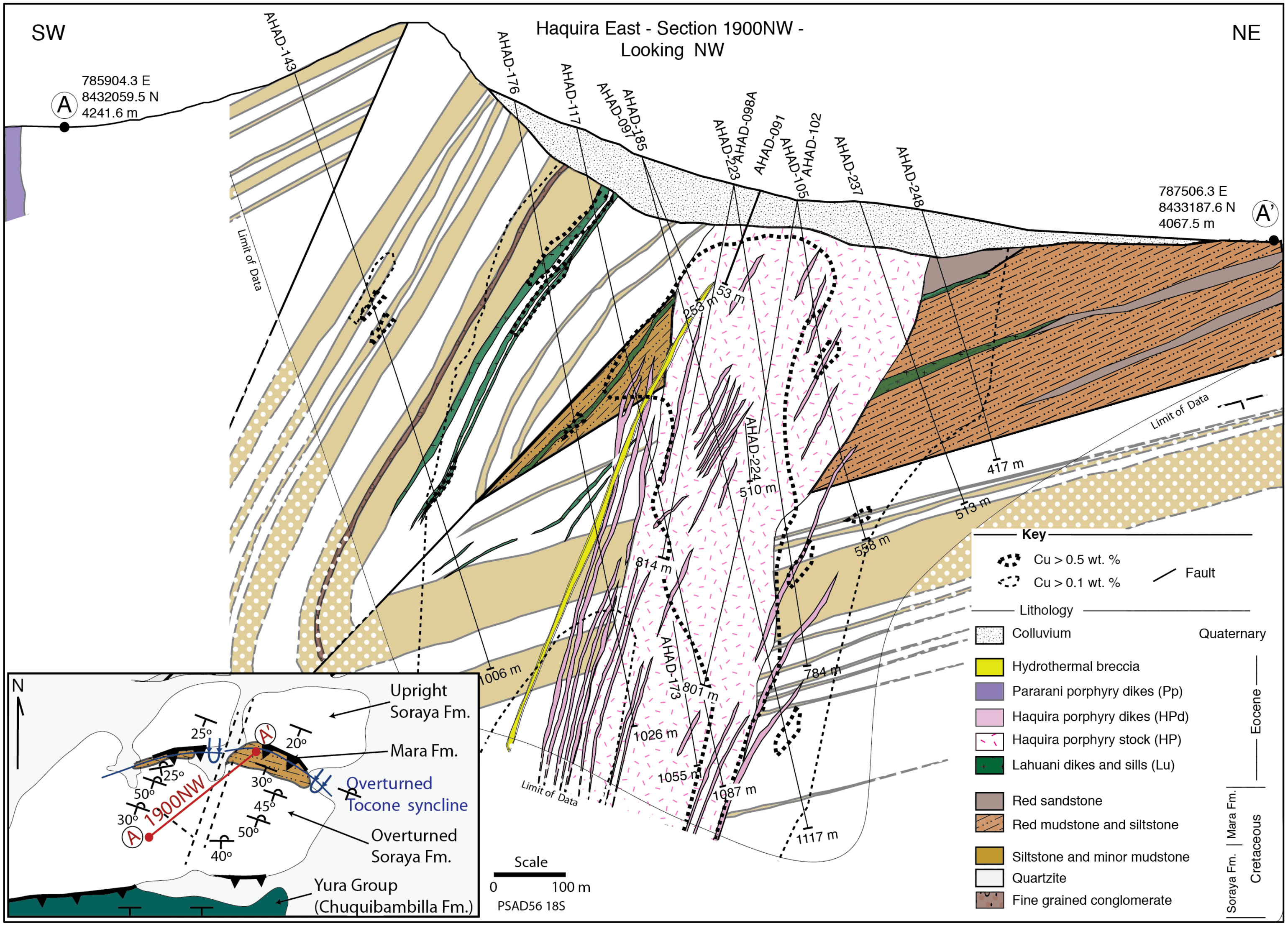

Figure 2.3. Cross-section 1900 NW through the Haquira East porphyry copper deposit

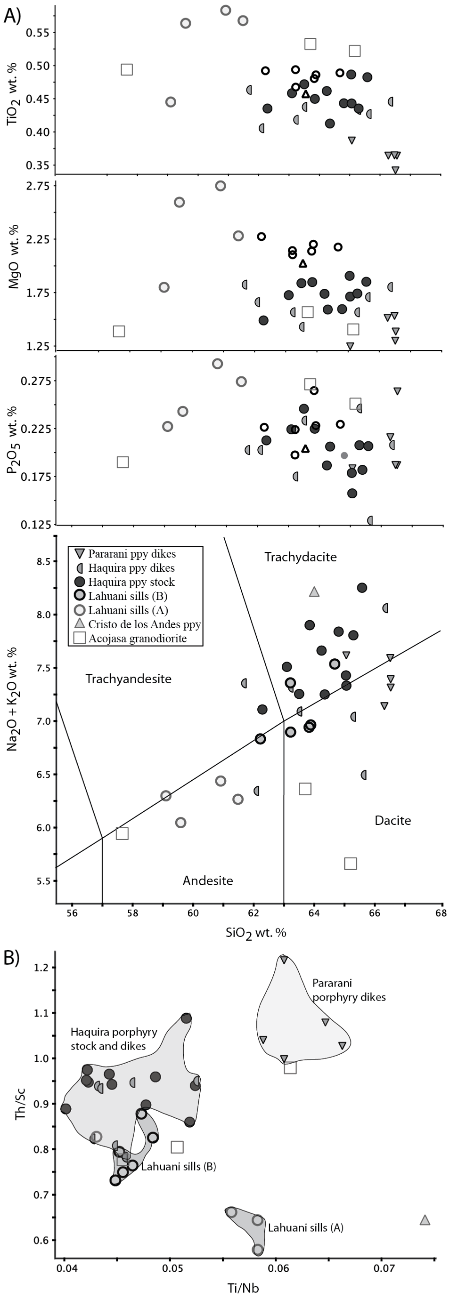

Figure 2.4. A) TiO_2, MgO, P_2O_5 and total alkalis (K_2O + N_2O) versus silica (SiO_2) (LeMaitre *et al.,* 1989) showing the composition of fresh and vein-less samples from Haquira East. Two samples from Cristo de los Andes and a nearby Andahuaylas-Yauri batholith intrusion are shown for comparison. The early Lahuani dikes and sills of type (A) are the only andesitic rocks from Haquira East. The rest of the intrusions present overlapping compositions that plot between the andesite, dacite and trachydacite fields. **B)** Th/Sc vs Ti/Nb plot showing distinct compositions for the Lahuani sills A and the Pararani porphyry dikes. The Haquira granodiorite stock and the Haquira porphyry dikes overlap in composition, while the Lh sills B only partially overlap.

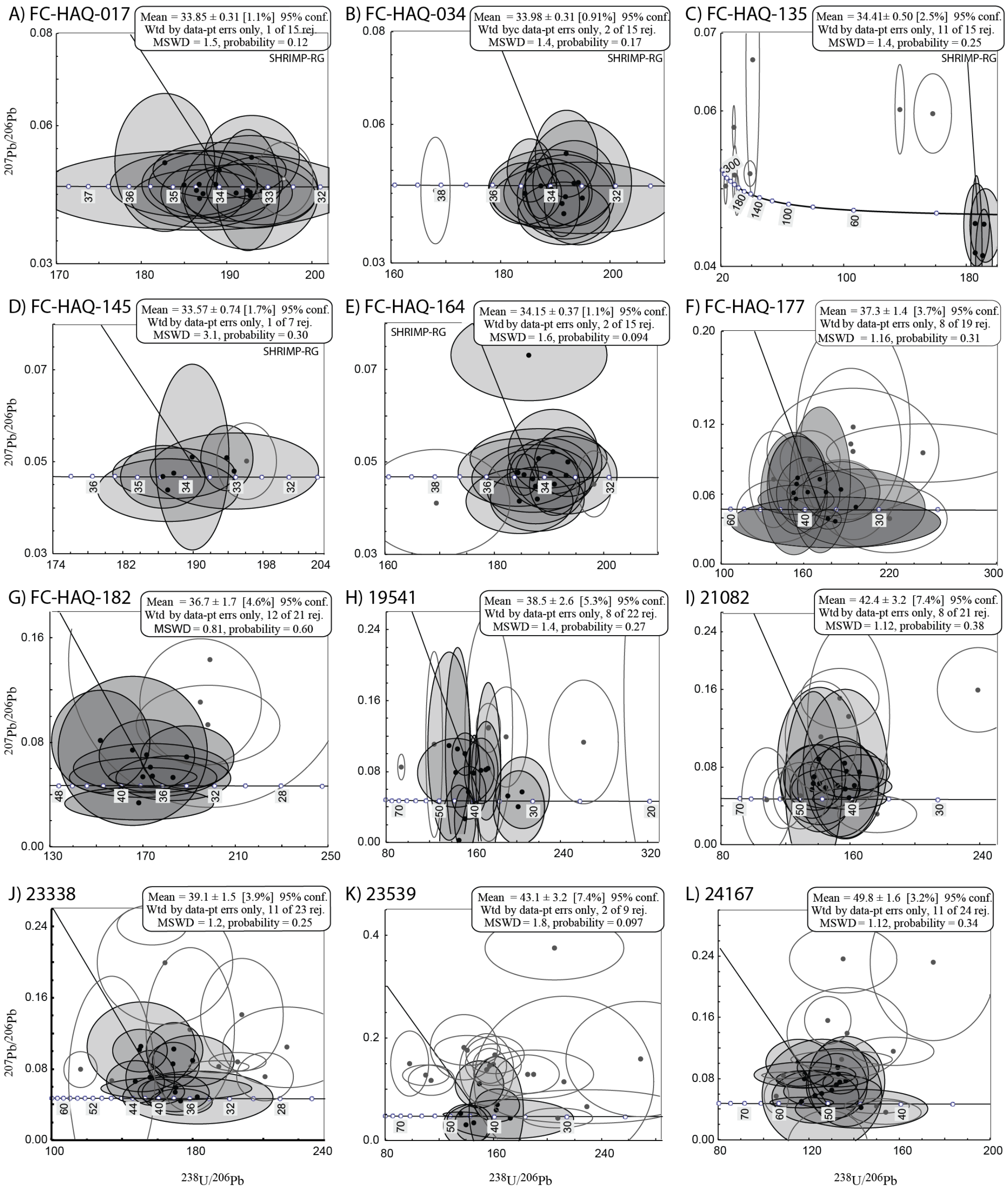

Figure 2.5. Inverse concordia plots for all the zircon samples dated by U-Pb. Ellipses are errors of two standard deviation (95 % confidence). Analyses in black were used to calculate the age, analyses in grey were discarded due to inheritance, discordance or Pb loss (see appendix). Weighted mean ages are also reported at 95% confidence.

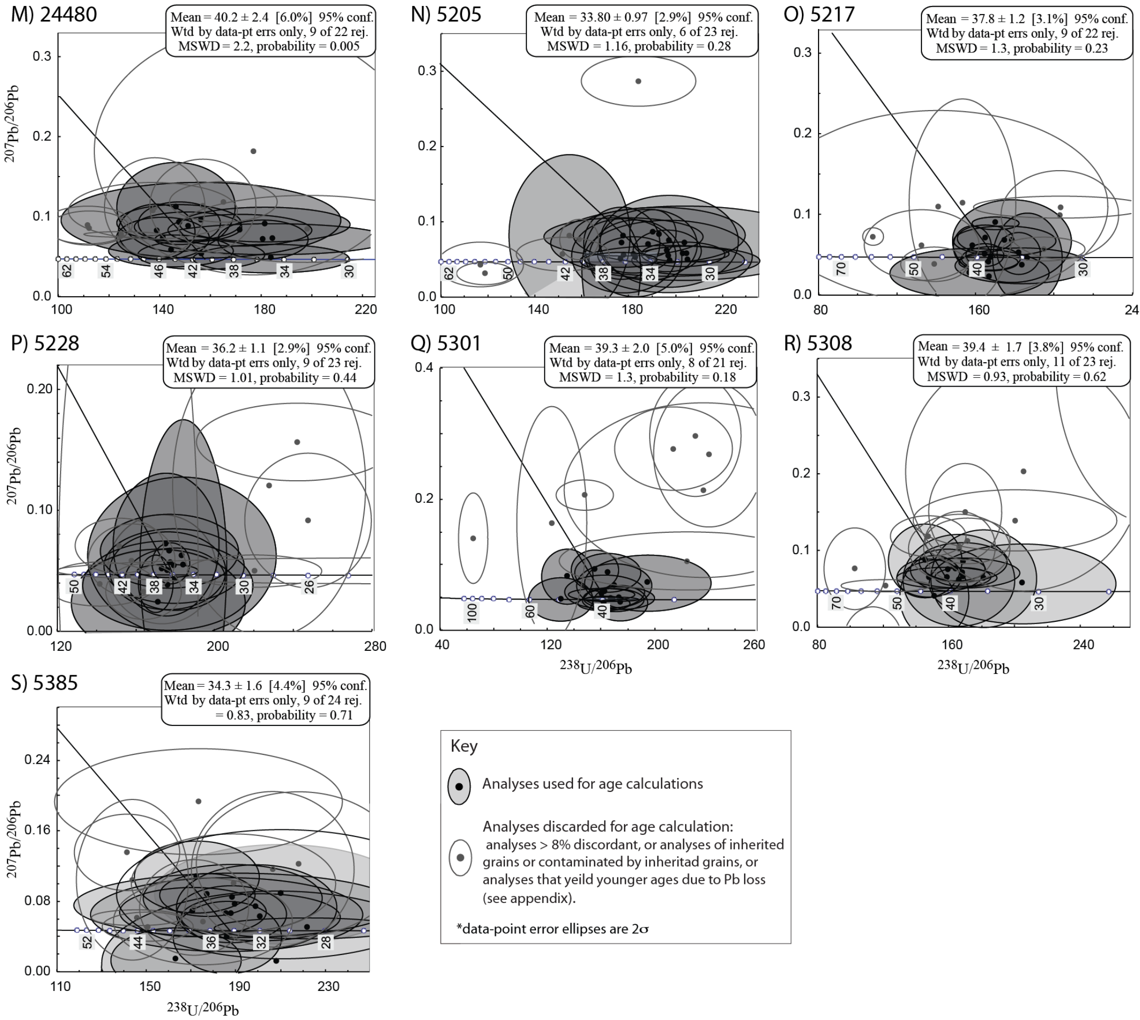

Figure 2.5. (Continued)

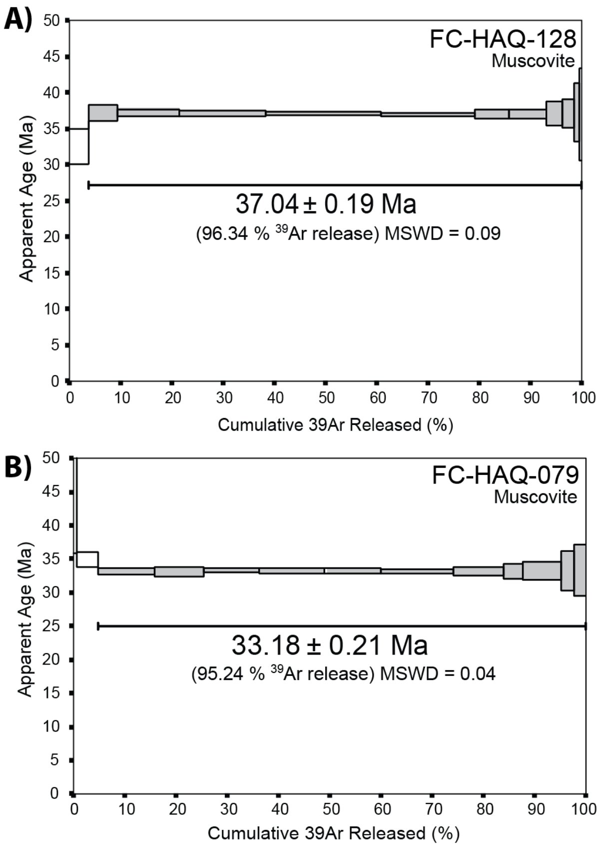

Figure 2.6. Apparent age versus cumulative ^{39}Ar release plots obtained by step heating for the two samples dated by ^{40}Ar/^{39}Ar in muscovite. The grey boxes indicate the steps that were used to calculate the plateau age.

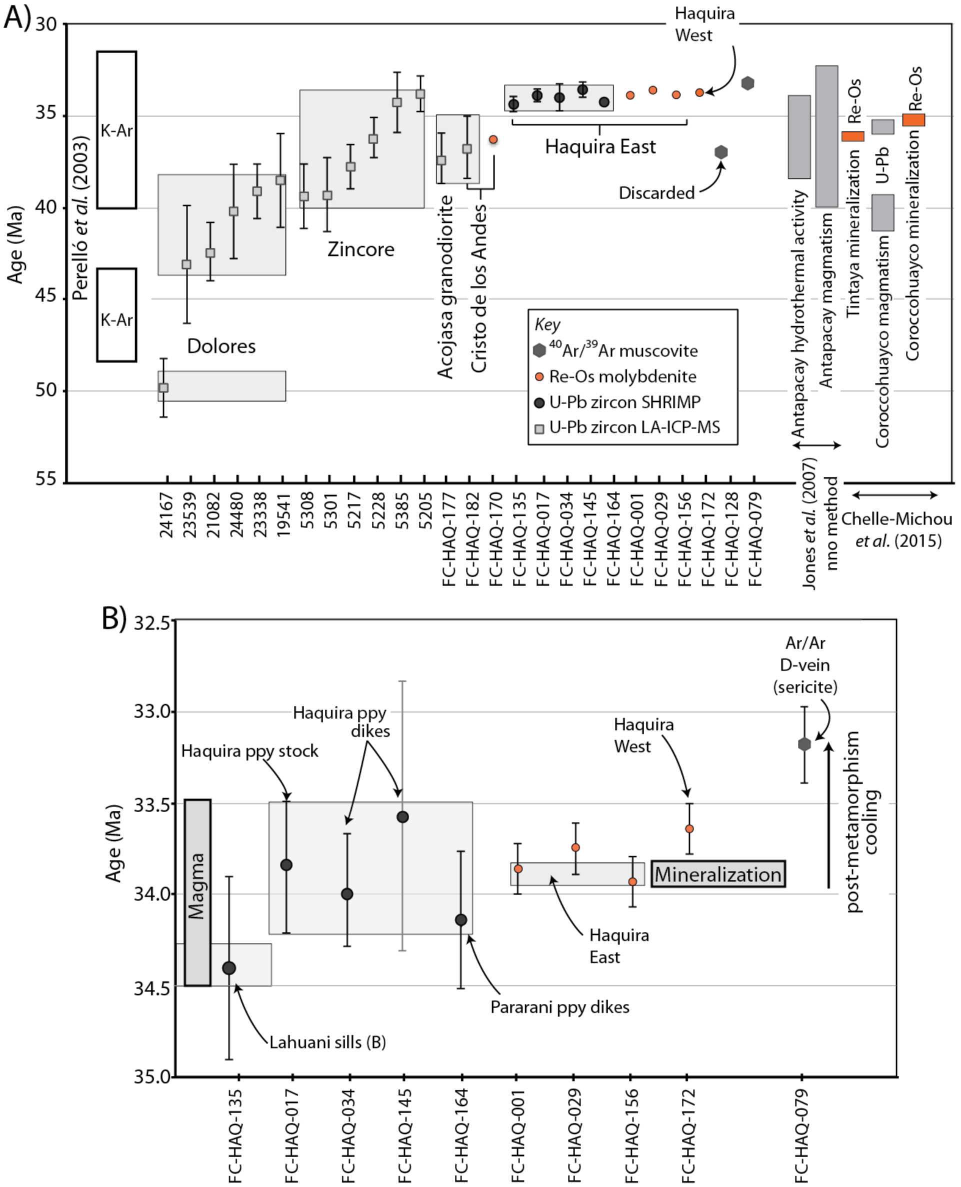

Figure 2.7. A) Ages of all the samples dated by U-Pb of zircon, Re/Os of molybdenite and ^{40}Ar/^{39}Ar of muscovite. Each of the copper-molybdenum deposits and prospects shows distinct but partially overlapping age ranges. Errors bars represent two standard deviations and in some cases they are included in the symbol size.**B)** The age of intrusions at Haquira-East range from ~34.5 to 33.5 Ma. Re/Os of molybdenite from banded quartz molybdentie and B veins overlap in average at ~33.85 ± 0.20 Ma. ^{40}Ar/^{39}Ar of muscovite from a quartz-pyrite-muscovite D vein has an age of 33.18 ± 0.18 Ma.

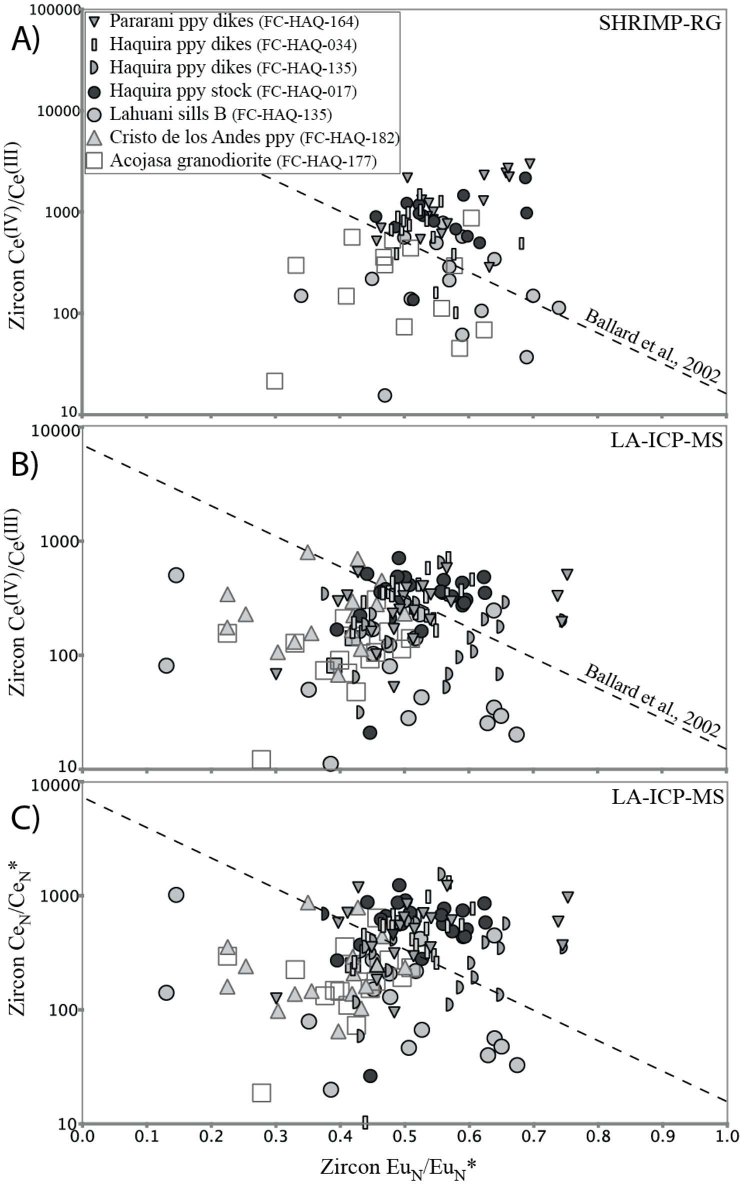

Figure 2.8. Different proxies for estimating the intensity of Ce anomaly plotted versus Eu_N/Eu_N* for zircon samples from Haquira East and Cristo de los Andes. The dotted line shows the boundary between non-productive intrusions and productive intrusions at higher $Ce^{(IV)}/Ce^{(III)}$ and Eu/Eu* from Ballard *et al.* (2002). Most of the analyses from the Haquira porphyry stock and dikes and the Pararani porphyry dikes plot here. **A)** $Ce^{(IV)}/Ce^{(III)}$ from SHRIMP-RG analyses, **B)** $Ce^{(IV)}/Ce^{(III)}$ from LA-ICP-MS analyses, **C)** Ce_N/Ce_N* from LA-ICP-MS analyses. See text for details on the calculation.

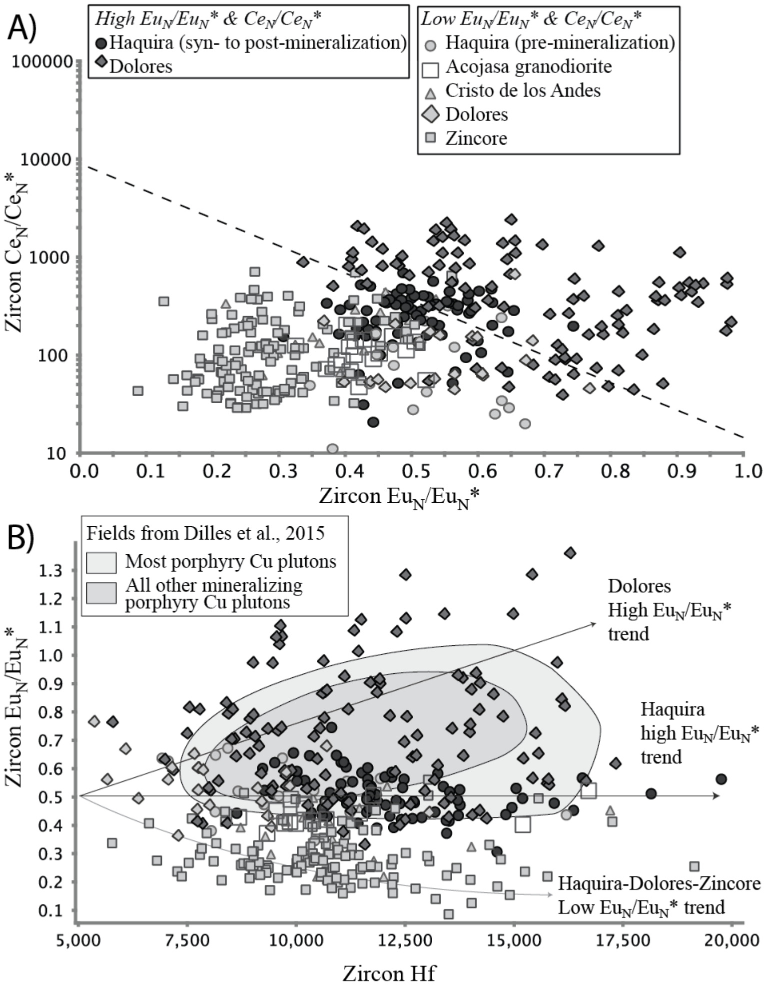

Figure 2.9. Zircon compositional data obtained with LA-ICP-MS from Dolores, Zincore, Haquira East and Cristo de los Andes. **A)** Ce_N/Ce_N^* versus Eu_N/Eu_N^*: all the samples from Dolores with the exception of samples 24167 plot in the productive field from Ballard *et al.* (2002) together with the syn- to post-mineralization samples from Haquira East (see Figure 2.10). **B)** $Eu/_NEu_N^*$ versus ^{179}Hf used as a proxy for fractionation, showing fields from Dilles *et al.* (2015). The pre-mineralization samples from Haquira East, all the samples from Zincore and sample 24167 from Dolores form a trend that reduces the Eu/Eu* as Hf increases. Syn- to post-mineralization samples from Haquira East form a trend at equal Eu_N/Eu_N^* as Hf increases, while ore-related samples form Dolores increase Eu_N/Eu_N^* as Hf increases.

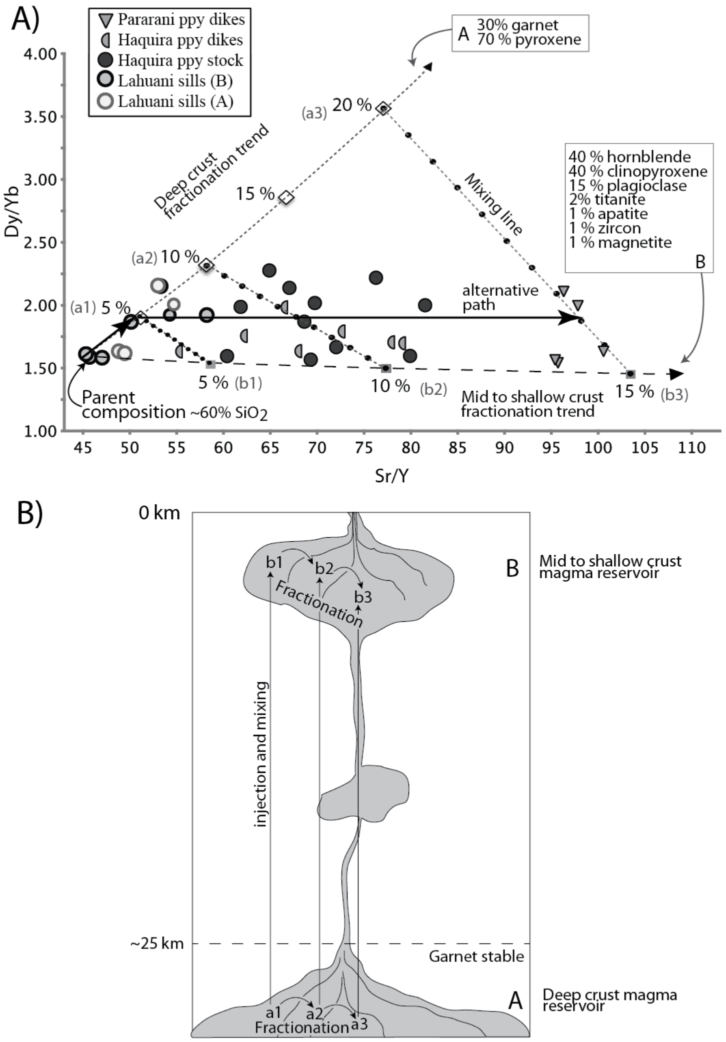

Figure 2.10. Sr/Y versus Dy/Yb plot. The samples of different intrusion from Haquira East plot between a deep crustal fractionation path responsible and a mid- to shallow-crust fractionation path. The samples aligned obliquely to the fractionation paths following mixing lines between end members.

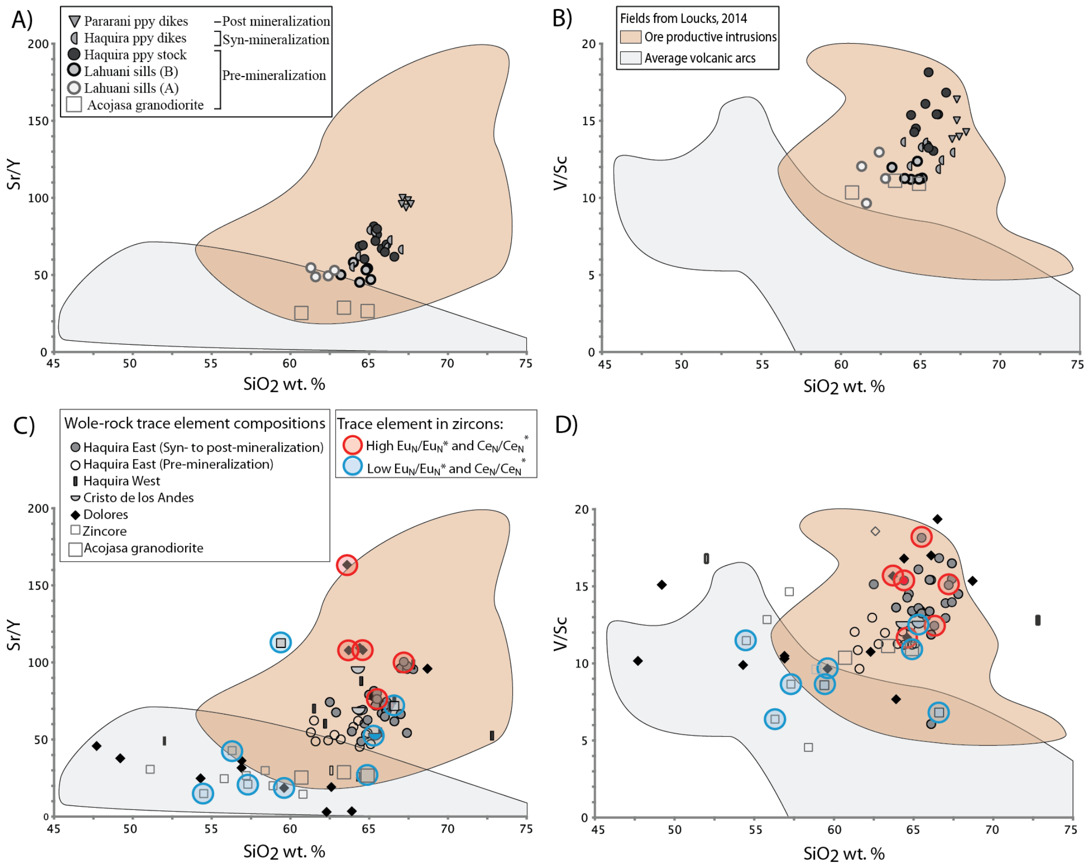

Figure 2.11. Whole-rock Sr/Y and V/Sc versus SiO_2 plots compared to the average volcanic arc and ore-productive intrusion fields from Loucks (2014). **A, B)** Only the samples from the Acojasa intrusion and some of the pre-mineralization Lahuani type A sills from Haquira East plot in the average volcanic arc fields. The syn- and post-mineralization samples from Haquira East plot on top of the ore productive intrusions field, or close to its boundary. **C, D)** Samples from Dolores, Zincore, Cristo de los Andes, Haquira East and Haquira West. The samples highlighted in red and blue where also analyzed for REE in zircons. The ones highlighted in red plot in the ore-related fields in a Eu_N/Eu_N* versus Ce_N/Ce_N^* plot, whereas the ones highlighted in blue plot in the normal-arc intrusion field.

Figure 2.12. Summary cartoon. **A)** The Lahuani sills intruded into meta-sedimentary contacts while the Tocone syncline was being folded during shortening. A shallow magma chamber, related to the Andahuaylas-Yauri batholith was created. **B)** Close to the time that the syncline is closed, overturned and thrusted, the Haquira granodiorite stock and the mineralizing Haquira porphyry dikes are intruded from a mid- to shallow-crust andesitic to dacitic magma chamber and form the Haquira Cu-Mo-mineralization. The Pararani porphyry dikes were emplaced shortly after from a deeper magma chamber. **C)** The geology tilted between ~10 and ~20^{o} to the northeast. The uplift and erosion during the compression shallowed the Haquira East intrusions and high grade Cu-Mo mineralization to close to surface levels.

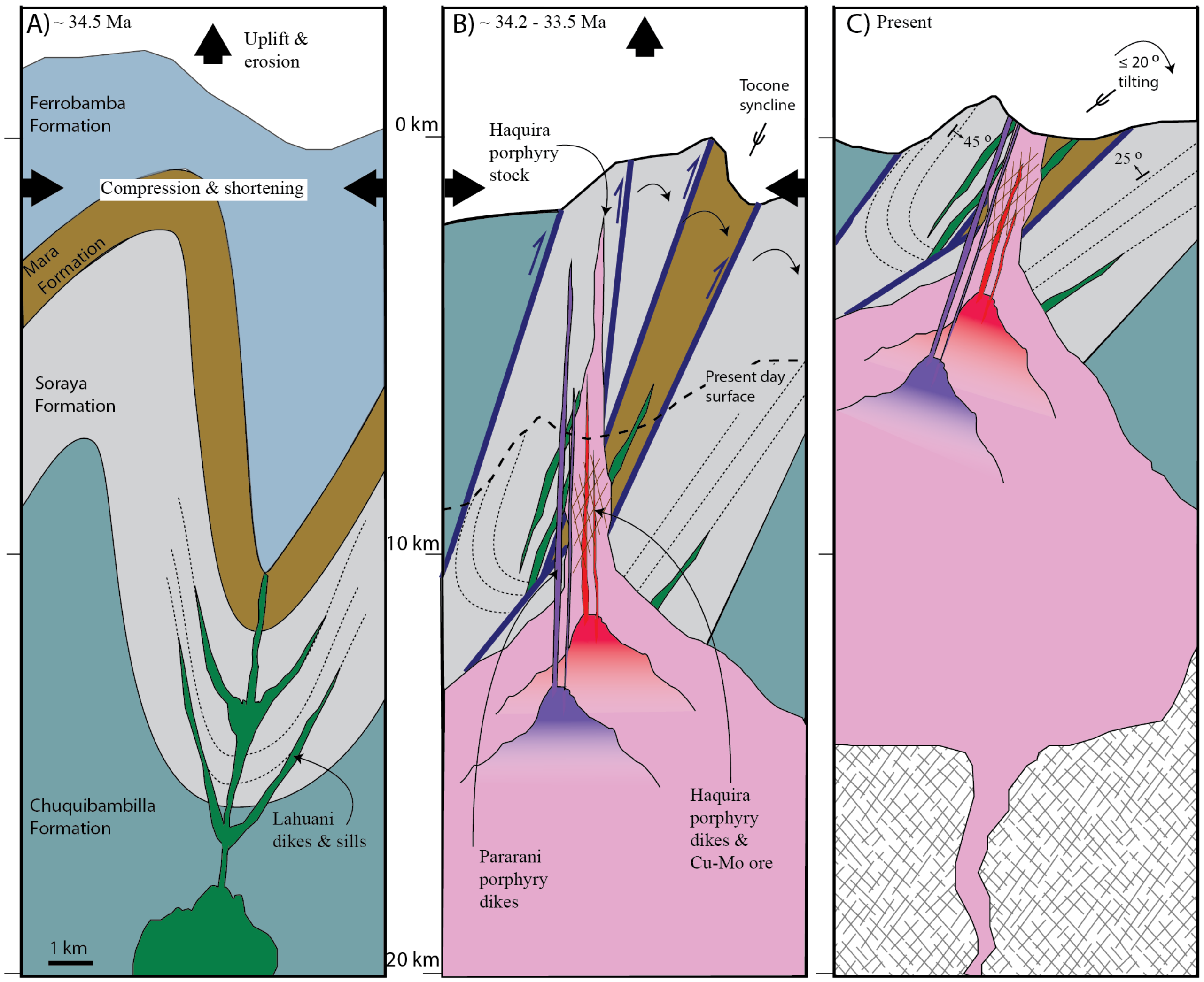

Figure 2.12. Summary cartoon.

Plate 2.1. Photographs of Haquira East intrusions and deformation recorded in quartz veins and aplites. **A)** Lahuani type A sill showing sheared-microporphyritic texture (AHAD089-96.85m). **B)** Lahuani type B sill showing alignment of the plagioclase phenocrysts (AHAD143-658m). There is a gradation of textures from Lahuani type A to Lahuani type B. **C, D, E)** Haquira granodiorite stock with up to 30% groundmass: **C, D)** slightly more mafic and finer-grained facies compared to E (AHAD105-205.9m; AHAD125-1091.15m), **E)** coarser-grained facies with occasional quartz phenocrysts (AHAD094-141.55m). **F, G, H)** Haquira porphyry dikes: **F)** Porphyry dike of similar composition to stock C, D, E but with 45-60% aplitic ground mass (AHAD117-731.95m), **G)** Haquira porphyry dike cross-cutting a folded aplite hosted in the Haquira granodiorite stock (AHAD181-661.2m), **H)** Bornite-chalcopyrite-bearing B vein cross-cutting the contact between the Haquira granodiorite stock and a Haquira porphyry dike (AHAD116-266m). **I)** Late Pararani porphyry dike with characteristic K-feldspar megacrysts (AHAD114-291.10m). **J)** Aplitic quartz and K-feldspar groundmass of a Haquira porphyry dike (FC-HAQ-151: AHAD108-475.25m), **K)** Alignment of hornblende between plagioclase phenocrysts in a Lahuani type A sill (FC-HAQ-140: AHAD166-443m). **L)** Folded banded quartz molybdenite vein re-opened by Cu-sulfides and cutting the Haquira granodiorite stock (AHAD185-834.5m) **M)** Folded deep quartz veins cutting meta-siltstones of the Soraya Formation (AHADXXX-105.35m).

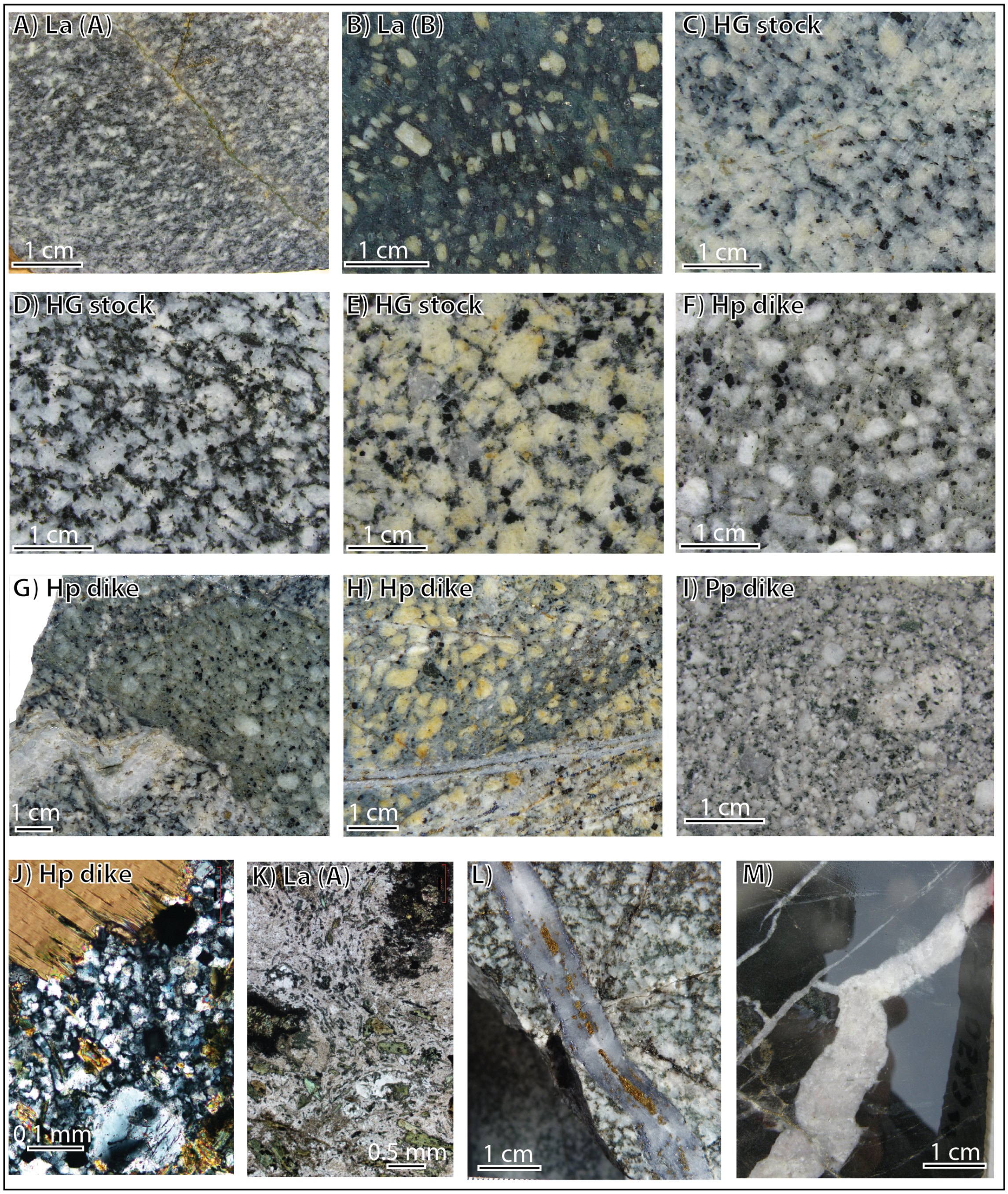

Plate 2.1. Photographs of Haquira East intrusions and deformation recorded in quartz and aplitic veins.

CHAPTER III

HYDROTHERMAL PARAGENESIS AND MINERALIZATION OF THE HAQUIRA EAST PORPHYRY COPPER DEPOSIT, PERU.

Federico Cernuschi
John H. Dilles
Marco T. Einaudi
Kalin Kouzmanov
Scott Halley

Draft to be submitted to Geosphere
A journal of the Geological Society of America

3.1 Abstract

Haquira East is a moderate-grade copper deposit with less molybdenum and gold, that is part of the Eocene-Oligocene Andahuaylas-Yauri porphyry belt of southern Peru. The subvertical Haquira granodiorite stock was emplaced at ~34 Ma in the southeast to northwest-trending and northeast-overturned quartzite and meta-siltstone Tocone syncline. New core logging observations, whole rock geochemistry and short wave infrared spectroscopy data are summarized in cross-sections and three-dimensional models and document the sequence and spatial distribution of veins, hydrothermal alteration and mineralization. From oldest to youngest, the sequence of veins and halos consists of biotite veins/micro-breccias, aplite dikes, deep quartz (DQ) veins, actinolite veins with plagioclase halos and epidote veins, early dark micaceous (EDM) halos with bornite-chalcopyrite, Cu-sulfide±quartz veinlets with chalcopyrite and/or bornite, banded molybdenite-quartz (BMQ) veins, B quartz-bornite-chalcopyrite veins, D pyrite-quartz-sericite veins with sericitic halos, and green and white intermediate argillic halos composed of illite-smectite-chlorite-kaolinite ± pyrite. EDM halos are alteration selvages formed around a central fracture that rarely have a central quartz vein. Scanning electron microscopy imaging (QMESCAN) reveals that the halos are composed of mixtures of hydrothermal biotite, muscovite, K-feldspar and rare quartz and corundum that replaces magmatic plagioclase and hornblendes of the Haquira granodiorite stock. EDM halos carry up to 10-15 % disseminated bornite and chalcopyrite and their distribution is correlated with the highest copper grades. The distribution of the latter BMQ veins is correlated with the highest molybdenum grades, whereas B veins are secondary but important contributors to both copper and molybdenum ores. The distribution of most Cu- and Mo-sulfide bearing halos and veins forms an inverted cup-shaped volume or shell above a K-silicate altered core zone of high-density aplites and DQ veins. The copper shell forms a continuous high-grade ore zone in the Haquira stock (>0.5 wt. %), but is low grade where it projects into the relatively non-reactive wall rock, mostly quartzites, likely as a result of a limited supply of iron to enable copper-iron sulfide precipitation. In contrast, molybdenite mineralization forms a roughly symmetric shell overlapping both stock and quartzite with an axis of symmetry located along the southwest flank of the Haquira granodiorite stock. The highest gold/copper ratios are coincident with the highest copper grades, suggesting that gold is hosted in bornite. Several sets of the narrow and subvertical Haquira porphyry dikes were emplaced synchronously with the development of K-silicate alteration, and the emplacement of aplites, DQ veins, EDM halos, BMQ and B veins. Whereas the K-silicate alteration and K-silicate stable veins dominate in the southwest-flank of the Haquira granodiorite stock where EDM halos,

BMQ and B veins constitute the Cu-Mo-ore, the actinolite veins are more abundant on sodic-calcic altered northeast-flank of the stock. The Pararani porphyry dike post date the copper and molybdenum ores and intruded synchronously with the development of sericitic alteration, D veins/sericitic halos and hydrothermal breccias.

3.2 Introduction

Porphyry Cu ± Mo ± Au deposits are large economic mineral deposits associated with shallowly emplaced arc-type granitoids mainly in convergent tectonic settings (Seedorff *et al.* 2005). Sulfide mineralization and hydrothermal alteration is intimately related to quartz-bearing veins and hydrothermal halos. Magmatic-hydrothermal fluid separates from cupolas atop a deep magma chamber and ascends by hydro-fracturing the overlying wall rock where it reacts with rock, cools, and depressurizes to form veins and Fe, Cu, Mo, and Au-bearing sulfides. Small volume porphyry dikes are emplaced synchronously (*e.g.* Burnham, 1979; Dilles, 1987).

The sequence, spatial distribution and paragenesis of veins and hydrothermal alteration relation to the distribution of the Cu- and Mo-ores have been studied in detail in a few porphyry deposits around the globe. The best know example is the seminal work by Gustafson and Hunt (1975) who described the intrusive and hydrothermal features at El Salvador in Chile. This and other similar work (*e.g.* Dilles and Einaudi, 1992; Atkinson *et al.,* 1996; Seedorff and Einaudi, 2004) enabled more recent detail studies and ultimately set the basis for the development of general models on porphyry deposit genesis. This type of research has also provided the basis for the development of successful exploration tools that contributed to the discovery of porphyry deposit elsewhere. Here we follow the approach of Gustafson and Hunt (1975) and present new vein and porphyry cross-cutting relations from the Haquira East Cu-Mo-Au porphyry deposit together with whole rock geochemistry, automated mineral analysis and textural imaging, and short wave infrared (SWIR) spectroscopy data.

Haquira East is a relatively high grade Cu-Mo deposit (689 Mt copper at 0.59% and a 0.3% cutoff and ~140 ppm Mo and containing a total of ~0.9 M oz of gold; Antares, 2010) hosted in a ~34 Ma subvertical granodiorite stock emplaced in the southeast to northwest-trending and northeast-overturned quartzite and meta-siltstone Tocone syncline (Fig. 3.1, Gans, 2009; Chapter 2). Haquira-East is part of the Eocene-Oligocene (~40-32 Ma) Andahuaylas-Yauri porphyry belt of southern Peru (Perello *et al*., 2003; Chapter 2).

The data presented here was obtained from previous exploration drill core from Antares Minerals LTD and First Quantum Minerals LTD that extensively sampled the concealed Haquira

East deposit. The data and interpretations are presented in a geologic map (Fig. 3.1), two parallel southwest to northeast cross-sections (Fig. 3.2 and 3.3) and one southeast to northwest cross-section (Fig. 3.4), together with short movies made with Leapfrog™ 3D modeling software that aids the visualization of the results (Movies 3.1 to 3.7). We reconstructed the relative timing of porphyry emplacement, vein/halo formation and hydrothermal paragenesis as well as the vein/halo distribution and their relation to the Cu-Mo ores.

3.3 Methods

Detailed core logging and geochemical sampling were conducted on cores from holes drilled at Haquira East and accompanied by reconnaissance geologic mapping (Fig. 3.1) of the area during several field seasons between 2011 and 2013. Core logging at 1/1,000 to 1/10,000 was conducted in all the drill-holes along cross-sections 1900NW (Fig. 3.2), 2100NW (Fig. 3.3) and 1200NE (Fig. 3.4). Along these cross-sections, 1,035 one-meter long split drill-hole core samples were analyzed at ALS-Global (Canada) using four acid digestion followed by inductively coupled plasma mass spectroscopy (ICP-MS). A total of 30,044 one-meter long split drill-hole core samples from all available drill-holes at Haquira East were analyzed at ALS-Global using aqua regia digestion followed by inductively coupled plasma optical emission spectrometry (ICP-OES). First Quantum Minerals LTD provided all the samples. Details on the whole rock methods can be found on the appendix. Standard transmitted and reflected light microscopy and petrographic techniques were used to describe the mineralogy and textures of the veins, hydrothermal halos and wall rock hydrothermal alteration.

Short wave infrared spectroscopy (SWIR) was used for the identification of hydrous minerals (Thompson *et al.,* 1999) and was performed on drill-hole split faces every 2 m throughout all the drill-hole core using an ASD Terraspec™. A total of 33,296 analyses were obtained with 2 cm diameter spots at a 5 nm spectral resolution (Zhaoshan and Yang, 2012) by First Quantum Minerals LTD staff in Arequipa, Peru. Reflected infrared radiation was measured between 400 to 2500 nm. The spectra were analyzed with the aid of The Spectral Geologist™ software which was used to identify the wavelength of each characteristic absorption feature and compare the obtained spectra with reference standards (see Clark *et al.,* 2007, Thompson *et al.,* 1999 and Goetz *et al.,* 2009). The mineral identifications were limited to hydrous minerals that are well characterized in SWIR, and that are common in porphyry copper deposits, including hornblende, biotite, muscovite-illite, kaolinite and smectites.

SWIR analyzes were also performed with a HCI-2 spectrometer by CORESCAN^{TM} on 176 thin section billets of wall rock and vein samples using a 0.5x0.5 mm analytical spot at 4 nm spectral resolution at CORESCAN facilities in Perth, Australia. The data were then analyzed with CORESCAN^{TM} software to identify a mineral on the basis of the strongest SWIR absorption (see ASD method above), and to produce a color-coded raster image of the identified minerals.

Ten samples were analyzed using X-Ray Diffraction (XRD) at Oregon State University, using a Philips XRG 3100 with Datascan 3.1 digital data collection. Scans were performed between 5 to 60 degrees at 0.04 degree steps and 1.5 seconds per step. Jade^{TM} 5.0 software was used for mineral identification using peak-fitting (ICDF, 1978).

Automated mineral analysis and textural imaging of the studied samples were performed using an FEI QEMSCAN® Quanta 650F facility at the Department of Earth Sciences, University of Geneva, Switzerland. The system is equipped with two Bruker QUANTAX light-element energy dispersive X-ray spectrometers. Analyses were conducted at high vacuum, accelerating voltage of 25 kV, and probe current of 10 nA on carbon-coated polished thin sections. FieldImage operating mode (Pirrie *et al.,* 2004) was used for analyses. Between 15 and 325 individual fields were measured per sample, with 1500, 1000 or 400 pixels per field, depending on the applied point spacing - 5, 3 or 1µm, respectively. X-ray spectra acquisition time was 10 ms per pixel. Gray-scale (GS) level of BSE images was calibrated using quartz (42), copper (130) and gold (232) standards. Data processing was performed using the iDiscover software package. Final results consist of: i) high-quality spatially resolved and fully quantified mineralogical maps enabling basic image analysis, including particle size and shape distribution, mineral assemblages and mineral proportion definitions; ii) BSE images with identical resolution as the mineralogical maps; iii) X-ray element distribution maps.

Three-dimensional models of the intrusions, vein distribution and ore grades were calculated using Leapfrog^{TM} software. Leapfrog implicit modeling (Cowan *et al.,* 2003) uses radial basis functions (RBFs) to model 3D wireframes from the data. The RBF modeling is mathematically equivalent to dual krigging (Carr *et al.,* 2001; Chiles and Delfiner, 1999; Costa *et al.,* 1999). In practice modeled ore grades using RBFs are virtually indistinguishable to those produced by the generally accepted method of ordinary krigging where the data spacing is less than the range of the variogram (Stewart *et al.,* 2014). To partially account for heterogeneity in the distribution of the drill-hole data, all the modeled volumes are shown in solid color where the data are abundant and the modeled results are included within drill-holes that overlap at < 100 m radius. The volumes are shown with a gray pattern overly where the data density is less and contiguous drill-holes do not overlap at < 100 m radius. The modeled volumes are shown in conjunction with the map, cross-sections and drill-hole core data in narrated Movies 3.1 to 3.7 for visualization purposes. The interpretations and conclusion presented here are drawn solely from the interpretation of porphyry and vein cross-cutting relations, drill-hole logs summarized in the cross-sections, geologic mapping and drill-hole core compositional data.

3.4 Results

3.4.1 *Geology*

The main geologic features of Haquira East (Fig. 3.1) are presented in Figure 2.3 of Chapter 2 in cross-section 1900NW (together with the petrography, whole-rock composition and isotopic ages of the freshest intrusion samples). Here we summarize the geology in cross-section 1900NW (Fig. 3.2) and present it in new cross-sections 2100 NW (Fig. 3.3) and 1200 NE (Fig. 3.4) as well as in 3D Movie 31. The location of the cross-sections are shown in Figure 3.1.

The quartzites, minor siltstones and carbonaceous mudstones of the Soraya formation (Pecho, 1981) are folded into the southeast to northwest-trending and southwest-verging overturned Tocone syncline, with the younger reddish mudstones and minor sandstones of the Mara formation (Pecho, 1981) in its center. The overturned syncline is accompanied by thrust faults parallel to its axial plane that displace the Soraya and Mara Formation (Figs. 3.1, 3.2, 3.3, 3.4).

The ~34.4 Ma pre-mineralization quartz-monzodiorite to granodiorite Lahuani intrusions were emplaced as 1 to 15 m thick sills, and were folded, faulted and sometimes sheared together with the Soraya and Mara formations (Gans, 2009; Chapter 2). Later intrusions overlap in age between ~34.2 and 33.5 Ma (U/Pb in zircons, Chapter 2), but their relative timing is resolvable by cross-cutting relationships.

Three end-member textural variations form the non-outcropping and northwest-elongated (~1 km x 0.5 km) plug-like body of the pre-mineralization Haquira granodiorite stock. The stock plunges 70º to 80º to the southwest and appears to continue below the maximum drilling depth of 1 km. It intruded both the upright and overturned limbs of the Tocone syncline, (Fig. 3.2, Gans, 2009).

The Haquira porphyry dikes are a set of narrow (20 cm to <10 m wide) and discontinuous sub-vertical dikes that cross cut the Haquira granodiorite stock and are compositionally indistinguishable from the stock (Chapter 1). The Haquira porphyry dikes are inferred to dominantly strike ~N50ºE but a northwest-striking set may also be present. The groundmass of the dikes differs from the groundmass of the stock and present a 45 to 60% quartz and K-feldspar aplitic matrix of 0.01 to 0.05 mm grain size, which has been identified in porphyry dikes related to porphyry copper mineralization elsewhere (*e.g.* Dilles, 1987).

Several sets of Haquira porphyry dikes were emplaced synchronously with the porphyry copper and molybdenum mineralization, veining and K-silicate hydrothermal alteration and are therefore possibly the causative intrusions (Cernuschi *et al.,* 2012; 2013; Chapter 2). The densest concentrations of the dikes were observed at depth in the low-grade Cu to "barren" core (Fig. 3.1; Movie 3.1).

At the waning stages of the magmatism (~33.5 Ma), the subvertical granodiorititic to quartz-monzodioritic Pararani porphyry dikes were emplaced along a north-south strike and closely in time with D veins, sericitic halos and sericitically altered hydrothermal breccias (Fig. 3.4).

3.4.2 Cu and Mo ores and sulfide distribution

When plotting the drill-hole core aqua regia whole rock analysis, the high-grade 0.5 wt. % Cu-ore forms an inverted cup shape (~ 850 m x 350 m) on top of a vertically elongated low-grade Cu to "barren" core (~ 500 m x 300 m, Cernuschi *et al.,* 2013; Figs. 3.2, 3.3, 3.4; Movie 3.2). The Haquira granodiorite stock is strongly mineralized in narrow sub-vertical zones with high density of bornite-chalcopyrite bearing EDM halos and B veins. However, where the copper shell projects into the meta-sedimentary wall rock, mainly composed of quartzites, the Cu-grades are low and hosted by a low density of Cu-sulfide±quartz veinlets. In the meta-sedimentary wall rock, the high-grade Cu-ore is only observed where the early Lahuani sills are intercepted, or where narrow carbonaceous silt intercalations within the quartzites present skarn-like replacements with Cu-sulfides that produce local intercepts of > 0.5 wt. % Cu (Fig. 3.2). The vein and halo distribution is reflected by the anomalous 0.1 wt. % Cu that is uniformly distributed through both wall rock types (Figs. 3.2, 3.3, 3.4; Movie 3.2). A very low-grade Cu (< 0.1 wt. %) to "barren" core is observed at depth and close to the southwest-flank of the Haquira granodiorite stock.

The anomalous Mo >5 ppm samples are uniformly distributed across the southwest contact of the Haquira granodiorite stock and the meta-sedimentary wall rock. The anomalous molybdenum shell (~ 900 m x 400 m) outboards the distribution of the low-grade Cu (>0.1 wt. %, Figs., 3.2, 3.3, 3.4; Movie 3.2). There is a low Mo-grade core (< 5 ppm) that is partially coincident with the location of the low-grade Cu core. The relatively high-grade Mo (>50 ppm) forms and inverted cup shape (~1.000 m x 550 m) and is partially coincident with, and outboards the high-grade Cu-ore (> 0.5 wt. %). However, the high-grade Mo is not restricted to the Haquira granodiorite stock, and extends into the meta-sedimentary wall rock (Figs. 3.2, 3.3, 3.4; Movie 3.2). At very high-grade Mo (> 100 ppm), the Mo-ore is partially restricted to the Haquira granodiorite stock similarly to the high-grade Cu-ore (Movie 3.2).

The sulfide distribution logged from drill-hole core is shown in the cross-sections in Figures 3.2, 3.3 and 3.4). The occurrence of bornite is restricted to a vertically elongated central zone (~900 m x 400 m), where it is commonly found with chalcopyrite. The bornite distribution mostly overlaps with the 0.5 wt. % Cu-ore shell in the Haquira granodiorite stock. This zone apparently dips 70º to 80º W and mimics the tilting of the Haquira granodiorite stock. The bornite center is surrounded by a chalcopyrite dominated zone with less pyrite that only partially overlaps with the outer margins of the 0.5 wt. % Cu-ore shell, and extends between ~100 to 200 m outside of the bornite zone. An outer zone of pyrite with less chalcopyrite surrounds the chalcopyrite dominated zone and extends at least 400 m from the chalcopyrite zone and only presents low-grade Cu (≤ 0.1 wt. % Cu). A weathered zone of up to 150 m overlies the center of the deposit where the Cu-Fe- and Fe-sulfides were oxidized to mixtures of goethite, hematite and Cu-oxides.

The sulfide mineralogy was also calculated from whole-rock analyses (aqua regia/ICP-OES). Based on the relative proportions of Cu, S and Fe in Cu-sulfides a ternary diagram was used to discriminate samples dominated by bornite (Bn), chalcopyrite (Cpy), mixtures of chalcopyrite-pyrite, pyrite (Py) and Cu-oxides (Fig. 3.5a). A plot of Cu versus Au (Fig. 3.5b) was used to aid the discrimination of bornite from chalcopyrite, as bornite incorporates larger quantities of Au and Ag (Au ≤ 0.5 ppm) than chalcopyrite (Au ≤ 0.1 ppm). Note that the logged Cu-sulfide distribution and zoning matches the Cu-sulfide distribution and zoning calculated from the whole-rock data (Movie 3.3).

3.4.3 Dikes, veins and alteration halos

Vein and porphyry dike cross-cutting relationships are summarized in Table 3.1. Only the vein and porphyry cross-cutting observations with unequivocal displacement (*e.g.* Plate 3.1E) were recorded in this table, following the approach of Seedorff and Einaudi (2004). The mineral paragenesis of each vein type are summarized in Table 3.2 and representative photographs are shown in Plates 3.1 to 3.4. The distribution and abundance of veins is shown in the three cross-sections (Fig. 3.2, 3.3, 3.4) and in Movie 3.4.

From oldest to youngest, the sequence of veins and halos consists of biotite veins/micro-breccias, aplite dikes, deep quartz (DQ) veins, actinolite veins with plagioclase halos and epidote veins, early dark micaceous (EDM) halos with bornite-chalcopyrite, Cu-sulfide±quartz veinlets with chalcopyrite and/or bornite, banded molybdenite-quartz (BMQ) veins, B quartz-bornite-chalcopyrite veins, D pyrite-quartz-sericite veins with sericitic halos, and green and white intermediate argillic halos composed of illite-smectite-chlorite-kaolinite ± pyrite.

3.4.3.1 Biotite veins and microbreccias

Steeply dipping, 0.5 to 3 cm thick biotite veins and microbreccias are rare, do not present sulfides, and are mostly observed in the low-grade Cu to “barren” core where they are usually cross-cut by aplites and deep quartz veins. However, the opposite cross-cutting relationship is also observed (Table 3.1). The biotite veins are composed of fine grained dark-brown biotite replacements of the Haquira granodiorite stock groundmass and partially of the feldspar phenocrysts. The biotite veins are sometimes incipiently aligned (Plate 3.1A). There is a continuum of veins textures that grade into microbreccias. The biotite microbreccias are composed by a biotitic matrix and clasts of feldspars that are 0.1 to 0.5 mm and rarely reach 1.5 mm in diameter (Plate 3.1B).

3.4.3.2 Aplites and vein-dikes

The 0.2 to 15 cm thick aplites are white to pink in color, composed of sugary K-feldspar and quartz with rare 0.1 to 0.2 mm K-feldspar and hornblende phenocrysts and do not carry sulfides (Plate 3.1B, C, D). The aplites cross cut the biotite veins/microbreccias, and are in turn commonly cross cut by DQ veins. However, the opposite cross-cutting relationships were also observed (Table 3.1). Some aplites are re-opened by DQ veins and vise versa, and were named vein-dikes (Plate 3.1D).

The aplites are abundant at depth (~5 to 20 vol. %) in the low-grade Cu core and two swarms can be identified. A more prominent swarm in the center of the low Cu-grade core and close to the southwest flank of the Haquira granodiorite stock (*e.g.* AHAD176, 900-1026 m in cross-section 1900NW, Fig. 3.2) and a second high density center close to the Northeast flank of the stock (*e.g.* AHAD-102, 639-64 9m in cross-section 1900NW, Fig. 3.2, 3.3, Movie 3.4).

Analysis of 100 core-angle measurements of aplites in cross-sections 1900NW and 2100NW indicates that core angles in drill-holes angled to the norhteast are greater (average =

35º) than in drill-holes angled to the southwest (average=10º), suggesting that the aplites steeply dip to the southwest, assuming there is only one dominant dip direction (Einaudi, 2008).

3.4.3.3 Deep quartz (DQ) veins

Deep quartz veins are straight-walled to sinuous, 0.2 to 3 cm thick, milky-white to gray-translucent quartz veins with rare sulfides (Plate 3.1B, E). They lack the sugary texture of typical A veins and the symmetrical growth textures of B veins (*cf.* Gustafson and Hunt, 1975). K-feldspar is rarely observed within the vein quartz as 1-3 mm anhedral crystals, but is more common as irregular pink-halos replacing plagioclase (Plate 3.1F). All the observations of K-feldspar halos were done in the low-grade Cu core. Below ~ 900 m depth, anhydrite is preserved in DQ veins intergrown with quartz and rarely with traces of chalcopyrite (Plate 3.1H). Above ~900 m depth, some DQ veins present irregular open space centerlines (Plate 3.1G) that were probably filled with anhydrite crystals that were later dissolved during weathering. DQ veins mostly postdate biotite veins/microbreccias and aplites, but the reverse relation has also been observed (Table 3.1), indicating alternating pulses of the three vein types. The DQ veins are more abundant in the southwest flank of the Haquira granodiorite stock where the aplites and the Haquira porphyry dikes are also abundant (Figs. 3.2, 3.3). There, steeply dipping stockworks of DQ veins reach densities of more than 15 vol. % (*e.g.* AHAD-176 900-1026m, Fig. 3.2) and locally reach up to 60 vol. %. A second and discontinuous high-density area partially overlaps with a high-density zone of aplites in the northwest margin of the Haquira granodiorite stock (Figs. 3.2, 3.3).

Analysis of 237 core-angle measurements for DQ veins on sections 1900NW and 2100NW indicates that the core angles in drill-holes angled to the northeast are greater (average = 43º) than in drill-holes angled to the southwest (average= 22º), suggesting that if there is only one dominant dip direction, the DQ veins dip to the SW (Einaudi, 2008).

3.4.3.4 Actinolite veins and epidote veins

Hydrothermal actinolite was found as replacement patches with minor albite and rare quartz (Plate 3.2A) and in pale green 1 to 5 mm thick veins, which sometimes show albite halos of up to 1 cm thickness (Plate 3.2B). Rarely, the actinolite veins also contain diopside, whereas sulfides are absent. The actinolite veins and patches are most abundant in the northeast flank of the Haquira granodiorite stock, and are rare in the southwest flank where all the other vein types and dikes are most abundant, therefore vein cross-cutting observations are sparse. When observed, actinolite veins cross cut DQ veins, and are in turn cross cut by Cu-sulfide±quartz and B veins.

Epidote veins were very rarely found, and only in the northeast flank of the stock within the actinolite vein zone (Plate 3.1D). Epidote was also observed replacing felsic sites in more distal-to-ore intercepts of Lahuani sills in the quartzite wall rock (Plate 3.1C).

3.4.3.5 Early dark micaceous (EDM) halos

Early dark micaceous (EDM) halos are green-dark brown micaceous alteration halos around fractures that commonly lack a quartz centerline and are mostly 0.2 to 1 cm thick and rarely reach up to 5 cm (Plate 3.1E). The EDM halos are the earliest mineralized vein/halo and carry up to 10-15% disseminated bornite and chalcopyrite. The bornite:chalcopyrite ratio ranges from 2:1 to 1:2. The EDM halos cross cut aplites and DQ veins (Plate 3.1F), and are in turn cross cut and/or re-opened by Cu-sulfide±quartz veinlets, B veins and BMQ veins (Table 3.1, Plate 3.1F, G, H, Plate 3.3B). The EDM halos at Haquira are similar to the EDM halos described at Butte (Montana, Meyer 1965; Brimhall, 1977), Los Pelambres (Chile, type 4 veins, Atkinson *et al.,* 1996) and Bingham (Utah, Redmond and Einaudi, 2010). As in Butte and Los Pelambres, the area of distribution of EDM halos at Haquira East is well correlated with the distribution of the high-grade Cu-ore in areas that reach a density of 1 to ~10 vol. % (Fig. 3.2, 3.3, 3.4 and Movie 3.4). The EDM halos locally reach 10-30 vol. % over core intercepts of up to 5 m (*e.g.* AHAD-98A, 240-400 m, Fig. 3.2; AHAD116, 290-350 m, Fig. 3.3). Analyses of 117 core-angle measurements for EDM halos in cross-sections 1900NW and 2100NW indicate that core angles are commonly < 10º to the core axis, and are independent whether the drill-holes are angled to the norhteast or southwest. The EDM halos are restricted to the Haquira granodiorite stock and are completely absent in the meta-sedimentary wall rock (Figs. 3.2, 3.3, 3.4 and Movie 3.4).

QEMSCAN^{TM} imaging reveals that in the EDM halos, mixtures of biotite, muscovite, K-feldspar and minor corundum and quartz replace both hornblendes and feldspars and are in contact with bornite and chalcopyrite (Plate 3.5 and 3.6). Andalusite has been described in EDM halos from Butte (Brimhall, 1977; Reed *et al.,* 2013), but has not yet been identified at Haquira East. Magmatic biotite is stable within the halos and only partially replaced by chlorite. Chlorite, however, replaces magmatic hornblende and biotite as well as hydrothermal biotite in the EDM halos and elsewhere in the Haquira granodiorite stock and is considered a latter event (Plate 3.5 and 3.6; Fig. 3.5c,f). Where rare quartz centerlines are present in the EDM halos, they are composed of mosaic-textured quartz that also carry bornite and chalcopyrite (see Chapters 4, 5).

Although dark-colored hydrous minerals are not readily identified by SWIR, CORESCAN^{TM} images identified mixtures of biotite-muscovite in some of the imaged EDM halos (Fig. 3.6C, H, M).

The higher Bn:Cpy ratios are found in the most abundant dark brown to green EDM halos (Plate 3.2E), whereas more rare pale green EDM halos (Plate 3.2H) are dominated by chalcopyrite with only traces of bornite. QEMSCAN^{TM} images (Plate 3.5, 3.6) reveal that the difference in color is due to the relative abundances of hydrothermal biotite and muscovite replacing the magmatic plagioclase. The darker EDM halos present similar amounts of biotite and muscovite, whereas the lighter colored halos are dominated by muscovite and lesser amounts of biotite. The latter resemble the Pale Green Sericite (PGS) halos of Butte (Reed, 1999), although at Haquira the lighter colored halos have significant amounts of hydrothermal biotite, and therefore where classified as EDM. At Butte, the PGS halos partially overlap with the EDM halos, but are also an upward and outward continuation of the EDM halo dominated zone (Rusk *et al.,* 2008). A similar but more diffuse and irregular zonation is present at Haquira East, where the darker EDM halos partially grade upward and outward to lighter colored EDM halos.

3.4.3.6 Cu-sulfide±quartz veinlets

One to three millimeter thick chalcopyrite and less commonly bornite veinlets are rare and very rarely accompanied by sugary quartz (Plate 3.3D). When quartz is present they resemble A veins (Einaudi, 2008) due to their similarity with A veins elsewhere (*c.f.* Gustafson and Hunt, 1975). The Cu-sulfide veinlets are observed as sparse single veinlets in 10 to 20 cm wide intercepts with a veinlet every 1 to 2 cm. Due to the low abundance of these veins they are not significant contributors to the high Cu-grade ore. However, the distribution of sparse Cu-sulfide veinlets correlates with the low-grade Cu distribution (>0.1 wt. %) that extends to the meta-sedimentary wall rock (Figs. 3.2, 3.3, 3.4; Movie 3.4). The Cu-sulfides veinlets together with sparse B veins, are the only Cu-sulfide-bearing veinlets observed in the meta-sedimentary wall rock.

The Cu-sulfide±quartz veinlets cross cut the biotite veins/microbreccias, aplites, DQ veins, EDM halos and actinolite veins (Table 3.1). More rarely they cross cut B veins, suggesting the presence of multiple Cu-sulfide venlets events. However, the late Cu-sulfide veinlets are only observed close to Cu-sulfide-bearing EDM halos and B veins and may represent a remobilization of earlier copper (Einaudi, 2008).

3.4.3.7 Banded molybdenite-quartz (BMQ) veins

Banded molybdenite-quartz veins are 0.2 to 4 cm thick straight walled gray-quartz veins that rarely reach 10 cm in thickness (Plate 3.3C). Fine grained (10's of μm to 1 mm in diameter) molybdenite grains concentrate in narrow (0.5 to 2 mm) and irregular bands in one or both sides of the quartz vein. Disseminated molybdenite in the quartz is less abundant, and sometimes aligns in discontinuous internal bands. When the molybdenite is micron-sized and barely visible in hand sample, it gives a transparent blue appearance to the quartz. The distribution of the BMQ veins overlap with most of the high-grade Mo (> 50 ppm, Figs. 3.2, 3.3, 3.4; Movie 3.4). The high-grade Mo is mostly hosted in BMQ veins, as the molybdenum concentrations are the highest (>100 ppm) in areas with high density of BMQ (Einaudi, 2008). However, more molybdenite is also present in later B veins.

BMQ veins cross cut DQ veins, EDM halos and the Cu-sulfide±quartz veinlets, and are in turn cross cut (Plate 3.3F) and re-opened by B veins (Table 3.1, Plate 3.3D). The re-opening of BMQ veins by B veins is further evidenced by SEM-CL imaging. The bright-CL mosaic textured BMQ quartz in contact with abundant molybdenite is re-opened by gray-CL mosaic to growth banded B vein quartz containing bornite and chalcopyrite and only traces of molybdenite (Chapter 4). The distribution of the BMQ veins outboards the distribution of the Cu-sulfide bearing EDM halos and B veins (Figs. 3.2, 3.3, 3.4; Movie 3.4).

The analysis of 49 core-angle average measurements in cross-sections 1900NW and 2100NW for different drill-holes range from 20º to 45º, and are steeper than previously emplaced veins and halos and independent of whether the drill-hole is angled to the norhteast or to the southwest (Einaudi, 2008).

3.4.3.8 B veins

Some of the B veins at Haquira East are straight-walled milky- to gray-quartz veins with continuous bornite-chalcopyrite±molybdenite centerlines (Plate 3.3B, D) and are similar to the B veins originally defined at El Salvador (*c.f.* Gustafson and Hunt, 1975). There are also more sinuous and irregular quartz veins with also irregular and/or discontinuous Cu-sulfide centerlines that could be cataloged as AB veins (Plate 3.3A, F). Since both AB and B vein types share the same cross-cutting relationships, for simplification purposes we refer to all as B veins. Based on 123 thickness measurements, two B vein populations are recognized. A dominant set of B veins that range from 0.1 to 0.4 cm (average = 0.2 cm) and a thicker set that ranges from 0.6 to 2 cm (average = 1.1 cm) (Einaudi, 2008). It is possible that the thicker sets are DQ veins re-opened by B veins (*e.g.* Plate 3.3A).

B veins cross cut biotite veins/microbreccias, aplites, DQ veins (Plate 3.3A), actinolite veins, EDM halos (Plate 3.3B), Cu-sulfide±quartz veinlets and BMQ veins (Plate 3.3D). Several generations of B veins are evidenced by the presence of different sets of B veins cross cutting each other (Plate 3.3E). The distribution of B veins partially overlaps and outboards the distribution of EDM halos (Figs. 3.2, 3.3, 3.4, Movie 3.4). In the Haquira granodiorite stock, the high-density B vein zone consists of > 5 vol. %, and locally 10 vol. %, and partially overlaps with the distribution of the >0.5 wt. % Cu. The B vein high-density zone truncates abruptly against the southwest contact of the Haquira granodiorite stock with the meta-sedimentary wall rock. Lesser amounts of B veins (>0.1 vol. %) penetrate the quartzite wall rock near the syncline axis where carbonaceous silts are more abundant than quartzites (Fig., 3.2).

The analyses of 238 core-angle measurements of B veins indicate more than one dipping population. Most B veins have core angles that range from 20º to 60º and average 30º. Exceptions to these angles were found in drill-holes AHAD-98A, -102, -116 and -107. B-veins in drillholes AHAD-98A (200 – 400 m) and -102 (180 – 270 m) angled to the southwest are defined by average angles to core between 4º and 5º. B-veins in drillholes AHAD-116 (300 – 350 m) and -107 (150 – 350 m) angled to the northeast are defined by average angles to core between 6º and 8º (Einaudi, 2008).

3.4.3.9 D veins, sericitic halos and hydrothermal breccias

D veins (*cf.* Gustafson and Hunt, 1975) are 0.2 mm to 2 cm thick pyrite veins with or without gray quartz (Plate 3.4A, B, D). Small amounts of fine-grained muscovite (sericite) are intergrown with the vein quartz (Cernuschi *et al.,* 2015b). The D veins always have gray alteration halos than range from 1 cm to 5 cm in thickness. The halos are formed by hydrothermal sericite and quartz that replace both felsic and mafic sites and the feldspars in the groundmass of the Haquira granodiorite stock as well as the Haquira and Pararani porphyry dikes. In opposition to the EDM halos, D veins never have hydrothermal biotite, and the magmatic biotites are always altered to muscovite±rutile.

D veins and sericitic halos are not abundant at Haquira East (less than 5 %), and are restricted to narrow and continuous zones that cross cut all the previous veins and halos and the Haquira porphyry dikes. The D veins are the first vein type that cross cut the late Pararani porphyry dikes (Figs. 3.3, 3.4).

Hydrothermal breccias (Plate 3.4D, E) form a distinct irregular but roughly tabular body of up to 15 m in thickness that follow a swarm of D vein/sericitic halos. Correlation between the three cross-sections indicates that the main breccia body strikes ~NS and dips ~70º W (Figs. 3.2, 3.3, 3.4). The breccias are composed of variable proportions of angular to sub-rounded clasts of 1 to 20 cm in size of quartzite, siltstone, Haquira granodiorite stock, as well as Haquira and Pararani porphyry dikes. In some intercepts, the clasts are rounded and evidence transport, and the breccia can be classified as a pebble dike (*e.g.* AHAD-166, 691.5-697.7m). The clasts include Mo-bearing BMQ veins and Cu-sulfide bearing B veins that are always truncated against the breccia matrix. The matrix is composed of fine-grained pyrite, quartz and sericite (<1 mm) sometimes with traces of chalcopyrite. Unaltered or previously K-silicate altered intrusive clasts have superimposed sericite.

3.4.3.10 White and green intermediate argillic halos

D veins commonly show green and white halos that are external to, and some times overlapping with, the gray sericitic halo of the D vein (Plate 3.4A). Green and white halos commonly occur together, most commonly as an inner white halo and an outer green halo (Plate 3.4C), but the opposite spatial relation has also been observed. Vein/halo cross-cutting observations suggests that the green and white halos post date the D veins/gray sericitic halos, although the green and white halos were mostly emplaced through the permeability discontinuities formed by the D veins. The green and white halos are not only observed parallel to the D vein/sericitic halo, but also as halos of very rare, thin and irregular pyrite veinlets with no quartz or muscovite (Plate 3.4C). Furthermore, the white and green halos were observed striking orthogonally to D veins (Plate 3.4D). The mineralogy of the white/green halos is distinct from the gray sericitic halos. White and green intermediate halos present small amounts of fine-grained hydrothermal phyllosilicates intergrown with clays, in comparison to the more obvious muscovite of the gray sericitic halos. The phyllosilicate of the white and green halos is likely illite, although the distinction of illite and muscovite through XRD is difficult due to the almost identical ~10 Å spacing of the (001) plane in both minerals, which produces overlapping XRD reflection peaks ($8.6^\circ < 2\theta < 8.8^\circ$). Empirical data, however, suggest that illite has a rather wide peak whereas muscovite present a narrower peak ($\Delta 2\theta < 0.25^\circ$, Meunier and Velde, 2004). The XRD spectra of white and green halos sampled several meters away from D veins show wider ~8.7º peaks, suggesting the presence of illite, whereas the gray sericitic halo of a D veins sample shows a narrower and much more intense ~8.8º peak, indicating muscovite (Fig. 3.7). Smectites were identified by XRD in green halos but not in the white halos (Fig. 3.7). Besides illite, the white halos have mixtures of kaolinite>smectites identified by SWIR in CORESCAN^{TM} images (Fig. 3.6E, J), whereas the green halos have smectites>kaolinite and chlorite (SWIR, Fig. 3.6D, I). Based on the mineralogy of the green and white halos, and the observation that they post-date D veins and gray sericitic halos, we name them here green and white intermediate argillic halos (see Fig. 5A in Seedorff *et al.,* 2005).

3.4.4 Wall rock hydrothermal alteration

The mapped extension of hydrothermal biotite replacing hornblende is shown in the cross-sections as a proxy of the extension of the K-silicate alteration. Both the low-grade Cu core and the Cu-Mo ore zones are contained within the 90% hydrothermal biotite zone (Figs. 3.2, 3.3, 3.4). Most of the earlier veins were mapped within this zone and are stable with K-silicate alteration (Table 3.2). Biotite veins/microbreccias, aplites and DQ veins are more abundant in the deep and low-grade Cu core, were K-silicate alteration appears to be more intense. Not only is magmatic hornblende altered to hydrothermal biotite, but the low-grade Cu core is the only area were K-feldspar replaces plagioclase in DQ vein selvages.

EDM halos, Cu-sulfide±quartz veinlets, BMQ veins and B veins form the Cu-Mo ore zones and are more abundant above the low-grade Cu core and to its sides (Figs. 3.2, 3.3, 3.4). The EDM halos are a particular between the veins in Cu-Mo ore zone, since they are stable with transitional alteration (Seedorff *et al.,* 2005) since they not only contain hydrothermal biotite but also contain muscovite.

The hydrothermal biotite was more easily mapped in the Haquira granodiorite stock in the northeast flank of the deposit. In the southwest the meta-sedimentary wall rock lacks indicative minerals to map the hydrothermal reaction with the exception of sparse intercepts of early Lahuani sills that were used as anchor observations to project the hydrothermal biotite limit (Figs. 3.2, 3.3).

Outside of the high-grade Cu-Mo and hydrothermal biotite, the northeast flank of the Haquira granodiorite stock has the highest density of actinolite veins with albite halos, and is the only area identified with sodic-calcic (Na-Ca) alteration. In-between actinolite veins/halos spaced <10 m hornblendes and biotites of the Haquira granodiorite stock are at least partially altered to actinolite. In areas were hornblendes were previously altered to hydrothermal biotite, both the relict hornblende and the hydrothermal biotite are altered to actinolite. The opposite relation has also been observed, however, suggesting that Na-Ca and K-silicate alteration partially overlapped in time, with each type of alteration dominating in different areas of the stock. Propylitic alteration is rare and only evidenced by the sparse occurrence of epidote veins within the area of Na-Ca alteration or replacing mafic and felsic sites in Lahuani sills intercepts more than 300 m away of the Haquira granodiorite stock.

Sericitic alteration is mostly restricted to the gray sericitic halos of D veins. Only in areas where D veins are closely spaced (<0.4 m) sericite partially replaces mafic and felsic sites of the Haquira granodiorite stock. Sericitic alteration forms narrow and mostly sub-vertical domains that cross cut through the K-silicate and Na-Ca alteration zones (Figs. 3.2, 3.3). The hydrothermal breccias and the late Pararani porphyry dikes are either cross cut by D veins, or apparently emplaced within swarms of D veins, and are pervasively altered to sericite (Fig., 3.2, 3.3). In the meta-sedimentary wall rock, sericite-illite replaces some of the rare feldspar grains in the quartzite, as identified by CORESCAN^{TM} imaging (Fig. 3.6N, O).

Intermediate argillic alteration postdates all the vein types and is more evident as the green and white intermediate argillic halos that were commonly mapped along earlier D vein structures (Figs. 3.2, 3.3). In drill-hole core samples where intermediate argillic halos are not developed and are not obvious in hand sample, small amounts of chlorite, smectites and kaolinite are commonly revealed as a late hydrothermal mineral in CORESCAN^{TM} images. Chlorite is commonly superimposed to magmatic and hydrothermal biotite (Fig. 3.6F), whereas smectites and kaolinite are commonly present in the outer margins of the EDM halos, B veins and D veins (Fig. 3.6G, H), or replacing magmatic feldspar in vein-less samples. Similarly, kaolinite was identified replacing feldspars grains in the quartzites (Fig. 3.6N, O).

Figure 3.6 shows a K/Al versus Na/Al molar plot of whole rock analyses of the Haquira granodiorite stock and Haquira porphyry dikes (4 acid digestion/ICP-MS) with the interpreted dominant hydrothermal alteration. The freshest samples plot close to the center of the diagram as the result of mixtures of magmatic plagioclase (~An_{45}) and K-feldspar. Na-Ca altered samples are displaced to higher Na/Al and lower K/Al ratios, towards the molar ratio composition of albite. K-silicate altered samples are displaced towards higher K/Al and lower Na/Al ratios, towards the molar composition of K-feldspar and biotite. Sericite-altered samples are displaced towards the molar ratio composition of muscovite. Most of the samples are either K-silicate or Na-Ca altered, as these are the two most abundant hydrothermal alteration types mapped at Haquira. Movie 3.5 shows the whole-rock samples color-coded according to dominant type of alteration shown in Figure 3.6. The hydrothermal alteration mapped by core-logging matches the alteration identified by the geochemical method (Movie 3.5).

3.4.5 SWIR-hydrous mineralogy

Movie 3.6 shows the SWIR-spectra obtained from drill-hole core by ASD-Terraspec^{TM}. Mixtures of relict magmatic hornblende and hydrothermal biotite were only identified in the central area of Haquira east where hydrothermal biotite was logged in drill core. The hydrothermal biotite zone identified by SWIR is mostly coincident with the location of the Cu-Mo ore in the Haquira granodiorite stock and is surrounded by an outer zone dominated by SWIR-identified muscovite-illite. This pattern is likely showing the logged sericite-illite that replaces some of the feldspar grains in the quartzite wall rock. Muscovite-illite was also identified in some samples of the Haquira granodiorite stock, and is partially correlated with the logged distribution of D veins and sericitic halos.

Pure muscovite can be differentiated from phengitic muscovite based on the wavelength of the 2,200 nm absorption feature that corresponds to the location of the Al-OH bond energy. The wavelength of the 2,200 nm absorption feature shifts from 2,195 nm in pure muscovite towards 2,220 nm in phengite. This is caused by the coupled Tschermak substitution of Al by (Fe, Mg) and Si controlled mainly by pH (Halley *et al.,* 2015). When only the SWIR-identified muscovite-illite are plotted and color-coded by the wavelength of their 2200 nm absorption features (Fig. 3.9), two zones can be distinguished (Movie 3.6). A central zone with mostly >2205 nm phengitic muscovite is roughly coincident with the Cu-Mo ores and the Haquira granodiorite stock, whereas an outer zone with 2195-2205 nm muscovite dominates in the meta-sedimentary wall rock.

When samples with SWIR-identified clays are plotted in 3D (Movie 3.6), the Haquira granodiorite stock and the K-silicate central zone is dominated by smectites, whereas the outer zone in the meta-sedimentary wall rock is dominated by kaolinite.

3.4.6 Trace elements in whole rock

The three cross-sections (Figs. 3.2, 3.3, 3.4) and Movie 3.7 show the distribution of selected trace elements in whole rock samples at the deposit scale (aqua regia/ICP-MS). The anomalous concentrations of trace elements reflect at least 3 times the average crust abundance (Halley *et al.,* 2015) and form coherent patterns at and around the Cu-ore. Mo and tungsten (W) concentrations above 5 ppm are common in most of the analyzed samples and particularly at and around the Cu-Mo ore and at the low Cu-grade barren core. Tin (Sn) above 4 ppm is restricted to the shallower areas of the Cu-Mo ore, whereas antimony (Sb) above 4 ppm and arsenic (As) above 40 ppm are only present in shallower areas in the periphery of the Cu-Mo ore and mostly in the quartzite wall rock.

3.5 Discussion

Vein cross-cutting relationships indicate that the Cu- and Mo-sulfides were introduced in three different stages (Fig. 3.10). The first copper stage precipitated most of the copper but completely lacks molybdenum. The high-grade copper was precipitated as bornite and less chalcopyrite in early EDM halos and was immediately followed by minor amounts of copper in chalcopyrite > bornite in Cu-sulfide±quartz veinlets. Following this stage, the bulk of the molybdenum ore was precipitated in molybdenite in BMQ veins. No copper was precipitated at this stage. The final mineralization stage introduced significant copper and less molybdenum in later B veins. The correlation of Au with Cu indicates that the Au-ore is hosted in bornite, and no significant Au is hosted in late pyrite-bearing D veins.

All veins are interpreted to be magmatic-hydrothermal in origin, except for the actinolite veinlets and patches with Na-Ca alteration selvages that are interpreted as produced by basinal brines, as has been interpreted for similar veins elsewhere (Dilles and Einaudi, 1992). Similarly, the rare epidote veinlets and replacements are interpreted to be distal and lower temperature propylitic alteration equivalents to the sodic-calcic alteration and formed by less briny meteoric water (eg. Seedorff *at al.,* 2005). The earlier veins and halos, stable with K-silicate alteration (DQ, BMQ and B veins), transitional alteration (EDM halos), sericitic alteration (D veins and sericitic halos) and intermediate argillic (green and white halos) are inferred to be magmatic-hydrothermal in origin as proposed for other porphyry copper deposits elsewhere (Seedorff *et al.,* 2005). The magmatic-hydrothermal fluid that produced the K-silicate to sericitic to intermediate argillic veins/halos and wall rock alteration are interpreted to derive from a progressively deeper magmatic source (Chapter 2 and 5) and formed by a fluid of similar composition as temperature decreases and acidity increases. This interpretation follows that proposed by Reed *et al.* (2013) for deposits elsewhere.

The distribution of the magmatic-hydrothermal veins and Cu-Mo ore are centered around the southwest flank of the Haquira granodiorite stock, whereas the possibly brine-related actinolite veins are mostly restricted to the northwest flank of the stock in the periphery of the Cu-Mo ore (Figs., 3.2, 3.3; Movie 3.5). As discussed below, the locus of the magmatic-hydrothermal fluid input is inferred to be located close to the southwest flank of the Haquira stock (Fig. 3.1OA). It is likely that the hydrostatic pressure of the magmatic-hydrothermal fluid up-flow restricted the possibility of the convecting basinal brines to circulate through the magmatic-hydrothermal center, confining them to the periphery. Drops in the hydrostatic pressure between the porphyry/vein pulses may have allowed the penetration of the basinal brines further to the southwest, explaining the rare observations of actinolite veinlets in the magmatic-hydrothermal zone.

3.5.1 The Haquira porphyry dikes and the Cu-Mo ore

The porphyry copper deposit magmatic-hydrothermal system at Haquira East postdates the intrusion of the early Lahuani sills, the bulk of folding and faulting of the metasedimentary wall rock into the Tocone syncline and the intrusion of the Haquira granodiorite stock (Fig. 3.1, 3.2; see Chapter 2).

The intrusion of the Haquira porphyry dikes into the Haquira granodiorite stock and the meta-sedimentary wall rock marks the beginning of the hydrothermal alteration and mineralization (Fig. 3.10B). Most of the aplites and DQ veins were emplaces synchronously with these dikes. Cross-cutting observations indicate that the much less abundant biotite veins/microbreccias are broadly contemporaneous with the earlier aplites and DQ veins, but pre-date later aplites and DQ veins emplaced with later batches of Haquira porphyry dikes. The close temporal spacing and repetition of magmatic and hydrothermal events is further indicated by the common observation of vein dikes. Aplites (magmatic) and re-opened by DQ veins (hydrothermal), as well as the opposite observation of DQ veins that are re-opened by aplites.

Some Haquira porphyry dikes also have ambiguous cross-cutting relationships with EDM halos, and BMQ and B veins (Chapter 2). Therefore, the Haquira porphyry dikes must have intruded in several pulses during K-silicate alteration from the emplacement of early low-Cu-grade aplites and DQ veins to the later Cu-Mo-ore forming EMD halos, BMQ and B veins. This suggests that the emplacement of the Haquira porphyry dikes was related to the input of magmatic-hydrothermal fluids (Chapter 2). Furthermore, the ~50% aplitic groundmass of the Haquira porphyry dikes, suggests that they formed during volatile exsolution and quenching as commonly described for porphyry dikes associated to the hydrothermal alteration and mineralization elsewhere (Dilles, 1987). The Haquira porphyry dikes may have intruded from a concealed magmatic cupola atop an inferred magma chamber concealed at depth, releasing the Cu-Mo-bearing fluids that ascended by hydro-fracturing the overlying wall rock (Fig. 3.10A). A similar mechanism for porphyry emplacement and magmatic-hydrothermal fluid release has been proposed elsewhere (Dilles, 1987). Drilling at Haquira East reaches ~ 1 km depth and both the

Haquira granodiorite stock and Haquira porphyry dikes remain open at depth and therefore the location and depth of the source intrusion cannot be constrained. However, the source cupola(s) should be located at some depth below the southwest flank of the Haquira granodiorite stock in order to explain the high density of Haquira porphyry dikes and veins found there (Fig. 3.10A). In other words, the locus of the magmatic-hydrothermal up-flow and K-silicate alteration was located close to the southwest flank of the stock. This is further suggested by the relatively symmetrical distribution of the mapped hydrothermal biotite around a symmetry axis roughly coincident with the southwest flank of the stock (Figs., 3.2, 3.3, 3.4, 3.10A). Similarly, the sparse Cu-sulfide±quartz veinlets and the BMQ veins, are roughly symmetrically distributed around the axis formed by the inferred magmatic-hydrothermal fluid flow center cross-cutting both the Haquira granodiorite stock and the meta-sedimentary wall rock (Figs., 3.2, 3.3, 3.4, 3.10A; Movie 3.2). Along the symmetry axis at the low-grade Cu core, the Haquira porphyry dikes intrude both wall rock types with equal density (Fig., 3.2). Similarly, the low-density distribution of DQ veins and aplites are also symmetrically distributed around the proposed symmetry axis (Figs., 3.2, 3.3, 3.4; Movies 3.2, 3.3). These observations indicate that similar quantities of the magmatic-hydrothermal fluid were input close to the southwest flank of the stock and migrated in a similar fashion through both wall rock types (Fig. 3.10A). This is further suggested by the distribution of copper and molybdenum anomalies in whole rock. The relatively low-grade Cu-ore shell (>0.1 wt. %) forms the shape of an inverted cup around a low-grade Cu (< 0.1 wt. %) core center that mimics the distribution of Cu-sulfide±quartz veinlets. A similar shape is formed by the anomalous Mo shell (>5 ppm) and the relatively high-grade Mo (>50 ppm) shell that mimics the distribution of the Mo-ore forming BMQ veins (Figs., 3.2, 3.3, 3.4; Movie 3.2). An inverted cup shape is the typical shape of the high-grade copper and molybdenum in several porphyry copper deposits around the world, and is governed by favorable pressure, temperature and fluid composition conditions for copper deposition during the hydrothermal and mineralizing fluid flow (e.g. Seedorff *et al.* 2005). The shape of an inverted cup surrounding a strongly veined but relatively low-grade Cu to “barren” core its thought to be formed mainly as a response to a temperature gradient from highest in the center of the rising hydrothermal fluid flow path to lower in the edges, creating a “bend” at the depth where copper precipitation in sulfides is triggered (~ 430 - 350 °C, Landtwing *et al.* 2010; Redmond and Einaudi 2010; ~550 - 500 ºC, Chapter 4).

3.5.2 The asymmetry of the high-grade Cu ore shell

The high-grade Cu ore shell (>0.5 wt.%) is evident in the Haquira granodiorite stock, but in the meta-sedimentary wall rock the copper grades are low (≤ 0.1 wt. %, Figs., 3.2, 3.3, 3.4; Movie 3.2) and half of the typical inverted cup shape is missing (Fig. 3.10A). The high-grade Cu is mostly controlled by the distribution of Cu-bearing EDM halos, and in less degree by the distribution of Cu-Mo-bearing B veins (Figs., 3.2, 3.3, 3.4; Movie 3.2). EDM halos are restricted to the Haquira granodiorite stock and completely absent in the meta-sedimentary wall rock. Since EDM halos are formed by alteration of mafic and felsic magmatic minerals, they cannot be formed in the less reactive meta-sedimentary wall rock, mostly composed of quartzites. If the EDM-forming fluid circulated through the quartzites, it did not form EDM halos or precipitate Cu-sulfides. Similarly, the >1 vol. % density of B vein is truncated against the southwest flank of the Haquira granodiorite stock, and less amounts of B veins (0.1 to 1 vol. %) are present in the meta-sedimentary wall rock. Therefore, if the B vein-forming fluid circulated through the quartzites, it formed B veins with Cu-sulfides in substantially lower quantities than in the stock.

Based on the symmetrical distribution of Haquira porphyry dikes, earlier aplites, DQ veins, and later Cu-sulfides±quartz veinlets and BMQ veins presented above, it is unlikely that a permeability contrast inhibited the EDM and B vein-forming fluid to circulate through the meta-sedimentary wall rock. An explanation for the absence of high Cu-grade ore in the quartzite wall rock is most likely due to a wall rock compositional contrast that inhibited the Cu-sulfide formation in the quartzite in similar quantities than in the Haquira granodiorite stock. This can be explain by the low availability of Fe to trigger the precipitation of Cu-sulfides in such wall rock (Cernuschi and Dilles, 2012).

The alteration of magmatic hornblende to hydrothermal biotite releases Fe upon reaction with the mineralizing acidic, K-, Cu- and S-rich hydrothermal fluid (1) and enables the precipitation of Fe-Cu sulfides (2, 3) (Dilles *et al., unpub.*).

(1) $Ca_2(Mg,Fe)_{4.5}AlSi_{7.5}O_{22}(OH)_2 + K^+ + 6H^+ =$

$K(Mg,Fe)_3AlSi_3O_{10}(OH)_2 + 1.5Fe_2^+ + 2Ca_2^+ + 4.5SiO_2 + 3H_2O$

(2) $Cu^+ + Fe^{2+} + 2H_2S + 0.25O_2 = CuFeS_2 + 3H^+ + 0.5H_2O$

(3) $Cu(HS)^{2-} + Fe^{2+} + 0.25O2 = CuFeS_2 + H^+ + 0.5H_2O$

In contrast, the sedimentary wall rock in Haquira, mainly quartzites, lacks Fe-bearing minerals and is low in total Fe content, and therefore Fe-Cu sulfides are not as readily precipitated. This phenomenon produces only a “half” high-grade Cu ore shell in the HG stock that disappears abruptly in the contact with the quartzites (Figs. 3.2, 3.3, 3.4; Movie 3.2). There, only minor amounts of Cu-sulfides were precipitated and therefore the relatively low-grade Cu forms a complete inverted cup shell that is continuous through both wall rock types (Cu ~ 0.1 wt. %). Molybdenum grade is not restricted by the protolith composition because precipitation of molybdenite (4) does not require iron, and explains the observed, more continuous inverted-cup shaped, Mo-ore shell at low- and relatively high Mo-grades.

(4) $Mo(OH)_4 + 2H_2S = MoS_2 + 4H_2O$

The expected symmetry of the high-grade Cu-ore shell, assuming homogenous wall rock, is evidenced in section 1900NW (Fig. 3.2) and sketched in Figure 3.10A. In the area of the projected inverted cup Cu-ore shell in the meta-sedimentary wall rock, the copper grades are high and similar to ones in the Haquira granodiorite stock in intercepts of the more reactive early Lahuani sills. Meta-siltstones are compositionally more similar to the quartzites than to the granodiorites and therefore generally affect the copper sulfide ore shell in a similar way. However, some siltstones are calcareous, and therefore more reactive to acidic fluids, and tend to form local hornfels and skarns that produce local spikes in copper grade (Fig. 3.2, 3.10A).

We can infer that the fluids that produced the high-grade mineralization flowed through the Haquira granodiorite stock and the meta-sedimentary wall rock, presumably in a symmetrical manner, but with some variations according to permeability contrasts. The >100 ppm Mo-ore shell is less symmetrical than the 50 ppm Mo-ore shell (Movie 3.2), and more restricted to the HG stock. This could be explained by a slightly less ability of the magmatic-hydrothermal fluid to create fractures through the meta-sedimentary wall rock than through the Haquira granodiorite stock. This is partially supported by a slightly less abundance of BMQ veins in the meta-sedimentary wall rock than in the stock (*e.g.* Fig. 3.2). However, since the Cu-Mo-bearing B veins also contribute to the Mo-ore and these are mostly restricted to the granodiorite stock, lower Mo-grades are expected in the meta-sedimentary wall rock.

3.5.3 Vein and dike attitudes

The lack of oriented drill-hole cores at Haquira East complicates the interpretation of strikes and dips of the porphyry dikes, aplites, veins and alteration halos. The Haquira porphyry dikes were interpreted to be dominantly emplaced in a northeast trend, as suggested by one

N50ºE striking and ~85ºNW dipping dike outcropping ~500 m east of Haquira (Fig. 3.1, Gans, 2008; Chapter 2). However, the dikes are narrow and discontinuous and it is difficult to correlate single dikes between the three cross-sections. It is possible that more than one strike and dip exists and some porphyry dikes may strike northwest following the elongation of the Haquira granodiorite stock as inferred for some veins that were emplaced synchronously.

Aplite and DQ vein-to-core angles are steeper in drill-holes angled to the southwest than in drill-holes angles to the northeast indicating that if there is one dominant strike for aplites and DQ veins, they dip steeply to the southwest and therefore likely strike northwest following the elongation of the Haquira granodiorite stock. However, the vein-to-core angles of the later Cu- and/or Mo-bearing EDM halos, BMQ and B veins do not evidence a most common dip direction. These veins are inferred to dominantly strike to the northeast and dip steeply to the northwest as the dominant set of Haquira porphyry dikes, and therefore the measured angles-to-core are similar in drill-holes angled to the northeast and southwest. A less abundant and conjugate northwest-striking set must exist, because occasionally two veins of the same type are observed crosscutting orthogonally in drill-hole core.

The main hydrothermal breccia forms a tabular body that can be correlated between the three cross-sections with a NS strike and dipping 70º to the W. Since this and other small breccias are intruded in swarms of D veins, it is likely that most of the D veins have a similar strike. This is consistent with the common core-to-angle of ~ 40º observed for D veins and breccias in the drill-holes angled to the northeast. The late Pararani porphyry dikes were emplaced close in time with the D veins and hydrothermal breccias and were also emplaced in a norhtwest strike as evidence by surface mapping (Fig. 3.1). Correlation between the three cross-sections indicate that the amalgamating and undulating Pararani dikes are close to sub-vertical.

It is possible that all the Haquira geology and hydrothermal veins were tilted between 10º and 20º to the northeast, as suggested by the dip of the Haquira granodiorite stock (Fig. 3.2, 3.3; Movie 3.1) and according to the southwest to northeast shortening direction of the Tocone syncline (Fig. 3.1). By removing the tilting, the aplites and DQ veins that were inferred to strike northwest and dip steeply to the southwest become closer to sub-vertical, whereas the northeast-striking porphyries and veins remain close to sub-vertical. Similarly, the angle-to-core of the plunge of the intersection of orthogonally cross-cutting BMQ veins range from 65º to 40º in drill-holes angled 70º to the northeast. By assuming that the orthogonal sets of BMQ veins were emplaced sub-vertically, after the hydrostatic overpressure of deep magmatic cupolas and hydro-fracturing of the wall rock, then the plunge-to-core angles indicate a possible tilting between 20º and 35º to the norhteast. Furthermore, the inverted cup shaped Cu-Mo-ores were formed upright, then its inclined orientation in cross-sections 1900NW and 2100NW suggests a ~10 to 20º tilting to the northeast (Fig. 3.2, 3.3). Due to the north-south strike of the Pararani porphyry dikes and their undulating shape, it is difficult to judge if they are tilted.

3.5.4 Trace elements in whole rock and hydrous mineral patterns

Anomalies of relatively immobile trace element at Haquira East are the expected for a porphyry copper deposit that was eroded close to the top of the Cu-Mo-ore according to what is described by Halley *et al.,* (2015) for porphyry deposits elsewhere. Molybdenum, tungsten and tin are interpreted to be introduced with K-silicate alteration, whereas antimony and arsenic was introduced with sericitic alteration. Molybdenum and tungsten anomalies (>5 ppm) are relatively deeper and closer to the Cu-Mo-ores and K-silicate altered area, however tin is anomalous (> 4 ppm) only in the shallower area of the Cu-Mo-ore (Movie 3.7). Antimony and arsenic are anomalous (>4 ppm and 40 ppm respectively) outside the Cu-Mo-ore zone and mostly at shallow depths in the sericitically altered quartzite wall rock.

The SWIR-hydrous mineralogy also produces consistent patterns that can be interpreted in terms of the hydrothermal alteration zoning (Movie 3.6). Mixtures of amphibole and biotite were only identified in the K-silicate and Na-Ca altered zones. The SWIR-mineral identifications can be produced by relict magmatic hornblende and biotite, hydrothermal biotite (K-silicate alteration) and hydrothermal actinolite (Na-Ca alteration). Sericite-illite was identified throughout the deposit. The SWIR-identified sericite-illite is interpreted to post-date the K-silicate alteration and their distribution evidences the extension of the sericitic alteration overprint. In the K-silicate zone, some of the SWIR-analyses that indicate sericite-illite were from swarms of D veins/sericitic halos and sericitically altered Pararani porphyry dikes and hydrothermal breccias.

Whereas phengitic muscovite dominates in in the Cu-Mo ore zone, the periphery of the deposit is dominated by more pure muscovite. This pattern is the opposite to the muscovite central zone and phengite periphery pattern described for porphyry copper deposit elsewhere by Halley *et al.* (2015). These authors interpret the muscovite center and phengite periphery as a result of the acidity of the sericitic alteration fluid. The center of the deposits experienced large quantities of sericitic fluid flowing through and most of the feldspars in the wall rock were transformed early to sericite. The consumption of feldspars diminishes the buffering capacity of the wall rock and subsequent fluid migrating through remains at high pH. Less quantities of sericitic fluid reach the outer portions of the deposit, where relict magmatic feldspar is commonly observed. There, the wall rock is able to buffer the acidity of the fluid as feldspar is consumed, and the precipitated muscovite tends to be more phengitic in composition. However, most of the porphyry copper deposits studied by Halley *et al.* (2015) intruded in a mostly uniform igneous wall rock. We interpret the pattern observed at Haquira East as a product of the compositional contrast of the Haquira granodiorite stock and meta-sedimentary wall rock. Magmatic feldspar is abundant in the stock in the center of the deposit, where it is only locally replaced by biotite and muscovite in EDM halos and by sericite in a minor volume of rock that was affected by sericitic halos of D veins. Large quantities of relict magmatic feldspar buffered the acidity of the sericitic fluid and therefore the precipitated muscovite in the center of the Haquira East deposit was mostly phengitic in composition. In contrast, the meta-sedimentary wall rock is mostly constituted by quartzites that only have traces amounts of feldspar grains, commonly replaced by muscovite-illite. Therefore, the meta-sedimentary wall rock had a low buffering capacity and the sericitic fluid that migrated to the periphery of Haquira East was more acidic and precipitated less phengitic muscovite and some nearly pure muscovite (Movie 3.6).

The late clay overprint, produced during intermediate argillic alteration, shows a mineralogical pattern that reflects a similar acidity zoning. Smectites form at relatively less acidic conditions than kaolinite (Seedorff *et al.,* 2005). Whereas the center of the deposit is dominated by smectites replacing the relict feldspar of the Haquira granodiorite stock, kaolinite is more commonly identified at the periphery of the deposit in the meta-sedimentary wall rock (Movie 3.6).

3.6 Conclusions

The presence of EDM halos and the scarcity of A veins, suggests that Haquira East was emplaced deeply, as proposed for other EDM-bearing deposits elsewhere (Proffett, 2009).

At Haquira East the copper and molybdenum was introduced from one or more inferred magmatic cupolas on top of a concealed granodioritic intrusion (Fig. 3.10A). The release of over-pressured magmatic-hydrothermal fluid from the cupolas, hydro-fractured the roof wall rock of the intrusion, creating a fracture-controlled upwards migration pathway. The upwards-migrating hydrothermal fluid produced K-silicate to transitional alteration in the wall rock, as well as the early veining and the Cu-Mo mineralization. Small batches of magma were released synchronously resulting in the emplacement of the Haquira porphyry dikes and aplites. The fluid pathway was located close to the southwest flank of the Haquira granodiorite and defines a symmetry axis, around which most vein types and sulfides are distributed equally, or forming an inverted cup-shape controlled by favorable precipitation temperatures (Fig. 3.10A). Notable exceptions to this process are the Cu-ore forming EDM halos and in less degree the B veins, which are restricted to the Haquira granodiorite stock wall rock. The EDM halos only develop in favorable reactive wall rocks, where its constitutive minerals become unstable and react with K-silicate to transitional hydrothermal fluid. Similarly, the availability of iron in the wall rock minerals limits the bulk precipitation of Cu-sulfides. At Haquira East the great reactivity contrast between the quartzite dominated meta-sedimentary wall rock to the southwest and the Haquira granodiorite stock to the norhteast, determined the asymmetry of the distribution of EDM halos, high density of B veins and high Cu-grade ore (Fig. 3.10A).

The Cu-Mo-ore was formed during three different stages of copper and/or molybdenum mineralization during K-silicate alteration (Fig. 3.10B). The Cu/Mo ratios of the magmatic-hydrothermal source fluctuated greatly through time. It is possible that during the generation of the first hydrothermal fluid batch, most of the copper in the magmatic source was efficiently fractionated into the fluid phase after fractional crystallization and depleting the intrusion from copper. An efficient fractionation of copper into the fluid phase is expected because experimental data suggest that copper is more compatible in Cl^- rich fluid than in a silicate melt ($D_{Cu(fluid)} >> D_{Cu(melt)}$, where D is the bulk partition coefficient; Candela and Holland, 1984). Experimental studies also suggests that in high Cl^- and oxidized magmas molybdenum is less compatible in the fluid phase than cooper ($D_{Mo(fluid)} << D_{Cu(fluid)}$, Candela and Holland, 1984). Therefore, molybdenum may have remained in the melt at this stage. The high Cu/Mo fluid migrated to the cupola of the intrusion, from where it was injected into the wall rock, forming Cu-rich EDM halos. Subsequent fractional crystallization enriched the fluid phase in molybdenum but not in copper, which was already depleted from the melt. Upon release, the second batch of hydrothermal fluid precipitated molybdenite in the Mo-ore forming BMQ veins. The third stage introduced both copper and molybdenum in B veins (Cu>Mo). This could be the result of basaltic-andesite injection into the magma source, which could reintroduce both copper and molybdenum. This scenario would also require a slightly lower concentration of Cl^- to produce a more similar fractionation of Cu and Mo into the fluid phase. Periodic low-crust basaltic-andesitie injection into a mid- to shallow-crust granodioritic magma chamber was suggested in Chapter 1, based on trace element fractionation modeling.

3.7 Acknowledgments

I would like to thank FQM for supporting this research. Many thanks to Matt Booth from FQM and the all the geologists that contributed to the understanding of the geology of the deposit while working with Antares and FQM. Matt Booth assisted the 3D modeling. I extend my gratitude to Neil Goodey, Ronell Carey and Brigetta Martini for providing and processing the CoreScan^{TM} data. Thanks to Jannina Micko and LeapFrog^{TM} that provided an academic license of its software and great assistance to produce the 3D models.

3.8 References

Antares, 2010, Antares press–release: New Haquira global resource, February 26th, 2010, p. 6.

Atkinson, W.W., Souviron, A., Vehrs, T.I., and Faunes G.A., 1996, Geology and mineral zoning of the Los Pelamberes porphyry copper deposit, Chile: Society of Economic Geologists Special Publication, v. 5, p. 131–156.

Brimhall, G.H.J., 1977, Early fracture–controlled disseminated mineralization at Butte, Montana: Economic Geology, v. 72, p. 37–59.

Burnham, C.W., 1979, Magmas and hydrothermal fluids, *in* Barnes, H.L., ed., Geochemistry of hydrothermal ore deposits, v. II, New York, Wiley Interscience, p. 71–136.

Candela, P.A. and Holland, H.D, 1984, The partitioning of copper and molybdenum between silicate melts and aqueous fluids: Geochimica et Cosmochimica Acta, v. 48, p. 373–388.

Carr, J.C., Beatson, R.K., Cherrie, J.B., Mitchell, T.J., Fright, W.R., McCallum, B.C. and Evans, T.R., 2001, Reconstruction and representation of 3D objects with radial basis functions, ACM SIGGRAPH 2001, August 12–17, 2001, Los Angeles, CA, USA.

Chiles, J.P. and Delfiner, P., 1999, Geostatistics: Modelling Spatial Uncertainty, Wiley Series in Probability and Statistics, Wiley, New York, 696 p.,

Clark, R.N., Swayze, G.A., Wise, R., Livo, E., Hoefen, T., Kokaly, Sutley, S.J., 2007, USGS digital spectral library splib06a: US Geological Survey, Digital Data Series, Vol. 231, (http://speclab.cr.usgs.gov/).

Costa, J.P., Pronzato, I. and Thierry, E., 1999, A comparison between krigin and radial basis functions networks for non–linear prediction, Proceedings IEEE–EURASIP Workshop on nonlinear signal and image processing, Bogazici, University Printhouse.

Cowan, E.J., Beastson, R.K., Ross, H.J., Fright, W.R., McLennan, T.J., Evans, T.R., Carr, J.C., Lane, R.G., Bright, D.V., Gillman, A.J., Oshurst, P.A., and Titley, M., 2003, Practical implicit geological modeling, *in* Proceedings Fifth International Mining Geology Conference: The Australasian Institute of Mining and Metallurgy, Melbourne.

Dilles, J.H., 1987, Petrology of the Yerington batholith, Nevada: Evidence for evolution of porphyry copper ore fluids: Economic Geology, v. 82, p. 1750–1789.

Dilles, J.H. and Einaudi, M.T., 1992, Wall–rock alteration and hydrothermal flow paths about the Ann–Mason Porphyry Copper Deposit, Nevada, A 6 km Vertical Reconstruction: Economic Geology, v. 87, p. 1963–2001.

Einaudi, M.T., 2008, Distribution of Vein Types, Alteration, Sulfides, and Metal Grades, Hp Cu–Mo–Au Deposit, Departamento De Apureímac, Perú: Unpublished Report for Antares Minerals Inc, (September): 47 p.

Gans, P., 2009, Geology of the Hp Copper Deposit: New Information and Synthesis: Internal report for Antares Minerals, 9 p.

Goetz, A.F.H., Curtiss, B., and Shiley, D.A., 2009, Rapid gangue mineral concentration measurement over conveyors by NIR reflectance spectroscopy, Minerals Engineering, Vol. 22. p. 490 – 499.

Gustafson, L.B., and Hunt, J.P., 1975, The porphyry copper deposit at El Salvador, Chile: Economic Geology and the Bulletin of the Society of Economic Geologists, v. 70, no. 5, p. 857–912

Halley, S., Dilles, J.H. and Tosdal, R.M., 2015, Footprints: Hydrothermal alteration and geochemical dispersion around porphyry copper deposits: Economic Geology Newsletter, v. 100, no. 1, p. 12–17.

Meunier, A. and Velde, B., 2004, Illite, Origins, evolution and metamorphism, Springer, 281 p.

Meyer, C., 1965, An early potassic type of wall–rock alteration at Butte, Montana, American Mineralogist, v. 50, no. 10, p.1717–1723.

Pecho, V., 1981, Geología de los cuadrángulos de Chalhuanca, Antabamba y Santo Tomás: Instituto de Geología, Minería y Metalurgia, Boletín n. 35, p. 67

Perelló, J., Carlotto, V., Zarate, A., Ramos, P., Posso, H., Neyra, C., Caballero, A., Fuster, N., and Muhr., R., 2003, Porphyry–style alteration and mineralization of the middle Eocene to early Oligocene Andahuaylas–Yauri belt: Economic Geology, v. 98, no. 8, p. 1575–1605.

Pirrie, D., Butcher, A.R., Power, M.R., Gottlieb, P., Miller, G.L., 2004, Rapid quantitative mineral and phase analysis using automated scanning electron microscopy (QEMSCAN); Potential applications in forensic geoscience, *in* Geological Society, London, Special Publication 232, 123–136 p.

Redmond, P.B. and Einaudi, M.T., 2010, The Bingham Canyon porphyry Cu–Mo–Au deposit. I. Sequence of intrusions, vein formation, and sulfide Deposition: Economic Geology, v. 105, no. 1, p. 43.

Reed, M., Rusk, B., and Palandri, J., 2013, The Butte magmatic–hydrothermal system: One fluid yields all alteration and veins: Economic Geology, v. 108, p. 1379–1396.

Reed, M.H., 1999, Zoning of metals and early potassic and sericitic hydrothermal alteration in the Butte, Montana, porphyry Cu–Mo deposit [abs.]: Geological Society of America Abstracts with Programs, v. 31, no. 7, p. A381.

Rusk, B.G., Reed, M.H. and Dilles, J.H., 2008, Fluid inclusion evidence for magmatic–hydrothermal fluid evolution in the porphyry copper–molybdenum deposit at Butte, Montana: Economic Geology, v. 103, no. 2, p. 307.

Seedorff, E., and Einaudi, M.T., 2004, Henderson porphyry molybdenum system, Colorado: I. Sequence and abundance of hydrothermal mineral assemblages, flow paths of evolving fluids, and evolutionary style: Economic Geology, v. 99, no. 1, 3–37.

Seedorff, E., Dilles, J.H., Proffett, J.M., Jr., Einaudi, M.T., Zurcher, L., Stavast, W.J.A., Johnson, D.A., and Barton, M.D., 2005, Porphyry deposits: Characteristics and origin of hypogene features: Economic Geology 100TH Anniversay Volume, p. 251−298.

Stewart, M., de Lacey, J, Hodkiewicz, P.F., and Lane, R., 2014, Grade estimation from radial basis functions – how does it compare with conventional geostatistical estimation?, *in* Proceedings Ninth International Mining Geology Conference 2014 , The Australasian Institute of Mining and Metallurgy: Melbourne. p. 129–140

Thompson, A.J.B., Hauff, P., Robitaille, J.A., 1999, Alteration Mapping in Exploration: Application of Short–wave Infrared (SWIR) Spectroscopy, SEG Newsletter v. 39, p. 16–27.

Zhaoshan, C., and Yang, Z., 2012, Evaluation of Inter–instrument Variations Among Short Wavelength Infrared (SWIR) Devices: Economic Geology v. 107: p. 1479 – 1488.

3.9 Figures and Tables

Table 3.1. Vein and porphyry dike cross-cutting log

Alteration:
Na-Ca / Propilitic
K-silicate
Sericitic
Intermediate argillic

These veins cut: ↓ / These veins are cut: →	Biotite microbreccias/veins	Aplites	Deep quartz veins (DQ) (no sulfides)	Actinolite veins with plagioclase haloes; epidote veins	Haquira porphyry dikes	Dark micaceous (EDM) halos (bornite-chalcopyrite)	Cu-sulfide±quartz veinlets	Banded molybdenite quartz veins (BMQ)	B veins (bornite-chalcopyrite±molybdenite)	D veins (pyrite±chalcopyrite) and sericitic halos	Illite±smectite±chlorite±kaolinite halos
Biotite microbreccias/veins		10									
Aplites	15		15		3	5					
Deep quartz veins (DQ, no sulfides)		30			5	5		8			
Actinolite veins with plagioclase halos; epidote veins			5								
Haquira porphyry dikes		15	12			3		4	3		
Dark micaceous (EDM) halos (bornite-chalcopyrite)		10	13		10						
Cu-sulfide±quartz veinlets	3	21	10	4		10			3		
Banded molybdenite quartz veins (BMQ)					6	15	3		1		
B veins (bornite-chalcopyrite±molybdenite)	2	15	12	3	10	35	5	42	7		
D veins (pyrite±chalcopyrite) and sericitic halos		8			6	2	3	5	2		
Illite±smectite±chlorite±kaolinite halos		2	4		3	2			3	5	

Note: Biotite veins, aplites, EDM halos, BMQ, veins, B veins and D veins cross-cut the chilled margins and internal contacts of the Haquira granodiorite stock and the early Lahuani sills. The Haquira porphyry dikes cross-cut all the Haquira granodiorite stock facies. Pararani dikes are only cross-cut by D veins and sericitic halos and later intermediate argillic halos. Numbers in red indicate reversals.

Table 3.2. Vein and halo mineralogy

Vein #	Vein type	Vein mineralogy	Halo mineralogy	Sulfides	Alteration	Location
1	Biotite veins and micro-breccias	Biotite		± Cpy	K-silicate	High density in low Cu-grade core. Less abundant in Cu-ore zone
2	DQ veins	Quartz ± K-feldspar ± anhydrite	Rare K-feldspar			
3	Aplites and vein dikes	Quartz, K-feldspar				
4	Actinolite veins	Actinolite ± quartz	Albite after plagioclase	± Py ± Cpy	Na-Ca	NE flank ± barren core
	Epidote veins	Epidote	Rare albite	Py	Propylitic	Distal: only observed in Lahuani sills
5	EDM halos		Biotite, muscovite, K-feldspar, corundum	Bn, Cpy	K-silicate	Cu-ore zone
6	Cu-sulfide±quartz veins	Bn, Cpy, rare sugary ("A type") quartz		Bn and/or Cpy		
7	BMQ veins	Quartz		Mo		Mo-ore zone
8	B veins	Quartz ± anhydrite		Cpy, Bn ± Mo		Cu-ore zone
9	D veins and sericitic halos	Quartz, muscovite	Quartz, muscovite	Py ± Cpy (in vein and halo)	Sericitic	Throughout the Haquira stock. Abundant in NE flank
10	White and green intermediate argillic halos		Illite, kaolinite, smectite, chlorite	± Py	Intermediate Argillic	Follow D-vein structures, abundant in low Cu-grade core

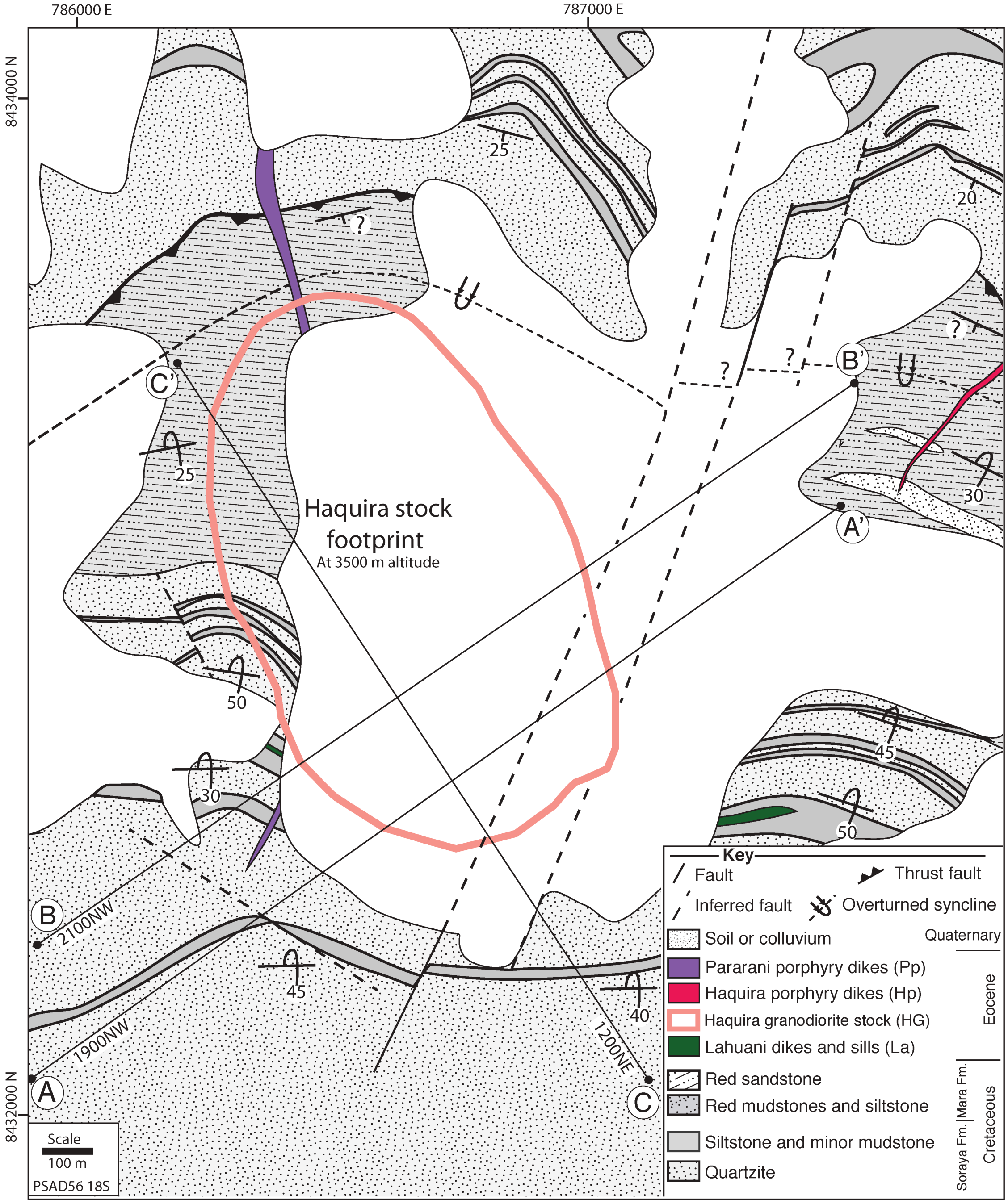

Figure 3.1. Geologic map of Haquira East modified from Gans (2009) showing the location of cross-sections 1900NW, 2100NW and 1200NE. The footprint of the non-outcropping Haquira granodiorite stock is projected from a 3500 m altitude.

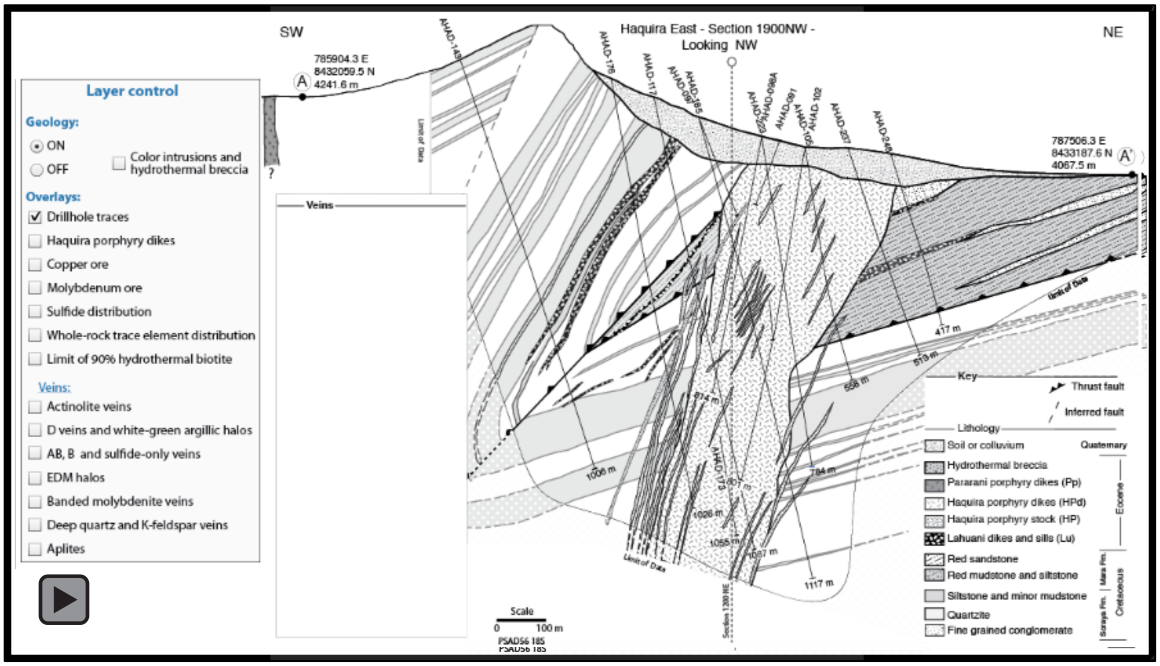

Layer control

Geology:
● ON
○ OFF
☐ Color intrusions and hydrothermal breccia

Overlays:
☑ Drillhole traces
☐ Haquira porphyry dikes
☐ Copper ore
☐ Molybdenum ore
☐ Sulfide distribution
☐ Whole-rock trace element distribution
☐ Limit of 90% hydrothermal biotite

Veins:
☐ Actinolite veins
☐ D veins and white-green argillic halos
☐ AB, B and sulfide-only veins
☐ EDM halos
☐ Banded molybdenite veins
☐ Deep quartz and K-feldspar veins
☐ Aplites

Figure 3.2. Cross-section 1900NW through the Haquira East porphyry copper deposit. Geology modified from Gans (2009) and veining from Einaudi (2008). Dynamic layers include the high Cu and Mo grade ore shells traced from whole rock analysis and the mapped sulfide and vein/halo distribution. Individual layers are printed in the appendix and the dynamic pdf can be found in the digital appendix. *Click here.* Password: Haquira-2015-

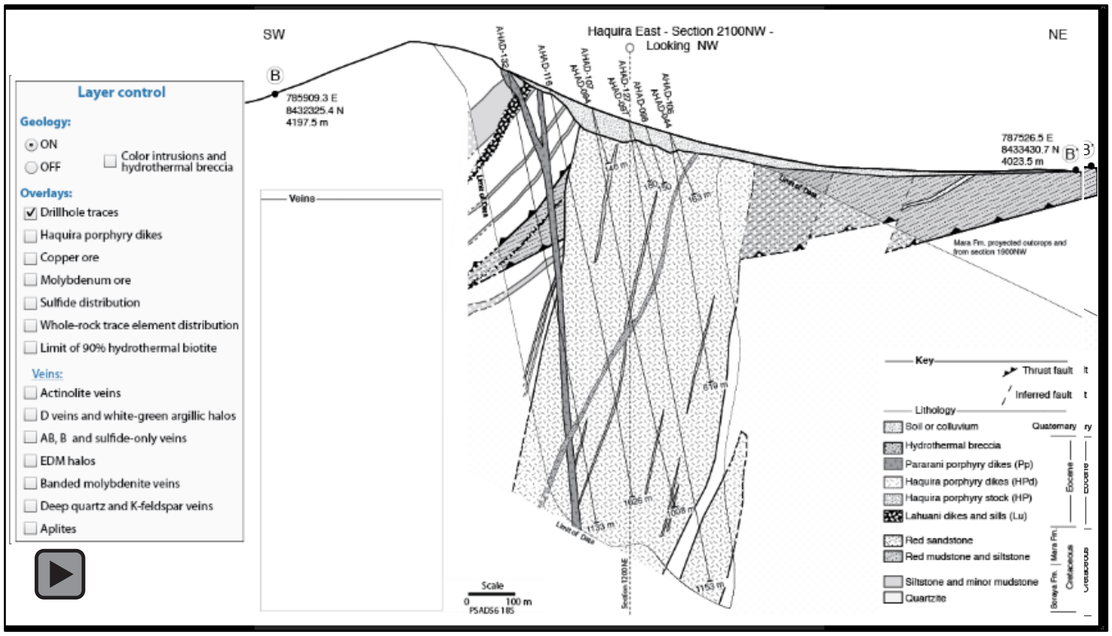

Layer control

Geology:

● ON
○ OFF
☐ Color intrusions and hydrothermal breccia

Overlays:

☑ Drillhole traces
☐ Haquira porphyry dikes
☐ Copper ore
☐ Molybdenum ore
☐ Sulfide distribution
☐ Whole-rock trace element distribution
☐ Limit of 90% hydrothermal biotite

Veins:

☐ Actinolite veins
☐ D veins and white-green argillic halos
☐ AB, B and sulfide-only veins
☐ EDM halos
☐ Banded molybdenite veins
☐ Deep quartz and K-feldspar veins
☐ Aplites

Figure 3.3. Cross-section 2100NW through the Haquira East porphyry copper deposit. Geology modified from Gans (2009) and veining from Einaudi (2008). Dynamic layers include the high Cu and Mo grade ore shells traced from whole rock analysis and the mapped sulfide and vein/halo distribution. Individual layers are printed in the appendix and the dynamic pdf can be found in the digital appendix. _Click here._ Password: Haquira-2015-

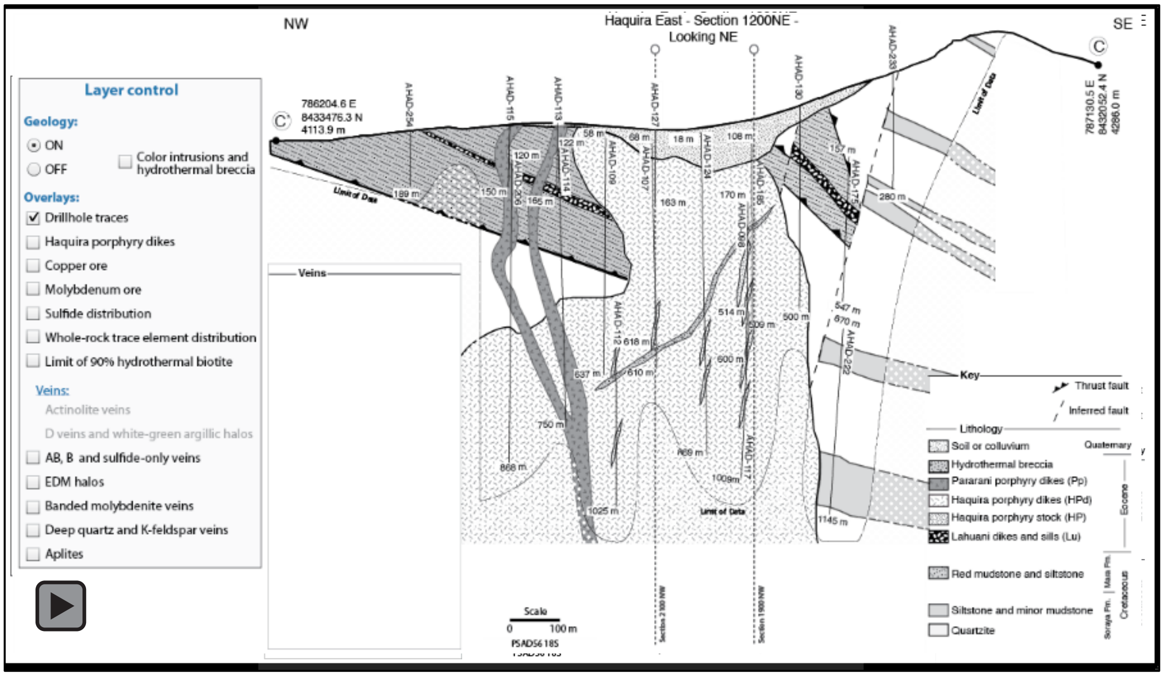

Layer control

Geology:
● ON
○ OFF
☐ Color intrusions and hydrothermal breccia

Overlays:
☑ Drillhole traces
☐ Haquira porphyry dikes
☐ Copper ore
☐ Molybdenum ore
☐ Sulfide distribution
☐ Whole-rock trace element distribution
☐ Limit of 90% hydrothermal biotite

Veins:
Actinolite veins
D veins and white-green argillic halos
☐ AB, B and sulfide-only veins
☐ EDM halos
☐ Banded molybdenite veins
☐ Deep quartz and K-feldspar veins
☐ Aplites

Figure 3.4. Cross-section 2100NW through the Haquira East porphyry copper deposit. Dynamic layers include the high Cu and Mo grade ore shells traced from whole rock analysis and the mapped sulfide and vein/halo distribution. Individual layers are printed in the appendix and the dynamic pdf can be found in the digital appendix. *Click here.* Password: Haquira-2015-

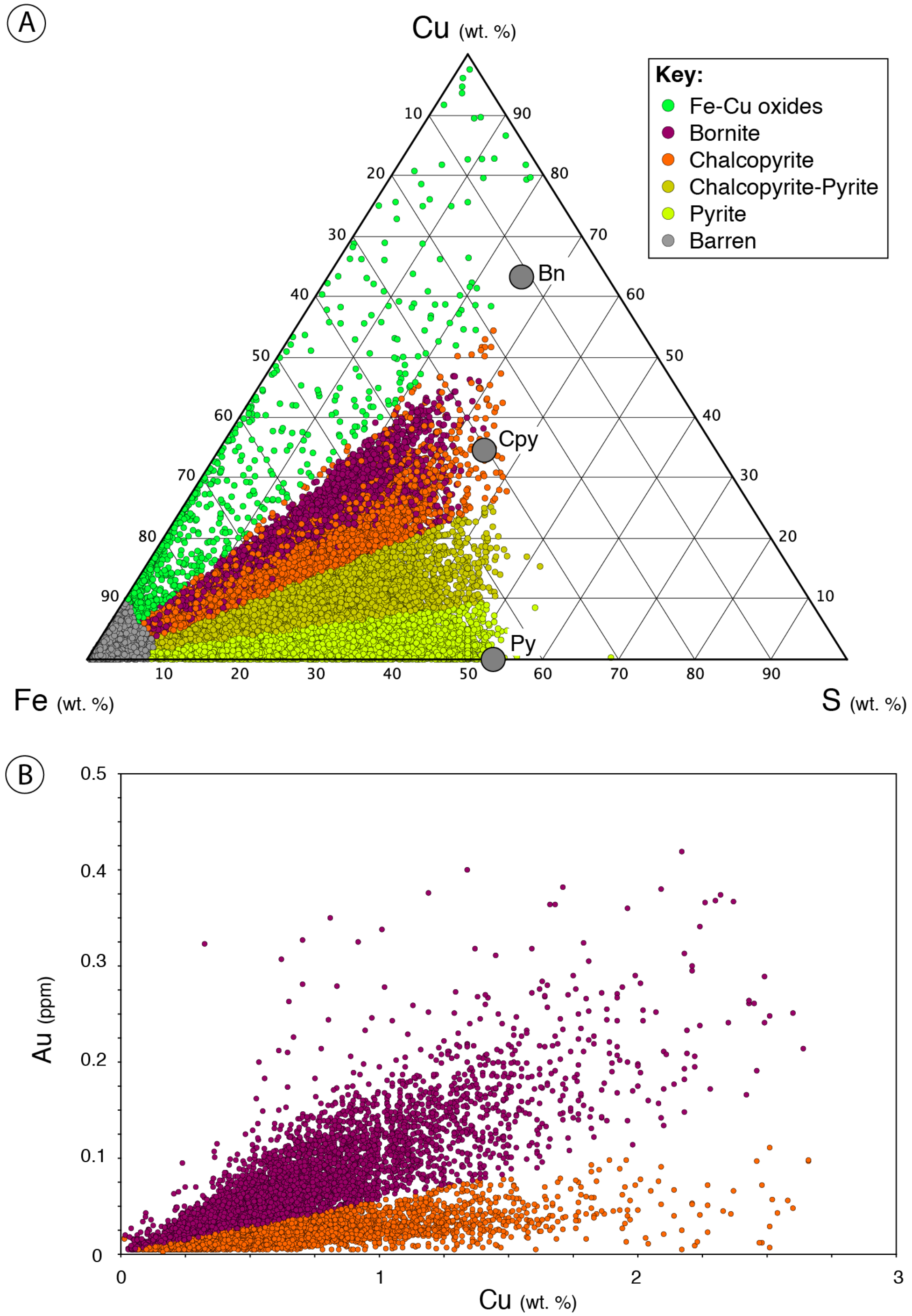

Figure 3.5. Interpreted sulfide/oxide mineralogy from whole rock samples analyzed by ICP-OES after aqua regia digestion. **A)** Ternary Cu-Fe-S plot and **B)** Au versus Cu plot.

Figure 3.6. Photographs and CORESCAN™ SWIR-maps of thin section billets. **A, B)** Hydrothermal biotite after hornblende in a K-silicate altered sample of the HG stock (FC-HAQ-225a, AHAD108-112m). **C)** Transmitted light thin section photograph of area marked in B, showing hydrothermal biotite replacing hornblende. **D, E)** D vein and gray sericitic halo. A kaolinitic outer halo post-dates the D vein and the gray sericitic halo (FC-HAQ-127, AHAD106-618m). **F)** Crossed polars thin section photograph of area marked in E, showing fine-grained muscovite replacing feldspar. **G, H)** EDM halo with hydrothermal biotite and sericite and later chlorite overprint. A kaolinite-smectite outer halo postdates the EDM halo (FC-HAQ-243, AHAD98A-267m). **I)** Transmitted light thin section photograph of area marked in H, showing hydrothermal biotite and muscovite replacing a plagioclase site. **J, K)** Green intermediate argillic halo formed by illite, smectite and chlorite. **L, M)** White intermediate argillic halo formed by illite, kaolinite and less smectite. **N, O)** Quartzite sample cross cut by an oxidized sulfide veinlet. The fine-grained feldspar is altered to muscovite-illite. Later kaolinite replaces feldspars locally mainly along the strike of the vein.

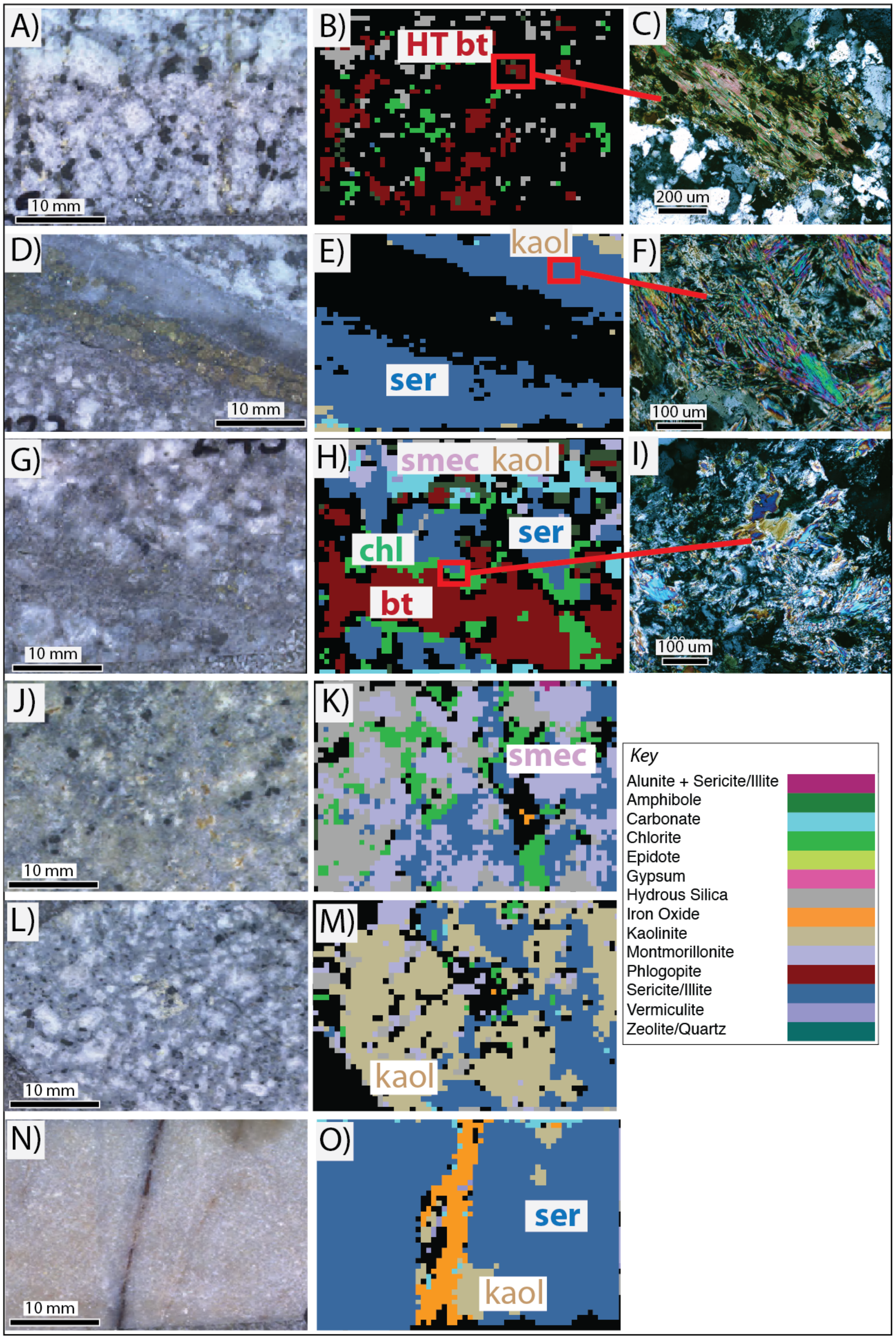

Figure 3.6. Photographs and CORESCAN™ SWIR-maps of thin section billets

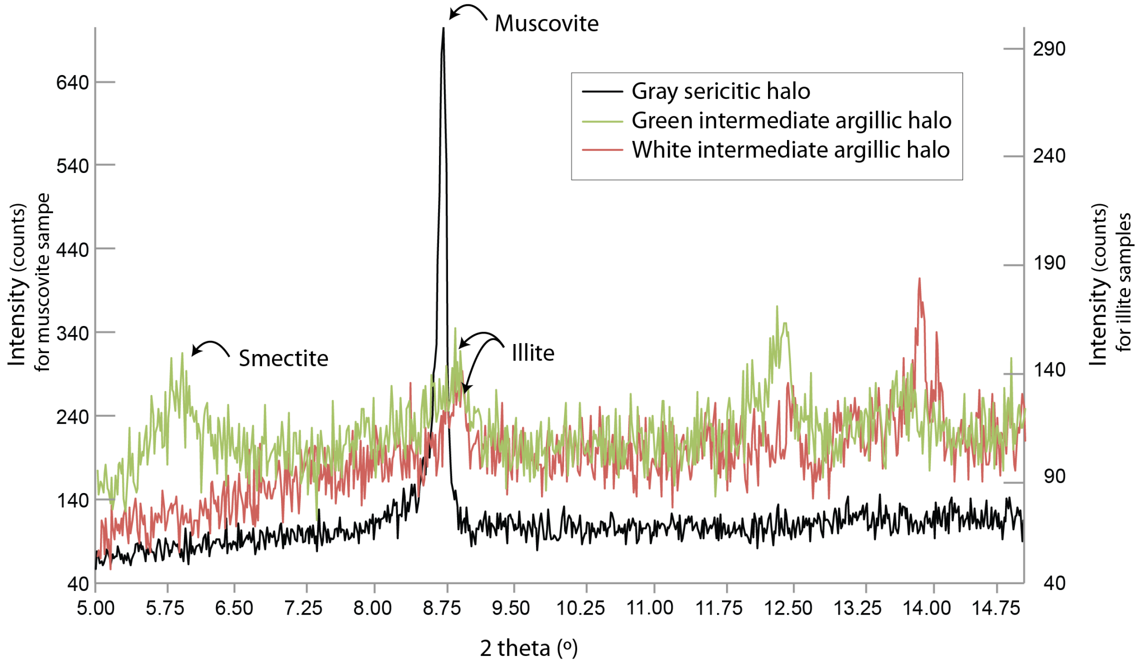

Figure 3.7. XRD spectra of a gray sericitic halo (AHAD233-330.5m) with a narrower and more intense muscovite peak at 2ϴ=8.762º (left hand Y-axis) in comparison to the slightly wider and much less intense illite peaks (righ hand Y-axis) of green (2ϴ=8.822º, AHAD185-354m) and white (2ϴ=8.878º, AHAD127-1107m) intermediate argillic halos. The green intermediate argillic halo also shows a smectite peak at 2ϴ=5.873º.

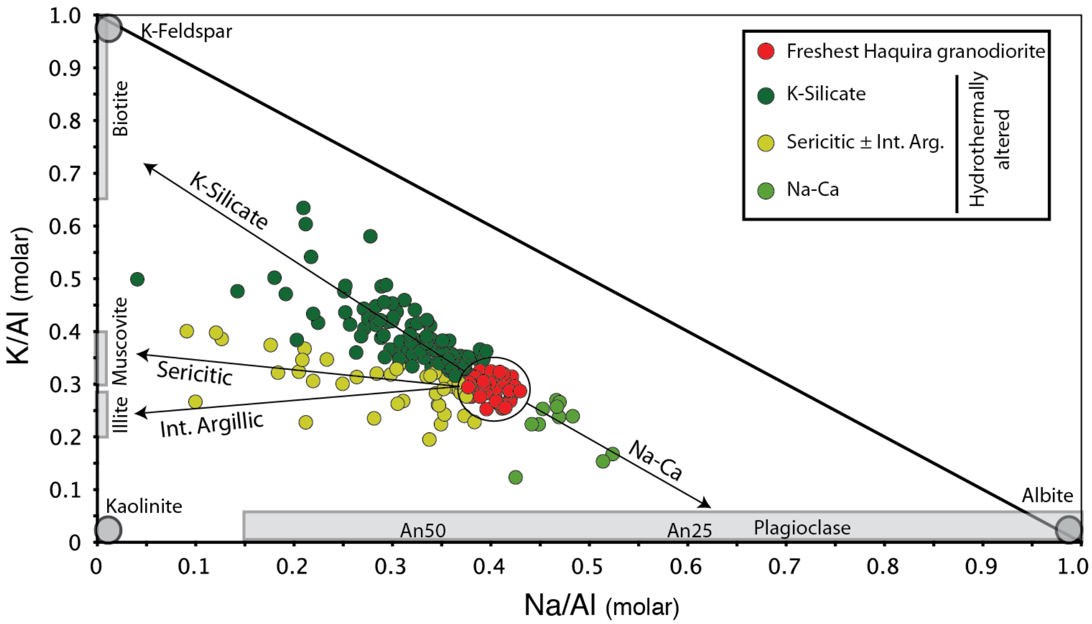

Figure 3.8. K/Al versus Na/Al molar plot showing the interpreted hydrothermal alteration for whole rock samples of the HG stock analyzed by ICP-MS after four acid digestion.

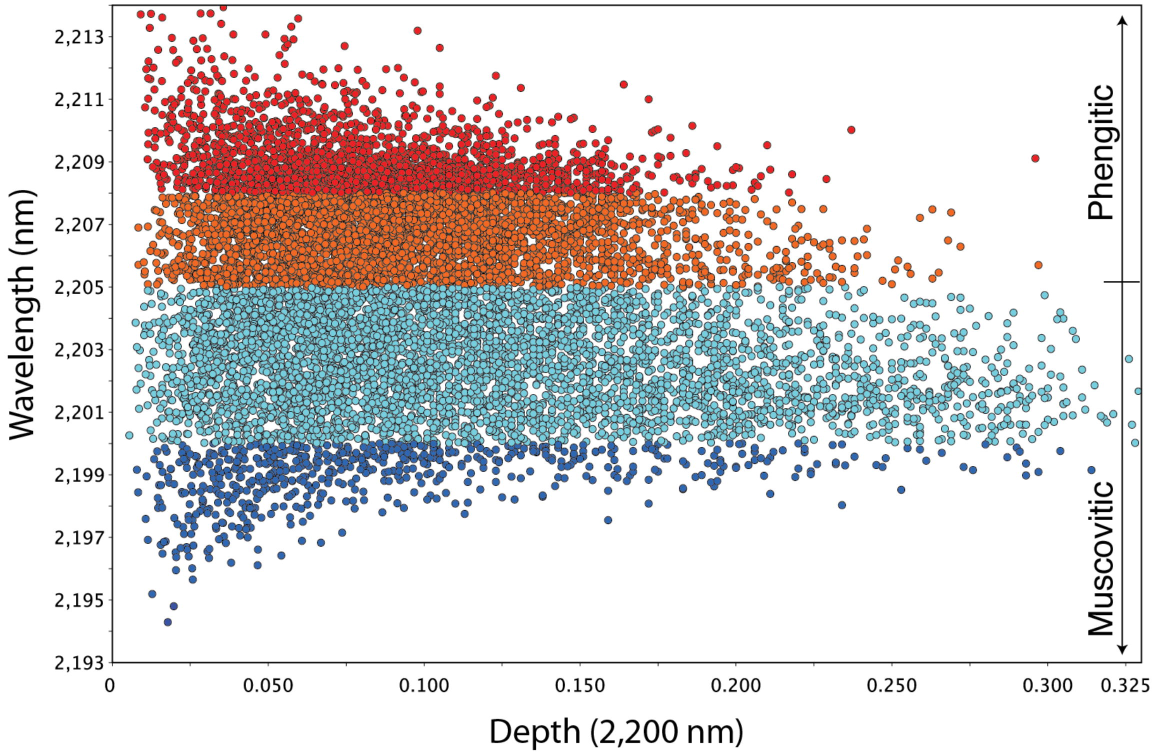

Figure 3.9. Samples with SWIR-identified muscovite-illite shown in a plot of the wavelength of the ~2,200 nm absorption feature versus its depth. The samples are color coded according to the wavelength of the 2,200 nm absorption feature. Samples in orange and red are phengitic muscovite (pure phengite ~ 2,220 nm) and samples in blue are muscovite (pure muscovite ~2,195 nm).

Figure 3.10. A) Schematic summary of some of the hydrothermal alteration and mineralization features at Haquira East. Same view as cross-section 1900NW. The magmatic-hydrothermal fluid migrated along a sub-vertical pathway close to the SW flank of the HG intrusion that defines a symmetry axis for the distributions of most veins, Mo-ore and low grade Cu. High grade Cu, EDM halos and high density of B veins is restricted to the HG stock and missing in the meta-sedimentary wall rock. **B)** Schematic sequence of intrusions, veins and mineralization. The width of the boxes reflects the relative volumes. The K-silicate alteration and Cu-Mo-mineralization was synchronous with the emplacement of the Hp dikes. The first and higher grade Cu is hosted in EDM halos, whereas most of the high-grade Mo is hosted in later BMQ veins. Later B veins host additional Cu and Mo.

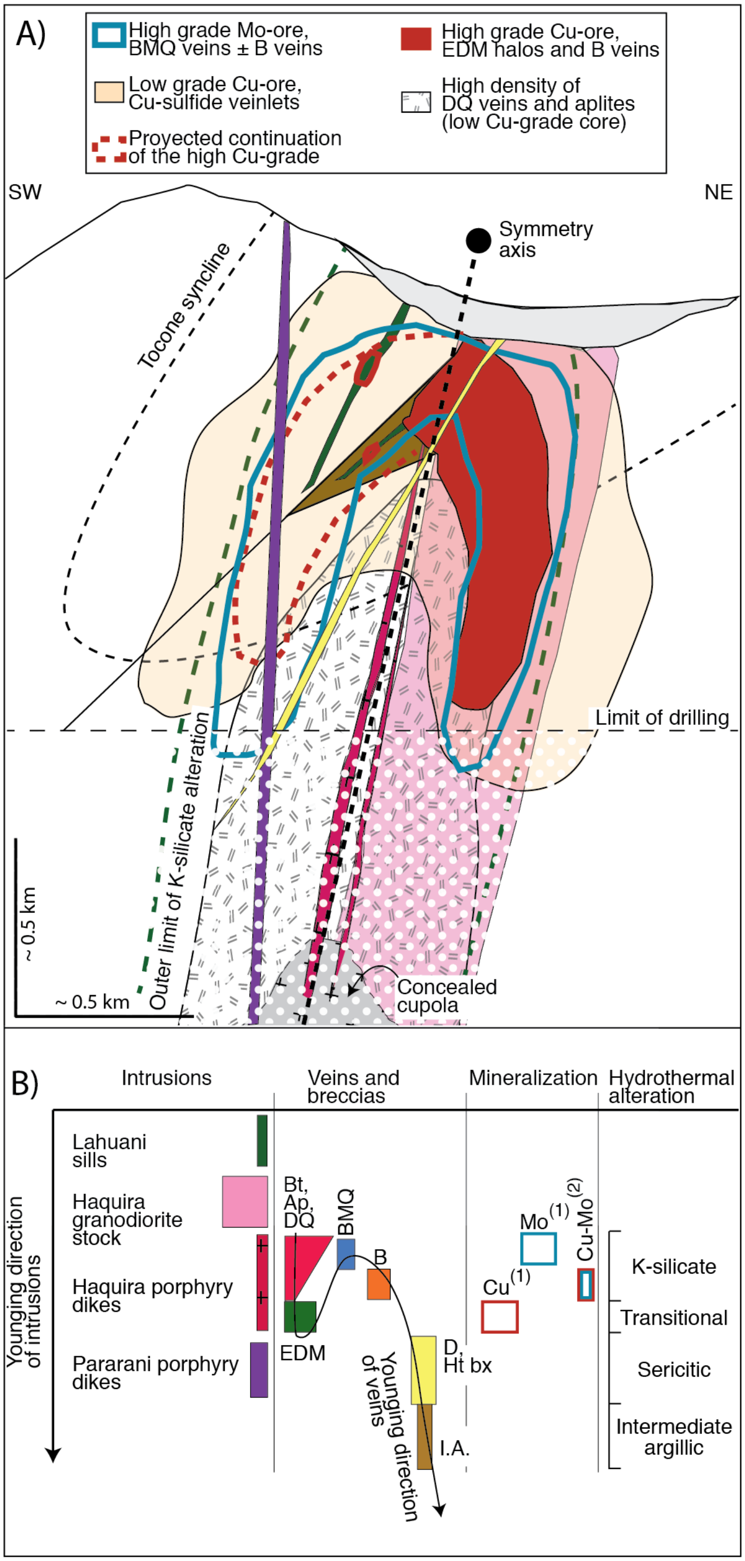

Figure 3.10. Schematic summary of some of the hydrothermal alteration and mineralization features at Haquira East, sequence of intrusions, veins and mineralization.

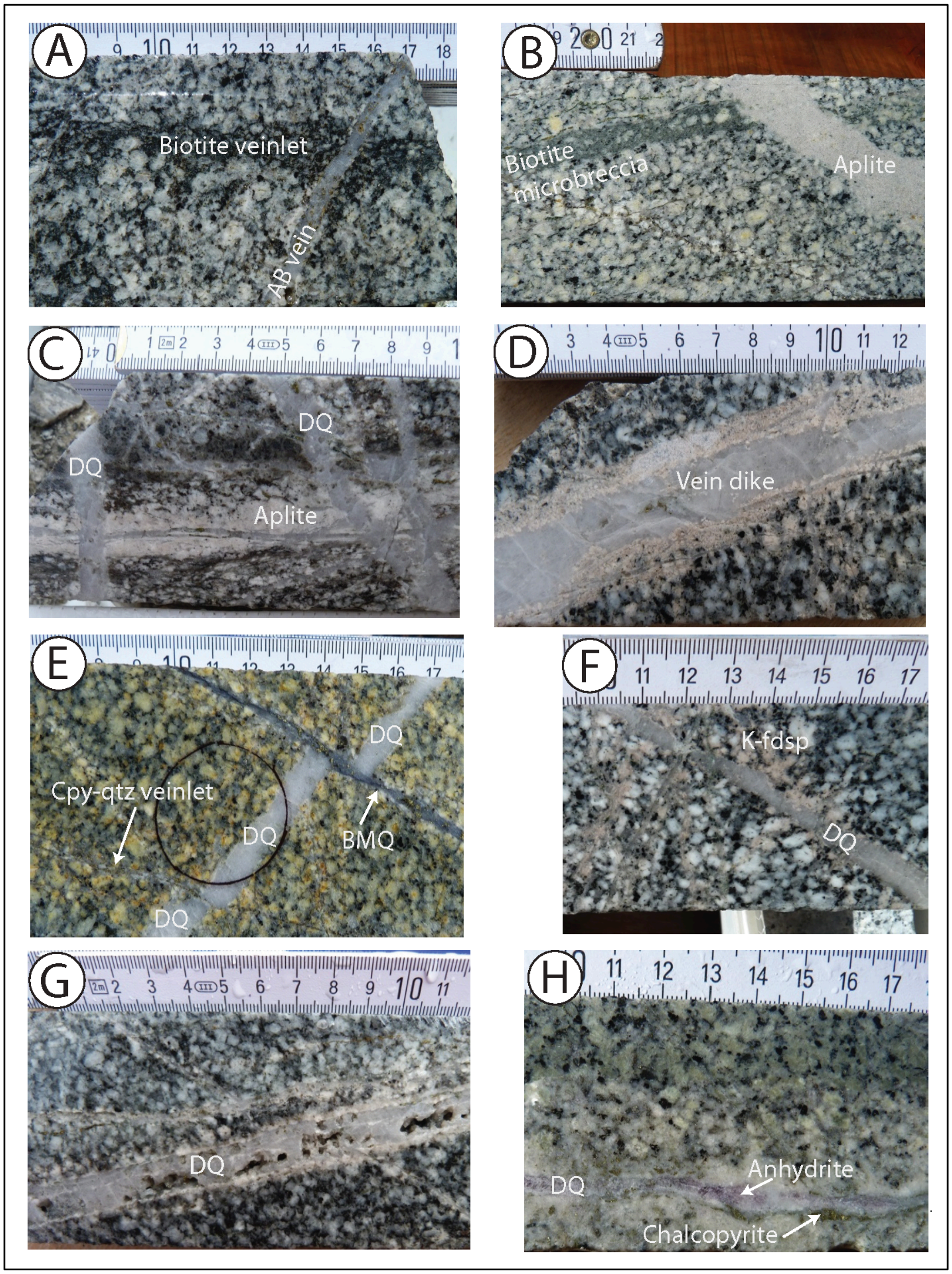

Plate 3.1. A) AHAD127-519.65m biotite veinlet cross-cut by an AB-vein with chalcopyrite **B)** AHAD116-278.3m biotite microbreccia cross-cut by an aplite. **C)** AHAD98A-361m Aplite crosscut by DQ veins. **D)** AHAD98A-495.7m vein dike (DQ vein re-opening an aplite). **E)** AHAD105-205.9m DQ vein cut and displaced by a narrow BMQ vein. **F)** AHAD176-1014m DQ vein from Haquira-East low Cu-grade core with a halo of hydrothermal K-feldspar replacing plagioclase. **G)** AHAD98A-450m DQ vein with vuggy centerline, probably after anhydrite dissolution at low temperature **H)** AHAD120-1022m DQ vein with quartz, anhydrite and less abundant chalcopyrite-pyrite.

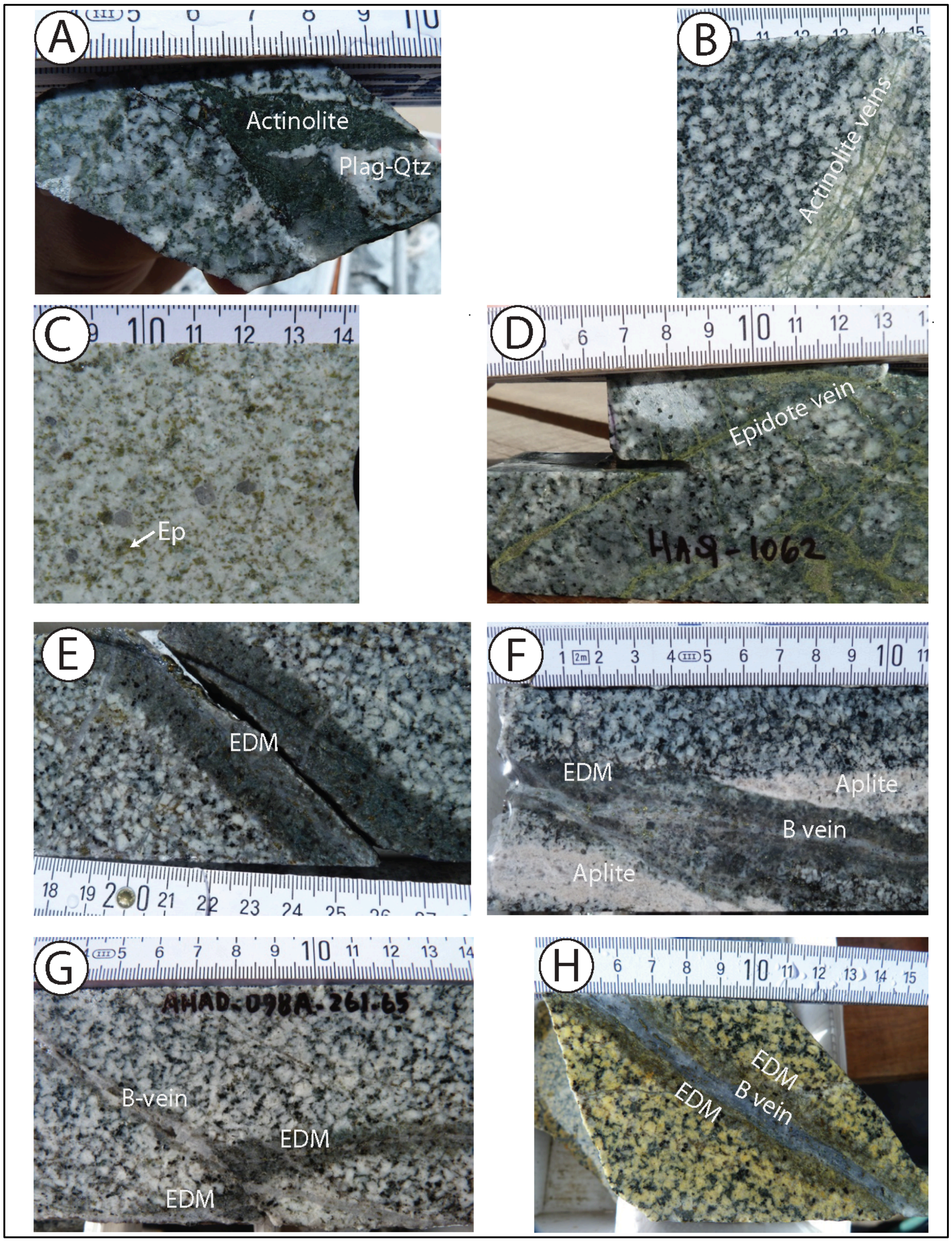

Plate 3.2. A) AHAD185-567 actinolite-plagioclase alteration patch with minor quartz. **B)** AHAD105-337.4m narrow actinolite veins with plagioclase halo. **C)** AHAD132-95.2m Epidote replacing plagioclase in a Lahuani sill. **D)** AHAD264-735.85m epidote±actinolite veins. **E)** AHAD98A-125.8m EDM halo with bornite-chalcopyrite and no quartz centerline. **F)** AHAD98A-426m aplite cut and displaced by EDM halo. EDM halos are re-opened by narrow B veins with bornite-chalcopyrite. **G)** AHAD98A-261.65m EDM halo cross-cutting a B vein with chalcopyrite. **H)** AHAD185-229m EDM halo with chalcopyrite and traces of bornite reopened by B-vein with chalcopyrite-bornite-molybdenite.

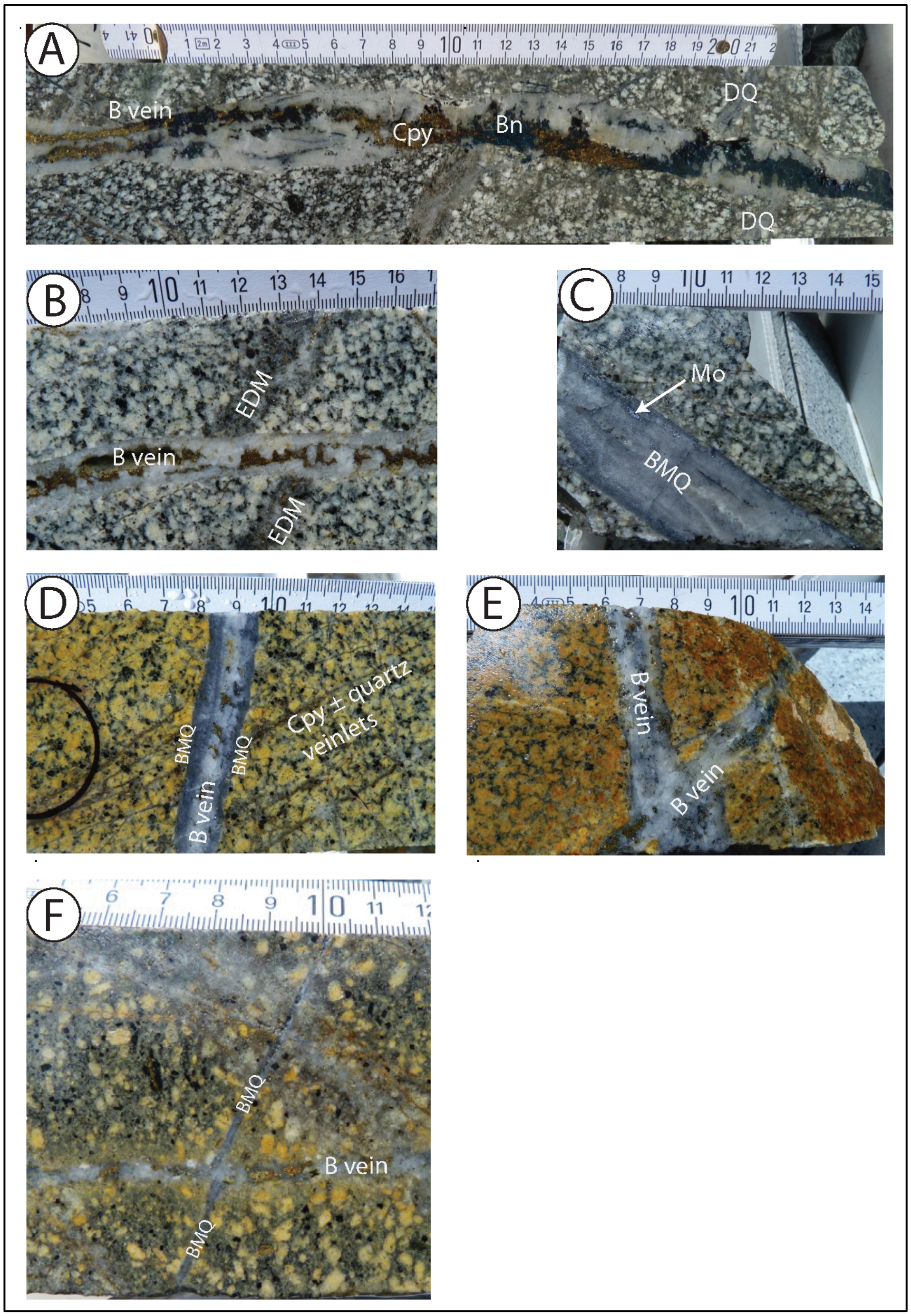

Plate 3.3. A) AHAD185-745m B-vein with bornite-chalcopyrite cross-cutting DQ veins. **B)** AHAD127-474m EDM halo cross-cut by a chalcopyrite rich B-vein. Vugs were probably filled by anhydrite. **C)** AHAD98A-127.7m typical BMQ with two narrow molybdenite bands on its edges. **D)** AHAD185-234m BMQ vein reopened by a B-vein with chalcopyrite-bornite. Both the BMQ and B vein cross-cut chalcopyrite veinlets with rare quartz. **E)** AHAD185-262m two B-vein with chalcopyrite-bornite cross-cutting and displacing each other. **F)** AHAD185-238m a molybdenite-bearing BMQ vein cross-cut and displaced by a B vein with bornite, chalcopyrite and molybdenite.

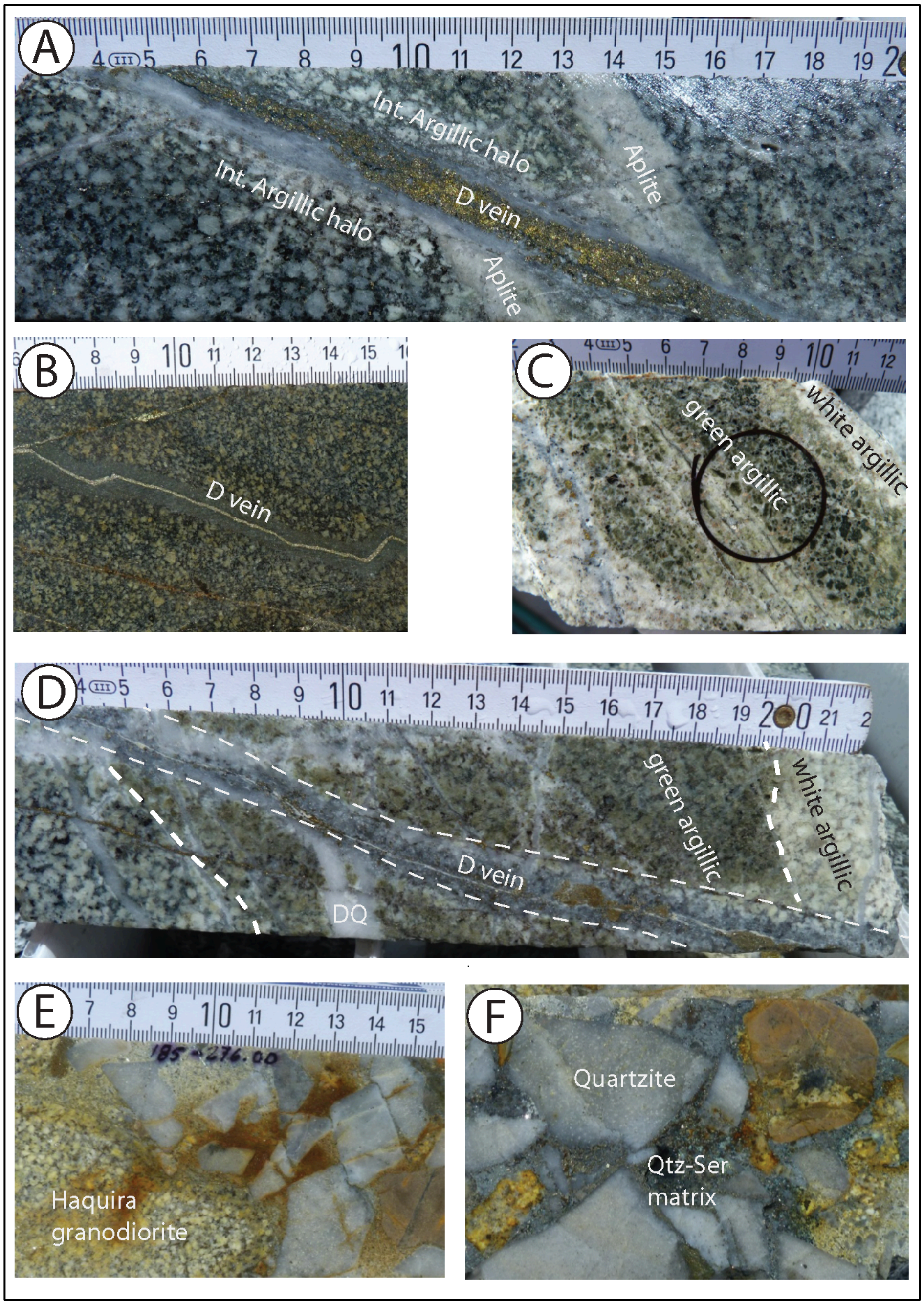

Plate 3.4. A) AHAD106-618.5m quartz-pyrite±chalcopyrite±muscovite D-vein with a sericitic quartz-muscovite±pyrite halo and cross-cutting and aplite. An intermediate argillic external halo with illite-kaolinite-smectite is later than the D-vein. **B)** AHAD175-537m D-vein with pyrite and less quartz and a sericitic halo of muscovite-quartz-pyrite cross-cut a Lahuani sill. **C)** AHAD185-354m intermediate argillic halos over imposed to early quartz rich veins. Green-argillic halo (chlorite-smectite-illite) parallel to a white-argillic halo (illite-kaolinite-smectite-chlorite). **D)** AHAD127-801.7m the strike of pyrite-muscovite rich D-vein is perpendicular to the strike of intermediate argillic halos. **E, F)** AHAD185-276m hydrothermal breccia consisting of quartzite and Haquira granodiorite clasts in a quartz-sericite matrix.

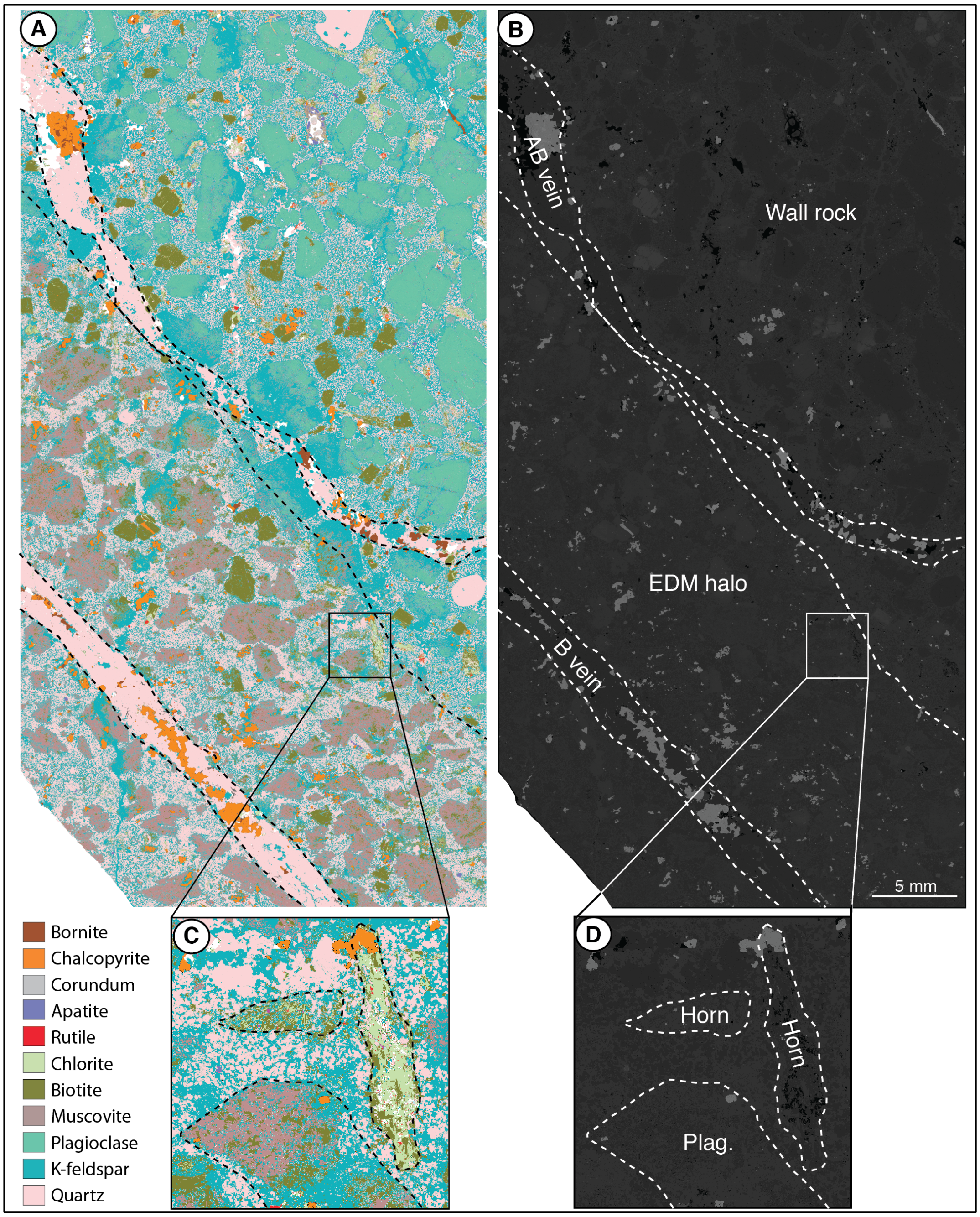

Plate 3.5. A), C) QEMSCAN image and **B), C)** back-scattered image of EDM halo sample FC-HAQ-002 (AHAD98A-125.8m) in a Haquira porphyry dike. The EDM halo is composed of hydrothermal biotite, muscovite, K-feldspar, corundum and quartz replacing plagioclase sites. Hornblende is replaced by hydrothermal biotite. Chalcopyrite and bornite are present both in the plagioclase and hornblende sites. Magmatic biotite is stable in the EDM halo. Later chlorite replaces magmatic and hydrothermal biotite. A chalcopyrite-bornite B vein re-opened the central fracture of the EDM halo. An AB vein at the edge of the EDM halo has a narrow K-feldspar halo. Thin K-feldspar veinlets are perpendicular to the EDM and B veins.

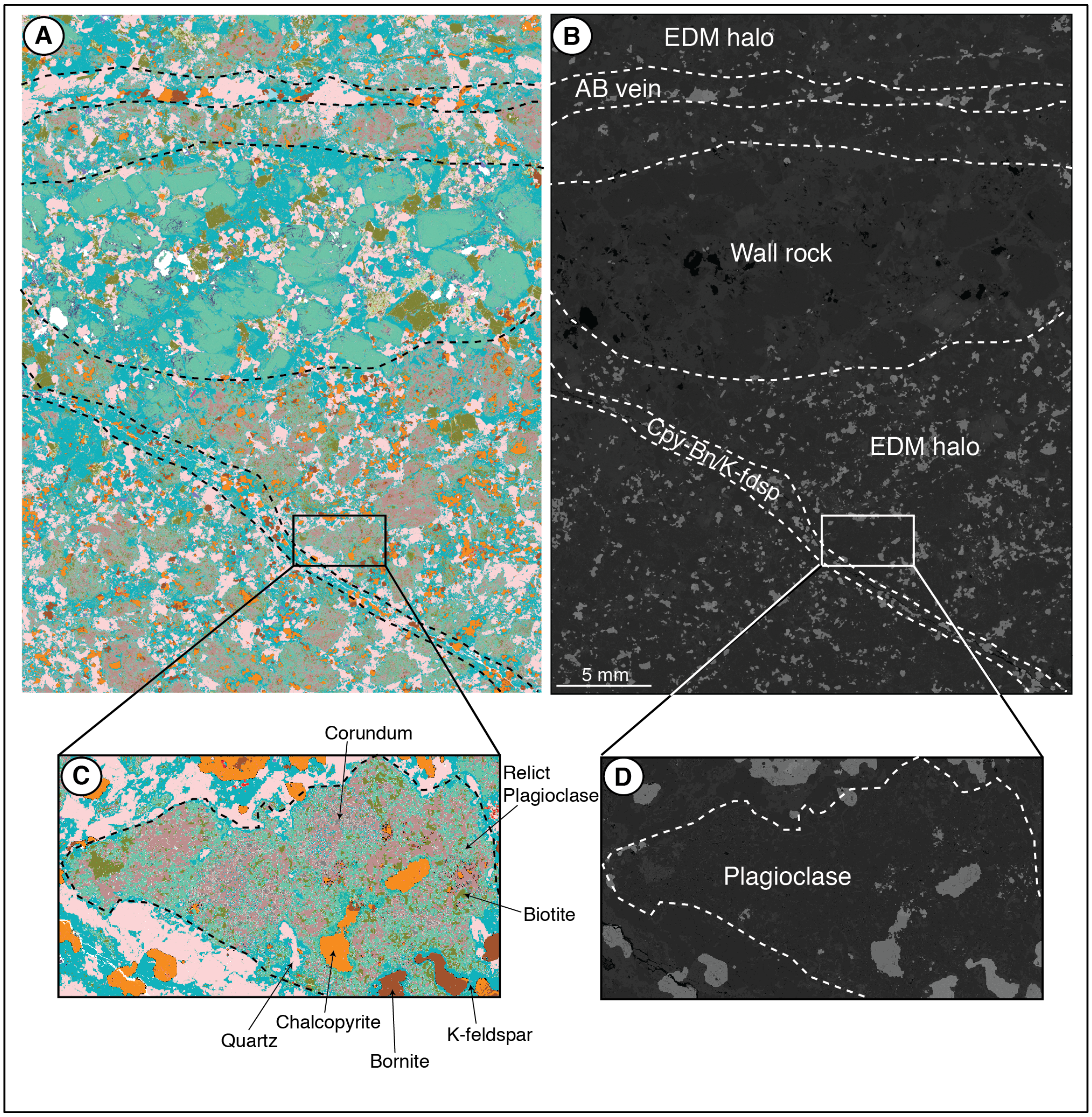

Plate 3.6. QEMSCAN image and **B), C)** back-scattered image of EDM halo sample FC-HAQ-253 (AHAD-224-568m). Two EDM halos cross-cut the Haquira granodiorite stock. The upper EDM halo is re-opened by a discontinuous quartz AB-vein with chalcopyrite and K-feldspar. The lower EDM halo is cross-cut by a chalcopyrite and bornite veinlet with a narrow K-feldspar halo. The Cu-sulfides are abundant in the veins and the EDM halos and are rare in their wall rock. **C), D)** Plagioclase sites are partially replaced by hydrothermal K-feldspar, biotite, muscovite, corundum, quartz, bornite and chalcopyrite.

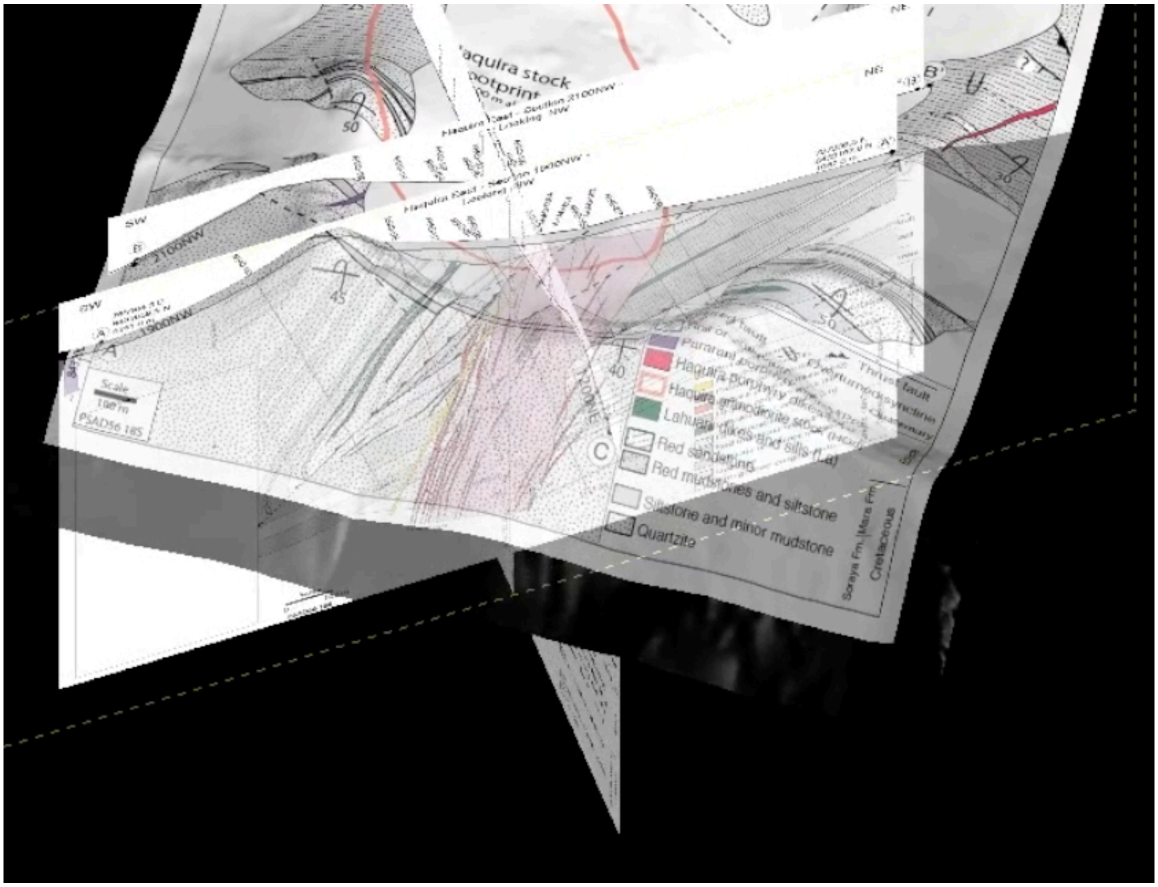

Movie 3.1. Geology of Haquira East. The location and shape of the Haquira granodiorite stock is shown in 2D in three cross-sections. A 3D model of the stock was made with all the drill-hole lithological logs. The solid pink model shows the areas that are within 100 m distance from drill holes, whereas the shaded pattern shows the areas where the 3D model is less constrained. The Haquira porphyry dikes are narrow and discontinuous and are only shown in the cross-sections. The later Pararani porphyry dikes are shown in purple. Click here. *Password: Haquira-2015-*

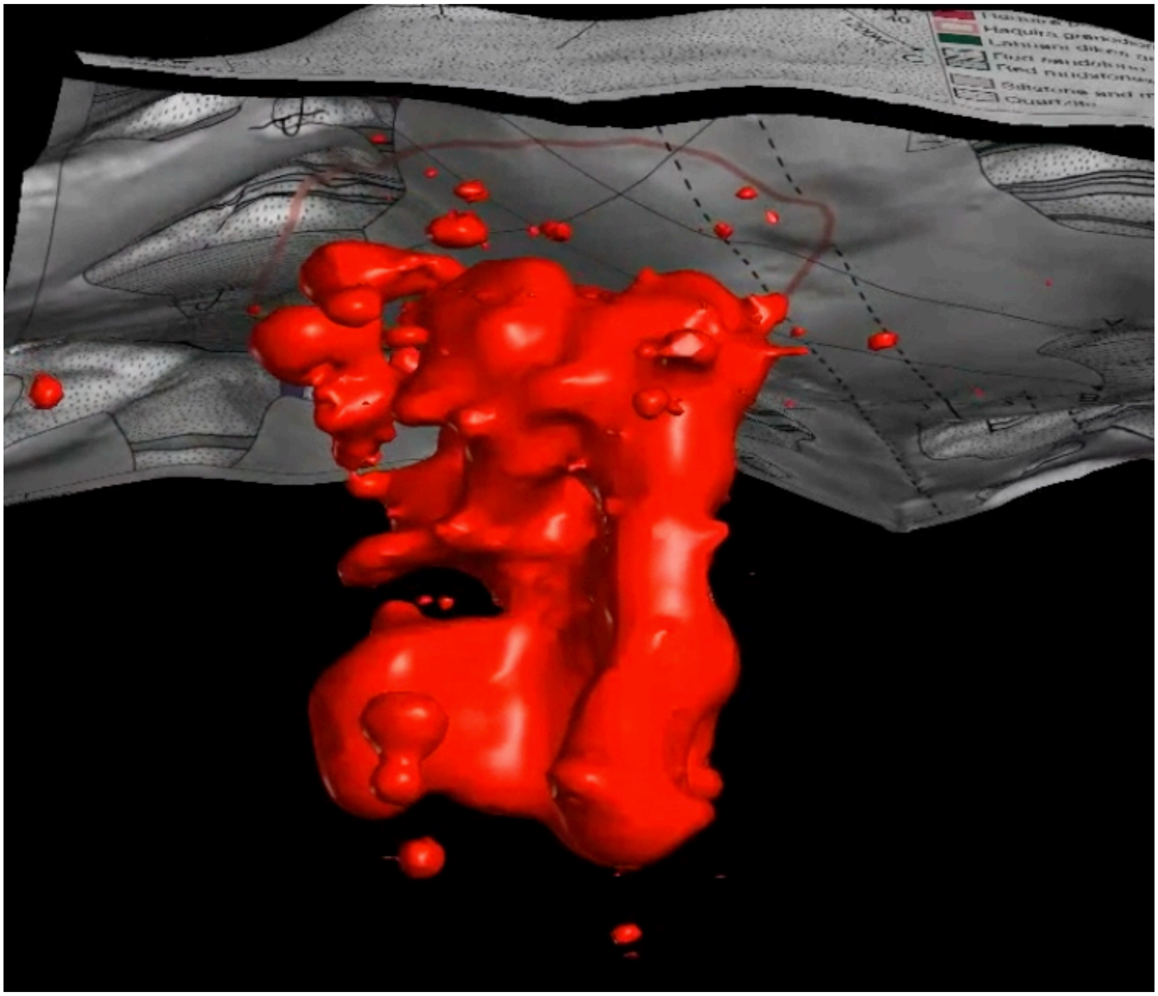

Movie 3.2. Cu- and Mo-ore shells. The modeled ore shells are shown in solid color in the areas within 100 m distance from the drill holes, whereas the shaded pattern shows the less constrained areas where drill holes are further apart. The 0.1 wt.% Cu is shown in yellow and the 0.5 wt. % shell is shown in red. The 5 ppm, 50 ppm and 100 ppm Mo-ore shells are shown in different shades of blue. The high grade Cu ore (> 0.5 wt. %) is mostly restricted to the granodiorite wall rock and is locally hosted in Lahuani dikes and in small replacements in the locally carbonaceous silt wall rock but absent in the quartzite wall rock. The high-grade Mo ore (> 50 ppm) is continuous through all the wall rock types, and an asymmetry is only observed at very high Mo concentrations (> 100 ppm). Click here. *Password: Haquira-2015-*

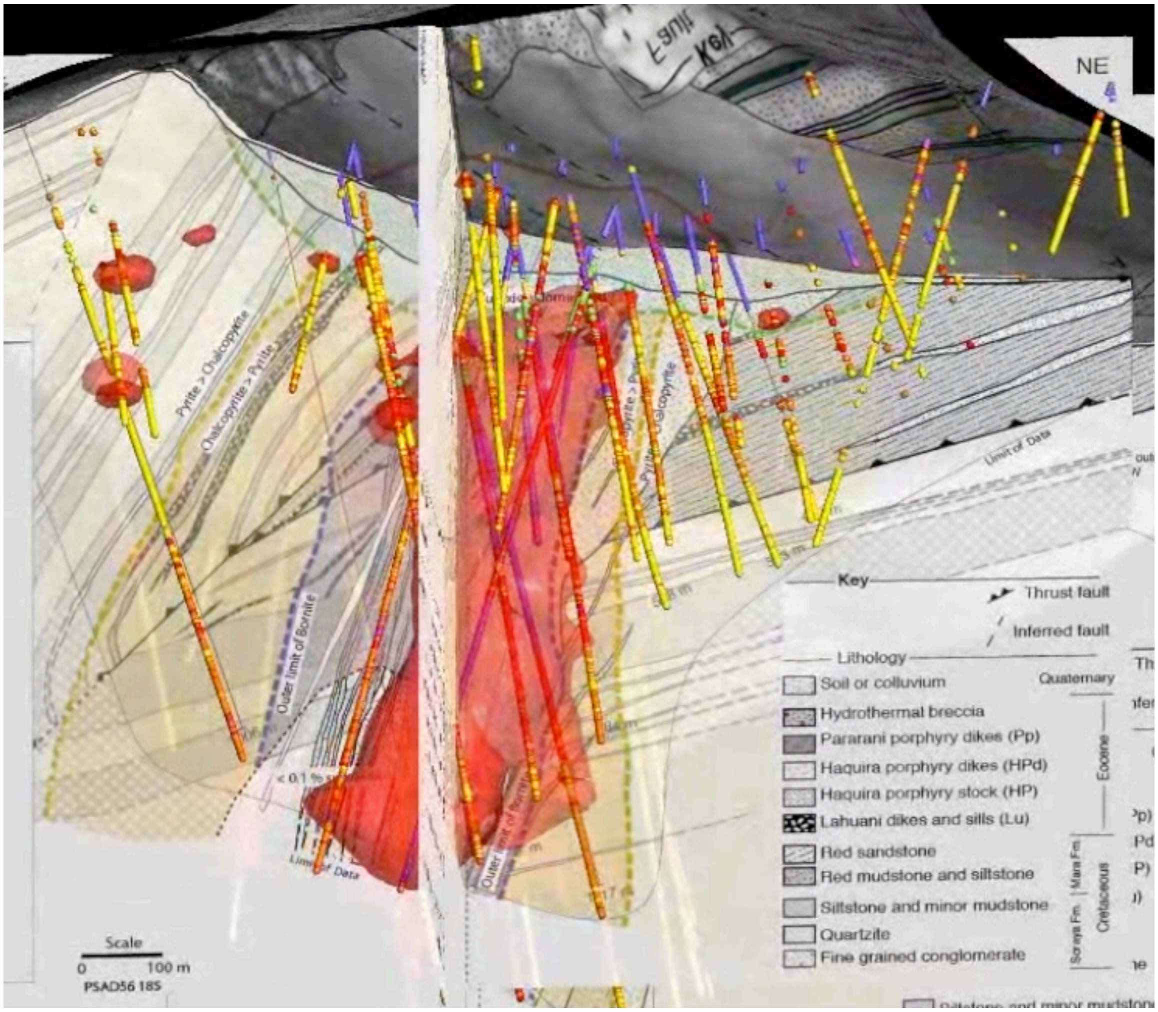

Movie 3.3. Copper sulfide distribution. The sulfide distribution in the cross-sections was contoured from the logged sulfide in the drill-hole core. Aqua regia ICP-OES exploration samples along drill-holes are color coded based on the dominant sulfide present as interpreted by the relative abundances of Cu, Fe, S, Au and Ag (Fig. 3.5). Click here. *Password: Haquira-2015-*

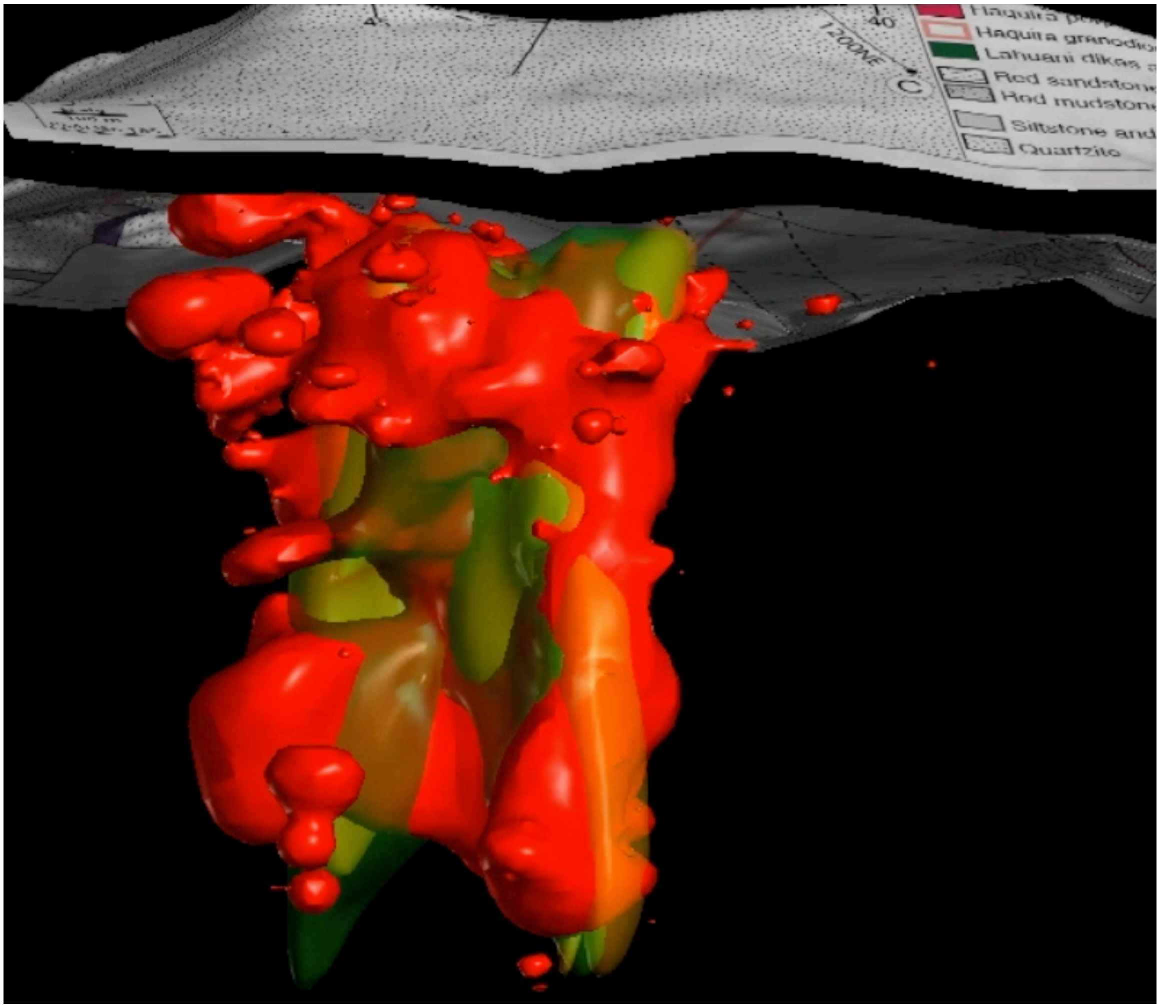

Movie 3.4. Vein distribution. 3D models of the distribution of the different vein types are modeled from the logged distribution of veins in the sections 1900NW, 2100NW and 12000NE. The modeled vein distributions are shown in solid color in the areas within 100 m distance from the drill holes, whereas the shaded pattern shows the less constrained areas where drill holes are further apart. Click here. *Password: Haquira-2015-*

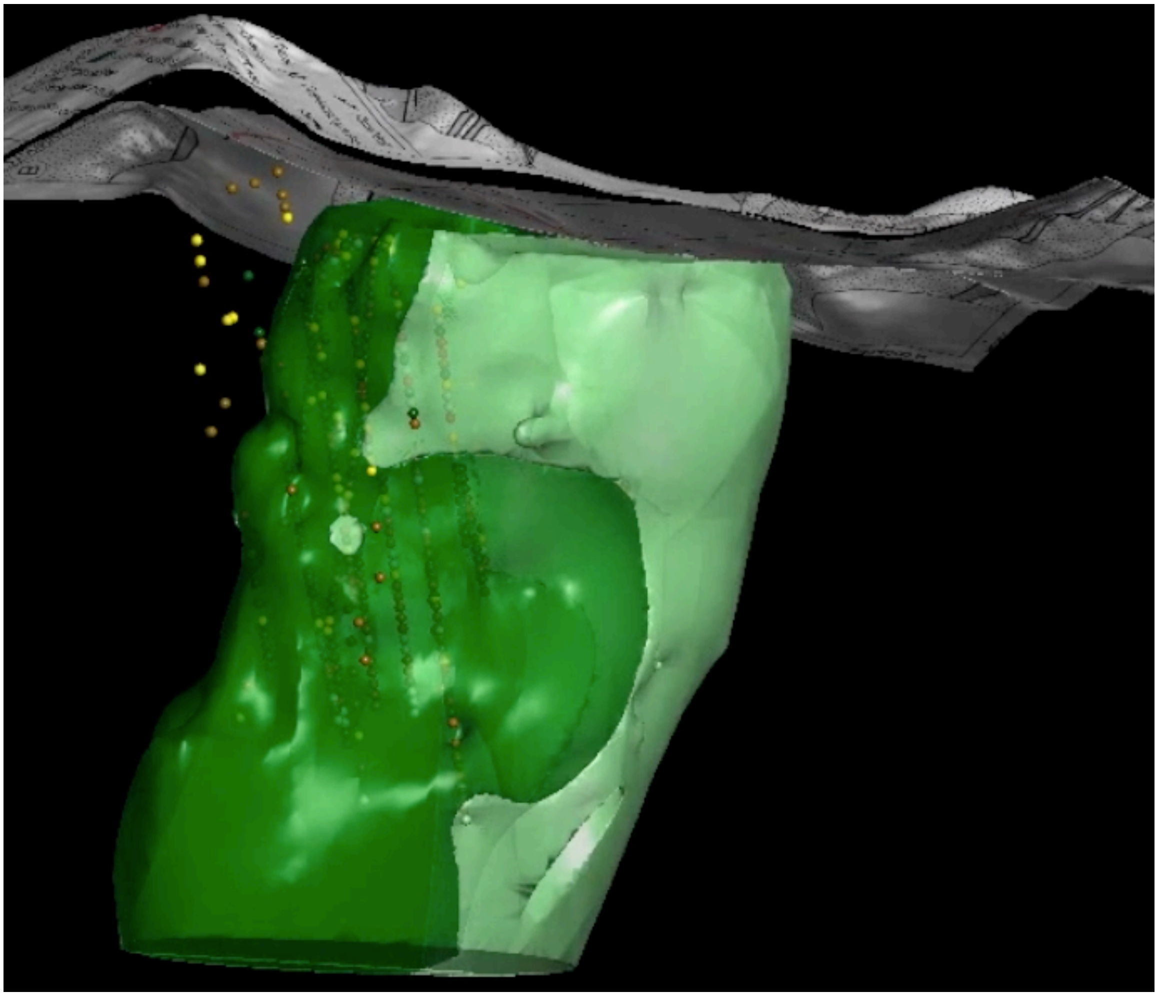

Movie 3.5. Hydrothermal alteration. Drill-hole core samples of the Haquira granodiorite stock and porphyry dikes analyzed by four acid digestion and ICP-MS are color coded according to the dominant hydrothermal alteration as interpreted using a molar ratio diagram of Na/Al versus K/Al (Fig. 3.8). Click here. *Password: Haquira-2015-*

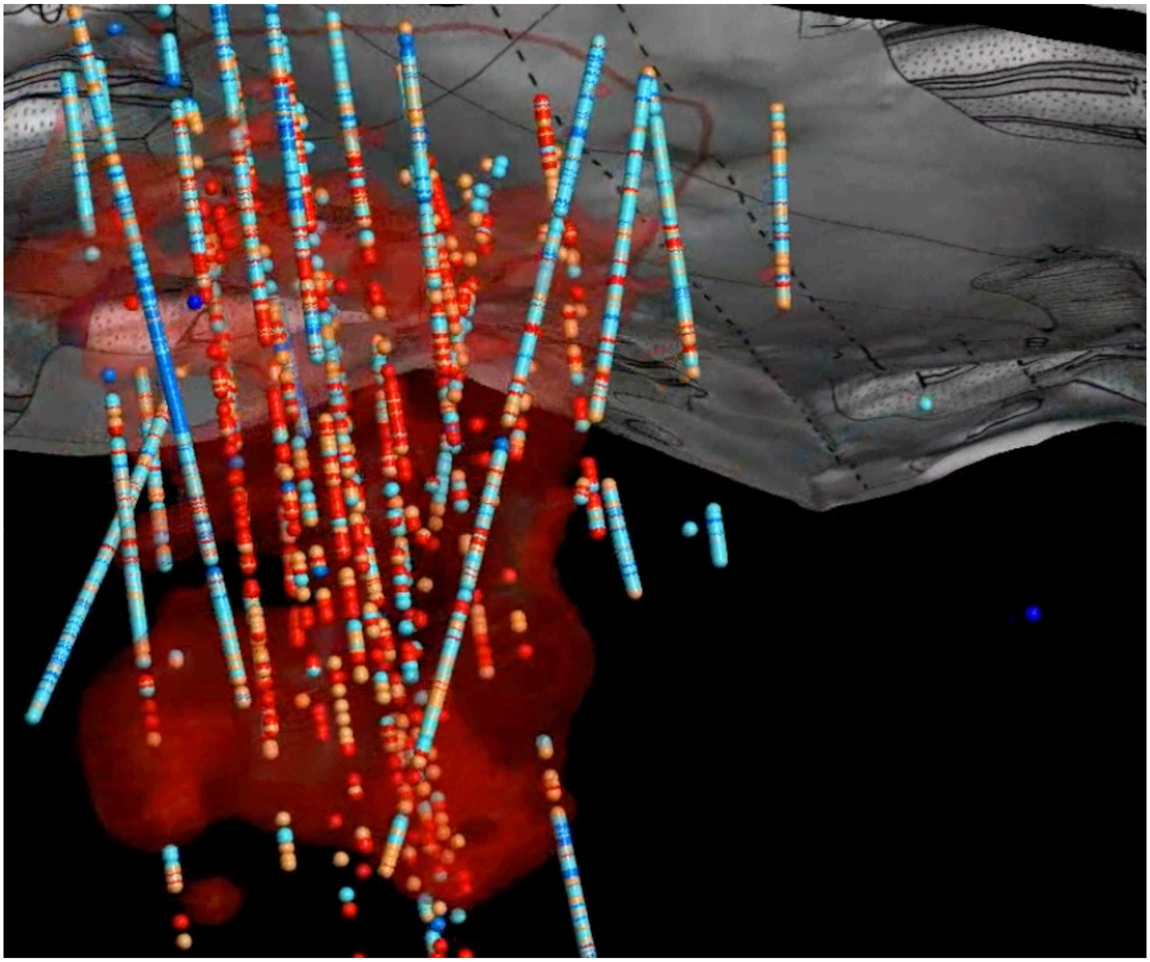

Movie 3.6. SWIR hydrous mineralogy. Drill-hole core intercepts analyzed by SWIR are color coded according to the main hydrous mineral identified. Part 1) Mixtures of hornblende and biotite versus muscovite. Part 2) Intercepts with muscovite-illite are color coded according to position of the 2,200 nm absorption feature to discriminate muscovite from phengitic muscovite (Fig. 3.9). Part 3) Intercepts were low temperature clays were identified are color coded according to presence of kaolinite or smectites. Click here. *Password: Haquira-2015-*

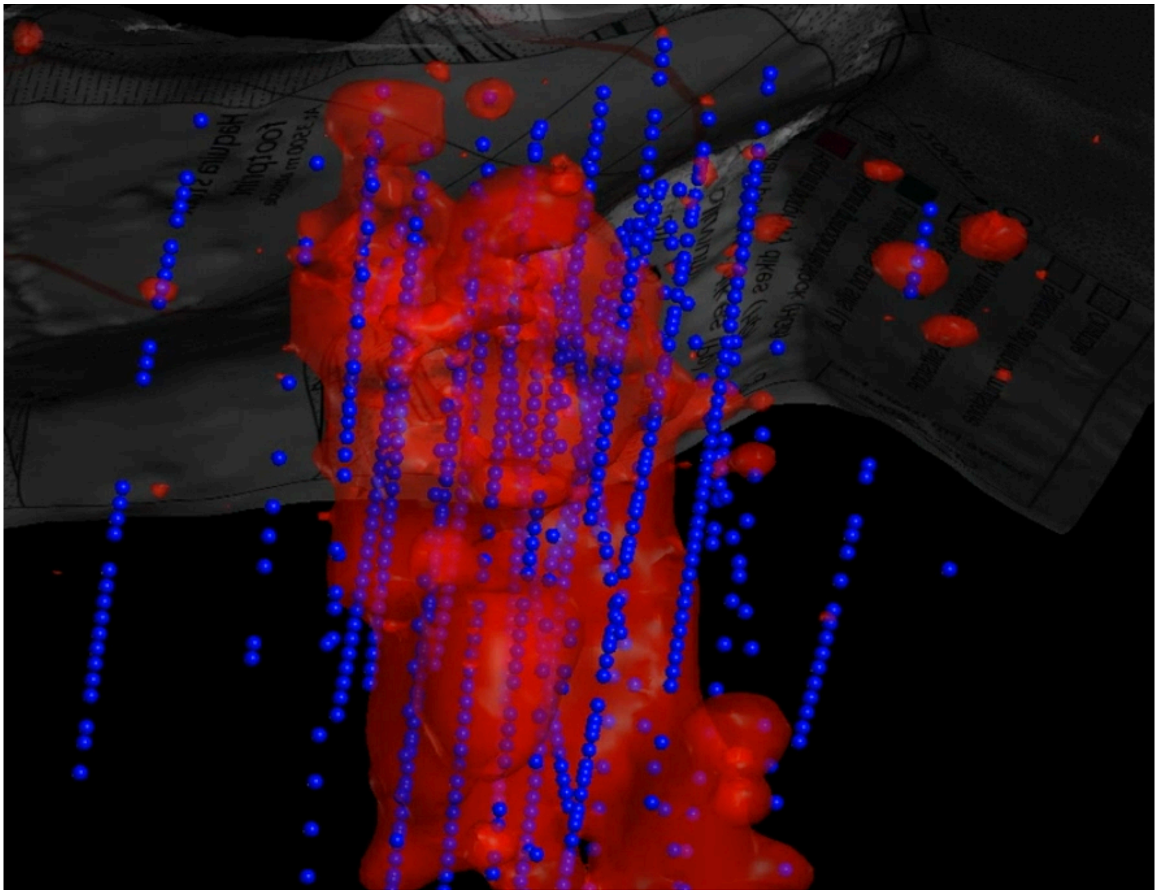

Movie 3.7. Whole rock trace element footprints. Drill-hole core intercepts analyzed with four acid digestion and ICP-MS are color coded according to the abundance trace elements that were introduced with the porphyry hydrothermal system. Blue: Mo > 5 ppm; purple: W > 5ppm; gray: Sn > 4 ppm; red: Sb > 4 ppm; yellow: As > 40 ppm. Click here. *Password: Haquira-2015-*

CHAPTER IV

COPPER MINERALIZATION ABOVE 400ºC IN PORPHYRY COPPER DEPOSITS?

Federico Cernuschi
John H. Dilles

Draft of an express letter to be submitted to Economic Geology
A journal of the Society of Economic Geologists

4.1 Abstract

The temperature of Cu-sulfide deposition and the formation of high grade copper ore in porphyry copper deposits has been the subject of strong debate for at least a decade. Vein cross-cutting relations, mineral phase equilibria and sulfur isotope data apparently indicate copper precipitation temperatures above 400ºC and stable with hydrothermal biotite and K-feldspar bearing K-silicate alteration. More recent studies, however, that employ secondary electron microscope cathodoluminescense (SEM-CL) imaging of quartz, coupled with in-situ TitaniQ geothermometry and fluid inclusion data, suggests that copper deposition took place at temperatures below 400ºC and therefore in stability with sericitic alteration. SEM-CL imaging enabled the differentiation of multiple quartz generations within a signle vein type and the observation that dark-CL and low temperature quartz is commonly in contact with Cu-sulfides.

In this study, we re-evaluate this apparent contradiction using previously published data combined with new vein cross-cutting observations and SEM-CL imaging of quartz veins from Haquira East porphyry copper deposit of southern Peru and Batu Hijau in Indonesia. We find that the evidence for Cu-sulfide deposition below 400ºC is ambiguos, and that the observations can be reconciliated with Cu-sulfide deposition above 400ºC in agreement with mineral phase equilibria predictions, vein cross-cutting observations and the the observed correlation of K-silicate stable Early Dark Micaceous (EDM) halos, A or B type veins with the high grade Cu-ore shell in porphyry copper deposits. Although the Cu-sulfides are sometimes in direct contact with the latest and darkest-CL quartz in microfractures, they are also in contact with earlier and brighter CL quartz of EDM halos, A and B veins. Cu-sulfides are only observed along the strike of bright- to gray-CL quartz bearing A and B veins and/or in EDM halos evidencing an intimate association with bright- to gray-CL quartz. The dark-CL quartz in microfractures is ubiquitous in Cu-bearing veins at Haquira and porphyry copper deposits elsewhere, but is equally common in earlier low-grade Cu or barren veins and magmatic quartz with no Cu-sulfides. Furthermore, the dark-CL quartz is texturally and compositionally indistinguishable from the equally dark-CL quartz in later low-grade Cu D veins.

We propose that Cu-sulfides are precipitated early, above ~400ºC and in stability with K-silicate alteration. In our preferred model, the late and lower temperature silica saturated fluid that produced the dark-CL quartz in microfractures also produced the pyrite-muscovite-quartz D veins and sericitic halos that cross-cuts all the earlier K-silicate stable veins/halos. Microfractures in earlier low- and high-grade Cu quartz veins are, thus, created after volume reduction upon cooling of the quartz in the vein. The contact between sulfides and quartz grains are pre-existing

discontinuities that provide a breaking surface during the volume contraction, facilitating the creation of open space. This mechanism can explain why late and low temperature dark-CL quartz is commonly observed in contact with earlier and higher temperature Cu-sulfides in the Cu-ore-forming veins.

4.2 Introduction

Porphyry Cu ± Mo ± Au are large economic mineral deposits that are associated with shallowly emplaced arc-type granitoids typically in convergent tectonic settings (Seedorff *et al.* 2005). Sulfide mineralization and hydrothermal alteration is intimately related to quartz-bearing veins. In a standard model, magmatic-hydrothermal fluid separates from cupolas atop a deep magma chamber and ascends by hydro-fracturing the overlying wall-rock where it reacts with rock, cools, and depressurizes to form veins and Fe, Cu, Mo, and Au-bearing sulfides (Fig. 4.1). Small volumes of magma are emplaced synchronously and form porphyry dikes (*i.e.* Burnham, 1979; Dilles, 1987). The magmatic-hydrothermal fluid flow ranges in temperature from >650ºC to <250ºC as recorded by the different hydrothermal alteration mineral assemblages that replace the wall-rock minerals and phase equilibria studies (*e.g.* Seedorff *et al.* 2005), TitaniQ geothermometry of quartz in porphyry and veins (Rusk *et al.,* 2012) and fluid inclusion data (Rusk *et al.,* 2008).

The timing and temperature of Cu-sulfide deposition and the formation of the high grade Cu-ore has been subject of signifiant debate. Whereas vein cross-cutting relations, mineral phase equilibria and sulfur isotopic composition of sulfide and sulfate pairs apparently indicate deposition temperatures above 400ºC (*e.g.* Seedorff *et al.,* 2005; Field *et al.,* 2005), secondary electron microscope cathodoluminescense (SEM-CL) imaging of quartz in veins and TitaniQ geothermometry suggest that Cu-sulfide deposition took place below 400ºC (*e.g.* Redmond *et al.* 2004).

In this study, we re-evaluate this apparent contradiction using previously published data combined with new vein cross-cutting observations and SEM-CL imaging of quartz veins from Haquira East porphyry copper deposit of southern Peru and Batu Hijau in Indonesia. We find that the evidence for Cu-sulfide deposition below 400ºC is ambiguos, and that the observations can be reconciliated with Cu-sulfide deposition above 400ºC in agreement with mineral phase equilibria predictions, vein cross-cutting observations and the the observed correlation of K-silicate stable Early Dark Micaceous (EDM) halos, A or B type veins with the high grade Cu-ore shell in porphyry copper deposits.

4.2.1 Copper ore, veining and hydrothermal alteration in porhyry copper deposits

In deeply emplaced porphyry copper deposits the high grade copper is hosted in bornite ± chalcopyrite ± digenite bearing Early Dark Micaceous (EDM, *cf.* Brimhall, 1977) halos, whereas in shallowly emplaced deposits it is hosted in bornite ± chalcopyrite ± digenite bearing A type quartz veins (Fig. 4.1; Proffett, 2009). A veins are stable with hydrothermal biotite and K-feldspar, however EDM halos are also stable with muscovite. Based on mineral phase equilibria, the temperature of Cu-sulfide precipitation in A veins should overlap with the temperature range of biotite–K-feldspar bearing K-silicate alteration above ~550ºC. In EDM halos, the Cu-sulfides precipitation overlaps with transitional potassic-sericitic alteration temperatures (Seedorff *et al.* 2005) ranging between ~550 and 400ºC. Some porphyry copper deposits have significant amounts of Cu-sulfides in later B type veins, which sometimes also include molybdenite and contributes to form the high grade Mo-ore (*i.e.* Gustafson and Hunt, 1975; Cernuschi *et al.,* 2013). B veins commonly post date EDM halos and/or A veins, and are also stable with K-silicate alteration. All the Cu-ore-forming veins and halos (EDM, A, B), normally cross-cut earlier low grade or barren veins, including aplite dikes, bioite veins, deep quartz veins (DQ) with or without K-feldspar and/or magnetie. However, vein cross-cuting reversals are sometimes observed, suggesting several veining episodes (*e.g.* Seedorff *et al.* 2005). The early low-grade Cu veins are also stable with K-silicate alteration, but generally more abundant below the Cu-ore forming veins and halos (Fig. 4.1). When present, high grade Mo-ore forming banded molybdenite quartz veins (BMQ) are also stable with K-silicate alteration and either pre-date the high-grade Cu EDM halos (*e.g.* Butte, Montana; Rusk *et al.,* 2008) or post-date EDM halos (*e.g.* Haquira East, Cernuschi *et al.,* 2013) and A veins (*e.g.* Bingham, Utah, Redmond and Einaudi, 2010). In contrast, quartz-pyrite-muscovite D type veins and sericitic halos post date the high grade Cu-Mo mineralization and commonly cross-cut all the previously mentioned veins and halos (Fig. 4.1, Gustafson and Hunt, 1975). D veins and their sericitic alteration halos are stable with hydrothermal muscovite whereas magmatic bioite is no longer stable. This indicates a lower formation temperature and more acidic conditions, stable with sericitic alteration between ~400 and 300ºC (Seedorff *et al.* 2005). D veins carry pyrite and less chalcopyrite, and do not constitute the high grade Cu-ore in porphyry copper deposits.

4.2.2 Quartz in veins and the temperature of Cu-sulfide deposition

Recent studies (*e.g.* Redmond *et al.,* 2004) suggest that the copper deposition in porphyry copper deposits takes place below 400ºC in contradiction with previous vein cross-cutting observations and the mineral equilibria predictions of their hydrothermal mineral paragenesis. SEM-CL imaging of quartz veins enabled the identification of different quartz generations characterized by different CL-brightness and texture, thus rasing questions of which quartz generation was truly precipitated together with the Cu-sulfides. CL-brightness of quartz increases with Ti content, which increases with temperature of formation (Rusk *et al.,* 2008) and growth rate as calibrated by the TitaniQ thermobarometer (Huang and Audétat, 2012). Cu-sulfides in Cu-sulfide bearing veins from Butte, Montana (Rusk *et al.,* 2006), El Salvador, Chile (Rusk *et al.,* 2008), El Teniente and Los Pelambres, Chile (Rusk, 2013), Bingham, Utah (Redmond *et al.* 2004; Landtwing and Pettke, 2005), Oyu Tolgoi, Mongolia (Müller *et al.,* 2010) and Altar, Argentina (Maydagan *et al.,* 2015) were reported to be always in contact with the darkest-CL and latest generation quartz in fractures. The Ti content of the Dark-CL quartz in each of these studied porphyry copper deposits commonly ranges between ~1 and 5 ppm, and are always less than 15 ppm (Rusk, 2012). Precipitation temperatures calculated with the TitaniQ geothermometer indicates temperatures broadly below 400ºC depending on the estimated formation pressures (*e.g.* Rusk, 2012). Furthermore, at Bingham, the later dark-CL quartz in fractures and in contact with the Cu-sulfides presents a Cu-depleted fluid inclusion population with lower homogenization temperature in comparison to the Cu-rich fluid inclusions in the bright-CL A vein quartz, that were assumed to be secondary (Redmond *et al.* 2004). Based on these observations and assumption Redmond *et al.* (2004) proposed that the Cu-sulfides were introduced at a later stage than the A vein quartz. The hydrothermal fluid got depleted in copper as it precipitated the Cu-suflides right before the precipitation of dark-CL quartz in microfractures at temperatures below 400ºC.

Upon new vein cross-cutting observations and SEM-CL imaging of quartz veins from the Haquira porphyry copper deposit of southern Peru and Batu Hijau deposit of Indonesia, together with the re-examination of previously published SEM-CL images from porphyry deposits elsewhere, we conclude that the observation of dark-CL quartz associated with Cu-sulfides is not a conclusive proof of copper precipitation at temperatures below ~400ºC. Although the Cu-sulfides are sometimes in direct contact with the latest and darkest-CL quartz in microfractures, they are also in contact with earlier and brighter CL quartz of EDM halos, A and B veins. Cu-sulfides are only observed along the strike of bright- to gray-CL quartz bearing A and B veins and/or in EDM halos evidencing an intimate association with bright- to gray-CL quartz. The dark-CL quartz in microfractures is ubiquitous in Cu-bearing veins at Haquira and porphyry copper deposits elsewhere, but is equally common in earlier low-grade Cu or barren veins and magmatic quartz with no Cu-sulfides. Furthermore, the dark-CL quartz is texturally and compositionally indistinguishable from the equally dark-CL quartz in later low-grade Cu D veins. We propose that the dark-CL quartz is precipitated during sericitic alteration and after the main introduction of Cu-sulfides in earlier and higher temperature EDM halos, and in A and B veins. The dark-CL quartz is precipitated both in pyrite-muscovite bearing D veins and in microfractures that are produced upon cooling and volume reduction of the pre-exiting quartz in all the earlier veins.

4.3 Ore Geology

Haquira East is a ~33.85 Ma relatively high grade Cu-Mo porphyry deposit hosted in a ~34 Ma subvertical granodiorite stock and cut by porphyry dikes emplaced into Jurassic-Cretaceous quartzite and meta-siltstone in the southeast to northwest-trending and northeast-overturned Tocone syncline (Cernuschi *et al.,* 2013). Haquira East is part of the Eocene-Oligocene (~ 40-32 Ma) Andahuaylas-Yauri porphyry belt of southern Perú (Perello *et al*., 2003, Chapter 2). At Haquira, veins follow a sequence, from oldest to youngest, of: 1) biotite micro-breccias/veins, 2) aplites, 2) deep quartz veins (DQ), 4) actinolite and epidote veins with plagioclase halos, 5) bornite-chalcopyrite early dark micaceous (EDM) halos, 6) Cu-sulfide±quartz veinlets with chalcopyrite or bornite, 7) banded molybdenite-quartz veins (BMQ), 8) B type open space quartz-bornite-chalcopyrite veins, 9) D type pyrite-quartz-sericite veins with sericitic halos, and 10) green and white intermediate argillic halos with smectite-chlorite-illite-kaolinite ± pyrite halos (Cernuschi *et al.,* 2013, Chapter 3).

In the center of the Haquira granodiorite stock, low Cu-Mo grade veins types 1 to 3 are cut off by narrow Haquira porphyry dikes, which are in turn cut by a second set of less abundant veins types 1 and 2, yielding reverse-age relations. A low-grade and deep core characterized by hydrothermal biotite alteration and abundant type 1 and 2 veins is overlain by the highest copper grade zone, which is also characterized by hydrothermal biotite and vein sets 5, 6 and 8 that both cut and are cross-cut by the Haquira porphyry dikes (Fig. 4.1). Except for the type 4 veins with sodic-calcic alteration selvages that are interpreted as produced by non-magmatic fluids elsewhere (Dilles and Einaudi, 1992), all veins are interpreted to be magmatic-hydrothermal in origin and formed progressively at lower temperatures.

The presence of EDM halos suggests that Haquira East is a relatively deep porphyry deposit (Proffett, 2009). The preliminary hornblende barometry and the lack of unmixed fluid inclusions, suggests deeper formation conditions than Butte, possibly in the range of ~10 km (Chapter 6). Since Haquira lacks A type veins, a sample from the shallowly (1-3 km) emplaced ~1.5 Ma Batu Hijau porphyry copper-gold deposit was analyzed for comparison. Batu Hijau is located in the southwest of Sumbawa Island in the Sunda-Banda archipielago of Indonesia and is related to an Early Miocene to Holocene volcanic arc in oceanic crust. The mineralization is hosted in bornite and chalcopyrite in A veins that are abundant in a K-silicate altered zone and associated with several tonalite porphyry dikes (Garwin, 2002).

4.4 Methods

Quartz in veins and porphyry phenocrysts in thirty thin and thick polished sections were imaged using a FEI Quanta 600 FEG scanning electron microscope equipped with a Gatan MiniCL cathodoluminiscense (SEM-CL) grayscale detector at Oregon State University (OSU). Ti content of quartz was obtained at OSU using a Cameca SX-100 electron microprobe (EMP) together with laser ablation inductively coupled mass spectroscopy (LA-ICP-MS) for quartz with Ti concentrations below 13 ppm. One mineral map of an EDM halo was constructed with data obtained with a FEI QEMSCAN Quanta 650F at University of Geneva. See the Chapter 3 and 6 and the Appendix for further details.

4.5 Results

SEM-CL images of veins and halos are presented in Plates 4.1-4.3. Ti compositions of the different CL-intensity types of quartz in different veins are summarized in Table 4.1 together with precipitation temperatures estimated by TitaniQ geothermometry (Huang and Audétat, 2012). Only the lowest Ti contents of quartz in each vein type were used for TitaniQ geothermometry. The bright-CL quartz grains with high Ti-contents common in DQ veins, BMQ veins and some growth bands in B veins are interpreted to be rapidly grown and not suitable for thermometry. At rates of 120 µm/day quartz incorporates up to ~100 ppm more Ti than slow growing quartz (4 µm/day) at ~700 ºC (Huang and Audétat, 2012). Therefore, high growth rates yield high apparent formation temperatures by amounts of up to ~100 ºC. TitaniQ geothermometry limitations and other temperature constrains are discussed in more detail in Chapter 6. After accounting for the kinetic effect, DQ and BMQ veins from Haquira are estimated to form at ~650ºC, and A veins from Batu Hijau at ~600ºC. Based on the darkest CL and lowest Ti growth bands in B veins, these are estimated to form at ~550ºC (Table 4.1). Quartz in EDM halos and D veins display narrow ranges of gray-CL, consistent with equilibrium crystallization. EDM quartz is estimated to form at ~500ºC whereas the dark gray-CL quartz in D veins was estimated at ~450ºC and the latest and darkest-CL in D veins at ~350ºC (Table 4.1). We assume that the 1 to 5 ppm Ti composition measured in the dark-CL quartz of D veins by LA-ICP-MS is also representative of the equally dark-CL quartz in microfractures and riming Cu-sulfides in earlier veins indicating a formation temperature of ~350 ºC. The dark-CL quartz in D veins and the quartz in microfractures, present identical oxygen isotopic compositions, providing more evidence of the equal composition of both types of quartz (see Chapter 5). Furthermore, dark-CL quartz in microfractures in veins from other deposits present similar Ti compositions ranging between 1 and 5 ppm (*e.g.* Butte, Mercer *et al.,* 2015). The estimated formation temperatures of quartz in veins summarized here are consistent with the mineral phase equilibria of the associated hydrothermal assemblages of each vein as summarized above (Table 4.1). Nonetheless, the estimated temperatures are only considered informative and the interpretations in this study are solely based on vein cross-cutting relationships and the identification of different quartz generations in SEM-CL imaging within them as shown in Plates 4.1, 4.2 and 4.3.

At Haquira East, at the deposit scale the Cu-sulfides are intimately associated with the distribution of B-veins and the EDM halos (Chapter 3). At the vein scale, Cu-sulfides are not only in direct contact with the late and dark-CL quartz in microfractures as previously reported for porphyry deposits elsewhere. Cu-sulfides are also in contact with the gray-CL and mosaic textured quartz centerline present in some of the EDM halos and with the gray- to bright-CL growth bands in the euhedral quartz of B veins (Plate 4.1A, B, C, D). At the vein scale, the chalcopyrite in the quartz centerline of the EDM halo in Plate 4.2A and B follows the strike of the mosaic textured gray-CL quartz of the EDM (Plate 4.2C). Plate 4.2A and B also shows two B veins with bright- and gray-CL euhedral quartz that cross-cut the EDM halo and its quartz centerline. The euhedral quartz in the B veins is seen in detail in Plate 4.2C, where different CL-intensity growth bands are observed. At the vein scale the chalcopyrite is correlated with the undulating strike of the B vein quartz and not with the distribution of the dark-CL quartz.

In EDM halos, bornite and chalcopyrite are rarely in contact with any type of quartz, but are commonly in contact with hydrothermal K-feldspar that together with hydrothermal biotite, muscovite, corundum and minor quartz replaced magmatic plagioclase and hornblende (Plate 4.1C, D). Dark-CL quartz in microfractures is virtually absent in the EDM halos. Furthermore, at the vein scale the Cu-sulfides follow the strike of EDM halos and B veins and are not correlated with the distribution of the dark-CL quartz in microfractures (Plate 4.2A, B, C).

The occurrence of dark-CL quartz is not restricted to veins and halos with Cu-sulfides. Dark-CL quartz also fills microfractures that cross-cut magmatic quartz and veins stable with K-silicate alteration but with low-grade Cu. Quartz phenocrysts in porphyry dikes as well as DQ veins that are cross-cut by high-grade Cu EDM halos and B veins have dark-CL quartz in microfractures but no Cu-sulfides (Plates 4.2D and 4.3E respectively). DQ veins are the most abundant below the high-grade Cu-ore in the low-grade Cu to “barren” core. There, DQ veins are cross-cut by the same density of dark-CL quartz in microfractures than veins in the shallower Cu-Mo-ore zone.

Dark-CL quartz is also in contact with molybdenite in high grade Mo-bearing BMQ veins and in some B veins. BMQ veins consist of straight to sinuous bright-CL quartz veins with one or two narrow bands of molybdenite along their edges and contain no Cu-sulfides. Molybdenite in BMQ veins is always in contact with the BMQ bright-CL quartz but sometimes is also in contact with late dark-CL quartz in microfractures that cross cut the BMQ (Plate 4.3A, B). At the deposit scale the distribution of molybdenite is correlated with the distribution of BMQ veins (Chapter 3), and at the vein scale molybdenite follows the distribution of bright-CL quartz (Plate 4.3A, B) in disregard of the distribution of dark-CL quartz. Cu-sulfides are never in contact with the bright-CL quartz of the BMQ veins. When BMQ veins have associated Cu-sulfides, these are only present in gray- to bright-CL B vein quartz that re-opens the center of some BMQ veins and in some cases have a less amounts of late molybdenite (Chapter 3, Plate 4.3C, D).

Late D veins, that post-date both the Cu and Mo ores, lack bright- and gray-CL quartz and only have dark-CL quartz in contact with muscovite, pyrite and rare chalcopyrite. At high SEM-CL contrast, growth banding is evidenced in D veins and two CL-types of quartz are revealed in the apparently dark-CL quartz: a slightly gray dark-CL quartz and an absolute-black dark-CL quartz (Plate 4.3F, G). At the SEM-CL contrast that CL images are shown in Plate 4.3F and G, the gray- and bright-CL quartz of earlier veins looks extremely bright (white) and saturated.

Similarly to the observations at Haquira East, at Batu Hijau the Cu-sulfides are not exclusively in contact with dark-CL quartz. Bornite and chalcopyrite in an A vein sample are in contact with the gray- to bright-CL quartz of the A vein and with dark-CL quartz in microfractures that cross-cut the vein (Plate 4.3H, I).

4.6 Discussion

4.6.1 Cu-sulfide precipitation in EDM halos-veins, A and B veins

At Haquira East the association of dark-CL quartz and Cu-sulfides is not exclusive, and at least some of the Cu-sulfides are also in contact with earlier and higher temperature types of quartz in EDM halos and B veins (Plates 4.1A-C and 4.2A-D). Furthermore, even where the Cu-sulfides are in contact with dark-CL quartz, they are contained within B veins or in EDM halos. Therefore, the correlation of EDM halos and B veins with the high-grade Cu shell at Haquira East (Cernuschi *et al.,* 2013) is confirmed at the vein scale under SEM-CL imaging. Most importantly, the Cu-sulfides that form most of the high-grade Cu-ore are intergrown with the hydrothermal mineral assemblage that constitutes the EDM halos where quartz is scarce. Mineral phase equilibria indicates that biotite, muscovite and K-feldspar bearing EDM halos are formed between ~550ºC and ~400ºC (Table 4.1, Seedorff *et al.,* 2005). Similarly, our TitaniQ geothermometry estimates indicates ~500ºC for the mosaic textured gray-CL quartz centerline in some EDM halos that also contains Cu-sulfides (Table 4.1). The TitaniQ geothermometry indicates ~550ºC for the later Cu-sulfide bearing B veins, in agreement with the mineral phase equilibria estimate of K-silicate alteration (>550ºC, Table 4.1). Besides the exact precipitation temperatures of B veins and EDM halos, the observations presented here argue that the Cu-sulfides were present in the EDM halos and B veins, before the formation of lower temperature dark-CL quartz in microfractures.

Batu Hijau is a contrasting porphyry copper deposit that provides a comparison to Haquira East. In discrepancy with observations from other A vein-bearing deposits, at Batu Hijau the Cu-sulfides are not completely contained within the dark-CL quartz. The bornite and chalcopyrite are also in contact with the A vein mosaic to wavy concentric banded textured and gray- to bright-CL quartz (Plate 4.3H, I). Our TitaniQ geothermometry estimates indicate ~600ºC for the formation of the A veins (Table 4.1), however, and most importantly than the exact temperature of precipitation of the A vein quartz is that this observation indicates that the copper sulfides were not necessarily precipitated with the dark-CL quartz, but may have been precipitated earlier with the higher temperature gray- to bright-CL A vein quartz.

4.6.2 Dark-CL quartz is ubiquitous in all types of veins

At Haquira East, low-grade Cu to “barren” DQ veins, BMQ veins and quartz phenocrysts in porphyry dikes show dark-CL fractures but no Cu-sulfides, further indicating that at the deposit scale the Cu-ore is not correlated with the distribution of the later dark-CL quartz (Plate 4.2E,

Plate 4.3A-E). Similarly to Haquira East, dark-CL quartz in microfractures is also ubiquitous in low-grade Cu to "barren" veins, Cu-bearing A veins and in later D veins of deposits elsewhere (*e.g.* Rusk, 2012).

At Haquira East, dark-CL quartz is commonly present in BMQ veins and sometimes in contact with molybdenite (Plate 4.3C). Similar observations of bright-CL quartz and molybdenite in BMQ veins with later dark-CL quartz in microfractures have been made in porphyry copper (*e.g.* Altar; Maydagan *et al.,* 2015) and porphyry molybdenum (*e.g.* Henderson; Rusk, 2013) deposits elsewhere. At Haquira East, at the vein scale, the molybdenite follows the bright-CL quartz bands of the BMQ veins, which are never in contact with Cu-sulfides. This suggests that the molybdenite in BMQ veins was precipitated with the bright-CL quartz estimated at ~650ºC.

Where BMQ veins are re-opened by later B veins, a second generation of bornite, chalcopyrite and less molybdenite are observed together in the later gray-CL quartz of the B vein (Plate 4.3C, D). Dark-CL quartz in microfractures cross-cut both the bright-CL quartz of the BMQ and the gray-CL quartz of the B vein (Plate 4.3A, B). These observations suggests that the microfractures were formed and filled with dark-CL quartz after the formation of BMQ and B veins.

Similarly, dark-CL quartz in microfractures is abundant in low-grade Cu to "barren" DQ veins (Plate 4.3E) and in quartz phenocrysts of porphyry dikes. At Bingham, DQ veins (named barren stockwork veins), also have dark-CL microfractures and no Cu-sulfides (Landtwing *et al.,* 2010). At Haquira East, where DQ veins and porphyry dikes are cross-cut by EDM halos and B veins, the dark-CL quartz in microfractures cross-cut all the veins, but the Cu-sulfides are restricted to EDM halos and B veins. This further argues that the Cu-sulfides are not correlated with the distribution of the dark-CL quartz, but with the distribution of EDM halos and B veins. As indicated by dike/vein cross-cutting relationships, the Cu-sulfide introduction in EDM halos and B veins post dates the formation of the DQ veins and some of the porphyry dikes. Therefore, a later and lower temperature fluid flowed through microfractures in all the earlier types of quartz and precipitated dark-CL quartz after the Cu-sulfide formation.

DQ veins with dark-CL quartz in microfractures are most abundant in the low-grade Cu to "barren" core below the high grade Cu-Mo-ore zone. This observation evidences that both the K-silicate altered low-grade Cu core with DQ veins and aplite dikes and the EDM-B-bearing high grade Cu-ore shell above and to its sides are equally cross-cut by late dark-CL quartz in microfractures (Fig. 4.1). The whole vertical section of the deposit had to experienced low temperatures at a late stage in order to precipitate dark-CL quartz in microfractures.

4.6.3 The hypothesis of low temperature precipitation of Cu-sulfides

The hypothesis of Cu-sulfide introduction with the low temperature dark-CL quartz (<400ºC) requires several generations of low temperature dark-CL quartz succeeding each other and in between the formation of higher temperature quartz in veins to explain why only some dark-CL quartz in fractures carry Cu-sulfides. Even in that scenario it is difficult to explain why the high grade Cu-ore is always very well correlated with either the EDM halo distribution (*e.g.* Los Pelambres, Chile; Atkinson *et al.,* 1996), EDM halos and B veins (Haquira East; Cernuschi *et al.*, 2013) or A vein distribution *(e.g.* El Salvador, Chile; Gustafson and Hunt, 1975). In the low temperature Cu deposition hypothesis, it is possible that the low temperature fluid batch that carried copper precipitated Cu-sulfides at shallower areas and at favorable precipitation temperature following the thermal gradient during the hydrothermal fluid up flow (Landtwing *et al.,* 2010). However, this implies that the inverted cup-shape and position of the thermal gradient remained constant through time and through significant temperature fluctuations. The shape of the thermal boundaries during the late and low temperature copper deposition had to coincided in space and shape with the earlier and higher temperature thermal boundaries that determined the areas of precipitation of EDM halos and B veins. The low temperature copper deposition hypothesis also requires a late generation of Cu-depleted fluid to precipitate dark-CL quartz in deeper zones of the system and through DQ veins after further thermal collapse of the porphyry system.

Our alternative hypothesis is that the Cu-sulfides were already precipitated in the EDM halos and B veins at temperatures >400ºC and the later and low temperature dark-CL quartz precipitated in microfractures throughout all the previously formed veins and close in time with the formation of D veins and sericitic halos (Fig. 4.1).

4.6.4 Late D veins and dark-CL quartz in microfractures post-date the Cu-ore

The dark-CL quartz in microfractures that cross-cut through the low- and high-grade Cu-veins is similar in CL intensity, Ti and oxygen isotope composition to the dark-CL quartz in D veins, suggesting a compositional and temperature precipitation correlation between both. Our TitaniQ geothermometer estimates indicate ~350ºC (Table 4.1) for the dark-CL quartz in D veins, in agreement with estimates for similar quartz in porphyries elsewhere (*e.g.* Rusk, 2012). This temperature estimate is in agreement with the temperature range of sericitic alteration of ~400 to 350ºC (Seedorff *et al.,* 2005). D veins are stable with sericitic alteration and are commonly the last quartz-bearing type of vein in porphyry deposits. As the dark-CL quartz in microfractures, D veins cross-cut all the earlier K-silicate-stable low-grade and high-grade Cu veins and halos (*i.e.* Seedorff *et al.,* 2005; Silllitoe, 2010) suggesting that the dark-CL quartz in microfractures and the dark-CL quartz in D veins where formed closely in time.

We propose that late and lower temperature dark-CL quartz was precipitated in microfractures through all the pre-sericitic alteration quartz veins and closely in time with the D vein formation and sericitic alteration (Fig. 4.1). The microfracturing of the early quartz was a product of volume reduction after formation and subsequent cooling and affected all the K-silicate stable quartz veins similarly. An abrupt volume reduction of ~0.8 % takes place at 573ºC at the transition from alpha to beta quartz. Another ~2.5% of the volume is reduce when reaching ~350ºC. (Fig. 4.2; Dilles, 1984). This volume reduction is enough to produce a net of microfractures through quartz in veins and microfractures and explains why microfractures are abundant in quartz and not in the wall-rock. It is likely that some of the newly formed open space would be accommodated between quartz and sulfide grains since these crystal boundaries are pre-existing discontinuities. Therefore, this process can explain the common observation of dark-CL quartz in contact with earlier Cu-sulfides.

4.6.5 Fluid inclusions in A vein quartz and dark-CL quartz in microfractures

Previously published low temperature copper precipitation arguments based on fluid inclusion studies can be reconciled with the earlier and higher temperature copper precipitation hypothesis discussed here. Fluid inclusions hosted in bright-CL A vein quartz (B1) at Bingham show a large span in copper composition, averaging ~26,000 µg/g. Later fluid inclusions in dark-CL quartz in microfractures through the A veins and in contact with Cu-sulfides (B2) present lower copper concentrations and a smaller range between 8,100 and 1,450 µg/g (Landtwing *et al.,* 2005). For the low temperature precipitation interpretation it was assumed that the B1 fluid inclusions hosted in the bright-CL A vein quartz are secondary and were formed during the later and low temperature microfracturing event, but immediately before the deposition of the B2-bearing dark-CL quartz within them. It follows that the B1 fluid inclusion represents a Cu-rich fluid that was progressively depleted in Cu as it was precipitated in Cu-sulfides by the time of the precipitation of dark-CL quartz with B2 fluid inclusions. However, there is no direct evidence that supports the assumption that B1 fluid inclusions are secondary. B1 fluid inclusions could be primary, and therefore trapped during the formation of bright-CL A vein quartz, in which case the measured homogenization temperatures of ~ 400ºC (Landtwing *et al.,* 2005) only represent the minimum trapping temperature. If the B1 fluid inclusions are primary, the interpreted mechanisms of Redmond *et al.* (2004) remains valid but if would suggest that the copper was depleted from the fluid during the A vein quartz precipitation. In this scenario, the fluid from which the latter, lower temperature and darker-CL quartz in microfractures was precipitated would be comparatively depleted in copper as expected for a sericitic alteration fluid.

4.7 Conclusions

The high grade Cu-ore in deep porphyry copper deposits such as Haquira East is formed by copper sulfides precipitated in EDM halos at ~500ºC during K-silicate alteration and after the formation of low-grade copper DQ veins and aplite dikes at ~650ºC (Fig. 4.3). In shallowly emplaced porphyries such as Batu Hijau, the ore-forming Cu-sulfides are precipitated at a similar timing and during K-silicate alteration but in A veins at ~600 ºC (Fig. 4.3). The high-grade Mo-ore is formed by molybdenite precipitated in BMQ veins during K-silicate alteration. In cases such as Butte, the BMQ veins were formed before the high-grade Cu-ore, and in cases like Haquira East the BMQ precipitated at ~650ºC during a thermal reversal after the formation of the Cu-ore in EDM halos (Fig. 4.3). In some cases such as Haquira, later B veins introduce more a second generation of molybdenite and copper sulfides at ~550ºC (Fig. 4.3).

The low temperature, dark-CL quartz that is commonly observed in contact with copper sulfides is a product of a later event and it is not related to copper precipitation. Dark-CL quartz is formed by the latest silica saturated fluids, which are stable with sericitic alteration, reach temperatures as low as ~350 ºC and produce pyrite-muscovite-quartz D veins and sericitic halos that cross-cut the earlier veins/halos and post date the high-grade Cu-Mo-ores. The ~350 ºC fluid also percolates through microfractures in all the earlier veins created after volume reduction of quartz upon cooling, and precipitate dark-CL quartz (Figs. 4.2, 4.3). Some of the volume reduction is also accommodated at previous discontinuities such as mineral grain boundaries, creating flow paths between copper sulfides and quartz grains and explaining why is it common to observe the low temperature and dark-CL quartz in contact with earlier copper sulfides.

4.8 Acknowledgments

We thank First Quantum Minerals LTD for supporting this research. To Kalin Kouzmanov for obtaining the QEMSCAN image presented here. To Brian Rusk and Andreas Audétat for the discussions about SEM-CL imaging and limitations of the Ti in quartz geothermometry.

4.9 References

Atkinson, W.W., Souviron, A., Vehrs, T.I., and Faunes G.A., 1996, Geology and mineral zoning of the Los Pelamberes porphyry copper deposit, Chile: Society of Economic Geologists Special Publication, v. 5, p. 131–156.

Brimhall, G.H.J., 1977, Early fracture–controlled disseminated mineralization at Butte, Montana: Economic Geology, v. 72, p. 37–59.

Burnham, C.W., 1979, The importance of volatile constituents, *in* Yoder, H.S. Jr., ed., The evolution of the igneous rocks: Fiftieth anniversary perspectives, Princeton University Press, Princeton, N. J., p. 439–482.

Cernuschi, F., Einaudi, M.T., Dilles, J.H., Heather, K.B., Barr, N.C., 2012, Hydrothermal Veins, porphyry Geochemistry and mineralization zonation of the Haquira East porphyry Cu–Mo deposit, Perú: SEG Conference 2012, Lima, Perú.

Cernuschi, F., Dilles, J.H., and Creaser, R., 2013, Hydrothermal alteration, SWIR–mineral mapping, vein distribution and age of the Haquira–East Cu–Mo porphyry: 12th SGA Biennial Meeting 2013, Proceedings, v. 2, p. 782–785.

Dilles, J.H. and Einaudi, M.T., 1992, Wall–rock Alteration and Hydrothermal Flow Paths about the Ann–Mason Porphyry Copper Deposit, Nevada, A 6 km Vertical Reconstruction: Economic Geology, v. 87, p. 1963–2001.

Dilles, J.H., 1984, The petrology and geochemistry of the Yerington batholith and the Ann–Mason porphyry copper deposit, Western Nevada: [Unpublished Ph.D. dissertation], Stanford, Stanford University, 389 p.

Dilles, J.H., 1987, Petrology of the Yerington batholith, Nevada: Evidence for evolution of porphyry copper ore fluids: Economic Geology, v. 82, p. 1750–1789.

Field, C.W., Zhang, L., Dilles, J.H., Rye, R.O., and Reed, M.H., 2005, Sulfur and oxygen isotopic record in sulfate and sulfide minerals of early, deep, pre–main stage porphyry Cu–Mo and late main stage base–metal mineral deposits, Butte district, Montana: Chemical Geology, v. 215 no.1–4, 61–93.

Garwin, S., 2002, The Geologic Setting of Intrusion–Related Hydrothermal Systems near the Batu Hijau Porphyry Copper–Gold Deposit, Sumbawa, Indonesia: Society of Economic Geologists Special Publication, v. 9, p. 333–366.

Gustafson, L.B., and Hunt, J.P., 1975, The porphyry copper deposit at El Salvador, Chile: Economic Geology and the Bulletin of the Society of Economic Geologists, v. 70, no. 5, 857–912.

Huang, R., and Audétat, A., 2012, The titanium–in–quartz (TitaniQ) thermobarometer: A critical examination and re–calibration: Geochimica et Cosmochimica Acta, v. 84, p. 75–89.

Landtwing, M.R., Pettke, T., Halter, W.E., Heinrich, C.A., Redmond, P.B., Einaudi, M.T., and Kunze, K., 2005, Copper deposition during quartz dissolution by cooling magmatic–hydrothermal fluids: The Bingham porphyry: Earth and Planetary Science Letters, v. 235 no. 1, 229–243.

Landtwing, M.R., Furrer, C., Redmond, P.B., Pettke, T., Guillong, M., and Heinrich, C.A., 2010, The Bingham Canyon porphyry Cu–Mo–Au deposit. III. Zoned copper–gold ore deposition by magmatic vapor expansion: Economic Geology, v. 105, no. 1, 91–118.

Maydagán, L., Franchini, M., Rusk, B., Lentz, D. R., McFarlane, C., Impiccini, A., and Rey, R., 2015, Porphyry to epithermal transition in the Altar Cu–(Au–Mo) Deposit, Argentina, studied by cathodoluminescence, LA–ICP–MS, and fluid Inclusion analysis: Economic Geology, v. 110, no. 4, 889–923.

Mercer, C.N., Reed, M.H., and Mercer, C.M., 2015, Time Scales of porphyry Cu deposit formation: Insights from titanium diffusion in quartz: Economic Geology, v. 110, no. 3, 587–602.

Müller, A., Herrington, R., Armstrong, R., Seltman, R., Kirwin, D., Stenina, N. and Kronz, A., 2010, Trace elements and cathodoluminescence of quartz in stockwork veins of Mongolian porphyry–style deposits: Mineralium Deposita, v. 45, p. 707–727.

Perello, J., Carlotto, V., Zarate, A., Ramos, P., Posso, H., Neyra, C., Caballero, A., Fuster, N. and Muhr, R., 2003, Porphyry–style alteration and mineralization of the m Eocene to early Oligocene Andahuaylas–Yauri belt, Cuzco Region, Peru: Economic Geology v. 98, no. 8, p. 1575.

Proffett, J.M., 2009, High Cu grades in porphyry Cu deposits and their relationship to emplacement depth of magmatic sources: Geology, v. 37, no. 8, 675–678, doi:10.1130/G30072A.1

Redmond, P.B. and Einaudi, M.T., 2010, The Bingham Canyon Porphyry Cu–Mo–Au Deposit. I. Sequence of intrusions, vein formation, and sulfide deposition: Economic Geology, v. 105, no.1, p. 43.

Redmond, P.B., Einaudi, M.T., Inan, E.E., Landtwing, M.R., and Heinrich, C.A., 2004, Copper deposition by fluid cooling in intrusion–centered systems; new insights from the Bingham porphyry ore deposit, Utah: Geology, v. 32, no. 3, p. 217–220.

Rusk, B.G., Lowers, H.A., and Reed, M.H., 2008, Trace elements in hydrothermal quartz: Relationships to cathodoluminescent textures and insights into vein formation: Geology, v. 36, no. 7, p. 547.

Rusk, B., 2012, Cathodoluminescent Textures and Trace Elements in Hydrothermal Quartz, *in* Götze, J. and Möckel, R., eds., Quartz: Deposits, Mineralogy and Analytics, Berlin, Springer, p. 307–329.

Rusk, B., and Reed, M., 2002, Scanning electron microscope–cathodoluminescence analysis of quartz reveals complex growth histories in veins from the Butte porphyry copper deposit, Montana: Geology, v. 30, no. 8, p. 727 – 730.

Seedorff. E., Dilles, J.H., Proffett, J.M. Jr, Einaudi, M.T., Zurcher, L., Stavast, W.J.A., Johnson, D.A., Barton, M.D., 2005, Porphyry Deposits: Characteristics and Origin of Hypogene Features: Economic Geology 100th Anniversary, v. 29, p. 251–298.

Sillitoe, R.H., 2010, Porphyry copper systems: Economic Geology, v. 105, no.1, p. 3–41.

Skinner, B.J., 1966, Thermal expansion, in Clark, S.P., Jr., ed., Handbook of physical constants: Geological Society of America Memoir v. 97, p. 75–96.

Zwyer, T., 2010, Temporal and spatial evolution of hydrotheraml, ore–related fluids in the Batu Hiaju porphyry copper–gold deposit, Sumbawa (Indonesia) [Unpublished master Thesis]: ETH Zürich, Switzerland, p. 57.

4.10 Figures and Tables

Table 4.1. Porphyry and vein formation temperatures based on phase equilibria, titaniq geothermometry and fluid inclusion data.

Quartz type	**Deposit**	**T(°C)** [phase]	**Ti** (ppm)	**T(°C)** [Ti]				**T(°C)** [pref.	**SEM-CL intensity**
				T (°C)	P (kbar)		αTiO2		
Igneous	Haquira	~700	27-40	662-703	3	L.	0.65	650	Gray-CL
DQ/BMQ		>550	60-70*	685-702	2.5	L.	1.0	650	Bright-CL
A	Batu Hijau		90-120*	624-656	0.5	L.-H.		600	Bright- to gray-CL
EDM	Haquira	550-400	15-30	505-561	1.1	L.-H.		500	Gray-CL
B		>550	18-40	541-598	1.6	L.-H.		550	Bright- to gray-CL
D (early quartz)		400-450	5-15	425-500	1	L.-H.		450	Dark-gray-CL
D (late quartz)		300-400	1-5	339-425	1	L.-H.		350	Dark-CL

Notes: **T (ºC) [phase]** was estimated based on the phase stability of quartz – K-feldspar – Muscovite – Andalusite (Seedorff *et al.,* 2005). **T (ºC) [Ti]** was calculated using the Ti-in-Q geothermometer (Huang and Audétat, 2012) of the lowest Ti zones, together with pressure constrains from fluid inclusion and hornblende baromethry. * Posibly all fast growing quartz. The Ti concentration might not reflect precipitation under equilibrium conditions. P (kbar) = Pressure in kbars, L. = Lithostatic, H. = Hydrostatic. **T (ºC) [pref.]** is the preferred formation temperature.

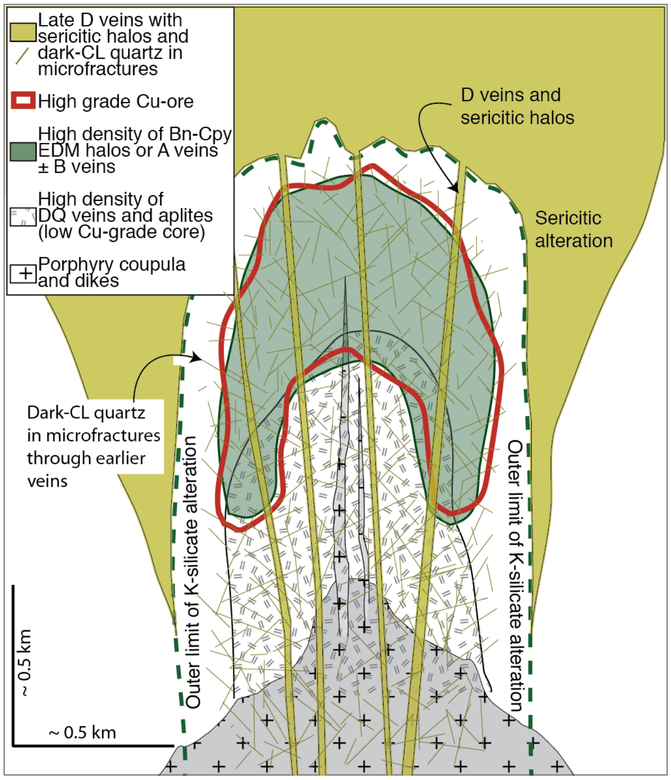

Figure 4.1. Schematic zonation of a typical porphyry copper deposit. The high-grade Cu-ore correlates with the distribution of Cu-sulfide bearing EDM halos or A veins and sometimes also with B veins. The high-grade Cu-ore is also included within the limits of the K-silicate alteration zone with hydrothermal biotite replacing magmatic hornblende and sits on top and to the sides of a K-silicate altered but low Cu-grade core with abundant DQ veins and aplites. Sericitic alteration dominates at shallower depths and to the sides of the K-silicate alteration and structurally controlled D vein and sericitic halos. Microfractures filled with dark-CL quartz are shown out of scale for illustration purposes. After Gustafson and Hunt, 1975; Seedorff et al., 2005; Sillitoe, 2010; Cernuschi *et al.,* 2013.

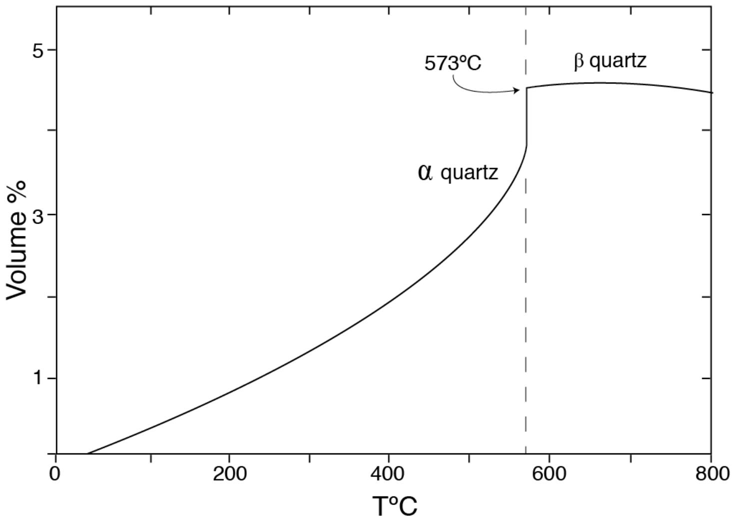

Figure 4.2. Thermal expansion of quartz versus temperature, reproduced from Dilles, 1984 and data from Skinner, 1966. Reference volume is at 20ºC. The volume of quartz increases gradually from low temperature up to 573ºC where it presents a discontinuity due to the α-β phase transformation.

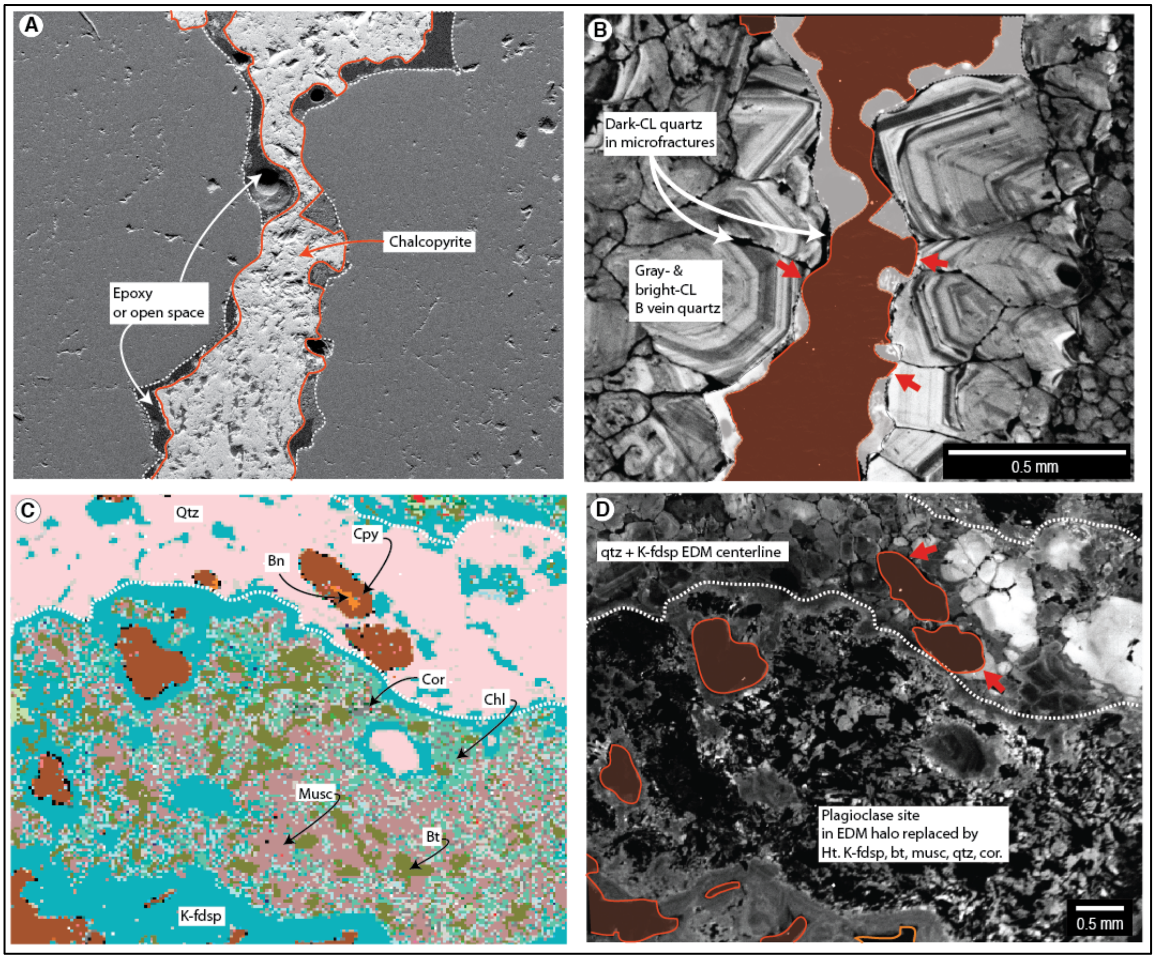

Plate 4.1. **A)** Haquira: BSE image of a chalcopyrite-bearing B vein. **B)** SEM-CL image of the same area showing the chalcopyrite in contact with the B vein gray- to bright-CL quartz and late dark-CL quartz in microfractures and partially riming the sulfides (FC-HAQ-027: AHAD-185-229m). **C)** Haquira: QEMSCAN image of an EDM halo and its quartz with K-feldspar centerline. A plagioclase site in the halo is replaced by hydrothermal K-feldspar, biotite, muscovite, quartz and corundum. **D)** SEM-CL image of the same area showing the Cu-sulfides are not in contact with quartz in the EDM halo but with K-feldspar. In the quartz centerline, chalcopyrite is in contact with K-feldspar and gray-CL quartz (FC-HAQ-242: AHAD98A-262m).

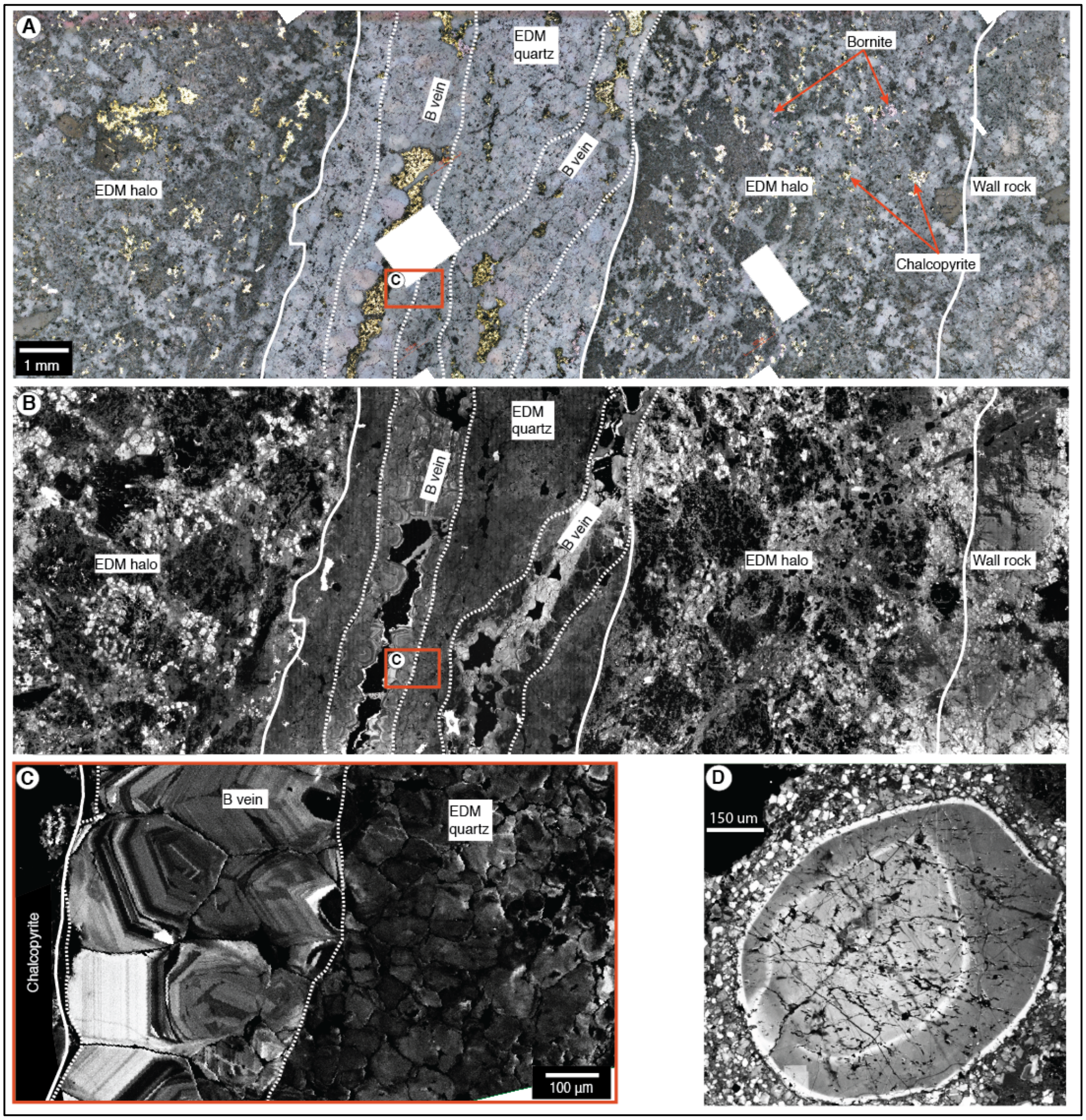

Plate 4.2. A) Haquira: reflected light microphotograph and **B)** SEM-CL image of a bornite-chalcopyrite bearing EDM halo with rare gray-CL quartz replacing magmatic hornblendes and plagioclase together with more abundant hydrothermal biotite, muscovite, K-feldspar and corundum. A chalcopyrite-bearing gray-CL mosaic quartz forms a centerline to the EDM halo. Two sinous B veins with banded gray- to bright-CL euhedral quartz with chalcopyrite cross cut the EDM halo and its quartz centerline. All the quartz types present dark-CL quartz in microfractures, sometimes in contact with the sulfides. (FC-HAQ-027: AHAD-185-229m). **C)** Detail of A and B, showing the EDM halo's gray-CL mosaic quartz, the banded bright- to gray-CL euhedral B vein quartz and dark-CL quartz in microfractures and riming most of the B-vein quartz contact with the chalcopyrite. **D)** Haquira: Quartz phenocryst of a porphyry dike intensely cross-cut by dark-CL quartz in microfractures (FC-HAQ-002: AHAD-98A-125.8m).

Plate 4.3. Reflected light microphotographs and SEM-CL images: **A**, **B)** Haquira: molybdenite contained or in contact with the bright-CL quartz of a BMQ band and sometimes in contact with later dark-CL quartz in microfractures (FC-HAQ-224: AHAD108-80m). **C, D)** Haquira: molybdenite follows the bright-CL quartz band a BMQ vein. Cu-sulfides are never in contact with the BMQ quartz, but in the gray-CL B-vein quartz that cross-cuts and re-opens the BMQ vein. Dark-CL quartz filled microfractures cross-cut the BMQ and the B vein quartz and are sometimes in contact both with the molybdenite in the BMQ veins and the Cu-sulfides in the B vein (FC-HAQ-224: AHAD108-80m). **E)** Haquira: Bright-CL quartz on a DQ vein with abundant dark-CL filled microfractures but no Cu-sulfides (FC-HAQ-122: AHAD127-739m). **F, G)** Haquira: Dark gray- and gray-CL quartz in a D vein. Both types of quartz are in contact with muscovite and pyrite±chalcopyrite. G) is shown at higher SEM-CL contrast than the previous CL images. All the quartz in this image appears as dark-CL quartz in the previous SEM-CL images (FC-HAQ-009: AHAD-98A-545m). **H)** Batu Hijau: BSE image and **I**) SEM-CL image of a bright- to gray-CL mosaic textured A vein quartz with incipient wavy concentric banding. Dark-CL quartz is common in microfractures and riming the chalcopyrite (SBD86-873m).

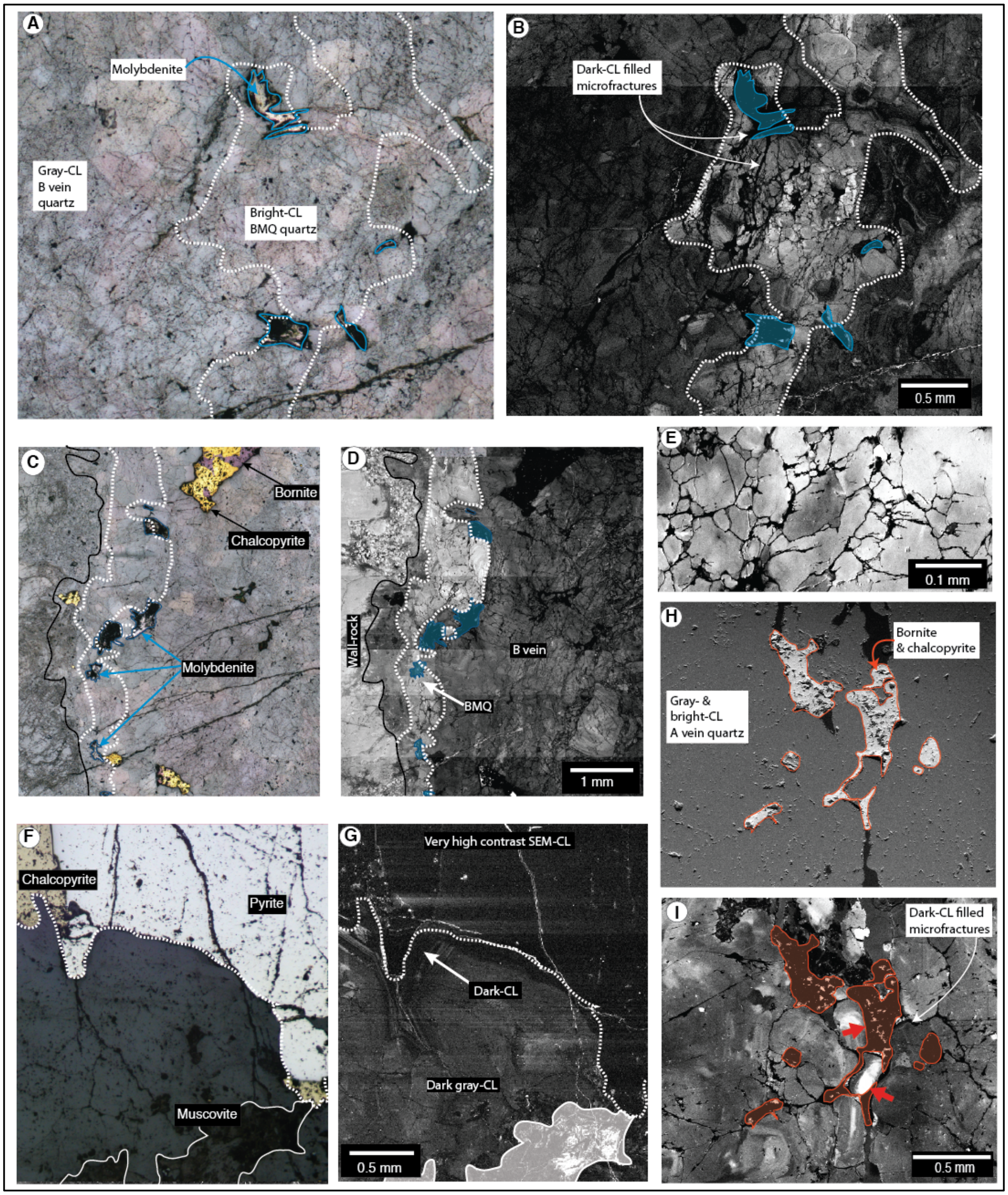

Plate 4.3. Reflected light microphotographs and SEM-CL images.

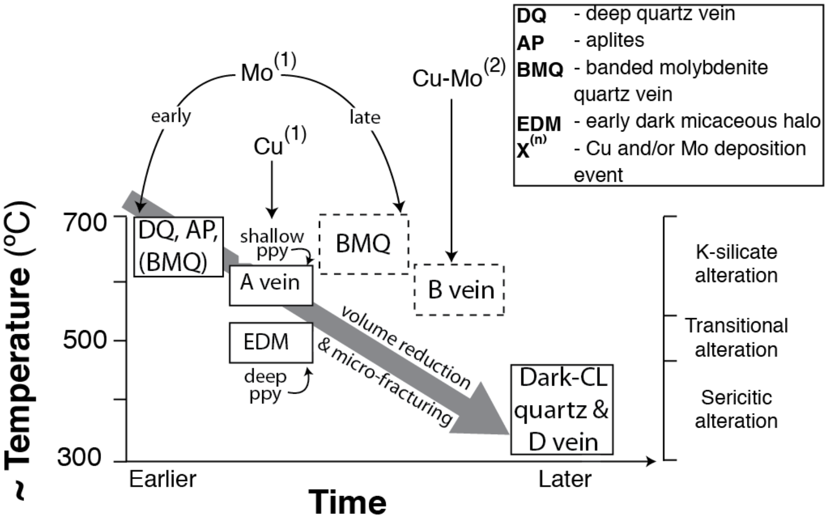

Figure 4.3. Schematic and generalized temperature versus time porphyry copper deposit evolution. DQ veins and aplites are precipitated early at high temperatures and during K-silicate alteration. In some deposits such as Butte, this stage also includes the precipitation of BMQ veins. In shallow porphyry copper deposits the high grade Cu-ore is formed by Cu-sulfides in K-silicate stable A veins whereas in deeper porphyry copper deposits is hosted by EDM halos. At some deposits such as Haquira East and Bingham, BMQ veins and the high Mo-grade ore were formed after the Cu-bearing halos and/or veins and during a temperature reversal. Some deposits have significant amounts of Cu and Mo in latter B veins, also stable with K-silicate alteration. The volume of the quartz in all the K-silicate stable veins is significantly reduced upon cooling which creates a network of microfractures. Later dark-CL quartz filled the microfractures and precipitated in pyrite rich D veins stable with sericitic alteration.

CHAPTER V

RAPID FORMATION OF PORPHYRY COPPER DEPOSITS EVIDENCED BY DIFFUSION OF OXYGEN AND TITANIUM IN QUARTZ

Federico Cernuschi
John H. Dilles
Stephanie B. Grocke
John W. Valley
Kouki Kitajima
Frank J. Tepley III

Submitted to Geology on 09/11/2015
A journal of the Geological Society of America

5.1 Abstract

Porphyry copper deposits are large and economic mineral deposits, yet their lifespan for formation is incompletely known. Here, we obtain estimates for the duration of the magmatic-hydrothermal fluid flow at >350ºC using diffusion profiles of titanium (Ti) and $\delta^{18}O$ analyzed along transects of quartz in Fe, Cu, and/or Mo sulfide-bearing hydrothermal veins and igneous quartz. The $\delta^{18}O$ of quartz analyzed by secondary ion mass spectrometry is a novel approach for quantifying hydrothermal timescales. At the Haquira porphyry Cu-Mo deposit, Peru, quartz Ti contents range from >100 ppm in porphyry quartz phenocryst overgrowths (~650 ºC) and early veins in K-silicate alteration to ~ 1 ppm in quartz in veins with associated muscovite and pyrite alteration (~350 ºC) as well as in fractures through earlier veins. The $\delta^{18}O$ of hydrothermal quartz varies from ~10.7 ‰ in Cu-sulfide bearing veins, to ~11.1 and ~12.7 ‰ in late quartz with ~1 ppm Ti. Diffusion modeling of both Ti and $\delta^{18}O$ gradients across initially abrupt quartz growth boundaries yields a calculated maximum lifespan for the Haquira porphyry of 170,000 years for the period from initial fluid injection at >650 ºC to cooling below ~ 350 ºC. The high-grade Cu-Mo ore formed in less than 30,000 years. These short diffusion timescales agree well with duration estimates from isotopic ages, and together suggest magmatic-hydrothermal metals ores may form rapidly.

5.2 Introduction

Porphyry copper deposits are large economic mineral deposits that are associated with shallowly emplaced arc-type granitoids mainly in convergent tectonic settings (Seedorff *et al.* 2005). Sulfide mineralization and hydrothermal alteration is intimately related to quartz-bearing veins. Magmatic-hydrothermal fluid separates from cupolas atop a deep magma chamber and ascends by hydro-fracturing the overlying wall-rock where it reacts with rock, cools, and depressurizes to form veins and Fe, Cu, Mo, and Au-bearing sulfides. Small volume porphyry dikes are emplaced synchronously (*e.g.* Burnham, 1979; Dilles, 1987).

The lifespan of magmatic-hydrothermal fluid flow that produces sulfide mineralization at *ca.* 650-350°C is incompletely known. U/Pb zircon ages of porphyry intrusions and Re/Os ages of hydrothermal molybdenite suggest fluid flow durations of <100,000 years for the entire ore-formation process at Bingham (Utah) and Bajo de la Alumbrera (Argentina) deposits (von Quadt *et al.,* 2011) and <100,000 years for each of several individual mineralizing fluid pulses at El Teniente deposit (Chile, Spencer *et al.,* 2015). Model ages of individual veins with sericitic (muscovite) alteration selvages yield estimates of ~100 years at 400°C at Butte (Montana, Geiger *et al.,* 2002) and ~20 to 900 years for K-silicate alteration at Bajo de la Alumbrera and Butte (Cathles and Shannon, 2007).

Scanning electron microscope cathodoluminescence (SEM-CL) imaging of magmatic and hydrothermal quartz can be used to image growth, dissolution, and vein textures. CL-brightness of quartz increases with Ti content, which increases with temperature of formation and growth rate as calibrated by the TitaniQ geothermometer (Huang and Audétat, 2012). At Butte, diffusion modeling of Ti-in-quartz gradients in growth zones imaged by CL suggests porphyry magma residence times of ~1,000s of years, and formation and cooling of various generations of hydrothermal vein quartz ranging from 10s to 10,000s of years (Mercer *et al.,* 2015).

In this study, we constrain the hydrothermal lifespan of the Haquira porphyry Cu-Mo deposit from southern Peru. We present CL images of quartz from porphyry and veins together with their Ti and $\delta^{18}O$ compositions. We assume that the observed boundaries initially had abrupt step-like changes in Ti and $\delta^{18}O$, and we model the time needed to produce the observed gradients using experimentally determined diffusivities at estimated temperatures. Determination of $\delta^{18}O$ gradients analyzed by secondary ion mass spectrometry **(**SIMS) is a novel approach, and enables quantification of timescales at low temperature because oxygen isotope diffusivity is ~10,000 times faster than Ti diffusivity in quartz.

5.3 Ore Geology

Haquira East is a Cu-Mo porphyry deposit located in the Andahuaylas-Yauri porphyry belt of southern Perú. It is hosted in a ~34 Ma subvertical granodiorite stock and cut by a series of porphyry dikes emplaced into Jurassic-Cretaceous quartzite and meta-siltstone. Sinuous and milky deep quartz veins (DQ) synchronous with porphyry dike emplacement are stable with K-silicate alteration and only carry traces of Cu-sulfides. The high grade Cu-ore is hosted in later biotite–K-feldspar–muscovite alteration halos (Early Dark Micaceous or EDM) with bornite-chalcopyrite and rare quartz vein centerlines. Most Mo occurs in later banded molybdenite-quartz veins (BMQ), which are similar to DQ veins but have molybdenite in their margins. Later B type quartz veins with open space filled with bornite-chalcopyrite±molybdenite also contribute to Cu and Mo ore. The youngest D veins contain quartz-pyrite with rare chalcopyrite and are the first veins stable with sericitic alteration (Cernuschi *et al.,* 2013).

Three Re/Os isotopic ages in molybdenite average 33.85 ± 0.15 Ma and one $^{40}Ar/^{39}Ar$ age of muscovite yields 33.18 ± 0.21 Ma, which suggest a maximum lifespan of the hydrothermal system of ~600,000 years (Cernuschi *et al.,* 2013). However, since Haquira East is a deep deposit

(~10 km, Cernuschi, *unpub. data*, Data Repository section 1), the $^{40}Ar/^{39}Ar$ age of muscovite likely reflects slow cooling and the hydrothermal lifespan may be shorter.

5.4 Methods

Quartz in twenty-five thin and thick polished sections was imaged using a FEI Quanta 600 FEG SEM equipped with a Gatan MiniCL cathodoluminescence grayscale detector at Oregon State University (OSU). Ti content of quartz was obtained using a CAMECA SX-100 electron microprobe (EMP). Low Ti quartz (< 13 ppm) was measured by laser ablation inductively coupled mass spectrometry (LA-ICP-MS) at OSU. The $\delta^{18}O$ of quartz (V-SMOW) was analyzed in situ with 10 μm spots using a CAMECA IMS-1280 SIMS at the University of Wisconsin. See the Data Repository for details.

5.5 Results

A quartz phenocryst from a Haquira porphyry dike has a gray-CL core with 24-54 ppm Ti and a ~10 μm thick bright-CL rim with ~75 ppm Ti (Fig. 5.1). Similar high Ti contents are present in the equally bright-CL quartz in the adjacent aplitic textured quartz–K-feldspar porphyry groundmass and in hydrothermal DQ, BMQ veins, and the brightest bands of B veins.

EDM halos rarely contain a central quartz vein, and many are re-opened by later B veins. The centerline of an EDM halo in Figure 2a contains bornite-chalcopyrite with mosaic-textured gray-CL quartz and ~30 to 50 ppm Ti. The EDM quartz is crosscut by a CL-banded B vein with euhedral quartz and central bornite-chalcopyrite. In the B vein, gray-CL quartz bands of different contrast range from ~30 to 50 ppm Ti and bright-CL quartz from ~70 to 80 ppm Ti. The $\delta^{18}O$ values of both the EDM quartz and the different B vein bands are indistinguishable and average 10.7 ‰ (Fig. 5.2b).

Figure 5.3a shows a B vein with bright-CL bands with ~80-100 ppm Ti, and an outer zone of gray-CL bands with ~40 to 60 ppm Ti. The B vein quartz is rimmed and crosscut by a fracture filled with dark-CL quartz in contact with chalcopyrite in the center of the vein. Whereas the B vein quartz averages 10.7 ‰ $\delta^{18}O$, the dark-CL quartz rim averages 12.7 ‰. The Ti concentrations of the dark-CL quartz in the rim is below detection limit (EMP < 13 ppm), and it is identical in CL intensity and texture to the dark-CL quartz present in later and lower temperature D veins with 1 to 5 ppm Ti in quartz (LA-ICP-MS). Similar dark-CL filled fractures and rims are also identified cross-cutting earlier types of veins at Haquira and other deposits elsewhere (Rusk and Reed, 2002; Redmond *et al.,* 2004). At Butte, the dark-CL quartz in fractures and in D veins also have 1 to 5 ppm Ti (Mercer *et al.,* 2015). In Figure 5.2a, a net of younger and ≤ 1 μm wide interconnected fractures and dissolution bands are commonly spaced every ~40 μm in the EDM and B vein quartz and penetrate into the adjacent wall-rock. Here, two fractures were analyzed. Dark-CL quartz has $\delta^{18}O$ = 12.4 ‰ and slightly brighter quartz has $\delta^{18}O$ = 11.3 ‰ (Fig. 5.2b).

D veins are composed of two types of growth-zoned quartz (dark-CL and dark gray-CL), which are CL- and isotopically indistinguishable from the quartz-filled fractures through earlier veins (Supp. Fig. A1). The dark-CL quartz ranges from ~1 to 5 ppm Ti and ~12 to 13 ‰ in $\delta^{18}O$, and overlaps in $\delta^{18}O$ composition with the dark-CL quartz rim in a B vein (Fig. 5.3a) and one of the quartz-filled fractures in an EDM sample (Fig. 5.2b). The slightly brighter dark gray-CL quartz ranges from ~ 5 to 20 ppm Ti and $\delta^{18}O$ = 10.5 to 11.7 ‰ and is similar in $\delta^{18}O$ composition to one quartz-filled fracture in an EDM sample (Fig. 5.2b).

5.6 Discussion

5.6.1 Diffusion models

Isothermal diffusion for varying lengths of time was modeled using the equation ($C=C_o \operatorname{erfc} [X/2\sqrt{Dt}]$) described in Valley (2001) for one-dimensional diffusion and the equation described in Crank (1975) for spherical diffusion (Data Repository). Experimental wet diffusivities are available at temperatures that overlap only with the upper range of porphyry hydrothermal quartz precipitation (*i.e.,* 648-1200°C for Ti (Cherniak *et al.,* 2007) and 515-850°C for oxygen (Dennis, 1984). The Arrhenius equation and experimentally determined activation energies were used to estimate diffusivities parallel to the c-axis of quartz to model diffusion perpendicular to growth zones of quartz, which are mainly on $\{10\bar{1}\bar{1}\}$ pyramidal faces.

Temperatures for calculating diffusivities were estimated by TitaniQ geothermometry and fluid inclusion data. Ti activity was estimated as 1 for the hydrothermal quartz based on the presence of rutile, and as 0.65 for the magmatic quartz based on estimates for similar arc rocks elsewhere (*e.g.* Walker *et al.,* 2013). Based on hornblende barometry and fluid inclusion data, pressures were estimated at ~ 3kb (lithostatic) for magmatic quartz, and between 1 and 1.6 kbar (lithostatic to hydrostatic) for the hydrothermal quartz (Data Repository section 1).

The bright-CL quartz in thin quartz phenocryst rims, aplitic ground mass, DQ and BMQ veins and some bands in B veins have high Ti concentrations. This is interpreted to result from non-equilibrium rapid growth that triggered the enhanced incorporation of Ti in crystal defects in fast-growing quartz (Huang and Audétat, 2012). Fast growing quartz can be a product of water exsolution and magmatic degassing, as proposed to explain the typical 50% aplitic groundmass in porphyry dikes (Burnham, 1979; Dilles, 1987). At growth rates of 120 µm/day, quartz incorporates up to ~100 ppm more Ti than slow-growing quartz (4 µm/day) at ~700 ºC (see Fig. 3 in Huang and Audétat, 2012). Therefore, high growth rates yield spuriously high apparent formation temperatures by amounts of up to ~100 ºC, and were therefore discarded for the temperature estimates.

The gray-CL core of a quartz phenocrysts suggest >650°C formation temperature for igneous quartz. B veins formed at ~550ºC based on the lowest Ti contents of their CL-zoned quartz. EDM veins display a narrow range of gray-CL quartz, consistent with equilibrium crystallization that suggests crystallization at ~500ºC. Similarly, in D veins the dark gray-CL quartz formed at ~450ºC whereas the dark-CL quartz formed at ~350°C. All the TitaniQ estimated temperatures are in agreement with phase equilibrium arguments (Seedorff *et al.,* 2005; Supp. Table A5).

5.6.2. Timescales

5.6.2.1. Stage 1: Magmatic and main Cu-Mo stage

The Ti-in-quartz gradient between the quartz phenocryst core and its rim (Fig. 5.1a) is interpreted to have formed at the time of the porphyry emplacement, and therefore represents the earliest and highest temperature stage of the magmatic-hydrothermal system (≥650ºC). This stage also includes the formation of aplite dikes, DQ veins, and BMQ veins that have similar bright-CL quartz. Younger Cu-bearing EDM halos are crosscut by Mo-bearing BMQ veins. Therefore, this initial stage includes the EDM halo formation and Cu-ore formation at moderate temperatures (~500 ºC) before a reversal to higher temperatures (≥650 ºC) in which BMQ veins form (Fig. 5.4a). A diffusion model for Ti gradients at the core - rim boundary of a porphyry phenocryst indicates a maximum timescale of 35,000 years at ~650°C for the porphyry to BMQ stage (Fig. 5.1b).

5.6.2.2. Stage 2: Second Cu-Mo stage

Subsequent to BMQ vein formation, the hydrothermal stages record a progressive decline in temperature (~650ºC to ~550ºC, Fig. 5.4a). Three diffusion models for the Ti concentration gradients observed in the B vein quartz bands indicate a maximum timescale of ~50,000 years at ~550 ºC (Fig. 5.2a, Supp. Fig. A3).

5.6.2.3. Stage 3: Early quartz in D veins and 450ºC homogenization

We assume that a single composition of magmatic-hydrothermal fluid produced all veins from high to low temperature (BQ to D veins), as proposed by Reed *et al.* (2013). The $\delta^{18}O$ of this hydrothermal water is restricted to a limited range of ~7.5 to ~8.0 ‰ by the observed quartz compositions and available quartz-water fractionation factors (Supp. Table A6). If we use $\delta^{18}O$ = 7.5 ‰ for magmatic water (Taylor, 1968) and a fractionation factor for quartz-water (Zhang *et al.,* 1989), then the estimated temperatures for dark gray-CL quartz with $\delta^{18}O$ ~11.1 ‰ and dark-CL quartz with ~12.7 ‰ from D veins are ~450 ºC and ~370 ºC, respectively (Supp. Table A6). The estimates agree with independent TitaniQ and fluid inclusion data (Supp. Table A5). In contrast, the independently estimated formation temperatures for EDM and B vein quartz are ~500 ºC and ~550 ºC, but quartz in both has average $\delta^{18}O$ ~ 10.7 ‰ calculated to be in equilibration with ~7.5 ‰ water at ~475-480°C (Supp. Table A6).

We propose that the dark gray-CL quartz in D veins, fractures, and dissolution bands ($\delta^{18}O$ ~11.1 ‰) formed at a ~450ºC stage via partial $\delta^{18}O$ exchange of earlier high temperature quartz (Fig. 5.2b and 5.4). Nonetheless, Ti contents of high temperature quartz did not re-equilibrate at ~450 ºC because of the low Ti diffusivity (Fig. 5.2a, 5.3 a). The planar dissolution bands suggest local one-dimensional diffusion, whereas the abundant 3D network of fractures and veins suggests that spherical 3D diffusion dominated. We calculate exchange times at 450°C between a 7.5 ‰ magmatic water and preexisting 9.6 ‰ B vein quartz (Fig. 5.5). We assume that magmatic water penetrated the older quartz along the observed microfractures and dissolution bands that are commonly spaced every 40 μm and at a maximum of 120 μm (Supp. Fig. A2). However, the spacing >40 μm could be an overestimate because more closely space fractures may exist in other dimensions. Spherical diffusion models yields timescales of ~1,000 years for a 20 μm radius and ~10,000 years for a 60 μm radius. The latter represents the maximum fracture spacing and therefore is the preferred maximum exchange time length. One-dimensional models are ~1 order of magnitude longer (Fig. 5.5, Supp. Fig. A7).

5.6.2.4 Stage 4: Late quartz in D veins and fractures

The dark-CL quartz precipitated in fractures and open space between sulfide and quartz likely after quartz contraction upon cooling. The 1 to 5 ppm Ti content of the dark-CL D vein quartz is assumed to also represent the dark-CL quartz in fractures (Fig. 5.2), indicative of a formation temperature of ~ 350 ºC (Supp. Table A5). Modeling at 350 °C of the $\delta^{18}O$ diffusion profile between a late 12.7 ‰ dark-CL quartz rim and earlier 10.7 ‰ B vein quartz (Fig. 5.3b) gives a maximum diffusion length of 75,000 years. This timescale likely includes regional slow cooling attending the deep emplacement of Haquira (~10 km), and therefore the lifespan of the 350 ºC hydrothermal event may be shorter.

5.7 Conclusions

The diffusion timescales reveal a maximum magmatic-hydrothermal lifespan of ~170,000 years for cooling from ~650 ºC to ~ 350 ºC. The four hydrothermal stages illustrated in Figure 5.4a and b suggest formation times of ≤30,000 years for stage 1 Cu-Mo ores. The ascent of hot magmatic-hydrothermal fluids, heated the surrounding wall-rock to produce a locally steepened geothermal gradient (Fig. 5.4c, d). During stage 1 and the formation of DQ veins, aplites, and Cu-bearing EDM veins, the temperature decreased from ~650 ºC to ~500 ºC. A thermal reversal heating to ~650ºC produced steeper geothermal gradients and Mo-ore hosted in BMQ veins. This was followed by cooling to ~550°C during stage 2 and Cu-Mo ores in B veins in a period of ≤50,000 years (Fig. 5.5a,c). During stage 3, the δ^{18}O of preexisting quartz was partially re-equilibrated in ≤10,000 years at ~ 450ºC. Further cooling to ~350ºC during stage 4 sericitic alteration and possibly during a post-hydrothermal stage took ≤75,000 years. The general and progressive temperature decline after stage 1 is inferred to result from deepening of the porphyry magma source as the magma chamber crystallized downward beneath the porphyry deposit (Dilles, 1987; Fig. 5.4c, d). Both this effect and reduced magmatic-hydrothermal fluid flux during late D vein and sericitic alteration of stages 3 and 4 decreased the local geothermal gradient (Fig. 5.4c, d).

5.8 Acknowledgments

To First Quantum Minerals Ltd. for supporting this research. To Brian Rusk and Andreas Audétat for the discussions about SEM-CL imaging and limitations of the Ti in quartz geothermometry. WiscSIMS is funded by NSF-EAR-1355590.

5.9 References

Burnham, C.W., 1979, Magmas and hydrothermal fluids, *in* Barnes, H.L., ed., Geochemistry of hydrothermal ore deposits, v. II, New York, Wiley Interscience, p. 71–136.

Cathles, L.M., and Shannon, R., 2007, How potassium silicate alteration suggests the formation of porphyry ore deposits begins with the nearly explosive but barren expulsion of large volumes of magmatic water: Earth and Planetary Science Letters, v. 262, no. 1–2, p. 92–108.

Cernuschi, F., Dilles, J.H., and Creaser, R., 2013, Hydrothermal alteration, SWIR–mineral mapping, vein distribution and age of the Haquira–East Cu–Mo porphyry: 12th SGA Biennial Meeting 2013, Proceedings, v. 2, p. 782–785.

Cherniak, D., Watson, E., and Wark, D., 2007, Ti diffusion in quartz: Chemical Geology, v. 236, no. 1–2, p. 65–74.

Crank, J., 1975, The mathematics of diffusion (2nd ed.): Oxford, Clarendon Press, 414 p.

Dennis, P.F., 1984, Oxygen self–diffusion in quartz under hydrothermal conditions: Journal of Geophysical Research, v. 89, no. B6, p. 4047–4057.

Dilles, J.H., 1987, Petrology of the Yerington batholith, Nevada: Evidence for evolution of porphyry copper ore fluids: Economic Geology, v. 82, p. 1750–1789.

Geiger, S., Haggerty, R., Dilles, J. H., Reed, M.H., and Matthäi, S.F., 2002, The evolution of the early hydrothermal alteration at Butte, Montana: New insights from reactive transport modeling: Geofluids, v. 2, p. 185–201.

Huang, R., and Audétat, A., 2012, The titanium–in–quartz (TitaniQ) thermobarometer: A critical examination and re–calibration: Geochimica et Cosmochimica Acta, v. 84, p. 75–89.

Mercer, C.N., Reed, M.H., and Mercer, C.M., 2015, Time scales of porphyry Cu deposit formation: Insights from titanium diffusion in quartz: Economic Geology, v. 110, no. 3, p. 587–602.

Redmond, P.B., Einaudi, M.T., Inan, E.E., Landtwing, M.R., and Heinrich, C.A., 2004, Copper deposition by fluid cooling in intrusion–centered systems: New insights from the Bingham porphyry ore deposit, Utah: Geology, v. 32, no. 3, p. 217–220.

Reed, M., Rusk, B., and Palandri, J., 2013, The Butte magmatic–hydrothermal system: One fluid yields all alteration and veins: Economic Geology, v. 108, p. 1379–1396.

Rusk, B., and Reed, M., 2002, Scanning electron microscope–cathodoluminescence analysis of quartz reveals complex growth histories in veins from the Butte porphyry copper deposit, Montana: Geology, v. 30, no. 8, p. 727–730.

Seedorff, E., Dilles, J.H., Proffett, J.M., Jr, Einaudi, M.T., Zurcher, L., Stavast, W.J.A., Johnson, D.A., and Barton, M.D., 2005, Porphyry deposits: Characteristics and origin of hypogene features, *in* Hedenquist, J. W., Thompson, J.F.H., Goldfarb, R. J., and Richards, J. P., eds.: Economic Geology 100th Anniversary Volume, p. 251–298.

Spencer, E.T., Wilkinson, J.J., Creaser, R.A., and Seguel, J., 2015, The distribution and timing of molybdenite mineralization at the El Teniente Cu–Mo porphyry deposit, Chile: Economic Geology, v. 110, p. 387–421.

Taylor H.P., Jr., 1968, The oxygen isotope geochemistry of igneous rocks: Contributions to Mineral Petrology, v.19, p. 185–219.

Valley, J. W., 2001, Stable isotope thermometry at high temperatures, *in* Reviews in Mineralogy and Geochemistry, v. 43, no. 1, p. 365–413.

Von Quadt, A., Erni, M., Martinek, K., Moll, M., Peytcheva, I., and Heinrich, C.A., 2011, Zircon crystallization and the lifetimes of ore–forming magmatic–hydrothermal systems: Geology, v. 39, no. 8, p. 731–734.

Walker, B.A., Klemetti, E.W., Grunder, A.L., Dilles, J.H., Tepley, F.J., and Giles, D., 2013, Crystal reaming during the assembly, maturation, and waning of an eleven–million–year crustal magma cycle: thermobarometry of the Aucanquilcha Volcanic Cluster: Contributions to Mineralogy and Petrology, v. 165, no. 4, p. 663–682.

Zhang L.G., Liu J.X., Zhou H.B. and Chen Z.S., 1989, Oxygen isotope fractionation in the quartz–water–salt system: Economic Geology, v. 89, p. 1643–1650.

5.10 Figures

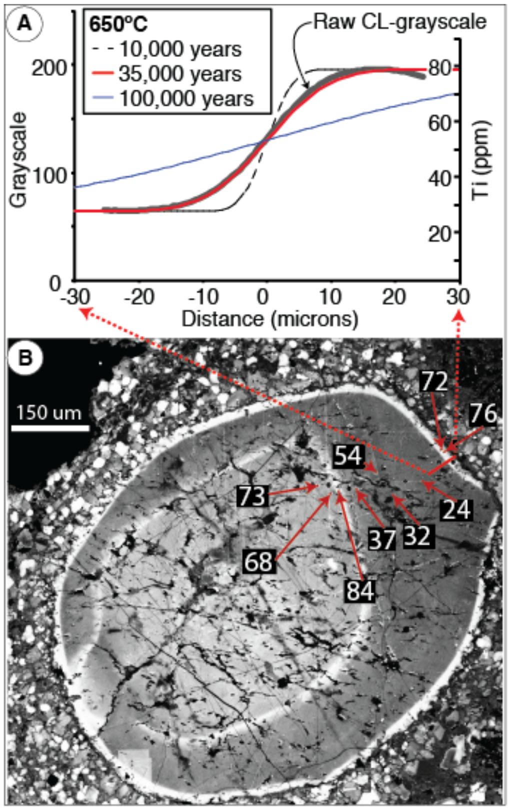

Figure 5.1. SEM-CL image of a quartz phenocryst in porphyry sample FC-HAQ-002. A narrow bright-CL and high Ti quartz band rims a gray-CL and lower Ti core. A model for the Ti diffusion profile across this boundary in quartz suggests a diffusion time of 35,000 years at ~650 ºC.

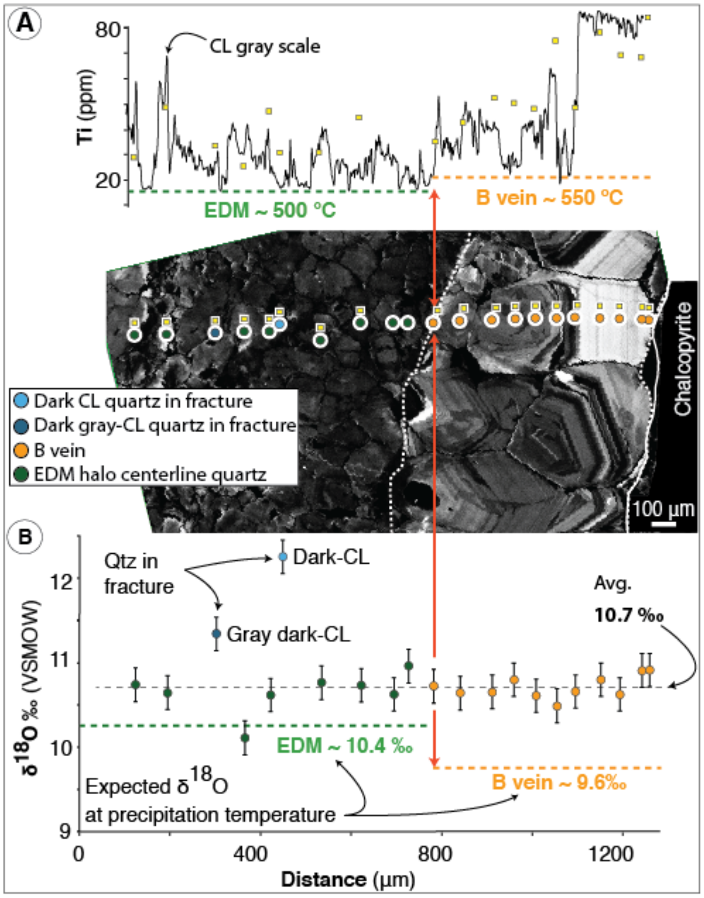

Figure 5.2. SEM-CL image of an EDM halo containing gray-CL mosaic quartz crosscut by a B vein with euhedral quartz showing growth bands of different CL intensity in sample FC-HAQ-027. **A)** Ti in quartz data (points) and CL grayscale profile along transect. Precipitation temperatures were calculated using the TitaniQ geothermometer of the lowest Ti zones in EDM and B vein quartz and $\alpha TiO2=1$. **B)** $\delta^{18}O$ ‰ (SIMS) along the transect showing reproducibility at 2 SD, and the expected $\delta^{18}O$ ‰ of EDM and B vein quartz based on the TitaniQ crystallization temperatures calculated in (A) and assuming $\delta^{18}O = 7.5$ ‰ for magmatic-hydrothermal fluids.

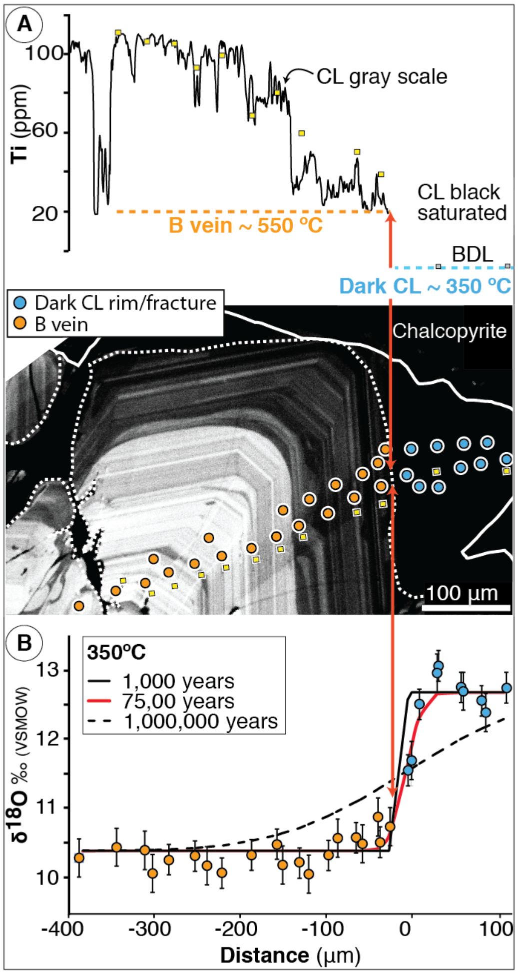

Figure 5.3. SEM-CL image of sample FC-HAQ-048 where euhedral B vein quartz shows different CL-intensity growth bands and a narrow rim of later and lower temperature dark-CL quartz. **A)** Ti in quartz data (points) and CL grayscale profile along transect. Precipitation temperatures were calculated using the TitaniQ geothermometer of the lowest Ti zones in the B vein quartz, the dark-CL D vein quartz and □TiO_2=1. **B)** Measured $\delta^{18}O$ ‰ along transect showing reproducibility at 2 SD. The $\delta^{18}O$ of the B vein quartz varies slightly from 10.1 to 10.7 ‰ whereas the dark-CL quartz rim has $\delta^{18}O$ of ~12.7 ‰. The diffusion model for the observed $\delta^{18}O$ gradient between gray-CL (B vein) and dark-CL zones provides an estimate for maximum diffusion time of 75,000 years at ~350ºC.

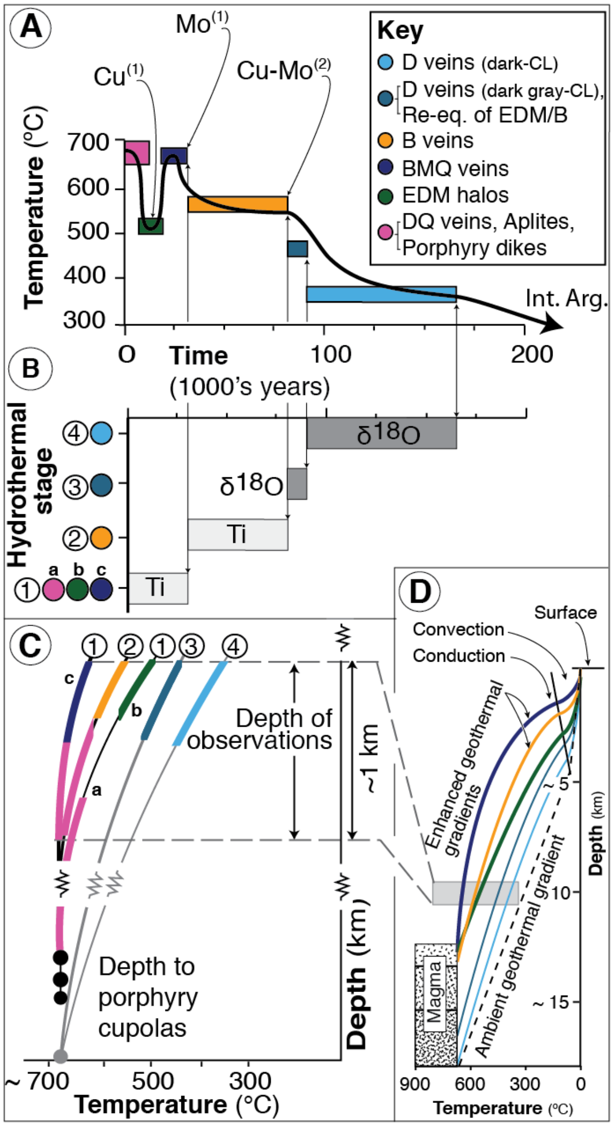

Figure 5.4. Summary of estimated timescales and evolution of the geothermal gradient. **A)** Temperature evolution of the different magmatic-hydrothermal stages and Cu-Mo-ore formation. **B)** Timescale of each hydrothermal stage based on Ti- and oxygen-in-quartz diffusion. **C, D)** Depth section illustrating schematically the evolution of the geothermal gradient resulting from porphyry intrusions and fluid ascent. Following early heating to form an enhanced geothermal gradient, the decrease in fluid flux and greater source depth of magmas and fluids leads to progressive temperature decline after stage 1. Exhumation is not considered. **C)** The relative depths of precipitation of each vein type are shown using the color scheme used in A. **D)** The enhanced geothermal gradients are color coded according to the main vein type precipitated during each hydrothermal stage.

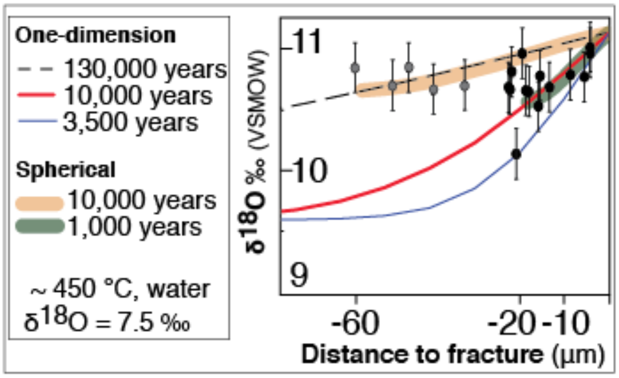

Figure 5.5. Quartz δ^{18}O ‰ (SIMS) versus measured distance to fracture or dissolution band in a B vein from sample FC-HAQ-027 (Fig. 3.2). Analyzed points < 20 µm from fracture/dissolution bands are black, points 30-60 µm from fracture are gray. Diffusion models for quartz with original δ^{18}O of 9.6 ‰ provide maximum time estimates to partially re-equilibrate by reaction with a ~450ºC and 7.5 ‰ magmatic-hydrothermal fluid present in fractures. For quartz <20 µm and < 60 µm from fracture, the preferred spherical models give 1,000 to 10,000 years, respectively. One-dimensional models are ~1 order of magnitude longer.

CHAPTER VI

PRESSURE-TEMPERATURE PATHWAYS OF MAGMATIC-HYDROTHERMAL FLUID IN PORPHYRY COPPER DEPOSITS

Federico Cernuschi
John H. Dilles
Brian Rusk
Yongmei Zhang

Extended abstract of ongoing reserach

6.1 Abstract

Porphyry Cu ± Mo ± Au are large economic mineral deposits that that are associated with shallowly emplaced arc-type granitoids typically in convergent tectonic settings. The hydrothermal alteration and mineralization is generally understood to form by magmatic-hydrothermal fluids that separate from cupolas atop a deep magma chamber and ascends by hydro-fracturing the overlying wall rock where it reacts with rock, cools, and depressurizes to form veins and/or hydrothermal halos with Fe, Cu, Mo, and Au-bearing sulfides. The pressure and temperature evolution of the magmatic-hydrothermal fluid through time, however, remains poorly understood. Here, we estimate the precipitation temperature and pressure of pre- to post-mineralization intrusions, porphyry dikes and veins using Ti-in-quartz, Ti-in-zircon and Ti-in-biotite geothermometry, hornblende barometry, fluid inclusion data and $\delta^{34}S$ compositions of sulfide-sulfate pairs. We interpret the results in the context of an adiabatic depressurization of the causative magmatic-hydrothermal fluid after its release from inferred magmatic cupolas. At the Haquira porphyry Cu-Mo deposit, Peru, magmatic temperatures before-to-during the porphyry dike emplacement is estimated between ~720 to 650 ºC. Early pre-mineralization veins and later Mo-bearing veins are estimated at ~650 ºC, whereas Cu-bearing hydrothermal halos and veins were estimated at ~550 to 500 ºC. Two generation of quartz in late and sericitic-stable veins with pyrite are estimated at ~450 ºC and 350 ºC. Copper-bearing quartz veins from the Batu Hijau porphyry Cu-Au deposit, Indonesia, are estimated to form between ~600 to 650 ºC. At the deeply emplaced Haquira East deposit, the magmatic hydrothermal fluid remained as one liquid phase during the different hydrothermal fluid releases and depressurization events. In contrast, at the shallowly emplaced Batu Hijau deposit, the magmatic-hydrothermal fluid un-mixed into a vapor and brine phase. These two distinct pressure-temperature trajectories could be key to elucidate observed differences between deep and shallow porphyry deposit globally.

6.2 Introduction

Porphyry Cu ± Mo ± Au are large economic mineral deposits that are associated with shallowly emplaced arc-type granitoids typically in convergent tectonic settings (Seedorff *et al.* 2005). In a standard model, magmatic-hydrothermal fluid separates from cupolas atop a deep magma chamber and ascends by hydro-fracturing the overlying wall rock, where it reacts with rock, cools, and depressurizes to form veins and/or hydrothermal halos with Fe, Cu, Mo, and Au-bearing sulfides (*e.g.* Dilles, 1987). Small volumes of magma are emplaced synchronously and form porphyry dikes (*e.g.* Burnham, 1979). The magmatic-hydrothermal fluid flow ranges in temperature from >650ºC to <250ºC as recorded by the different hydrothermal alteration mineral assemblages that replace the wall-rock minerals and by phase equilibria studies (Seedorff *et al.* 2005), TitaniQ geothermometry (Wark and Watson, 2006; Thomas *et al.,* 2010; Huang and Audétat, 2012) of quartz in porphyry and veins (*e.g.* Mercer *et al.,* 2013) and fluid inclusion data (*e.g.* Rusk *et al.,* 2008). However, the details of the temperature and pressure evolution and the temperature of formation of the different vein types and mineralization are not completely known.

TitaniQ geothermometry is a convenient tool to estimate formation temperatures that range from magmatic to hydrothermal as quartz is commonly an abundant mineral that forms both in magmatic and hydrothermal conditions. In porphyry deposits, quartz is present in the aplitic groundmass of porphyry dikes and as quartz phenocrysts, as well as in veins that formed before, during and after Cu±Mo±Au ore precipitation. However, accuratly calculating the temperature of formation of quartz through TitaniQ geothermometry requires the correct estimation of the pressure of formation (Thomas *et al.,* 2010). This is a complicated task as porphyry deposits may form at a variety of depths in the upper crust, ranging from as shallow as ~1 km for copper mineralization (*e.g.*, Batu Hijau, Inonesia; Yerington Mine, Nevada) to ~8 km (*e.g.*, Butte, Montana; 6-8 km) (Seedorff *et al.* (2005). Furthermore, the emplacement depth is not the only factor that controls the formation pressure of quartz in veins and porphyry dikes. Pressure fluctuates from lithostatic to close to hydrostatic conditions during each pulse of hydrothermal fluid over-pressurization and expulsion from the source magma chamber and the consequent hydro-fracturing of the roof wall rock (*e.g.* Dilles, 1987; Weis *et al.,* 2012). Additionally, the correct calculation of formation temperatures of quartz using the TitaniQ geothermometer requires accounting for kinetic effects. As reported by Huang and Audétat (2012), the non-equilibrium rapid growth of quartz enhances the incorporation of Ti in defects in fast-growing crystals. Therefore, fast-grown quartz yield spuriously high apparent formation temperatures. This is not a minor complication, as at least some of the porphyry-related hydrothermal quartz is thought to precipitate rapidly, possibly as a product of water exsolution and magmatic degassing, as proposed to explain the typical 50% aplitic groundmass in porphyry dikes (Burnham, 1979; Dilles, 1987).

Here, we present new Ti-in-quartz data from porphyry dikes and veins of the deeply emplaced EDM-bearing Haquira East porphyry Cu±Mo±Au deposit of southern Peru and one vein sample from the shallowly emplaced Batu Hijau porphyry Cu-Au deposit from Indonesia. To partially account for the pressure and kinetic effect on TitaniQ geothermometry we interpret the Ti-in-quartz data in terms of the pressure-temperature evolution of the magmatic-hydrothermal fluid that formed the different veins types by using a pressure-temperature (P-T) diagram. This method enables screening for samples that can be interpreted as precipitated at equilibrium conditions according to independent pressure and temperature estimates using fluid inclusion data, hornblende baromethry and the $\delta^{34}S$ composition of sulfate-sulfide pairs. The Ti-in-quartz analyses were coupled with secondary electron microscope cathodoluminescense (SEM-CL) imaging of the analyzed quartz to aid in the identification of different generations of quartz within a vein sample.

Geologic and thermodynamic considerations constrain the trajectory of the possible fluid pathways, limiting the range of possible formation temperatures at a giving pressure. The heat loss through the wall rock can be considered minimum during the release of magmatic-hydrothermal fluid, therefore, close to adiabatic depressurization pathways can be assumed. The pathways were inferred to begin at lithostatic pressures at the estimated emplacement depth and to terminate at the equivalent hydrostatic pressures at the same depth, in order to account for the depressurization dinamics after each hydro-fracturing event and fluid release described above (see Weis et al., 2012).

The Ti-in-quartz analyses of quartz precipitated in equilibrium conditions yield TitaniQ temperatures that agree with the temperatures calculated by independent thermometers and phase mineral equilibria estimates. The magmatic-hydrothermal fluid of the deep EDM-bearing Haquira East porphyry deposits depressurized from lithostatic to close to hydrostatic pressures as one liquid phase. In contrast, at the shallow A vein-bearing Batu Hijau porphyry deposit, the magmatic hydrothermal fluid depressurized and un-mixed into two immiscible vapor and a brine phases.

6.3 Ore Geology

The ore geology of Haquira East is described in detail in Chapters 2 through 4. The key features of the geology of Batu Hijau is summarized in Chapter 4.

6.4 Methods

Quartz grains in thirty thin and thick polished sections were imaged using a FEI Quanta 600 FEG SEM equipped with a Gatan MiniCL cathodoluminescence grayscale detector at Oregon State University (OSU). Ti contents of quartz (n=145) and biotite (n=163) were obtained using a CAMECA SX-100 electron microprobe (EMP) at OSU. Additional Ti-in-quartz data were measured by laser ablation inductively coupled mass spectrometry (LA-ICP-MS) at OSU (Photon

Machines Analyte G2 coupled with a Thermo XseriesII Quadrupole, n=28) and at Western Washington University (WWU, NewWave 213 nm Nd YAG laser coupled to an Agilent 7500ce mass spectrometer, n=116). Ti concentrations in zircons (n=82) were measured using a Sensitive High Resolution Ion-Microprobe in reverse geometry (SHRIMP-RG) at the Stanford-USGS Micro Analysis Center (SUMAC) at Stanford University. The $\delta^{34}S$ values of sulfate and sulfide pairs were measured on SO_2 gas in a continuous-flow gas-ratio mass spectrometer (ThermoQuest Finnigan Delta PlusXL, n=4) at University of Arizona. Data for these measurements are presented in Appendix 6. Thirteen thick polished sections of samples from different vein types were observed for fluid inclusion type, abundance, spatial distribution and size. These samples were previously imaged by SEM-CL and the different types of quartz were analyzed bye EMP and/or LA-ICP-MS. Microthermometry was carried out using a Linkam stage at WWU in 349 fluid inclusions from 6 representative samples. Most analyzed fluid inclusions were liquid-vapor inclusions that formed clathrate upon cooling. Salinities, CO_2 contents, and densities were estimated using the computer program ICE (Bakker, 1997) and the data of Duan *et al.* (1992a, b).

6.5 Building a pressure-temperature diagram

A diagram of apparent temperature against pressure is shown in Figure 6.1. Pressure at hydrostatic depth was estimated at ~2.7 times less than the lithostatic pressure at the same depth, using the formula $P = \rho . g . z$ where P is pressure, ρ is density, g is the gravitational constant and z is depth. Ti-in-quartz data is color coded according to the quartz type and the key is shown in Figure 6.1. The hydrous-granite solidus line (dashed gray line, Holtz *et al.,* 2001) divides the magmatic field at high P-T from the hydrothermal field at lower P-T. Ti-isopleths were calculated using the TitaniQ geothermometer (Huang and Audétat, 2012). Ti activity was estimated as 1 for the hydrothermal quartz based on the presence of rutile (gray Ti-isopleths), and as 0.65 for the magmatic quartz based on estimates for similar arc rocks elsewhere (orange Ti-isopleths, *e.g.* Walker *et al.,* 2013, Grocke, 2014). Where apparent formation temperatures of hydrothermal quartz overlap with the position of the magmatic field, the Ti-isopleths of the hydrothermal field are projected to higher magmatic P-T.

6.5.1 Magmatic temperature constrains

Zircon crystallization temperatures for the Haquira East intrusions were estimated using Ti-in-zircon (Watson and Harrison, 2005) assuming a Ti activity of 0.70. With the exception of the pre-mineralization Lahuani sills (Chapter 2), the zircon crystallization of the Haquira intrusions mostly range from ~650 to 720 ºC. Ti-in-biotite temperatures estimates (Henry *et al.,* 2005) for magmatic biotite in the Haquira granodiorite stock range from ~700º to 750ºC.

6.5.2 Pressure estimates

A variety of evidence suggests significant (~10 km) emplacement depths at Haquira East. The Haquira East deposit is hosted in a granodiorite stock that intrudes a folded and ductily deformed quartzite sequence. Hydrothermal banded molybdenite-quartz (BMQ) veins cutting the quartzite are locally folded, and hydrothermal biotite in the porphyry plug is aligned into a foliation by deformation. This deformation does not affect the last porphyry dikes, which has an isotopic age that is indistinguishable from the earlier porphyries. Therefore, deformation was ongoing during porphyry emplacement, and suggests significant depth (Chapter 2).

Shallow porphyry deposits are characterized by A type granular quartz-sulfide veins, whereas deep deposits lack these veins but instead contain early dark micaceous (EDM) veins, as observed at the Butte porphyry copper deposit in Montana (Proffett, 2009). At Haquira East, A quartz veins are absent, and EDM veins are the most important contributors to the high-grade Cu ore (Cernuschi *et al.,* 2012), suggesting emplacement depths similar to Butte (~ 8 km, Rusk *et al.,* 2008).

The observed fluid inclusions trapped in quartz veins were classified according to their bubble size (*e.g.* Rusk *et al.,* 2008) and all samples are dominated by B30 and B50 inclusions. Halite-saturated B15H and vapor-rich B85 inclusions, typical in many porphyry-type deposits are rare in samples observed from Haquira. B30 fluid inclusions homogenize between ~260ºC to 300ºC and are 4 to 6.5 wt. % NaCl and ~5 mol % CO_2. B30s are common in bright-CL quartz of early BQ veins and in dark gray-CL quartz of late D veins (see Chapter 4). B50 fluid inclusions homogenize between ~350ºC and ~380ºC, are ~2.5 to 6 wt. % NaCl and ~5 mol % CO_2. Both B30 and B50 inclusions were trapped in the single phase field at pressures and temperatures greater than those that lead to fluid immiscibility (Fig. 6.1). The dominance of B30 and B50 inclusions that trapped a single phase fluid, and the dearth of B15H and B85 inclusions, suggests that the veins in which these inclusions are trapped formed at pressures higher than the typical in many other porphyry type ore deposits, where unmixed fluid inclusion assemblages are more common (*e.g.* Bingham, Utah; Landtwing *et al.,* 2010). The fluid inclusion population more closely resembles those at Butte (Rusk *et al.,* 2008), however, B15H and B85 fluid inclusions are more abundant at Butte, indicating that some fluid un-mixing occurred. Therefore it is likely that Haquira was emplaced at a greater depth than Butte, likely at ~10 km.

Geologic considerations also indicate great depth. Hornblende barometry of the nearby exposed and shallower Acojasa granodiorite pluton (Chapter 2) yields a pressure estimate of ~ 2 (±0.5) kb. At Haquira East, 1 km deep drill-holes did not reach the top of the inferred source intrusion below it. Therefore, the lithostatic pressure during the emplacement of Haquira East is considered > 2 kb, and likely ~ 3 kb, which indicates ~10 km.

In contrast to Haquira, geologic evidence indicates that Batu Hijau is a shallowly emplaced porphyry deposit (~ 1 km, Seedorff *et al.,* 2005). Fluid inclusions in the Cu-ore forming A veins evidence that fluid un-mixing into a vapor and brine phase was a common process (Zwyer, 2010). Therefore, fluid inclusions were trapped at low pressure, below the immiscibility field of water (<1 kb).

6.5.3 Pressure-temperature fluid paths

The first adiabatic depressurization fluid pathway at Haquira East (A, shown in red in Fig. 6.1) is interpreted to start at ~3 kb at lithostatic pressure and end at ~1.2 kb at close to hydrostatic pressures. Because fluid inclusion assemblages indicate that the magmatic-hydrothermal fluid did not un-mix into brine and vapor, the depressurization path has to terminate above the liquid to brine+vapor boundry (Fig. 6.1). At the estimated pressure, the maximum starting temperature of the adiabatic depressurization pathways is constrained by the position of the boundary of a granodioritic magma with ~50 % crystals. This is a common assumption for the crystal fraction of the magmatic source based on the typical ~50 % ground mass of the porphyry dikes associated with the hydrothermal system at Haquira East and porphyry deposits elsewhere (*e.g.* Dilles, 1987).

Based on cross-cutting relationships and spatial distribution (Chapter 3, 4) the K-silicate to transitional alteration-stable veins and halos (DQ, EDM, BMQ and B) are assumed to have formed by several consecutive magmatic-fluid releases that followed the trajectory of pathway A (shown in red in Fig. 6.1). Later D veins, stable with lower temperature sericitic alteration (*e.g.* Seedorff *et al.,* 2005) cross-cut all the earlier and higher temperature K-silicate veins and halos throughout all the deposit. Therefore, we assume that D veins formed from a magmatic-hydrothermal fluid ejected from a deeper cupola as the magmatic hydrothermal system retracted underneath Haquira East (see Chapters 4 and 5). The starting pressure of this pathway is unconstrained, but it is assumed to started at >3kb. Further constrains of the P-T trajectories are discussed in the next section.

At the shallowly emplaced Batu Hijau deposit, the pressure-temperature trajectories of the magmatic-hydrothermal fluid were different than at Haquira East. Based on the fluid inclusion assemblage of A veins, we infer that the source of the magmatic-hydrothermal fluid was emplaced at a maximum of ~1.2 kb below the miscibility curve of water.

6.5.4 Fluid inclusions isochores and Ti-in-quartz isopleths

Individual fluid inclusion data was interpreted in the P-T diagram together with Ti-in-quartz data of the quartz that hosts them (Fig. 6.1). The density of individual fluid inclusions was calculated after heating/freezing experiments and representative iochores are shown in Figure 6.1. The maximum formation pressure and temperature for some types of hydrothermal quartz was estimated graphically by the intersection of fluid inclusion isochores with the Ti-isopleth that indicates the Ti concentration of the quartz that hosts them (*e.g.* Maydagan *et al.,* 2015).

The intersection of the 0.74 g/cm^3 isochore of a B30 fluid inclusion with the 80 ppm Ti-isopleth of the DQ vein that hosts it indicates that it was trapped at ~ 4 kb and 750 ºC. However, the uncertainties in the isochore calculations are large, and the 80 ppm Ti concentration of the DQ quartz is considered to be the result of rapid crystallization and not reflecting the P-T formation conditions. Therefore, ~ 4 kb and 750 ºC are considered an overestimation and DQ veins were likely formed at a maximum lithostatic pressure of ~3 kb as previously estimated. The Ti-in-zircon and Ti-in-biotite data indicate that magmatic temperatures ranged between ~650 and 750 ºC. It is likely that the maximum hydrothermal temperatures overlap with the lower end of the estimated magmatic temperature and therefore did not reach 750 ºC. The maximum pressure and temperature precipitation conditions of the DQ veins are constrained by the starting point of pathway A at a lithostatic pressure of ~ 3kb and ~700 ºC in a granitoid magma with ~50 % crystals (Fig. 6.1).

The end of the depressurization pathway A, at close to hydrostatic pressures is constrained by the fluid inclusions in B veins and quartz centerlines of EDM halos. The intersection of the 0.56 g/cm^3 isochore of a B50 fluid inclusion with the 20 ppm Ti-isopleth of the host B vein quartz, indicate that it was trapped at ~ 1.3 kb and 550 ºC. Similarly, the end of the depressurization pathway B at close to hydrostatic pressures is constrained by the fluid inclusions in dark gray-CL quartz of D veins (see Chapter 4 and 6). The intersection of the 0.66 g/cm^3 isochore of a B30 fluid inclusion with the 7 ppm Ti-isopleth of the host D vein dark gray-CL quartz, indicates that it was trapped at ~ 1.25 kb and 400 ºC.

6.5.5 Ti-in-quartz and temperature estimates

The Ti-in-quartz analyses were plotted along the corresponding Ti-isopleths within the permisible boundries indicated by the independent pressure and temperature estimates and following an adiabatic depressurization path from lithostatic pressure to close to hydrostatic pressures. Equilibrium precipitation temperatures were then estimated for the Ti-in-quartz analyses that plot along said pathways. High Ti-in-quartz compositions due to fast-grown quartz plot away from the adiabatic depressurization pathways towards higher appartent temperatures and are discussed in the following section. The estimated temperatures agree with mineral phase equilibria estimates and are summarized in Table 6.1. SEM-CL observations are discussed in detail in Chapters 4 and 5.

The bright-CL quartz in thin quartz phenocryst rims, aplitic ground mass, DQ and BMQ veins and some bands in B veins have high Ti concentrations. This is interpreted to result from non-equilibrium rapid growth that triggered the enhanced incorporation of Ti in crystal defects in fast-growing quartz. The gray-CL outer core of a quartz phenocryst in a Haquira porphyry dike (Chapter 5) is considered to have precipitated in equilibrium at magmatic conditions before the dike emplacement. The TitaniQ temperature yields a range from ~662 to 703 ºC at the assumed Ti activity of 0.65 and pressure $\geq$ 3 kbar. This is interpreted to be representative of the formation temperature of the quartz in aplitic groundmass in porphyry dikes and DQ and BMQ veins. A temperature of ~650 ºC is assumed as the minimum formation temperature. This temperature estimate is in agreement with the magmatic temperatures estimated by Ti-in-zircon and Ti-in-biotite methodology. Ti-in-biotite of hydrothermal biotite replacing hornblende that formed during K-silicate alteration give temperatures that range from ~630 to ~740 ºC with most of the analyses yielding temperatures of ~720 ºC (Fig. 6.1). As stated above, it is likely that the Ti-in-biotite estimated temperatures for hydrothermal biotite overestimates the precipitation temperature (Mercer *et al.,* 2013).

B veins formed at ~550ºC based on the lowest Ti contents of their CL-zoned quartz at pressures intermediate from lithostatic to hydrostatic (~1.6 kb). The estimated temperature overlaps with the estimated precipitation temperature of ~500 to 540 ºC for a B vein-like quartz-anhydrite-pyrite vein, based on the $\delta^{34}S$ composition of pyrite-anhydrite (Fig. 6.1). This temperature only slightly overlaps with the estimated precipitation temperatures of ~570 to 650 ºC for a B vein-like quartz-anhydrite-chalcopyrite vein, based on the $\delta^{34}S$ composition of chalcopyrite-anhydrite (Fig. 6.1).

The majority of the quartz centerline in EDM halos display a narrow range of gray-CL quartz, consistent with equilibrium crystallization that suggests crystallization at ~500ºC and ~ 1.6 kb. Similarly, in D veins the dark gray-CL quartz formed at ~450ºC whereas the dark-CL quartz formed at ~350°C at ~1kb. The estimates are consistent with the precipitation temperature of ~350 ºC for dark-CL quartz and ~370 ºC for dark gray-CL quartz estimated with de $\delta^{18}O$ data (Fig. 6.1; Chapter 5).

6.5.6 Kinetic effects in TitaniQ

The Ti-in-quartz analyses of quartz that grew in equilibrium are expected to plot along the depressurization path and reflect the P-T precipitation conditions. High Ti-in-quartz analyses interpreted to be product of fast growing quartz, however, plot in a trend that departs from the adiabatic path to higher apparent temperature (Fig. 6.1 upper insert). Experimental data can be used to constrain the magnitude of this departure. At growth rates of 120 μm/day, quartz incorporates up to ~100 ppm more Ti than slow-growing quartz (4 μm/day) at ~700 ºC (see Fig. 3 in Huang and Audétat, 2012). We assume that quartz will be more likely to precipitate at higher rates at the beginning of each depressurization cycle due to water exsolution and magma degassing as each hydrothermal fluid batch is released. As the fluid depressurizes, it is more likely that the quartz will grow at a slower rate. In a simple model, it can be expected that quartz grows faster at higher pressures and then progressively approaches the equilibrium precipitation conditions as pressure decreases. In the P-T diagram of Figure 6.1, fast grown quartz plots away from the adiabatic depressurization path by as much as ~100ºC (upper insert). In this simple model, intermediate apparent temperatures represent intermediate growth rates and not necessarily intermediate precipitation temperatures.

6.6 Conclusions

In Figure 6.2 we present the evolution of the thermal gradient a top of an inferred magma chamber's cupola from where the magmatic-hydrothermal fluid was expelled below Haquira East. This figure summarizes the pressure and temperature constraines presented here, as well as the temporal sucesion of veins and mineralization described in chapters 3, 4 and 5.

The early K-silicate stable magmatic-hydrothermal fluid depressurized from ~3 kb to ~1.2 kb along fluid pathway A. Several successive fluid releases formed the observed sequence of DQ veins, EDM halos, BMQ veins and B veins (Figure 6.1).

During hydro-fracturing and porphyry emplacement the geothermal gradient is enhanced as the hot magmatic-hydrothermal flows upwards and heats up the wall rock (Fig. 6.2A). The temperature gradient is the highest in the center of the rising hydrothermal fluid flow path and decreases in the edges, creating a "bend" in depth of the iso-temperature surfaces that represent the geothermal gradient. The shape of the geothermal gradient will later control the depth of precipitation of sulfides resulting in the typical inverted cup shaped high grade Cu and Mo ores (*e.g.* Seedorff *et al.,* 2005; Landtwing *et al.,* 2010).

During the first magmatic-hydrothermal up-flow and hydro-fracturing of the roof wall rock (Fig. 6.2A), DQ veins are emplaced in a central and deeper area at ~3 kb lithostatic pressure and ~650 ºC, together with most of the Haquira porphyry dikes and aplites that crystallized from a synchronous magma. The same magmatic-hydrothermal fluid precipitated EDM halos at ~500 ºC above the DQ vein dominated zone (Fig. 6.2A) as the depressurization after hydro-fracturing drives the pressure down to ~1.6 to 1.2 kb (Fig. 6.1). The inverted cup-shaped high-grade Cu-ore shell is formed at this stage by the distribution of the bornite-chalcopyrite-bearing EDM halos, above and around a DQ vein dominated low-grade Cu core, as discussed in Chapter 3.

Several subsequent pulses of magmatic-hydrothermal fluid up-flow further steepened the geothermal gradient. A later Mo-mineralizing fluid pulse (see Chapter 3) precipitated BMQ veins at ~650ºC in a zone that is roughly coincident with, but outboards, the distribution of EDM halos (Fig. 6.2A'). As the amount of fluid up-flow decreased, the geothermal gradient retracted. A latter Cu-Mo-mineralizing fluid precipitated B veins at ~550ºC (Fig. 6.2A'').

After the magmatic system below Haquira East started to retract, fluid released from deeper cupolas reached the observed depth with higher acidity and lower temperature than the previous batches. This fluid is stable with sericitic alteration and folows the trajectory of pathway B in Figure 6.1. The earlier fluid releases at this stage precipitated D veins with sericitic halos at ~450ºC (dark gray-CL quartz in Fig. 6.1). Later fluids were released as the thermal gradient collapsed and reached quartz in D veins reached ~350 ºC (dark CL quartz in Fig. 1; see Chapter 2).

At the deeply emplaced Haquira East porphyry deposit, the magmatic hydrothermal fluid remained as one liquid phase during the different fluid releases and depressurization of the system, (Fig. 6.1, paths A and B). A tentative fluid pathway for a shallowly porphyry copper deposit is exemplified by Baju Hijau. There, the high-grade Cu-mineralization is hosted in A veins. Fluid inclusions in A veins evidence that fluid un-mixing into a vapor and brine phase was a common process (Zwyer, 2010). At Batu Hijau the depressurization followed a trajectory entirely in the vapor and brine field (Fig. 6.1, path C). The very high Ti concentration of the sugary textured A vein quartz is likely due to fast growing quartz triggered by the rapid un-mixing of the magmatic hydrothermal fluid. The lowest Ti zones in A vein quartz the ones that precipitated the closest to equilibrium conditions. TitaniQ estimates of these zones yield apparent temperatures of ~624 to 655 ºC at ~0.5 kb. However, since all the A vein quartz is grown at fast rates, the TitaniQ temperatures are considered an overestimate, and ~600 ºC is a more plausible equilibrium precipitation temperature.

6.7 Acknowledgements

I am indebted to Nansen Olson for his excellent help with hornblende barometry, Frank Tepley for the assistance with EMP analyses, Richard Bradshaw for the assistance with LA-ICP-MS analyses at OSU and Matt Coble for the assistance with the SIMS at Stanford. I extend my gratitude to Chris Eastoe for analyzing the sulfide-sulfate pairs at University of Arizona.

6.8 References

Bakker, R.J., 1997, Clathrates: Computer programs to calculate fluid inclusion V–X properties using clathrate melting temperatures: Computers and Geosciences, v. 23, p. 1–18.

Bodnar, R.J., and Sterner, S.M., 1987, Synthetic fluid inclusions *in* Hydrothermal Experimental Techniques, Ulmer, G.C., and Barnes, H.L., eds., Wiley–Interscience, New York. p. 423–457.

Cernuschi, F., Einaudi, M.T., Dilles, J.H., Heather, K.B., Barr, N.C., 2012, Hydrothermal veins, porphyry geochemistry and mineralization zonation of the Haquira East porphyry Cu–Mo deposit, Perú: SEG Conference 2012, Lima, Perú.

Dilles, J.H., 1987, Petrology of the Yerington batholith, Nevada: Evidence for evolution of porphyry copper ore fluids: Economic Geology, v. 82, p. 1750–1789.

Duan, Z., Moller, N., and Weare, J.H., 1992a, and equation of state for the CH4–CO2–H2O system: I. Pure systems from 0 to 1000°C and 0 to 8000 bars: Geochimica et Cosmochimica Acta, v. 56, p. 2605–2617.

Duan, Z., Moller, N., and Weare, J.H., 1992b, and equation of state for the CH4–CO2–H2O system: II. Mixtures from 50 to 1000°C and 0 to 1000 bars: Geochimica et Cosmochimica Acta, v. 56, p. 2619–2631.

Grocke, S.B., 2014, Magma dynamics and evolution in continental arcs: Insights from the Central Andes [Unpublished PhD thesis]: Oregon State University, 303 p.

Holtz, F., Becker, A., Freise, M., and Johannes, W., 2001, The water–undersaturated and dry Qz–Ab–Or system revisited. Experimental results at very low water activities and geological implications: Contributions to Mineralogy and Petrology, v. 141, p. 347−357.

Huang, R., and Audétat, A., 2012, The titanium–in–quartz (TitaniQ) thermobarometer: A critical examination and re–calibration: Geochimica et Cosmochimica Acta, v. 84, p. 75–89.

Landtwing, M.R., Furrer, C., Redmond, P. B., Pettke, T., Guillong, M., and Heinrich, C.A., 2010, The Bingham Canyon porphyry Cu–Mo–Au deposit. III. Zoned copper–gold ore deposition by magmatic vapor expansion: Economic Geology, v. 105, no. 1, 91–118.

Maydagán, L., Franchini, M., Rusk, B., Lentz, D. R., McFarlane, C., Impiccini, A., and Rey, R., 2015, Porphyry to epithermal transition in the Altar Cu–(Au–Mo) deposit, Argentina, studied by cathodoluminescence, LA–ICP–MS, and fluid inclusion analysis: Economic Geology, v. 110, no. 4, 889–923.

Mercer, C.N., and Reed, M.H., 2013, Porphyry Cu–Mo stockwork formation by dynamic, transient hydrothermal pulses: Mineralogic insights from the deposit at Butte, Montana: Economic Geology, v. 108, no 6, p. 1347–1377, doi:10.2113/econgeo.108.6.1347

Proffett, J.M., 2009, High Cu grades in porphyry Cu deposits and their relationship to emplacement depth of magmatic sources. Geology, v. 37, no. 8, p. 675–678, doi:10.1130/G30072A.1

Rusk, B.G., Lowers, H.A., and Reed, M.H., 2008, Trace elements in hydrothermal quartz: Relationships to cathodoluminescent textures and insights into vein formation: Geology, v. 36, n 7, 547.

Seedorff. E., Dilles, J.H., Proffett, J.M. Jr, Einaudi, M.T., Zurcher, L., Stavast, W.J.A., Johnson, D.A., and Barton, M.D., 2005, Porphyry deposits: Characteristics and origin of hypogene features: Economic Geology 100th Anniversary, v. 29, p. 251–298.

Thomas, J.B., Watson, E.B., Spear, F.S., Shemella, P.T., Nayak, S.K., and Lanzirotti, A., 2010, TitaniQ under pressure; the effect of pressure and temperature on the solubility of Ti in quartz: Contributions to Mineralogy and Petrology, v. 160, no. 5, p. 743–759, doi:10.1007/s00410–010–0505–3

Walker, B.A., Klemetti, E.W., Grunder, A.L., Dilles, J.H., Tepley, F.J., and Giles, D., 2013, Crystal reaming during the assembly, maturation, and waning of an eleven–million–year crustal magma cycle: Thermobarometry of the Aucanquilcha Volcanic Cluster: Contributions to Mineralogy and Petrology, v. 165, no. 4, 663–682.

Wark, D.A., and Watson, E.B., 2006, TitaniQ: a titanium–in–quartz geothermometer: Contributions to Mineralogy and Petrology, v. 152, no. 6, 743–754, doi:10.1007/s00410–006–0132–1

Watson, E.B., and Harrison, T.M., 2005, Zircon thermometer reveals minimum melting conditions on earliest Earth: Science, v. 308, p. 841–844, doi:10.1126/science.1110873.

Weis, P., Driesner, T., and Heinrich, C.A., 2012, Porphyry–copper ore shells form at stable pressure–temperature fronts within dynamic fluid plumes: Science, v. 338, no. 6114, 1613–1616, doi:10.1126/science.1225009

Zwyer, T., 2010. Temporal and Spatial Evolution of Hydrotheraml, Ore–related Fluids in the Batu Hiaju Porphyry Copper–Gold Deposit, Sumbawa (Indonesia) [Unpublished master thesis]: ETH Zürich, Switzerland, 57 p.

6.9 Figures and Tables

Table 6.1. Porphyry and vein formation temperatures based on phase equilibria, titaniq geothermometry and fluid inclusion data.

Quartz type	**Deposit**	**T(°C)** [phase]	**Ti** (ppm)	**T(°C)** [Ti]				**T(°C)** [pref.	**SEM-CL intensity**
				T (°C)	P (kbar)		αTiO2		
Igneous	Haquira	~700	27-40	662-703	3	L.	0.65	650	Gray-CL
DQ/BMQ		>550	60-70*	685-702	2.5	L.		650	Bright-CL
A	Batu Hijau		90-120*	624-656	0.5	L.-H.		600	Bright- to gray-CL
EDM	Haquira	550-400	15-30	505-561	1.1	L.-H.	1.0	500	Gray-CL
B		>550	18-40	541-598	1.6	L.-H.		550	Bright- to gray-CL
D (early quartz)		400-450	5-15	425-500	1	L.-H.		450	Dark-gray-CL
D (late quartz)		300-400	1-5	339-425	1	L.-H.		350	Dark-CL

Notes: T (°C) [phase] was estimated based on the phase stability of quartz – K-feldspar – Muscovite – Andalusite (Seedorff *et al.,* 2005). **T (°C) [Ti]** was calculated using the Ti-in-Q geothermometer (Huang and Audétat, 2012) of the lowest Ti zones, together with pressure constrains from fluid inclusion and hornblende baromethry. * Posibly all fast growing quartz. The Ti concentration might not reflect precipitation under equilibrium conditions. P (kbar) = Pressure in kbars, L. = Lithostatic, H. = Hydrostatic. **T (°C) [pref.]** is the preferred formation temperature.

Figure 6.1. Diagram of apparent temperature versus pressure modified from Bodnar and Sterner (1987) showing EMP (circles) and LA-ICP-MS (squares) Ti-in-quartz data, selected fluid inclusion data and inferred adiabatic depressurization paths. The left vertical axis also shows hydrostatic depths, whereas the right vertical axis shows lithostatic depths. The thick black line shows the miscibility curve for the H_2O + 35 wt. % NaCl system Hornblende barometry, Ti-in-biotite, Ti-in-zircon and $\delta^{34}S$ data are shown outside of the diagram. $\delta^{18}O$ estimated temperatures are taken from Chapter 5. See text for details.

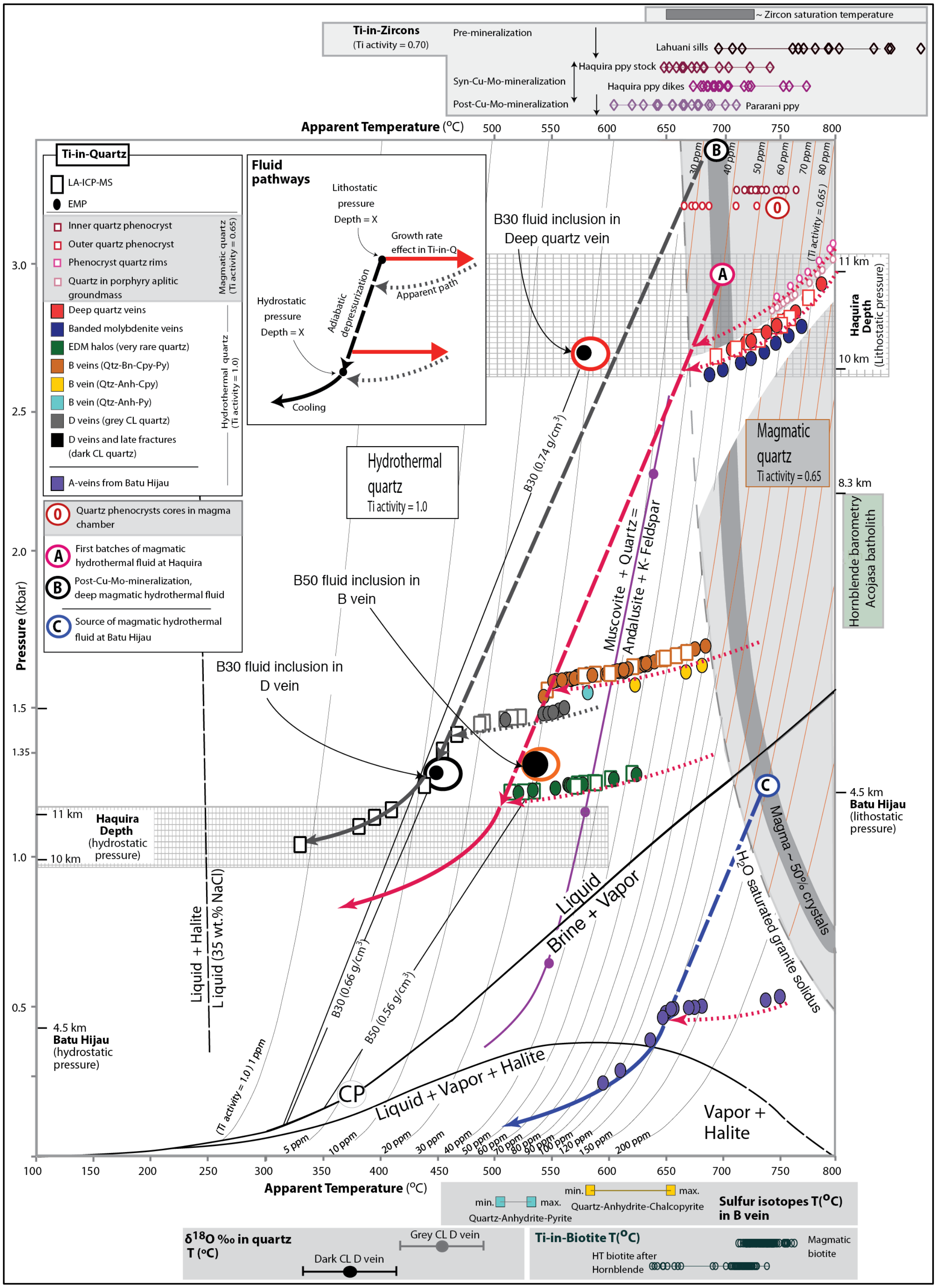

Figure 6.1. Diagram of apparent temperature versus pressure

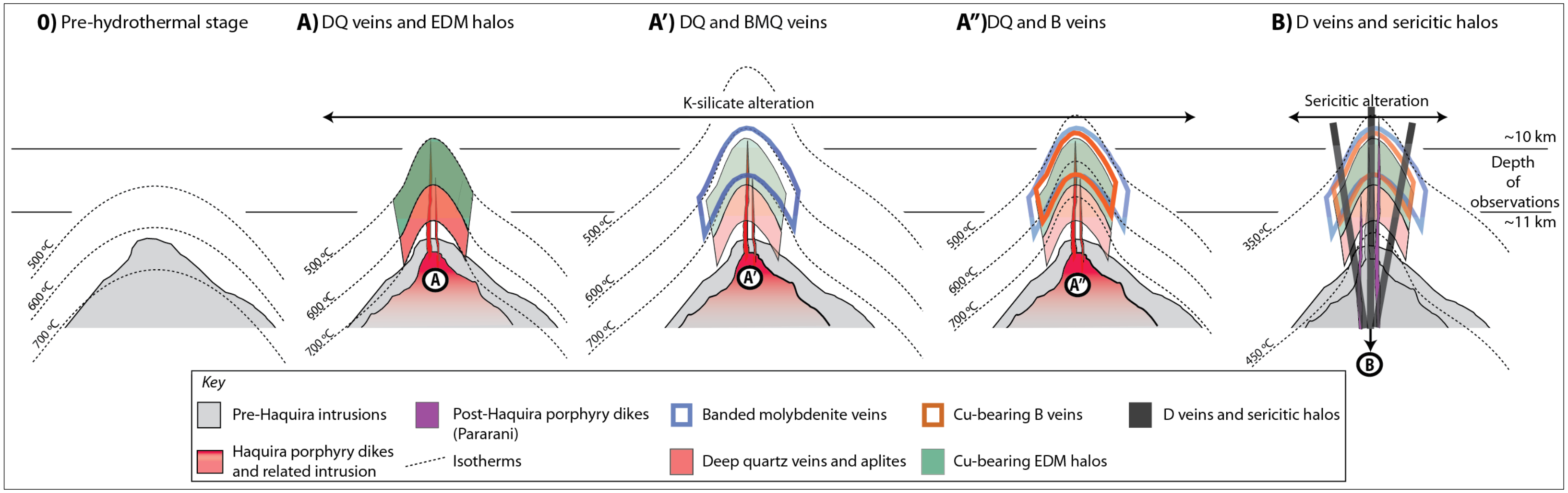

Figure 6.2. Schematic evolution of the geothermal gradient a top of a concealed cupola at Haquira East porphyry copper deposit and relation to the precipitation of the different veins and halos. Panels 0) precedes the hydrothermal fluid flow. Panels A through B show steepened geothermal gradients due to the magmatic-hydrothermal fluid up-flow.

CHAPTER VII

TEST OF A USER DEFINED CALIBRATION IN A PORTABLE XRF FOR LITHOGEOCHEMISTRY APPLICATIONS

Federico Cernuschi
Mark T. Ford
Darrick Boschmann
John H. Dilles
Richard Conrey

Draft to be submitted to Bulletin
A journal of the Geological Society of America

7.1 Abstract

Lithogeochemistry is a commonly used tool in petroleum and mineral exploration for mapping and correlating rocks. It is particularly useful to aid the identification of fine-grained shale or aphanitic or aphiric igneous rocks or rocks that have been heavily weathered/altered and lack mineralogical and textural characterization features that can be observed at hand sample. Portable X-ray fluorescence spectrometers (pXRF) have the potential to be used for lithogeochemical purposes and the convenience of rapid and low cost analyses. However, many of the commercially available devices only provide pre-set calibrations that are suitable for restricted uses (*e.g.* ore grade control), where the analysis do not have to be compared with commercially available chemical analysis or data gathered with pXRFs of different brands. We produced and tested two calibrations, one for basaltic compositions and another one for rhyolitic compositions, using whole-rock powdered samples and influence coefficient calibrations in a Bruker Tracer IV XRF spectrometer with SPECTRA EDX software. Calibrations and tests were performed using rock powders previously analyzed by bench top WD-XRF at Washington State University. We were able to reproduce concentrations for a wide range of major elements, including Al_2O_3, CaO, FeO*, K_2O, MnO, TiO_2 and less accurately SiO_2 in powdered basaltic and rhyolitc samples. Several trace elements were accurately reproduced, including Cr, Cu, Nb, Ni, Sr, Y, Zr and less accurately V in powdered basaltic samples, as well as Nb, Pb, Rb, Sr, Y, Zn, Zr and less accurately Ba in powdered rhyolitic samples. The bias of the replicated analysis mostly varies between 5% and 20%, and precision between 1% and 5%. Portable XRF analysis properly calibrated for similar compositions and matrix to the unknowns can be reliably used to measure a selected set of elements for igneous rocks.

7.2 Introduction

Lithogeochemical methods are commonly used in petroleum and mineral exploration to aid the mapping and correlation of rocks from grassroots exploration to mine site. Portable X-ray fluorescence spectrometers (pXRF) have been used in several applications (*e.g.* archeology, soil analyses) in the last few years, and can be helpful tools in lithogeochemistry applications due to rapid, low cost and sometimes field-based analyses. In particular, pXRF can be an important tool to aid the geologic correlation of basaltic or rhyolitic rocks that are fine grained, aphanitic or aphiric and are difficult to identify solely based on mineralogical and textural variation on hand sample (*e.g.* Boschmann, 2012; Cernuschi *et al.,* 2015). Similarly, weathering or metasomatic alteration can obscure to obliterate the distinctive mineralogical and textural features of even coarse grained igneous rocks. However, some immobile trace elements such as Ti, Y, Nb and Zr tend to remain unchanged during weathering or hydrothermal alteration, preserving the geochemical footprint of the rock (McLean and Barrett, 1993).

Most of the commercially available pXRF devices provide pre-set calibrations that are only suitable for narrowly defined uses, were the gathered data does not need to be compared with geochemical data obtained with other instruments. Current pre-set calibrations produce results that are not comparable between different pXRF brands (Goodale *et al.,* 2011) or against commercially available wave dispersive X-ray fluorescence (WD-XRF), inductively coupled plasma optical emission spectrometry (ICP-OES) or inductively coupled plasma mass spectrometry (ICP-MS) analyses. Some user-defined pXRF calibrations rely on multivariate statistical analysis to correct intensities of one element based on other elements that are supposed to be proxies. As pointed out by Conrey *et al.* (2012), in many cases no physical reasons support these corrections, inducing error in the analysis. We produced and tested two calibrations for a Bruker Tracer IV XRF spectrometer, one for basaltic rock powders and one for rhyolitic rock powders using previously analyzed samples by standard and commercially available WD-XRF. We tested the accuracy of the newly developed calibrations by analyzing a different set of previously analyzed basaltic and rhyolitic whole rock powders (WD-XRF) that covered the whole compositional range of the calibrations. We tested the reproducibility of the calibrations by repeated pXRF analyses (n=28) of one basaltic and one rhyolitic USGS standard to calculate the precision of the analyses.

7.3 Methods

Eighteen whole rock basaltic powders and fourteen whole rock rhyolitic powders were analyzed with a Bruker Tracer IV to produce two calibrations, one for the analysis of basaltic rock powders and one for rhyolitic rock powders. The calibrations were then tested by analyzing twenty two whole rock basaltic powders, twenty six whole rock rhyolitic powders and twenty eight consecutive measurements of USGS standards RGM-1 (rhyolite, Abbey, 1983, Gladney and Roelandts, 1988, Govindaraju, 1994) and BCR-2 (basalt, Wilson, 1997).

The samples were selected to cover a broad range of compositions in each of the groups, especially in trace elements and metals (Table 7.1, 7.2). Both the samples used to make and to test the calibration were either powders previously analyzed at Washington State University (WSU) by WD-XRF (Johnson *et al.,* 1999) and selected from the Oregon State University (OSU) collection, or USGS standards (Appendix: Tables A1, A2, A3, A4).

Analyses were performed on uniformly ground powders placed in sample cups with prolene 6 µm thick film window bottoms. No filters were used in the pXRF, which used a Rh filament operated at 45keV, 25 µA and a 240 second dwell for each sample.

The data were treated independently for each composition and the calibration was done using SPECTRA EDX software following the procedure described by Conrey *et al.* (2012). The measured peaks were manually selected at full width at half maximum (FWHM) and minimizing inter-element peak overlap. The calibration calculations were done in SPECTRA EDX using influence coefficient calibrations (ICC) (Figure 7.1). ICC calibrations (empirical or calculated) are traditionally used in bench top XRFs to compensate element peak intensities from the interference produced by the presence of other elements in the sample.

7.4 Results

Al_2O_3, CaO, FeO*, K_2O, MnO, P_2O_5, SiO_2, TiO_2, Cr, Cu, Nb, Ni, Rb, Sr, V, Y, Zn and Zr for basaltic samples and Al_20_3, CaO, FeO*, K_2O, MnO, SiO_2, TiO_2, Ba, Nb, Pb, Rb, Sr, Y, Zn and Zr for the rhyolitic samples produced resolvable individual peaks (*i.e.* peaks that can be distinguished from the background and other elemental peaks) in the X-ray spectra and were selected for the calibration.

The measured concentration for each element using the newly developed calibrations in the pXRF were plotted against the WD-XRF concentrations, and compared to a 1:1 line to evaluate how accurate the original values were reproduced.

The test results for basaltic rock powders are presented in Figure 7.2 and results for rhyolitic rock powders in Figure 7.3. P, Rb and Zn for basalt powders yield poor results that did not reproduced the previously known compositions and were discarded from this evaluation. Average lower limits of detection (LLD) and average bias % for each element are summarized in Tables 7.1 and 7.2. LLD were calculated by SPECTRA EDX by projecting the background level below each element peak in each analysis from contiguous areas in the spectra and using the formula: [LLD = 3 standard deviations of background (cps) * calibration (ppm/cps)]. The calculated LLD for each individual analysis were then averaged for each element in each calibration. The LLD for each element/calibration is reported as the average LLD + 3 standard deviations.

The bias %, based on the accuracy, was calculated using the formula:
Bias % = {([*measured*]-[*certified*])/[*certified*]}*100 where [*measured*] is the measured concentration of an element using the pXRF and [*certified*] is the measured concentration for the

same element using the bench-top WD-XRF. Bias % are reported as averages for each element/calibration.

The reproducibility results of USGS basalt standard BCR-2 and rhyolite standard RGM-1 and are presented in Figure 7.4 and 7.5 respectively. The error % was calculated as 100*[standard deviation]/[mean] and are reported as averages for each element/calibration together with the bias % in Tables 7.1 and 7.2.

7.5 Discussion

CaO, FeO*, K_2O, MnO, TiO_2, Cr, Cu, Nb, Ni, Sr, Y and Zr all fit close to the 1:1 line for basaltic rock powders (Figure 2). The same was observed for Al_2O_3, CaO, FeO*, K_2O, MnO, SiO_2, TiO_2, Nb, Pb, Rb, Sr, Y, Zn and Zr in the rhyolitic powdered samples (Figure 7.3). The original bench top analyses were accurately reproduced with the pXRF for these elements. The bias % for these elements ranges from 3 % to 17% for the basaltic rock powders and 2 % to 20 % for the rhyolitic rock powders.

Al_2O_3, SiO_2, and V in basaltic powders are departed from the 1:1 correlation line between WD-XRF and pXRF analyses. However, these analyses present a linearly correlated arrangement from the lowest to the highest measured concentrations ($R^2 > 0.7$, Table 7.1) and the average bias ranges only from 6 to 12 %. SiO_2 pXRF analyses form a trend with the same slope of the 1:1 line, but the pXRF concentration are systematically lower by ~ 5 wt.%. This might be due to an error in the calibration for that element. However, a correction factor could be applied to reproduce the WD-XRF SiO_2 contents more accurately.

Lead in rhyolites yield average bias is ~34 % and therefore the pXRF analyses can only be consider informative. However, there is better correlation at concentrations over ~12 ppm. Similarly, Ba results depart from the 1:1 and the average bias is ~ 23 %.

Reproducibility analyses of BCR-2 using the basalt calibration show Al_2O_3, MnO, TiO_2, Cu, Nb, Sr, Y and Zr concentrations that overlap at 3 standard deviation with the accepted values of the standard. However, the bias of Cu and Nb from the accepted value is ~28 %, possibly as an effect of the low concentration of these elements in BCR-2 (19 and 13 ppm respectively), relatively close to the reported lower limit of detection of the instrument (5.9 and 3.4 ppm respectively). CaO, FeO, and K_2O pXRF composition overlap at 4 standard deviations, but are only biased ~6 %, ~6% and ~12 % respectively. SiO_2 and V do not overlap and biased by a ~17% and ~34 % respectively. With the exception of SiO_2, Cu, Nb and V, the reproducibility indicates average precisions that range from 0.5 % to 4.6 %. Ni and Cr concentration in BCR-2 (10.8 and

18 ppm respectively) are close to the reported LLD of the pXRF (6.8 and 12.3 ppm respectively). Analyses of Ni and Cr yield results below detection limit and therefore were not evaluated.

Analyses of RGM-1 using the rhyolite calibration indicate CaO, FeO, K_2O, MnO, TiO_2, Pb, Rb, Sr, Y and Zr concentrations that overlap at 3 standard deviation with the accepted values of the standard and are only biased between 1 and 10%. Al_2O_3, Nb and Zn partially overlap at 4 standard deviations, whereas SiO_2 and Ba analyses do not. However, all the measured elements are only biased by 1.6% to 12%, and only Ba, Nb and Zn reach >15% bias. All the measured elements present a precision between 0.01 to ~5%, with the exception of Nb (5%).

7.6 Conclusions

When calibrated using influence coefficient calibrations for compositions similar to the unknowns, pXRF analysis on samples of a similar matrix can be reliably used to accurately measure a selected set of elements over a wide range of compositions.

The pXRF calibrated with the method used in this article is particularly capable of confidently measuring the high field strength elements Ti, Zr, Y and Nb, together with Al, Ca, K, Mn, Ca, Fe and Sr and reproduced commercially available bench top WD-XRF at a maximum of ~3-4 standard deviations. Alumina, however, is better reproduced in rhyolites than in basalts, and analyses of this element in basalts are less accurate. Silica, is reproducible in rhyolites, but at more than 4 standard deviation from the standard used in the reproducibility analyses. In basalts, however, Si yield spuriously but uniformly low concentrations. Transition metals Cr, Cu and Ni can confidently be reproduced in basalts, as well as Pb (> 12 ppm), Zn and the alkali metal Rb in rhyolites.

For both basaltic and rhyolitic rock compositions, the relatively immobile elements (*e.g.* Nb, Zr, Ti and Y), which are often resistant to hydrothermal alteration and weathering, are measured with high accuracy and precision, enabling the use of pXRFs for lithogeochemistry in mineral exploration. Other elements, commonly more mobile, such as Sr, and K are confidently measured and can also aid lithogeochemistry applications in fresh or slightly altered rocks.

7.7 Acknowledgments

We thank Alexander Seyfarth from Bruker for his great assistance in operating the pXRF

7.8 References

Abbey, S., 1983, Studies in "standard samples" of silicate rocks and minerals 1969–1982: Canadian Geological Survey Paper 83–15, p. 114.

Boschmann, D., 2012, Structural and volcanic evolution of the Glass Buttes area, high lava plains, Oregon [Unpublished Masters Thesis]: Oregon State University, 100 p.

Cernuschi, F., Dilles, J.H., Kent, A.J.R., Schroer, G., Raab, A.K., Conti, B., and Muzio, R., 2015, Geology, geochemistry and geochronology of the Cretaceous Lascano East intrusive complex and magmatic evolution of the Laguna Merín basin, Uruguay: Gondwana Research, v. 28, no. 2, p. 837–857, doi:10.1016/j.gr.2014.07.007

Conrey, R.M., Wolff, J. A., Seyfarth, A., Vanhoose, A., Goodman Elgar, A., Betterncourt, N., Boschmann, D., and Werling, K., 2012, Portable XRF calibration using influence coefficients: 8th International conference on the analysis of geological and environmental materials, 67: Buzios, Rio de Janeiro, Brazil.

Flanagan, F.J., 1976, Descriptions and Analyses of Eight New USGS Rock Standards: U.S.: Geological Survey Professional Paper 840, 192 p.

Gladney, E.S., and Roelandts, I., 1988, Compilation of elemental concentration data for USGS BHVO–1, MAG–1, QLO–1, RGM–1, SCo–1, SDC–1, SGR–1, and STM–1: Geostandards Newsletter, v. 12, p. 253–362.

Goodale, N., Bailey, D.G., Jones, G.T., Prescott, C., Scholz, E., Stagliano, E., and Lewis, C., 2011, pXRF: a study of inter–instrument performance: Journal of Archaeological Science.

Govindaraju, K., 1994, Compilation of working values and descriptions for 383 geostandards: Geostandards Newsletter, v. 18, p. 1–158.

Johnson, D.M., Hooper, P.R., and Conrey, R.M., 1999, XRF Analysis of rocks and minerals for major and trace elements on a single low dilution Li–tetraborate fused bead: Advances in X–ray Analysis, v. 41, no. 843–867.

Mclean, W.H., and Barrett, T.J., 1993, Lithogeochemical techniques using immobile elements: Journal of Geochemical Exploration, v. 48, p. 109–133.

Wilson, S.A., 1997, The collection, preparation, and testing of USGS reference material BCR–2, Columbia River, Basalt: U.S. Geological Survey Open–File Report 98.

7.9 Figures and Tables

Table 7.1. Basalt powder calibration and tests

		Calibration (18 samples)		Calibration test (22 samples)					Reproducibility (n=28)	
		[Minimum]	[Maximum]	R^2	Coefficient *	Intercept *	Average LLD (BKG+ 3stdv)	Average Bias %	Average Bias %	Average precision %
Al_2O_3	wt%	14.82	17.83	0.708	0.505	6.8018	0.14	9.5%	2.9%	1.4%
CaO		8.51	12.03	0.989	0.879	0.759	0.03	4.2%	6.3%	0.5%
FeO*		8.24	15.40	0.928	1.099	1.023	0.01	3.9%	6.3%	0.5%
K_20		0.12	1.32	0.995	0.920	0.024	0.01	5.3%	12.5%	0.9%
MnO		0.16	0.27	0.928	1.060	-0.0160	0.01	4.4%	11.7%	4.6%
SiO_2		45.83	54.24	0.870	0.923	-1.953	0.09	11.6%	17.0%	140.0%
TiO_2		0.68	3.69	0.982	0.976	0.044	0.03	3.0%	1.4%	0.5%
Cr	ppm	11.3	269.8	0.952	0.976	0.506	12.3	14.2%	BDL in pXRF	
Cu		37.8	109.6	0.961	1.097	-10.925	5.9	10.1%	28.0%	22.3%
Nb		7.9	29.2	0.951	0.882	0.852	3.4	17.5%	28.0%	14.3%
Ni		23.0	193.2	0.990	0.966	0.750	6.8	7.4%	BDL in pXRF	
Sr		194.5	665.6	0.996	0.969	7.156	3.8	1.9%	9.7%	0.9%
V		194.0	329.9	0.784	0.681	52.141	15.8	10.8%	35.7%	9.5%
Y		20.4	62.9	0.864	1.210	-4.447	3.2	6.2%	3.7%	3.6%
Zr		43.5	295.6	0.997	1.003	0.945	5.0	3.5%	8.9%	1.4%

Note: **[Minimum]** and **[Maximum]** = lowest and highest measured composition to construct the calibration respectively **LLD:** lower limit of detection, **BKG:** background, **STDV**: standard deviation, **BDL:** below detection limit. ***** [pXRF] = Coefficient [WD-XRF] + Intercept

Table 7.2. Rhyolite powder calibration and tests

		Calibration (14 samples)		Calibration test (26 samples)					Reproducibility (n=28)	
		[Minimum]	[Maximum]	R^2	Coefficient *	Intercept *	Average LLD (BKG+ 3stdv)	Average Bias %	Average Bias %	Average precision %
Al_2O_3	wt%	10.43	15.46	0.882	0.866	2.273	0.22	4.4%	5.8%	0.9%
CaO		0.18	2.18	0.996	1.189	-0.260	0.01	6.0%	1.6%	0.3%
FeO*		0.44	4.40	0.935	0.934	0.439	0.01	12.5%	4.2%	0.3%
K_20		3.18	5.49	0.978	0.913	0.470	0.04	4.8%	6.0%	0.3%
MnO		0.03	0.10	0.907	0.773	0.018	0.01	8.5%	12.0%	1.2%
SiO_2		66.60	77.30	0.934	1.073	4.798	0.09	2.0%	5.6%	0.4%
TiO_2		0.05	0.66	0.967	0.834	0.087	0.02	19.6%	7.4%	0.0%
Ba	ppm	8.9	1880.0	0.854	1.457	-295.306	191.4	23.7%	36.0%	5.0%
Nb		6.5	80.5	0.986	1.001	1.6527	3.4	17.7%	30.5%	15.9%
Pb		11.7	42.0	0.630	0.910	3.338	3.9	30.4%	8.0%	4.8%
Rb		47.1	1770.0	0.996	1.013	0.033	3.8	5.2%	8.2%	0.8%
Sr		0.5	478.0	0.992	1.065	-8.125	3.9	6.3%	10.0%	1.6%
Y		11.0	144.2	0.984	0.973	0.073	3.9	10.7%	8.1%	4.2%
Zn		21.0	233.9	0.947	0.923	1.262	4.2	16.1%	17.9%	5.1%
Zr		50.0	1157.4	0.994	1.137	-26.587	4.6	9.9%	7.4%	0.7%

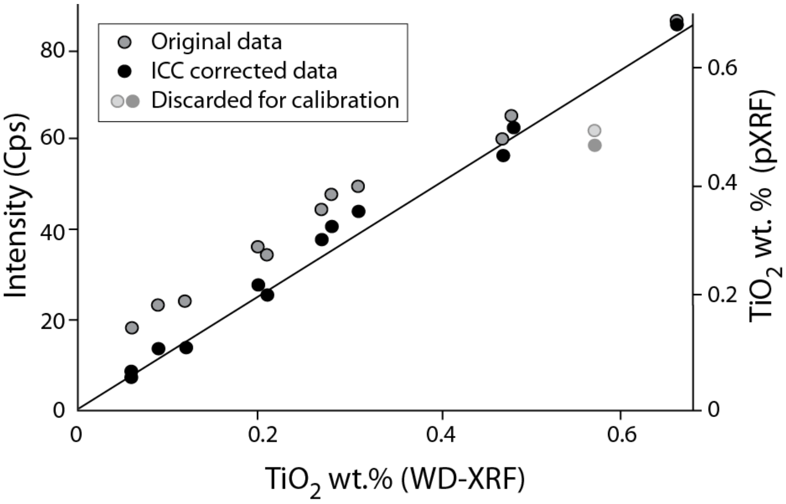

Figure 7.1 Example of a calibration for TiO_2 using basaltic rock powders in SPECTRA EDX. Gray circles are the original data and black symbols are corrected values using ICC.

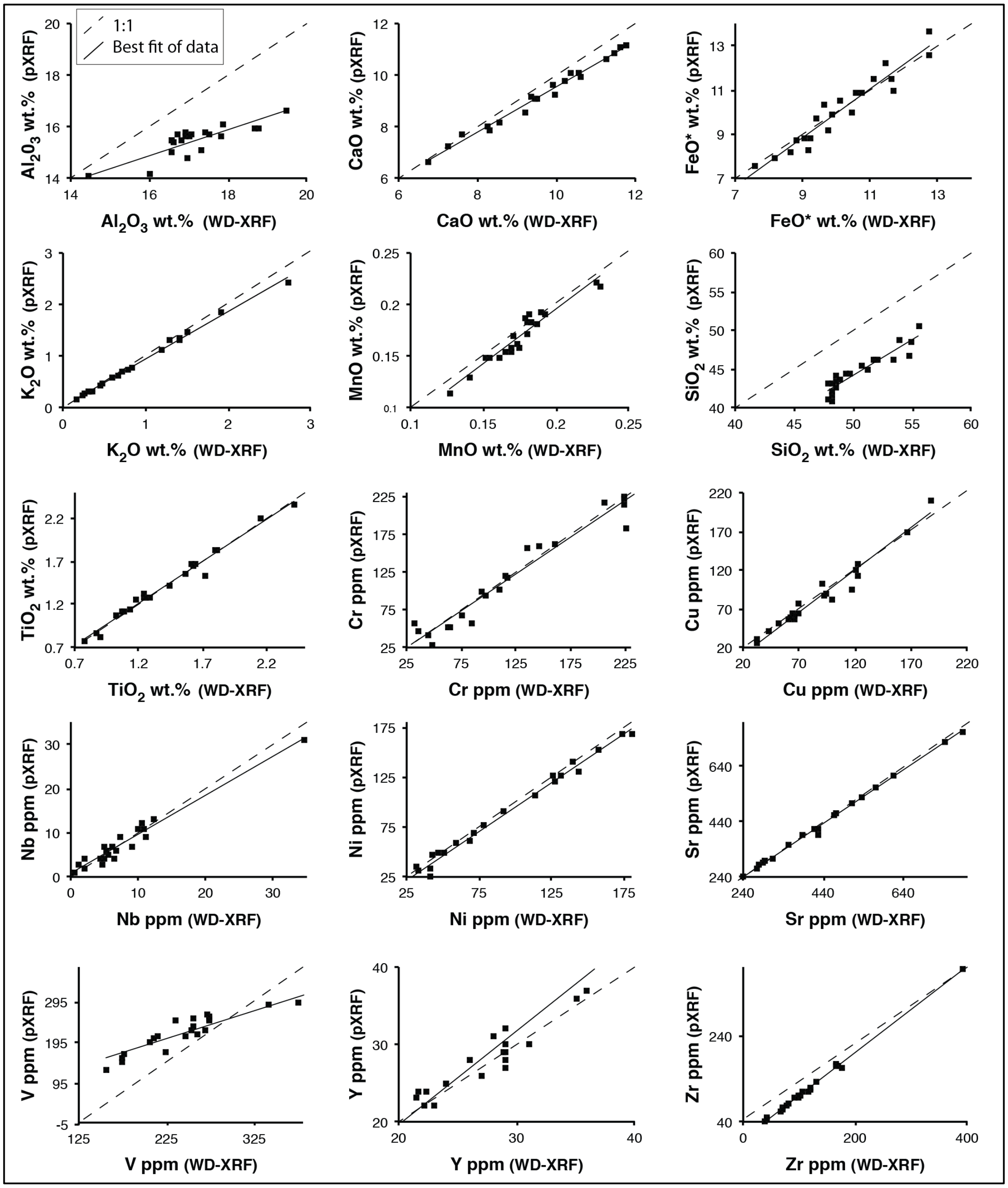

Figure 7.2 Comparison of pXRF data with bench top WD-XRF analyses for basalts samples used in the test of the basaltic powder calibration. Black lines are 1:1 and dashed line is the best fit linear regression of the data.

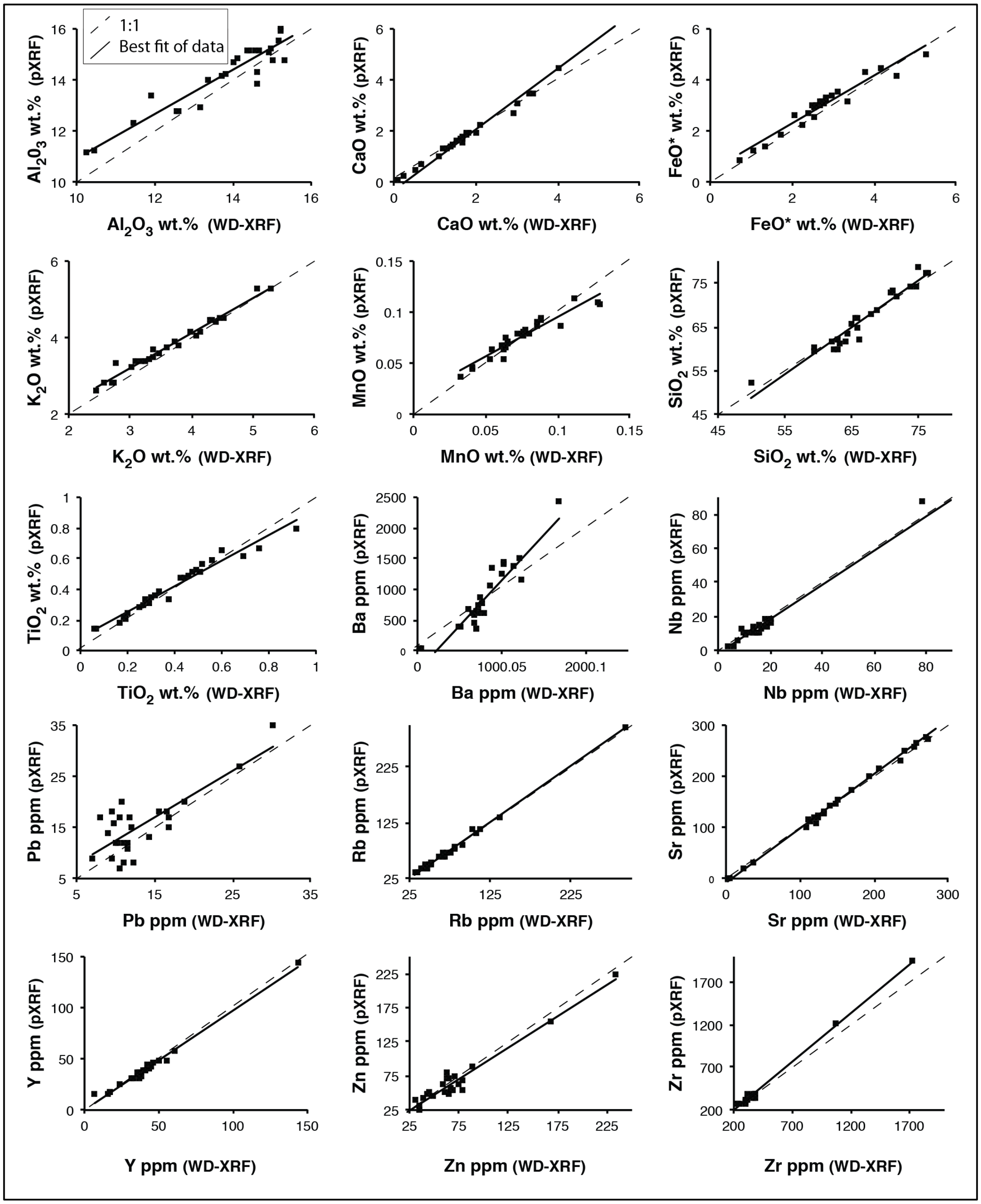

Figure 7.3. Comparison of pXRF data with bench top WD-XRF analyses for rhyolite samples used in the test of the basaltic powder calibration. Black lines are 1:1 and dashed line is the best fit linear regression of the data.

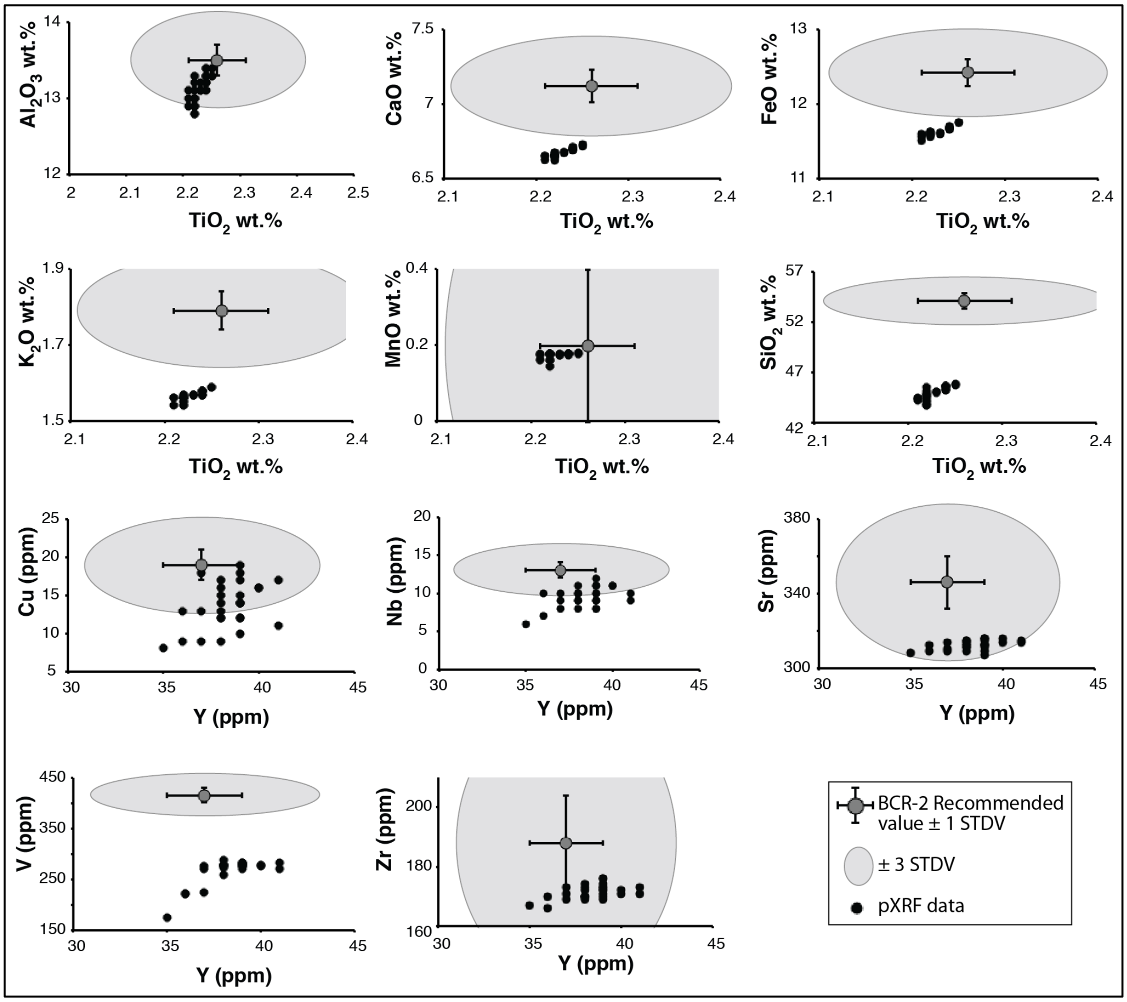

Figure 7.4. Reproducibility test of BCR-2 using the basaltic powder calibration. Error bars are 1 standard deviation and gray circle represent 3 standard deviations.

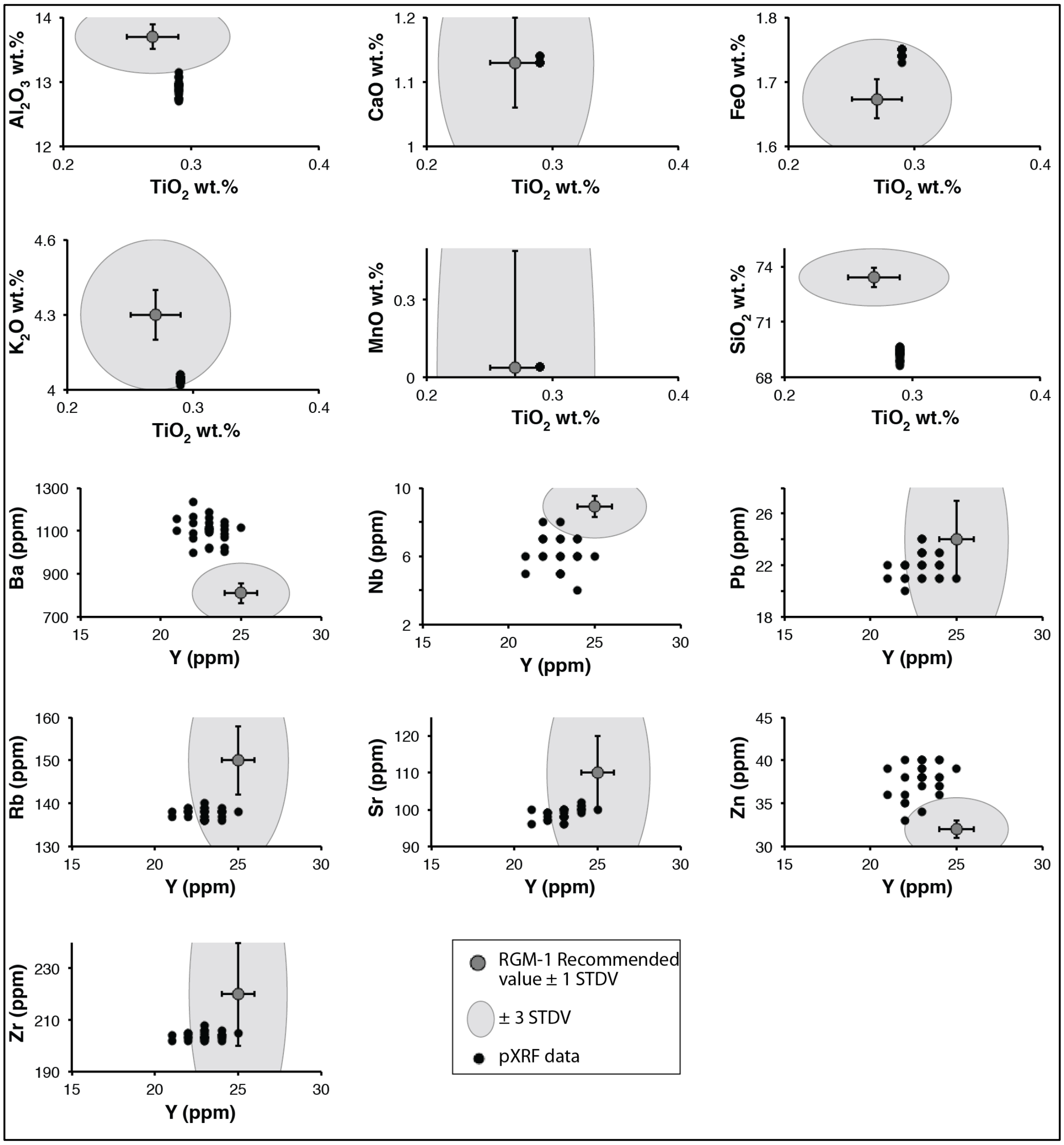

Figure 7.5. Reproducibility test of RGM-1 using the basaltic powder calibration. Error bars are 1 standard deviation and gray circle represent 3 standard deviations.

CHAPTER VIII

GENERAL CONCLUSIONS

This dissertation examines the ages, petrology and geochemistry of intrusions at the Haquira East porphyry Cu-Mo-Au deposit of southern Peru, as well as the timing, duration and pressure-temperature evolution of the Haquira East magmatic-hydrothermal alteration and mineralization. The last chapter contributes to the development of portable-XRF calibration that could be used in the future to further investigate the geochemistry of porphyry-type deposits.

Chapter 1 studied the ages and petrology of the intrusions at Haquira East and their relationship with the copper and molybdenum mineralization. The magmatism at Haquira East took place in the late Eocene to earliest Oligocene between ~34.5 to 33.5 Ma during the regional compression related to the east/northeast subduction of the Nazca plate under the western margin of the South American plate. Most of the magmatism at Haquira East was emplaced closely in time with the formation of the copper and molybdenum mineralization, and it comprises some of the youngest magmatism related to the large Andahuaylas-Yauri batholith of southern Peru (~40 to 32 Ma). The magmatism began with the emplacement of the andesitic to dacitic Lahuani sills at ~34.5 Ma, whereas the more voluminous granodioritic magmatism took place between ~34.2 and 33.5 Ma. On the basis of trace element modeling we infer that a hydrous and oxidized magma fractionated hornblende, small amounts of plagioclase and trace mineral phases while periodically re-injected with basaltic andesite and andesite from a garnet-fractionating lower crust MASH zone. This petrogenesis is responsible for high Sr/Y and V/Sc ratios in whole-rock and high Eu_N/Eu_N* and Ce_N/Ce_N* ratios in zircon observed in the immediately pre-mineralization Haquira granodiorite stock, the syn-mineralization Haquira porphyry dikes and the immediately post-mineralization Pararani porphyry dikes. As previously suggested by other authors, Sr/Y and V/Sc ratios in whole-rock and high Eu_N/Eu_N* and Ce_N/Ce_N* ratios in zircon are reliable indicators of intrusions that were related to the formation of porphyry copper deposits or intrusions that were emplaced closely in time.

The Haquira granodiorite stock was emplaced as a series of dike-like bodies that intruded in a short period of time and amalgamated into a single 0.5 x 1 km northwest-southeast elongate stock while temperatures remained high. The slightly later Haquira porphyry dikes were emplaced in several successive sets together with the K-silicate alteration-stable magmatic-hydrothermal veins and the Cu-Mo-mineralization at ~ 33.85 Ma and during compression. The emplacement of the Pararani porphyry dikes followed immediately while the inferred magma chamber below Haquira East diminished its activity and likely retracted to further depth. The sericitically altered hydrothermal breccias and quartz-sericite-pyrite veins and halos were emplaced closely in time with the Pararani porphyry dikes. Deep magma injection ceased after the intrusion of the Pararani porphyry dikes (~33.5 Ma) producing the consequent end of the magmatism at Haquira East. Rapid uplift and erosion shallowed the Haquira East intrusions and the high grade Cu-Mo mineralization from an inferred depth of formation of ~10 km at ~33.85 Ma, to its close-to-surface position before the deposition of the ~28 Ma Tacaza volcanics further to the southwest. Further compression tilted the geology at Haquira East between 10º and 20º to the north/northeast.

Chapter 3 describes in detail the mineralization and hydrothermal alteration at Haquira East. New core logging observations, geochemical data, cross-sections, 3D modeling, petrography, QEMSCAN and short wave infrared analyses of hydrothermally altered samples document the vein sequence, alteration mineralogy and their spatial distribution. From oldest to youngest, the sequence consists of biotite veins/micro-breccias, aplite dikes, deep quartz (DQ) veins, actinolite veins with plagioclase halos and epidote veins, early dark micaceous (EDM) halos with bornite-chalcopyrite, Cu-sulfide±quartz veinlets with chalcopyrite and/or bornite, banded molybdenite-quartz (BMQ) veins, B quartz-bornite-chalcopyrite veins, D pyrite-quartz-sericite veins with sericitic halos, and illite-smectite-chlorite-kaolinite ± pyrite green and white intermediate argillic halos. EDM halos are alteration selvages formed around a central fracture that rarely have a central quartz vein. The halos are composed of mixtures of hydrothermal biotite, muscovite, K-feldspar and rare quartz and corundum that replace magmatic plagioclase and hornblendes of the Haquira granodiorite stock. EDM halos carry up to 10-15 % disseminated bornite and chalcopyrite and their distribution is correlated with the highest copper grades. The distribution of the latter BMQ veins is correlated with the highest molybdenum grades. Latter B veins are secondary but important contributors to both copper and molybdenum ores.

At Haquira East the copper and molybdenum was introduced from one or more inferred magmatic cupolas on top of a concealed granodioritic intrusion. As evidenced by the vein cross-cutting relationship, the copper and molybdenum ore was formed during three different stages of copper and/or molybdenum mineralization during K-silicate alteration and indicate that the Cu/Mo ratios of the magmatic-hydrothermal source fluctuated greatly through time.

The release of over-pressured magmatic-hydrothermal fluid from the cupolas, hydro-fractured the roof wall rock of the intrusion, creating a fracture-controlled upwards migration pathway. The upwards-migrating hydrothermal fluid produced K-silicate to transitional alteration in the wall rock, as well as the early veining and the copper-molybdenum mineralization. Small batches of magma were released synchronously resulting in the emplacement of the Haquira porphyry dikes and aplites. The fluid pathway was located close to the southwest flank of the Haquira granodiorite stock and defines a symmetry axis, around which most vein types and sulfides are distributed equally and form an inverted cup-shape controlled by favorable precipitation temperatures. Notable exceptions are the distribution of the copper-ore forming EDM halos and in less degree the B veins, which are restricted to the Haquira granodiorite stock. The EDM halos only develop in favorable reactive wall rocks, where magmatic hornblende and plagioclase minerals become unstable as they react with a K-silicate to transitional alteration-stable hydrothermal fluid. Similarly, the availability of iron in the wall-rock minerals greatly limits the precipitation of copper-sulfides. At Haquira East the great reactivity contrast between the quartzite dominated meta-sedimentary wall rock to the southwest and the Haquira granodiorite stock to the northeast, determined the asymmetry of the distribution of EDM halos, high density of B veins and high Cu-grade ore.

Chapter 4 describes the temperature of precipitation of copper at Haquira East and compares it with previously published data from other deposits. The results suggest that the previous evidence for copper precipitation below ~400ºC (based on SEM-CL imaging) is, at best, ambiguous. The SEM-CL observations can be reconciliated with Cu-sulfide deposition above 400ºC in agreement with mineral phase equilibria predictions, vein cross-cutting observations and the the observed correlation of K-silicate stable Early Dark Micaceous (EDM) halos, A or B type veins with the high grade Cu-ore shell in porphyry copper deposits. Although the Cu-sulfides are sometimes in direct contact with the latest and darkest-CL quartz in microfractures, they are also in contact with earlier and brighter CL quartz of EDM halos, A and B veins. Cu-sulfides are only observed along the strike of bright- to gray-CL quartz bearing A and B veins and/or in EDM halos evidencing an intimate association with bright- to gray-CL quartz. The dark-CL quartz in microfractures is ubiquitous in Cu-bearing veins at Haquira and porphyry copper deposits elsewhere, but is equally common in earlier low-grade Cu or barren veins and magmatic quartz with no Cu-sulfides. Furthermore, the dark-CL quartz is texturally and compositionally indistinguishable from the equally dark-CL quartz in later low-grade Cu D veins.

We propose that Cu-sulfides are precipitated early, above ~400ºC and in stability with K-silicate alteration. In our preferred model, the late and lower temperature silica saturated fluid that produced the dark-CL quartz in microfractures also produced the pyrite-muscovite-quartz D veins and sericitic halos that cross-cuts all the earlier K-silicate stable veins/halos. Microfractures in earlier low- and high-grade Cu quartz veins are, thus, created after volume reduction upon cooling of the quartz in the vein. The contact between sulfides and quartz grains are pre-existing discontinuities that provide a breaking surface during the volume contraction, facilitating the creation of open space. This mechanism can explain why late and low temperature dark-CL quartz is commonly observed in contact with earlier and higher temperature Cu-sulfides in the Cu-ore-forming veins.

Chapter 5 describes new investigations into the timescales of porphyry formation. Titanium and δ^{18}O diffusion timescales reveal a maximum magmatic-hydrothermal lifespan of ~170,000 years for cooling from ~650 ºC to ~ 350 ºC, whereas the bulk of the high-grade Cu-Mo ores formed relatively rapidly in ≤30,000 years. The ascent of hot magmatic-hydrothermal fluids heated the surrounding wall rock to produce a locally steepened geothermal gradient. During the formation of DQ veins, aplites, and Cu-bearing EDM veins, the temperature decreased from ~650 ºC to ~500 ºC. A thermal reversal heating to ~650ºC produced steeper geothermal gradients and precipitated the molybdenum-ore hosted in BMQ veins. This was followed by cooling to ~550°C during a second stage of copper and molybdenum ore formation in B veins in a period of ≤50,000 years. At a later and lower temperature stage, the δ^{18}O of preexisting quartz was partially re-equilibrated in ≤10,000 years at ~ 450ºC. Further cooling to ~350ºC took place during sericitic alteration and possibly during a post-hydrothermal stage took ≤75,000 years. The general and progressive temperature decline after the formation of the copper and molybdenum ores is inferred to result from deepening of the porphyry magma source as the magma chamber crystallized downward beneath the porphyry deposit. Both this effect and reduced magmatic-hydrothermal fluid flux during the formation of late D vein and sericitic alteration decreased the local geothermal gradient.

Chapter 6 presents the study of the pressure and temperature evolution of the Haquira East porphyry copper deposit based on Ti-in-quartz, Ti-in-zircon and Ti-in-biotite geothermometry, hornblende barometry, fluid inclusion data and δ^{34}S compositions of sulfide-sulfate pairs. The temperature estimation results are also used in chapters 4 and 5. Based on comparison with EDM-bearing porphyry copper deposits elsewhere, hornblende barometry and fluid inclusion assemblages the depth of emplacement of Haquira East was estimated at ~10 km. During the magmatic-hydrothermal up-flow at Haquira East, the fluid remained as one liquid phase during the different fluid releases that produced the K-silicate alteration, the copper and molybdenum ores and the later sericitic alteration and pyrite-sericite-quartz D veins. During each magmatic-hydrothermal fluid release and porphyry dike emplacement, the system depressurized from a lithostatic pressure estimated at ~3kb to close to lithostatic pressures of ~1.2 kb. In contrast, preliminarily data of the shallowly emplaced Batu Hijau deposit of Indonesia indicate that the magmatic-hydrothermal fluid was released and depressurized at much lower estimated pressures (<1.4 kb), resulting in the un-mixing of the fluid into immiscible phases of vapor and brine. These two contrasting depressurization trajectories and the implied consequences for the magmatic hydrothermal fluid could be important in elucidating the observed differences between deep and shallow porphyry deposit globally.

In chapter 7, two new calibrations of a portable-XRF (pXRF) are presented and tested. When calibrated using influence coefficient calibrations for compositions similar to the unknowns, pXRF analysis on samples of a similar matrix can be reliably used to accurately measure a selected set of elements over a wide range of compositions. The pXRF calibrated with this method is capable of confidently measuring the high field strength elements Ti, Zr, Y and Nb, together with Al, Ca, K, Mn, Ca, Fe and Sr and reproduced commercially available bench top WD-XRF at a maximum of ~3-4 standard deviations. Alumina, however, is better reproduced in rhyolites than in basalts. Silica compositions are only partially reproducible in rhyolites, and with low accuracy at more than 4 standard deviations. In basalts, however, silica yield spuriously but uniformly low concentrations. Transition metals Cr, Cu and Ni can confidently be reproduced in basalts, as well as Pb (> 12 ppm), Zn and the alkali metal Rb in rhyolites.

Relatively immobile elements (*e.g.* Nb, Zr, Ti and Y), which are often resistant to hydrothermal alteration and weathering, are measured with high accuracy and precision, enabling the use of pXRFs for lithogeochemistry in hydrothermally altered rock such as the ones commonly found in porphyry copper deposits.

BIBLIOGRAPHY

Abbey, S., 1983, Studies in "standard samples" of silicate rocks and minerals 1969–1982: Canadian Geological Survey Paper 83–15, p. 114.

Antares, 2010, Antares press–release: New Haquira global resource, February 26th, 2010, 6 p.

Atkinson, W.W., Souviron, A., Vehrs, T.I., and Faunes G.A., 1996, Geology and mineral zoning of the Los Pelamberes porphyry copper deposit, Chile: Society of Economic Geologists Special Publication, v. 5, p. 131–156.

Ayusso, R.A., 2010, Trace element geochemistry, *in* porphyry copper model: Scientific Investigation Report 2010–5070–B. U.S. Department of the Interior U.S. Geological Survey.

Bakker, R.J., 1997, Clathrates: Computer programs to calculate fluid inclusion V–X properties using clathrate melting temperatures: Computers and Geosciences, v. 23, p. 1–18.

Ballard, J.R., Palin, J.M., and Campbell, I.H., 2002, Relative oxidation states of magmas inferred from $Ce^{(IV)/}Ce^{(III)}$ in zircon: Application to porphyry copper deposits of northern Chile: Contributions to Mineralogy and Petrology, v. 144, p. 347–364.

Barth, A.P., and Wooden, J.L., 2010, Coupled elemental and isotopic analyses of polygenetic zircons from granitic rocks by ion microprobe, with implications for melt evolution and the source of granitic magmas: Chemical Geology, v. 277, p. 149–159.

Black, L.P., Kamo, S.L., Allen, C.M., Davis, D.W., Aleinikoff, J.N., Valley, J.W., Mundil, R., Campbell, I.H., Korsch, R.J., Williams, I.S., Foudoulis, C., 2004, Improved $^{206}Pb/^{238}U$ microprobe geochronology by the monitoring of a trace–element–related matrix effect; SHRIMP, ID–TIMS, ELA–ICP–MS and oxygen isotope documentation for a series of zircon standards: Chemical Geololgy, v. 205, p. 115–140.

Bodnar, R.J., and Sterner, S.M., 1987, Synthetic fluid inclusions *in* Hydrothermal Experimental Techniques, Ulmer, G.C., and Barnes, H.L., eds., Wiley–Interscience, New York. p. 423–457.

Boschmann, D., 2012, Structural and volcanic evolution of the Glass Buttes area, high lava plains, Oregon [Unpublished Masters Thesis]: Oregon State University, 100 p.

Brimhall, G.H.J., 1977, Early fracture–controlled disseminated mineralization at Butte, Montana: Economic Geology, v. 72, p. 37–59.

Burnham, A.D., and Berry, A.J., 2012, An experimental study of trace element partitioning between zircon and melt as a function of oxygen fugacity: Geochimica et Cosmochimica, Acta, v. 95, p. 196–212.

Burnham, C.W., 1979, Magmas and hydrothermal fluids, *in* Barnes, H.L., ed., Geochemistry of hydrothermal ore deposits, v. II, New York, Wiley Interscience, p. 71–136.

Burnham, C.W., 1979, The importance of volatile constituents, *in* Yoder, H.S. Jr., ed., The evolution of the igneous rocks: Fiftieth anniversary perspectives, Princeton University Press, Princeton, N. J., p. 439–482.

Camus, F., 2003, Geología de las sistemas porfíricos en los Andes de Chile: Santiago de Chile, Servicio Nacional de Geología y Minera, 267 p.

Candela, P.A. and Holland, H.D, 1984, The partitioning of copper and molybdenum between silicate melts and aqueous fluids: Geochimica et Cosmochimica Acta, v. 48, p. 373–388.

Carlotto, V., 1998, Evolution andine et raccourcissement au niveau de Cusco (13º–16º), Pérou: Enregistrement sédimentaire, chronologie, contrôles paléogeógraphiques, évolution cinématique [Unpublished Ph.D. thesis]: Grenoble, France, Université Joseph Fourier, 203 p.

Carr, J.C., Beatson, R.K., Cherrie, J.B., Mitchell, T.J., Fright, W.R., McCallum, B.C. and Evans, T.R., 2001, Reconstruction and representation of 3D objects with radial basis functions, ACM SIGGRAPH 2001, August 12–17, 2001, Los Angeles, CA, USA.

Castillo, P.R., Janney, P.E., and Solidum, R.U., 1999, Petrology and geochemistry of Camiguin Island, southern Philippines: Insights to the source of adakites and other lavas in a complex arc setting: Contributions to Mineralogy and Petrology, v. 134, p. 33–51.

Cathles, L.M., and Shannon, R., 2007, How potassium silicate alteration suggests the formation of porphyry ore deposits begins with the nearly explosive but barren expulsion of large volumes of magmatic water: Earth and Planetary Science Letters, v. 262, no. 1–2, p. 92–108.

Cernuschi, F., Dilles, J. H., and Creaser, R., 2013, Hydrothermal alteration, SWIR–mineral mapping, vein distribution and age of the Haquira–East Cu–Mo porphyry: 12th SGA Biennial Meeting 2013, Proceedings, v. 2, p. 782–785.

Cernuschi, F., Dilles, J.H., Kent, A.J.R., Schroer, G., Raab, A.K., Conti, B., and Muzio, R., 2015, Geology, geochemistry and geochronology of the Cretaceous Lascano East intrusive complex and magmatic evolution of the Laguna Merín basin, Uruguay: Gondwana Research, v. 28, no. 2, p. 837–857, doi:10.1016/j.gr.2014.07.007

Cernuschi, F., Einaudi, M.T, Dilles, J.H., Heather, K.B., and Barr, N. C., 2012, Hydrothermal veins, porphyry geochemistry and mineralization zonation of the Haquira–East Porphyry Cu–Mo Deposit, Perú: SEG Conference 2012, Lima, Peru.

Chelle–Michou, C., Chiaradia, M., Ovtcharova, M., Ulianov, A., and Wotzlaw, J.F., 2014, Zircon petrochronology reveals the temporal link between porphyry systems and the magmatic evolution of their hidden plutonic roots (the Eocene Coroccohuayco Deposit, Peru): Lithos v. 198–199, no. 0, p. 129–40.

Cherniak, D., Watson, E., and Wark, D., 2007, Ti diffusion in quartz: Chemical Geology, v. 236, no. 1–2, p. 65–74.

Chiaradia, M., 2009, Adakite–like magmas from fractional crystallization and melting–assimilation of mafic lower crust (Eocene Macuchi arc, Western Cordillera, Ecuador): Chemical Geology, v. 265, p. 468–487.

Chiles, J.P. and Delfiner, P., 1999, Geostatistics: Modelling Spatial Uncertainty, Wiley Series in Probability and Statistics, Wiley, New York, 696 p.

Clark, R.N., Swayze, G.A., Wise, R., Livo, E., Hoefen, T., Kokaly, Sutley, S.J., 2007, USGS digital spectral library splib06a: US Geological Survey, Digital Data Series, Vol. 231, (http://speclab.cr.usgs.gov/).

Clement, S.W.J., and Compston, W., 1994, Ion probe parameters for very high resolution without loss of sensitivity: U.S. Geological Survey Circular, no. 1107, 62 p.

Conrey, R.M., Wolff, J. A., Seyfarth, A., Vanhoose, A., Goodman Elgar, A., Betterncourt, N., Boschmann, D., and Werling, K., 2012, Portable XRF calibration using influence coefficients: 8th International conference on the analysis of geological and environmental materials, 67: Buzios, Rio de Janeiro, Brazil.

Costa F., Scaillet, B., and Pichavant, M., 2004, Petrological and experimental constraints on the pre–eruption conditions of Holocene dacite from Volcan San Pedro (36_S, Chilean Andes) and the importance of sulphur in silicic subduction–related magmas: Journal of Petrology, v. 45, p. 855–881.

Costa, J.P., Pronzato, I. and Thierry, E., 1999, A comparison between krigin and radial basis functions networks for non–linear prediction, Proceedings IEEE–EURASIP Workshop on nonlinear signal and image processing, Bogazici, University Printhouse.

Cowan, E.J., Beastson, R.K., Ross, H.J., Fright, W.R., McLennan, T.J., Evans, T.R., Carr, J.C., Lane, R.G., Bright, D.V., Gillman, A.J., Oshurst, P.A., and Titley, M., 2003, Practical implicit geological modeling, *in* Proceedings Fifth International Mining Geology Conference: The Australasian Institute of Mining and Metallurgy, Melbourne.

Cox, S., 2005, Coupling between deformation, fluid pressures and fluid flow in ore–producing hydrothermal environments: Economic Geology 100th Anniversary Volume, p. 39–75.

Crank, J., 1975, The mathematics of diffusion (2nd ed.): Oxford, Clarendon Press, 414 p.

DeBari, S.M., and Sleep, N.H., 1991, High–Mg, low–Al bulk composition of the Talkeetna island arc, Alaska: Implications for primary magmas and the nature of arc crust: Geological Society of America, Bulletin, v. 103, p. 37–47.

Dennis, P.F., 1984, Oxygen self–diffusion in quartz under hydrothermal conditions: Journal of Geophysical Research, v. 89, no. B6, p. 4047–4057.

Dilles, J.H. and Einaudi, M.T., 1992, Wall–rock Alteration and Hydrothermal Flow Paths about the Ann–Mason Porphyry Copper Deposit, Nevada, A 6 km Vertical Reconstruction: Economic Geology, v. 87, p. 1963–2001.

Dilles, J.H., 1984, The petrology and geochemistry of the Yerington batholith and the Ann–Mason porphyry copper deposit, Western Nevada: [Unpublished Ph.D. dissertation], Stanford, Stanford University, 389 p.

Dilles, J.H., 1987, Petrology of the Yerington batholith, Nevada: Evidence for evolution of porphyry copper ore fluids: Economic Geology, v. 82, p.1750–1789.

Dilles, J.H., 1987, Petrology of the Yerington batholith, Nevada: Evidence for evolution of porphyry copper ore fluids: Economic Geology, v. 82, p. 1750–1789.

Dilles, J.H., 1987, Petrology of the Yerington batholith, Nevada: Evidence for evolution of porphyry copper ore fluids: Economic Geology, v. 82, p. 1750–1789.

Dilles, J.H., Kent, A.J.R., Wooden, J.L., Tosdal, R.M., Koleszar, A., Lee, R.G., and Farmer, L.P., 2015, Zircon compositional evidence for sulfur–degassing from ore–forming arc magmas: Economic Geology, v. 110, no. 1, p. 241–51, doi:10.2113/econgeo.110.1.241.

Duan, Z., Moller, N., and Weare, J.H., 1992a, and equation of state for the CH4–CO2–H2O system: I. Pure systems from 0 to 1000°C and 0 to 8000 bars: Geochimica et Cosmochimica Acta, v. 56, p. 2605–2617.

.

Dumitru, T.A., Ernst, W.G., Wright, J.E., Wooden, J.L., Wells, R.E., Farmer, L.P., Kent, A.J.R., and Graham, S.A., 2013, Eocene extension in Idaho generated massive sediment floods into the Franciscan Trench and into the Tyee, Great Valley, and Green River Basins: Geology, v. 41, no. 2, p. 187–190.

Einaudi, M.T., 2008, Distribution of vein types, alteration, sulfides, and metal grades. Haquira Cu–Mo–Au deposit, departamento de Apureímac, Perú: Unpublished Report for Antares Minerals Inc. (September): 47 p.

Field, C.W., Zhang, L., Dilles, J.H., Rye, R.O., and Reed, M.H., 2005, Sulfur and oxygen isotopic record in sulfate and sulfide minerals of early, deep, pre–main stage porphyry Cu–Mo and late main stage base–metal mineral deposits, Butte district, Montana: Chemical Geology, v. 215 no.1–4, 61–93.

Flanagan, F.J., 1976, Descriptions and Analyses of Eight New USGS Rock Standards: U.S.: Geological Survey Professional Paper 840, 192 p.

Foley, S.F., and Wheller, G.E., 1990, Parallels in the origin of the geochemical signatures of island arc volcanics and continental potassic igneous rocks: The role of residual titanites: Chemical Geology, v. 85, p. 1–18.

Gans, P., 2009, Geology of the Haquira copper deposit: New information and iynthesis: Internal report for Antares Minerals, 9 p.

Garwin, S., 2002, The Geologic Setting of Intrusion–Related Hydrothermal Systems near the Batu Hijau Porphyry Copper–Gold Deposit, Sumbawa, Indonesia: Society of Economic Geologists Special Publication, v. 9, p. 333–366.

Geiger, S., Haggerty, R., Dilles, J. H., Reed, M.H., and Matthäi, S.F., 2002, The evolution of the early hydrothermal alteration at Butte, Montana: New insights from reactive transport modeling: Geofluids, v. 2, p. 185–201.

Geissman, J., Van Der Voo, R., Kelly, W., and Brimhall, Jr., G., 1980, Paleomagnetism, rock magnetism, and aspects of structural deformation of the Butte mining district, Butte, Montana: Journal of Geology, v. 88, p. 129–159.

Germ, 2014, Geochemical earth reference model. Partition coefficient database: http://earthref.org/KDD/

Gladney, E.S., and Roelandts, I., 1988, Compilation of elemental concentration data for USGS BHVO–1, MAG–1, QLO–1, RGM–1, SCo–1, SDC–1, SGR–1, and STM–1: Geostandards Newsletter, v. 12, p. 253–362.

Goetz, A.F.H., Curtiss, B., and Shiley, D.A., 2009, Rapid gangue mineral concentration measurement over conveyors by NIR reflectance spectroscopy, Minerals Engineering, Vol. 22. p. 490 – 499.

Goodale, N., Bailey, D.G., Jones, G.T., Prescott, C., Scholz, E., Stagliano, E., and Lewis, C., 2011, pXRF: a study of inter–instrument performance: Journal of Archaeological Science.

Govindaraju, K., 1994, Compilation of working values and descriptions for 383 geostandards: Geostandards Newsletter, v. 18, p. 1–158.

Grocke, S.B., 2014, Magma dynamics and evolution in continental arcs: Insights from the Central Andes [Unpublished PhD thesis]: Oregon State University, 303 p.

Gustafson, L.B., and Hunt, J.P., 1975, The porphyry copper deposit at El Salvador, Chile: Economic Geology and the Bulletin of the Society of Economic Geologists, v. 70, no. 5, p. 857–912

Halley, S., Dilles, J.H. and Tosdal, R.M., 2015, Footprints: Hydrothermal alteration and geochemical dispersion around porphyry copper deposits: Economic Geology Newsletter, v. 100, no. 1, p. 12–17.

Hamilton, W.B., 1981, Crustal evolution by arc magmatism. Philosophical Transactions: Royal Society of London, v. 301, p. 279–291.

Heather, K.B., Black, J.E., Gamarra, H., Einaudi, M., Barr, N.C. and Robeto, J., 2012, Discovery and development of the Haquira Cu–Mo–Au porphyry deposit, Peru: A super giant in the making? SEG Orange NSW talk, presentation, 27–06–2012.

Hildreth, W., and Moorbath, S., 1988, Crustal Contributions to Arc Magmatism in the Andes of Central Chile: Contributions to Mineralogy and Petrology, v. 98, n. 4, p. 455–489.

Holtz, F., Becker, A., Freise, M., and Johannes, W., 2001, The water–undersaturated and dry Qz–Ab–Or system revisited. Experimental results at very low water activities and geological implications: Contributions to Mineralogy and Petrology, v. 141, p. 347−357.

Houston, R.A., and Dilles, J.H., 2013, Structural geologic evolution of the Butte district, Montana: Economic Geology, v. 108, no. 6, p. 1397–1424, doi:10.2113/econgeo.108.6.1397.

Huang, R., and Audétat, A., 2012, The titanium–in–quartz (TitaniQ) thermobarometer: A critical examination and re–calibration: Geochimica et Cosmochimica Acta, v. 84, p. 75–89.

INGEMMET, 2001, Geologic maps from the instituto geoloógico, minero y metalúrgico del Perú, digital edition. Including: Mapa geológico del cuadrángulo Santo Tomás, hojas 29r–I, 29r–II, 29r–III, 29r–IV, escala 1:50.000, Mapa geológico del cuadrángulo Livitaca, hoja 29–s, escala 1:100.0000.

Ireland, T., 2010, Geological framework of the mineral deposits of the Collahuasi district, Región de Tarapacá, Chile [unpublished PhD Thesis]: University of Tasmania, 412 pp.

Ireland, T.R., and Williams, I.S., 2003, Considerations in zircon geochronology by SIMS, Reviews in Mineralogy and Geochemistry, v. 53, p. 215–241, Hanchar, J.M., and Hoskin, W.O., editors.

Johnson, D.M., Hooper, P.R., and Conrey, R.M., 1999, XRF Analysis of rocks and minerals for major and trace elements on a single low dilution Li–tetraborate fused bead: Advances in X–ray Analysis, v. 41, no. 843–867.

Jones, B., Kamenetsky, V.S., Davidson, P., and Allen, C.M., 2007, Antapaccay porphyry Cu–Au deposit: A product of Andean tectonism and evolving magmatism, late Eocene–early Oligocene Abancay batholith, Altiplano, southern Peru, *in* Ores and orogenesis: A symposium honoring the career of William R. Dickinson: Tucson, Arizona, Arizona Geological Society, p. 132–133.

Kent, A.J.R., Jacobsen, B., Peate, D.W., Waight, T.E., and Baker, J.A., 2004, Isotope dilution MC–ICP–MS rare earth element analysis of geochemical reference materials NIST SRM 610, NIST SRM 612, NIST SRM 614, BHVO–2G, BHVO–2, BCR–2G, JB–2, WS–1, W–2, AGV–1, AGV–2: Geostandards Newsletter, v. 28, no. 3, p. 417–430.

Klein, M., Stosch, H.G., and Seck, H.A., 1997, Partitioning of high field strength and rare–earth elements between amphibole and quartz–dioritic to tonalitic melts: An experimental study: Chemical Geology, v. 138, p. 257–271.

Klinck, B.A., Ellison, R.A., and Hawkins, M.P., 1986, The geology of the Cordillera Occidental and Altiplano west of Lake Titicaca, southern Peru: Lima, British Geological Survey, Instituto Geológico Minero y Metalúrgico, 353 p.

Koppers, A., and Duncan, B., 2003, High–resolution 40Ar/39Ar dating of the oldest oceanic basement basalts in the western Pacific basin: Geochemistry, Geophysics, Geosystems v. 4, no. 11, p. 1–20.

Landtwing, M.R., Furrer, C., Redmond, P.B., Pettke, T., Guillong, M., and Heinrich, C.A., 2010, The Bingham Canyon Porphyry Cu–Mo–Au Deposit. III. Zoned copper–gold ore deposition by magmatic vapor expansion: Economic Geology, v. 105, no. 1, p. 91–118.

Landtwing, M.R., Pettke, T., Halter, W.E., Heinrich, C.A., Redmond, P.B., Einaudi, M.T., and Kunze, K., 2005, Copper deposition during quartz dissolution by cooling magmatic–hydrothermal fluids: The Bingham porphyry: Earth and Planetary Science Letters, v. 235 no. 1, 229–243.

Le Maitre, R.W., Bateman, P., Dudek, A., Keller, J., Lameyre, J., Le Bas, M.J., Sabine, P.A., Schmid, R., Sorensen, H., Streckeisen, A., Woolley, A.R., and Zanettin, B., 1989, A classification of igneous rocks and glossary of terms: Recommendations of the international union of geological sciences subcommission on the systematics of igneous rocks, Blackwell Scientific, Oxford.

Lee, R.G., 2008, Genesis of the El Salvador porphyry copper deposit, Chile and distribution of epithermal alteration at Lassen Peak, California [unpublished Ph.D. thesis]: Corvallis, OR, Oregon State University, 322 p.

Ligarda, R., 1989, Estudio geológico del cuadrángulo de Curahuasi (Departamento deApurimac) [Bachelor thesis]: Cusco, Universidad Nacional San Antonio Abad.

Loewen, M.W., and Kent, A.J., 2012, Sources of elemental fractionation and uncertainty during the analysis of semi–volatile metals in silicate glasses using LA–ICP–MS: Journal of Analytical and Atomic Spectrometry, v. 27, p. 1502–1508

Loucks, R.R., 2014, Distinctive Composition of Copper–Ore–Forming Arcmagmas: Australian Journal of Earth Sciences, v. 61, no, 1, p 5–16.

Ludwig, K.R., 2009, Squid 2, A user's manual, Berkeley Geochronology Center Special, Publication No. 5, 110 p.

Ludwig, K.R., 2012, Isoplot 3.75, a geochronological toolkit for Excel, Berkeley Geochronology Center Special Publication No. 5, 75 p.

Maher, K.C., 2010, Skarn alteration and mineralization at Coroccohuayco, Tintaya district, Peru: Economic Geology, v. 105, p. 263–283.

Mamani, M., Wörner, G., and Sempere, T., 2010, Geochemical variations in igneous rocks of the Central Andean orocline (13ºS to 18ºS): Tracing crustal thickening and magma generation through time and space: Geological Society of America Bulletin, v. 122, p. 162–182.

Markey, R.J., Stein, H.J., and Morgan, J.W., 1998, Highly precise Re–Os dating for molybdenite using alkaline fusion and NTIMS, Talanta, v. 45, p. 935–946.

Markey, R.J., Stein, H.J., Hannah, J.L., Selby, D., and Creaser, R.A., 2007, Standardizing Re–Os geochronology: A new molybdenite Reference Material (Henderson, USA) and the stoichiometry of Os salts: Chemical Geology, v. 244, p. 74–87.

Maydagán, L., Franchini, M., Rusk, B., Lentz, D. R., McFarlane, C., Impiccini, A., and Rey, R., 2015, Porphyry to epithermal transition in the Altar Cu–(Au–Mo) Deposit, Argentina, studied by cathodoluminescence, LA–ICP–MS, and fluid Inclusion analysis: Economic Geology, v. 110, no. 4, 889–923.

Mclean, W.H., and Barrett, T.J., 1993, Lithogeochemical techniques using immobile elements: Journal of Geochemical Exploration, v. 48, p. 109–133.

Mercer, C.N., Reed, M.H., and Mercer, C.M., 2015, Time scales of porphyry Cu deposit formation: Insights from titanium diffusion in quartz: Economic Geology, v. 110, no. 3, p. 587–602.

Meunier, A. and Velde, B., 2004, Illite, Origins, evolution and metamorphism, Springer, 281 p.

Meyer, C., 1965, An early potassic type of wall–rock alteration at Butte, Montana, American Mineralogist, v. 50, no. 10, p.1717–1723.

Mondillo, N., Boni, M., Balassone, G., and Villa, I.M., 2014, The Yanque prospect (Peru): From polymetallic Zn–Pb mineralization to a nonsulfide deposit: Economic Geology, v. 109, p. 1735–1762.

Moore, G.M., and Carmichael, I.S.E., 1998, The hydrous phase equilibria (to 3 kbar) of an andesite and basaltic andesite from western Mexico: Constraints on water content and conditions of phenocryst growth: Contributions to Mineralogy and Petrology, v. 130, p. 304–319.

Müller, A., Herrington, R., Armstrong, R., Seltman, R., Kirwin, D., Stenina, N. and Kronz, A., 2010, Trace elements and cathodoluminescence of quartz in stockwork veins of Mongolian porphyry–style deposits: Mineralium Deposita, v. 45, p. 707–727.

Naney, M.T., 1977, Phase Equilibria and Crystallization in Iron and Magnesium–bearing Granitic Systems [Unpublished Ph.D. thesis]: Stanford University.

Noble, D.C., McKee, E.H., Eyzaguirre, V.R., and Marocco, R., 1984, Age and regional tectonic and metallogenetic implications of igneous activity and mineralization in the Andahuaylas–Yauri belt of southern Peru: Economic Geology, v. 79, p. 172–176.

Oncken, O., Hindle, D., Kley, J., Elger, K., Victor, P., and Schemmann, K., 2006, Deformation of the Central Andean Upper Plate system—Facts, Fiction, and Constraints for Plateau Models: The Andes, p. 3–27.

Pecho, V., 1981, Geología de los cuadrángulos de Chalhuanca, Antabamba y Santo Tomás: Instituto de Geología, Minería y Metalurgia, Boletín n. 35, p. 67

Perelló, J. and Posso, C., 2011, Antilla: a supergene enriched porphyry copper deposit in the Andahuaylas–Yauri belt: ^{11}th SGA Biennial Metting, 26th–29th September 2011, Antofagasta, Chile, p. 917–920.

Perello, J., Carlotto, V., Zarate, A., Ramos, P., Posso, H., Neyra, C., Caballero, A., Fuster, N. and Muhr, R., 2003, Porphyry–style alteration and mineralization of the m Eocene to early Oligocene Andahuaylas–Yauri belt, Cuzco Region, Peru: Economic Geology v. 98, no. 8, p. 1575.

Perelló, J., Carlotto, V., Zarate, A., Ramos, P., Posso, H., Neyra, C., Caballero, A., Fuster, N., and Muhr, R., 2003, Porphyry–style alteration and mineralization of the middle Eocene to early Oligocene Andahuaylas–Yauri Belt: Economic Geology, v. 98, no. 8, p. 1575–1605.

Pirrie, D., Butcher, A.R., Power, M.R., Gottlieb, P., Miller, G.L., 2004, Rapid quantitative mineral and phase analysis using automated scanning electron microscopy (QEMSCAN); Potential applications in forensic geoscience, *in* Geological Society, London, Special Publication 232, 123–136 p.

Proffett, J.M., 1979, Ore deposits of the western United States, A summary: Nevada Bureau of Mines and Geology, Report 33, p. 13–32.

Proffett, J.M., 2009, High Cu grades in porphyry Cu deposits and their relationship to emplacement depth of magmatic sources: Geology, v. 37, no. 8, 675–678, doi:10.1130/G30072A.1

Proffett, J.M., 2009, High Cu grades in porphyry Cu deposits and their relationship to emplacement depth of magmatic sources. Geology, v. 37, no. 8, p. 675–678, doi:10.1130/G30072A.1

Redmond, P.B., and Einaudi, M.Y., 2010, The Bingham Canyon Porphyry Cu–Mo–Au Deposit. I. Sequence of Intrusions, Vein Formation, and Sulfide Deposition: Economic Geology, v. 105, no. 1, p. 43.

Redmond, P.B., Einaudi, M.T., Inan, E.E., Landtwing, M.R., and Heinrich, C.A., 2004, Copper deposition by fluid cooling in intrusion–centered systems: New insights from the Bingham porphyry ore deposit, Utah: Geology, v. 32, no. 3, p. 217–220.

Reed, M., Rusk, B., and Palandri, J., 2013, The Butte magmatic–hydrothermal system: One fluid yields all alteration and veins: Economic Geology, v. 108, p. 1379–1396.

Reed, M.H., 1999, Zoning of metals and early potassic and sericitic hydrothermal alteration in the Butte, Montana, porphyry Cu–Mo deposit [abs.]: Geological Society of America Abstracts with Programs, v. 31, no. 7, p. A381.

Richards, J.P., 2011, High Sr./Y Arc magmas and porphyry Cu ±Mo ±Au deposits: Just add water: Economic Geology, v. 106, no. 7, p. 1075–1081.

Richards, J.P., Spell, T., Rameh, E., Razique, A., and Fletcher, T., 2012, High Sr/Y magmas reflect arc maturity, high magmatic water content, and porphyry Cu ± Mo ± Au potential: Examples from the Tethyan arcs of central and eastern Iran and western Pakistan: Economic Geology, v. 107, p. 295–332.

Rollinson, H.R., 1993, Using geochemical data: Evaluation, presentation, interpretation. J. Wiley & Sons, New, 352 pp.

Romick, J.D., Kay, S.M., and Kay, R.W., 1992, The influence of amphibole fractionation on the evolution of calc–alkaline andesite and dacite tephra from the central Aleutians, Alaska: Contributions to Mineralogy and Petrology, v. 112, p. 101–118.

Rooney, T.O., Franceschi, P., and Hall, C.M., 2011, Water–saturated magmas in the Panama Canal region: A precursor to adakite–like magma generation?: Contributions to Mineralogy and Petrology, v. 161, p. 373–388.

Rusk, B., 2012, Cathodoluminescent Textures and Trace Elements in Hydrothermal Quartz, *in* Götze, J. and Möckel, R., eds., Quartz: Deposits, Mineralogy and Analytics, Berlin, Springer, p. 307–329.

Rusk, B., and Reed, M., 2002, Scanning electron microscope–cathodoluminescence analysis of quartz reveals complex growth histories in veins from the Butte porphyry copper deposit, Montana: Geology, v. 30, no. 8, p. 727–730.

Rusk, B.G., Lowers, H.A., and Reed, M.H., 2008, Trace elements in hydrothermal quartz: Relationships to cathodoluminescent textures and insights into vein formation: Geology, v. 36, no. 7, p. 547.

Rusk, B.G., Reed, M.H. and Dilles, J.H., 2008, Fluid inclusion evidence for magmatic–hydrothermal fluid evolution in the porphyry copper–molybdenum deposit at Butte, Montana: Economic Geology, v. 103, no. 2, p. 307.

Seedorff, E., and Einaudi, M.T., 2004, Henderson porphyry molybdenum system, Colorado: I. Sequence and abundance of hydrothermal mineral assemblages, flow paths of evolving fluids, and evolutionary style: Economic Geology, v. 99, no. 1, 3–37.

Seedorff, E., Dilles, J.H., Proffett, J.M., Jr, Einaudi, M.T., Zurcher, L., Stavast, W.J.A., Johnson, D.A., and Barton, M.D., 2005, Porphyry deposits: Characteristics and origin of hypogene features, *in* Hedenquist, J. W., Thompson, J.F.H., Goldfarb, R. J., and Richards, J. P., eds.: Economic Geology 100th Anniversary Volume, p. 251–298.

Selby, D. and Creaser, R.A., 2004, Macroscale NTIMS and microscale LA–MC–ICP–MS Re–Os isotopic analysis of molybdenite: Testing spatial restrictions for reliable Re–Os age determinations, and implications for the decoupling of Re and Os within molybdenite: Geochimica et Cosmochimica, Acta, v. 68, p. 3897–3908.

Sillitoe, R.H., 1998, Major regional factors favoring large size, high hypogene grade, elevated gold content and supergene oxidation and enrichment of porphyry copper deposits, *in* Porter, T.M., ed., Porphyry and hydrothermal copper and gold deposits: A global perspective: Adelaide, Australian Mineral Foundation, p. 21−34.

Sillitoe, R.H., 2010, Porphyry Copper Systems: Economic Geology, v. 105, no. 1, p. 3–41.

Sillitoe, R.H., and Perelló, J., 2005, Andean copper province: Tectonomagmatic settings, deposit types, metallogeny, exploration, and discovery: Economic Geology 100TH Anniversary Volume, p. 845−890.

Sisson, T.W., 1994, Hornblende–melt trace–element partitioning measured by ion microprobe: Chemical Geology, v. 117, p. 331–344.

Skinner, B.J., 1966, Thermal expansion, in Clark, S.P., Jr., ed., Handbook of physical constants: Geological Society of America Memoir, v. 97, p. 75–96.

Sláma, J., Košler, J., Condon, D.J., Crowley, J.L., Gerdes, A., Hanchar, J.M., Horstwood, M.S.A., Morris, G.A., Nasdala, L., Norberg N., Schaltegger, U., Schoene, B., Tubrett, M.N., and Whitehouse, M.J., 2008, Plešovice zircon – a new natural reference material for U–Pb and Hf isotopic microanalysis: Chemical Geology, v. 249, no. 1–2, p. 1–35.

Spencer, E.T., Wilkinson, J.J., Creaser, R.A., and Seguel, J., 2015, The distribution and timing of molybdenite mineralization at the El Teniente Cu–Mo porphyry deposit, Chile: Economic Geology, v. 110, p. 387–421.

Stacey, J. and Kramers, J.D., 1975, Approximation of terrestrial lead isotope evolution by a two–stage model: Earth and Planetary Science Letters, v. 26, p. 207–221.

Stewart, M., de Lacey, J, Hodkiewicz, P.F., and Lane, R., 2014, Grade estimation from radial basis functions – how does it compare with conventional geostatistical estimation?, *in* Proceedings Ninth International Mining Geology Conference 2014 , The Australasian Institute of Mining and Metallurgy: Melbourne, p. 129–140.

Stolper E., 1982, Water in silicate glasses: An infrared spectroscopic technique, Contributions to Mineralogy and Petrology, v. 81, p. 1–17.

Streck, M.J., and Dilles, J.H., 1998, Sulfur Evolution of Oxidized Arc Magmas as Recorded in Apatite from a Porphyry Copper Batholith: Geology, v. 26, no. 6, p. 523.

Takada, A., 1994, The influence of regional stress and magmatic input on styles of monogenetic and polygenetic volcanism: Journal of Geophysical Research, v. 99, p. 563−573.

Taylor H.P., Jr., 1968, The oxygen isotope geochemistry of igneous rocks: Contributions to Mineral Petrology, v.19, p. 185–219.

Thomas, J.B., Watson, E.B., Spear, F.S., Shemella, P.T., Nayak, S.K., and Lanzirotti, A., 2010, TitaniQ under pressure; the effect of pressure and temperature on the solubility of Ti in quartz: Contributions to Mineralogy and Petrology, v. 160, no. 5, p. 743–759, doi:10.1007/s00410–010–0505–3

Thompson, A.J.B., Hauff, P., Robitaille, J.A., 1999, Alteration Mapping in Exploration: Application of Short–wave Infrared (SWIR) Spectroscopy, SEG Newsletter v. 39, p. 16–27.

Tosdal, R.M., and Richards, J.P., 2001, Magmatic and structural controls on the development of porphyry Cu ± Mo ± Au deposits: Reviews in Economic Geology, v. 14, p. 157−181.

Tosdal, R.M., Dilles, J.H., and Cooke, D.R., 2009, From Source to Sinks in Auriferous Magmatic–Hydrothermal Porphyry and Epithermal Deposits, Elements v. 5, p. 289–295, doi:10.2113/gselements.5.5.289.

Trail, D., Watson, E.B., and Tailby, N.D., 2011, The oxidation state of Hadean magmas and implications for early Earth's atmosphere: Nature, v. 480, p. 79−82.

Valley, J. W., 2001, Stable isotope thermometry at high temperatures, *in* Reviews in Mineralogy and Geochemistry, v. 43, no. 1, p. 365–413.

Von Quadt, A., Erni, M., Martinek, K., Moll, M., Peytcheva, I., and Heinrich, C.A., 2011, Zircon crystallization and the lifetimes of ore–forming magmatic–hydrothermal systems: Geology, v. 39, no. 8, p. 731–734.

Walker, B.A., Klemetti, E.W., Grunder, A.L., Dilles, J.H., Tepley, F.J., and Giles, D., 2013, Crystal reaming during the assembly, maturation, and waning of an eleven–million–year crustal magma cycle: thermobarometry of the Aucanquilcha Volcanic Cluster: Contributions to Mineralogy and Petrology, v. 165, no. 4, p. 663–682.

Walker, B.A., Klemetti, E.W., Grunder, A.L., Dilles, J.H., Tepley, F.J., and Giles, D., 2013, Crystal reaming during the assembly, maturation, and waning of an eleven–million–year crustal magma cycle: Thermobarometry of the Aucanquilcha Volcanic Cluster: Contributions to Mineralogy and Petrology, v. 165, no. 4, 663–682.

Wang, F., Liu, S–A; Li, S., and He, Y., 2013, Contrasting zircon Hf–O isotopes and trace elements between ore–bearing and ore–barren adakitic rocks in central–eastern China: Implications for genetic relation to Cu–Au mineralization: Lithos, v. 156−159, p. 97−111.

Wark, D.A., and Watson, E.B., 2006, TitaniQ: a titanium–in–quartz geothermometer: Contributions to Mineralogy and Petrology, v. 152, no. 6, 743–754, doi:10.1007/s00410–006–0132–1

Watson, E.B., and Harrison, T.M., 2005, Zircon thermometer reveals minimum melting conditions on earliest Earth: Science, v. 308, p. 841–844, doi:10.1126/science.1110873.

Weis, P., Driesner, T., and Heinrich, C.A., 2012, Porphyry–copper ore shells form at stable pressure–temperature fronts within dynamic fluid plumes: Science, v. 338, no. 6114, 1613–1616, doi:10.1126/science.1225009

Williams, I.S., 1998, U–Th–Pb geochronology by ion microprobe, *in* McKibben, M.A., Shanks III, W.C., Ridley, W.I., (Editors), Applications of microanalytical techniques to understanding mineralizing processes, Reviews in Economic Geology Special Publication 7: p. 1–35

Wilson, S.A., 1997, The collection, preparation, and testing of USGS reference material BCR–2, Columbia River, Basalt: U.S. Geological Survey Open–File Report 98.

Xstrata, 2014, Mineral resources and ore reserves as at 31 December 2014: Annual Report, 64 p. glencorexstrata.com.

Zhang L.G., Liu J.X., Zhou H.B. and Chen Z.S., 1989, Oxygen isotope fractionation in the quartz–water–salt system: Economic Geology, v. 89, p. 1643–1650.

Zhaoshan, C., and Yang, Z., 2012, Evaluation of Inter–instrument Variations Among Short Wavelength Infrared (SWIR) Devices: Economic Geology v. 107: p. 1479 – 1488.

Zwyer, T., 2010, Temporal and spatial evolution of hydrotheraml, ore–related fluids in the Batu Hiaju porphyry copper–gold deposit, Sumbawa (Indonesia) [Unpublished master Thesis]: ETH Zürich, Switzerland, p. 57.

APPENDICES

APPENDIX 1
Cross-section 1900NW

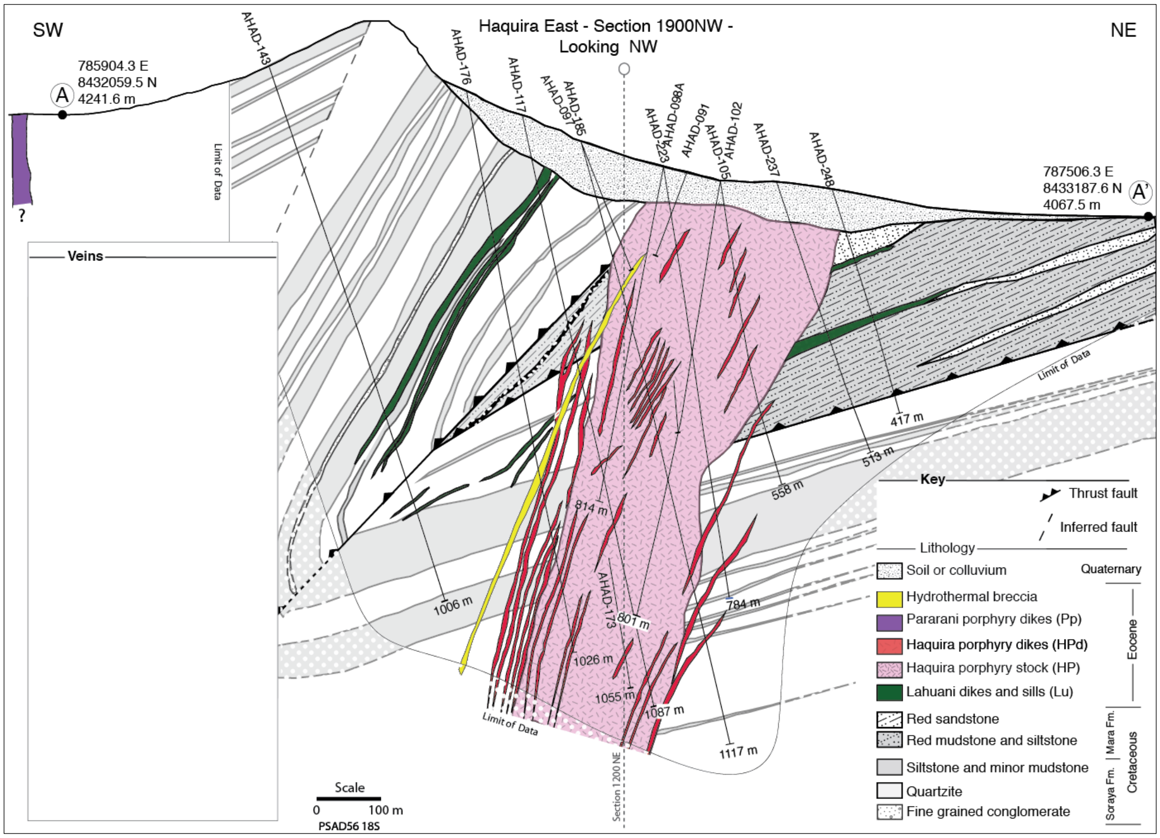
Haquira East - Section 1900NW -
Looking NW
SW
NE
785904.3 E
8432059.5 N
4241.6 m
A
787506.3 E
8433187.6 N
4067.5 m
A'
?
Limit of Data
Veins
AHAD-143
AHAD-176
AHAD-117
AHAD-097
AHAD-185
AHAD-223
AHAD-098A
AHAD-091
AHAD-105
AHAD-102
AHAD-237
AHAD-248
AHAD-173
417 m
513 m
558 m
784 m
801 m
814 m
1006 m
1026 m
1055 m
1087 m
1117 m
Limit of Data
Section 1200 NE
Scale
0
100 m
PSAD56 18S
Key
Thrust fault
Inferred fault
Lithology
Soil or colluvium
Quaternary
Hydrothermal breccia
Pararani porphyry dikes (Pp)
Haquira porphyry dikes (HPd)
Haquira porphyry stock (HP)
Lahuani dikes and sills (Lu)
Eocene
Red sandstone
Red mudstone and siltstone
Mara Fm.
Siltstone and minor mudstone
Quartzite
Fine grained conglomerate
Soraya Fm.
Cretaceous

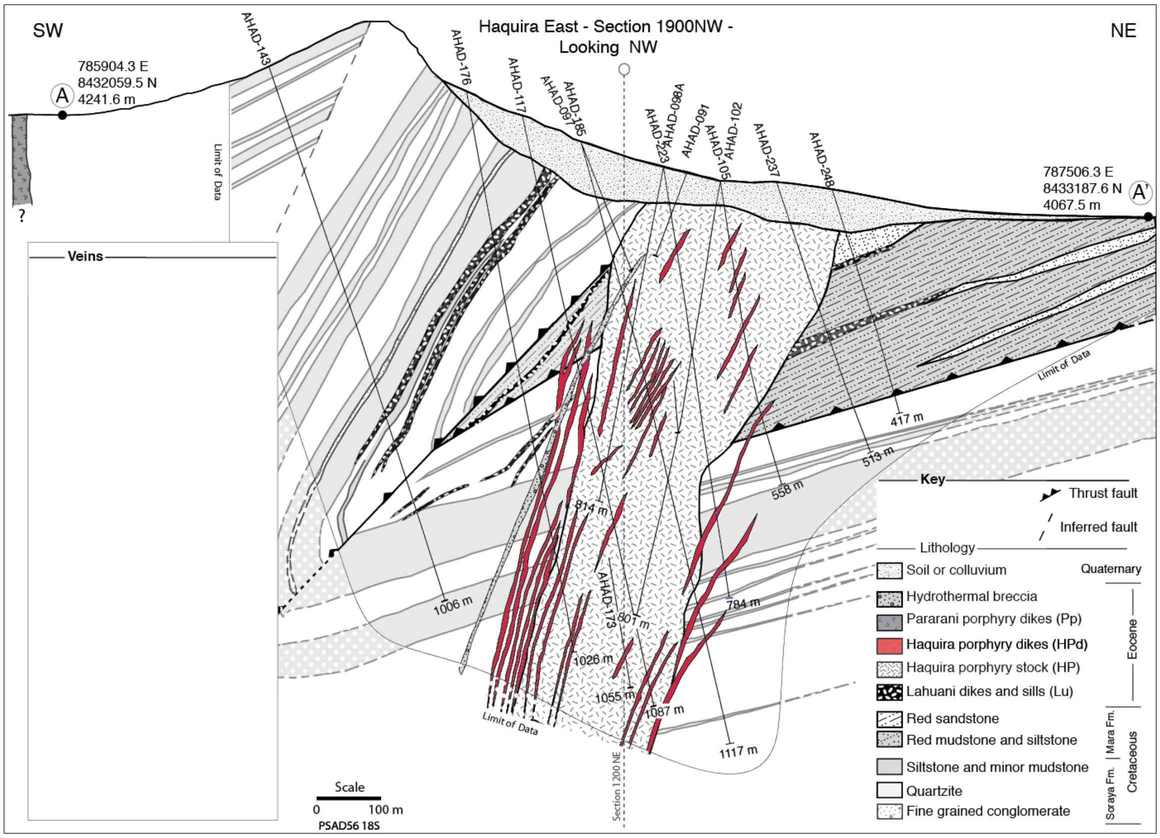
Haquira East - Section 1900NW -
Looking NW
SW
NE
785904.3 E
8432059.5 N
4241.6 m
A
787506.3 E
8433187.6 N
4067.5 m
A'
?
Limit of Data
Veins
AHAD-143
AHAD-176
AHAD-117
AHAD-097
AHAD-185
AHAD-223
AHAD-098A
AHAD-091
AHAD-105
AHAD-102
AHAD-237
AHAD-248
AHAD-173
417 m
513 m
558 m
784 m
801 m
814 m
1006 m
1026 m
1055 m
1087 m
1117 m
Limit of Data
Section 1200 NE
Scale
0
100 m
PSAD56 18S
Key
Thrust fault
Inferred fault
Lithology
Soil or colluvium
Quaternary
Hydrothermal breccia
Pararani porphyry dikes (Pp)
Haquira porphyry dikes (HPd)
Haquira porphyry stock (HP)
Lahuani dikes and sills (Lu)
Eocene
Red sandstone
Red mudstone and siltstone
Mara Fm.
Siltstone and minor mudstone
Quartzite
Fine grained conglomerate
Soraya Fm.
Cretaceous

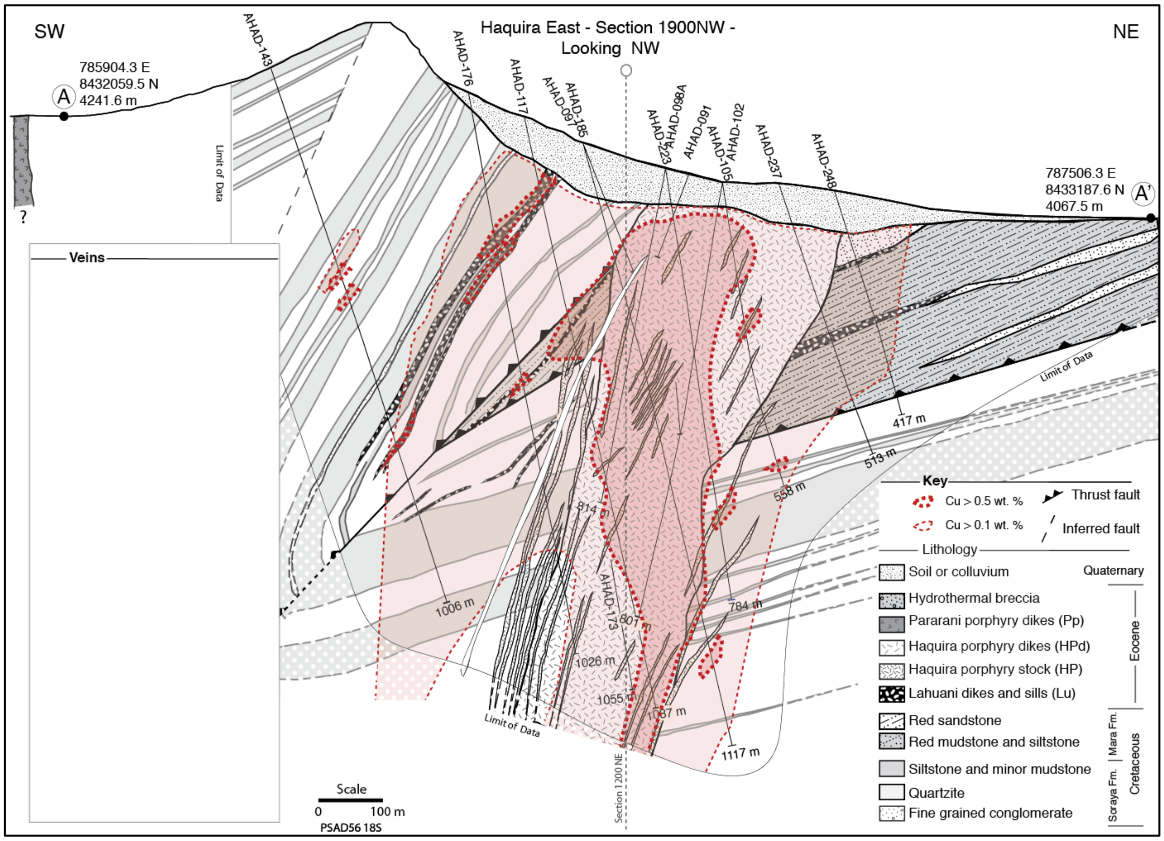
SW
Haquira East - Section 1900NW -
Looking NW
NE
785904.3 E
8432059.5 N
4241.6 m
A
787506.3 E
8433187.6 N
4067.5 m
A'
?
Limit of Data
Veins
AHAD-143
AHAD-176
AHAD-117
AHAD-097
AHAD-185
AHAD-223
AHAD-098A
AHAD-091
AHAD-105
AHAD-102
AHAD-237
AHAD-248
AHAD-173
417 m
513 m
558 m
784 m
814 m
807 m
1006 m
1026 m
1055 m
1087 m
1117 m
Limit of Data
Section 1200 NE
Scale
0
100 m
PSAD56 18S
Key
Cu > 0.5 wt. %
Cu > 0.1 wt. %
Thrust fault
Inferred fault
Lithology
Soil or colluvium
Quaternary
Hydrothermal breccia
Pararani porphyry dikes (Pp)
Haquira porphyry dikes (HPd)
Haquira porphyry stock (HP)
Lahuani dikes and sills (Lu)
Eocene
Red sandstone
Red mudstone and siltstone
Siltstone and minor mudstone
Quartzite
Fine grained conglomerate
Mara Fm.
Soraya Fm.
Cretaceous

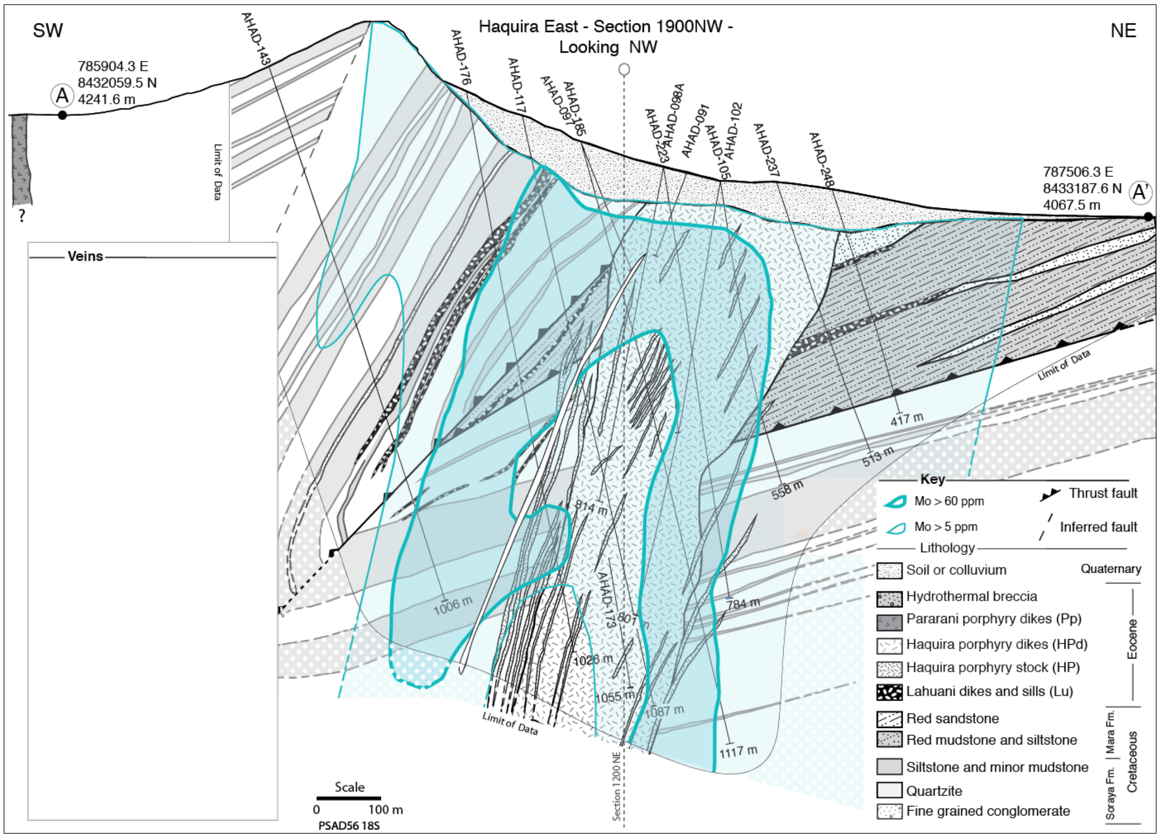
SW
Haquira East - Section 1900NW -
Looking NW
NE
785904.3 E
8432059.5 N
4241.6 m
A
787506.3 E
8433187.6 N
4067.5 m
A'
?
Limit of Data
Veins
AHAD-143
AHAD-176
AHAD-117
AHAD-097
AHAD-185
AHAD-223
AHAD-098A
AHAD-091
AHAD-105
AHAD-102
AHAD-237
AHAD-248
AHAD-173
417 m
513 m
558 m
784 m
814 m
807 m
1006 m
1026 m
1055 m
1087 m
1117 m
Limit of Data
Section 1200 NE
Scale
0
100 m
PSAD56 18S
Key
Mo > 60 ppm
Mo > 5 ppm
Thrust fault
Inferred fault
Lithology
Soil or colluvium
Quaternary
Hydrothermal breccia
Pararani porphyry dikes (Pp)
Haquira porphyry dikes (HPd)
Haquira porphyry stock (HP)
Lahuani dikes and sills (Lu)
Eocene
Red sandstone
Red mudstone and siltstone
Siltstone and minor mudstone
Quartzite
Fine grained conglomerate
Mara Fm.
Soraya Fm.
Cretaceous

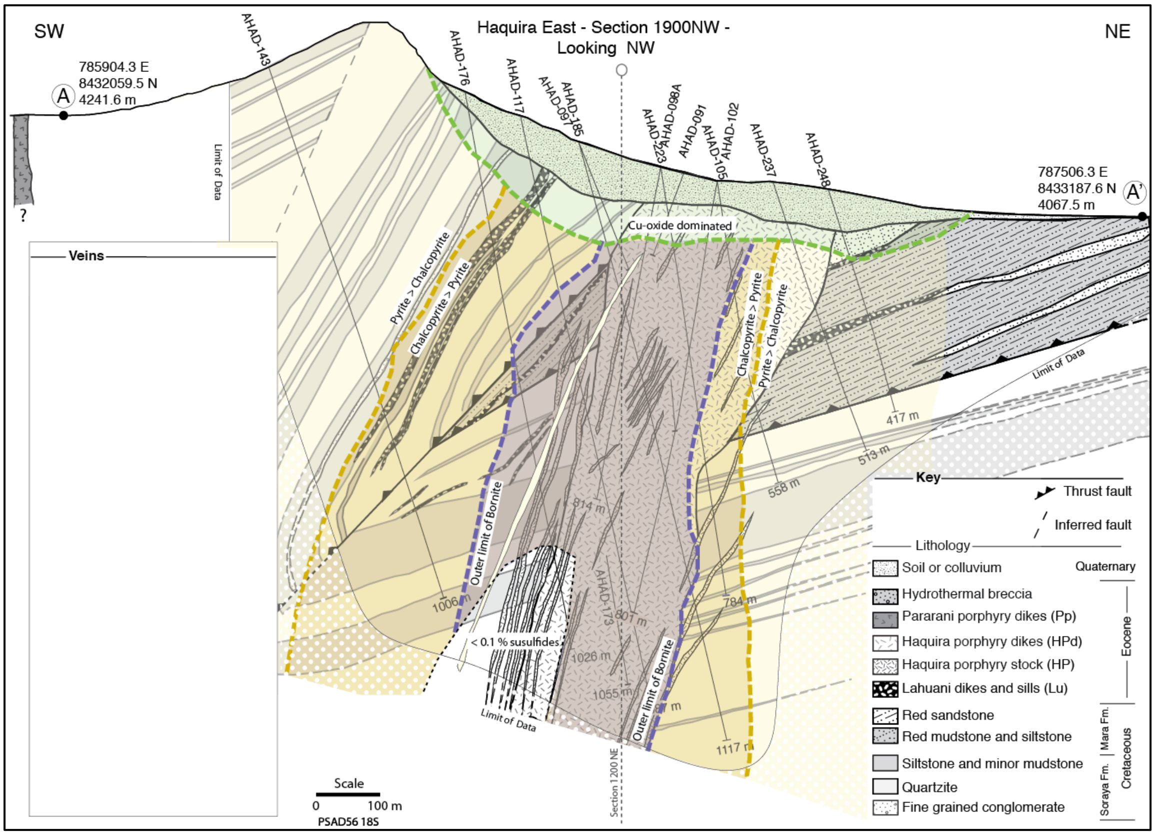
SW
Haquira East - Section 1900NW -
Looking NW
NE
A
785904.3 E
8432059.5 N
4241.6 m
A'
787506.3 E
8433187.6 N
4067.5 m
?
Limit of Data
AHAD-143
AHAD-176
AHAD-117
AHAD-097
AHAD-185
AHAD-223
AHAD-098A
AHAD-091
AHAD-105
AHAD-102
AHAD-237
AHAD-248
AHAD-173
Cu-oxide dominated
Pyrite > Chalcopyrite
Chalcopyrite > Pyrite
Chalcopyrite > Pyrite
Pyrite > Chalcopyrite
Outer limit of Bornite
Outer limit of Bornite
< 0.1 % susulfides
417 m
513 m
558 m
784 m
807 m
814 m
1006 m
1026 m
1055 m
1087 m
1117 m
Limit of Data
Limit of Data
Section 1200 NE
Veins
Scale
0
100 m
PSAD56 18S
Key
Thrust fault
Inferred fault
Lithology
Soil or colluvium
Quaternary
Hydrothermal breccia
Pararani porphyry dikes (Pp)
Haquira porphyry dikes (HPd)
Haquira porphyry stock (HP)
Lahuani dikes and sills (Lu)
Eocene
Red sandstone
Red mudstone and siltstone
Mara Fm.
Siltstone and minor mudstone
Quartzite
Fine grained conglomerate
Soraya Fm.
Cretaceous

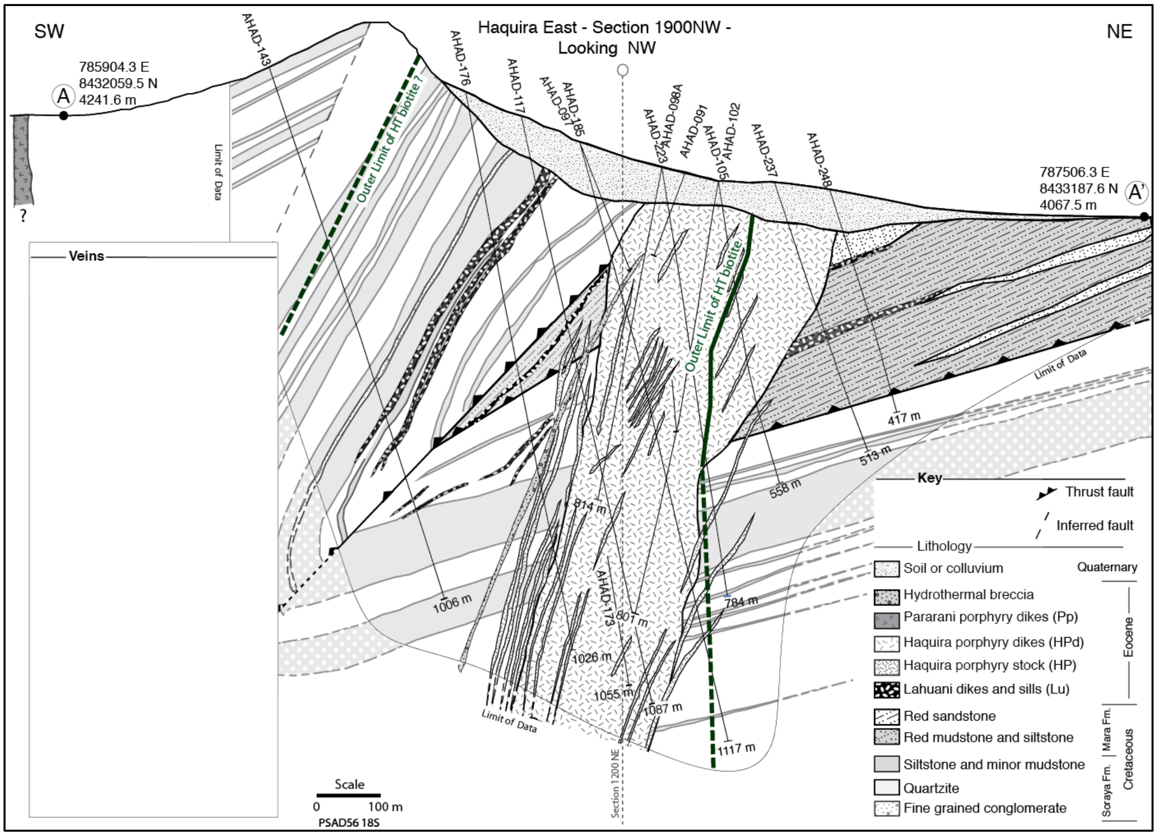
SW
Haquira East - Section 1900NW -
Looking NW
NE
A
785904.3 E
8432059.5 N
4241.6 m
A'
787506.3 E
8433187.6 N
4067.5 m
?
Limit of Data
AHAD-143
AHAD-176
AHAD-117
AHAD-097
AHAD-185
AHAD-223
AHAD-098A
AHAD-091
AHAD-105
AHAD-102
AHAD-237
AHAD-248
AHAD-173
Outer Limit of HT biotite ?
Outer Limit of HT biotite
417 m
513 m
558 m
784 m
807 m
814 m
1006 m
1026 m
1055 m
1087 m
1117 m
Limit of Data
Limit of Data
Section 1200 NE
Veins
Scale
0
100 m
PSAD56 18S
Key
Thrust fault
Inferred fault
Lithology
Soil or colluvium
Quaternary
Hydrothermal breccia
Pararani porphyry dikes (Pp)
Haquira porphyry dikes (HPd)
Haquira porphyry stock (HP)
Lahuani dikes and sills (Lu)
Eocene
Red sandstone
Red mudstone and siltstone
Mara Fm.
Siltstone and minor mudstone
Quartzite
Fine grained conglomerate
Soraya Fm.
Cretaceous

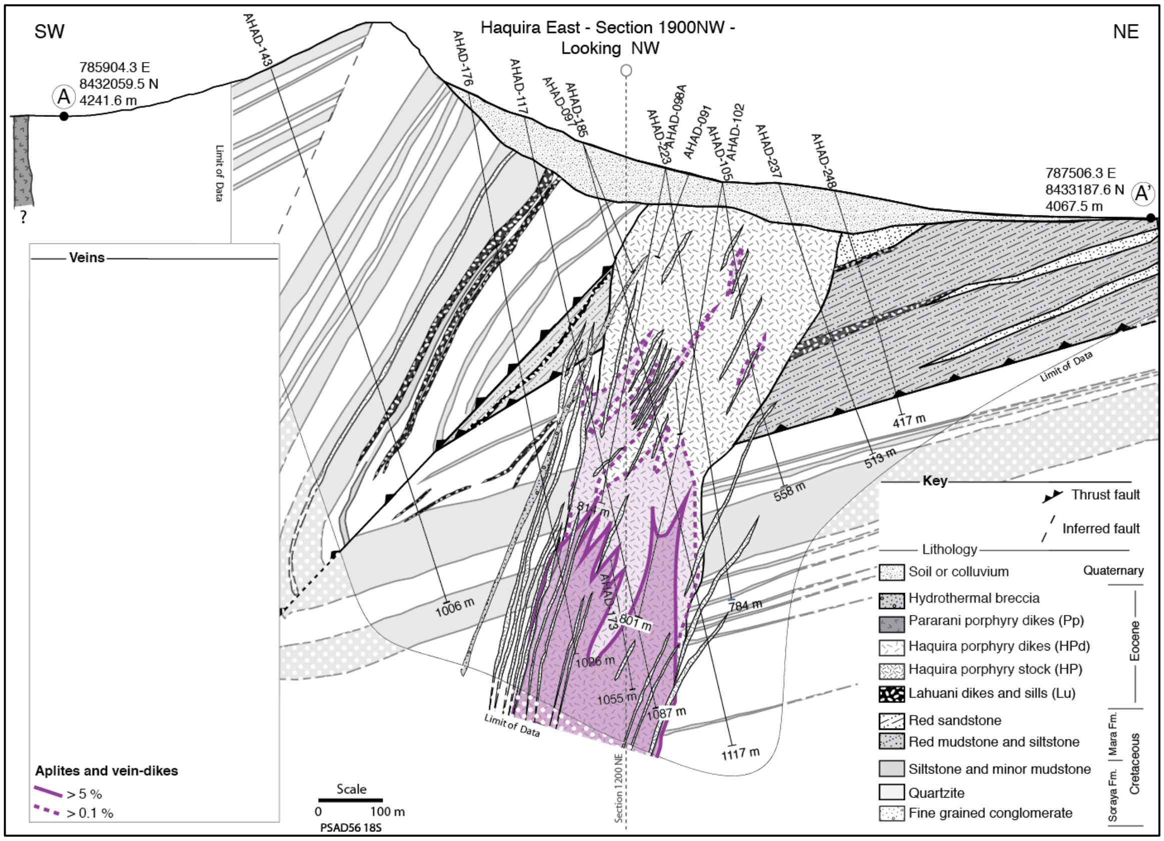
SW
Haquira East - Section 1900NW - Looking NW
NE
785904.3 E
8432059.5 N
4241.6 m
A
787506.3 E
8433187.6 N
4067.5 m
A'
AHAD-143
AHAD-176
AHAD-117
AHAD-097
AHAD-185
AHAD-223
AHAD-098A
AHAD-091
AHAD-105
AHAD-102
AHAD-237
AHAD-248
AHAD-173
Limit of Data
417 m
513 m
558 m
784 m
814 m
801 m
1006 m
1026 m
1055 m
1087 m
1117 m
Section 1200 NE
Veins
Aplites and vein-dikes
> 5 %
> 0.1 %
Scale
0
100 m
PSAD56 18S
Key
Thrust fault
Inferred fault
Lithology
Soil or colluvium
Quaternary
Hydrothermal breccia
Pararani porphyry dikes (Pp)
Haquira porphyry dikes (HPd)
Haquira porphyry stock (HP)
Lahuani dikes and sills (Lu)
Eocene
Red sandstone
Red mudstone and siltstone
Mara Fm.
Siltstone and minor mudstone
Quartzite
Fine grained conglomerate
Soraya Fm.
Cretaceous

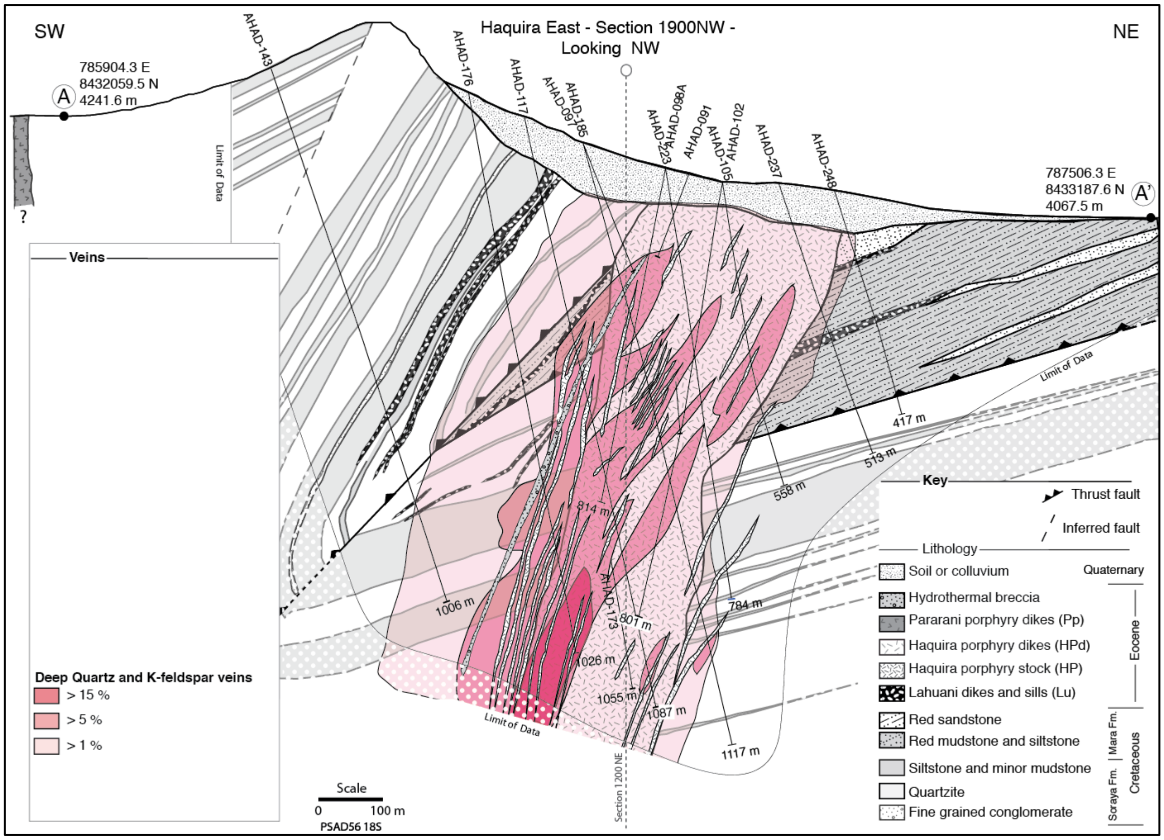
SW
Haquira East - Section 1900NW - Looking NW
NE
785904.3 E
8432059.5 N
4241.6 m
A
787506.3 E
8433187.6 N
4067.5 m
A'
AHAD-143
AHAD-176
AHAD-117
AHAD-097
AHAD-185
AHAD-223
AHAD-098A
AHAD-091
AHAD-105
AHAD-102
AHAD-237
AHAD-248
AHAD-173
Limit of Data
417 m
513 m
558 m
784 m
814 m
801 m
1006 m
1026 m
1055 m
1087 m
1117 m
Section 1200 NE
Veins
Deep Quartz and K-feldspar veins
> 15 %
> 5 %
> 1 %
Scale
0
100 m
PSAD56 18S
Key
Thrust fault
Inferred fault
Lithology
Soil or colluvium
Quaternary
Hydrothermal breccia
Pararani porphyry dikes (Pp)
Haquira porphyry dikes (HPd)
Haquira porphyry stock (HP)
Lahuani dikes and sills (Lu)
Eocene
Red sandstone
Red mudstone and siltstone
Mara Fm.
Siltstone and minor mudstone
Quartzite
Fine grained conglomerate
Soraya Fm.
Cretaceous

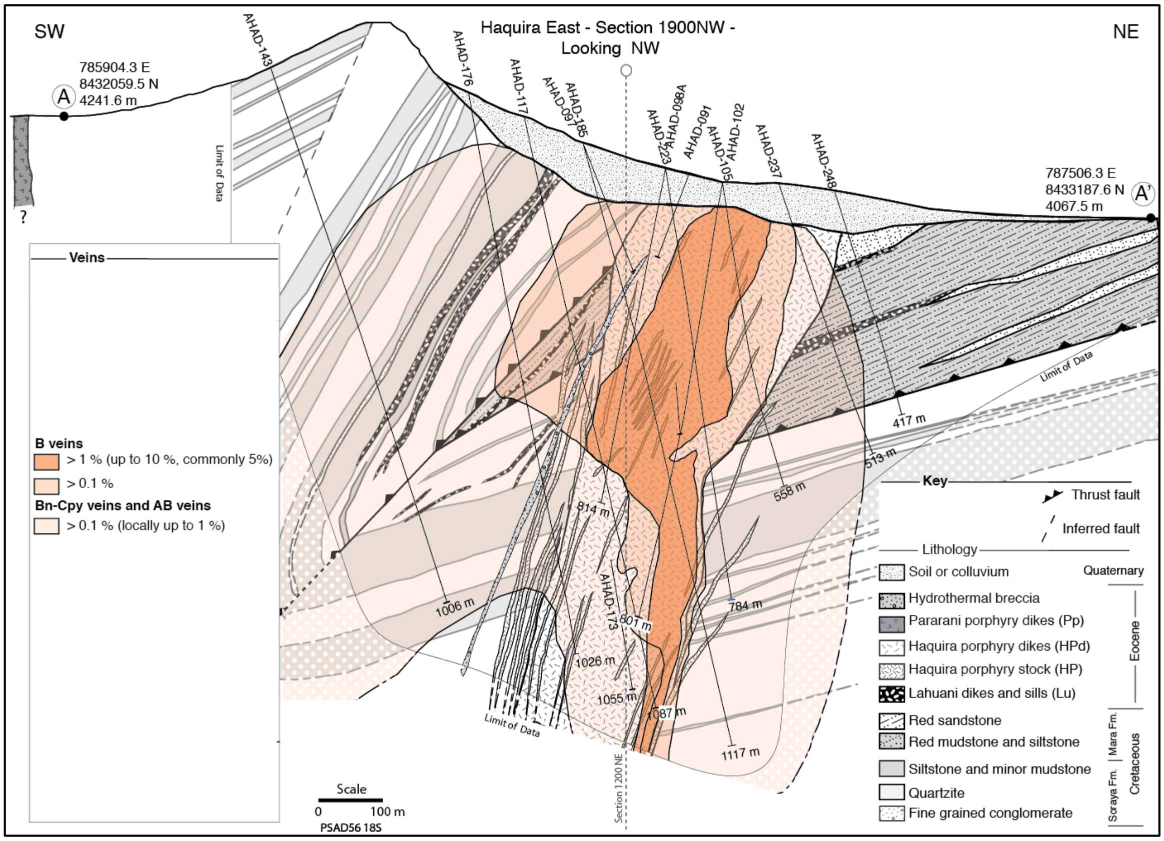
SW
Haquira East - Section 1900NW - Looking NW
NE
785904.3 E
8432059.5 N
4241.6 m
A
787506.3 E
8433187.6 N
4067.5 m
A'
?
Limit of Data
AHAD-143
AHAD-176
AHAD-117
AHAD-097
AHAD-185
AHAD-223
AHAD-098A
AHAD-091
AHAD-105
AHAD-102
AHAD-237
AHAD-248
AHAD-173
417 m
513 m
558 m
814 m
1006 m
807 m
784 m
1026 m
1055 m
1087 m
1117 m
Limit of Data
Section 1200 NE
Veins
B veins
> 1 % (up to 10 %, commonly 5%)
> 0.1 %
Bn-Cpy veins and AB veins
> 0.1 % (locally up to 1 %)
Key
Thrust fault
Inferred fault
Lithology
Soil or colluvium
Quaternary
Hydrothermal breccia
Pararani porphyry dikes (Pp)
Haquira porphyry dikes (HPd)
Haquira porphyry stock (HP)
Lahuani dikes and sills (Lu)
Eocene
Red sandstone
Red mudstone and siltstone
Mara Fm.
Siltstone and minor mudstone
Quartzite
Fine grained conglomerate
Soraya Fm.
Cretaceous
Scale
0
100 m
PSAD56 18S

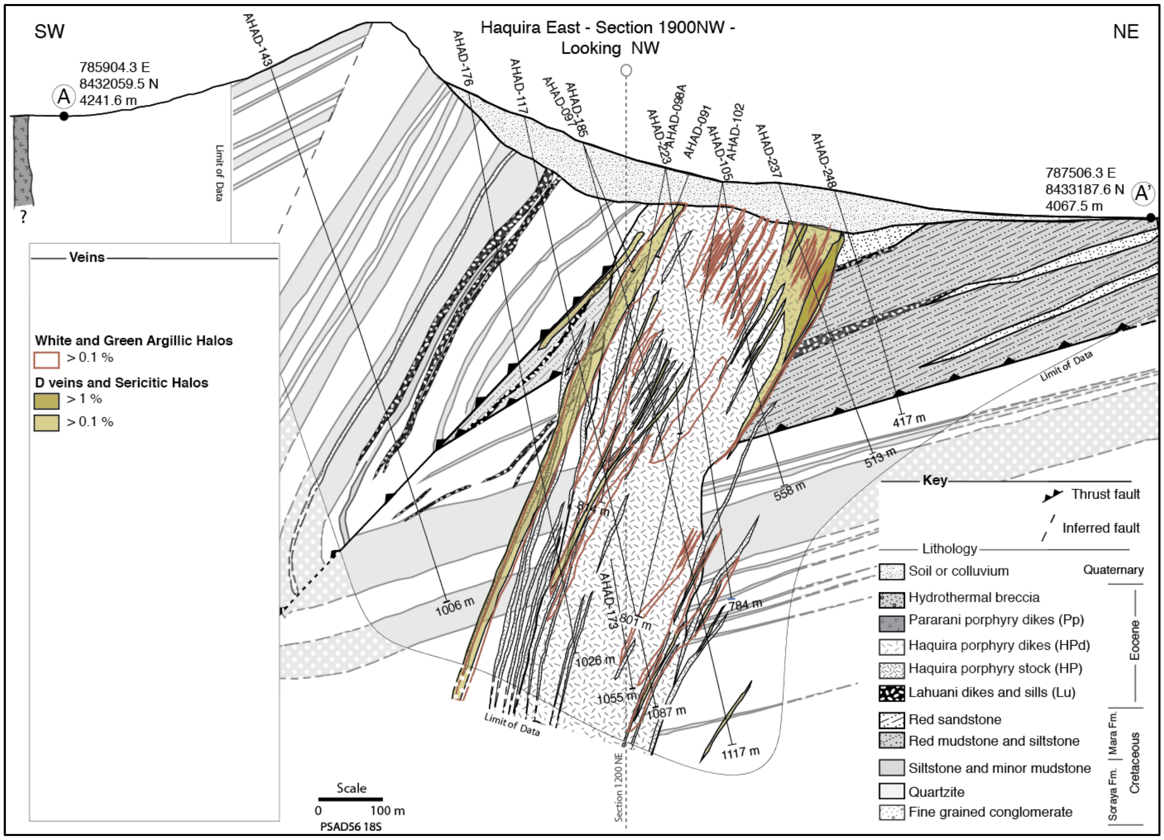
SW
Haquira East - Section 1900NW - Looking NW
NE
785904.3 E
8432059.5 N
4241.6 m
A
787506.3 E
8433187.6 N
4067.5 m
A'
?
Limit of Data
AHAD-143
AHAD-176
AHAD-117
AHAD-097
AHAD-185
AHAD-223
AHAD-098A
AHAD-091
AHAD-105
AHAD-102
AHAD-237
AHAD-248
AHAD-173
417 m
513 m
558 m
814 m
1006 m
807 m
784 m
1026 m
1055 m
1087 m
1117 m
Limit of Data
Section 1200 NE
Veins
White and Green Argillic Halos
> 0.1 %
D veins and Sericitic Halos
> 1 %
> 0.1 %
Key
Thrust fault
Inferred fault
Lithology
Soil or colluvium
Quaternary
Hydrothermal breccia
Pararani porphyry dikes (Pp)
Haquira porphyry dikes (HPd)
Haquira porphyry stock (HP)
Lahuani dikes and sills (Lu)
Eocene
Red sandstone
Red mudstone and siltstone
Mara Fm.
Siltstone and minor mudstone
Quartzite
Fine grained conglomerate
Soraya Fm.
Cretaceous
Scale
0
100 m
PSAD56 18S

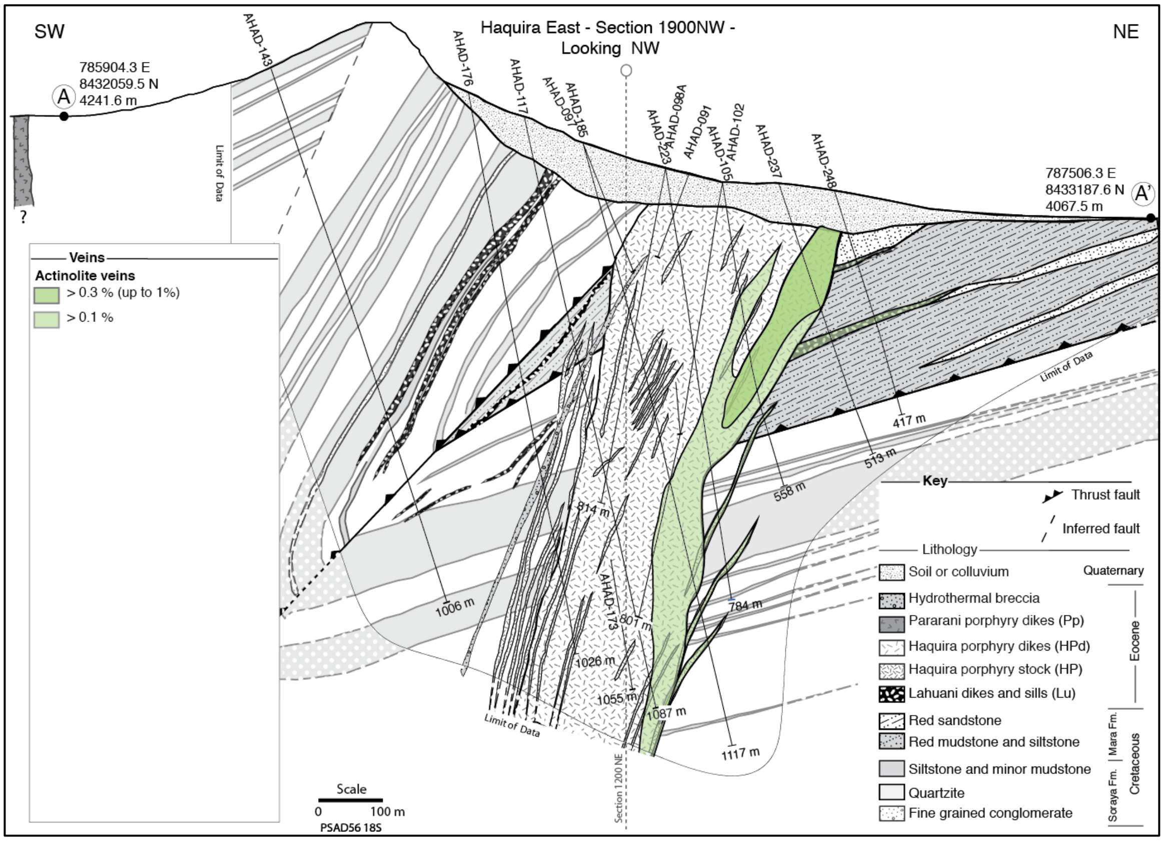
SW
NE
Haquira East - Section 1900NW -
Looking NW
A
785904.3 E
8432059.5 N
4241.6 m
A'
787506.3 E
8433187.6 N
4067.5 m
?
Limit of Data
AHAD-143
AHAD-176
AHAD-117
AHAD-097
AHAD-185
AHAD-223
AHAD-098A
AHAD-091
AHAD-105
AHAD-102
AHAD-237
AHAD-248
AHAD-173
1006 m
814 m
801 m
1026 m
1055 m
1087 m
1117 m
784 m
558 m
513 m
417 m
Limit of Data
Limit of Data
Section 1200 NE
Veins
Actinolite veins
> 0.3 % (up to 1%)
> 0.1 %
Scale
0
100 m
PSAD56 18S
Key
Thrust fault
Inferred fault
Lithology
Soil or colluvium
Quaternary
Hydrothermal breccia
Pararani porphyry dikes (Pp)
Haquira porphyry dikes (HPd)
Haquira porphyry stock (HP)
Lahuani dikes and sills (Lu)
Eocene
Red sandstone
Red mudstone and siltstone
Mara Fm.
Siltstone and minor mudstone
Quartzite
Fine grained conglomerate
Soraya Fm.
Cretaceous

APPENDIX 2
Cross-section 2100NW

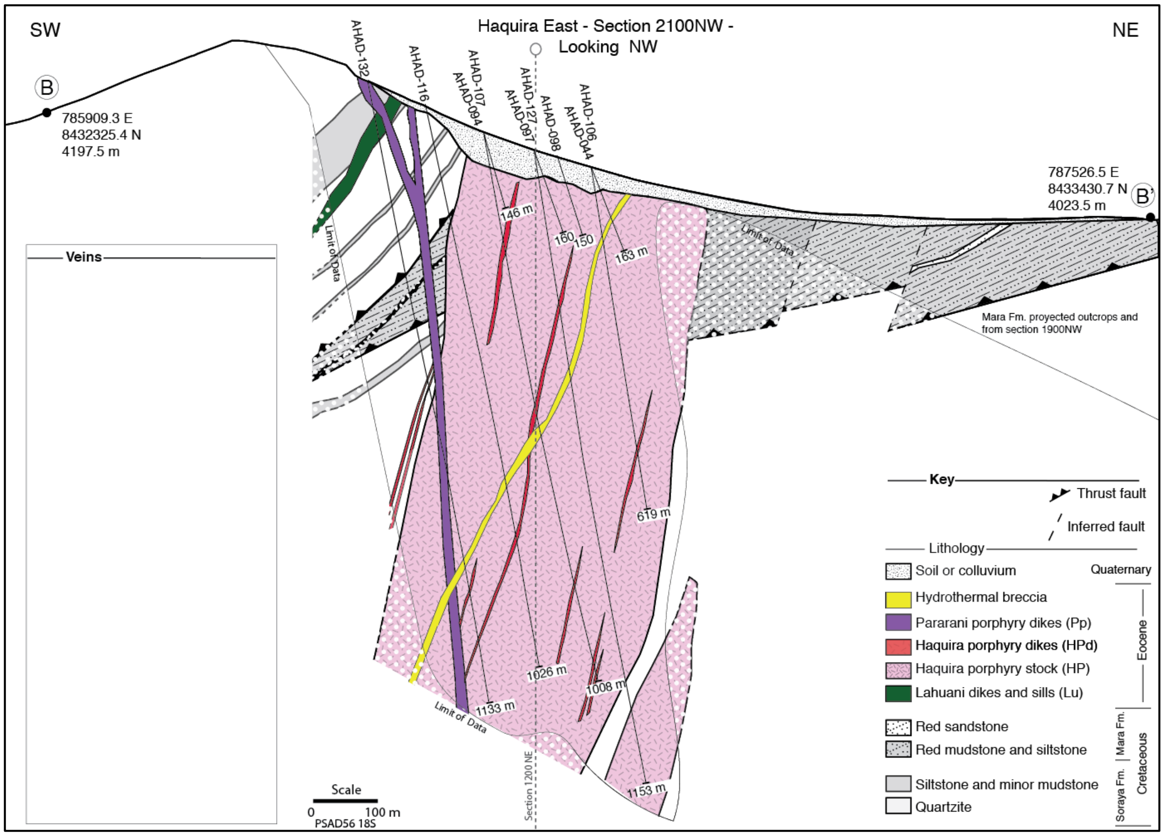
Haquira East - Section 2100NW -
Looking NW
SW
NE
B
785909.3 E
8432325.4 N
4197.5 m
787526.5 E
8433430.7 N
4023.5 m
B'
AHAD-132
AHAD-116
AHAD-107
AHAD-094
AHAD-127
AHAD-097
AHAD-098
AHAD-106
AHAD-044
146 m
160
150
163 m
619 m
1026 m
1008 m
1133 m
1153 m
Limit of Data
Limit of Data
Limit of Data
Mara Fm. proyected outcrops and from section 1900NW
Veins
Section 1200 NE
Scale
0
100 m
PSAD56 18S
Key
Thrust fault
Inferred fault
Lithology
Soil or colluvium
Quaternary
Hydrothermal breccia
Pararani porphyry dikes (Pp)
Haquira porphyry dikes (HPd)
Haquira porphyry stock (HP)
Lahuani dikes and sills (Lu)
Eocene
Red sandstone
Red mudstone and siltstone
Mara Fm.
Siltstone and minor mudstone
Quartzite
Soraya Fm.
Cretaceous

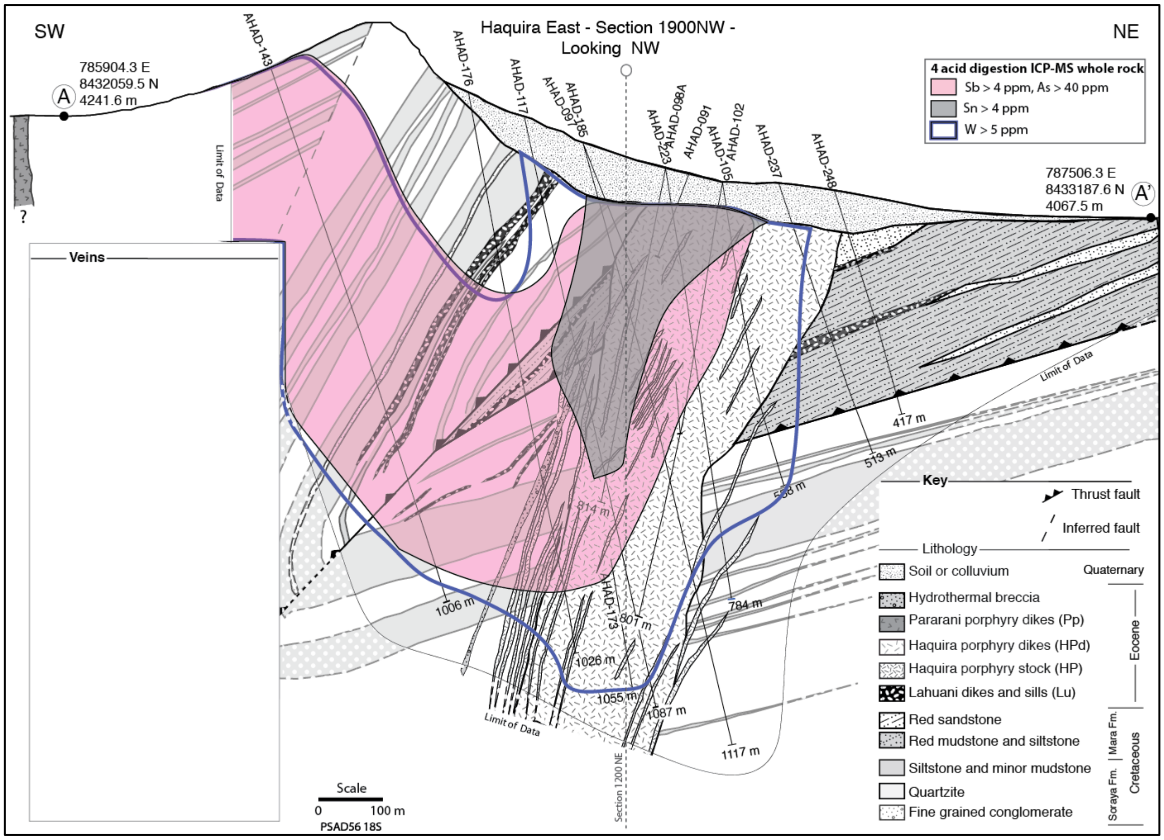
Haquira East - Section 1900NW -
Looking NW
SW
NE
A
785904.3 E
8432059.5 N
4241.6 m
787506.3 E
8433187.6 N
4067.5 m
A'
?
4 acid digestion ICP-MS whole rock
Sb > 4 ppm, As > 40 ppm
Sn > 4 ppm
W > 5 ppm
AHAD-143
AHAD-176
AHAD-117
AHAD-097
AHAD-185
AHAD-223
AHAD-098A
AHAD-091
AHAD-105
AHAD-102
AHAD-237
AHAD-248
AHAD-173
417 m
513 m
588 m
814 m
784 m
807 m
1006 m
1026 m
1055 m
1087 m
1117 m
Limit of Data
Limit of Data
Limit of Data
Veins
Section 1200 NE
Scale
0
100 m
PSAD56 18S
Key
Thrust fault
Inferred fault
Lithology
Soil or colluvium
Quaternary
Hydrothermal breccia
Pararani porphyry dikes (Pp)
Haquira porphyry dikes (HPd)
Haquira porphyry stock (HP)
Lahuani dikes and sills (Lu)
Eocene
Red sandstone
Red mudstone and siltstone
Mara Fm.
Siltstone and minor mudstone
Quartzite
Fine grained conglomerate
Soraya Fm.
Cretaceous

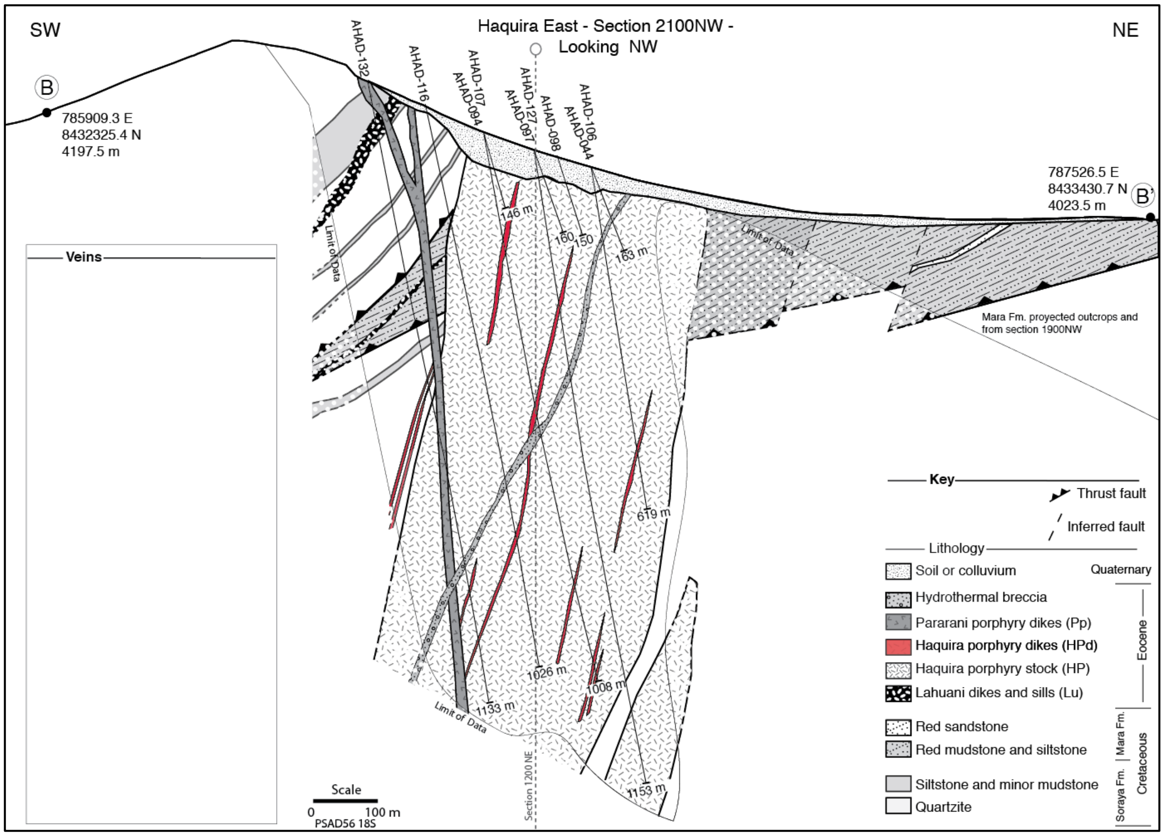
Haquira East - Section 2100NW -
Looking NW
SW
NE
B
785909.3 E
8432325.4 N
4197.5 m
B'
787526.5 E
8433430.7 N
4023.5 m
AHAD-132
AHAD-116
AHAD-107
AHAD-094
AHAD-127
AHAD-097
AHAD-098
AHAD-106
AHAD-044
146 m
160
150
163 m
619 m
1026 m
1008 m
1133 m
1153 m
Limit of Data
Mara Fm. proyected outcrops and from section 1900NW
Section 1200 NE
Veins
Scale
0
100 m
PSAD56 18S
Key
Thrust fault
Inferred fault
Lithology
Soil or colluvium
Quaternary
Hydrothermal breccia
Pararani porphyry dikes (Pp)
Haquira porphyry dikes (HPd)
Haquira porphyry stock (HP)
Lahuani dikes and sills (Lu)
Eocene
Red sandstone
Red mudstone and siltstone
Mara Fm.
Siltstone and minor mudstone
Quartzite
Soraya Fm.
Cretaceous

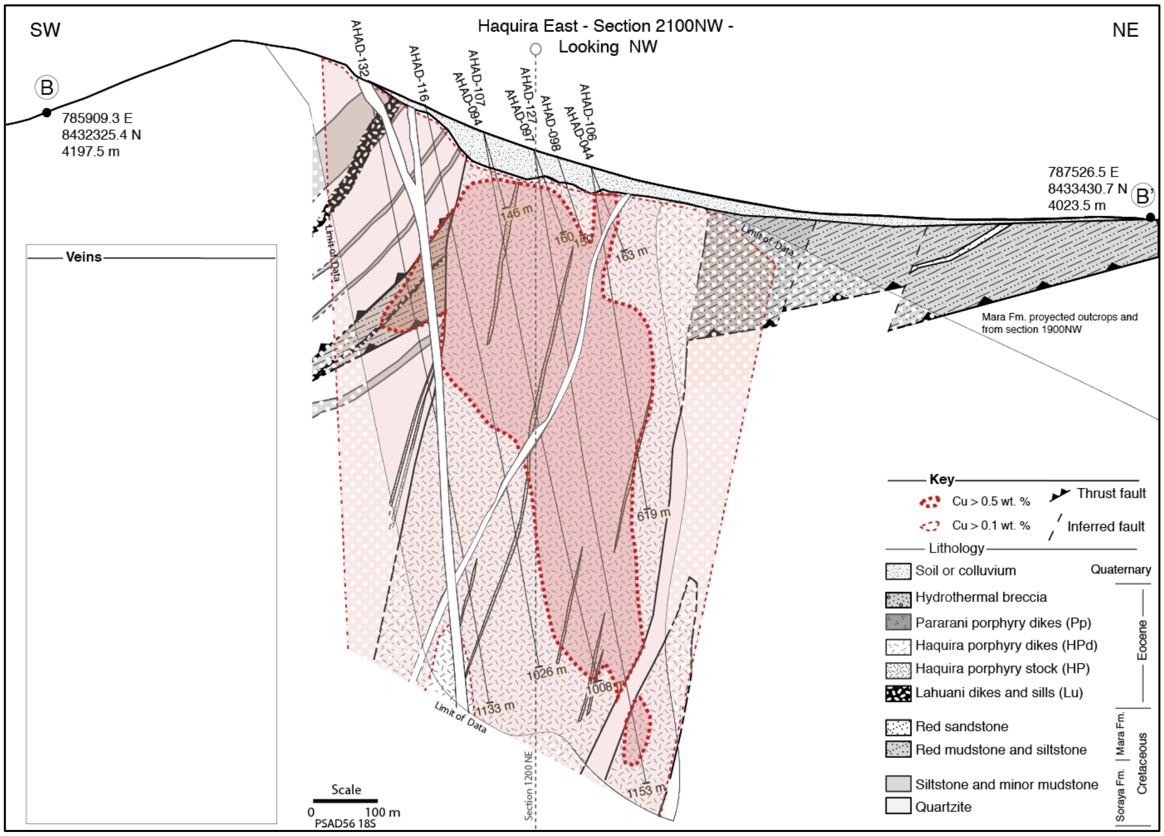
Haquira East - Section 2100NW -
Looking NW
SW
NE
B
785909.3 E
8432325.4 N
4197.5 m
B'
787526.5 E
8433430.7 N
4023.5 m
AHAD-132
AHAD-116
AHAD-107
AHAD-094
AHAD-127
AHAD-097
AHAD-098
AHAD-106
AHAD-044
146 m
160
150
163 m
619 m
1026 m
1008 m
1133 m
1153 m
Limit of Data
Mara Fm. proyected outcrops and from section 1900NW
Section 1200 NE
Veins
Scale
0
100 m
PSAD56 18S
Key
Cu > 0.5 wt. %
Cu > 0.1 wt. %
Thrust fault
Inferred fault
Lithology
Soil or colluvium
Quaternary
Hydrothermal breccia
Pararani porphyry dikes (Pp)
Haquira porphyry dikes (HPd)
Haquira porphyry stock (HP)
Lahuani dikes and sills (Lu)
Eocene
Red sandstone
Red mudstone and siltstone
Mara Fm.
Siltstone and minor mudstone
Quartzite
Soraya Fm.
Cretaceous

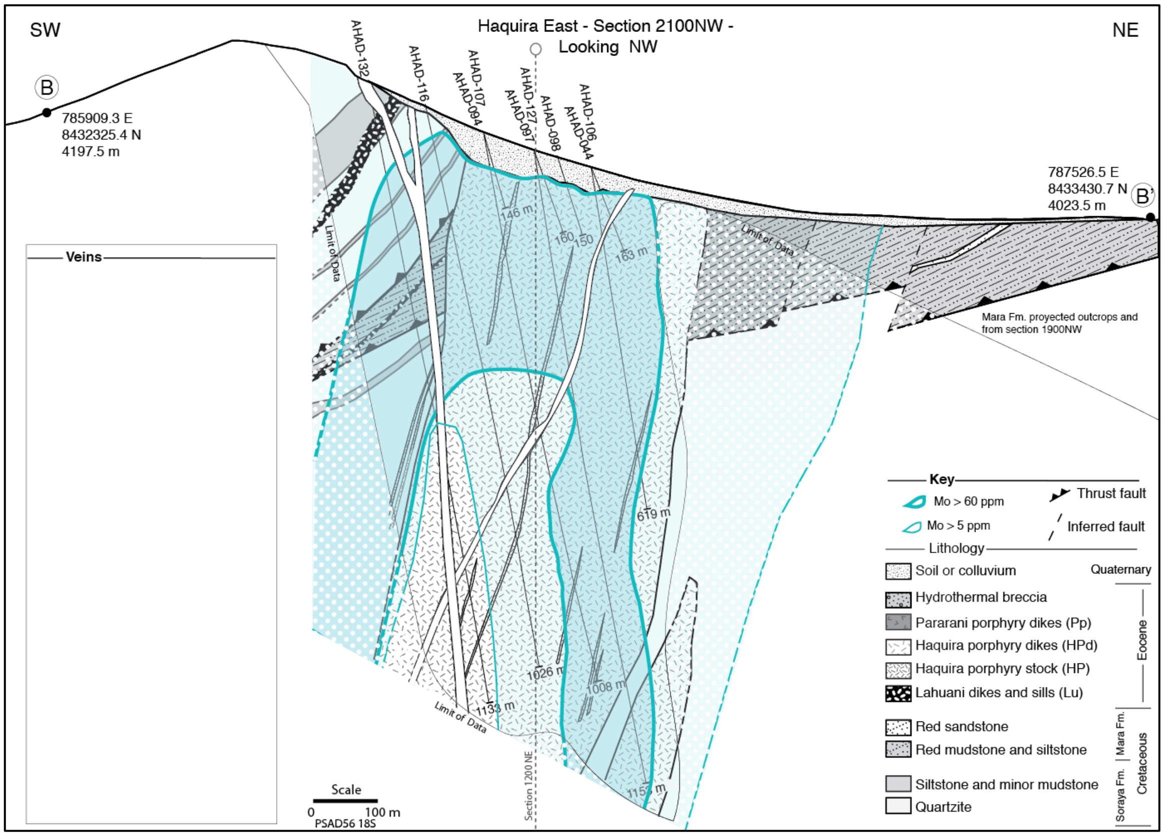
SW
Haquira East - Section 2100NW - Looking NW
NE
B
785909.3 E
8432325.4 N
4197.5 m
AHAD-132
AHAD-116
AHAD-107
AHAD-094
AHAD-127
AHAD-097
AHAD-098
AHAD-106
AHAD-044
787526.5 E
8433430.7 N
4023.5 m
B'
Veins
Limit of Data
146 m
160
150
163 m
Limit of Data
Mara Fm. proyected outcrops and from section 1900NW
619 m
1026 m
1008 m
1133 m
1153 m
Limit of Data
Section 1200 NE
Scale
0
100 m
PSAD56 18S
Key
Mo > 60 ppm
Mo > 5 ppm
Thrust fault
Inferred fault
Lithology
Soil or colluvium
Quaternary
Hydrothermal breccia
Pararani porphyry dikes (Pp)
Haquira porphyry dikes (HPd)
Haquira porphyry stock (HP)
Lahuani dikes and sills (Lu)
Eocene
Red sandstone
Red mudstone and siltstone
Mara Fm.
Siltstone and minor mudstone
Quartzite
Soraya Fm.
Cretaceous

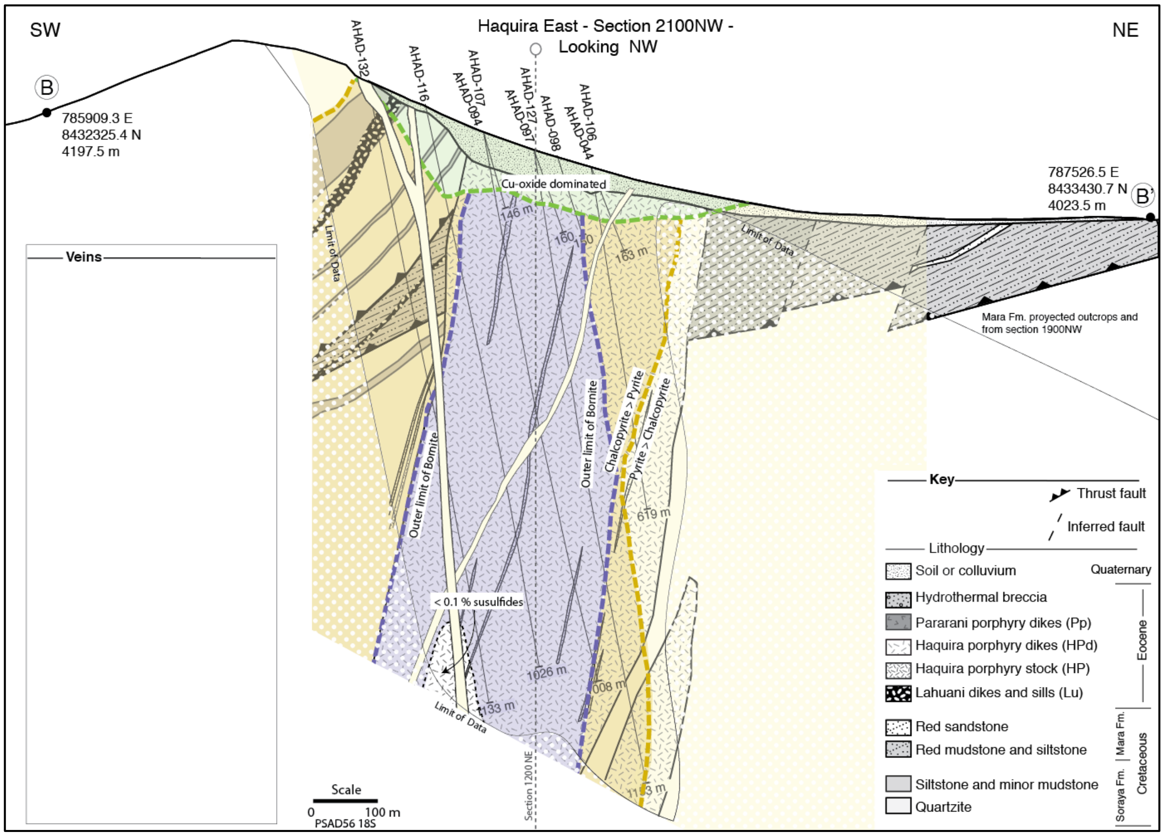
SW
Haquira East - Section 2100NW - Looking NW
NE
B
785909.3 E
8432325.4 N
4197.5 m
AHAD-132
AHAD-116
AHAD-107
AHAD-094
AHAD-127
AHAD-097
AHAD-098
AHAD-106
AHAD-044
787526.5 E
8433430.7 N
4023.5 m
B'
Veins
Cu-oxide dominated
Limit of Data
146 m
160
150
163 m
Limit of Data
Mara Fm. proyected outcrops and from section 1900NW
Outer limit of Bornite
Outer limit of Bornite
Chalcopyrite > Pyrite
Pyrite > Chalcopyrite
619 m
< 0.1 % susulfides
1026 m
1008 m
1133 m
1153 m
Limit of Data
Section 1200 NE
Scale
0
100 m
PSAD56 18S
Key
Thrust fault
Inferred fault
Lithology
Soil or colluvium
Quaternary
Hydrothermal breccia
Pararani porphyry dikes (Pp)
Haquira porphyry dikes (HPd)
Haquira porphyry stock (HP)
Lahuani dikes and sills (Lu)
Eocene
Red sandstone
Red mudstone and siltstone
Mara Fm.
Siltstone and minor mudstone
Quartzite
Soraya Fm.
Cretaceous

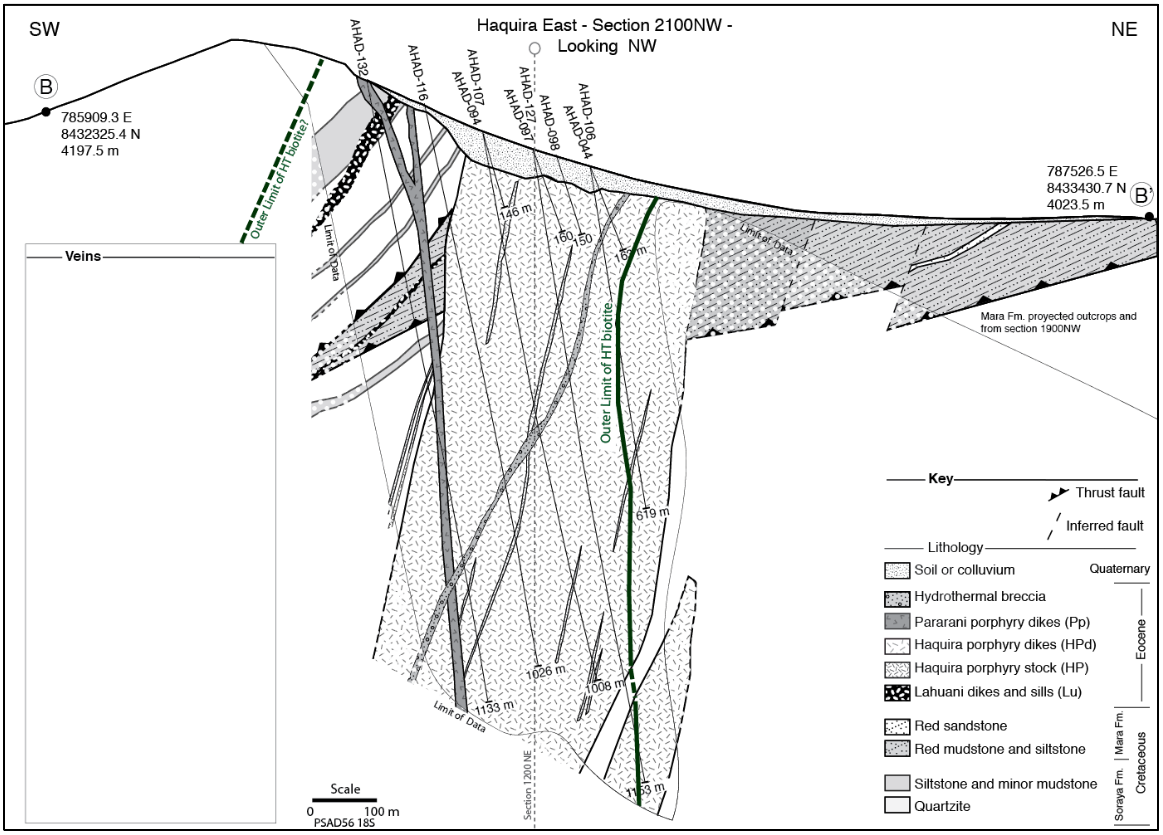
SW
Haquira East - Section 2100NW - Looking NW
NE
B
785909.3 E
8432325.4 N
4197.5 m
B'
787526.5 E
8433430.7 N
4023.5 m
AHAD-132
AHAD-116
AHAD-107
AHAD-094
AHAD-127
AHAD-097
AHAD-098
AHAD-106
AHAD-044
Outer Limit of HT biotite?
Outer Limit of HT biotite
Limit of Data
146 m
160
150
163 m
619 m
1026 m
1008 m
1133 m
1153 m
Mara Fm. proyected outcrops and from section 1900NW
Veins
Scale
0
100 m
PSAD56 18S
Section 1200 NE
Key
Thrust fault
Inferred fault
Lithology
Soil or colluvium
Quaternary
Hydrothermal breccia
Pararani porphyry dikes (Pp)
Haquira porphyry dikes (HPd)
Haquira porphyry stock (HP)
Lahuani dikes and sills (Lu)
Eocene
Red sandstone
Red mudstone and siltstone
Mara Fm.
Siltstone and minor mudstone
Quartzite
Soraya Fm.
Cretaceous

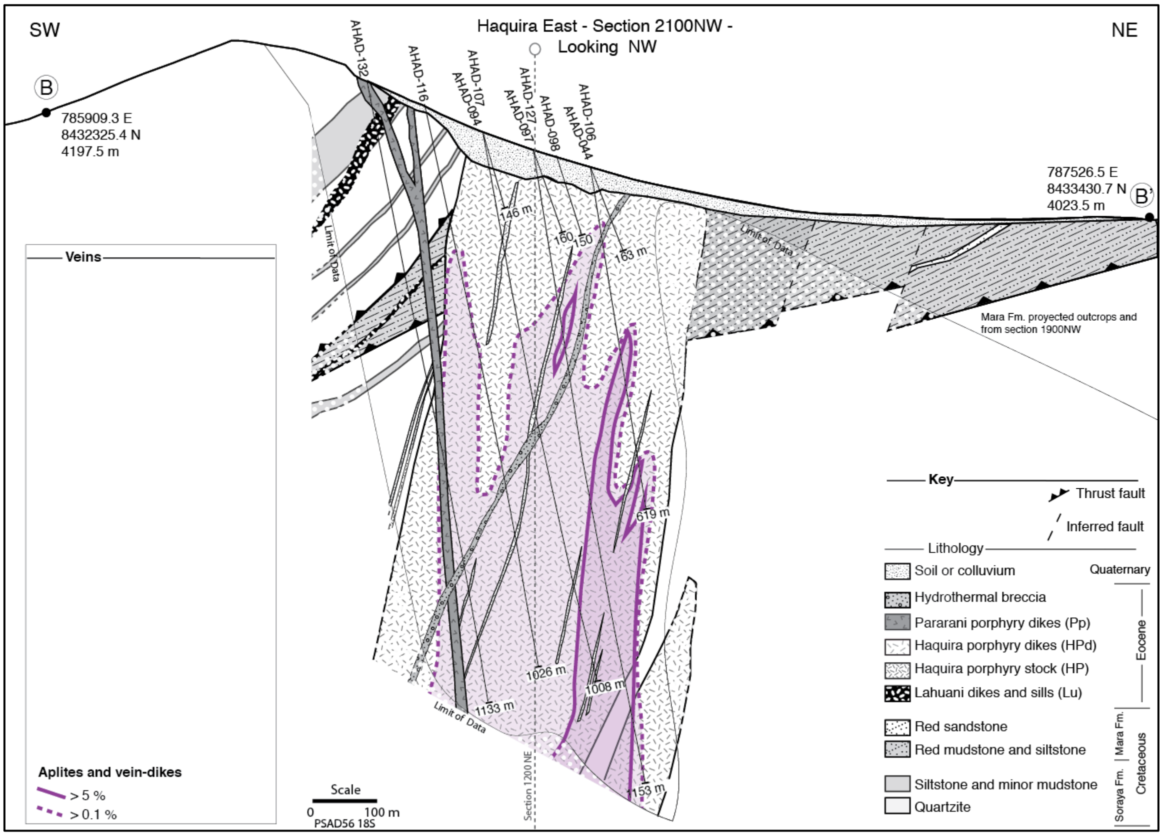
SW
Haquira East - Section 2100NW - Looking NW
NE
B
785909.3 E
8432325.4 N
4197.5 m
B'
787526.5 E
8433430.7 N
4023.5 m
AHAD-132
AHAD-116
AHAD-107
AHAD-094
AHAD-127
AHAD-097
AHAD-098
AHAD-106
AHAD-044
Limit of Data
146 m
160
150
163 m
619 m
1026 m
1008 m
1133 m
1153 m
Mara Fm. proyected outcrops and from section 1900NW
Veins
Aplites and vein-dikes
> 5 %
> 0.1 %
Scale
0
100 m
PSAD56 18S
Section 1200 NE
Key
Thrust fault
Inferred fault
Lithology
Soil or colluvium
Quaternary
Hydrothermal breccia
Pararani porphyry dikes (Pp)
Haquira porphyry dikes (HPd)
Haquira porphyry stock (HP)
Lahuani dikes and sills (Lu)
Eocene
Red sandstone
Red mudstone and siltstone
Mara Fm.
Siltstone and minor mudstone
Quartzite
Soraya Fm.
Cretaceous

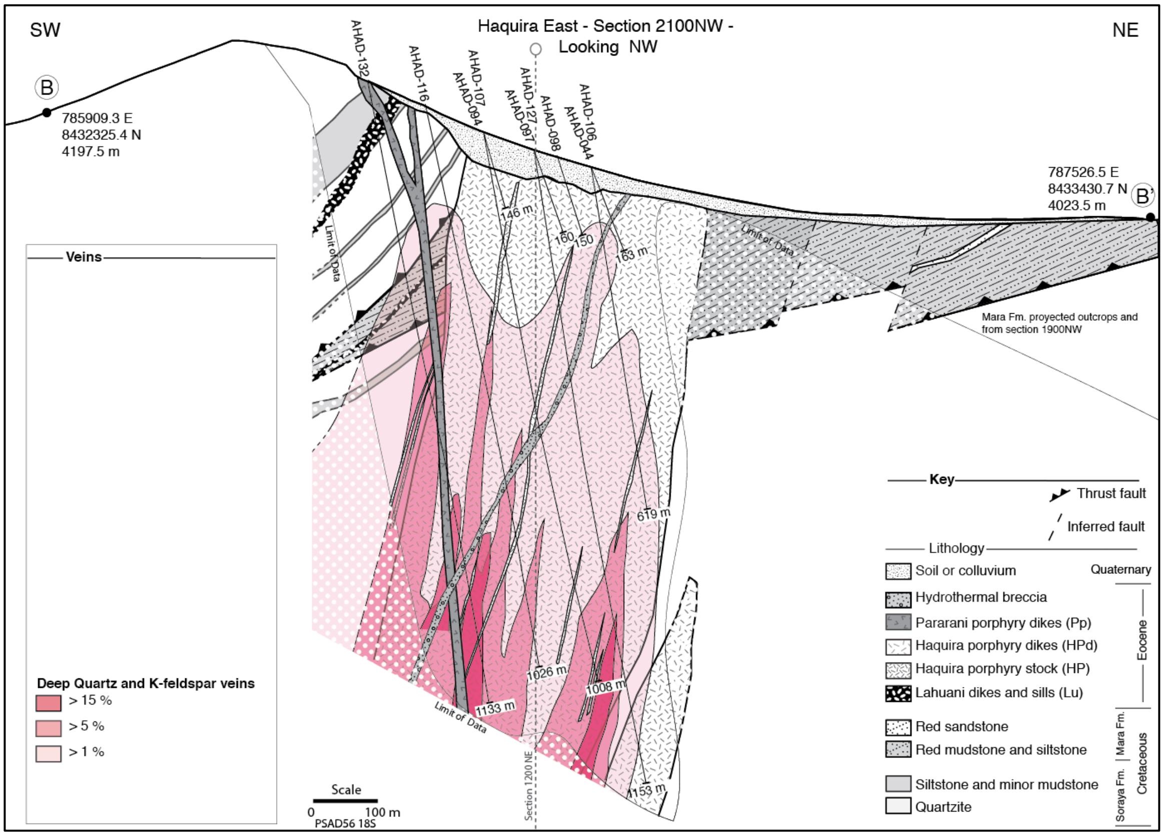
SW
Haquira East - Section 2100NW - Looking NW
NE
B
785909.3 E
8432325.4 N
4197.5 m
787526.5 E
8433430.7 N
4023.5 m
B'
AHAD-132
AHAD-116
AHAD-107
AHAD-094
AHAD-127
AHAD-097
AHAD-098
AHAD-106
AHAD-044
146 m
150
150
163 m
619 m
1026 m
1008 m
1133 m
1153 m
Limit of Data
Limit of Data
Limit of Data
Section 1200 NE
Mara Fm. proyected outcrops and from section 1900NW
Veins
Deep Quartz and K-feldspar veins
> 15 %
> 5 %
> 1 %
Scale
0
100 m
PSAD56 18S
Key
Thrust fault
Inferred fault
Lithology
Soil or colluvium
Quaternary
Hydrothermal breccia
Pararani porphyry dikes (Pp)
Haquira porphyry dikes (HPd)
Haquira porphyry stock (HP)
Lahuani dikes and sills (Lu)
Eocene
Red sandstone
Red mudstone and siltstone
Mara Fm.
Siltstone and minor mudstone
Quartzite
Soraya Fm.
Cretaceous

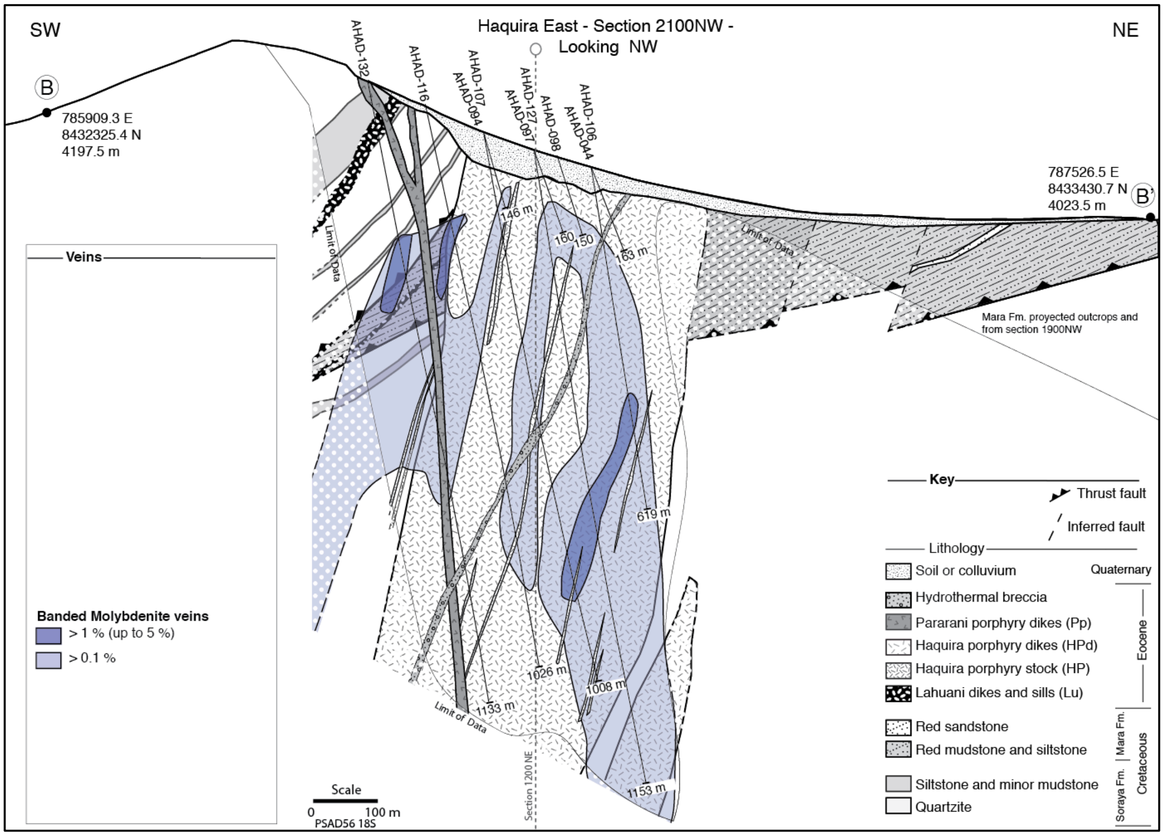
SW
Haquira East - Section 2100NW - Looking NW
NE
B
785909.3 E
8432325.4 N
4197.5 m
787526.5 E
8433430.7 N
4023.5 m
B'
AHAD-132
AHAD-116
AHAD-107
AHAD-094
AHAD-127
AHAD-097
AHAD-098
AHAD-106
AHAD-044
146 m
150
150
163 m
619 m
1026 m
1008 m
1133 m
1153 m
Limit of Data
Limit of Data
Limit of Data
Section 1200 NE
Mara Fm. proyected outcrops and from section 1900NW
Veins
Banded Molybdenite veins
> 1 % (up to 5 %)
> 0.1 %
Scale
0
100 m
PSAD56 18S
Key
Thrust fault
Inferred fault
Lithology
Soil or colluvium
Quaternary
Hydrothermal breccia
Pararani porphyry dikes (Pp)
Haquira porphyry dikes (HPd)
Haquira porphyry stock (HP)
Lahuani dikes and sills (Lu)
Eocene
Red sandstone
Red mudstone and siltstone
Mara Fm.
Siltstone and minor mudstone
Quartzite
Soraya Fm.
Cretaceous

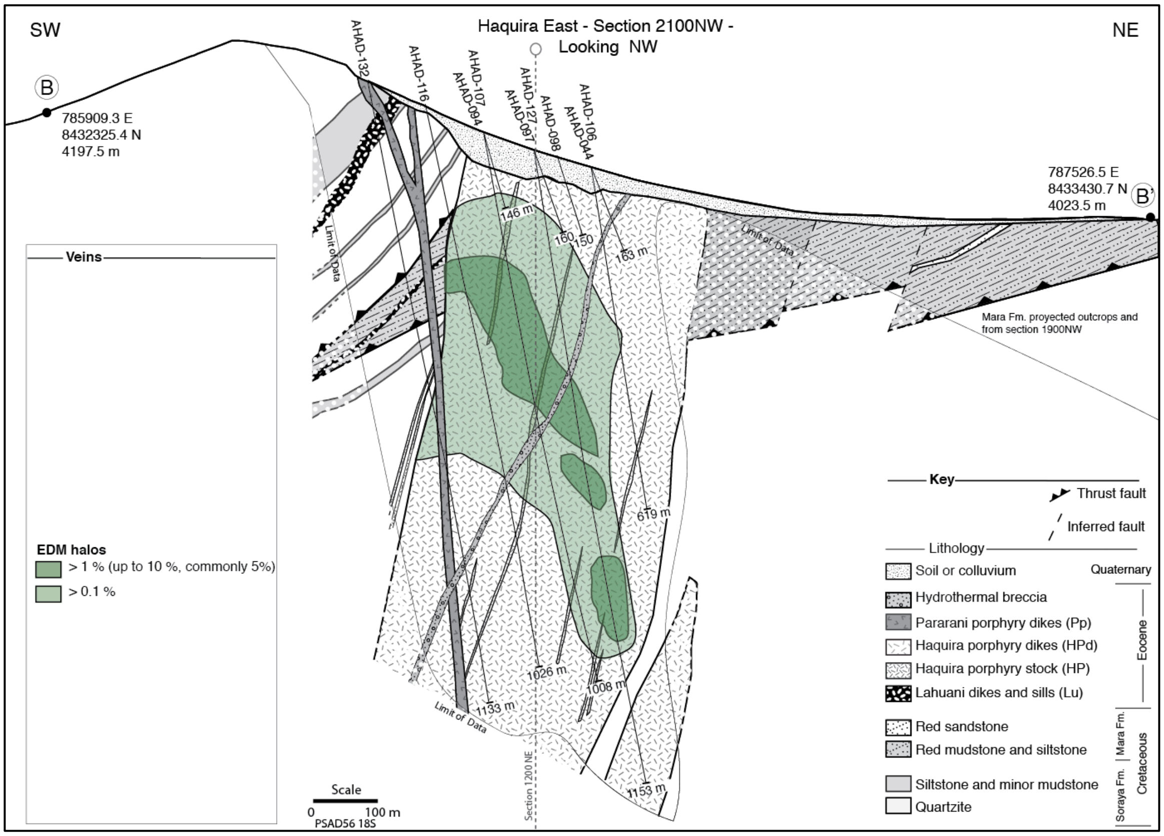
SW
Haquira East - Section 2100NW - Looking NW
NE
B
785909.3 E
8432325.4 N
4197.5 m
787526.5 E
8433430.7 N
4023.5 m
B'
AHAD-132
AHAD-116
AHAD-107
AHAD-094
AHAD-127
AHAD-097
AHAD-098
AHAD-106
AHAD-044
146 m
160
150
163 m
619 m
1026 m
1008 m
1133 m
1153 m
Limit of Data
Limit of Data
Limit of Data
Mara Fm. proyected outcrops and from section 1900NW
Section 1200 NE
Veins
EDM halos
> 1 % (up to 10 %, commonly 5%)
> 0.1 %
Scale
0
100 m
PSAD56 18S
Key
Thrust fault
Inferred fault
Lithology
Soil or colluvium
Quaternary
Hydrothermal breccia
Pararani porphyry dikes (Pp)
Haquira porphyry dikes (HPd)
Haquira porphyry stock (HP)
Lahuani dikes and sills (Lu)
Eocene
Red sandstone
Red mudstone and siltstone
Mara Fm.
Siltstone and minor mudstone
Quartzite
Soraya Fm.
Cretaceous

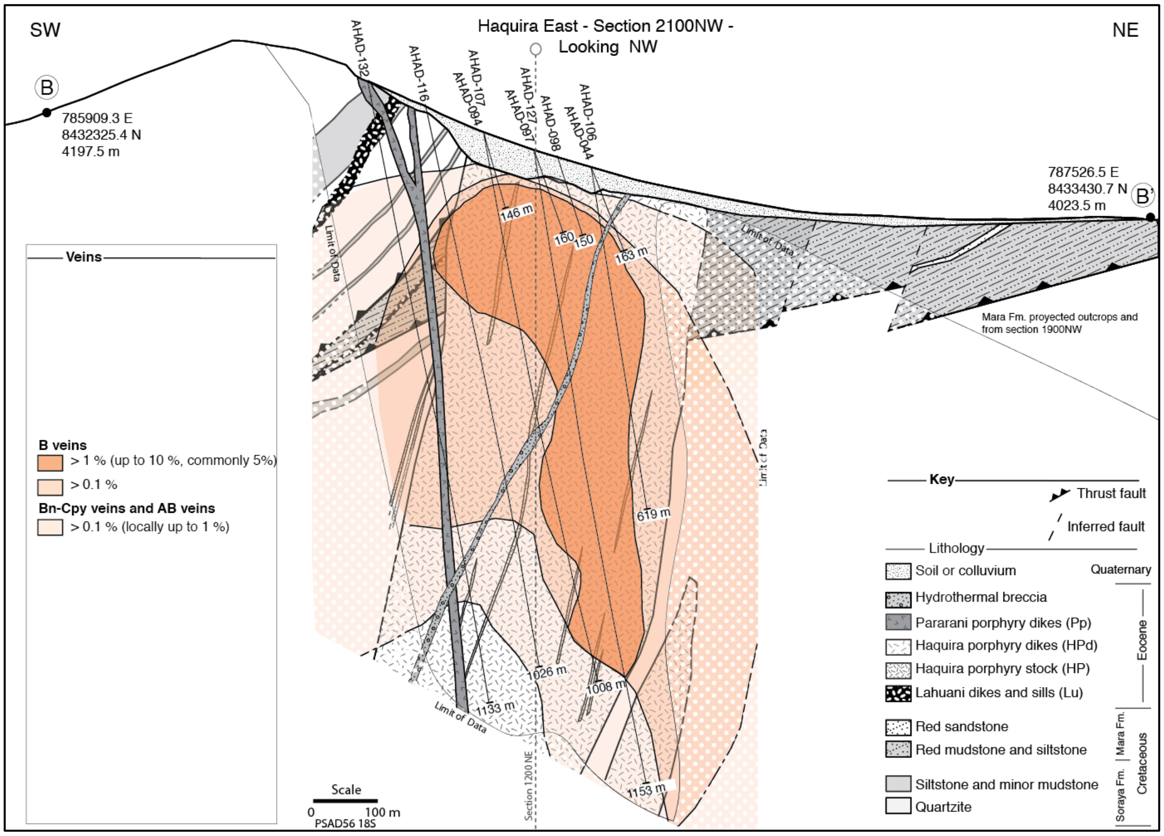
SW
Haquira East - Section 2100NW - Looking NW
NE
B
785909.3 E
8432325.4 N
4197.5 m
787526.5 E
8433430.7 N
4023.5 m
B'
AHAD-132
AHAD-116
AHAD-107
AHAD-094
AHAD-127
AHAD-097
AHAD-098
AHAD-106
AHAD-044
146 m
160
150
163 m
619 m
1026 m
1008 m
1133 m
1153 m
Limit of Data
Limit of Data
Limit of Data
Limit of Data
Mara Fm. proyected outcrops and from section 1900NW
Section 1200 NE
Veins
B veins
> 1 % (up to 10 %, commonly 5%)
> 0.1 %
Bn-Cpy veins and AB veins
> 0.1 % (locally up to 1 %)
Scale
0
100 m
PSAD56 18S
Key
Thrust fault
Inferred fault
Lithology
Soil or colluvium
Quaternary
Hydrothermal breccia
Pararani porphyry dikes (Pp)
Haquira porphyry dikes (HPd)
Haquira porphyry stock (HP)
Lahuani dikes and sills (Lu)
Eocene
Red sandstone
Red mudstone and siltstone
Mara Fm.
Siltstone and minor mudstone
Quartzite
Soraya Fm.
Cretaceous

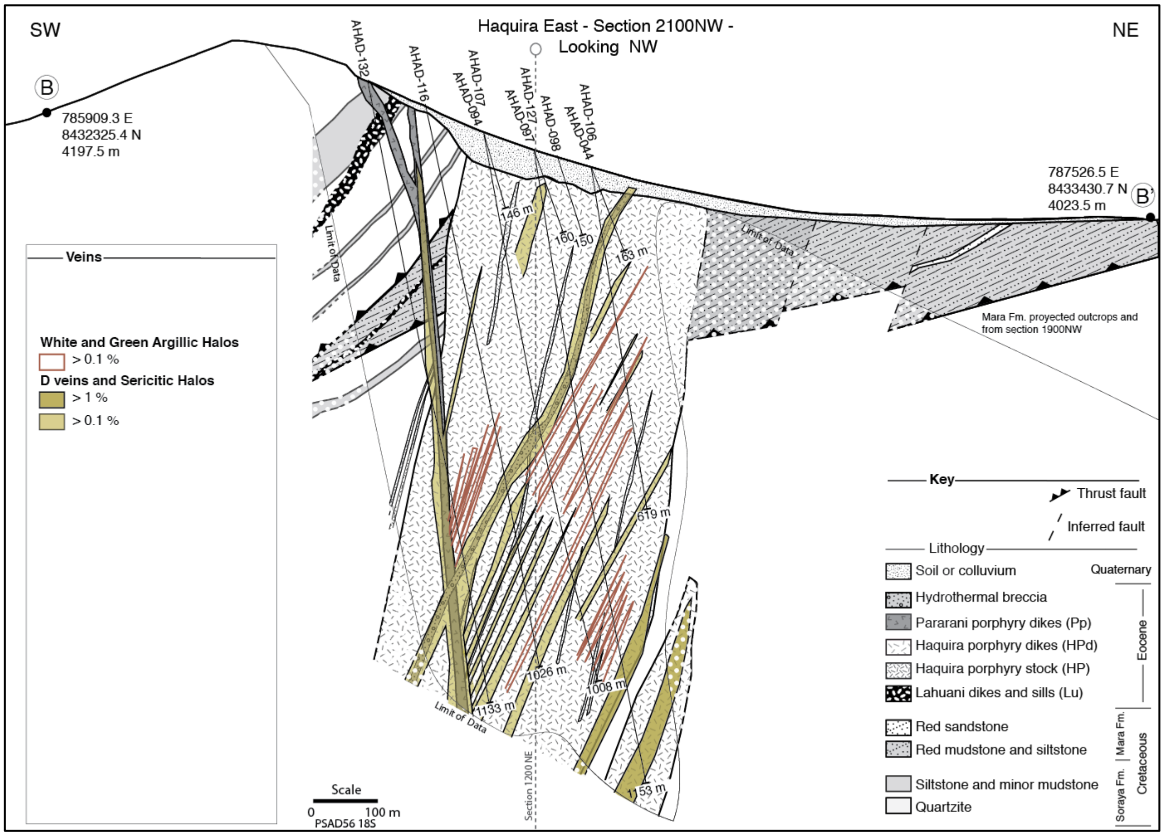
SW
NE
Haquira East - Section 2100NW - Looking NW
B
785909.3 E
8432325.4 N
4197.5 m
B'
787526.5 E
8433430.7 N
4023.5 m
AHAD-132
AHAD-116
AHAD-107
AHAD-094
AHAD-127
AHAD-097
AHAD-098
AHAD-106
AHAD-044
146 m
150
150
163 m
619 m
1026 m
1008 m
1133 m
1153 m
Limit of Data
Limit of Data
Limit of Data
Section 1200 NE
Mara Fm. proyected outcrops and from section 1900NW
Veins
White and Green Argillic Halos
> 0.1 %
D veins and Sericitic Halos
> 1 %
> 0.1 %
Key
Thrust fault
Inferred fault
Lithology
Soil or colluvium
Quaternary
Hydrothermal breccia
Pararani porphyry dikes (Pp)
Haquira porphyry dikes (HPd)
Haquira porphyry stock (HP)
Lahuani dikes and sills (Lu)
Eocene
Red sandstone
Red mudstone and siltstone
Mara Fm.
Siltstone and minor mudstone
Quartzite
Soraya Fm.
Cretaceous
Scale
0
100 m
PSAD56 18S

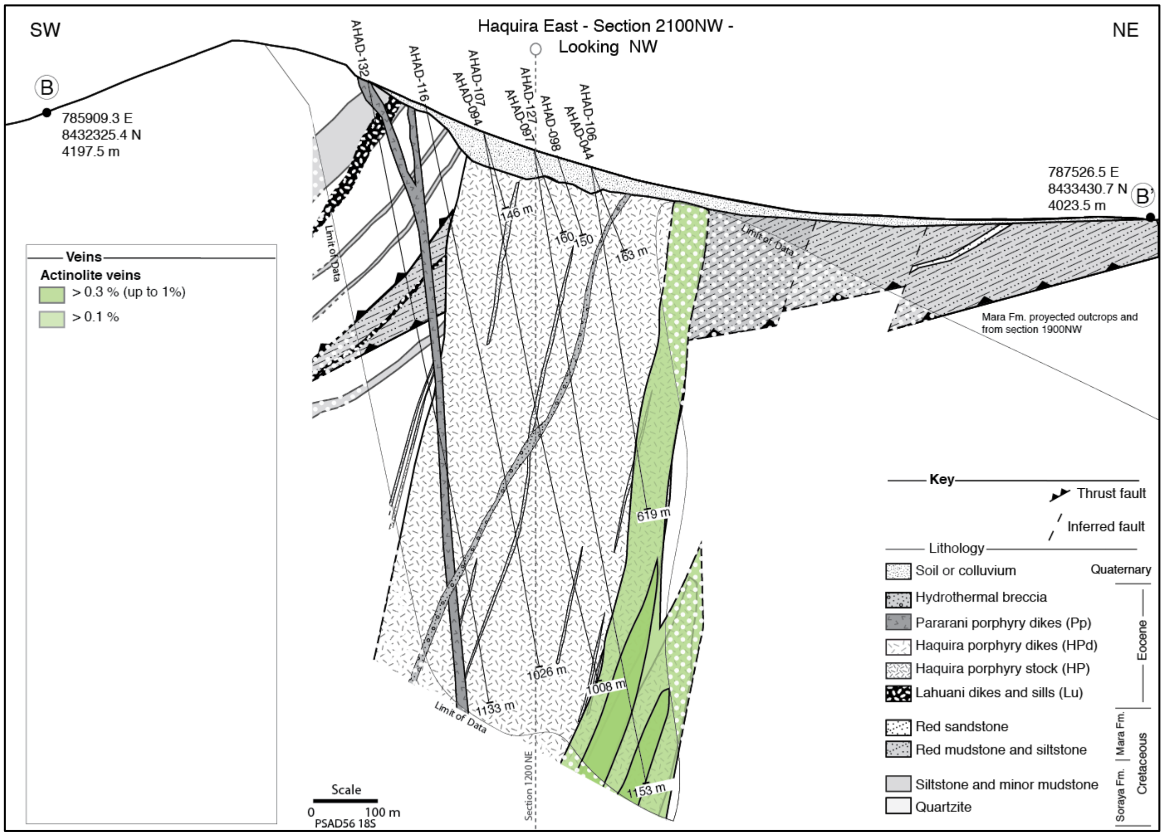
SW
NE
Haquira East - Section 2100NW - Looking NW
B
785909.3 E
8432325.4 N
4197.5 m
B'
787526.5 E
8433430.7 N
4023.5 m
AHAD-132
AHAD-116
AHAD-107
AHAD-094
AHAD-127
AHAD-097
AHAD-098
AHAD-106
AHAD-044
146 m
150
150
163 m
619 m
1026 m
1008 m
1133 m
1153 m
Limit of Data
Limit of Data
Limit of Data
Section 1200 NE
Mara Fm. proyected outcrops and from section 1900NW
Veins
Actinolite veins
> 0.3 % (up to 1%)
> 0.1 %
Key
Thrust fault
Inferred fault
Lithology
Soil or colluvium
Quaternary
Hydrothermal breccia
Pararani porphyry dikes (Pp)
Haquira porphyry dikes (HPd)
Haquira porphyry stock (HP)
Lahuani dikes and sills (Lu)
Eocene
Red sandstone
Red mudstone and siltstone
Mara Fm.
Siltstone and minor mudstone
Quartzite
Soraya Fm.
Cretaceous
Scale
0
100 m
PSAD56 18S

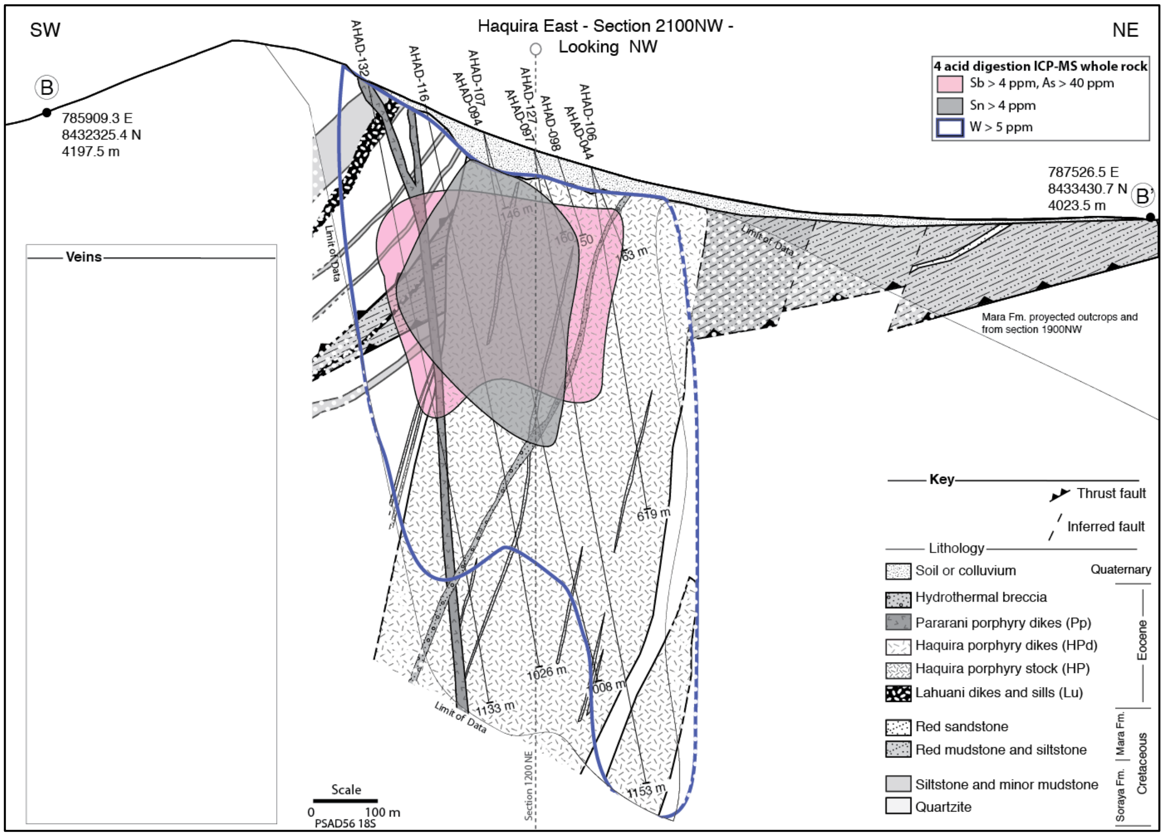
SW
Haquira East - Section 2100NW - Looking NW
NE
B
785909.3 E
8432325.4 N
4197.5 m
787526.5 E
8433430.7 N
4023.5 m
B'
AHAD-132
AHAD-116
AHAD-107
AHAD-094
AHAD-127
AHAD-097
AHAD-098
AHAD-106
AHAD-044
4 acid digestion ICP-MS whole rock
Sb > 4 ppm, As > 40 ppm
Sn > 4 ppm
W > 5 ppm
Veins
Limit of Data
146 m
160
50
163 m
619 m
1026 m
1008 m
1133 m
1153 m
Mara Fm. proyected outcrops and from section 1900NW
Key
Thrust fault
Inferred fault
Lithology
Soil or colluvium
Quaternary
Hydrothermal breccia
Pararani porphyry dikes (Pp)
Haquira porphyry dikes (HPd)
Haquira porphyry stock (HP)
Lahuani dikes and sills (Lu)
Eocene
Red sandstone
Red mudstone and siltstone
Mara Fm.
Siltstone and minor mudstone
Quartzite
Soraya Fm.
Cretaceous
Scale
0
100 m
PSAD56 18S
Section 1200 NE

APPENDIX 3
Cross-section 1200NE

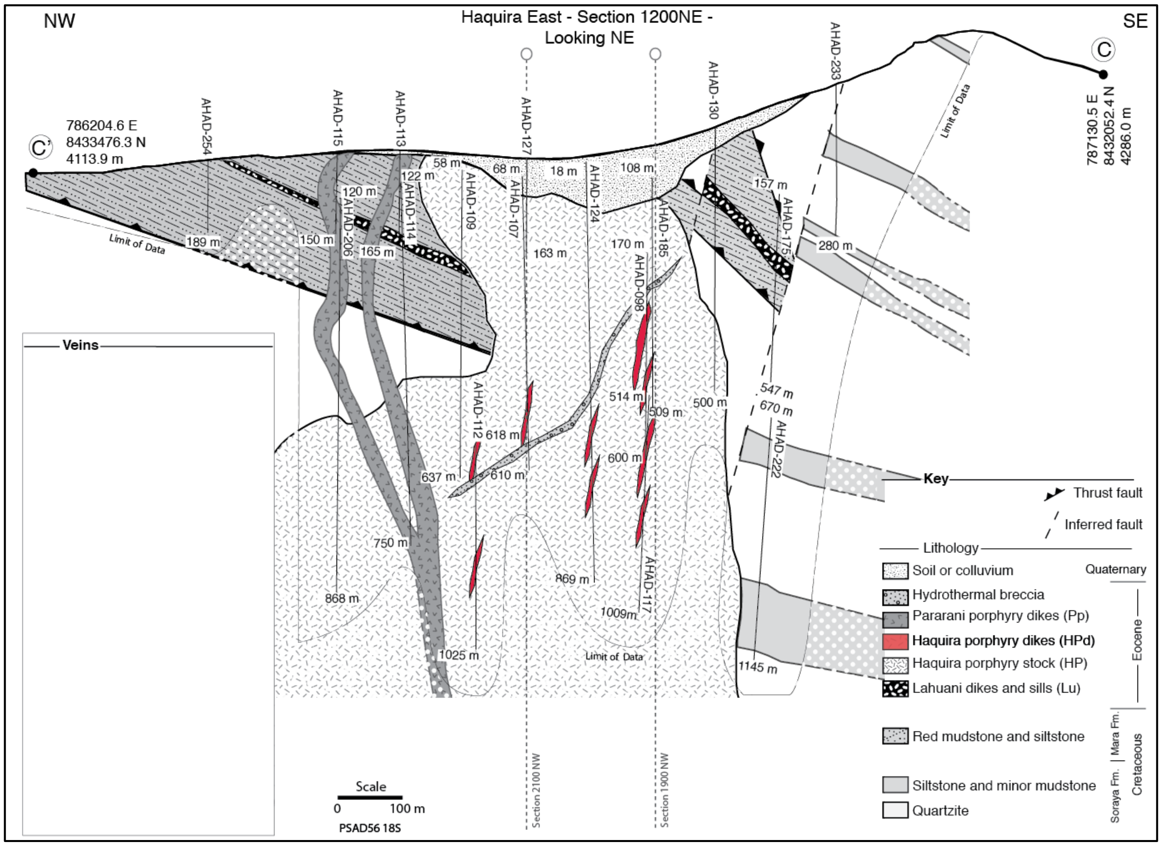
NW
Haquira East - Section 1200NE - Looking NE
SE
C'
786204.6 E
8433476.3 N
4113.9 m
C
787130.5 E
8432052.4 N
4286.0 m
AHAD-254
AHAD-115
AHAD-113
AHAD-127
AHAD-130
AHAD-233
AHAD-206
AHAD-114
AHAD-109
AHAD-107
AHAD-124
AHAD-185
AHAD-098
AHAD-175
AHAD-112
AHAD-117
AHAD-222
58 m
68 m
18 m
108 m
120 m
122 m
150 m
165 m
189 m
163 m
170 m
157 m
280 m
514 m
509 m
500 m
547 m
670 m
618 m
600 m
637 m
610 m
750 m
869 m
868 m
1009m
1025 m
1145 m
Limit of Data
Limit of Data
Limit of Data
Veins
Scale
0
100 m
PSAD56 18S
Section 2100 NW
Section 1900 NW
Key
Thrust fault
Inferred fault
Lithology
Soil or colluvium
Quaternary
Hydrothermal breccia
Pararani porphyry dikes (Pp)
Haquira porphyry dikes (HPd)
Haquira porphyry stock (HP)
Lahuani dikes and sills (Lu)
Eocene
Red mudstone and siltstone
Mara Fm.
Siltstone and minor mudstone
Quartzite
Soraya Fm.
Cretaceous

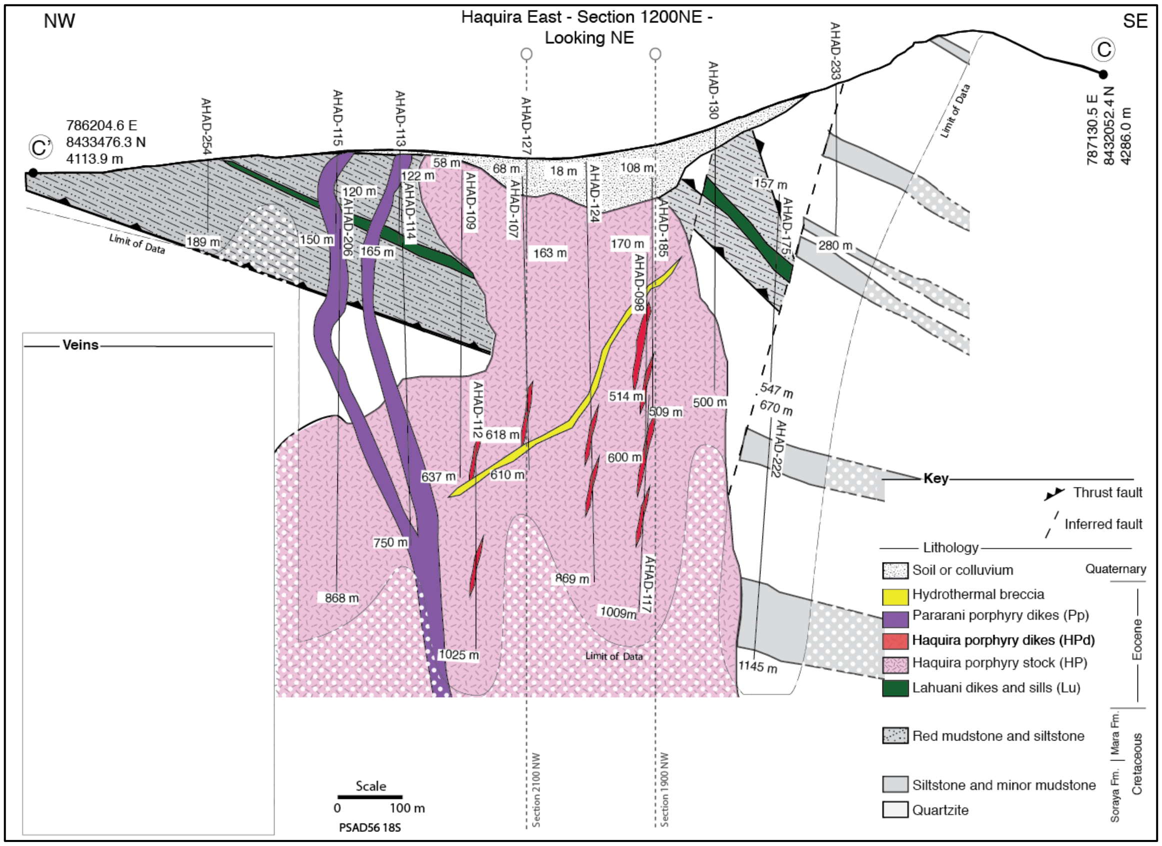
NW
Haquira East - Section 1200NE - Looking NE
SE
C'
786204.6 E
8433476.3 N
4113.9 m
C
787130.5 E
8432052.4 N
4286.0 m
AHAD-254
AHAD-115
AHAD-113
AHAD-127
AHAD-130
AHAD-233
AHAD-206
AHAD-114
AHAD-109
AHAD-107
AHAD-124
AHAD-185
AHAD-098
AHAD-175
AHAD-112
AHAD-117
AHAD-222
58 m
68 m
18 m
108 m
120 m
122 m
150 m
165 m
189 m
163 m
170 m
157 m
280 m
514 m
509 m
500 m
547 m
670 m
618 m
600 m
637 m
610 m
750 m
869 m
868 m
1009m
1025 m
1145 m
Limit of Data
Limit of Data
Limit of Data
Veins
Scale
0
100 m
PSAD56 18S
Section 2100 NW
Section 1900 NW
Key
Thrust fault
Inferred fault
Lithology
Soil or colluvium
Quaternary
Hydrothermal breccia
Pararani porphyry dikes (Pp)
Haquira porphyry dikes (HPd)
Haquira porphyry stock (HP)
Lahuani dikes and sills (Lu)
Eocene
Red mudstone and siltstone
Mara Fm.
Siltstone and minor mudstone
Quartzite
Soraya Fm.
Cretaceous

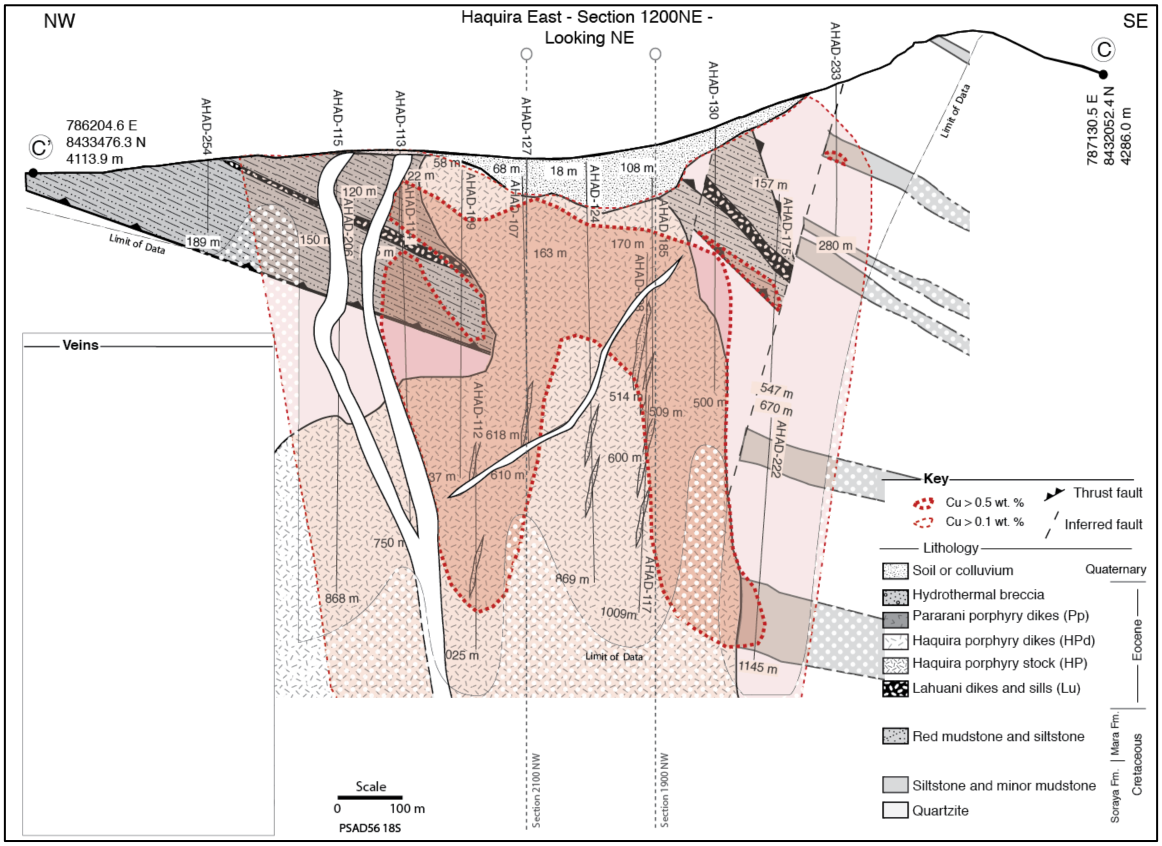
NW
Haquira East - Section 1200NE -
Looking NE
SE
C'
786204.6 E
8433476.3 N
4113.9 m
C
787130.5 E
8432052.4 N
4286.0 m
AHAD-254
AHAD-115
AHAD-113
AHAD-127
AHAD-130
AHAD-233
AHAD-206
AHAD-114
AHAD-109
AHAD-107
AHAD-124
AHAD-185
AHAD-175
AHAD-112
AHAD-117
AHAD-222
Limit of Data
Veins
Key
Cu > 0.5 wt. %
Cu > 0.1 wt. %
Thrust fault
Inferred fault
Lithology
Soil or colluvium
Hydrothermal breccia
Pararani porphyry dikes (Pp)
Haquira porphyry dikes (HPd)
Haquira porphyry stock (HP)
Lahuani dikes and sills (Lu)
Red mudstone and siltstone
Siltstone and minor mudstone
Quartzite
Quaternary
Eocene
Mara Fm.
Soraya Fm.
Cretaceous
Scale
0
100 m
PSAD56 18S
Section 2100 NW
Section 1900 NW

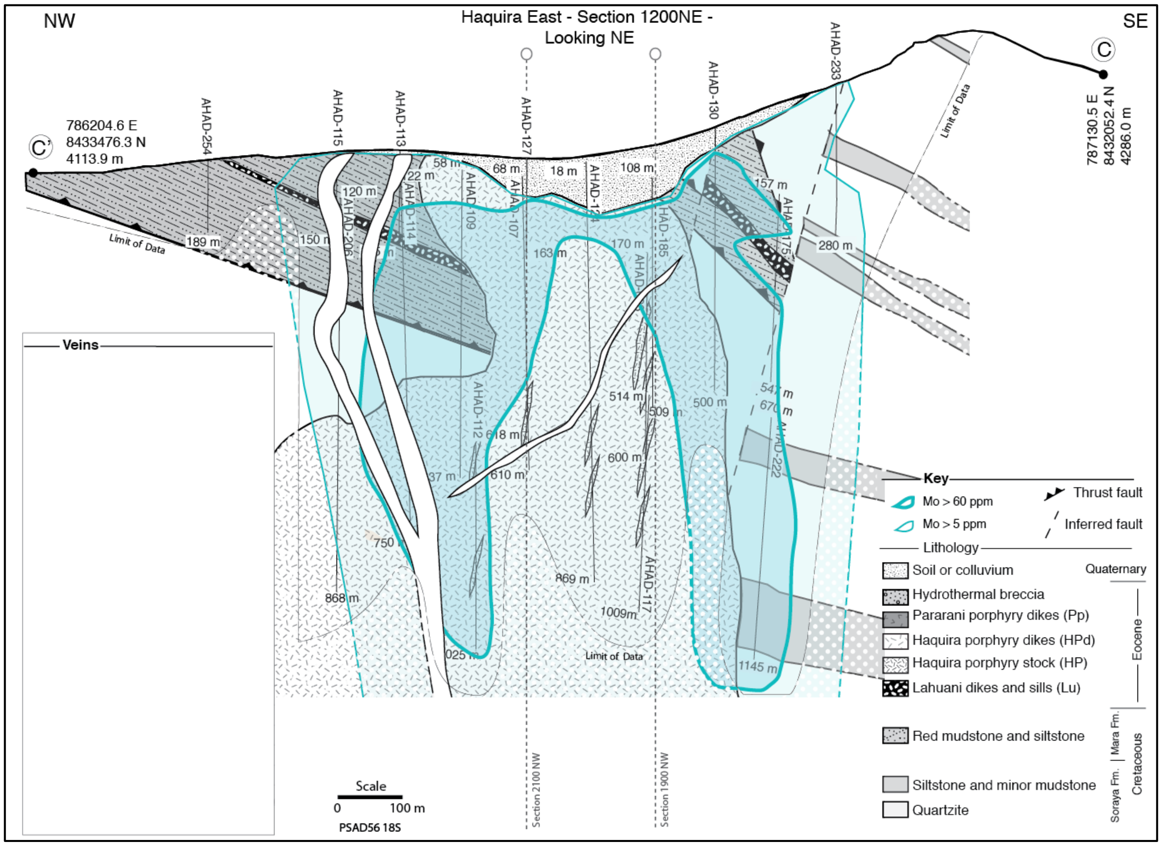
NW
Haquira East - Section 1200NE -
Looking NE
SE
C'
786204.6 E
8433476.3 N
4113.9 m
C
787130.5 E
8432052.4 N
4286.0 m
AHAD-254
AHAD-115
AHAD-113
AHAD-127
AHAD-130
AHAD-233
Limit of Data
Veins
Key
Mo > 60 ppm
Mo > 5 ppm
Thrust fault
Inferred fault
Lithology
Soil or colluvium
Hydrothermal breccia
Pararani porphyry dikes (Pp)
Haquira porphyry dikes (HPd)
Haquira porphyry stock (HP)
Lahuani dikes and sills (Lu)
Red mudstone and siltstone
Siltstone and minor mudstone
Quartzite
Quaternary
Eocene
Mara Fm.
Soraya Fm.
Cretaceous
Scale
0
100 m
PSAD56 18S
Section 2100 NW
Section 1900 NW

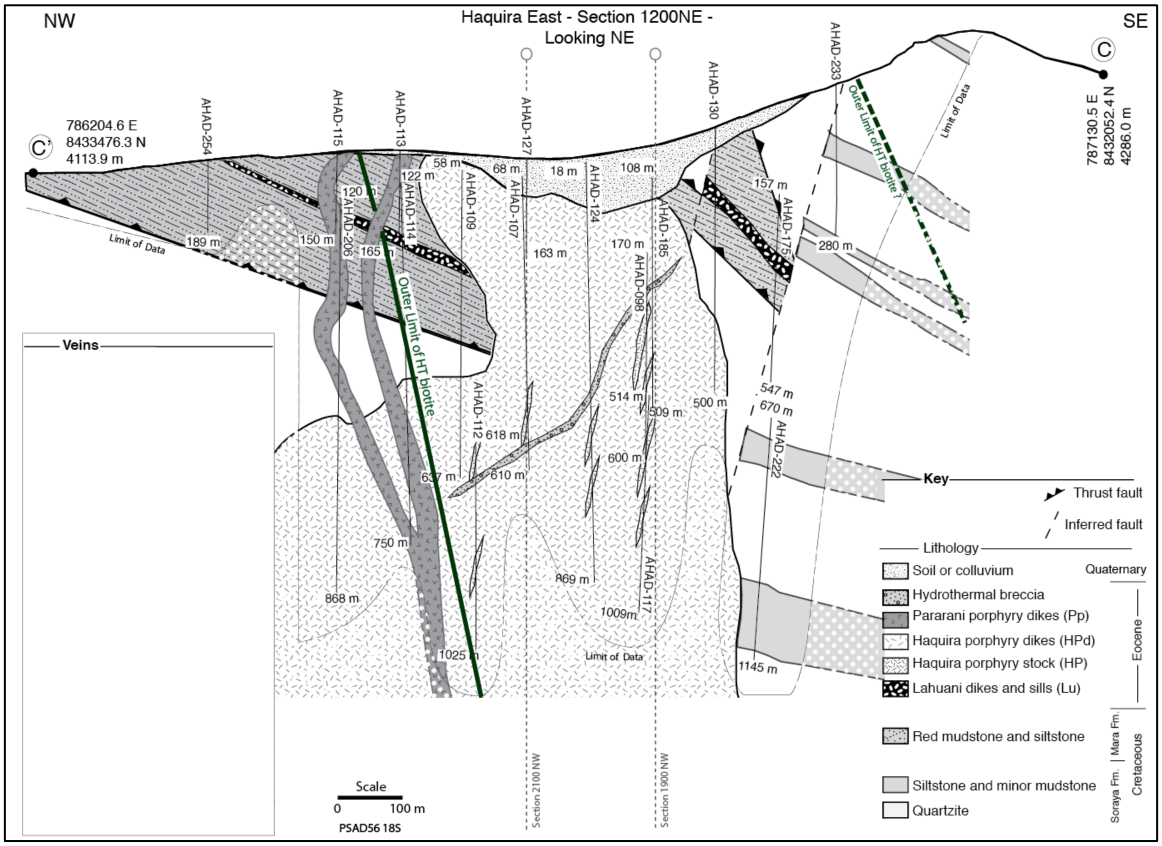
NW
Haquira East - Section 1200NE - Looking NE
SE
C'
786204.6 E
8433476.3 N
4113.9 m
C
787130.5 E
8432052.4 N
4286.0 m
AHAD-254
AHAD-115
AHAD-113
AHAD-127
AHAD-130
AHAD-233
AHAD-206
AHAD-114
AHAD-109
AHAD-107
AHAD-124
AHAD-185
AHAD-098
AHAD-175
AHAD-112
AHAD-117
AHAD-222
58 m
68 m
18 m
108 m
122 m
120 m
150 m
165 m
189 m
163 m
170 m
157 m
280 m
514 m
509 m
500 m
547 m
670 m
618 m
637 m
610 m
600 m
750 m
868 m
869 m
1009m
1025 m
1145 m
Outer Limit of HT biotite
Outer Limit of HT biotite ?
Limit of Data
Veins
Scale
0
100 m
PSAD56 18S
Section 2100 NW
Section 1900 NW
Key
Thrust fault
Inferred fault
Lithology
Soil or colluvium
Quaternary
Hydrothermal breccia
Pararani porphyry dikes (Pp)
Haquira porphyry dikes (HPd)
Haquira porphyry stock (HP)
Lahuani dikes and sills (Lu)
Eocene
Red mudstone and siltstone
Mara Fm.
Siltstone and minor mudstone
Quartzite
Soraya Fm.
Cretaceous

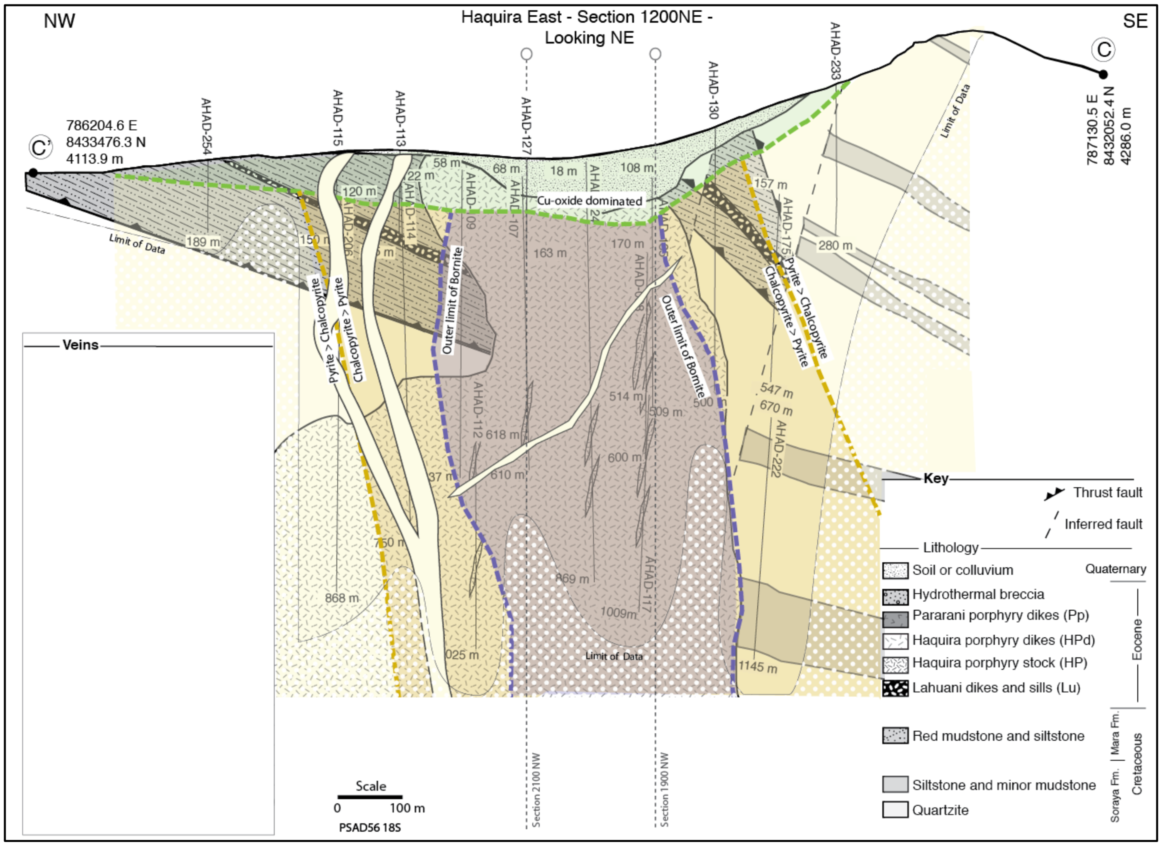
NW
Haquira East - Section 1200NE - Looking NE
SE
C'
786204.6 E
8433476.3 N
4113.9 m
C
787130.5 E
8432052.4 N
4286.0 m
AHAD-254
AHAD-115
AHAD-113
AHAD-127
AHAD-130
AHAD-233
Cu-oxide dominated
Pyrite > Chalcopyrite
Chalcopyrite > Pyrite
Outer limit of Bornite
Outer limit of Bornite
Chalcopyrite > Pyrite
Pyrite > Chalcopyrite
58 m
68 m
18 m
108 m
120 m
189 m
163 m
170 m
157 m
280 m
514 m
509 m
547 m
670 m
618 m
610 m
600 m
750 m
868 m
869 m
1009m
1145 m
Limit of Data
Veins
Scale
0
100 m
PSAD56 18S
Section 2100 NW
Section 1900 NW
Key
Thrust fault
Inferred fault
Lithology
Soil or colluvium
Quaternary
Hydrothermal breccia
Pararani porphyry dikes (Pp)
Haquira porphyry dikes (HPd)
Haquira porphyry stock (HP)
Lahuani dikes and sills (Lu)
Eocene
Red mudstone and siltstone
Mara Fm.
Siltstone and minor mudstone
Quartzite
Soraya Fm.
Cretaceous

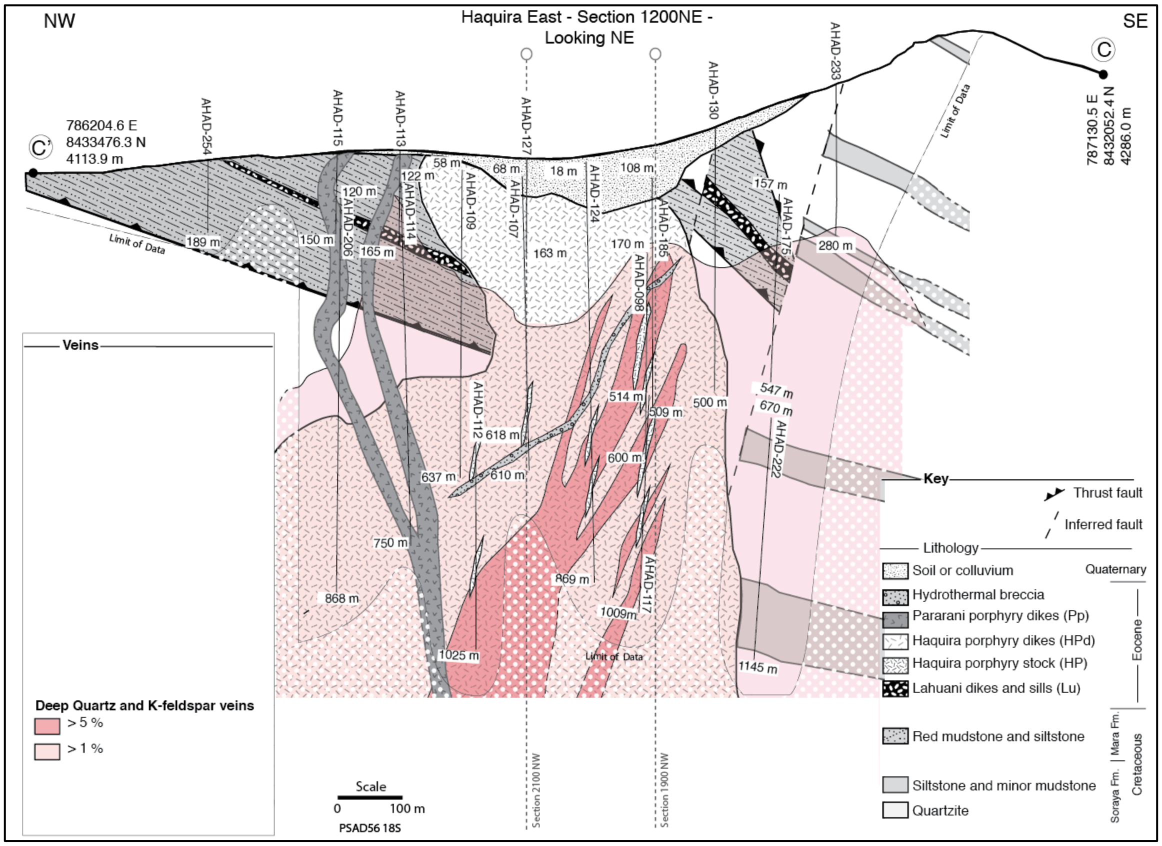
NW
Haquira East - Section 1200NE -
Looking NE
SE
C'
786204.6 E
8433476.3 N
4113.9 m
C
787130.5 E
8432052.4 N
4286.0 m
AHAD-254
AHAD-115
AHAD-113
AHAD-127
AHAD-130
AHAD-233
AHAD-206
AHAD-114
AHAD-109
AHAD-107
AHAD-124
AHAD-185
AHAD-098
AHAD-175
AHAD-112
AHAD-117
AHAD-222
58 m
68 m
18 m
108 m
120 m
122 m
157 m
189 m
150 m
165 m
163 m
170 m
280 m
514 m
509 m
500 m
547 m
670 m
618 m
600 m
637 m
610 m
750 m
869 m
868 m
1009m
1025 m
1145 m
Limit of Data
Veins
Deep Quartz and K-feldspar veins
> 5 %
> 1 %
Scale
0
100 m
PSAD56 18S
Section 2100 NW
Section 1900 NW
Key
Thrust fault
Inferred fault
Lithology
Soil or colluvium
Quaternary
Hydrothermal breccia
Pararani porphyry dikes (Pp)
Haquira porphyry dikes (HPd)
Haquira porphyry stock (HP)
Lahuani dikes and sills (Lu)
Eocene
Red mudstone and siltstone
Mara Fm.
Siltstone and minor mudstone
Quartzite
Soraya Fm.
Cretaceous

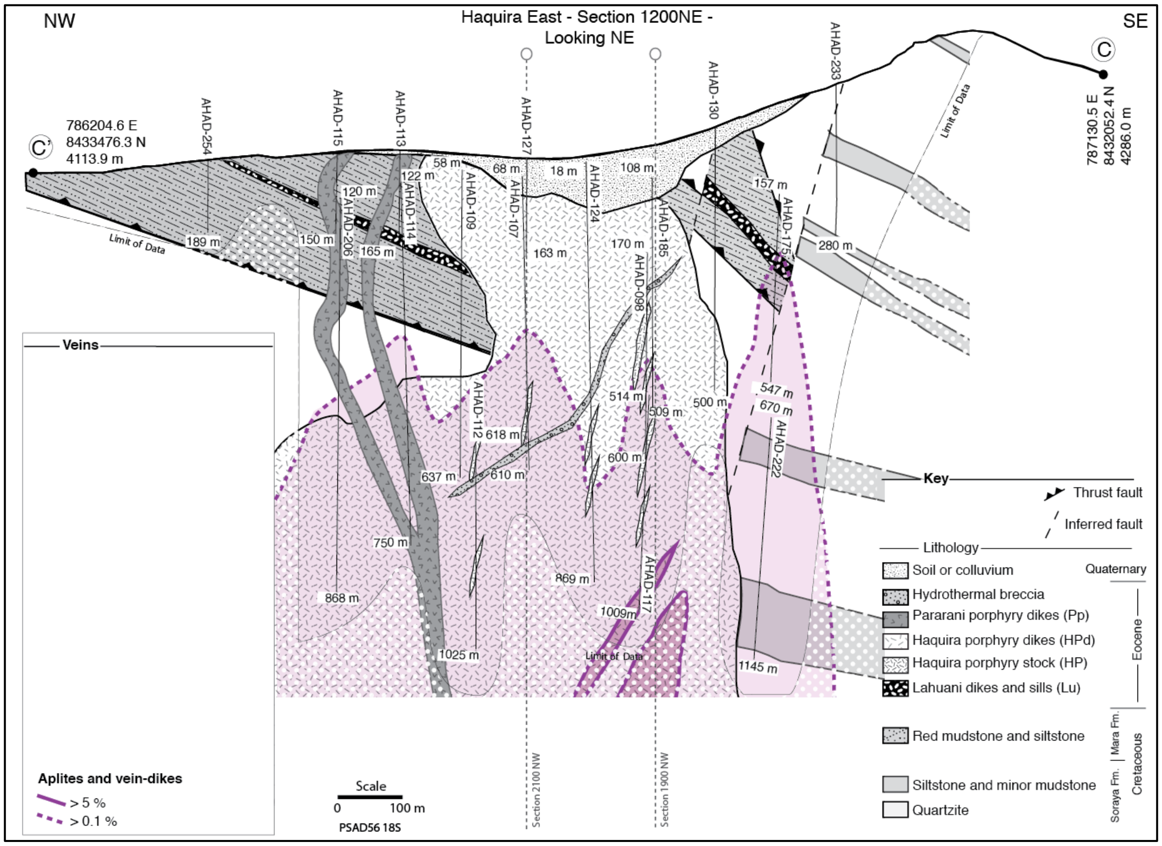
NW
Haquira East - Section 1200NE -
Looking NE
SE
C'
786204.6 E
8433476.3 N
4113.9 m
C
787130.5 E
8432052.4 N
4286.0 m
AHAD-254
AHAD-115
AHAD-113
AHAD-127
AHAD-130
AHAD-233
AHAD-206
AHAD-114
AHAD-109
AHAD-107
AHAD-124
AHAD-185
AHAD-098
AHAD-175
AHAD-112
AHAD-117
AHAD-222
58 m
68 m
18 m
108 m
120 m
122 m
157 m
189 m
150 m
165 m
163 m
170 m
280 m
514 m
509 m
500 m
547 m
670 m
618 m
600 m
637 m
610 m
750 m
869 m
868 m
1009m
1025 m
1145 m
Limit of Data
Veins
Aplites and vein-dikes
> 5 %
> 0.1 %
Scale
0
100 m
PSAD56 18S
Section 2100 NW
Section 1900 NW
Key
Thrust fault
Inferred fault
Lithology
Soil or colluvium
Quaternary
Hydrothermal breccia
Pararani porphyry dikes (Pp)
Haquira porphyry dikes (HPd)
Haquira porphyry stock (HP)
Lahuani dikes and sills (Lu)
Eocene
Red mudstone and siltstone
Mara Fm.
Siltstone and minor mudstone
Quartzite
Soraya Fm.
Cretaceous

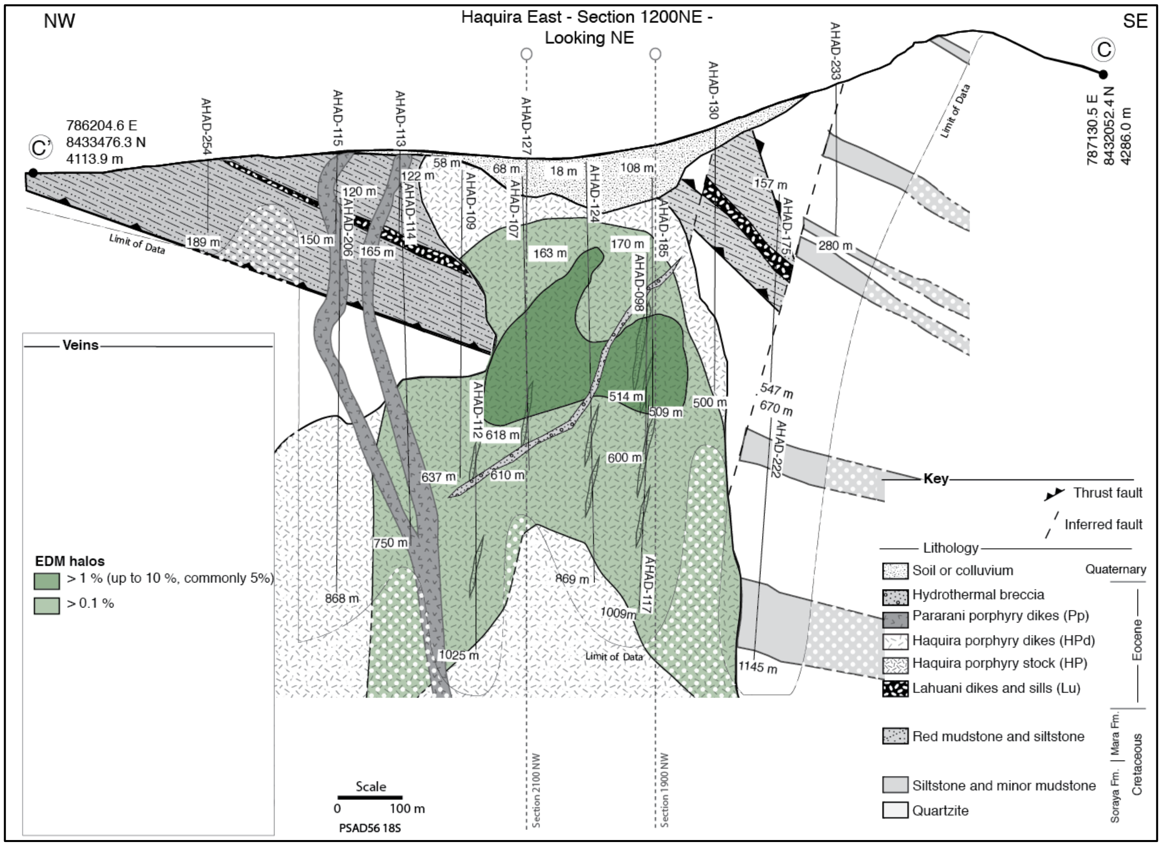
NW
Haquira East - Section 1200NE - Looking NE
SE
C'
786204.6 E
8433476.3 N
4113.9 m
C
787130.5 E
8432052.4 N
4286.0 m
AHAD-254
AHAD-115
AHAD-113
AHAD-127
AHAD-130
AHAD-233
AHAD-206
AHAD-114
AHAD-109
AHAD-107
AHAD-124
AHAD-185
AHAD-098
AHAD-175
AHAD-112
AHAD-222
AHAD-117
58 m
68 m
18 m
108 m
120 m
122 m
157 m
150 m
165 m
189 m
163 m
170 m
280 m
514 m
509 m
500 m
547 m
670 m
618 m
637 m
610 m
600 m
750 m
869 m
868 m
1009m
1025 m
1145 m
Limit of Data
Limit of Data
Limit of Data
Veins
EDM halos
> 1 % (up to 10 %, commonly 5%)
> 0.1 %
Key
Thrust fault
Inferred fault
Lithology
Soil or colluvium
Quaternary
Hydrothermal breccia
Pararani porphyry dikes (Pp)
Haquira porphyry dikes (HPd)
Haquira porphyry stock (HP)
Lahuani dikes and sills (Lu)
Eocene
Red mudstone and siltstone
Mara Fm.
Siltstone and minor mudstone
Quartzite
Soraya Fm.
Cretaceous
Scale
0
100 m
PSAD56 18S
Section 2100 NW
Section 1900 NW

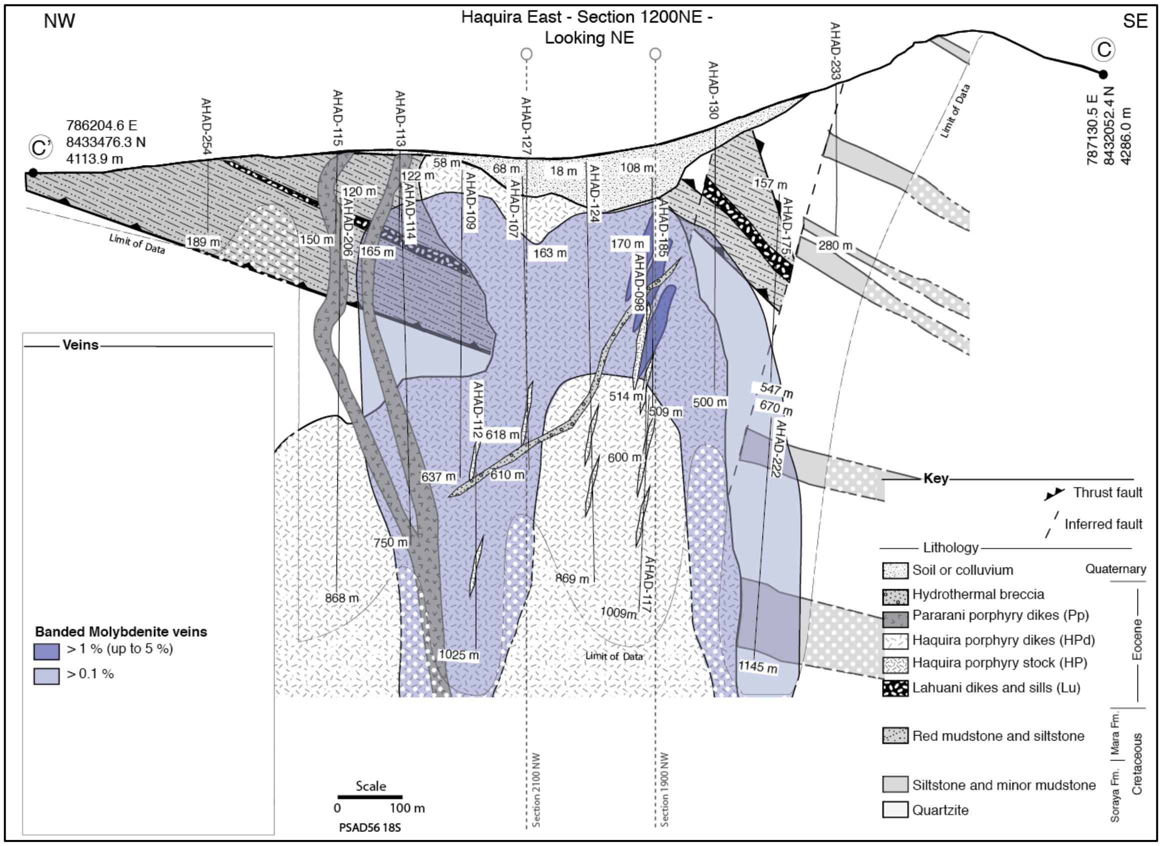
NW
Haquira East - Section 1200NE - Looking NE
SE
C'
786204.6 E
8433476.3 N
4113.9 m
C
787130.5 E
8432052.4 N
4286.0 m
AHAD-254
AHAD-115
AHAD-113
AHAD-127
AHAD-130
AHAD-233
AHAD-206
AHAD-114
AHAD-109
AHAD-107
AHAD-124
AHAD-185
AHAD-098
AHAD-175
AHAD-112
AHAD-222
AHAD-117
58 m
68 m
18 m
108 m
120 m
122 m
157 m
150 m
165 m
189 m
163 m
170 m
280 m
514 m
509 m
500 m
547 m
670 m
618 m
637 m
610 m
600 m
750 m
869 m
868 m
1009m
1025 m
1145 m
Limit of Data
Limit of Data
Limit of Data
Veins
Banded Molybdenite veins
> 1 % (up to 5 %)
> 0.1 %
Key
Thrust fault
Inferred fault
Lithology
Soil or colluvium
Quaternary
Hydrothermal breccia
Pararani porphyry dikes (Pp)
Haquira porphyry dikes (HPd)
Haquira porphyry stock (HP)
Lahuani dikes and sills (Lu)
Eocene
Red mudstone and siltstone
Mara Fm.
Siltstone and minor mudstone
Quartzite
Soraya Fm.
Cretaceous
Scale
0
100 m
PSAD56 18S
Section 2100 NW
Section 1900 NW

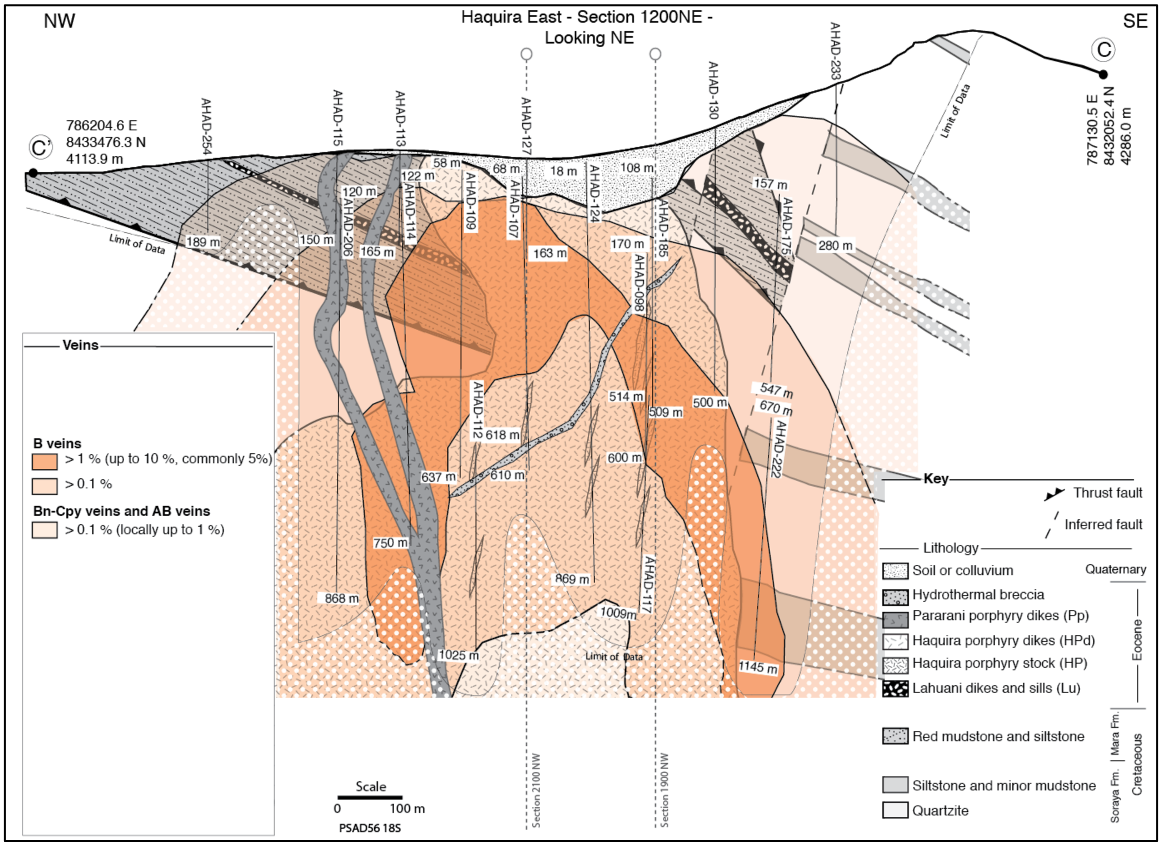
NW
Haquira East - Section 1200NE -
Looking NE
SE
C
C'
786204.6 E
8433476.3 N
4113.9 m
787130.5 E
8432052.4 N
4286.0 m
AHAD-254
AHAD-115
AHAD-113
AHAD-127
AHAD-130
AHAD-233
AHAD-206
AHAD-114
AHAD-109
AHAD-107
AHAD-124
AHAD-185
AHAD-098
AHAD-175
AHAD-112
AHAD-117
AHAD-222
58 m
68 m
18 m
108 m
122 m
120 m
150 m
165 m
163 m
170 m
157 m
189 m
280 m
514 m
509 m
500 m
547 m
670 m
618 m
610 m
600 m
637 m
750 m
868 m
869 m
1009m
1025 m
1145 m
Limit of Data
Veins
B veins
> 1 % (up to 10 %, commonly 5%)
> 0.1 %
Bn-Cpy veins and AB veins
> 0.1 % (locally up to 1 %)
Key
Thrust fault
Inferred fault
Lithology
Soil or colluvium
Quaternary
Hydrothermal breccia
Pararani porphyry dikes (Pp)
Haquira porphyry dikes (HPd)
Haquira porphyry stock (HP)
Lahuani dikes and sills (Lu)
Eocene
Red mudstone and siltstone
Mara Fm.
Siltstone and minor mudstone
Quartzite
Soraya Fm.
Cretaceous
Scale
0
100 m
PSAD56 18S
Section 2100 NW
Section 1900 NW

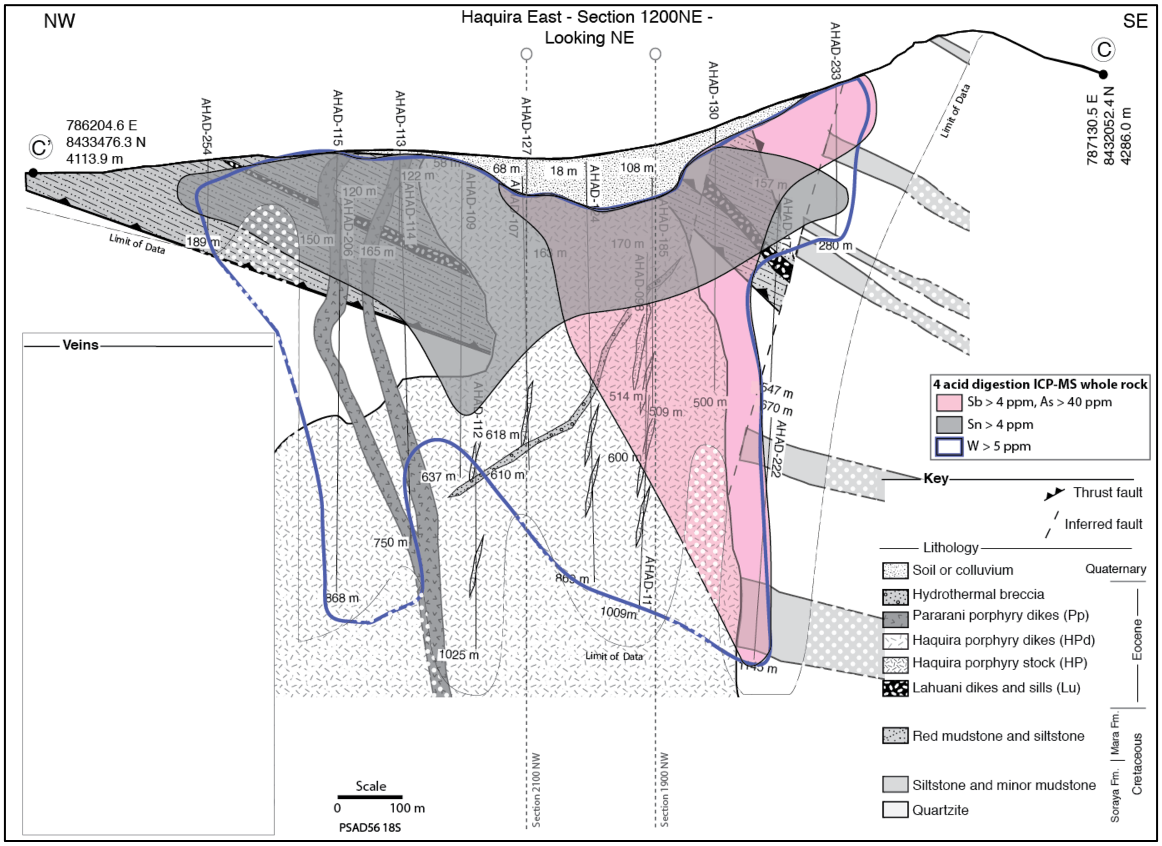
NW
Haquira East - Section 1200NE -
Looking NE
SE
C
C'
786204.6 E
8433476.3 N
4113.9 m
787130.5 E
8432052.4 N
4286.0 m
AHAD-254
AHAD-115
AHAD-113
AHAD-127
AHAD-130
AHAD-233
AHAD-206
AHAD-114
AHAD-109
AHAD-107
AHAD-124
AHAD-185
AHAD-098
AHAD-175
AHAD-112
AHAD-117
AHAD-222
58 m
68 m
18 m
108 m
122 m
120 m
150 m
165 m
163 m
170 m
157 m
189 m
280 m
514 m
509 m
500 m
547 m
670 m
618 m
610 m
600 m
637 m
750 m
868 m
869 m
1009m
1025 m
1145 m
Limit of Data
Veins
4 acid digestion ICP-MS whole rock
Sb > 4 ppm, As > 40 ppm
Sn > 4 ppm
W > 5 ppm
Key
Thrust fault
Inferred fault
Lithology
Soil or colluvium
Quaternary
Hydrothermal breccia
Pararani porphyry dikes (Pp)
Haquira porphyry dikes (HPd)
Haquira porphyry stock (HP)
Lahuani dikes and sills (Lu)
Eocene
Red mudstone and siltstone
Mara Fm.
Siltstone and minor mudstone
Quartzite
Soraya Fm.
Cretaceous
Scale
0
100 m
PSAD56 18S
Section 2100 NW
Section 1900 NW

APPENDIX 4
Supplementary data and figures for chapter 5

1) INTRODUCTION

Porphyry Cu±Mo±Au Deposits

Porphyry-type deposits include porphyry Cu±Mo±Au deposits in which copper is the chief economic metal. These deposits are large, ranging from <100 Mt (million metric tons) to >5 Bt (million metric tons) ore materials grading from <0.2 to >1.2 wt.% Cu with variable amounts of Mo and Au. The largest single deposit, albeit formed in multiple temporally spaced hydrothermal events introduced over several million years, is the El Teniente deposit, Chile (~96 Mt contained Cu), and perhaps the largest single hydrothermal event (<100,000 years; von Quadt *et al.,* 2011) is the Bingham, Utah, Cu-Au orebody (~28 Mt contained Cu).

In well-exposed porphyry deposits, a deep source intrusion, commonly estimated at >50 km^3 but as much as 500 km^3 (Ruby Star Granodiorite: Stavast *et al.,* 2008; El Abra Fiesta Granodiorite; Brimhall *et al.,* 2006; Dilles *et al.,* 2011) that is an equigranular granitoid is commonly exposed (see Burnham, 1979). These intrusions range from quartz diorite to granite to monzonite, and span the range from Na-rich to K-rich calc-alkaline to alkaline. Most intrusions are metaluminous, but some are weakly peraluminous or near the boundary of metaluminous to peralkaline (Seedorff *et al.,* 2005). The deep granitoid is the source of porphyry dikes of identical composition but with a porphyritic texture characterized by ~50 vol.% fine-grained groundmass that is commonly <0.1 mm in grain size, granitic in composition, and aplitic in texture. Such aplite represents a pressure-quench via water-vapor loss on ascent of magma at relatively low temperature (~700°C) (Burnham, 1979; Dilles, 1987). At Yerington and several porphyry deposits in the southwest of the USA, such porphyry dikes can be observed to grade downward into the deep granite, and moreover that younger dikes are more deeply sourced and cross-cut older dikes with slightly coarser groundmass (Dilles, 1987).

As reviewed by Seedorff *et al.* (2005), porphyry deposits may form at a variety of depths in the upper crust ranging from as shallow as ~1 km for copper mineralization (*e.g.*, Batu Hijau, Yerington Mine) to ~10 km (*e.g.*, Butte, Montana; 6-8 km). Shallow deposits are characterized by A type granular quartz-sulfide veins, whereas deep deposits lack these veins but instead contain early dark micaceous (EDM) veins as at Butte (Proffett, 2009). Shallower deposits likely form at slightly lower temperature and presumably may cool more quickly after fluid flow ceases. The range of observed hydrothermal temperatures in such deposits ranges from ~700°C at Butte (Brimhall, 1977; Field *et al.,* 2005; Rusk *et al.,* 2006; Mercer *et al.,* 2013) to about 300°C for late base metal veins associated with strong sericitic alteration (*e.g.* Rusk *et al.,* 2008; Landtwing *et al.,* 2005).

The Haquira East Porphyry Copper Deposit

The Haquira district contains two known porphyry copper centers. Haquira East is the focus of this study (-14.164877º, -72.345922º), and is the subject of the PhD thesis of Federico Cernuschi so many of the relevant parts of the geology are currently being submitted for publication. Haquira East is a moderate-sized porphyry copper deposit with minor Mo and Au that contains measured, indicated, and inferred resources of 689 Mt ore containing 4.2 Mt Cu (~9 B lb), about 37,000 t Mo, and 28 t (0.9 M oz) Au (Antares, 2010). Haquira East is a relatively typical, but also relatively deeply formed porphyry copper deposit. A variety of evidence suggests significant depth at Haquira. A quartz veins are absent, and EDM veins are important contributors to Cu-Mo grades (Cernuschi *et al.,* 2012). Late, low-temperature ~350 °C D pyrite-quartz veins with sericitic selvages and late <300 ℃ pyrite veins with intermediate argillic alteration are rare (affecting <5% of the granodiorite porphyry stock). Fluid inclusions trapped in quartz veins were all trapped in the single phase field, and there are no observations of brine or vapor-rich inclusions indication fluid immiscibility. These inclusion were therefore trapped at >1.0 kb and more likely at >1.4 kb pressure. Fluid inclusion heating / freezing experiments (Brian Rusk, Federico Cernuschi, *unpub.* data) suggest hydrothermal fluids were trapped at pressures in excess of 1.6 kb to as much as ~3 kb, under conditions ranging for lithostatic at high temperature to intermediate between lithostatic and hydrostatic at low temperature. Moreover, geologic considerations also indicate ~10 km depth. Hornblende barometry of a nearby exposed and shallower granodiorite pluton yields a pressure estimates of ~ 2 (±0.5) kb. The Haquira East deposit is hosted in a granodiorite porphyry plug that intrudes a folded and ductily deformed quartzite sequence. Hydrothermal banded molybdenite-quartz (BMQ) veins cutting the quartzite are locally folded, and hydrothermal biotite in the porphyry plug is aligned into a foliation by deformation. This deformation does not affect the last porphyry dikes, which has an isotopic age that is indistinguishable from the earlier porphyries. Therefore, deformation was ongoing during porphyry emplacement, and suggests significant depth and >350°C for the rocks surrounding the deposit. As muscovite has a closure temperature to Ar diffusion of ~325-350°C (depending on grain size), the $^{40}Ar/^{39}Ar$ age of muscovite likely reflects slow cooling after the end of hydrothermal alteration. Hence, the hydrothermal lifespan is likely shorter than the 200,000 to 600,000 year interval defined by the Re-Os age of molybdenite and the $^{40}Ar/^{39}Ar$ age of muscovite. Average of 3 molybdenite ages is 33.75 ± 0.15 Ma and one $^{40}Ar/^{39}Ar$ age of muscovite yields 33.18 ± 0.21 Ma (Cernuschi *et al.*, 2013).

REFERENCES FOR INTRODUCTION

Antares, 2010, Antares press-release: New Haquira global resource. February 26th, 2010. 6 p.

Brimhall, G.H, Dilles, J.H., and Proffett, J.M., Jr., 2006, The role of geologic mapping in mineral exploration, in Doggett, M. D., and Parry, J. R., eds., Wealth creation in the minerals industry: Integrating, science, business, and education: Society of Economic Geologists Special Publication 12, p. 221-241.

Brimhall, G.H, Jr., 1977, Early fracture-controlled disseminated mineralization at Butte, Montana: Economic Geology, v. 72, p. 37-59.

Burnham, C.W., 1979, Magmas and hydrothermal fluids, *in* Barnes, H.L., ed., Geochemistry of hydrothermal ore deposits: New York, Wiley Interscience, v. II, p. 71-136.

Cernuschi, F., Einaudi, M.T, Dilles, J.H., Heather, K.B., and Barr, N.C., 2012, Hydrothermal veins, porphyry geochemistry and mineralization zonation of the Haquira-East porphyry Cu-Mo deposit, Perú: SEG Conference 2012, Lima, Perú.

Cernuschi, F., Dilles, J.H., and Creaser, R., 2013, Hydrothermal alteration, SWIR-mineral mapping, vein distribution and age of the Haquira-East Cu-Mo porphyry: 12th SGA Biennial Meeting 2013, Proceedings, v. 2, p. 782-785.

Dilles, J.H., Tomlison, A.H., Garcia, M., and Alcota, H., 2011, The geology of the Fortuna Granodiorite Complex, Chuquicamata district, Northern Chile. Relation to porphyry copper deposits: 11th SGA Biennial Meeting 2011, Proceedings, v. 2, p. 398-400.

Field, C.W., Zhang, L., Dilles, J.H., Rye, R. O., and Reed, M.H., 2005, Sulfur and oxygen isotopic record in sulfate and sulfide minerals of early, deep, pre-main stage porphyry Cu-Mo and late main stage base-metal mineral deposits, Butte district, Montana: Chemical Geology, v. 215, no. 1-4, p. 61–93.

Landtwing, M.R., Pettke, T., Halter, W.E., Heinrich, C.A., Redmond, P.B., Einaudi, M.T., and Kunze, K., 2005, Copper deposition during quartz dissolution by cooling hydrothermal fluids: The Bingham porphyry: Earth and Planetary Science Letters, v. 235, p. 229-243.

Mercer, C.N., and Reed, M.H., 2013, Porphyry Cu-Mo stockwork formation by dynamic, transient hydrothermal pulses: mineralogic insights from the deposit at Butte, Montana: Economic Geology, v. 108, no. 6, p. 1347–1377.

Proffett, J.M., 2009, High Cu grades in porphyry Cu deposits and their relationship to emplacement depth of magmatic sources: Geology, v. 37 (8), p. 675–678.

Rusk, B.G., Reed, M.H., Dilles, J.H., and Kent, A.J.R., 2006, Intensity of quartz cathodoluminescence and trace element content of quartz from the porphyry copper deposit in Butte, Montana: American Mineralogist, v. 91, p. 1300-1312.

Rusk, B.G., Reed, M.H., and Dilles, J.H., 2008, Fluid inclusion evidence for magmatic-hydrothermal fluid evolution in the porphyry copper-molybdenum deposit at Butte, Montana: Economic Geology, v. 103, p. 307-334.

Seedorff, E., Dilles, J.H., Proffett, J.M., Jr, Einaudi, M.T., Zurcher, L., Stavast, W.J.A., Johnson, D.A., Barton, M.D., 2005, Porphyry deposits: Characteristics and origin of hypogene features, *in* Hedenquist, J. W., Thompson, J. F. H., Goldfarb, R. J., and Richards, J. P., eds., Economic Geology 100th Anniversary Volume, p. 251-298.

Stavast, W.J.A., Butler, B.F., Seedorff, E., Barton, M.D., and Ferguson, C.A., 2008, Tertiary tilting and dismemberment of the Laramide arc and related hydrothermal systems, Sierrita Mountains, Arizona: Economic Geology, v. 103, p. 629-636.

Von Quadt, A., Erni, M., Martinek, K., Moll, M., Peytcheva, I., and Heinrich, C.A., 2011, Zircon crystallization and the lifetimes of ore-forming magmatic-hydrothermal systems: Geology, v. 39, no. 8, p. 731–734.

2) EXTENDED METHODS

Secondary Electron Microscope Cathodoluminescence (SEM-CL)

SEM-CL images of 30 and 200 µm thick polished sections were obtained at the Oregon State University Microscopy facility using a FEI Quanta 600FEG with a Gatan mini-CL detector with a wavelength range between 185 and 850 nm. Images were obtained while operating the instrument between 10 and 15 KeV, a spot size of 6 µm, scanning time between 50 and 200 µs and resolution of 1024x884 pixels. Thin sections were carbon coated or gold coated (< 100 nm thick) prior to the analyses. Gray scale profiles were obtained with image-J software. For each profile the gray line shows the raw gray scale data and the black line represents a smoothed profile calculated by image-J. The smoothed profile is calculated by averaging contiguous pixel scale CL-intensity variations and is considered a better representation of the gray scale variations at the micron scale.

Electron Microprobe (EMP)

Titanium and aluminum in quartz on the thin section samples previously imaged by SEM-CL were obtained at Oregon State University using a CAMECA SX-100 Electron microprobe (EMP), by simultaneously collecting Ti x-rays on one LPET and two PET diffracting crystals, and collecting Al x-rays on one TAP and one LTAP diffracting crystals, a 15 keV accelerating voltage, a 200 nA beam current, a 1 um spot diameter and 600 second counting times on peak and 300 seconds on each background peak to achieve a 13 ppm detection limit (3 sigma). With multiple diffraction crystals, this is the equivalent of 1800 seconds on peak and 900 seconds on each background peak for Ti, and 1200 seconds on peak and 600 seconds on each background peak for Al. We analyzed a secondary quartz standard (Shandong, Audétat *et al.,* 2014) routinely for Ti and Al concentrations between analyzes of unknown samples (Table A1).

Laser Ablation Inductively Coupled Plasma Mass Spectroscopy (LA-ICP-MS)

The LA-ICP-MS analyses at Oregon State University used a Photon Machines Analyte G2 coupled with a Thermo XseriesII Quadrupole mass spectrometer, operating at

7 Hz with a 85 µm fixed spot and ~ 20 µm depth (Loewen and Kent, 2012; Dumitru et al., 2013). The total shot count was of 225 with a pre-ablation shot count of 2. Measured trace elements include 7Li, 11B, 23Na, 27Al, ^{31}P, ^{39}K, ^{47}Ti, ^{48}Ti, ^{49}Ti, ^{55}Mn, ^{56}Fe, ^{65}Cu, ^{72}Ge, ^{85}Rb, ^{88}Sr, ^{205}Tl, ^{208}Pb and concentrations were standardized using NIST-612 (Jochum *et al.,* 2011) using an Excel application (LaserTram, Kent *et al.* 2004). Spot analyses that included melt or fluid inclusions or accidental analyses of other minerals (i.e. sericite in D veins) were discarded by monitoring P, Al, Si, K, Sr, Rb. NIST-616 (Jochum *et al.,* 2011) was analyzed in between unknowns as a secondary standard. Based on the reproducibility its compositions, ^{49}Ti was preferred over ^{47}Ti and ^{50}Ti. Detection limit of 0.2 ppm (Table 2).

Secondary Ion Mass Spectrometer (SIMS)

In situ SIMS δ^{18}O measurements were made on the CAMECA IMS-1280 ion microprobe at the University of Wisconsin-Madison WiscSIMS lab. Oxygen isotope measurements were collected along several traverses with a 1.7-1.9 nA Cs^{+} primary beam. Analyses spots were ~10 µm wide and 1 µm deep. Operating and analytical conditions are described in detail by Kita *et al.* (2009); Valley and Kita (2009) and Ferry *et al.* (2010). Secondary ^{16}O, ^{16}O^{1}H^{-} and ^{18}O^{-} ions were measured simultaneously using three Faraday cup detectors (C, FC2 and H1, respectively). ^{16}O^{1}H^{-}ions were measured for monitoring OH in quartz and contaminant such as mineral inclusions. The duration of the analyses was 3-4 minutes and the working standard was UWQ1 quartz (see Kelly et al. (2007), Ferry *et al.* (2014) appendix A for composition). The working standard was measured 4-5 times before and after every 10 to 15 unknown analyses on every sample. The average of the 2 standard deviation for each bracketing set of the UWQ1 analyses was 0.27‰. The raw δ^{18}O data were corrected using standard procedures described by Ushikubo *et al.* (2012); Nakashima *et al.* (2013) and Tenner *et al.* (2013) and Ferry *et al.* (2014). The 2 standard deviation of the analyses was ~ 0.2-0.3 ‰ (Table 3).

REFERENCES FOR EXTENDED METHODS

Audétat, A., Garbe-Schönberg, D., Kronz, A., Pettke, T., Rusk, B., Donovan, J. J. and Lowers, H. A., 2014, Characterisation of a Natural Quartz Crystal as a Reference Material for

Microanalytical Determination of Ti, Al, Li, Fe, Mn, Ga and Ge: Geostandards and Geoanalytical Research, v. 39, no. 2, p. 171-184.

Dumitru, T.A., Ernst, W.G., Wright, J.E., Wooden, J.L., Wells, R.E., Farmer, L.P., Kent, A.J.R., Graham, S.A., 2013, Eocene extension in Idaho generated massive sediment floods into the Franciscan Trench and into the Tyee, Great Valley, and Green River Basins: Geology 41 (2), 187–190.

Ferry, J. M., Kitajima, K., Strickland, A and Valley, J. W., 2014, Ion microprobe survey of the grain-scale oxygen isotope geochemistry of minerals in metamorphic rocks: Geochimica et Cosmochimica Acta, v. 144, p. 403-433.

Jochum, K. P., Weis, U., Stoll, B., Kuzmin, D., Yang, Q., Raczek, I., Jacob, D. E., Stracke, A., Birbaum, K., Frick, D. A., Günther, D. and Enzweiler, J., 2011, Determination of Reference Values for NIST SRM 610-617 Glasses Following ISO Guidelines: Geostandards and Geoanalytical Research, v. 35, no. 4, p. 397-429.

Kelly JL, Fu B, Kita NT, Valley JW (2007) Optically Continuous Silcrete Cements Of The St. Peter Sandstone: Oxygen Isotope Analysis By Ion Microprobe And Laser Fluorination. Geochem. Cosmochim. Acta. 71:3812-3832.

Kent, A.J.R., Jacobsen, B., Peate, D.W., Waight, T.E., and Baker, J.A., 2004, Isotope dilution MC-ICP-MS rare earth element analysis of geochemical reference materials NIST SRM 610, NIST SRM 612, NIST SRM 614, BHVO-2G, BHVO-2, BCR-2G, JB-2, WS-1, W-2, AGV-1, AGV-2. Geostandards Newsletter, 28(3), 417-430.

Kita, N.T., Ushikubo, T., Fu, B., Valley, J.W., 2009, High precision SIMS oxygen isotope analysis and the effect of sample topography: Chemical Geology, v. 264, p. 43–57.

Loewen, M.W., and Kent, A.J., 2012, Sources of elemental fractionation and uncertainty during the analysis of semi-volatile metals in silicate glasses using LA-ICP-MS: Journal of Analytical and Atomic Spectrometry, v. 27, p. 1502-1508

Nakashima D., Kita N. T., Ushikubo T., Noguchi T., Nakamura T. and Valley J. W. (2013) Oxygen three-isotope ratios of silicate particles returned from asteroid Itokawa by the Hayabusa spacecraft: a strong link with equilibrated LL chondrites: Earth and Planetary Science Letters, v. 379, p. 127–136.

Tenner T. J., Ushikubo T., Kurahashi E., Kita N. T. and Nagahara H. (2013) Oxygen isotope systematics of chondrule phenocrysts from the CO3.0 chondrite Yamato 82120: evidence for two distinct oxygen isotope reservoirs: Geochimica et Cosmochimica Acta, v. 102, p. 226–245.

Ushikubo T., Kimura M., Kita N. T. and Valley J. W. (2012) Primordial oxygen isotope reservoirs of the solar nebula recorded in chondrules in Acfer 094 carbonaceous chondrite: Geochimica et Cosmochimica Acta, v. 90, p. 242–264.

Valley, J.W., Kita, N.T., 2009, In situ oxygen isotope geochemistry by ion microprobe, *in* Fayek, M. Ed., Secondary ion mass spectrometry in the earth sciences: Mineralogical Society of Canada Short Course, p. 19–63.

3) ADDITIONAL TABLES

Table 1. TITANIUM IN QUARTZ (EMP)

	Sample/Spot	**Al** (ppm)	**Ti** (ppm)
Correlative to δ^{18}O Transect 027	FC-HAQ-027	157	84
	FC-HAQ-027	121	68
	FC-HAQ-027	84	69
	FC-HAQ-027	64	77
	FC-HAQ-027	38	47
	FC-HAQ-027	126	75
	FC-HAQ-027	100	47
	FC-HAQ-027	100	51
	FC-HAQ-027	107	53
	FC-HAQ-027	78	43
	FC-HAQ-027	28	36
	FC-HAQ-027	44	45
	FC-HAQ-027	34	31
	FC-HAQ-027	49	31
	FC-HAQ-027	54	47
	FC-HAQ-027	41	27
	FC-HAQ-027	48	33
	FC-HAQ-027	35	49
	FC-HAQ-027	60	34
Correlative to δ^{18}O Transect 048	FC-HAQ-048	97	39
	FC-HAQ-048	23	49
	FC-HAQ-048	45	59
	FC-HAQ-048	55	79
	FC-HAQ-048	59	65
	FC-HAQ-048	115	98
	FC-HAQ-048	80	92
	FC-HAQ-048	123	105
	FC-HAQ-048	278	114
	FC-HAQ-048	250	109
	FC-HAQ-027-b1	63	26
	FC-HAQ-027-b2	125	40
	FC-HAQ-027-b3	152	50
	FC-HAQ-027-b4	203	42
	FC-HAQ-027-b5	189	46
	FC-HAQ-027-b6	162	39
	FC-HAQ-027-b7	191	48
	FC-HAQ-027-b8	218	51
	FC-HAQ-027-b9	177	49
	FC-HAQ-027-b10	190	59
	FC-HAQ-027-b11	179	55
	FC-HAQ-027-b12	111	42
	FC-HAQ-027-b13	101	59
	FC-HAQ-027-b14	612	57
	FC-HAQ-027-b15	82	18
	FC-HAQ-002-1	42	73
	FC-HAQ-002-2	47	68
	FC-HAQ-002-3	79	84
	FC-HAQ-002-4	47	37
	FC-HAQ-002-5	43	54
	FC-HAQ-002-6	27	32
	FC-HAQ-002-7	30	24
	FC-HAQ-002-8	19	72
	FC-HAQ-002-8	26	76

	Spot	**Al** (ppm)	**Ti** (ppm)
Shandong Standard	1	145	57
	1	146	60
	3	146	62
	4	131	57
	5	138	59
	6	130	53
	7	133	56
	8	131	55
	9	130	58
	10	131	57
	11	132	56
	12	132	65
	13	130	57
	14	129	54
	15	132	59
	16	121	59
	17	128	55
	18	128	64
	Average:	**133**	**58**
	2 Stdev:	**7**	**6**
	Preferred values	Audetat *et al.,* 2015	
	Average:	**154**	**57**
	2 stdev:	**15**	**4**

Table 2. TITANIUM IN QUARTZ (LA-ICP-MS)

Sample	**Li** (ppm)	**^{49}Ti** (ppm)	**Ge** (ppm)
FC-HAQ-009-1	5.75	2.23	1.07
FC-HAQ-009-2	3.35	3.26	1.00
FC-HAQ-009-21	0.77	5.65	1.32
FC-HAQ-009-32	2.62	0.73	1.79
Average:	**3.12**	**2.97**	**1.30**
2 stdev:	**4.13**	**4.13**	**0.72**

Standard	**Li** (ppm)	**^{49}Ti** (ppm)	**Ge** (ppm)
NISTSRM616-1	0.95	1.83	0.20
NISTSRM616-2	0.91	1.70	0.24
NISTSRM616-4	0.91	1.59	0.28
NISTSRM616-3	0.81	1.93	0.25
NISTSRM616-4b	0.90	2.23	-
NISTSRM616-7	0.82	2.75	0.24
NISTSRM616-8	0.87	2.05	0.17
NISTSRM616-9	0.79	1.83	0.23
NISTSRM616-10	1.02	2.26	0.20
NISTSRM616-12	1.05	2.23	0.21
NISTSRM616-13	0.85	2.06	0.40
Average:	**0.90**	**2.04**	**0.24**
2 stdev:	**0.17**	**0.65**	**0.13**

NISTSRM616 **preferred values**	Jochum *et al.,* 2011		
Average:	**0.895**	**2.65**	**0.283**
2 stdev:	**0.059**	**0.29**	**0.039**

Table 3. δ18O ‰ IN QUARTZ (SIMS)

File	Comment	**δ^{18}O ‰ VSMOW**	**2SD (ext.)**	**Mass Bias (‰)**	**δ^{18}O ‰ measured**	**2SE (int.)**	**^{16}O (Gcps)**	**IP (nA)**	**Yield (Gcps/nA)**	**Date**	**Time**	**X**	**Y**	**DTFA-X**	**DTFA-Y**	**^{16}OH/^{16}O**
SAMPLE:	**FC-HAQ-009**															
~~20150203@31.asc~~	~~009 UWQ-1 g0~~				~~5.963~~	~~0.234~~	~~2.833~~	~~**1.828**~~	~~1.550~~	~~2/3/15~~	~~8:45~~	~~-485~~	~~138~~	~~-8~~	~~-13~~	~~6.805E-05~~
20150203@32.asc	009 UWQ-1 g0				5.456	0.238	2.892	**1.829**	1.581	2/3/15	8:49	-412	-57	-9	-16	6.680E-05
20150203@33.asc	009 UWQ-1 g1				5.585	0.273	2.849	**1.821**	1.564	2/3/15	8:53	1066	1462	-12	-15	6.453E-05
20150203@34.asc	009 UWQ-1 g1				5.669	0.319	2.805	**1.810**	1.550	2/3/15	8:56	1243	1322	-12	-15	6.215E-05
20150203@35.asc	009 UWQ-1 g0				5.872	0.230	2.836	**1.805**	1.572	2/3/15	9:00	-425	-20	-9	-17	7.126E-05
	average and 2SD				**5.646**	**0.349**										
20150203@36.asc	009 D-vein	**9.71**	**0.32**		3.072	0.301	2.784	**1.800**	1.547	2/3/15	9:06	430	-2199	-2	-25	7.710E-05
20150203@37.asc	009 D-vein	**13.62**	**0.32**		6.952	0.414	2.755	**1.794**	1.536	2/3/15	9:10	447	-2111	-2	-27	6.281E-05
20150203@38.asc	009 D-vein	**10.78**	**0.32**		4.131	0.493	2.740	**1.788**	1.533	2/3/15	9:13	474	-2060	-1	-26	8.297E-05
20150203@39.asc	009 D-vein	**13.60**	**0.32**		6.937	0.216	2.709	**1.779**	1.522	2/3/15	9:17	567	-2035	-5	-25	6.201E-05
20150203@40.asc	009 D-vein	**10.60**	**0.32**		3.950	0.532	2.739	**1.773**	1.545	2/3/15	9:21	614	-2070	-4	-25	9.359E-05
20150203@41.asc	009 D-vein	**11.49**	**0.32**		4.832	0.215	2.754	**1.764**	1.562	2/3/15	9:25	437	-1830	-4	-24	1.651E-04
20150203@42.asc	009 D-vein	**11.13**	**0.32**		4.481	0.334	2.755	**1.756**	1.569	2/3/15	9:29	411	-1889	-3	-24	5.760E-05
20150203@43.asc	009 D-vein	**11.38**	**0.32**		4.723	0.234	2.716	**1.748**	1.554	2/3/15	9:33	345	-1947	-2	-25	5.491E-05
20150203@44.asc	009 D-vein	**10.89**	**0.32**		4.238	0.297	2.716	**1.738**	1.563	2/3/15	9:37	209	-2105	0	-26	5.232E-05
20150203@45.asc	009 D-vein	**11.02**	**0.32**		4.371	0.328	2.677	**1.729**	1.548	2/3/15	9:40	165	-2193	1	-27	5.229E-05
20150203@46.asc	009 UWQ-1 g0				5.637	0.188	2.675	**1.713**	1.562	2/3/15	9:44	-464	-200	-8	-19	5.278E-05
~~20150203@47.asc~~	~~009 UWQ-1 g0~~				~~5.208~~	~~0.352~~	~~2.637~~	~~**1.704**~~	~~1.548~~	~~2/3/15~~	~~9:48~~	~~-467~~	~~-275~~	~~-7~~	~~-21~~	~~5.325E-05~~
20150203@48.asc	009 UWQ-1 g0 Cs-Res=118				5.904	0.266	2.736	**1.752**	1.561	2/3/15	9:53	-525	-144	-7	-20	4.923E-05
20150203@49.asc	009 UWQ-1 g0				5.733	0.268	2.742	**1.760**	1.558	2/3/15	9:57	-546	-234	-6	-21	5.064E-05
20150203@50.asc	009 UWQ-1 g0				5.514	0.218	2.772	**1.761**	1.574	2/3/15	10:00	-456	-131	-8	-19	4.898E-05
	average and 2SD				**5.697**	**0.329**										
	bracket average and 2SD	**12.33**		**-6.58**	**5.671**	**0.319**										
SAMPLE:	**FC-HAQ-048**															
20150203@51.asc	048 UWQ-1 g0				5.819	0.251	2.782	**1.746**	1.594	2/3/15	10:09	166	-538	3	12	3.998E-05
20150203@52.asc	048 UWQ-1 g0				5.582	0.241	2.801	**1.743**	1.607	2/3/15	10:13	248	-520	1	13	4.106E-05
20150203@53.asc	048 UWQ-1 g1				5.742	0.241	2.790	**1.744**	1.599	2/3/15	10:16	297	1182	0	6	4.301E-05
20150203@54.asc	048 UWQ-1 g1				5.604	0.353	2.790	**1.740**	1.603	2/3/15	10:20	323	1071	0	6	4.292E-05
	average and 2SD				**5.687**	**0.226**										

Table 3. (Cont.)

File	Comment	δ^{18}O ‰ VSMOW	2SD (ext.)	Mass Bias (‰)	δ^{18}O ‰ measured	2SE (int.)	^{16}O (Gcps)	IP (nA)	Yield (Gcps/nA)	Date	Time	X	Y	DTFA-X	DTFA-Y	^{16}OH/^{16}O
20150203@55.asc	048 Late dark CL quartz	**12.75**	**0.22**		6.178	0.230	2.687	**1.737**	1.546	2/3/15	10:26	-1565	1716	-8	5	4.167E-05
20150203@56.asc	048 Late dark CL quartz	**12.57**	**0.22**		5.993	0.331	2.737	**1.733**	1.580	2/3/15	10:31	-1590	1736	-8	7	4.403E-05
20150203@57.asc	048 Late dark CL quartz	**12.76**	**0.22**		6.184	0.227	2.728	**1.727**	1.580	2/3/15	10:34	-1610	1749	-7	8	4.270E-05
20150203@58.asc	048 Late dark CL quartz	**13.07**	**0.22**		6.490	0.246	2.724	**1.721**	1.583	2/3/15	10:38	-1643	1752	-8	9	4.179E-05
20150203@59.asc	048 Late dark CL quartz	**12.52**	**0.22**		5.944	0.261	2.710	**1.714**	1.581	2/3/15	10:42	-1657	1769	-8	8	4.064E-05
20150203@60.asc	048 Late dark CL quartz	**11.57**	**0.22**		5.002	0.236	2.703	**1.707**	1.584	2/3/15	10:46	-1660	1795	-8	8	4.030E-05
20150203@61.asc	048 B vein	**10.54**	**0.22**		3.981	0.267	2.702	**1.700**	1.589	2/3/15	10:50	-1687	1803	-9	9	4.318E-05
20150203@62.asc	048 B vein	**10.61**	**0.22**		4.046	0.259	2.692	**1.694**	1.589	2/3/15	10:54	-1715	1813	-8	8	4.164E-05
20150203@63.asc	048 B vein	**10.35**	**0.22**		3.794	0.232	2.686	**1.690**	1.590	2/3/15	10:58	-1749	1823	-8	8	4.081E-05
20150203@64.asc	048 B vein	**10.24**	**0.22**		3.685	0.329	2.686	**1.687**	1.593	2/3/15	11:02	-1784	1839	-8	8	4.043E-05
20150203@65.asc	048 B vein	**10.51**	**0.22**		3.954	0.256	2.662	**1.683**	1.582	2/3/15	11:06	-1811	1849	-8	7	4.172E-05
20150203@66.asc	048 B vein	**10.36**	**0.22**		3.801	0.295	2.670	**1.681**	1.588	2/3/15	11:10	-1840	1861	-7	8	4.117E-05
20150203@67.asc	048 B vein	**10.10**	**0.22**		3.544	0.276	2.677	**1.679**	1.594	2/3/15	11:14	-1869	1880	-7	8	4.444E-05
20150203@68.asc	048 B vein	**10.34**	**0.22**		3.784	0.251	2.669	**1.676**	1.593	2/3/15	11:17	-1897	1895	-7	7	4.850E-05
20150203@69.asc	048 B vein	**10.29**	**0.22**		3.733	0.303	2.662	**1.673**	1.592	2/3/15	11:21	-1925	1910	-6	8	4.148E-05
20150203@70.asc	048 UWQ-1 g0				5.794	0.326	2.648	**1.661**	1.594	2/3/15	11:25	299	-565	-2	13	3.973E-05
20150203@71.asc	048 UWQ-1 g0				5.881	0.290	2.654	**1.658**	1.601	2/3/15	11:29	307	-600	-2	12	4.039E-05
20150203@72.asc	048 UWQ-1 g0				5.798	0.262	2.640	**1.656**	1.595	2/3/15	11:32	324	-644	-3	11	4.029E-05
20150203@73.asc	048 UWQ-1 g0				5.847	0.283	2.636	**1.653**	1.595	2/3/15	11:36	343	-685	-2	11	4.008E-05
	average and 2SD				**5.830**	**0.083**										
	bracket average and 2SD	**12.33**		**-6.49**	**5.758**	**0.220**										
20150203@74.asc	048 B vein	**10.42**	**0.27**		3.946	0.251	2.623	**1.651**	1.589	2/3/15	11:41	-1950	1922	-7	7	4.447E-05
20150203@75.asc	048 B vein	**10.47**	**0.27**		3.995	0.161	2.612	**1.647**	1.586	2/3/15	11:45	-1979	1938	-8	7	4.533E-05
20150203@76.asc	048 B vein	**10.31**	**0.27**		3.837	0.245	2.606	**1.642**	1.587	2/3/15	11:49	-2017	1960	-7	7	4.000E-05
20150203@77.asc	048 Late dark CL quartz	**12.40**	**0.27**		5.906	0.236	2.587	**1.635**	1.582	2/3/15	11:53	-1570	1752	-8	8	4.952E-05
20150203@78.asc	048 Late dark CL quartz	**12.71**	**0.27**		6.214	0.256	2.565	**1.629**	1.574	2/3/15	11:57	-1587	1772	-8	9	4.454E-05
20150203@79.asc	048 Late dark CL quartz	**12.96**	**0.27**		6.466	0.239	2.566	**1.624**	1.579	2/3/15	12:00	-1610	1792	-9	8	4.029E-05
20150203@80.asc	048 Late dark CL quartz	**11.71**	**0.27**		5.223	0.214	2.561	**1.620**	1.582	2/3/15	12:04	-1629	1809	-10	8	3.910E-05
20150203@81.asc	048 B vein	**10.76**	**0.27**		4.281	0.204	2.571	**1.617**	1.589	2/3/15	12:08	-1653	1828	-10	8	4.051E-05
20150203@82.asc	048 B vein	**10.90**	**0.27**		4.420	0.267	2.551	**1.614**	1.580	2/3/15	12:12	-1674	1824	-10	8	4.841E-05
20150203@83.asc	048 B vein	**10.52**	**0.27**		4.038	0.275	2.550	**1.611**	1.583	2/3/15	12:16	-1692	1831	-10	8	4.240E-05
20150203@84.asc	048 B vein	**10.60**	**0.27**		4.118	0.314	2.547	**1.607**	1.585	2/3/15	12:20	-1724	1842	-9	8	4.246E-05
20150203@85.asc	048 B vein	**10.08**	**0.27**		3.606	0.248	2.544	**1.604**	1.586	2/3/15	12:24	-1757	1854	-9	8	4.040E-05
20150203@86.asc	048 B vein	**10.21**	**0.27**		3.738	0.158	2.541	**1.601**	1.587	2/3/15	12:27	-1784	1864	-9	8	4.408E-05
20150203@87.asc	048 B vein	**10.20**	**0.27**		3.728	0.267	2.523	**1.599**	1.578	2/3/15	12:31	-1867	1907	-8	8	2.460E-04

Table 3. (Cont.)

File	Comment	$\delta^{18}O$ ‰ VSMOW	2SD (ext.)	Mass Bias (‰)	$\delta^{18}O$ ‰ measured	2SE (int.)	^{16}O (Gcps)	IP (nA)	Yield (Gcps/nA)	Date	Time	X	Y	DTFA-X	DTFA-Y	$^{16}OH/^{16}O$
20150203@88.asc	048 B vein	**10.09**	**0.27**		3.615	0.289	2.531	**1.597**	1.585	2/3/15	12:35	-1926	1938	-8	8	4.432E-05
20150203@89.asc	048 UWQ-1 g0				5.749	0.283	2.518	**1.584**	1.590	2/3/15	12:38	210	-518	1	12	3.702E-05
20150203@90.asc	048 UWQ-1 g0				5.684	0.314	2.519	**1.581**	1.594	2/3/15	12:42	136	-538	2	11	3.720E-05
20150203@91.asc	048 UWQ-1 g0 Cs-Res=119				6.144	0.245	2.584	**1.642**	1.574	2/3/15	12:48	148	-560	2	11	3.624E-05
20150203@92.asc	048 UWQ-1 g0				5.826	0.245	2.638	**1.649**	1.600	2/3/15	12:51	148	-505	2	12	3.699E-05
	average and 2SD				**5.851**	**0.408**										
	bracket average and 2SD	**12.33**		**-6.41**	**5.840**	**0.273**										
SAMPLE:	**FC-HAQ-027**															
20150203@93.asc	027 UWQ-1 g0				6.121	0.280	2.564	**1.651**	1.553	2/3/15	13:02	-907	289	12	-6	2.819E-05
20150203@94.asc	027 UWQ-1 g0				5.617	0.274	2.599	**1.651**	1.574	2/3/15	13:05	-1004	186	12	-7	2.926E-05
20150203@95.asc	027 UWQ-1 g1				5.738	0.211	2.594	**1.646**	1.575	2/3/15	13:09	486	-403	10	-8	2.893E-05
20150203@96.asc	027 UWQ-1 g1				5.569	0.306	2.588	**1.648**	1.571	2/3/15	13:12	537	-544	9	-10	2.938E-05
20150203@97.asc	027 UWQ-1 g0				5.806	0.288	2.587	**1.645**	1.572	2/3/15	13:16	-983	164	-12	-7	2.962E-05
	average and 2SD				**5.683**	**0.218**										
20150203@98.asc	027 B vein	**10.91**	**0.20**		4.286	0.220	2.533	**1.643**	1.541	2/3/15	13:22	-1080	2045	7	9	2.959E-05
20150203@99.asc	027 B vein	**10.91**	**0.20**		4.281	0.223	2.564	**1.640**	1.563	2/3/15	13:28	-1082	2030	7	9	3.035E-05
20150203@100.asc	027 B vein	**10.63**	**0.20**		4.000	0.210	2.592	**1.636**	1.584	2/3/15	13:32	-1084	1980	6	7	3.080E-05
20150203@101.asc	027 B vein	**10.80**	**0.20**		4.172	0.328	2.595	**1.632**	1.590	2/3/15	13:36	-1084	1937	7	7	2.943E-05
20150203@102.asc	027 B vein	**10.66**	**0.20**		4.031	0.302	2.583	**1.627**	1.588	2/3/15	13:40	-1086	1887	7	6	2.908E-05
20150203@103.asc	027 B vein	**10.49**	**0.20**		3.863	0.245	2.587	**1.625**	1.591	2/3/15	13:44	-1082	1842	7	4	3.319E-05
20150203@104.asc	027 B vein	**10.61**	**0.20**		3.982	0.295	2.567	**1.623**	1.581	2/3/15	13:47	-1082	1794	7	3	2.992E-05
20150203@105.asc	027 B vein	**10.80**	**0.20**		4.170	0.207	2.569	**1.622**	1.584	2/3/15	13:51	-1080	1749	7	2	2.922E-05
20150203@106.asc	027 B vein	**10.65**	**0.20**		4.028	0.269	2.558	**1.621**	1.578	2/3/15	13:55	-1077	1706	6	1	3.235E-05
20150203@107.asc	027 B vein	**10.64**	**0.20**		4.013	0.251	2.575	**1.621**	1.588	2/3/15	13:58	-1075	1634	6	1	3.188E-05
20150203@108.asc	027 B vein	**10.72**	**0.20**		4.095	0.255	2.554	**1.619**	1.577	2/3/15	14:02	-1070	1576	7	0	2.900E-05
20150203@109.asc	027 EDM	**10.96**	**0.20**		4.332	0.266	2.599	**1.617**	1.607	2/3/15	14:06	-1071	1519	7	-1	1.158E-04
20150203@110.asc	027 EDM	**10.63**	**0.20**		4.000	0.310	2.543	**1.614**	1.576	2/3/15	14:09	-1070	1476	7	-1	2.906E-05
20150203@111.asc	027 EDM	**10.73**	**0.20**		4.106	0.204	2.538	**1.610**	1.576	2/3/15	14:13	-1070	1404	7	-2	2.911E-05
20150203@112.asc	027 EDM	**10.76**	**0.20**		4.135	0.214	2.531	**1.607**	1.575	2/3/15	14:17	-1030	1315	7	-4	2.880E-05

Table 3. (Cont.)

File	Comment	$\delta^{18}O$ ‰ VSMOW	2SD (ext.)	Mass Bias (‰)	$\delta^{18}O$ ‰ measured	2SE (int.)	^{16}O (Gcps)	IP (nA)	Yield (Gcps/nA)	Date	Time	X	Y	DTFA-X	DTFA-Y	$^{16}OH/^{16}O$
20150203@113.asc	027 UWQ-1 g0				5.764	0.354	2.517	**1.603**	1.570	2/3/15	14:21	-795	267	6	-8	2.870E-05
20150203@114.asc	027 UWQ-1 g0				5.824	0.221	2.514	**1.602**	1.570	2/3/15	14:25	-847	300	6	-8	2.875E-05
20150203@115.asc	027 UWQ-1 g0 Cs-Res=120				5.613	0.243	2.620	**1.660**	1.578	2/3/15	14:31	-974	311	7	-6	2.569E-05
20150203@116.asc	027 UWQ-1 g0				5.608	0.233	2.649	**1.671**	1.585	2/3/15	14:35	-1038	307	8	-6	2.707E-05
	average and 2SD				**5.702**	**0.218**										
	bracket average and 2SD	**12.33**		**-6.56**	**5.692**	**0.203**										
20150203@117.asc	027 EDM	**12.39**	**0.20**		5.807	0.186	2.663	**1.680**	1.585	2/3/15	14:39	-1067	1224	7	-5	5.659E-05
20150203@118.asc	027 EDM	**10.62**	**0.20**		4.044	0.214	2.657	**1.680**	1.582	2/3/15	14:43	-1050	1201	7	-5	3.215E-05
20150203@119.asc	027 EDM	**10.11**	**0.20**		3.541	0.246	2.733	**1.679**	1.628	2/3/15	14:47	-1053	1146	7	-6	3.413E-05
20150203@120.asc	027 EDM	**11.32**	**0.20**		4.747	0.371	2.691	**1.676**	1.606	2/3/15	14:50	-1047	1084	8	-6	1.337E-04
20150203@121.asc	027 EDM	**10.64**	**0.20**		4.072	0.251	2.628	**1.672**	1.571	2/3/15	14:54	-1044	974	8	-8	2.771E-05
20150203@122.asc	027 EDM	**10.74**	**0.20**		4.165	0.282	2.604	**1.667**	1.562	2/3/15	14:58	-1044	902	8	-9	2.757E-05
20150203@123.asc	027 EDM	**10.78**	**0.20**		4.202	0.299	2.535	**1.665**	1.523	2/3/15	15:02	-1038	820	8	-12	2.906E-05
20150203@124.asc	027 B vein	**10.59**	**0.20**		4.014	0.215	2.604	**1.667**	1.563	2/3/15	15:06	-345	2130	4	7	2.314E-05
20150203@125.asc	027 B vein	**10.49**	**0.20**		3.915	0.246	2.624	**1.662**	1.578	2/3/15	15:10	-346	2100	2	6	4.955E-05
20150203@126.asc	027 B vein	**10.39**	**0.20**		3.823	0.252	2.623	**1.654**	1.585	2/3/15	15:15	-311	2060	3	6	3.850E-05
20150203@127.asc	027 B vein	**10.44**	**0.20**		3.864	0.240	2.621	**1.647**	1.592	2/3/15	15:19	-319	2023	3	7	2.697E-05
20150203@128.asc	027 B vein	**10.48**	**0.20**		3.905	0.227	2.628	**1.644**	1.599	2/3/15	15:22	-324	2003	3	7	2.858E-05
20150203@129.asc	027 B vein	**10.36**	**0.20**		3.786	0.201	2.625	**1.646**	1.595	2/3/15	15:26	-215	2018	2	6	2.734E-05
20150203@130.asc	027 B vein	**10.84**	**0.20**		4.265	0.327	2.580	**1.645**	1.568	2/3/15	15:31	-277	989	5	-5	2.831E-05
20150203@131.asc	027 B vein	**10.85**	**0.20**		4.280	0.309	2.551	**1.643**	1.553	2/3/15	15:35	-365	825	6	-7	1.006E-03
20150203@132.asc	027 UWQ-1 g1				5.733	0.246	2.590	**1.629**	1.590	2/3/15	15:40	401	-301	10	-7	2.590E-05
20150203@133.asc	027 UWQ-1 g1				5.701	0.300	2.560	**1.630**	1.571	2/3/15	15:43	447	-353	9	-8	3.396E-05
20150203@134.asc	027 UWQ-1 g1				5.864	0.270	2.560	**1.630**	1.570	2/3/15	15:47	445	-452	9	-9	2.566E-05
20150203@135.asc	027 UWQ-1 g1				5.865	0.282	2.564	**1.629**	1.574	2/3/15	15:50	598	-465	7	-10	2.604E-05
	average and 2SD				**5.791**	**0.172**										
	bracket average and 2SD	**12.33**		**-6.50**	**5.747**	**0.205**										
20150203@136.asc	009 UWQ-1 g0				5.872	0.301	2.527	**1.619**	1.560	2/3/15	15:59	-496	-183	-8	-14	2.853E-05
20150203@137.asc	009 UWQ-1 g0				5.878	0.273	2.524	**1.618**	1.560	2/3/15	16:02	-540	-198	-6	-15	2.909E-05
20150203@138.asc	009 UWQ-1 g0				6.040	0.211	2.533	**1.617**	1.567	2/3/15	16:06	-566	-138	-5	-15	2.979E-05
20150203@139.asc	009 UWQ-1 g0				5.770	0.239	2.530	**1.614**	1.568	2/3/15	16:10	-561	-83	-6	-14	2.959E-05
	average and 2SD				**5.890**	**0.223**										

Table 3. (Cont.)

File	Comment	δ^{18}O ‰ VSMOW	2SD (ext.)	Mass Bias (‰)	δ^{18}O ‰ measured	2SE (int.)	^{16}O (Gcps)	IP (nA)	Yield (Gcps/nA)	Date	Time	X	Y	DTFA-X	DTFA-Y	^{16}OH/^{16}O
SAMPLE: FC-HAQ-009																
20150203@140.asc	009 D-vein	**13.34**	**0.22**		6.889	0.271	2.493	**1.616**	1.542	2/3/15	16:15	477	-1795	-4	-19	1.249E-04
20150203@141.asc	009 D-vein	**12.53**	**0.22**		6.081	0.291	2.521	**1.613**	1.563	2/3/15	16:19	501	-1773	-5	-18	1.389E-04
20150203@142.asc	009 D-vein	**13.01**	**0.22**		6.560	0.261	2.509	**1.610**	1.559	2/3/15	16:23	537	-1761	-5	-18	3.625E-05
20150203@143.asc	009 D-vein	**12.93**	**0.22**		6.481	0.249	2.496	**1.608**	1.552	2/3/15	16:26	562	-1740	-5	-18	3.530E-05
20150203@144.asc	009 D-vein	**13.10**	**0.22**		6.651	0.354	2.483	**1.605**	1.547	2/3/15	16:30	598	-1713	-6	-18	6.744E-04
20150203@145.asc	009 D-vein	**11.39**	**0.22**		4.951	0.382	2.493	**1.603**	1.556	2/3/15	16:33	628	-1680	-6	-17	3.317E-05
20150203@146.asc	009 UWQ-1 g0				5.858	0.308	2.480	**1.592**	1.557	2/3/15	16:38	-507	-219	-6	-15	3.080E-05
20150203@147.asc	009 UWQ-1 g0				5.720	0.282	2.482	**1.591**	1.560	2/3/15	16:41	-584	-171	-5	-15	3.020E-05
20150203@148.asc	009 UWQ-1 g0 Cs-Res=121				6.014	0.295	2.564	**1.654**	1.550	2/3/15	16:48	-602	-148	-5	-15	3.011E-05
20150203@149.asc	009 UWQ-1 g0				5.898	0.269	2.590	**1.663**	1.557	2/3/15	16:51	-646	-130	-4	-15	3.077E-05
	average and 2SD				**5.873**	**0.243**										
	bracket average and 2SD	**12.33**		**-6.37**	**5.881**	**0.217**										
20150203@150.asc	009 D-vein	**13.15**	**0.25**		6.648	0.261	2.583	**1.673**	1.544	2/3/15	16:56	663	-1647	-7	-16	3.363E-04
20150203@151.asc	009 D-vein	**11.18**	**0.25**		4.700	0.237	2.637	**1.674**	1.575	2/3/15	17:00	692	-1617	-7	-16	2.822E-05
20150203@152.asc	009 D-vein	**11.19**	**0.25**		4.707	0.248	2.612	**1.674**	1.560	2/3/15	17:04	744	-1589	-8	-16	5.766E-05
20150203@153.asc	009 D-vein	**11.09**	**0.25**		4.605	0.287	2.625	**1.672**	1.570	2/3/15	17:07	782	-1559	-7	-15	3.380E-05
20150203@154.asc	009 D-vein	**11.13**	**0.25**		4.646	0.225	2.632	**1.671**	1.575	2/3/15	17:11	825	-1532	-8	-15	6.250E-05
20150203@155.asc	009 D-vein	**10.69**	**0.25**		4.211	0.275	2.683	**1.670**	1.606	2/3/15	17:14	870	-1508	-8	-14	1.097E-04
20150203@156.asc	009 D-vein	**12.98**	**0.25**		6.482	0.263	2.571	**1.665**	1.545	2/3/15	17:19	230	-1804	-2	-19	3.252E-05
20150203@157.asc	009 D-vein	**13.15**	**0.25**		6.651	0.226	2.576	**1.662**	1.549	2/3/15	17:23	255	-1768	-2	-19	4.722E-05
20150203@158.asc	009 D-vein	**13.02**	**0.25**		6.527	0.233	2.583	**1.660**	1.556	2/3/15	17:27	279	-1725	-2	-19	3.412E-05
20150203@159.asc	009 D-vein	**13.14**	**0.25**		6.643	0.240	2.578	**1.659**	1.554	2/3/15	17:30	304	-1683	-3	-18	3.440E-05
20150203@160.asc	009 D-vein	**11.91**	**0.25**		5.417	0.252	2.593	**1.657**	1.564	2/3/15	17:34	318	-1643	-4	-18	5.878E-05
20150203@161.asc	009 D-vein	**12.02**	**0.25**		5.530	0.343	2.594	**1.657**	1.566	2/3/15	17:37	340	-1614	-4	-18	8.513E-05
20150203@162.asc	009 D-vein	**11.43**	**0.25**		4.941	0.295	2.581	**1.655**	1.560	2/3/15	17:41	354	-1573	-4	-18	3.033E-05
20150203@163.asc	009 D-vein	**12.41**	**0.25**		5.921	0.214	2.574	**1.651**	1.559	2/3/15	17:45	368	-1527	-5	-17	3.305E-05
20150203@164.asc	009 D-vein	**10.84**	**0.25**		4.358	0.300	2.688	**1.646**	1.633	2/3/15	17:49	384	-1484	-5	-17	3.872E-05
20150203@165.asc	009 UWQ-1 g0				5.917	0.276	2.539	**1.631**	1.557	2/3/15	17:54	-505	-265	-15	-15	2.857E-05
20150203@166.asc	009 UWQ-1 g0				5.829	0.306	2.555	**1.628**	1.570	2/3/15	17:58	-443	-240	-16	-14	2.833E-05
20150203@167.asc	009 UWQ-1 g0				5.851	0.285	2.553	**1.625**	1.571	2/3/15	18:01	-493	-114	-16	-13	2.899E-05

Table 3. (Cont.)

File	Comment	$\delta^{18}O$ ‰ VSMOW	2SD (ext.)	Mass Bias (‰)	$\delta^{18}O$ ‰ measured	2SE (int.)	^{16}O (Gcps)	IP (nA)	Yield (Gcps/nA)	Date	Time	X	Y	DTFA-X	DTFA-Y	$^{16}OH/^{16}O$
20150203@168.asc	009 UWQ-1 g0				5.615	0.215	2.556	**1.625**	1.573	2/3/15	18:05	-415	-122	-17	-12	2.858E-05
	average and 2SD				**5.803**	**0.262**										
	bracket average and 2SD	**12.33**		**-6.41**	**5.838**	**0.245**										
SAMPLE:	**FC-HAQ-004**					**Cs-Res=122**										
20150203@169.asc	004 UWQ-1 g0				5.851	0.278	2.666	**1.683**	1.584	2/3/15	18:16	-1393	-389	2	5	2.602E-05

Table 3. (Cont.)

20150203@170.asc	004 UWQ-1 g0				5.691	0.204	2.702	**1.691**	1.598	2/3/15	18:19	-1406	-332	3	6	2.644E-05
20150203@171.asc	004 UWQ-1 g0				5.655	0.270	2.718	**1.692**	1.606	2/3/15	18:23	-1355	-359	3	5	2.813E-05
20150203@172.asc	004 UWQ-1 g0				5.566	0.221	2.713	**1.696**	1.600	2/3/15	18:26	-1326	-409	2	3	2.738E-05
	average and 2SD				**5.691**	**0.238**										
20150203@173.asc	004 Late dark CL quartz	**13.14**	**0.22**		6.453	0.264	2.715	**1.703**	1.594	2/3/15	18:31	1734	-660	-1	-3	2.686E-05
20150203@174.asc	004 B vein	**10.66**	**0.22**		3.990	0.268	2.698	**1.702**	1.585	2/3/15	18:35	1692	-627	-2	-3	3.773E-05
20150203@175.asc	004 B vein	**10.46**	**0.22**		3.794	0.263	2.699	**1.700**	1.588	2/3/15	18:38	1648	-577	-2	-2	3.181E-05
20150203@176.asc	004 B vein	**10.43**	**0.22**		3.765	0.238	2.703	**1.699**	1.591	2/3/15	18:42	1614	-550	-2	-2	3.023E-05
20150203@177.asc	004 B vein	**10.61**	**0.22**		3.939	0.236	2.688	**1.698**	1.583	2/3/15	18:46	1555	-507	-1	-2	3.852E-05
20150203@178.asc	004 B vein	**10.51**	**0.22**		3.840	0.283	2.685	**1.695**	1.584	2/3/15	18:49	1388	-421	0	-2	3.072E-05
20150203@179.asc	004 B vein	**12.88**	**0.22**		6.199	0.266	2.669	**1.696**	1.574	2/3/15	18:53	1732	-694	-2	-3	4.054E-05
20150203@180.asc	004 B vein	**10.79**	**0.22**		4.117	0.282	2.674	**1.694**	1.579	2/3/15	18:57	1708	-672	-2	-3	3.411E-05
20150203@181.asc	004 B vein	**10.62**	**0.22**		3.952	0.296	2.672	**1.692**	1.580	2/3/15	19:01	1691	-655	-1	-3	3.183E-05
20150203@182.asc	004 Late dark CL quartz	**13.08**	**0.22**		6.396	0.265	2.660	**1.690**	1.574	2/3/15	19:04	1757	-660	-1	-3	2.826E-05
20150203@183.asc	004 Late dark CL quartz	**11.28**	**0.22**		4.612	0.186	2.650	**1.685**	1.573	2/3/15	19:09	1802	-749	-2	-2	2.611E-05
20150203@184.asc	004 Late dark CL quartz	**11.05**	**0.22**		4.383	0.262	2.655	**1.682**	1.579	2/3/15	19:13	1938	-889	-2	-4	2.821E-05
20150203@185.asc	004 B vein	**10.74**	**0.22**		4.074	0.301	2.670	**1.678**	1.591	2/3/15	19:16	2063	-1125	-3	-6	3.168E-05
20150203@186.asc	004 UWQ-1 g0				5.726	0.226	2.639	**1.673**	1.577	2/3/15	19:21	-1395	-280	6	6	2.713E-05
20150203@187.asc	004 UWQ-1 g0				5.645	0.191	2.699	**1.679**	1.608	2/3/15	19:25	-1364	-320	8	6	2.849E-05
20150203@188.asc	004 UWQ-1 g0				5.588	0.236	2.668	**1.675**	1.593	2/3/15	19:28	-1372	-425	7	2	2.799E-05
20150203@189.asc	004 UWQ-1 g0				5.482	0.238	2.669	**1.667**	1.601	2/3/15	19:32	-1418	-424	7	2	2.762E-05
	average and 2SD				**5.610**	**0.205**										
	bracket average and 2SD	**12.33**		**-6.60**	**5.651**	**0.223**										

Note: IP values in the table are 110pA lower than acutal PA

Table 4. SAMPLE LOCATION

Sample	Drillhole	Depth (m)	Latitude	Longitude
FC-HAQ-002	AHAD-098A	125.8	-14.16567	-72.34654
FC-HAQ-009	AHAD-098A	545		
FC-HAQ-027	AHAD-185	235.3	-14.16678	-72.34653
FC-HAQ-048	AHAD-185	640.5		

Table A5. PORPHYRY AND VEIN FORMATION TEMPERATURES BASED ON PHASE EQUILIBRIA, TITANIQ GEOTHERMOMETER AND FLUID INCLUSION DATA

Quartz type	**T(°C)** [phase]	**Ti** (ppm)	**T(ºC)** [Ti]			**T(°C)** [pref. min.]
			T (ºC)	P (kbar)	αTiO2	
Igneous	~700	27-40	662-703	3.0 L.	0.65	650
B	>550	18-40	541-598	1.6 L.-H.	1.0	550
EDM	550-400	15-30	505-561	1.1 L.-H.	1.0	500
D (dark gray-CL)	400-450	5-15	425-500	1.0 L.-H.	1.0	450
D (dark-CL)	300-400	1-5	339-425	1.0 L.-H.	1.0	350

Notes: T (ºC) [phase] was estimated based on the phase stability of quartz – K-feldspar – Muscovite – Andalusite (Seedorff *et al.,* 2005). **T (ºC)** [Ti] was calculated using the Ti-in-Q geothermometer (Huang and Audétat, 2012) of the lowest Ti zones, together with pressure constraints from fluid inclusion and hornblende baromethry (Cernuschi *unpub.*). P (kbar) = Pressure in kbars, L. = Lithostatic, H. = Hydrostatic, αTiO_2 = Titanium activity. **T (ºC) [pref. min.]** is the preferred minimum formation temperature used for the diffusion modeling.

INTRODUCTION TO TABLE A6

Known fractionation factors for $\delta^{18}O$ of quartz-water were used to estimate the range of permissive $\delta^{18}O$ of the magmatic water (Table A6). Depending on the fractionation factor used, the possible values for water range from ~7.5 to 8.0 ‰ to yield the observed $\delta^{18}O$ of quartz at temperatures that are estimated independently from TitaniQ, fluid inclusion data and phase petrology. Note that since the EDM and B vein quartz appears to have partially re-equilibrated at ~ 450 ºC, the calculations of magmatic water composition are based on the ~450 ºC and ~350 ºC D vein quartz.

We assume that a single composition of magmatic-hydrothermal fluid produced all veins from high to low temperature (BQ to D veins), as proposed by Reed *et al.* (2013). It is not possible to assess whether a) $\delta^{18}O$ of the magmatic water changes from one fluid input to another. However, this seems unlikely given that the composition of the intrusions in porphyry copper deposits is relatively fixed. Where the roots of other large porphyry copper deposits can be observed (*e.g.* Yerington, Dilles, 1987), they are underlain by a source granite that has uniform composition. The intrusions range from tonalite to granite, but at Haquira East are presumed to be granodiorite as this is the composition of the Haquira stock and the porphyry dikes; b) whether the $\delta^{18}O$ of the water is significantly modified from the magmatic value by water-rock exchange between ~700 °C magmatic temperatures and the ~450 °C temperatures at which we calculate the quartz-water fractionation factor and water composition. However, it is unlikely that the magmatic water changed significantly on the basis that the quartz vein volume is very high (3 to >10 vol. %) and therefore the water : rock ratio was also high. Quartz solubility changes suggest that ~1000 ppm quartz would be precipitated during cooling, so this would require ~1000:1 water mass to vein quartz mass precipitated (Fournier, 1985). Furthermore, the water is ascending from the magma quickly by hydro-fracturing the wall-rock and therefore quickly depressurizing and cooling along a path that is close to adiabatic. Therefore, it is unlikely that at >350°C there is any meteoric water that mixes with the magmatic fluid (*cf.* Weis *et al.,* 2012)

References

Dilles, J.H., 1987, Petrology of the Yerington batholith, Nevada: Evidence for evolution of porphyry copper ore fluids: Economic Geology, v. 82, p. 1750–1789.

Fournier, R.O., 1985, The behavior of silica in hydrothermal solution: Reviews in Economic Geology, v. 2, p. 45-72.

Reed, M., Rusk, B., and Palandri, J., 2013, The Butte magmatic-hydrothermal system: One fluid yields all alteration and veins: Economic Geology, v. 108, p. 1379–1396.

Weis, P., Driesner, T. & Heinrich, C. A., 2012, Porphyry-copper ore shells form at stable pressure–temperature fronts within dynamic fluid plumes: Science, v. 338, p. 1613–1616.

Table A6. ESTIMATED FORMATION TEMPERATURES BASED ON MEASURED OXYGEN ISOTOPIC COMPOSITION OF QUARTZ AND DIFFERENT FRACTIONATION FACTORS

Quartz type	T(°C) [preferred minimum estimate]	**T (°C) estimates from δ ^{18}O ‰ data**										
		Measured δ ^{18}O ‰ in quartz			**Frac. factor** Matsuhisa *et al.,* 1979 (250 - 500 °C) *	**T (°C)**		**Frac. factor** Zhang *et al.,* 1989 (180 - 550 °C) *	**T (°C)**		**Frac. factor** Hu & Clayton, 2003 (450 - 700 °C) *	**T (°C)**
D vein (Dark-CL quartz)	350	Max.	13.6	Magmatic water δ^{18}O = 8.0 ‰	**5.7**	335	Magmatic water δ^{18}O = 7.5 ‰	**6.1**	340	Magmatic water δ^{18}O = 7.7 ‰	**5.9**	305
		Avg.	**12.7**		**4.8**	**370**		**5.3**	**370**		**5.0**	**345**
		Min.	11.8		**3.8**	410		**4.4**	410		**4.1**	395
D vein (Dark gray-CL quartz)	450	Max.	11.7		**3.7**	415		**4.2**	420		**4.0**	405
		Avg.	**11.1**		**3.1**	**450**		**3.6**	**450**		**3.3**	**450**
		Min.	10.5		**2.5**	485		**3.0**	485		**2.7**	505
Requilibrated EDM	500	Max.	11.2		**3.2**	445		**3.6**	450		**3.5**	440
		Avg.	**10.7**		**2.7**	**475**		**3.1**	**480**		**3.0**	**480**
		Min.	10.2		**2.2**	505		**2.6**	515		**2.5**	530
Requilibrated B vein	550	Max.	11.1		**3.1**	450		**3.6**	450		**3.4**	445
		Avg.	**10.7**		**2.7**	**475**		**3.1**	**480**		**3.0**	**480**
		Min.	10.3		**2.3**	500		**2.6**	515		**2.6**	520

Note: T (°C) [preferred minimum estimate] taken from Table A5. * Experimental range for each fractionation calibration. Min. = Minimum, Avg. = Average, Max. = Maximum. Minimum and maximum represent the range of the average ± 2 standard deviations. Different magmatic water compositions are assumed in order to fix the calculated temperature of the dark gray-CL quartz at 450 °C and the dark-CL quartz at ~345 to 370 °C using different fractionation factors. The dark-CL and dark gray-CL temperatures are reproduced well in all the calculations. EDM and B vein quartz show almost identical oxygen isotope compositions that always yield equal and lower than expected temperatures. For the discussion we assume a magmatic water composition of δ18O = 7.5 ‰ (Taylor, 1968) and fractionation factors from Zhang et al., 1989 since the experimental temperature range overlaps with the porphyry hydrothermal temperature range. However, the temperature estimates using the other fractionation factors show minimal variation.

References

Hu, G., & Clayton, R. N., 2003, Oxygen isotope salt effects at high pressure and high temperature and the calibration of oxygen isotope geothermometers. A Special Issue Dedicated to Robert Clayton, 67(17), 3227–3246.

Taylor H.P., Jr., 1968, The oxygen isotope geochemistry of igneous rocks. Contributions to Mineral Petrology, v.19, p. 185-219.

Matsuhisa, Y., Goldsmith, J.R., and Clayton, R.N., 1979, Oxygen isotopic fractionation in the system quartz-albite-anorthite-water: Geochimica et Cosmochimica Acta, v. 43, no. 7, p. 1131–1140.

Zhang L.-G., Liu J.-X., Zhou H.B. and Chen Z.-S., 1989, Oxygen isotope fractionnation in the quartz-water-salt system. Economic Geology, 89, p. 1643-1650.

Table A7. Diffusion timescales

T(°C)	Stage	Diffusion		D (m^2/s)	**Timescale** (years)		
					Min.	**Calc.**	**Max.**
650	1- Ppy, Ap, DQ, EDM, BMQ	1D	Ti	2.50x10^{-23}	3,500	**35,000**	520,000
550	2- B vein			9.82x10^{-24}	4,000	**50,000**	740,000
450	3- Requilibration EDM/B vein		δ^{18}O	2.14x10^{-21}	3,000	**10,000**	50,000
		3D (20 µm)			300	**1,000**	4,800
		3D (60 µm)			2,500	**10,000**	45,000
350	4- D vein	1D		5.38x10^{-23}	17,000	**75,000**	350,000

Note: Ppy = porphyry, Ap = aplite, DQ = deep quartz veins, EDM = early dark micaceous halos, BMQ = banded molybdenite quartz veins. Calc. = Calculated, Min. = Minimum, Max. = Maximum. Min. and Max. estimated by varying the diffusion temperature by 10 %. 1D = one dimensional diffusion. 3D=spherical diffusion, sphere radius in microns reflects the spacing of fractures in quartz.

4) δ^{18}O DATA

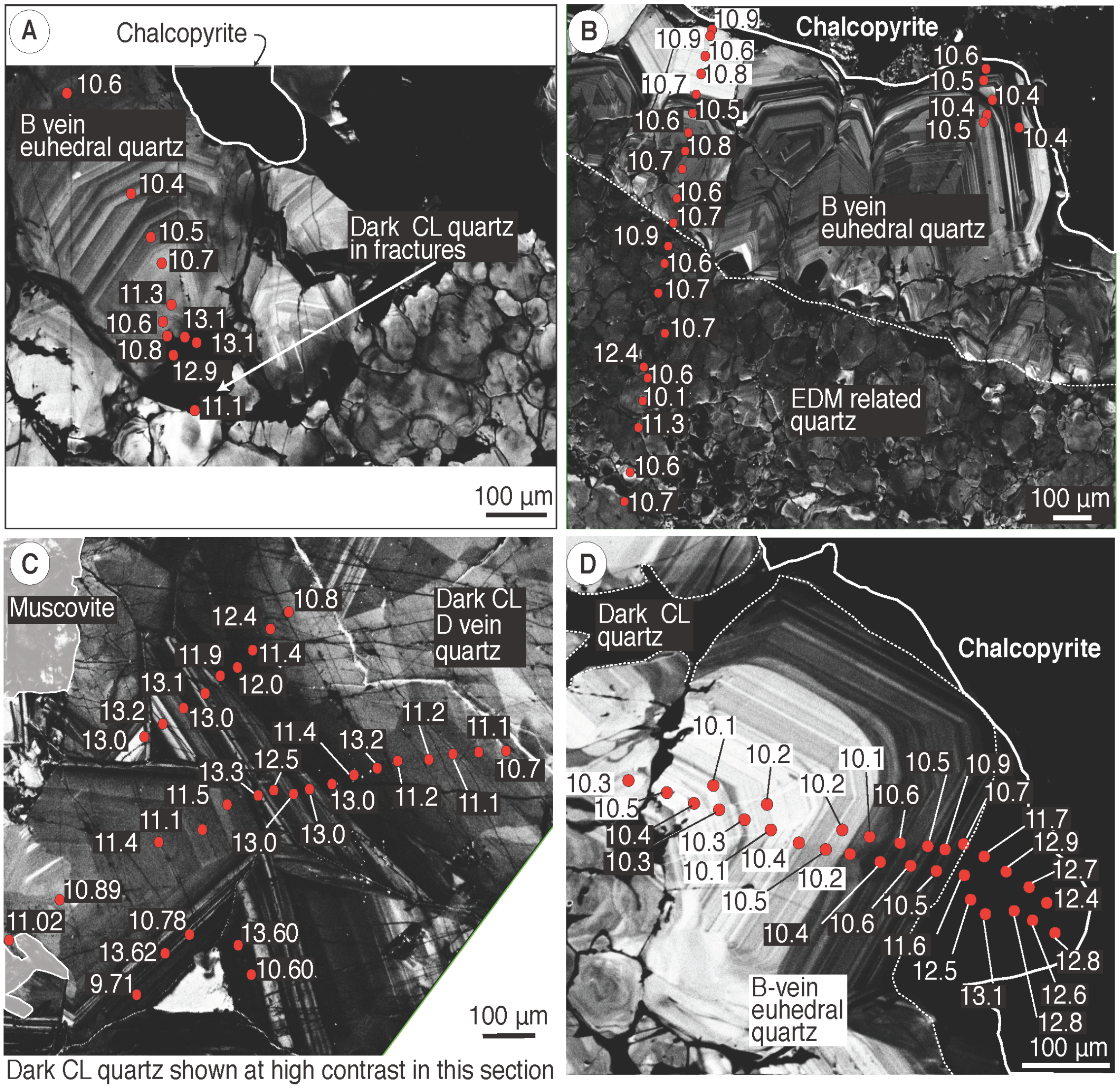

Figure A1. δ^{18}O on SEM-CL images. **A)** B vein with chalcopyrite and late dark-CL quartz in fractures in sample FC-HAQ-004. **B)** Mosaic textured EDM related quartz and euhedral B vein quartz in contact with chalcopyrite in sample FC-HAQ-027. **C)** Euhedral quartz in D vein sample FC-HAQ-009 with gray-dark-CL quartz and dark-CL quartz in contact with muscovite and pyrite. **D)** Euhderal quartz in B vein sample FC-HAQ-048, rimed by dark-CL quartz in contact with chalcopyrite.

5) DIFFUSION CALCULATIONS

Isothermal diffusion expression:

One-dimensional

$$C = C_o \operatorname{erfc}\left(\frac{X}{2\sqrt{Dt}}\right)$$

C_o is the composition of mineral A
C is the composition at distance X in mineral B
D is the diffusion constant
t is time
erfc = 1-erf (error function)

See Valley (2001) for additional information

Spherical

$$\frac{C - C_1}{C_0 - C_1} = 1 + \frac{2a}{\Pi r} \sum_{n=1}^{\infty} \frac{(-1)^n}{n} \sin \frac{n\Pi r}{a} \exp(-Dn^2\Pi^2 t/a^2)$$

C_o is the composition at the surface of the sphere
C_1 is the initial composition of the sphere
C is the composition at distance a
r is the radius of the sphere
D is the diffusion constant
t is time

See Crank (1975) for additional information

Titanium (perpendicular to c-axis)

$D_{Ti} = 7 \times 10^{-8} \exp(-273 \pm 12 \text{kJ mol}^{-1}/RT) \text{m}^2 \text{sec}^{-1}$ (Cherniak *et al.*, 2007)

Experimental temperature range: 700 to 1150ºC

Oxygen (perpendicular to c-axis)

$D_{oxygen} = 2.09 \times 10^{-11} \exp(-138.54 \pm 19.1 \text{kJ mol}^{-1}/RT) \text{m}^2 \text{sec}^{-1}$ (Dennis, 1984)

Experimental temperature range: 515 to 850ºC

---

6) Ti in quartz transects

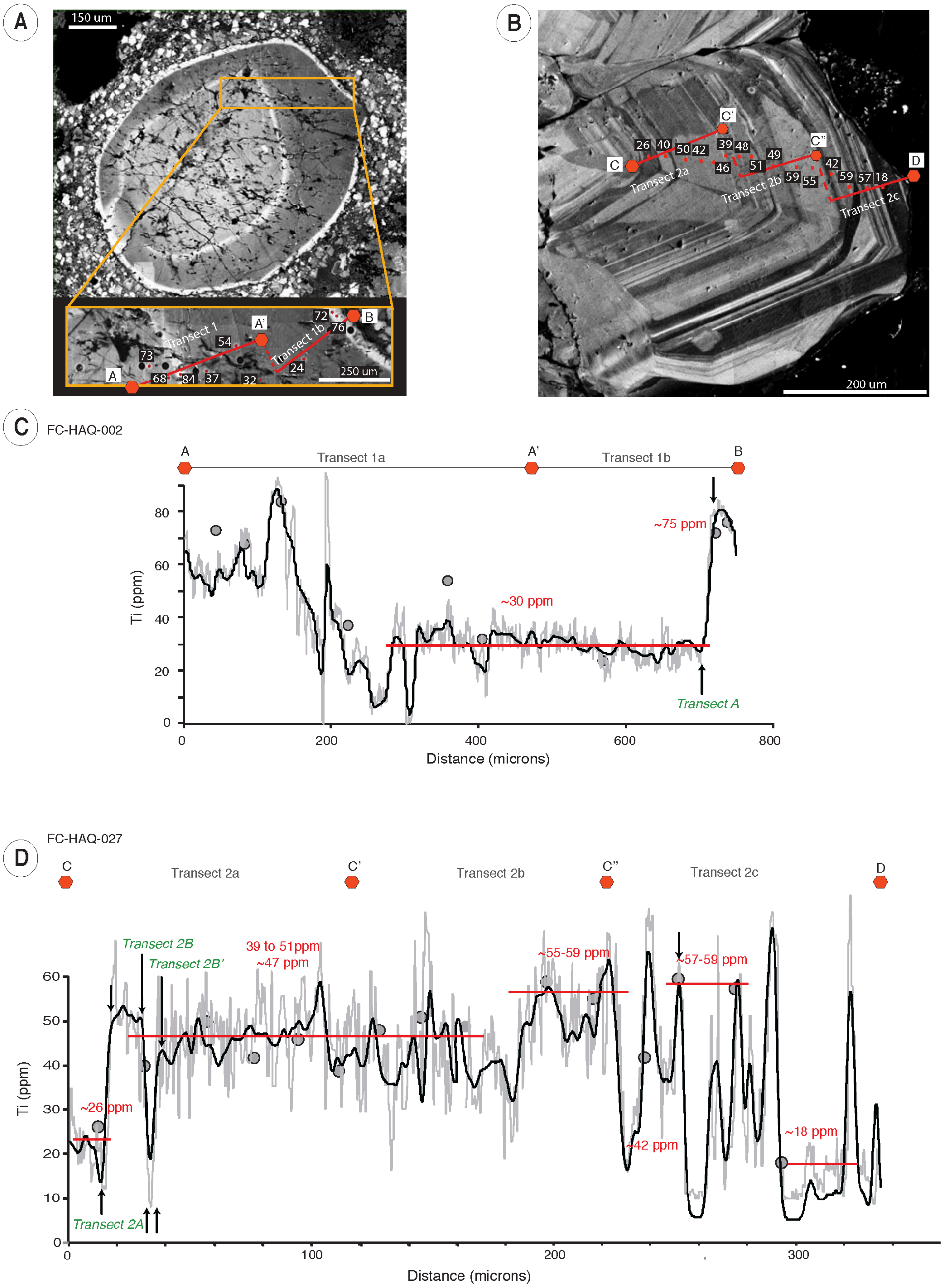

Figure A3. Ti (ppm) in quartz spot analyses by EMP (gray circles) and SEM-CL grayscale images for A) FC-HAQ-002 and **B)** FC-HAQ-027. SEM-CL grayscale raw values (gray line) and smoothed grayscale (blak lines) for **C)** FC-HAQ-002 and **D)** FC-HAQ-027 are shown for transects perpendicular to growth zones and used used for diffusion profile modelling along marked transects A, 2A and 2B.

7) Ti in quartz diffusion profiles

FC-HAQ-002 Ti profile 1

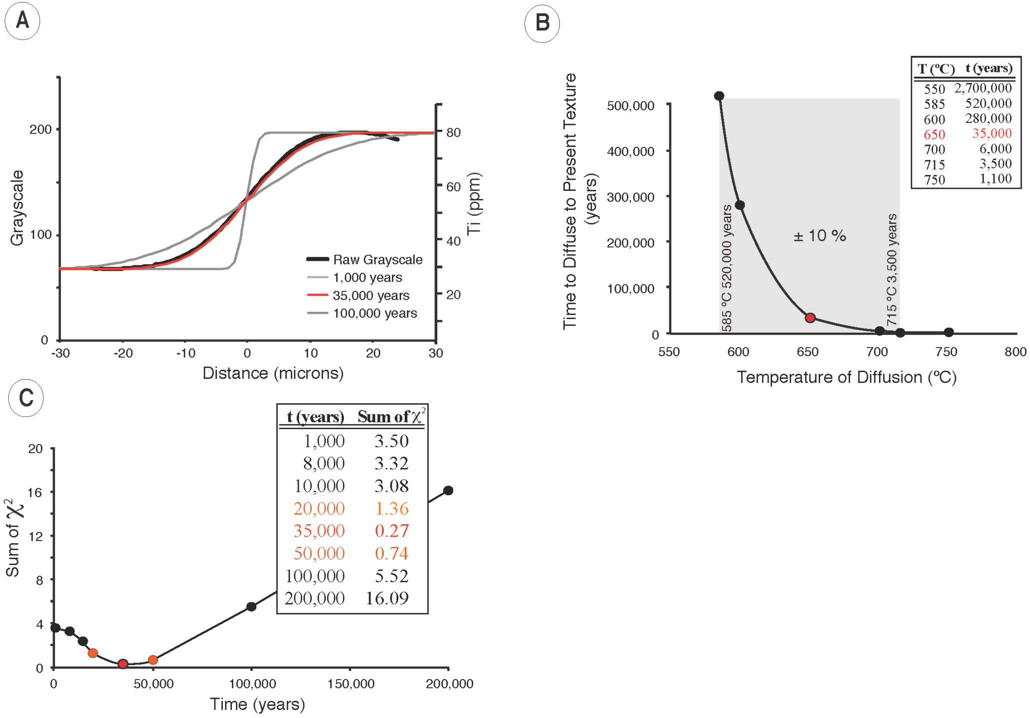

T (°C)	t (years)
550	2,700,000
585	520,000
600	280,000
650	35,000
700	6,000
715	3,500
750	1,100

t (years)	Sum of χ^2
1,000	3.50
8,000	3.32
10,000	3.08
20,000	1.36
35,000	0.27
50,000	0.74
100,000	5.52
200,000	16.09

Figure A4. Ti in quartz diffusion models for sample FC-HAQ-002. A, C, E) Using calculated diffusivities. B, D, F) Using extrapolated diffusivities. C, D) Modeled diffusion timescales versus temperature of diffusion used in the model at a fixed Sum of $\chi 2$ .The grey box shows the range of diffusion timescales by varying the preferred quartz crystalization temperature by a 10 %. E, F) Sum of $\chi 2$ versus time. The red circles show the preferred timescale based on the best fit of the model to the data as represented by the Sum of $\chi 2$. The orange circles show the range of timescales that produce a reasonable fit of the model to the data as represented by a Sum of $\chi 2$ smaller than 2..

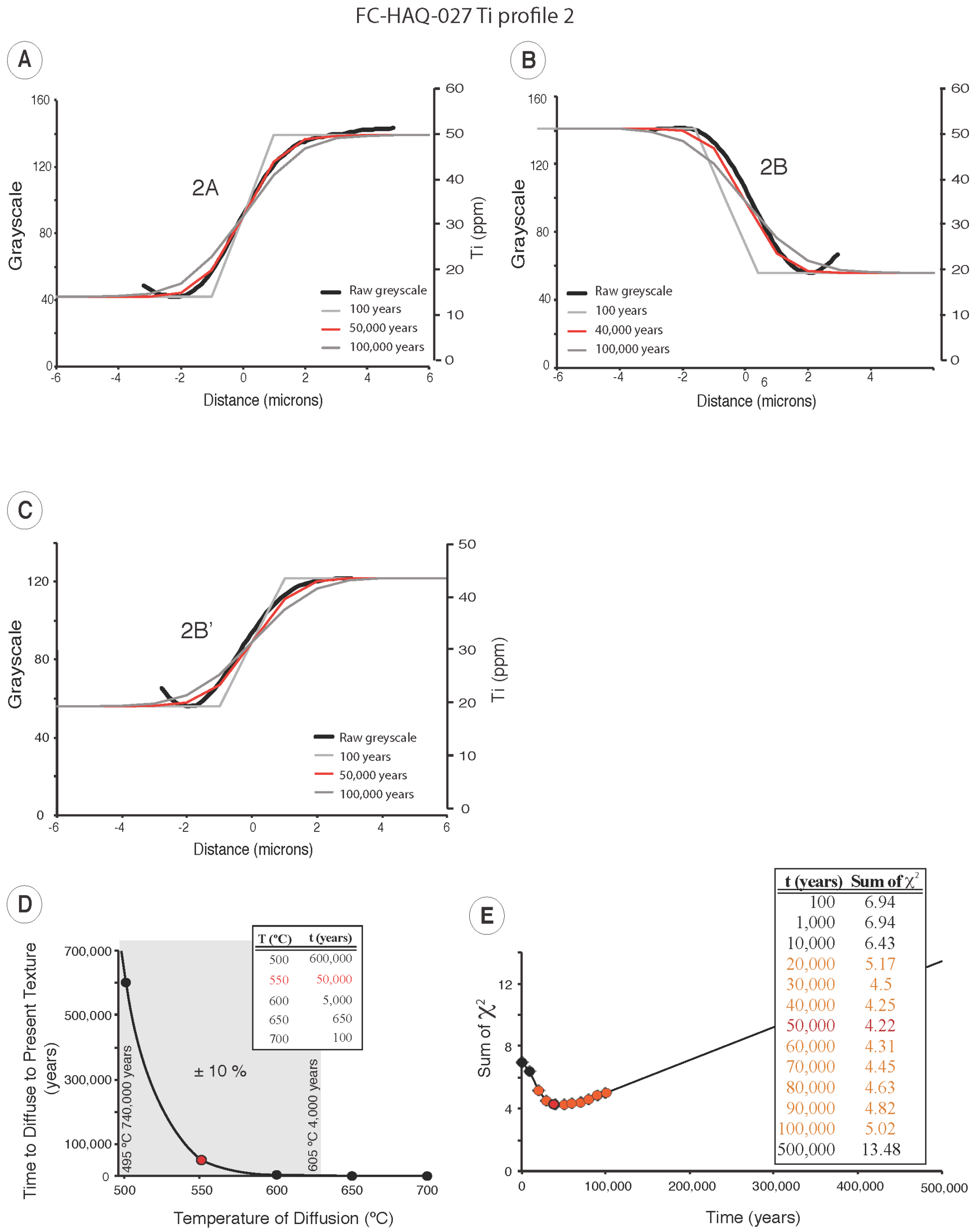

FC-HAQ-027 Ti profile 2

T (ºC)	t (years)
500	600,000
550	50,000
600	5,000
650	650
700	100

t (years)	Sum of χ^2
100	6.94
1,000	6.94
10,000	6.43
20,000	5.17
30,000	4.5
40,000	4.25
50,000	4.22
60,000	4.31
70,000	4.45
80,000	4.63
90,000	4.82
100,000	5.02
500,000	13.48

Figure A5. Part 1: A, B, C) Ti in quartz diffusion models for sample FC-HAQ-027. D) Modeled diffusion timescales versus temperature of diffusion used in the model at a fixed Sum of $\chi 2$ for profile B' .The grey box shows the range of diffusion timescales by varying the preferred quartz crystalization temperature by a 10 %. E,) Sum of $\chi 2$ versus time for profile B'. The red circles show the preferred timescale based on the best fit of the model to the data as represented by the Sum of $\chi 2$. The orange circles show the range of timescales that produce a reasonable fit of the model to the data as represented by a Sum of $\chi 2$ smaller than 2.

8) δ^{18}O in quartz diffusion profiles

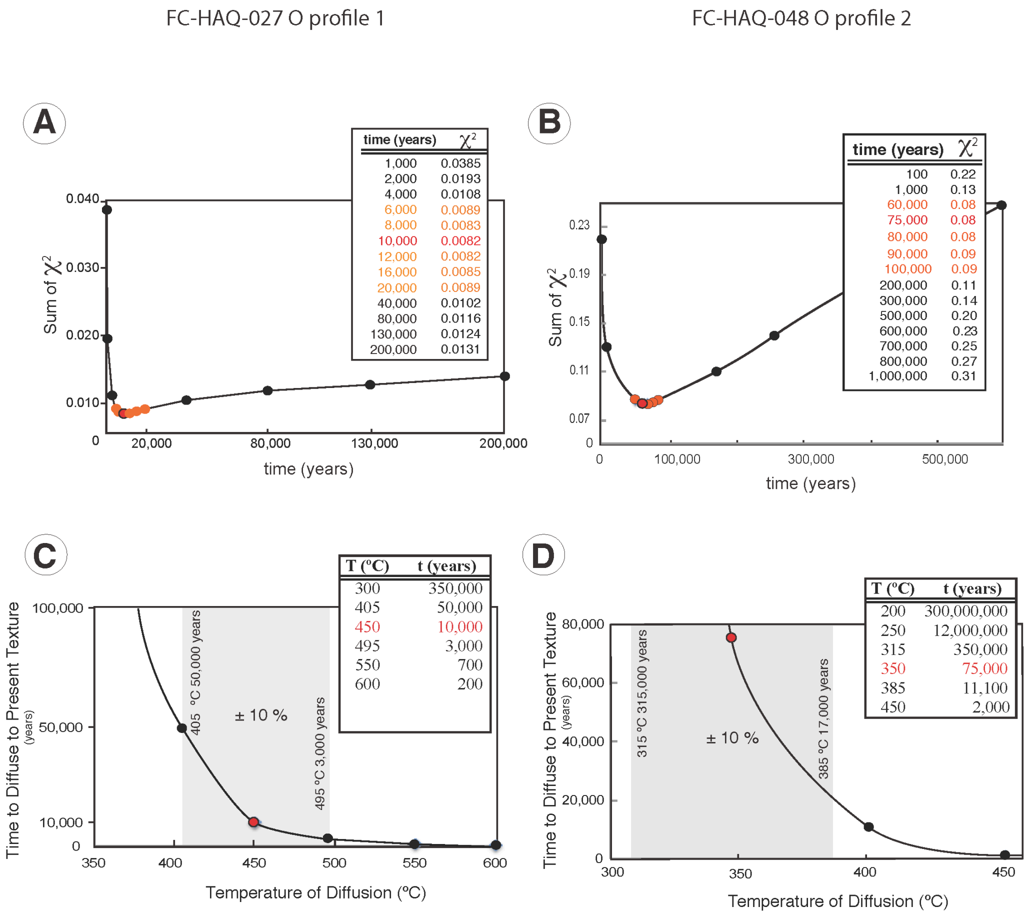

A)

time (years)	χ^2
1,000	0.0385
2,000	0.0193
4,000	0.0108
6,000	0.0089
8,000	0.0083
10,000	0.0082
12,000	0.0082
16,000	0.0085
20,000	0.0089
40,000	0.0102
80,000	0.0116
130,000	0.0124
200,000	0.0131

B)

time (years)	χ^2
100	0.22
1,000	0.13
60,000	0.08
75,000	0.08
80,000	0.08
90,000	0.09
100,000	0.09
200,000	0.11
300,000	0.14
500,000	0.20
600,000	0.23
700,000	0.25
800,000	0.27
1,000,000	0.31

C)

T (°C)	t (years)
300	350,000
405	50,000
450	10,000
495	3,000
550	700
600	200

D)

T (°C)	t (years)
200	300,000,000
250	12,000,000
315	350,000
350	75,000
385	11,100
450	2,000

Figure A6. δ^{18}O in quartz diffusion models. A, C) samples FC-HAQ-027 and B, D) FC-HAQ-048s. A, B) Sum of χ2 versus time. The red circles show the preferred timescale based on the best fit of the model to the data as represented by the Sum of χ2 . The orange circles show the range of timescales that produce a reasonable fit of the model to the data as represented by a Sum of χ2. C, D) Modeled diffusion timescales versus temperature of diffusion used in the model at a fixed Sum of χ2.The grey box shows the range of diffusion timescales by varying the preferred quartz crystalization temperature by a 10 %.

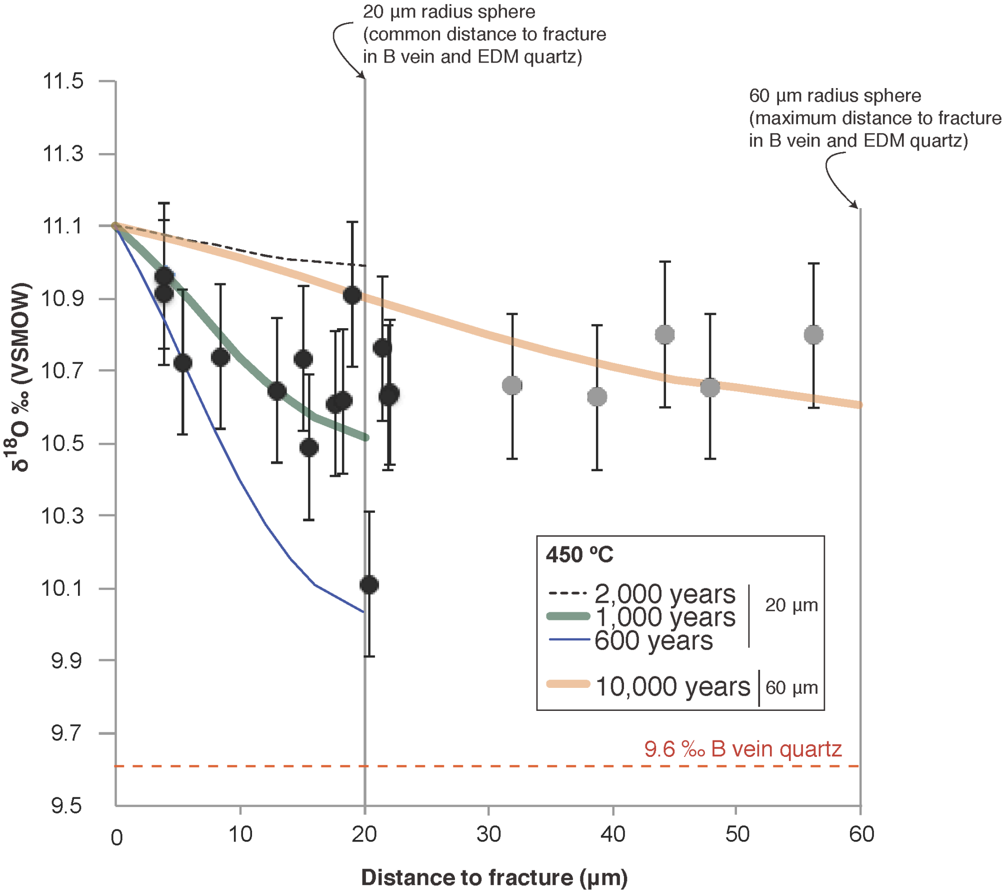

Figure A7. Spherical diffusion models for partial re-equilibration of B vein and EDM quartz at 450 °C. Partial re-equilibration can be achieved in ~ 1,000 years at a common distances to fracture of a maximum of 20 um (SIMS analyses plotted in black). Distance to fracture from 20 um to 60 um (SIMS analyses plotted in gray) are considered to be overestimated, and that closer fractures are present in other directions than the observed surface. A partial re-equilibration of the quartz to the maximum distance to fracture (~60 um) requires ~ 10,000 years.